DE GRUYTER OPEN

Acta Geophysica
vol. 64, no. 4, Aug. 2016, pp. 841-852
DOI: 10.1515/acgeo-2016-0031

# On the Motivation and Foundation of Natural Time Analysis: Useful Remarks

Panayiotis A. VAROTSOS, Nicholas V. SARLIS, and Efthimios S. SKORDAS

Section of Solid State Physics and Solid Earth Physics Institute, Department of Physics, School of Science, National and Kapodistrian University of Athens, Athens, Greece; e-mail: pvaro@otenet.gr

A b s t r a c t

Since its introduction in 2001, natural time analysis has been applied to diverse fields with remarkable results. Its validity has not been doubted by any publication to date. Here, we indicate that frequently asked questions on the motivation and the foundation of natural time analysis are directly answered if one takes into account the following two key points that we have considered as widely accepted when natural time analysis was proposed: first, the aspects on the energy of a system forwarded by Max Planck in his *Treatise on Thermodynamics*; second, the theorem on the characteristic functions of probability distributions which Gauss called *Ein Schönes Theorem der Wahrscheinlichkeitsrechnung* (beautiful theorem of probability calculus). The case of the time series of earthquakes and of the precursory Seismic Electric Signals are discussed as typical examples.

**Key words:** natural time analysis, complex systems, energy, dichotomous signals.

## 1. INTRODUCTION

Since 2001 (Varotsos *et al.* 2001, 2002a, b), it has been proposed that unique dynamic features hidden behind can be revealed from the time series of complex systems, if we analyze them in terms of a new time domain termed

Ownership: Institute of Geophysics, Polish Academy of Sciences;
© 2016 Varotsos *et al.* This is an open access article distributed under the Creative Commons Attribution-NonCommercial-NoDerivs license, http://creativecommons.org/licenses/by-nc-nd/3.0/.

natural time $\chi$. Examples of data analysis in this time domain carried out by a multitude of authors (*e.g.*, Vargas *et al.* 2015, Flores-Márquez *et al.* 2014, Ramírez-Rojas *et al.* 2011, Rundle *et al.* 2012, Holliday *et al.* 2006) have appeared in diverse fields, including Biology, Cardiology, Condensed Matter Physics, Environmental Sciences, Geophysics, Physics of Complex Systems, Statistical Physics, and Seismology. Several of these applications have been compiled in a monograph by Varotsos *et al.* (2011a), where the foundations of natural time analysis have been also explained in detail by providing the necessary mathematical background in each step. It is the objective of this short paper to shed more light on frequently asked questions related to the motivation and the foundation of natural time analysis. For example, although this analysis does not make use of any adjustable parameter, a question raises on why the selection of the normalized energy for each event is preferred in this analysis (see below) compared to other physical quantities. For a time series comprising $N$ events, we define as natural time $\chi_k$ for the occurrence of the $k$-th event the quantity $\chi_k = k/N$. In doing so, we ignore the time intervals between consecutive events, but preserve their order and energy $Q_k$. The analysis in natural time is carried out (Varotsos *et al.* 2001, 2002a, b) by studying the evolution of the pair $(\chi_k, p_k)$, where the quantity

$$p_k = \frac{Q_k}{\sum_{n=1}^{N} Q_n} \tag{1}$$

is the normalized energy for the $k$-th event, and using the normalized power spectrum (*cf.* $\omega$ stands for the angular natural frequency):

$$\Pi(\omega) \equiv \left|\Phi(\omega)\right|^2 \tag{2}$$

defined by

$$\Phi(\omega) = \sum_{k=1}^{N} p_k \exp\left(i\omega\chi_k\right) \tag{3}$$

$\Phi(\omega)$ is (Varotsos *et al.* 2011a) the characteristic function of $p_k$ for all $\omega \in R$ since $p_k$ can be regarded as a probability for the occurrence of the $k$-th event at $\chi_k$. This is obvious for dichotomous signals as it is frequently the case of Seismic Electric Signals (SES) activities (but holds for other signals as well (Varotsos *et al.* 2001, 2002a, b; 2009, 2011a); see also Section 3), because $Q_k$ is then proportional to the duration of the $k$-th event and $\sum_{n=1}^{N} Q_n$ to the total duration of $N$ events recorded, thus the ratio $Q_k \Big/ \sum_{n=1}^{N} Q_n \left(= p_k\right)$ gives the

probability to observe the $k$-th event among the other events (see Fig. 1) at the natural time $\chi_k = k/N$.

In natural time analysis, the behavior of $\Pi(\omega)$ is studied at $\omega \to 0$, because all the moments of the distribution of $p_k$ can be estimated from the derivatives $d^m\Phi(\omega)/d\omega^m$ (for $m$ positive integer) of the characteristic function $\Phi(\omega)$ at $\omega \to 0$ (see page 512 of Feller (1971)). For this purpose, a quantity $\kappa_1$ was defined (Varotsos *et al.* 2001, 2002a) from the Taylor expansion (see also the Appendix):

$$\Pi(\omega) = 1 - \kappa_1\omega^2 + \kappa_2\omega^4 + \ldots \tag{4}$$

where

$$\kappa_1 = \left\langle \chi^2 \right\rangle - \left\langle \chi \right\rangle^2 = \sum_{k=1}^{N} p_k \chi_k^2 - \left( \sum_{k=1}^{N} p_k \chi_k \right)^2 . \tag{5}$$

It has been shown (Varotsos *et al.* 2011a, b) that $\kappa_1$ becomes equal to 0.070 at the critical state for a variety of dynamical systems. Once $N$ consecutive events have been observed, the $k$-th event that occurred at natural time $\chi_k = k/N$ $(k \le N)$ will be hereafter called, for the sake of convenience, "$k/N$

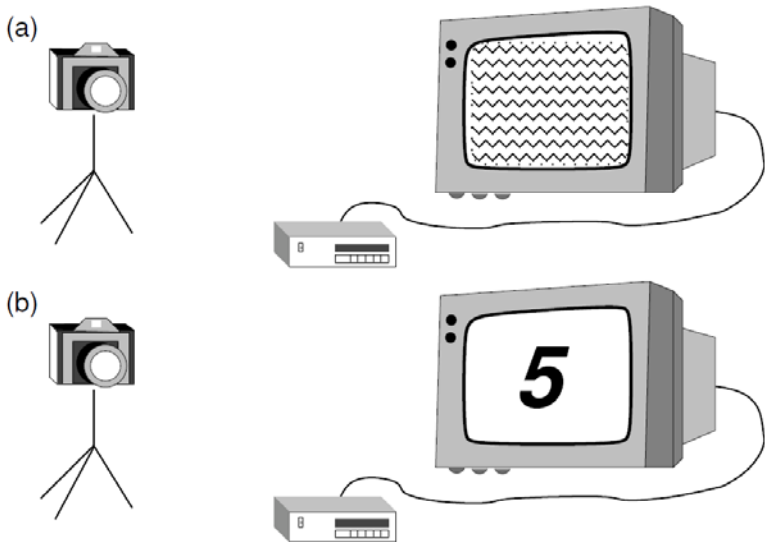


Fig. 1. Assume that $N$ events have been recorded: The observer reports the occurrence of each consecutive event as long as it lasts, *e.g.*, the fifth one (b), but marks nothing during periods of absence of events (a). The reading is replayed and a camera takes a snapshot. Upon discarding the "empty" snapshots, the probability to observe, for example the fifth event, is $Q_5 \Big/ \sum_{n=1}^{N} Q_n$ .

event". Note that upon the occurrence of an additional event, the value of $\chi_k$ changes from $k/N$ to $k/(N+1)$ together with the change of $p_k$ from $Q_k \Big/ \sum_{n=1}^{N} Q_n$ to $Q_k \Big/ \sum_{n=1}^{N+1} Q_n$, thus leading to changes of $\Pi(\omega)$ and $\kappa_1$ as well. Such changes are important, for example, when analyzing in natural time the small earthquakes that occur after the initiation of an SES activity in the candidate epicentral area in order to estimate the occurrence time of the forthcoming mainshock (*e.g.*, Varotsos *et al.* 2008; see also Huang 2015). Hence, when dealing with the possible outcomes of a yet-to-be-performed experiment (as well as when studying the behavior of an evolving dynamical system), where the total number of events that will be recorded is not known in advance, the $\chi_k$ values that are always discrete rational numbers in (0,1] vary until the occurrence of the last event.

Using $p(\chi) = \sum_{k=1}^{N} p_k \delta\left(\chi - \frac{k}{N}\right)$, which is the distribution corresponding to $p_k$, the normalized power spectrum $\Pi(\omega)$ of Eq. 2 can be rewritten in terms of $p(\chi)$ as (Varotsos *et al.* 2011b)

$$\Pi(\omega) = \int_0^1 \int_0^1 p(\chi) p(\chi') \cos\left[\omega(\chi - \chi')\right] d\chi d\chi' \tag{6}$$

and its Taylor expansion around $\omega \to 0$ leads to the value

$$\kappa_1 = \frac{1}{2} \int_0^1 \int_0^1 p(\chi) p(\chi') (\chi - \chi')^2 d\chi d\chi' \ . \tag{7}$$

Alternative expressions for $\Pi(\omega)$ and $\kappa_1$ are given in the Appendix.

## 2. RANDOM VARIABLE. CHARACTERISTIC FUNCTION. BACKGROUND

### 2.1 Random variable

Since 1933, Kolmogorov has first made it clear that a random variable is nothing but a measurable function on a probability space. Let (Ω, A, P) be a probability space, where Ω stands for the sample space (the set of world states, sometimes called outcomes), A the event space (the set of subsets of Ω), and P the probability measure. A single-valued real-valued function $X = X(\omega)$ defined on $\Omega$ ($\omega \in \Omega$) is called a random variable if for any real $x$ the set $\{\omega: X(\omega) < x\}$ belongs to the class A (*e.g.*, see Random variable. Encyclopedia of Mathematics, available from: http://www.encyclopediaofmath.org/index.php?title=Random_variable&oldid=29510; access 2 February 2015). In simple words, a random variable $X$ is a function that associates a unique

numerical value with every outcome of an experiment (*e.g.*, see Statistics Glossary v. 1.1 (STEPS), available from: http://www.stats.gla.ac.uk/steps/glossary/probability_distributions.html#probdistn; access 2 February 2015), or more simply (*e.g.*, see Summary of Chapter 8 in Finite Mathematics and Finite Mathematics and Applied Calculus, available from: http://www.zweigmedia.com/ThirdEdSite/Summary7.html; access 2 February 2015) it is just a rule that assigns a numerical value to each outcome in the sample space of an experiment. Also a random variable is sometimes described as a variable whose value is subject to variations due to chance, *i.e.*, randomness in a mathematical sense, *e.g.*, see page 391 of Yates *et al*. (2002) (but see also page 500 of Jaynes (2003), where the following is written: "However, although the property of being «random» is considered a real objective attribute of a variable, orthodoxy has never produced any definition of the term «random variable» that could actually be used in practice to decide whether some specific quantity, such as the number of beans in a can, is or is not «random». Therefore, although the question «which quantities are random?» is crucial to everything an orthodox statistician does, we are unable to explain how he actually decides this; we can only observe what decisions he makes."). A random variable differs essentially from other mathematical variables since it conceptually does not have a single, fixed value (even if unknown), but it can take on a set of possible different values each with an associated probability (if discrete) or a probability density function (if continuous).

A random variable's possible values might represent the possible outcomes of either a past experiment whose already existing value is uncertain (*e.g.*, as a result of incomplete information or imprecise measurements), or a yet-to-be-performed experiment. A typical example is the case of the analysis of a series of seismic events, which for instance should be carried out for the time series of small earthquakes occurring in the candidate area after the SES initiation in order to estimate the occurrence time of an impending mainshock, as mentioned earlier. In this example, the values of $k/N$ depend of course on the magnitude threshold adopted. In addition, for each threshold selected, the values of $k/N$ are subject to variations due to experimental error in the determination of the magnitude, which may result in the observation or not of the smaller events, especially the ones in the vicinity of the threshold in a way explained in Varotsos *et al.* (1996). In other words, due to the experimental error, events slightly exceeding the threshold selected may not be reported in the measurement while others slightly smaller than the threshold may be reported, thus affecting the $k/N$ values. Also, we clarify that random variable's values may conceptually represent either the results of an "objectively" random process (*e.g.*, rolling a die) or the "subjective" randomness that results from incomplete knowledge of a measurable quantity.

The latter is the case of the aforementioned example of analyzing a series of seismic events in which, as mentioned, an experimental error in the magnitude determination may affect the values of $k/N$.

### 2.2 Characteristic function

Let $X$ be a random variable. The characteristic function of a continuous distribution with cumulative distribution function $F(x)$ is defined as

$$\left(\omega \in R\right): \Phi(\omega) = E\left[e^{i\omega X}\right] = \int_{-\infty}^{\infty} e^{i\omega x} dF(x) \tag{8}$$

which is a complex-valued function. $E$ stands for the expectation value. For a discrete distribution on the non-negative integers $j$, it is defined as

$$\Phi(\omega) = E\left[e^{i\omega X}\right] = \sum_{j=0}^{\infty} e^{i\omega j} \Pr\left[X = j\right] \tag{9}$$

where $\Pr[X = j]$, or simply $p_j$ (if we follow the symbol used in Eq. 1 in Section 1), denotes for the random variable $X$ its associated probability at the non-negative integer value $X = j$.

The characteristic function uniquely determines the probability density function of a continuous distribution (see page 509 of Feller (1971) and page 48 of Johnson *et al.* (1992)); we have

$$f(x) = \frac{1}{2\pi} \int_{-\infty}^{\infty} e^{-i\omega x} \Phi(\omega) d\omega \ . \tag{10}$$

Gauss called this theorem *Ein Schönes Theorem der Wahrscheinlichkeitsrechnung* (beautiful theorem of probability calculus). The corresponding inversion formula for discrete distributions on the non-negative integers is

$$\Pr\left[X = x\right] = \frac{1}{2\pi} \int_{-\pi}^{\pi} e^{-i\omega x} \Phi(\omega) d\omega \ . \tag{11}$$

## 3. CHARACTERISTIC FUNCTION AND NATURAL TIME ANALYSIS

In accordance to Eq. 9, the function $\Phi(\omega)$ in Eq. 3 introduced in natural time analysis (Varotsos *et al.* 2001, 2002a, b), *i.e.*,

$$\Phi(\omega) = \sum_{k=1}^{N} p_k \exp\left(i\omega \frac{k}{N}\right) \tag{12}$$

constitutes the characteristic function of the random variable $(X =) k/N$. This is so, because $p_k$ − as given by Eq. 1 − can be regarded (Varotsos *et al.* 2001, 2002a, b) as the probability associated with $X = k/N$ (moreover, $\Phi(\omega)$ of Eq. 12 is positive definite for all $\omega \in R$, $\Phi(0) = 1$ and the map $\omega \rightarrow \Phi(\omega)$

is continuous at the origin, thus satisfying the conditions of the theorem 1.1.12 in page 17 of Applebaum (2013) to be characteristic function of a probability distribution). In other words, $p_k$ is the probability for observing the $k/N$ event. The latter becomes clear if we focus on the question "What is energy?" by considering the authoritative aspects of Max Planck to which we now turn. These aspects also show an insight into the use of the quantity of energy when natural time analysis was proposed (Varotsos *et al.* 2001, 2002a, b).

### 3.1 What is energy?

Recent relevant books (*e.g.*, see Coopersmith 2010) note that "most physicists are unable to provide a satisfactory answer to this question" (see also Crystal 2011).

Max Planck, in §58 of his *Treatise on Thermodynamics* (see page 41 in Planck (1945)) states:

"The energy of a body, or system of bodies, is a magnitude depending on the momentary condition of the system. In order to arrive at a definite numerical expression for the energy of a system in a given state, it is necessary to fix upon a certain normal arbitrarily selected state (*e.g.*, 0°C and atmospheric pressure). The energy of the system in a given state, referred to the arbitrarily selected state, is then equal to the algebraic sum of the mechanical equivalents of all the effects produced outside the system when it passes in any way from the given to the normal state. The energy of a system is, therefore, sometimes briefly denoted as the faculty to produce external effects".

This definition suggests the following answer to the aforementioned question on "what is energy", *e.g.*, for a recent reference see Bauer (2011): "The energy of the system is a measure of its presence in the universe".

We now proceed to the change of energy, $U_1 - U_2$, accompanying the transition of the system from a state 1 to a state 2 (which may probably happen when observing an event). Max Planck in §63 of his *Treatise on Thermodynamics* (see pages 44-45 in Planck (1945)) states:

"The energy, as stated, depends on the momentary condition of the system. To find the change of energy, $U_1 - U_2$, accompanying the transition of the system from a state 1 to a state 2, we should, according to the definition of the energy in §58 (this is the definition mentioned above), have to measure $U_1$ as well as $U_2$ by the mechanical equivalent of the external effects produced in passing from the given states to the normal state. But, supposing we so arrange matters that the system passes from state 1, through state 2, into the normal state, it is evident then that $U_1 - U_2$ is simply the mechanical equivalent of the external effects produced in passing from 1 to 2. The decrease of the energy of a system subjected to any change is, then, the me-

chanical equivalent of the external effects resulting from that change; or, in other words, the increase of the energy of a system which undergoes any change, is equal to the mechanical equivalent of the heat absorbed and the work expended in producing the change:

$$U_1 - U_2 = Q + W \tag{13}$$

$Q$ is the mechanical equivalent of the heat absorbed by the system, *e.g.*, by conduction, and $W$ is the amount of work expended on the system. …" and in §64 of his *Treatise on Thermodynamics* Max Planck clarifies:

"The difference $U_1 - U_2$ may also be regarded as the energy of the system in state 2, referred to state 1 as the normal state …"

Hence, the aforementioned answer to the question on "what is energy?" also holds for the difference $U_1 - U_2$.

### 3.2 Why it is logical to consider $p_k$ as a probability for the observation of the $k/N$ event

In the light of the above authoritative aspects of Max Planck summarized by Bauer (2011), and assuming that $N$ events have been observed, we think along the following lines: since $Q_k$ stands for the energy of the $k$-th event and $\sum_{n=1}^{N} Q_n$ for the total energy of $N$ events, their ratio $Q_k \Big/ \sum_{n=1}^{N} Q_n \left(= p_k\right)$ can be considered as a probability for the occurrence (observation) of the $k/N$ event. (The quantities $p_k$ are, of course, probabilities according to Kolmogorov (1950), since $\sum_{k=1}^{N} p_k = 1$.) This, however, should not be considered as being illogical with the following claim: "this is illogical since one never has the situation that the $k/N$ event occurred with probability 20% and did not occur with probability 80%, for example". This should be understood in the context that 80% refers to the sum of the probabilities of all the other $N-1$ events to occur.

## 4. CONCLUSIONS

The analysis in natural time $\chi$ is based on the study of the evolution of the pair $(\chi_k, p_k)$. On the basis of the authoritative aspects forwarded by Max Planck concerning the energy of a system, it becomes evident that $p_k$ can be considered as the probability for observing the event at $\chi_k = k/N$. By means of $\chi_k$ and $p_k$ that are experimentally accessible, the characteristic function $\Phi(\omega)$ is obtained. This function, upon recalling the theorem which Gauss called "beautiful theorem of probability calculus", uniquely determines the probability distribution of $p_k$. Thus, in short, the transparency of the analysis

in natural time cannot be doubted, in any terms, since it is based on celebrated aspects in Physics and in Probability Calculus, and in addition it does not make use of any adjustable parameter.

# Appendix

## Alternative expressions for $\Pi(\omega)$ and $\kappa_1$

We first give a general expression for $\Pi(\omega)$ valid for any value of $\omega$:
By writing $\Phi(\omega) = \sum_{k=1}^{N} p_k e^{i\omega\chi_k}$ and $\Phi^*(\omega) = \sum_{m=1}^{N} p_m e^{-i\omega\chi_m}$ we have:

$$\Pi(\omega) = \Phi(\omega)\Phi^*(\omega) = \sum_{k,m=1}^{N} p_k p_m e^{i\omega(\chi_k - \chi_m)} = \sum_{k=1}^{N} p_k^2 + \sum_{k=1}^{N-1}\sum_{i=1}^{N-k} p_k p_{k+i} \underbrace{\left(e^{i\omega\chi_i} + e^{-i\omega\chi_i}\right)}_{2\cos(\omega\chi_i)} \quad , \text{(A1)}$$

where we used the fact that

$$\chi_{k+i} - \chi_k = \chi_i \tag{A2}$$

because $\chi_l = l/N$.

Since

$$\sum_{k=1}^{N} p_k = 1 \Rightarrow \left(\sum_{k=1}^{N} p_k\right)^2 = 1 \Rightarrow \sum_{k=1}^{N} p_k^2 + 2\sum_{k=1}^{N-1}\sum_{i=1}^{N-k} p_k p_{k+i} = 1 \ ,$$

we have

$$\Pi(\omega) = 1 - 2\sum_{k=1}^{N-1}\sum_{i=1}^{N-k} p_k p_{k+i} + 2\sum_{k=1}^{N-1}\sum_{i=1}^{N-k} p_k p_{k+i}\cos\left(\omega\chi_i\right) . \tag{A3}$$

Thus,

$$\Pi(\omega) = 1 - 2\sum_{k=1}^{N-1}\sum_{i=1}^{N-k} p_k p_{k+i}\left[1 - \cos\left(\omega\chi_i\right)\right] = 1 - 4\sum_{k=1}^{N-1}\sum_{i=1}^{N-k} p_k p_{k+i}\sin^2\left(\frac{\omega\chi_i}{2}\right) \tag{A4}$$

valid for any value of $\omega$.

When $\omega \to 0$ (and since $\max[\chi_i] = 1$), we have $\sin(\omega\chi_i/2) \approx \omega\chi_i/2$ and hence Eq. A4 simplifies to:

$$\Pi(\omega) \approx 1 - \omega^2 \sum_{k=1}^{N-1}\sum_{i=1}^{N-k} p_k p_{k+i}\chi_i^2 \ . \tag{A5}$$

By comparing with Eq. 4 and using Eq. A2, we find for the $\kappa_1$ value the following expression:

$$\kappa_1 = \sum_{k=1}^{N-1} \sum_{i=1}^{N-k} p_k p_{k+i} \left( \chi_{k+i} - \chi_k \right)^2 \ . \tag{A6}$$

Note that there exists compatibility of the $\kappa_1$ value obtained from Eq. 7 with Eq. A6, which can be shown as follows:

We consider that

$$\sum_{l=1}^{N} \sum_{m=1}^{N} p_l p_m \left( \chi_l - \chi_m \right)^2 = 2 \sum_{k=1}^{N-1} \sum_{i=1}^{N-k} p_k p_{k+i} \left( \chi_{k+i} - \chi_k \right)^2 \ . \tag{A7}$$

In view of Eq. A7, Eq. A6 turns to

$$\begin{aligned} \kappa_1 &= \frac{1}{2} \sum_{l=1}^{N} \sum_{m=1}^{N} p_l p_m \left( \chi_l^2 - 2\chi_l \chi_m + \chi_m^2 \right) = \\ &= \frac{1}{2} \left\{ \sum_{l=1}^{N} p_l \chi_l^2 \underbrace{\sum_{m=1}^{N} p_m}_{1} - 2 \sum_{l=1}^{N} p_l \chi_l \sum_{m=1}^{N} p_m \chi_m + \underbrace{\sum_{l=1}^{N} p_l}_{1} \sum_{m=1}^{N} p_m \chi_m^2 \right\} \\ &= \frac{1}{2} \left\{ \left\langle \chi^2 \right\rangle - 2 \left\langle \chi \right\rangle^2 + \left\langle \chi^2 \right\rangle \right\} = \left\langle \chi^2 \right\rangle - \left\langle \chi \right\rangle^2 \ . \end{aligned} \tag{A8}$$

Hence in general

$$\kappa_1 = \left\langle \chi^2 \right\rangle - \left\langle \chi \right\rangle^2 = \frac{1}{2} \int_0^1 \int_0^1 p(\chi) p(\chi') \left( \chi - \chi' \right)^2 d\chi d\chi' \ , \tag{A9}$$

*i.e.*, Eq. 7, or

$$\kappa_1 = \left\langle \chi^2 \right\rangle - \left\langle \chi \right\rangle^2 = \sum_{k=1}^{N-1} \sum_{i=1}^{N-k} p_k p_{k+i} \left( \chi_{k+i} - \chi_k \right)^2 \ , \tag{A10}$$

*i.e.*, Eq. A6 shown above.

Alternatively, if instead of Eq. A1, we use the following expression for $\Pi(\omega)$:

$$\Pi(\omega) = \sum_{k=1}^{N} p_k^2 + \sum_{l=1}^{N-1} \sum_{i=1}^{N-l} p_i p_{i+l} \underbrace{\left( e^{i\omega\chi_l} + e^{-i\omega\chi_l} \right)}_{2\cos\left(\omega\chi_l\right)} \tag{A11}$$

we obtain

$$\Pi(\omega) = 1 - 4 \sum_{l=1}^{N-1} \sum_{i=1}^{N-l} p_i p_{i+l} \sin^2 \left( \frac{\omega\chi_l}{2} \right), \tag{A12}$$

which, when $\omega \to 0$, leads to

$$\kappa_1 = \sum_{l=1}^{N-1} \left( \sum_{i=1}^{N-l} p_i p_{i+l} \right) \chi_l^2 \quad . \tag{A13}$$

## References


Applebaum, D. (2013), *Lévy Processes and Stochastic Calculus*, Cambridge Studies in Advanced Mathematics, Vol. 116, Cambridge University Press, Cambridge.

Bauer, M. (2011), A definition of energy, *Physics Today* **64**, 8, 10, DOI: 10.1063/PT.3.1198.

Coopersmith, J. (2010), *Energy, the Subtle Concept. The Discovery of Feynman's Blocks from Leibniz to Einstein*, Oxford University Press, Oxford, 416 pp.

Crystal, L. (2011), Review of "Energy, the subtle concept: The discovery of Feynman's blocks from Leibniz to Einstein" by J. Coopersmith, *Physics Today* **64**, 4, 61-62, DOI: 10.1063/1.3580497.

Feller, W. (1971), *An Introduction to Probability Theory and Its Applications*, 2nd ed., John Wiley & Sons, New York.

Flores-Márquez, E.L., C.A. Vargas, L. Telesca, and A. Ramírez-Rojas (2014), Analysis of the distribution of the order parameter of synthetic seismicity generated by a simple spring-block system with asperities, *Physica A* **393**, 508-512, DOI: 10.1016/j.physa.2013.07.015.

Holliday, J.R., J.B. Rundle, D.L. Turcotte, W. Klein, K.F. Tiampo, and A. Donnellan (2006), Space-time clustering and correlations of major earthquakes, *Phys. Rev. Lett.* **97**, 23, 238501, DOI: 10.1103/PhysRevLett.97.238501.

Huang, Q. (2015), Forecasting the epicenter of a future major earthquake, *Proc. Natl. Acad. Sci. USA* **112**, 4, 944-945, DOI: 10.1073/pnas.1423684112.

Jaynes, E.T. (2003), *Probability Theory: The Logic of Science*, Cambridge University Press, Cambridge.

Johnson, N.L., S. Kotz, and A.W. Kemp (1992), *Univariate Discrete Distributions*, John Wiley & Sons, New York, 565 pp.

Kolmogorov, A.N. (1950), *Foundations of the Theory of Probability,* Chelsea Publishing Co., New York.

Planck, M. (1945), *Treatise on Thermodynamics,* Dover Publ., New York, 297 pp.

Ramírez-Rojas, A., L. Telesca, and F. Angulo-Brown (2011), Entropy of geoelectrical time series in the natural time domain, *Nat. Hazards Earth Syst. Sci.* **11**, 219-225, DOI: 10.5194/nhess-11-219-2011.

Rundle, J.B., J.R. Holliday, W.R. Graves, D.L. Turcotte, K.F. Tiampo, and W. Klein (2012), Probabilities for large events in driven threshold systems, *Phys. Rev. E* **86**, 2, 021106, DOI: 10.1103/PhysRevE.86.021106.

Vargas, C.A., E.L. Flores-Márquez, A. Ramírez-Rojas, and L. Telesca (2015), Analysis of natural time domain entropy fluctuations of synthetic seismicity generated by a simple stick-slip system with asperities, *Physica A* **419**, 23-28, DOI: 10.1016/j.physa.2014.10.037.

Varotsos, P., N. Sarlis, and M. Lazaridou (1996), Reply to "Rebuttal to reply by Varotsos and Lazaridou: Towards plainly successful prediction" by Paul W. Burton, *Geophys. Res. Lett.* **23**, 11, 1389-1390, DOI: 10.1029/96GL01259.

Varotsos, P.A., N.V. Sarlis, and E.S. Skordas (2001), Spatio-temporal complexity aspects on the interrelation between seismic electric signals and seismicity, *Pract. Athens Acad.* **76**, 294-321.

Varotsos, P.A., N.V. Sarlis, and E.S. Skordas (2002a), Long-range correlations in the electric signals that precede rupture, *Phys. Rev. E* **66**, 011902, DOI: 10.1103/PhysRevE.66.011902.

Varotsos, P., N. Sarlis, and E. Skordas (2002b), Seismic electric signals and seismicity: On a tentative interrelation between their spectral content, *Acta Geophys. Pol.* **50**, 3, 338-354.

Varotsos, P.A., N.V. Sarlis, E.S. Skordas, and M.S. Lazaridou (2008), Fluctuations, under time reversal, of the natural time and the entropy distinguish similar looking electric signals of different dynamics, *J. Appl. Phys.* **103**, 014906, DOI: 10.1063/1.2827363.

Varotsos, P.A., N.V. Sarlis, and E.S. Skordas (2009), Detrended fluctuation analysis of the magnetic and electric field variations that precede rupture, *Chaos* **19**, 2, 023114, DOI: 10.1063/1.3130931.

Varotsos, P.A., N.V. Sarlis, and E.S. Skordas (2011a), *Natural Time Analysis: The New View of Time. Precursory Seismic Electric Signals, Earthquakes and other Complex Time Series*, Springer Verlag, Berlin Heidelberg.

Varotsos, P.A., N.V. Sarlis, and E.S. Skordas, S. Uyeda, and M. Kamogawa (2011b), Natural time analysis of critical phenomena, *Proc. Natl. Acad. Sci. USA* **108**, 28, 11361-11364, DOI: 10.1073/pnas.1108138108.

Yates, D.S., D.S. Moore, and D.S. Starnes (2002), *The Practice of Statistics*, 2nd ed., W.H. Freeman, New York.

Received 3 February 2015
Received in revised form 24 April 2015
Accepted 22 May 2015

DE GRUYTER OPEN

Acta Geophysica
vol. 64, no. 4, Aug. 2016, pp. 853-884
DOI: 10.1515/acgeo-2016-0011

# Site-specific Probabilistic Seismic Hazard Map of Himachal Pradesh, India. Part II. Hazard Estimation

Prabhu MUTHUGANEISAN and S.T.G. RAGHUKANTH

Department of Civil Engineering, Indian Institute of Technology Madras, Chennai, India; e-mail: raghukanth@iitm.ac.in

Abstract

This article presents site-specific probable seismic hazard of the Himachal Pradesh province, situated in a seismically active region of northwest Himalaya, using the ground motion relations presented in a companion article. Seismic recurrence parameters for all the documented probable sources are established from an updated earthquake catalogue. The contour maps of probable spectral acceleration at 0, 0.2, and 1 s (5% damping) are presented for 475 and 2475 years return periods. Also, the hazard curves and uniform hazard response spectrums are presented for all the important cities in this province. Results indicate that the present codal provision underestimates the seismic hazard at cities of Bilaspur, Shimla, Hamirpur, Chamba, Mandi, and Solan. In addition, regions near Bilaspur and Chamba exhibit higher hazard levels than what is reported in literature.

**Key words:** PSHA, GMPE, seismic hazard, site coefficients, Himalaya.

## 1. INTRODUCTION

The state of Himachal Pradesh, is situated in the north-western part of Himalayas which is seismically very active. The high seismic activity in this region can be attributed to the Himalayan orogeny and to the numerous major

Ownership: Institute of Geophysics, Polish Academy of Sciences;
© 2016 Muthuganeisan and Raghukanth. This is an open access article distributed under the Creative Commons Attribution-NonCommercial-NoDerivs license, http://creativecommons.org/licenses/by-nc-nd/3.0/.

seismic faults present in this region. Some of the major Himalayan faults, such as the Main Frontal Thrust (MFT), Main Central Thrust (MCT), and Main Boundary Thrust (MBT), are present here. As a result, this region has been subjected to several major earthquakes in the past, namely, the Kangra earthquake ($M_w$ 7.8, 1905), Uttarkashi earthquake ($M_w$ 7, 1991), and Chamoli earthquake ($M_w$ 6.8, 1999), which resulted in extensive damages to infrastructure and human life. Hence, this region comes under the Zone IV (severe) and Zone V (very severe) of the seismic zone map of India (IS:1893 2002) with damage intensity of VIII and IX, respectively. Despite the seismicity, the increase in the population in the high seismicity regions of this state has led to increase in the seismic vulnerability (Chandel and Brar 2010). The vulnerability of the local population can be greatly lessened through creating awareness on disaster preparedness and recovery. Some of the aspects of disaster reduction strategies in place for India are discussed in Bansal and Verma (2013). On the other hand, there is an imperative need to assess the seismic hazard of this region as robustly as possible.

The review of earlier seismic hazard studies for this region (Khattri *et al.* 1984, Bhatia *et al.* 1999, Parvez *et al.* 2003, Mahajan *et al.* 2010, Patil *et al.* 2014) indicates that the previous estimates are based on ground motion relations developed for entirely different geological regions. This issue was addressed by NDMA (2011) which presented ground motion relations for class A sites taking into account the regional geological and seismogenic characteristics of India. However, these ground motion relations proposed cannot be applied to the study region without incorporating the local site effects as shown in the preliminary version of this paper (Prabhu and Raghukanth 2014), using fewer seismic sources and recurrence parameters derived from an already existing catalogue (upto 2009 A.D.) presented by Raghukanth (2011). Therefore, in the companion article (Muthuganeisan and Raghukanth 2016), the regional ground motion relations (GMPE) were developed for the widely prevalent class C and D site conditions in the study region.

In this article, the ground motion relations presented in the companion article shall be used to evaluate the site-specific seismic hazard of the study region (between 75°30′ E to 79° E and 30°30′ N to 33°30′ N) at a grid interval of 0.1°. The probabilistic seismic hazard analysis (PSHA) has been carried out by the widely used Cornell–McGuire approach (Cornell 1968, McGuire 1976). Among the 32 seismogenic zones delineated in NDMA (2011), 6 of them are located in a 500 km radius of the study domain (USNRC 1997) are considered and 301 faults located within these zones, published by GSI (2000), are considered as probable sources. The recurrence parameters are estimated for all the individual faults using a simple heuristic deaggregation approach (Iyengar and Ghosh 2004, NDMA 2011) from a

homogeneous earthquake catalogue that spans from 270 B.C. to 2013 A.D. prepared by updating the existing catalogue (Raghukanth 2011).

The hazard estimates are presented as contour maps for three ground motion parameters, namely, peak ground acceleration (PGA), short and long period spectral acceleration. These maps are presented for the widely prevalent class C and D sites for two return periods of 475 (~500) and 2475 (~2500) years which correspond to 10 and 2% probability of exceedance in 50 years. In addition, site-specific uniform hazard response spectrum (UHRS) and hazard curves (HC) for some important cities are also presented. These results are necessary to update the design standards for this region and are useful for designers to estimate the expected ground motion at the ground level and for risk assessment.

## 2. SEISMO-TECTONIC SETTING OF HIMACHAL PRADESH

### 2.1 Geography

The state of Himachal Pradesh lies between 30°20′ N to 33°15′ N latitudes and 75°45′ E to 79°00′ E longitudes, as shown in Fig. 1, and covers an area of 55 673 km$^2$. Figure 1 shows the division of this region into two major geological provinces, namely, Indo-Gangetic and Himalayan regions. The district of Una and parts of the districts of Sirmaur, Solan, Bilaspur, Hamirpur and Kangra lie in the Indo-Gangetic plain. The districts of Mandi, Shimla, Chamba, Kullu and parts of the districts of Bilaspur, Hamirpur, Kangra, Sirmaur, and Solan are located in the lower hills of Himalayas while the districts of Kinnaur and Lahaul & Spiti lie in the outer Himalayas (Karan 1966). The districts of Bilaspur, Hamirpur, Kangra, Mandi, Sirmaur, Solan, and Una generally have brown, alluvial, and grey brown podzolic soils, the districts of Kullu and Shimla have grey-wooded podzolic soils, while Kinnaur, Lahaul & Spiti, and some parts of Chamba have humus mountain speletal soils (Department of Planning 2003).

The topographic slope variation in the state is from 0.5 to above 70% (Department of Planning 2003) and the altitude varies from 320 m (Una District) in the Siwalik range in the south to 6975 m (Kinnaur District) in the mountainous regions of the greater Himalayas in the north. According to the recent data (Census 2011), the total population of the state is 68.56 million with the current population density of 123 persons per km$^2$. This indicates a growth of +32.58% in 20 years (Census 1991). Typical to the Himalayan region, the population in the high altitude region is sparse (only 2% in Lahaul & Spiti with 36% of total area) while it is denser in the lower Himalayan regions. The Kangra district sustains 22% of the total population in just 10% of the total area, which is equivalent to the combined population of Una, Hamirpur, and Bilaspur district. Hence, the seismic risk in the Kangra dis-

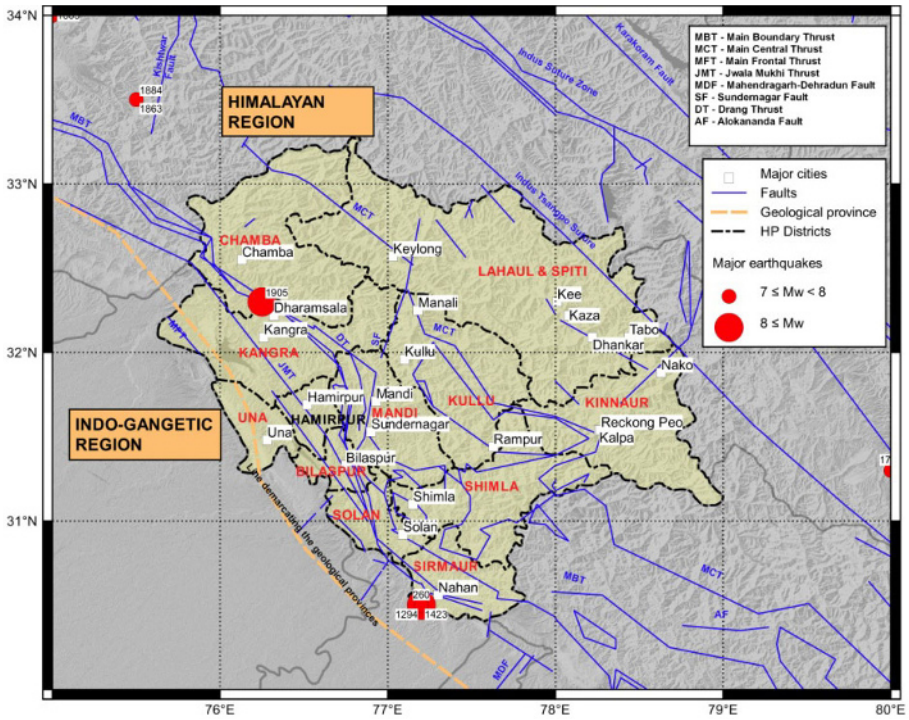


Fig. 1. Fault map of the study region with the location of the test cities shown along with the administrative districts of the state of Himachal Pradesh, India. The demarcation between the two geological divisions, namely the Himalayan and the Indo-gangetic regions, is shown. The epicentral location of historical great earthquakes of magnitude $M_w \geq 7$ and their year of occurrence is marked here. Extreme variability of the altitude, which varies from 320 m (in Una district) to 6975 m (in Kinnaur district), can be seen from the terrain map embossed in the background.

trict is only much greater and emphasizes the need to prevent the disastrous consequences of the 1905 Kangra earthquake (Ambraseys and Bilham 2000).

## 2.2 Seismotectonics

The Himalayan orogeny resulted in the formation of a large number of major faults in this region. Thus, the frequent seismic activities observed in this region are due to ruptures at these thrust faults formed by the subduction of the Indian plate below the slow moving Eurasian plate (Valdiya 2002). Some of these prominent faults are the Main Frontal Thrust (MFT) (Valdiya 1976) separating the Indo-Gangetic plain from the Siwalik ranges, the Main Boundary Thrust (MBT) separating the Siwalik ranges from the Lesser Hi-

malaya, and Main Central Thrust (MCT) separating the Lesser Himalaya from the Greater Himalaya and Tibet. Due to the presence of such large number of faults, some of the major earthquakes have occurred here, such as the Kangra ($M_w$ 7.8, 1905), Uttarkashi ($M_w$ 7, 1991), Killari ($M_w$ 6.2, 1993), and Chamoli ($M_w$ 6.8, 1999) earthquakes causing severe damages.

The estimation of the probable ground motion intensity at a site by McGuire–Cornell approach relies on the complete information of the location and seismic activity of all the faults within an effective distance from the site. The faults whose seismic activity can affect Himachal Pradesh have been identified from the Seismotectonic Atlas of India (GSI 2000) and are shown in Fig. 2. NDMA (2011) has delineated these faults into 32 seismogenic zones based on their distribution and known seismicity. The important features of 7 of these zones that are situated within 500 km from HP state are considered for this study. These zones are the Western Himalaya (SZ-1), Central Himalaya-I (SZ-2), Central Himalaya-II (SZ-3), Altya

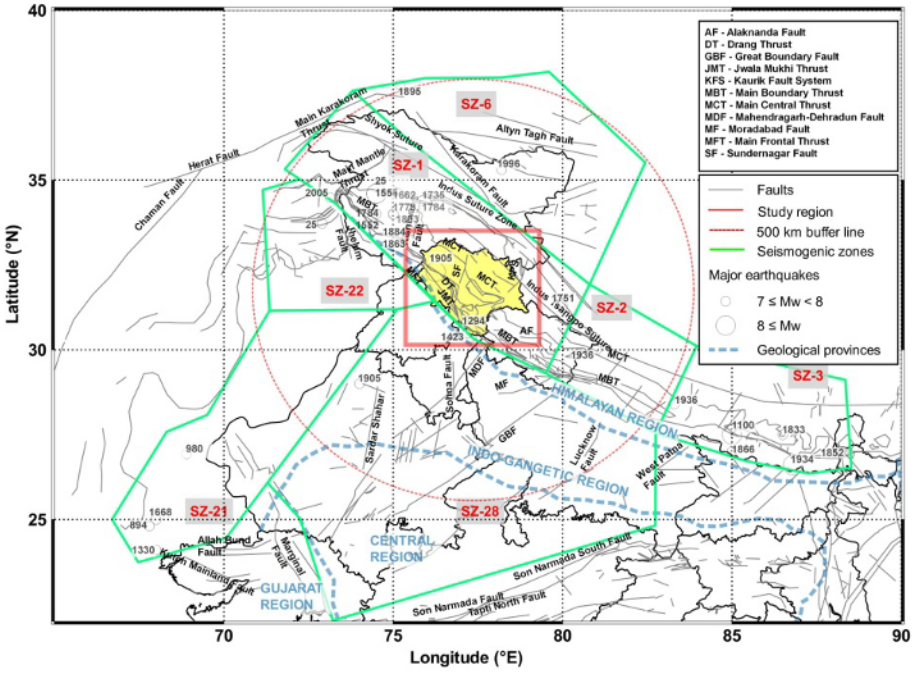


Fig. 2. Faults located in and around Himachal Pradesh and the seismogenic zones from NDMA (2011) considered in this study. A total of 301 fault segments located in seven zones (SZ-1, SZ-2, SZ-3, SZ-6, SZ-21, SZ-22, SZ-28) that control the hazard level of the study region (highlighted in yellow) are considered as probable sources. The epicentres of major seismic events given in Table 1 with magnitude $M_w \geq 7$ are indicated here.

Tegh & Karakoram (SZ-6), Sindh-Punjab (SZ-21), Upper Punjab (SZ-22), and the Aravali-Bundelkhand (SZ-28) zones and are indicated in Fig. 2.

The HP state lies entirely within the Western Himalaya zone (SZ-1) which is the plate boundary region marked by several prominent tectonic sequences. It can be seen from Fig. 1 that some major faults are situated near important cities. The city of Hamirpur lies on the active Jwala Mukhi Thrust (JMT), which is a neotectonic fault. The MFT, an active neotectonic fault, runs through the south-west of the state and within 10 km from the city of Una. Drang Thrust (DT), a non-active thrust, runs through the south of the state passing close to the cities of Nahan, Solan, Hamirpur, Mandi, and Dharamshala. The MBT runs to the south of the state passing through the cities of Solan, Mandi, and Dharamsala. The MCT, a non-active thrust, runs through the state through the region between the lower and outer Himalayas bordering the district of Lahaul & Spiti on the south and runs very close to the cities of Kullu, Manali, Kalpa, and Keylong. This is also referred to as the Zanskar shear zone. The Sundernagar Fault (SF) is a right-lateral shear fault runs through the Sundernagar city.

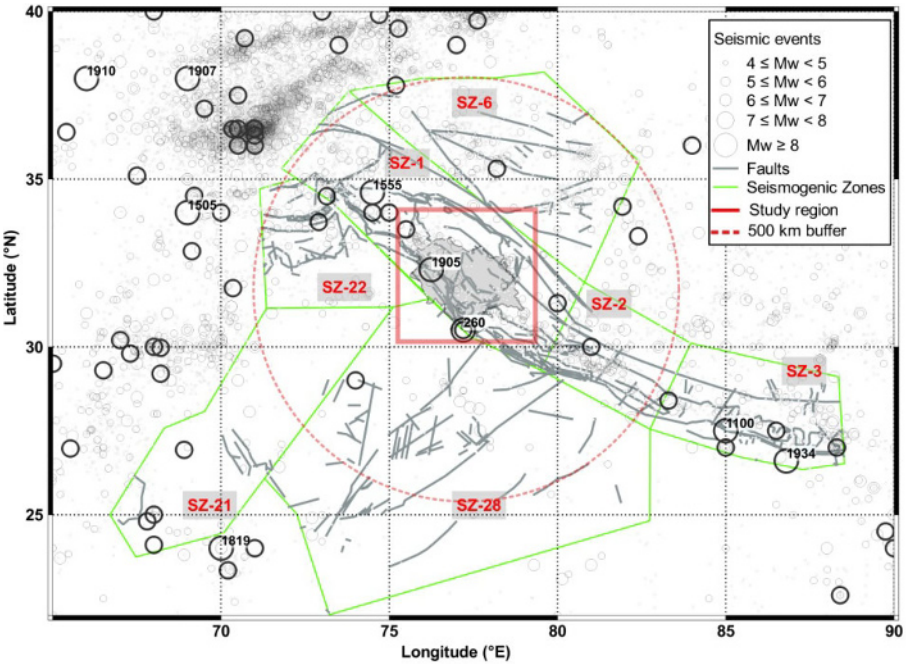


Fig. 3. Declustered seismicity map (from 25 up to 2013 A.D.) observed within the considered seismogenic zones. A total of 3070 independent events are located within the considered seismogenic zones. The major events from the catalogue with magnitude $M_w \geq 7$ are marked along with their date of occurrence.

The source zones SZ-2 and SZ-3 are the continuation of the Himalayan fault sequences comprising of the MBT and MCT along with several transverse faults. It can be seen from Fig. 2 that several large seismic events have been reported in these zones. Zone SZ-6 contains the Karakoram fault and the Altyn Tagh faults. Zones SZ-28 contains several faults such as the Mahendragarh-Dehradun Fault, Moradabad Fault, Sohna Fault, Great Boundary Thrust, and Lucknow Fault. This zone comprises of the Siwalik ranges in the north followed by the alluvial plains of the Indo-Gangetic foredeep. The faults and the seismicity of these considered source zones are shown in Figs. 2 and 3. A total of 301 line fault segments located in these 7 source zones are considered in this study. From Fig. 3, it can be observed that some of the past earthquakes can be associated with existing faults or rupture zones while it is not so straightforward in many cases. In order to carry out PSHA, the seismicity of all the probable sources is characterized in terms of the Gutenberg–Richter (G–R) recurrence relationship using an updated catalogue which will be discussed in the following section.

## 3. UPDATED EARTHQUAKE CATALOGUE

An earthquake catalogue is a collection of the location, time, and magnitude of the past seismicity of a region. A reliable, complete and homogenous catalogue is a prerequisite for deriving the seismicity parameters of the faults within the region. Such a catalogue has been presented by NDMA (2011) (records up to 2008 A.D.) and Raghukanth (2011) (records up to 2009 A.D.) for the source zones used in this study. The above two catalogues are composite and homogeneous comprising of instrumental data, data from historical government archives, and data gathered from paleo-seismic investigations. The most reliable records are the instrumental data obtained from the seismic instrumentation network of Indian Meteorological Department (IMD), International Seismological Centre (ISC), U.S. Geological Survey (USGS), and Pakistan Meteorological Department (PMD). Earlier historical events in these regions have been reported by Oldham (1883), Milne (1911) for the period between 1664 and 1899 A.D., and Quittmeyer and Jacob (1979) for the period between 1914 and 1965 A.D. The data from paleo-seismic investigations based on the available geomorphologic evidences helps to identify large magnitude events that have recurrence period of several 100 years.

In this study, the present catalogue (Raghukanth 2011) for these source zones was updated by including the events of magnitude $M_w \geq 4$ recorded during the period 2010-2013 A.D. These additional event included in this study are obtained from instrumented data available at the earthquake databases of the International Seismological Centre (ISC). The additional events have been homogenised to a single magnitude scale $M_w$ using the magnitude

conversions adopted by Raghukanth (2011) and NDMA (2011). The large events in the updated catalogue with magnitude $M_w$ exceeding 7 within a 500 km radius from the study region are listed in Table 1. The earliest event

Table 1

List of earthquakes of magnitude ≥ 7 within a 500 km radius of Himachal Pradesh

| Date (A.D.) | Latitude | Longitude | Magnitude $M_w$ | Depth [km] | Reference |
|---|---|---|---|---|---|
| 25 | 33.72 | 72.9 | 7.5 | – | PMD |
| 250 | 34.60 | 74.5 | 8.5 | | Iyengar *et al*. (1999) |
| 260 | 30.50 | 77.2 | 8 | – | Kumar *et al*. (2001) |
| 894 | 24.80 | 67.8 | 7.7 | | PMD |
| 980 | 26.93 | 68.9 | 7.6 | | Bilham *et al*. (2007) |
| 1100 | 27.50 | 85 | 8.5 | | Lave *et al*. (2005) |
| 1294 | 30.50 | 77.2 | 7.5 | – | Kumar *et al*. (2001) |
| 1330 | 24.10 | 68 | 7.6 | | Montessus de Ballore (1911) |
| 1423 | 30.50 | 77.2 | 7.5 | – | Kumar *et al*. (2001) |
| 1552 | 34 | 74.5 | 7.5 | – | IMD |
| 1555 | 34.60 | 74.5 | 8.5 | | Iyengar *et al*. (1999) |
| 1662 | 34 | 75 | 7.5 | – | IMD |
| 6 May 1668 | 25 | 68 | 7 | | IMD |
| 1735 | 34 | 75 | 7.5 | – | IMD |
| 1751 | 31.30 | 80 | 7 | – | Ambraseys and Jackson (2003) |
| 1778 | 34 | 75 | 7.7 | – | IMD |
| 1784 | 34 | 75 | 7.3 | – | IMD |
| 1803 | 34 | 75 | 7 | – | IMD |
| 26 Aug 1833 | 27.50 | 86.5 | 7.5 | | IMD |
| 1 May 1852 | 27 | 88.3 | 7 | | Oldham (1883) |
| 1 Jan 1863 | 33.50 | 75.5 | 7 | – | IMD |
| 23 May 1866 | 27 | 85 | 7 | | IMD |
| 30 May 1884 | 33.50 | 75.5 | 7.3 | – | IMD |
| 5 Jul 1895 | 37.80 | 75.2 | 7 | | IMD |
| 4 Apr 1905 | 32.30 | 76.25 | 8 | – | IMD |
| 26 Sep 1905 | 29 | 74 | 7.1 | – | IMD |
| 28 Aug 1916 | 30 | 81 | 7.5 | 35 | ISC |
| 15 Jan 1934 | 26.60 | 86.8 | 8.3 | – | IMD |
| 27 May 1936 | 28.40 | 83.3 | 7 | – | IMD |
| 19 Nov 1996 | 35.31 | 78.2 | 7 | – | ISC |
| 8 Oct 2005 | 34.49 | 73.14 | 7.6 | 10 | IMD |

record for the considered source zones is 25 A.D. reported by PMD (2007) and the largest event magnitude observed was $M_w$ 8.5. The following section discusses on the declustering of the catalogue and the identification of the completeness intervals.

### 3.1 Declustering and completeness check of the catalogue

As the earthquake occurrences in this PSHA framework are assumed to be Poissonian, the foreshocks and aftershocks present in the updated data have been identified and excluded using the widely adopted declustering approach of Gardner and Knopoff (1974) improved by Uhrhammer (1986). This method identifies event clusters based on a temporal and spatial window. As a result, additional 314 independent events with magnitudes $M_w$ ranging from 4-6.9 were added to the database of Raghukanth (2011) for these 7 source zones. The resultant catalogue for these 7 source zones contains a total of 3070 independent events for a period ranging from 25 to 2013 A.D., which comprises of 2554, 403, 82, 25, and 6 events in the magnitude range of $4 \le M_w < 5$, $5 \le M_w < 6$, $6 \le M_w < 7$, $7 \le M_w < 8$, and $M_w \ge 8$, respectively. The spatial distribution of these events is shown in Fig. 3.

The temporal distribution of the event magnitudes from the catalogue presented in Fig. 4 highlights two issues with the catalogue. The smaller magnitude events are available only for the last few decades and the larger magnitude events occur at a larger temporal interval, which in most cases extend beyond the catalogue period. Due to the limited availability of data or the lack of it for certain magnitude and temporal intervals, it is necessary to determine the completeness intervals of the present catalogue for different magnitude ranges. These complete parts of the catalogue will give a more re-

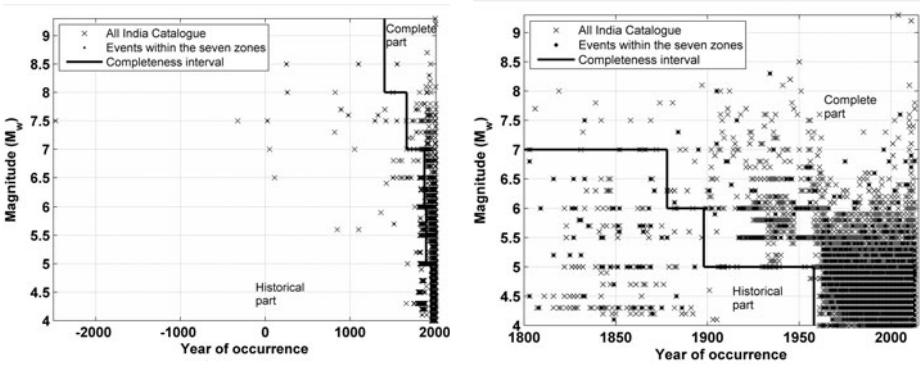


Fig. 4. Temporal distribution of the earthquakes observed within the seven considered seismogenic zones (from 25 up to 2013 A.D.) overlaid on the earthquake catalogue of India (from –2475 B.C. up to 2013 A.D.). The completeness interval obtained by Stepp (1972) approach is also indicated by the solid line.

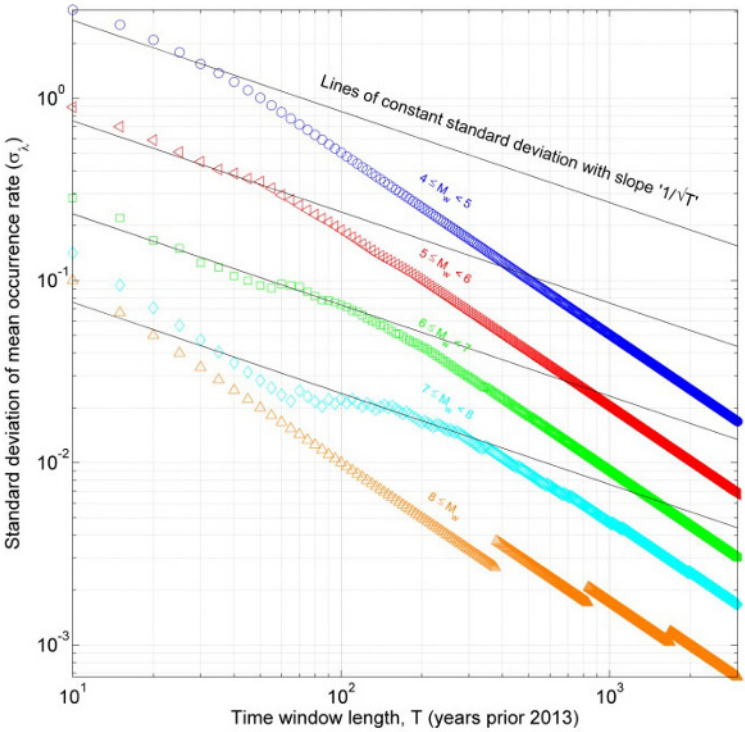


Fig. 5. Completeness test for earthquake data using Stepp (1972) method. Straight lines indicate the theoretical slope of complete data range.

liable estimate of the recurrence parameters. In this study, the widely used completeness test of Stepp (1972) has been used to identify the complete and the incomplete (or historic) part of the catalogue. The complete and the historic part of the catalogue are clearly demarcated and shown in Figs. 4 and 5. In this method, the annual event occurrence rates for several magnitude ranges are estimated for several time windows (10, 20 years, and so on) that extend backwards in time from the last catalogue period (2013 A.D.). The standard deviation of these mean occurrence rates are plotted as a function of the time window $T$. It can be seen from Fig. 5 that as long as the data is complete these values vary at a constant standard deviation of $1/\sqrt{T}$ and the completeness interval for each of the magnitude ranges can thus be identified. By this method, the catalogue has been found to be complete in the magnitude ranges of $4 \le M_w \le 5$, $5 \le M_w \le 6$, $6 \le M_w \le 7$, $7 \le M_w \le 8$, and $M_w > 8$, for a period of 54 years (1960-2013), 114 years (1900-2013), 134 years (1880-2013), 344 years (1670-2013), and 604 years (1410-2013), respectively.

## 4. RECURRENCE PARAMETERS FOR SEISMIC SOURCES

In the PSHA framework, the seismic activity of the sources present in the considered seismogenic regions are quantified by means of Gutenberg–Richter recurrence relations. These relations express the frequency at which these sources can generate seismic events of certain magnitude and their maximum magnitude potential. Thus, if $N(M)$ represents the number of events greater than or equal to a magnitude $M$ recorded during a time period $T$ due to activity at each of the identified seismic sources, then the mean annual rate of exceedance $\lambda_M$ of an earthquake of magnitude $M$ at the source can be given as follows

$$\log_{10}(\lambda_M) = a - bM \ , \tag{1}$$

where $a$ is the logarithmic value of the mean annual value of $N(M > M_0)$; where $M_0$ is the smallest significant magnitude that had occurred at the seismic source; and $b$ indicates the activity rate of the seismic sources and their potential to produce larger or smaller earthquakes. In this study, the value of $M_0$ is taken to be 4 as the occurrence of earthquakes of magnitudes $M_w < 4$ are not significant from design considerations and are usually not strong enough to cause significant structural damages. Knopoff and Kagan (1977) noted that the above recurrence relation needs to have an upper bound to reflect the fault potential realistically but this information cannot be obtained precisely from the catalogue due to the uncertain nature of future events.

In order to estimate the bounded G–R recurrence parameters ($a$, $b$, and $M_{\max}$), complete information on the seismicity of all the individual faults is necessary, but not always available for all the faults. Hence, it is common to estimate these parameters for the source zones and assign it to all the faults located within the source zones resulting in a conservative and higher hazard estimate. A viable alternative method is to estimate the recurrence parameters for the source zones and deaggregate it to fault level recurrences based on available fault specific information such as fault length and fault seismicity (Iyengar and Ghosh 2004, NDMA 2011). In this study, the latter method has been adopted and the zonal values of $a$, $b$, and $M_{\max}$ for all the 7 considered seismic source zones have been estimated from the updated catalogue using the Kijko and Graham (1998) and Kijko (2004) method. This statistical procedure takes into account the uncertainty in the catalogue information and incompleteness of the catalogue data. In this procedure, the updated catalogue is partitioned into a complete part and an extreme part based on the completeness interval determined using the Stepp (1972) method discussed earlier. The magnitude uncertainty is taken as 0.5 and 0.3 for the incomplete and complete part respectively (NDMA 2011).

Table 2

Updated seismicity parameters
for the seven seismogenic zones in Himachal Pradesh

| Source no. | Zones | *b* value | N(4) | Max. potential magnitude $M_{max}$ | Number of earthquakes | Number of faults |
|---|---|---|---|---|---|---|
| SZ-1 | Western Himalaya | 0.81±0.02 | 3.70 | 8.8 | 1025 | 97 |
| SZ-2 | Central Himalaya -I | 0.67±0.04 | 2.80 | 7.8 | 353 | 27 |
| SZ-3 | Central Himalaya-II | 0.70±0.04 | 1.80 | 8.8 | 382 | 39 |
| SZ-6 | Altya Tegh & Karakoram | 0.82±0.03 | 4.50 | 7.3 | 827 | 31 |
| SZ-21 | Sindh-Punjab | 0.71±0.06 | 0.58 | 8.0 | 102 | 11 |
| SZ-22 | Upper Punjab | 0.95±0.05 | 1.95 | 8.0 | 255 | 27 |
| SZ-28 | Aravali-Bundelkhand | 0.75±0.06 | 0.80 | 7.0 | 126 | 68 |

The estimated zonal seismicity parameters and the total number of faults present in all the 7 seismogenic zones considered in the study are listed in Table 2. It can be seen that all of these zones have a maximum magnitude potential of $M_w \geq 7$ and 3 of these zones have $N(4) > 2$ which means that they produce, on an average, 2 events of $M_w \geq 4$ every year. The SZ-1, which encompasses the study region, has the largest number of faults and experiences the largest number of earthquakes. The source zone pairs that exhibit similar seismic activity levels are SZ-1 and SZ-6, SZ-2 and SZ-3, SZ-21 and SZ-28. These updated source zone recurrence parameters are compared with the previously reported NDMA (2011) values, as shown in Fig. 6. It can be seen that there is only a slight variation in these values and

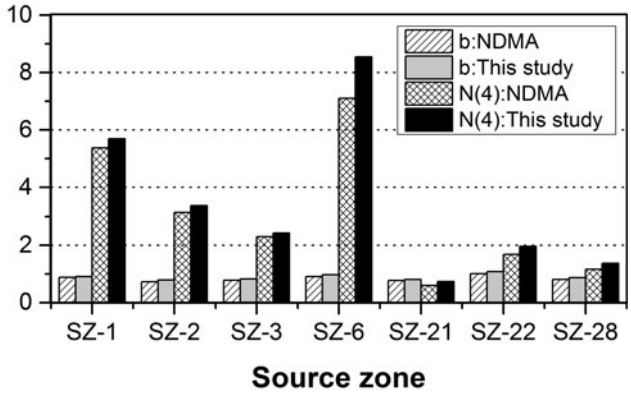


Fig. 6. Comparison of the updated source zone recurrence parameters with the NDMA (2011) values.

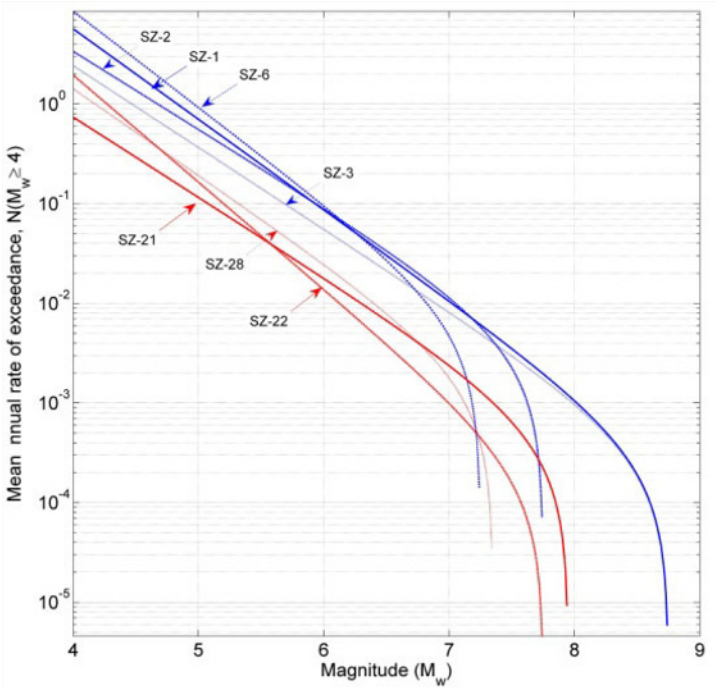


Fig. 7. Bounded Gutenberg–Richter magnitude-frequency relationship for the seven seismogenic zones. $N$ indicates the mean annual occurrence of $M_w \geq 4$ events.

the additional data has contributed to reducing the uncertainty in the $b$-value marginally. Since there had not been any major event in this region, the $M_{\max}$ values remain unchanged. Thus, the uncertainty in the parameters for a particular seismogenic region reduces when the catalogue becomes more complete for that region. The bounded G–R recurrence curve by plotting $\log(\lambda_M)$ against magnitude $M_w$ for all the seismic source zones considered in this study is shown in Fig. 7.

### 4.1 Fault deaggregation

Since the faults within the same zone exhibit varying levels of seismicity, it may be even more appropriate to consider the fault level recurrences. However, the gaps in the existing catalogue and lack of information on the slip characteristics of the faults make it difficult to achieve a clear consensus on the rupture potential of all the identified faults. Hence, the heuristic approach of Iyengar and Ghosh (2004) is used in this study. In this method, the total seismicity within a zone is conserved while estimating the $a$ value of all the faults. These fault specific $a$ values are estimated by taking into considera-

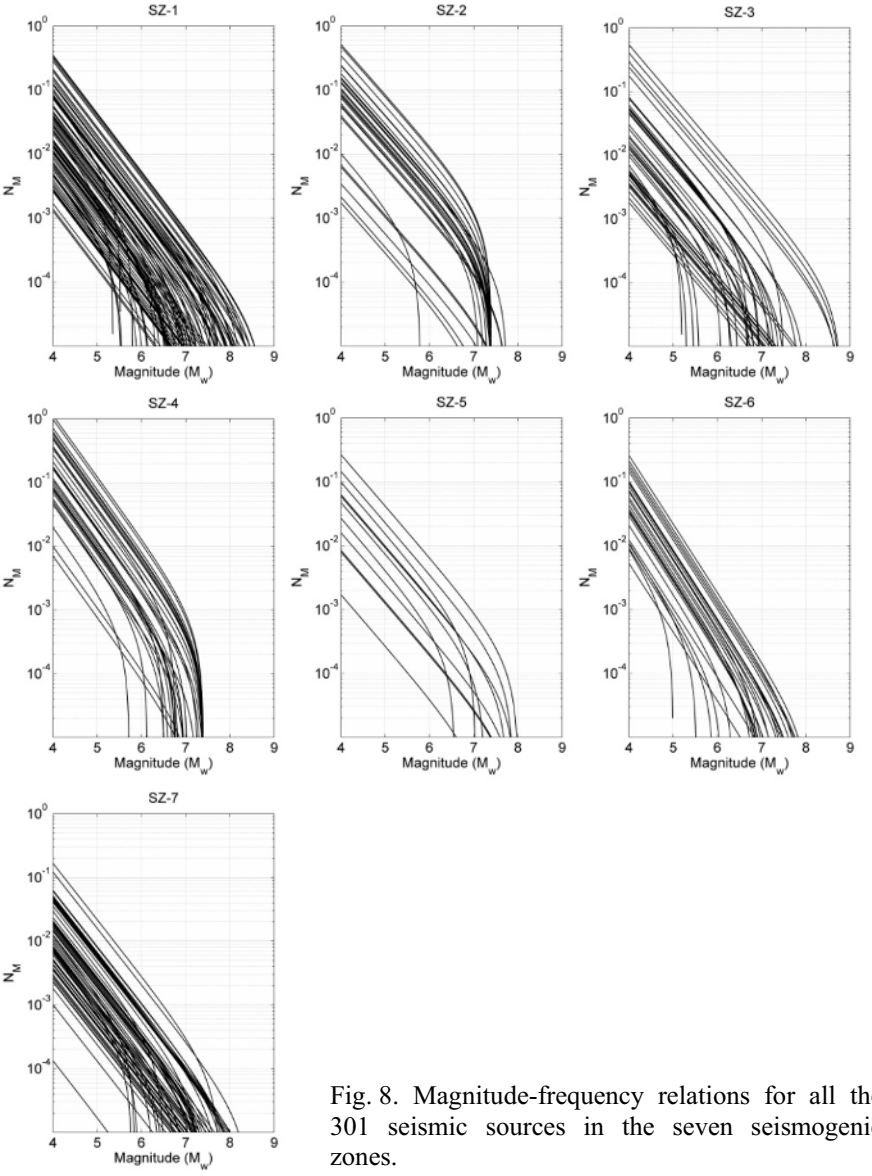


Fig. 8. Magnitude-frequency relations for all the 301 seismic sources in the seven seismogenic zones.

tion the potential of a fault to rupture and known activity. In this study, the background seismicity within a source zone is also taken into consideration by associating these events with the nearest faults in the zone. Thus, the value of $a$ of $i$-th fault is taken as the zonal $a$ value proportioned by a factor determined by fault length ratio and fault activity ratio. Thus, $a_i$ will be

$$a_i = N_i(m_0) = 0.5\left(\frac{L_i}{L_z} + \frac{n_i}{N_z}\right) N(m_0) \ , \tag{2}$$

where the fault length ratio is the ratio of the fault length of the $i$-th fault $L_i$ to the sum of the fault lengths of all the zonal faults ( $L_z = \sum_{i=1}^{Ns} L_i$ ). The fault activity ratio is the ratio of the event occurrences at the fault $n_i$ to total events in the zone $N_z$. $N_s$ is the number of faults present in a zone and $N(m_0)$ is the total number of annual events of magnitude greater than 4 due to all sources within a zone. Since, it is difficult to ascertain the magnitude *versus* rupture potential of individual faults due to the uncertainties in the fault activity, the $b$ value of all the faults within a zone is assumed to be same as the zonal $b$ value. The value of $M_{\max}$ for all the faults in each zone are taken as the maximum magnitude of past events associated with the fault plus 0.5 units, in order to account for uncertainty in the past data. For faults lacking past event records, Wells and Coppersmith (1994) relation has been used to evaluate $M_{\max}$ based on rupture length. Furthermore, the $M_{\max}$ values for individual faults are constrained by the zonal $M_{\max}$ values. These fault level recurrence parameters are estimated for all the 301 faults identified in the 7 seismogenic zones considered in this study. The fault level recurrence relations obtained from the above procedure are shown in Fig. 8. These values define the seismicity of all these causative faults while performing the PSHA.

## 5. PROBABILISTIC SEISMIC HAZARD ANALYSIS (PSHA)

The estimation of the seismic forces, which are expected to act on a structure during its design life, in a deterministic manner, can be unreliable due to the various uncertainties involved in the source and site characteristics. In order to address this problem, Cornell (1968) introduced the concept of PSHA to estimate the seismic hazard level (in terms of a ground motion intensity measure) at a site by taking into account the uncertainties associated with the probable sources, seismicity and the source-to-site path. Der Kiureghian and Ang (1977), in order to include a finite source and its uncertainty, later improved Cornell's assumption of point-source model to characterize sources. Addressing the uncertainties, which are broadly classified into aleatory and epistemic uncertainties, is the main idea behind PSHA. In this methodology, the aleatory uncertainty is addressed by the usage of probability distributions of the source to site distance, magnitude and the ground motion relations. The PSHA estimations become more reliable as the uncertainties reduce as more data becomes available on seismicity, rupture characteristics, *etc*., in the future.

The methodology of PSHA implemented for this study is widely discussed in the available literatures (Kramer 1996, NDMA 2011). Here, the hazard level estimations are simplified by making an assumption that these seismic events recorded on a fault are independent and hence can be assumed as a stationary Poisson process. This simplifies the computation of probability of exceedance of the monitored intensity level (can be PGA, for example) in a time frame of next $T$ years and can be expressed as

$$P\left(Y > y^* \text{ in } T \text{ years}\right) = 1 - e^{-\mu_{y^*} T} \quad . \tag{16}$$

Here, $\mu_{y^*}$ indicates the mean annual rate of exceedance of the ground motion measure $y^*$ (and its reciprocal is the average return period $T_r$ of the event capable of producing $y^*$). If there were $K$ number of probable sources or faults in the region, then $\mu_{y^*}$ can be computed as

$$\mu_{y^*} = \sum_{i=1}^{K} N_i\left(m_0\right) \times \int_{m=m_0}^{m_u} \int_{r=r_{\min}}^{r_{\max}} P\left[Y > y^* \mid m, r\right] p_{R|M}\left(r \mid m\right) p_M\left(m\right) dr dm \; . \tag{17}$$

where $m_0$ and $m_u$ indicate the minimum and the maximum threshold magnitude observed at the fault; $r_{\min}$ and $r_{\max}$ are the minimum and maximum site distances from the fault; $p_M(m)$ is the probability density function of the exponentially distributed magnitude which can be obtained through the G–R relationship; $p_{R|M}(r|m)$ is the conditional probability density function of hypocentral distance which can be obtained numerically for the identified probable sources; $P[Y > y^*|m, r]$ denotes the conditional probability that the chosen ground motion intensity level is exceeded for a given magnitude and distance which can be determined using the ground motion relationship. As discussed earlier, this value is obtained as a lognormal random variable with the mean value given by the attenuation equation and the standard deviation given by the error term $\ln(\varepsilon)$. All the causative faults within a radius of 500 km have been considered in accordance with the international guidelines (USNRC 1997) for estimating the seismic hazard at a site. The seismicity characteristics of each of these sources are expressed in terms of fault-level recurrence parameters. Finally, with the regional site-specific ground motion models presented in the companion paper (Muthuganeisan and Raghukanth (2016), the seismic hazard levels of the state of Himachal Pradesh can be estimated.

## 6. SEISMIC HAZARD OF HIMACHAL PRADESH

In this study, the seismic hazard of the state of Himachal Pradesh has been evaluated at a 0.1° grid interval covering the region between the longitudes 75°30′ E to 79° E and the latitudes 30°30′ N to 33°30′ N. Even though separate ground motion models are presented for class C and D conditions, it is not possible to identify the exact spatial distribution of the soil conditions

throughout the state. Hence, this study presents two sets of hazard maps for both class C and D site conditions in terms of the three ground motion parameters, namely, PGA, $Sa(0.2\,s)$ and $Sa(1.0\,s)$. Thus, for any site located within the study region, the uniform hazard response spectrums can be constructed, by IBC (2009) approach, by picking the values from the hazard map of that specific site class. In addition to the hazard maps, the seismic hazard curves for PGA values for both the site classes are presented for the 12 district-headquarters of Himachal Pradesh and are shown in Fig. 9. It can be seen that Una, being the only test site in the Indo-Gangetic region, experiences lower hazard values than the other cities.

As hazard estimation considering the regional geology and local site characteristics has not been reported by the previous studies for this region, a

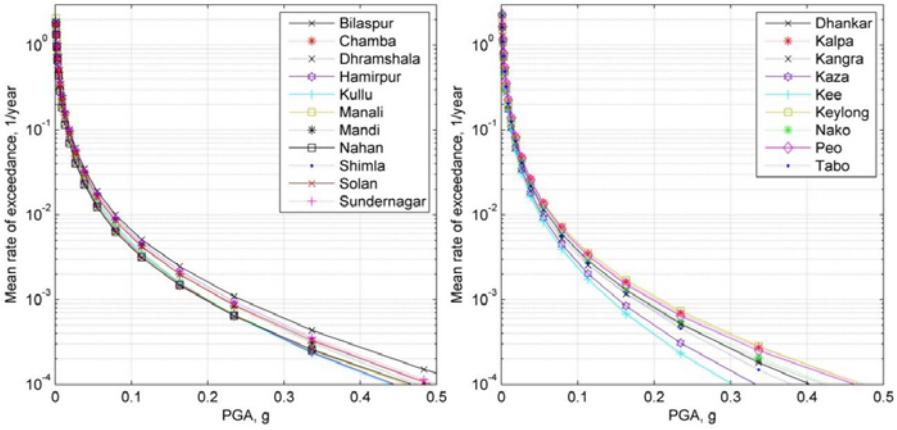


Fig. 9a. Seismic hazard curves for class C sites in some important cities.

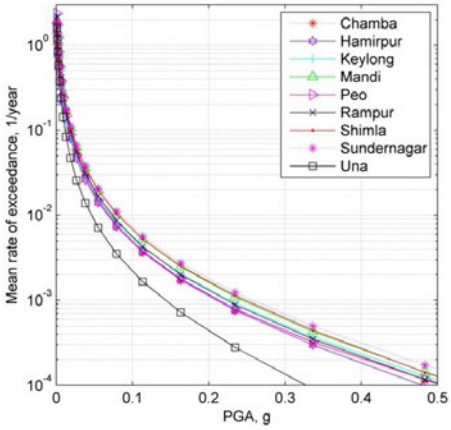


Fig. 9b. Seismic hazard curves for class D sites in some important cities.

reasonable comparison cannot be made. However, it is generally observed that the site effects play an important role in seismic hazard estimation. For the return period of 475 years, the estimated PGA values for class C and D sites reported in this study are in the ranges of 0.04-0.2 and 0.04-0.21 g, respectively. Due to the site amplification effects, the values reported in this study are found to be higher in comparison with the values reported by NDMA (2011) for the same return period, whose PGA values presented for class A sites range from 0.05-0.12 g. Similarly, these values are higher than those reported by Parvez *et al.* (2003), obtained by a deterministic approach (design ground acceleration ranges from 0.08-0.15 g). When compared with the case 1 (varying *b* value) estimates of Patil *et al.* (2014) that range between 0.078-0.15 g, it can be seen that their values underestimates the hazard in this region. When compared with their case 2 (constant *b* value), the hazard is in the range of 0.12-0.26 g which shows higher estimates for the region except for the Bilaspur and Chamba region. Hence, consideration of the fault level seismicity is found to map the seismic hazard more realistically.

The seismic zoning map of India (IS:1893 2002) designates the entire central part of HP as Zone V (very severe) and the peripheral regions are designated as Zone IV (severe) with zero period acceleration values as 0.36 and 0.24 g, respectively, for maximum considered earthquake (MCE) scenario. On comparison with the PGA values at class D sites with 2475 year return period, it can be seen that values estimated are in the ranges of 0.23-0.38 and 0.18-0.38 g for the regions designated as Zone V and Zone IV, respectively. The annex E of the IS:1893 (2002) provides the ZPA for Shimla as 0.24 g (for MCE) whereas the predicted value from this study is around 0.35 g (for 2475 years return period). Similarly, the hazard levels are underestimated for the cities of Chamba, Nahan Solan, Bilaspur, and Shimla which are depicted as Zone IV. On the other hand, the PGA values of the regions depicted as Zone V in the Indian code (IS:1893 2002) are found to be lower than the values reported by the Indian code.

Similarly, the seismic hazard curves can also be built for other spectral acceleration values, apart from PGA, for period ranging from 0.01 to 4 s using the corresponding attenuation coefficients given in Tables 3 to 6 of the companion paper (Muthuganeisan and Raghukanth 2016). Using these curves, it is possible to extract the response spectrums for design basis earthquake and maximum considered earthquake which correspond to 10 and 2% probability of exceedance during the design life of 50 years (IBC 2009). The resulting response spectra are known as uniform hazard response spectrum (UHRS) due to the assumption of uniform probability of exceedance throughout the frequency ranges. The UHRS curves for class C and D sites

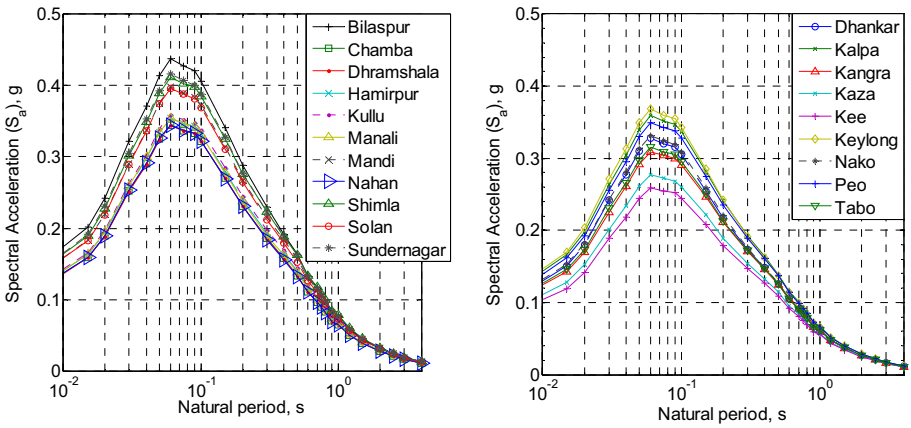


Fig. 10a. UHRS curve for class C sites in some important cities (return period: 475 years).

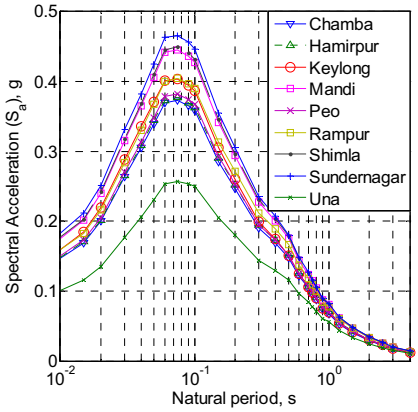


Fig. 10b. UHRS for class D sites in some important cities (return period: 475 years).

of some important cities in HP are shown in Figs. 10 to 11 for two return periods of 475 and 2475 years, respectively.

It is well known that characterization of ground motion in terms of peak measures such as the PGA may be sufficient for analyzing simple regular structures by equivalent static analysis method. However, for structures that are tall or irregular and exhibit complex behavior, it becomes necessary to conduct a dynamic analysis and the same has been recommended by design codes (IS:1893 2002, IBC 2009). Hence, in this work, the contour plots of short period $Sa\,(0.2\ s)$ and long period $Sa\,(1.0\ s)$ spectral accelerations have been also been estimated. The NDMA (2011) report has already published the contour maps of these three parameters for class A sites. It has been

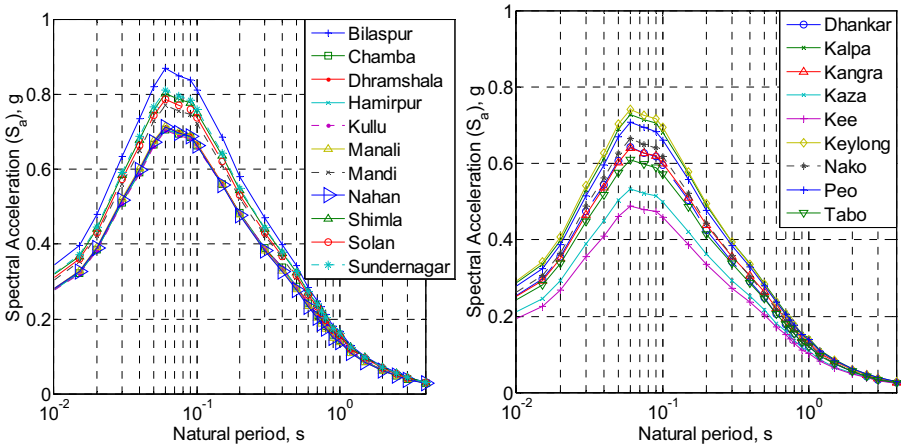


Fig. 11a. UHRS curve for class C sites in some important cities (return period: 2475 years).

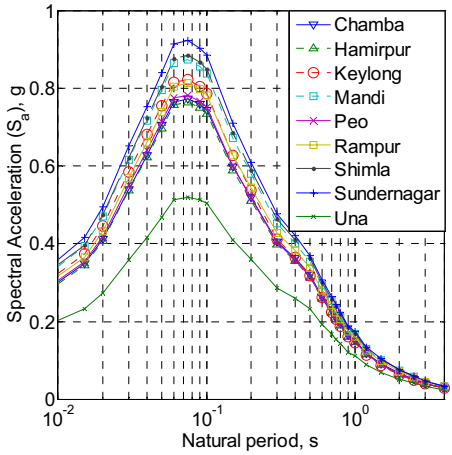


Fig. 11b. UHRS for class D sites in some important cities (return period: 2475 years).

shown earlier that the test sites were primarily of classes C and D with few exceptions. Since the determination of the site conditions throughout the region is not a feasible exercise, it becomes reasonable to provide these contour plots for both the class C (Figs. 12 to 17) and class D site conditions (Figs. 18 to 23).

The spatial variation of peak ground acceleration (PGA), the short period spectral acceleration $Sa\,(0.2\,s)$ and the long period spectral acceleration $Sa\,(1.0\,s)$ for the two return periods of 475 and 2475 years can be observed from these contour plots. It can be observed that the hazard values in the

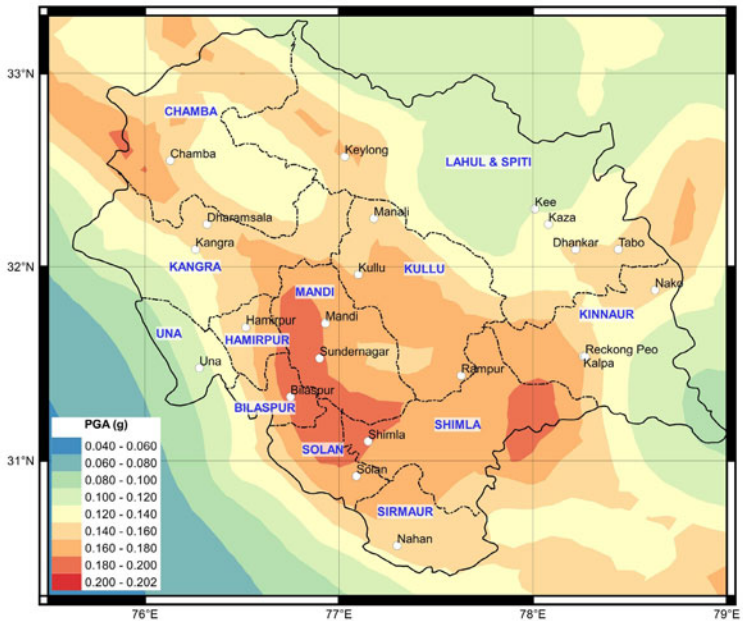


Fig. 12. PGA contours with a return period of 475 years for C type sites.

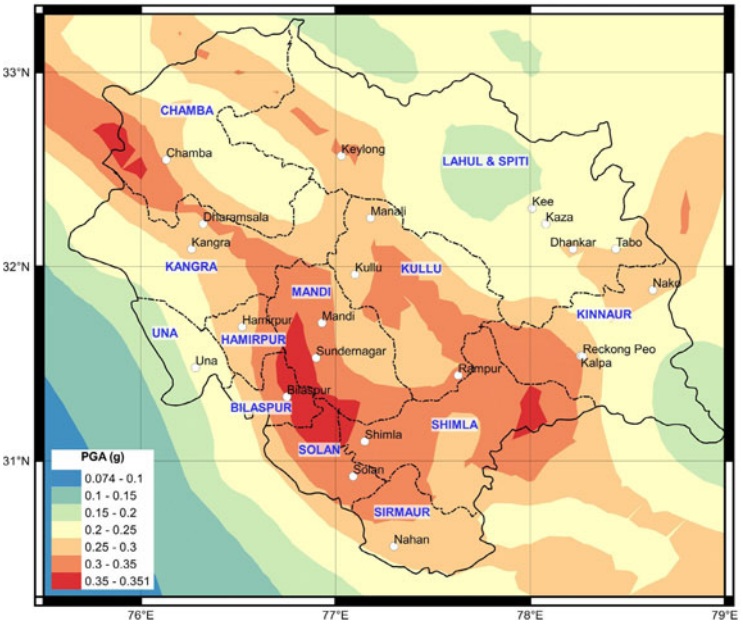


Fig. 13. PGA contours with a return period of 2475 years for C type sites.

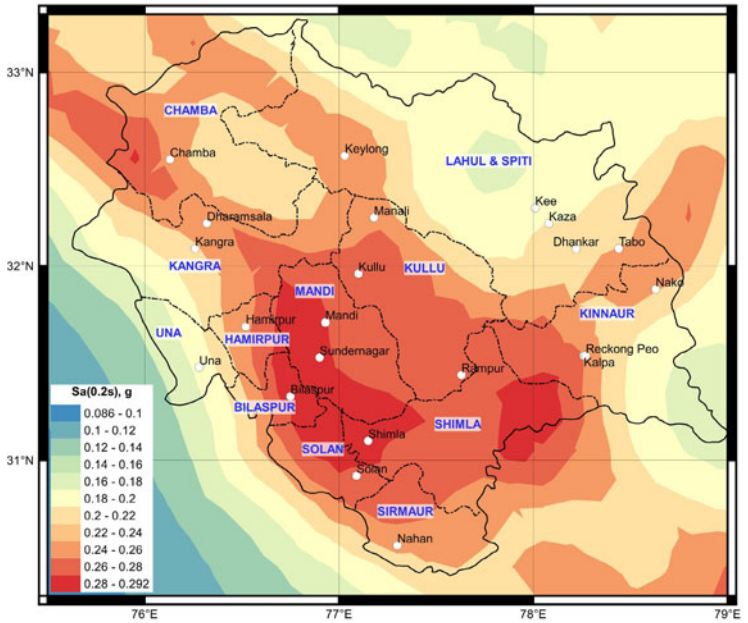


Fig. 14. *Sa* (0.2 *s*) contours with a return period of 475 years for C type sites.

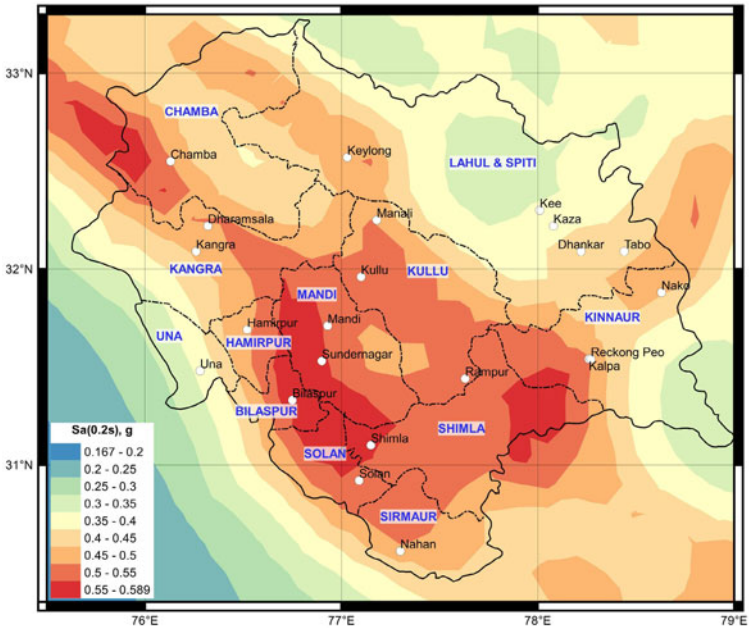


Fig. 15. *Sa* (0.2 *s*) contours with a return period of 2475 years for C type sites.

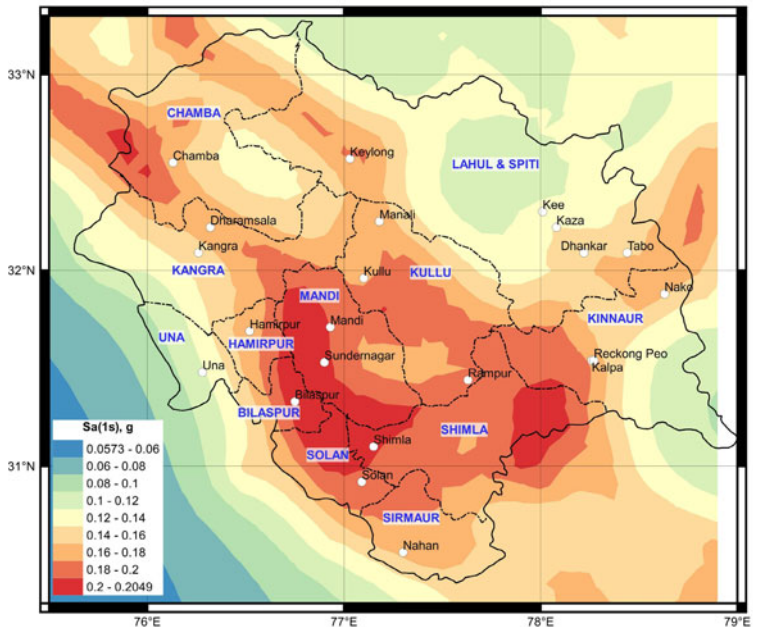


Fig. 16. *Sa* (1.0 *s*) contours with a return period of 475 years for C type sites.

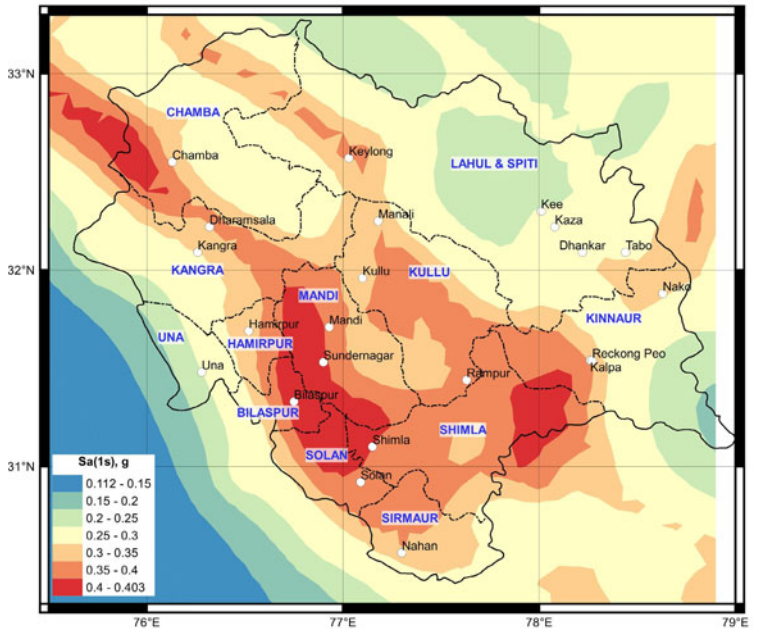


Fig. 17. *Sa* (1.0 *s*) contours with a return period of 2475 years for C type sites.

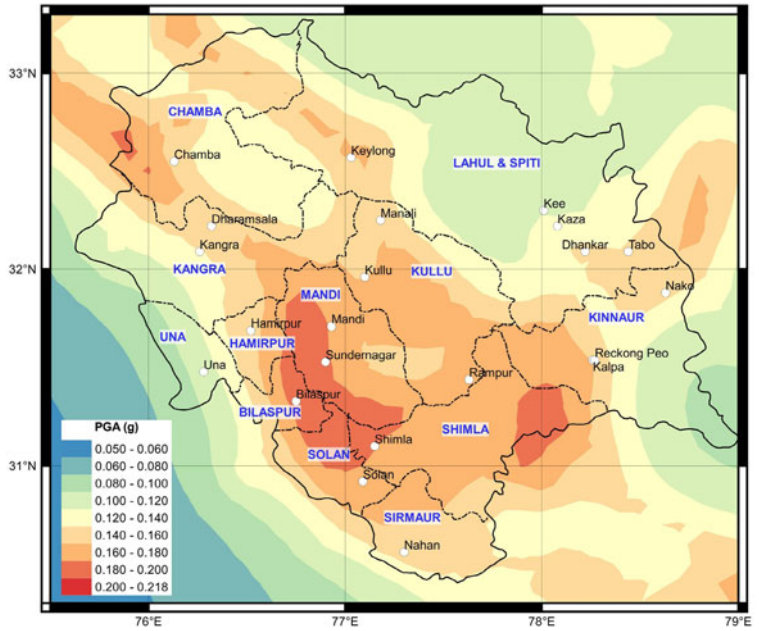


Fig. 18. PGA contours with a return period of 475 years for D type sites.

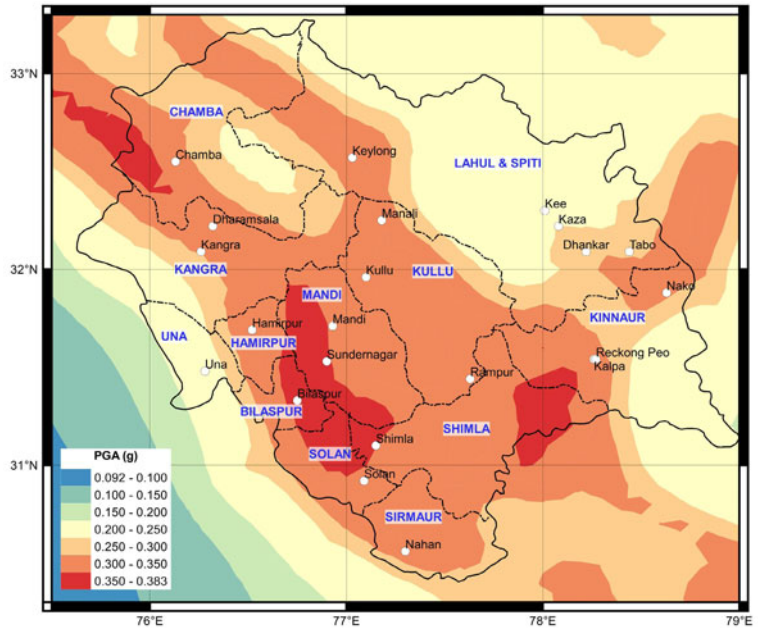


Fig. 19. PGA contours with a return period of 2475 years for D type sites.

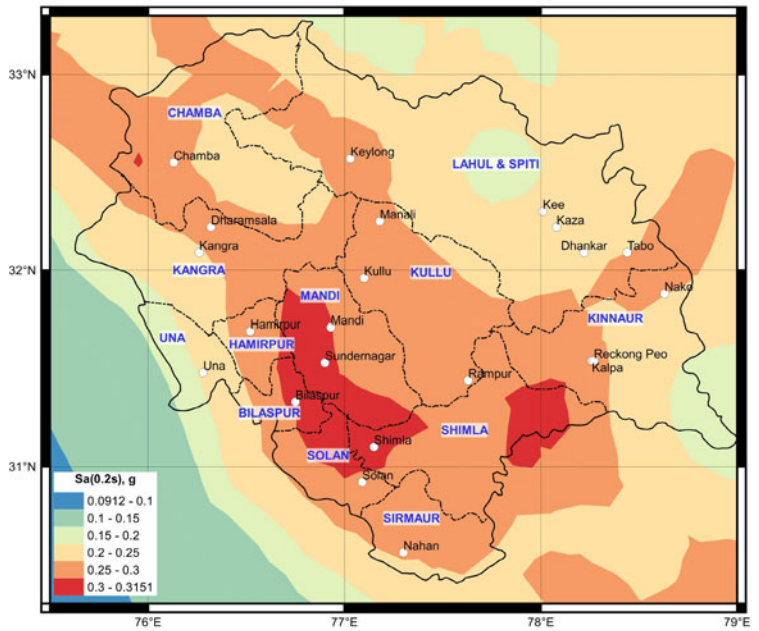


Fig. 20. *Sa* (0.2 *s*) contours with a return period of 475 years for D type sites.

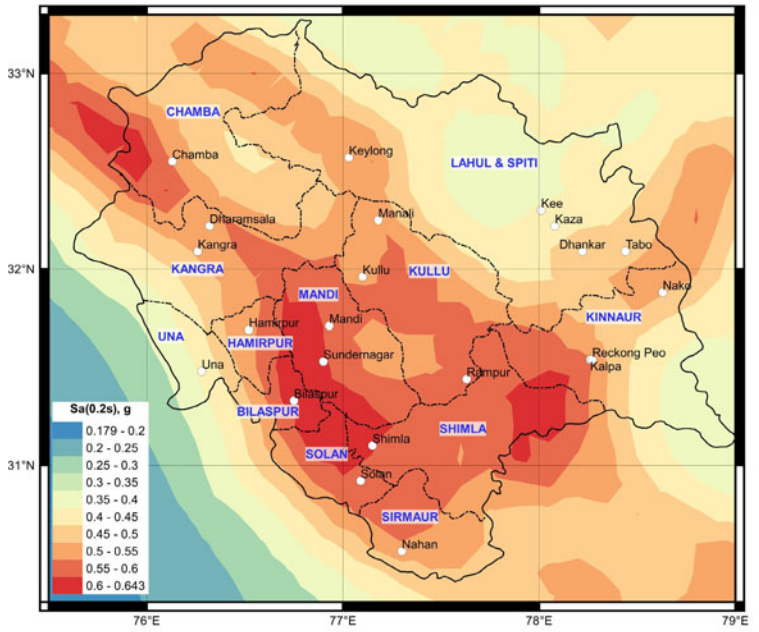


Fig. 21. *Sa* (0.2 *s*) contours with a return period of 2475 years for D type sites.

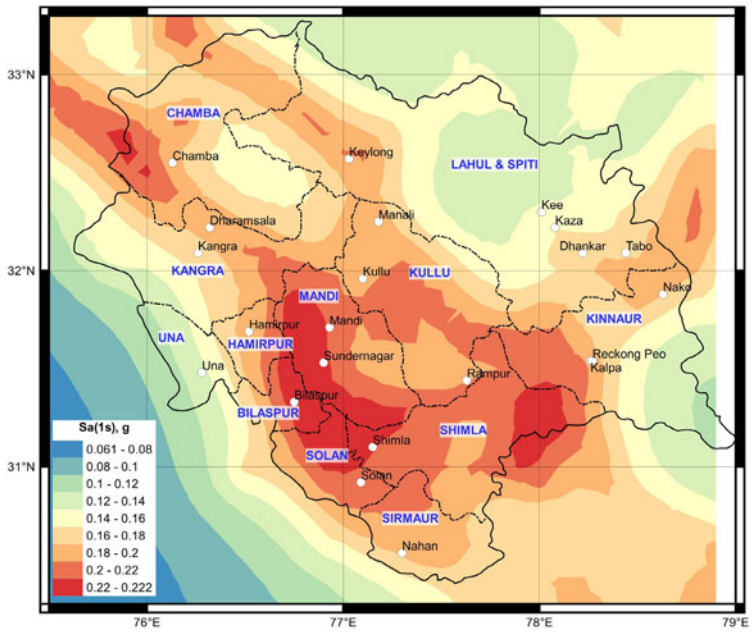


Fig. 22. $Sa\,(1.0\ s)$ contours with a return period of 475 years for D type sites.

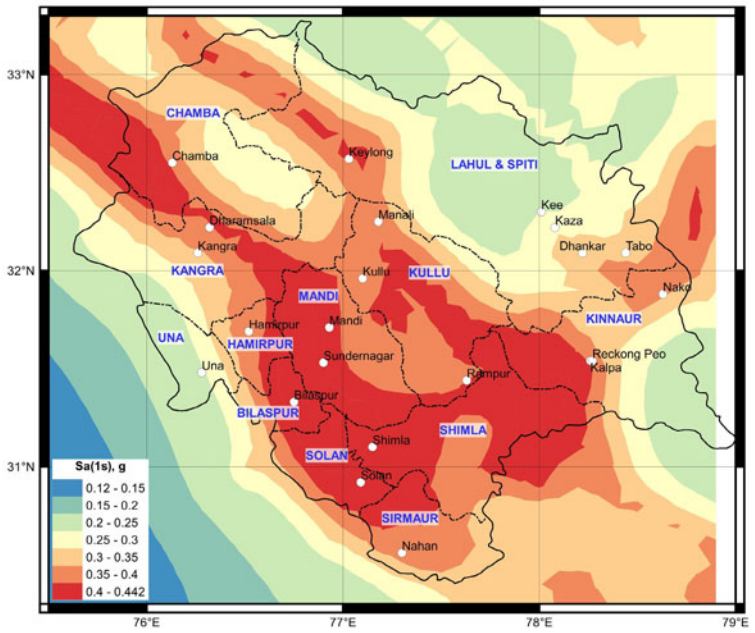


Fig. 23. $Sa\,(1.0\ s)$ contours with a return period of 2475 years for D type sites.

Himalayan region are higher than the IG region, as expected. For example, the PGA values for a 475 year return period and class C site, the hazard values at Hamirpur and Bilaspur, located in the Himalayan region, are greater than 0.14 g while it reduces to below 0.1 g in the Una city located in IG region less than 50 km away. It can be seen that the sparsely populated Lahaul & Spiti district shows lower hazard when compared to the densely populated cities in the lower Himalayan region, namely, Bilaspur, Shimla, Hamirpur, Chamba, Mandi, Solan, *etc*. This reiterates the need to evaluate the seismic risk and design sufficiency for the structures located in these regions. Similar trends are observed for the short and long period acceleration maps. Also, the difference in the PGA values for class C and D type can be observed in the range of 0.005-0.02 and 0.02-0.04 g for 475 and 2475 return periods, respectively. These differences are very similar for the $Sa$ (0.2 s) and $Sa$ (1.0 $s$) values and are in the range of 0.01-0.02 and 0.02-0.05 g for 475 and 2475 return periods, respectively. From the PGA values at class-D for 2475 year return period, the districts of Hamirpur, Bilaspur, Solan, Mandi, Shimla, Kullu, northern parts of Kangra, and the southern parts of Chamba exhibit nearly 35-65% more hazard levels than the districts of Una, Lahaul & Spiti, northern Chamba, eastern Sirmaur, and a small region in the southern part of Kullu. Most importantly, the seismic hazard of the region surrounding Bilaspur, Chamba, and Kullu are found to be the highest within the study region and hazard of this region is higher than the previous studies (NDMA 2011, Patil *et al.* 2014).

The two return periods of 475 and 2475 years, for which hazard analysis has been carried out, are considered equivalent to the design basis earthquake (DBE) and the maximum considered earthquake (MCE). It would be interesting to compare the ratio MCE to DBE for the study region with the value of 2 suggested in the Indian codal provisions (IS:1893 2002). On analyzing the PGA hazard values presented in this study, it was found that this scaling factor lies in the range of 1.67 to 2.18 ($\mu \pm \sigma = 1.965 \pm 0.072$) and 1.68 to 2.2 ($\mu \pm \sigma = 1.98 \pm 0.075$) for the class C- and D-site conditions, as shown in Fig. 24. The scaling factor for $Sa$ (0.2 $s$) hazard values lie in the range of 1.77 to 2.19 ($\mu \pm \sigma = 1.97 \pm 0.07$) and 1.78 to 2.22 ($\mu \pm \sigma = 1.99 \pm 0.072$) for the class C- and D-site conditions. For $Sa$ (1.0 $s$) hazard, these values are in the range of 1.69 to 2.12 ($\mu \pm \sigma = 1.974 \pm 0.05$) and 1.7 to 2.15 ($\mu \pm \sigma = 1.99 \pm 0.053$) for the class C and D-site conditions. Generally, these values were observed to be more than 2 in high hazard Himalayan regions and less than 2 in the IG regions (and within a small northern part of the Lahaul & Spiti region). Thus, the period and site dependency of this scaling factor indicates that a uniform factor of 2 as per IS:1893 (2002) may not appropriately scale the DBE event from MCE event for various regions.

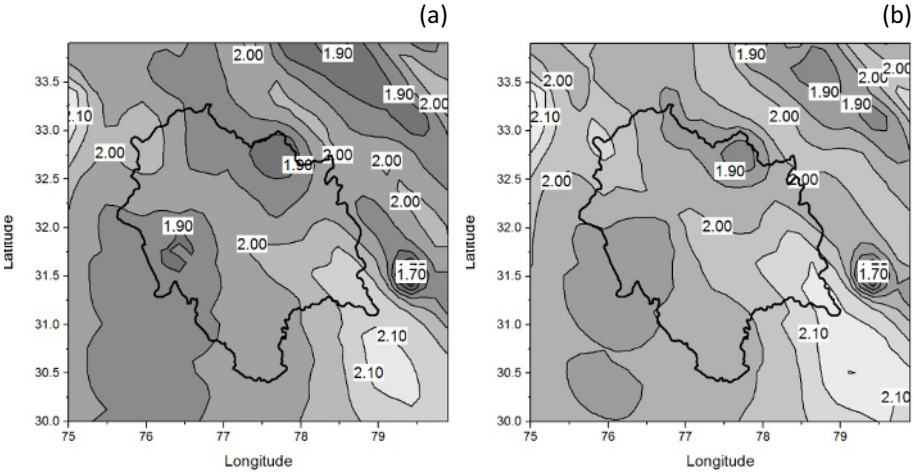


Fig. 24. Spatial variation of the MCE/DBE ratio of PGA values at class C (a) and class D (b) sites for 2475 year return period.

Similarly, it will be interesting to see the scaling of the hazard levels due to local site conditions. In this study region, it is observed that, on an average, the PGA values of the class D sites were 6.7 and 7.75% more than the class C sites for 475 and 2475 years return periods, respectively. For the $Sa\,(0.2\ s)$ and $Sa\,(1.0\ s)$, the increase in the value from class C to D was estimated as 6.5 and 5.7% for 475 years return period, while it was estimated to be 7.3 and 6.6% for 2475 years return period. Hence, the spectral acceleration coefficient used to account for the site effects in the Indian codal provisions, which is taken as 1 for scaling the PGA values for different soil types, is not appropriate.

Therefore, with the help of these contour plots, it is possible to construct a 5% damped design response spectrum for class C and D sites located within this region for the return periods of 475 and 2475 years with the help of the two parameters, $Sa\,(0.2\ s)$ and $Sa\,(1.0\ s)$, using the methodology presented in IBC (2009).

## 7. SUMMARY AND CONCLUSIONS

The increase in population and development activities in the seismically vulnerable regions of Himachal Pradesh (HP) necessitates a robust estimation of the regional seismic hazard. This article presents state of the art hazard maps for this region with due consideration of the active seismicity, the regional geology and the local site effects. In this paper, the probabilistic seismic hazard analysis of this region has been carried out using the Cornell–McGuire approach. An updated catalogue containing event records from

25-2013 A.D. has been used to characterize the source level seismicity of all the probable 301 faults that are presently identified in and around this region. In the companion paper, regional site-specific ground motion relations have been developed for C and D type sites in the two geological regions of HP. These relations are used to compute the surface-level spectral hazard curves for the important cities in Himachal Pradesh. From these seismic hazard curves, the site-specific uniform hazard response spectra for twelve important cities have been presented for 475 and 2475 year return periods.

Also, the contour maps of three ground motion parameters, namely, peak ground acceleration (PGA), short period $Sa(0.2\ s)$ and long period $Sa(1.0\ s)$ spectral acceleration, are presented for this region. The comparison of the present estimates with the recent hazards estimates by NDMA (2011) and Patil *et al.* (2014) highlights the need to consider the local site variability in the hazard computation. Also, the regions surrounding the city of Bilaspur and Chamba were found to have much higher seismic hazard levels than previously reported. The estimated hazard values for these regions highlight that the zonal spectral values are underestimated in the Indian codal provisions. Hence, the maps developed in this study using a detailed probabilistic framework are more reliable and can be used for the seismic design of new structures in HP and also for assessing the seismic vulnerability of the existing structures. The obtained hazard curves combined with UHRS can be used to construct risk maps for HP.

In the present scenario with the limited amount of ground motion data available for this seismically active region, the estimates presented in this study should be the most practical estimates of surface hazard available for this region so far. However, the hazard estimates should become more reliable as more ground motion data become available in the future. Also, there is a need for estimating the seismic hazard of this region in terms of other ground motion parameters such as spectral velocity, spectral displacements, *etc*., which are necessary for the performance based design of structures.

## References

Ambraseys, N., and R. Bilham (2000), A note on the Kangra $M_s = 7.8$ earthquake of 4 April 1905, *Curr. Sci. India* **79**, 1, 45-50.

Ambraseys, N., and D. Jackson (2003), A note on the early earthquakes in northern India and southern Tibet, *Curr. Sci. India* **84**, 4, 570-582.

Bansal, B.K., and M. Verma (2013), Science and technology based earthquake risk reduction strategies: The Indian scenario, *Acta Geophys*. **61**, 4, 808-821, DOI: 10.2478/s11600-013-0105-5.

Bhatia, S.C., R.M. Kumar, and H.K. Gupta (1999), A probabilistic seismic hazard map of India and adjoining regions, *Ann. Geophys*. **42**, 6, 1153-1164, DOI: 10.4401/ag-3777.

Bilham, R., S. Lodi, S. Hough, S. Bukhary, A.M. Khan, and S.F.A. Rafeeqi (2007), Seismic hazard in Karachi, Pakistan: Uncertain past, uncertain future, *Seismol. Res. Lett*. **78**, 6, 601-631, DOI: 10.1785/gssrl.78.6.601.

Census (1991), Census of India 1991, Directorate of Census Operations, Himachal Pradesh, India.

Census (2011), Census of India 2011, Directorate of Census Operations, Himachal Pradesh, India.

Chandel, V.B.S., and K.K. Brar (2010), Seismicity and vulnerability in Himalayas: the case of Himachal Pradesh, India, *Geomat. Nat. Hazard. Risk* **1**, 1, 69-84, DOI: 10.1080/19475701003643441.

Cornell, C.A. (1968), Engineering seismic risk analysis, *Bull. Seismol. Soc. Am*. **58**, 5, 1583-1606.

Department of Planning (2003), An overview of planning in Himachal Pradesh, Planning Department, State Government of Himachal Pradesh, India.

Der Kiureghian, A., and A.H.S. Ang (1977), A fault-rupture model for seismic risk analysis, *Bull. Seismol. Soc. Am.* **67**, 4, 1173-1194.

Gardner, J.K., and L. Knopoff (1974), Is the sequence of earthquakes in southern California, with aftershocks removed, Poissonian? *Bull. Seismol. Soc. Am.* **64**, 5, 1363-1367.

GSI (2000), *Seismotectonic Atlas of India and its Environs*, Geological Survey of India, Bangalore, India.

IBC (2009), International Building Code, International Code Council, International Seismological Centre (ISC), Thatcham, United Kingdom, on-line bulletin, available from http://www.isc.ac.uk.

IS:1893 (2002), Criteria for earthquake resistant design of structures: Part 1 – General provisions and buildings, Bureau of Indian Standards (BIS), New Delhi, India.

Iyengar, R.N., and S. Ghosh (2004), Microzonation of earthquake hazard in Greater Delhi area, *Curr. Sci. India* **87**, 9, 1193-1202.

Iyengar, R.N., D. Sharma, and J.M. Siddiqui (1999), Earthquake history of India in medieval times, *Indian J. History Sci*. **34**, 3.

Karan, P.P. (1966), Geographic regions of the Himalayas, *Bull. Tibetology* **3**, 5-26.

Khattri, K.N., A.M. Rogers, D.M. Perkins, and S.T. Algermissen (1984), A seismic hazard map of India and adjacent areas, *Tectonophysics* **108**, 1-2, 93-134, DOI: 10.1016/0040-1951(84)90156-2.

Kijko, A. (2004), Estimation of the maximum earthquake magnitude, $m_{max}$, *Pure Appl. Geophys*. **161**, 8, 1655-1681, DOI: 10.1007/s00024-004-2531-4.

Kijko, A., and G. Graham (1998), Parametric-historic procedure for probabilistic seismic hazard analysis: Part I: Estimation of maximum regional magnitude $M_{max}$, *Pure Appl. Geophys*. **152**, 3, 413-442, DOI: 10.1007/s000240050161.

Knopoff, L., and Y. Kagan (1977), Analysis of the theory of extremes as applied to earthquake problems, *J. Geophys. Res*. **82**, 36, 5647-5657, DOI: 10.1029/JB082i036p05647.

Kramer, S.L. (1996), *Geotechnical Earthquake Engineering*, Pearson Education, 672 pp.

Kumar, S., S.G. Wesnousky, T.K. Rockwell, D. Ragona, V.C. Thakur, and G.G. Seitz (2001), Earthquake reccurrence and rupture dynamics of Himalayan Frontal Thrust, India, *Science* **294**, 5550, 2328-2331, DOI: 10.1126/science.1066195.

Lave, J., D. Yule, S. Sapkota, K. Basant, C. Madden, M. Attal, and R. Pandey (2005), Evidence for a great medieval earthquake (~1100 A.D.) in the Central Himalayas, Nepal, *Science* **307**, 5713, 1302-1305, DOI: 10.1126/science.1104804.

Mahajan, A.K., V.C. Thakur, M.L. Sharma, and M. Chauhan (2010), Probabilistic seismic hazard map of NW Himalaya and its adjoining area, India, *Nat. Hazards* **53**, 3, 443-457, DOI: 10.1007/s11069-009-9439-3.

McGuire, R.K. (1976), FORTRAN computer program for seismic risk analysis, Open-file Report 76-67, U.S. Geological Survey, Denver, USA.

Milne, J. (1911), A catalogue of destructive earthquakes: A.D. 7 to A.D. 1899, British Association for the Advancement of Science, London, UK, 92 pp.

Montessus de Ballore, F. (1911), The seismic phenomena in British India and their connection with its geology, *Mem. Geol. Surv. India* **35**, part 3 (reprint).

Muthuganeisan, P., and S.T.G. Raghukanth (2016), Site-specific probabilistic seismic hazard map of Himachal Pradesh, India. Part I. Site-specific ground motion relations, *Acta Geophys*. **64**, 2, 336-361, DOI: 10.1515/acgeo-2016-0010

NDMA (2011), Development of probabilistic seismic hazard map of India, Tech. Report of the Working Committee of Experts (WCE), National Disaster Management Authority (NDMA), Govt. of India, New Delhi, India.

Oldham, T. (1883), Catalogue of Indian earthquakes from the earliest times to the end of 1869, *Mem. Geol. Surv. India* **19**, 3, 1-53.

Parvez, I.A., F. Vaccari, and G.F. Panza (2003), A deterministic seismic hazard map of India and adjacent areas, *Geophys. J. Int*. **155**, 2, 489-508, DOI: 10.1046/j.1365-246X.2003.02052.x.

Patil, N.S., J. Das, A. Kumar, M.M. Rout, and R. Das (2014), Probabilistic seismic hazard assessment of Himachal Pradesh and adjoining regions, *J. Earth Syst. Sci*. **123**, 1, 49-62, DOI: 10.1007/s12040-013-0378-8.

PMD (2007), Seismic hazard analysis and zonation for Pakistan, Azad-Jammu and Kashmir, Pakistan Meteorological Department (PMD), Pakistan and NORSAR, Norway.

Prabhu, M., and S.T.G. Raghukanth (2014), Development of surface level probabilistic seismic hazard map of Himachal Pradesh. **In:** *Proc. 9th Structural Engineers Convention (SEC 2014), 22-24 December 2014*, Indian Institute of Technology, Delhi, India.

Quittmeyer, R.C., and K.H. Jacob (1979), Historical and modern seismicity of Pakistan, Afghanistan, northwestern India, and southeastern Iran, *Bull. Seismol. Soc. Am.* **69**, 3, 773-823.

Raghukanth, S.T.G. (2011), Seismicity parameters for important urban agglomerations in India, *Bull. Earthq. Eng.* **9**, 5, 1361-1386, DOI: 10.1007/s10518-011-9265-3.

Stepp, J.C. (1972), Analysis of completeness of the earthquake sample in the Puget sound area and its effect on statistical estimates of earthquake hazard. **In:** *Proc. 1st Int. Conf. on Microzonation, Seattle, USA*, Vol. 2, 897-909.

Uhrhammer, R.A. (1986), Characteristics of northern and central California seismicity, *Earthq. Notes* **57**, 1, 21.

USNRC (1997), USNRC Regulatory Guide 1.165: Identification and characterization of seismic sources and determination of safe shutdown earthquake ground motion, Unites States Nuclear Regulatory Commission, Washington D.C., USA.

Valdiya, K.S. (1976), Himalayan transverse faults and folds and their parallelism with subsurface structures of North Indian plains, *Tectonophysics* **32**, 3-4, 353-386, DOI: 10.1016/0040-1951(76)90069-X.

Valdiya, K.S. (2002), Emergence and evolution of Himalaya: reconstructing history in the light of recent studies, *Prog. Phys. Geog.* **26**, 3, 360-399, DOI: 10.1191/0309133302pp342ra.

Wells, D.L., and K.J. Coppersmith (1994), New empirical relationships among magnitude, rupture length, rupture width, rupture area, and surface displacement, *Bull. Seismol. Soc. Am.* **84**, 4, 974-1002.

Received 16 September 2014
Received in revised form 27 March 2015
Accepted 10 April 2015

DE GRUYTER OPEN

**Acta Geophysica**
vol. 64, no. 4, Aug. 2016, pp. 885-903
DOI: 10.1515/acgeo-2016-0037

# Scaling Analysis of Time Distribution between Successive Earthquakes in Aftershock Sequences

Elisaveta MAREKOVA

Plovdiv University "Paisiy Hilendarski", Plovdiv, Bulgaria
e-mail: eligeo@uni-plovdiv.bg

A b s t r a c t

The earthquake inter-event time distribution is studied, using catalogs for different recent aftershock sequences. For aftershock sequences following the Modified Omori's Formula (MOF) it seems clear that the inter-event distribution is a power law. The parameters of this law are defined and they prove to be higher than the calculated value $(2 - 1/p)$. Based on the analysis of the catalogs, it is determined that the probability densities of the inter-event time distribution collapse into a single master curve when the data is rescaled with instantaneous intensity, $R(t; M_{th})$, defined by MOF. The curve is approximated by a gamma distribution. The collapse of the data provides a clear view of aftershock-occurrence self-similarity.

**Key words:** earthquakes, aftershocks, Omori's law, inter-event time distribution, self-similarity.

## 1. INTRODUCTION

In seismology the distribution of the basic earthquake quantities is the most often studied; these include magnitude, time of occurrence, and localization. The simplest description of seismicity is as a point process in space, time and energy (or magnitude). At present, the distribution of derivative quantities such as times and distances between successive events is also studied

Ownership: Institute of Geophysics, Polish Academy of Sciences;
© 2016 Marekova. This is an open access article distributed under the Creative Commons Attribution-NonCommercial-NoDerivs license,
http://creativecommons.org/licenses/by-nc-nd/3.0/.

with increasing interest and ambition to understand the spatial and temporal complexity of the earthquake realization and interaction.

Nowadays, the attention paid to the statistics of the inter-event time (also called waiting time, interoccurrence time, *etc*.) between the consecutive earthquakes is continuously growing (Bak *et al.* 2002, Corral 2004a, b, 2005; Talbi and Yamazaki 2009, Lippiello *et al.* 2012, Davidsen and Kwiatek 2013).

Bak *et al.* (2002) studied the distribution of the inter-event times $\Delta t$ between successive earthquakes for all earthquakes in different regions, by putting all events on the same footing (no distinction between mainshocks and aftershocks), therefore considering seismicity as a unique process.

After that, Corral (2004a, 2005) showed that under certain conditions the inter-event times in each region follow a specific probabilistic distribution, which is universal, *i.e*., it depends neither on the geographic region nor on the mean seismic activity rate. This distribution can be written in the following form:

$$D\left(\Delta t, M_{th}\right) = R\left(M_{th}\right) f\left(R\left(M_{th}\right)\Delta t\right) \ , \tag{1}$$

where $D(\Delta t; M_{th})$ is the inter-event time probability density, $R(M_{th})$ is the mean seismic rate, defined as the number of earthquakes per unit time, and $M_{th}$ is the minimum magnitude threshold included in the analysis. It should be noted that $R(M_{th})$ controls the scale of $D(\Delta t; M_{th})$, but not its shape. The latter is defined by the scaling function *f*. In his studies Corral has shown that for stationary seismicity, *i.e*., when $R(M_{th})$ is almost constant in time, the scaling function *f* well approximates with a gamma distribution:

$$f\left(x\right) \propto \frac{1}{x^{1-\gamma}} e^{-x/a} \ , \tag{2}$$

where $x \equiv R.\Delta t$; $\gamma$ and $a$ are parameters. For a stationary case the best fit gives a value of approximately 0.7 for the parameter $\gamma$ (Corral 2004b, 2005; Marekova 2012).

The validity of Eq. 2 has also been examined for non-stationary periods (Corral 2006a), Omori sequences (Shcherbakov *et al.* 2005, Bottiglieri *et al.* 2010), volcanic earthquakes (Bottiglieri *et al.* 2009a), and even picoseismicity (Davidsen and Kwiatek 2013). Talbi *et al*. (2013) used the analysis of the inter-event times to suggest a new measure of earthquake clustering. This can be used as a procedure for declustering catalogs.

All studies so far have demonstrated that the analysis of inter-event times gives important insight into the physical mechanisms of the earthquake process.

The existence of earthquake sequences (foreshocks, aftershocks, and swarms/clusters) considerably complicates the picture in terms of modelling the distribution of the events in time. A lot of attention is paid to the aftershock sequences, since they are the obvious manifestation of dependent events, following the main earthquake. The assumption for a Poisson distribution with intensity, different from constant, is basic in studying the aftershock activity (Utsu 2002). The decrease in this activity is most frequently approximated by the Modified Omori's Formula (MOF) (Utsu 2002):

$$n(t) = \frac{K}{(t+c)^p} \ , \tag{3}$$

where $t$ is the time elapsed after the main shock; $K$, $c$, and $p$ are constants.

The Japanese seismologist Tomoda (1954) stated that the time intervals $\tau$ between successive shocks in two aftershock sequences – 1927 Tango and 1948 Fukui – had the following type of distribution:

$$f(\tau) = k\tau^{-q} \ , \tag{4}$$

where $k$ and $q$ are constants. When the aftershock sequences are presented as a non-stationary Poisson process, whose intensity can be written in the form

$$n(t) = \frac{K}{t^p} \ , \tag{5}$$

then, for the above-mentioned sequences, the value of $q$ is 1.23 and 1.48, respectively.

In this case another Japanese seismologist, Senshu (1959), showed that the distribution 4 is obtained directly from Eq. 3 and the relation between $p$ and $q$ has to be:

$$q = 2 - \frac{1}{p} \ . \tag{6}$$

The inter-event time distribution is analyzed for aftershock sequences of certain strong contemporary earthquakes in California: the *M*7.3 Landers, the *M*6.7 Hector Mine, and the *M*7.1 Northridge (Shcherbakov *et al.* 2005). When considering sequences with different magnitude thresholds within one and the same aftershock sequence, rescaling leads to collapse of data in accordance with Eq. 2, wherein $f$ follows a power law with exponent $(2 - 1/p \approx 1)$, followed by an exponential cutoff.

Relation 6 was also obtained by Jonsdottir *et al*. (2006), Lindman (2009) and Shcherbakov *et al*. (2006) in an analytical way, based on the proposition that the aftershock sequences can be regarded as a Poisson process with in-

stantaneous intensity, defined on the basis of the Modified Omori's law at the considered moment $t$.

A number of studies have focused on the Modified Omori's Formula inter-event time probability density distributions (Utsu 1971, Utsu *et al*. 1995, Jonsdottir *et al*. 2006, Lindman 2009). They all have shown that individual aftershock sequences are characterized by a power law distribution of the intermediate inter-event times. Jonsdottir *et al*. (2006) analytically and numerically demonstrated that, by catalog incompleteness immediately after the main shock, the probability density distribution of the inter-event times is roughly constant for very short times (*i.e*., for $\Delta t < c$), while a power law decay dominates for $\Delta t < c$. For the longest inter-event times, a fall-off related to the finiteness of the considered time window is observed.

The present work investigates the temporal organization of the aftershock occurrence. The analysis is also focused on the inter-event time distributions. Formula 4 is used, giving the distribution of the inter-event times as a power law. The parameters of this power law are defined for the studied aftershock sequences and it is established that they are higher than the calculated value $(2 - 1/p)$.

The inter-event time distributions evaluated for the different main shock magnitudes collapse onto a single master curve when the inter-event time is rescaled with instantaneous intensity $R(t; M_{th})$, defined by the MOF. This implies that the aftershock temporal organization is independent of the main shock magnitude $M_{ms}$. The curve is approximated by a gamma distribution. The collapse of the data provides a clear illustration of aftershock-occurrence self-similarity. This result suggests again the existence of a universal mechanism for aftershock generation.

## 2. DATA

Aftershock sequences of relatively strong earthquakes are studied in the present paper. The data has been taken from California, Alaska, Canada, and Europe, from chosen seismic catalogs, on which detailed studies related to their completeness and homogeneity are focused. The identification of aftershock sequences is a complex problem which requires assumptions on the spatial and temporal clustering of aftershocks (see van Stiphout *et al*. 2012 for a complete review, Talbi *et al*. 2013). In this work it is assumed that all events which have occurred after a main shock within a given time interval $T$ and a square (or polygon) area are aftershocks. The events in the spatial windows, described in Table 1, have been selected based on the published descriptions (References in Table 1). The maximum duration of the sequences is chosen to be $T_{\max} = 1$ year (where the catalog allows that).

Table 1

Spatial regions, data sources, and references about some of the studied sequences

| Earthquake | Space window | Catalog source | References |
|---|---|---|---|
| Joshua Tree | 33.75÷34.80°N;<br>116.0÷117.5°W | Advanced National Seismic System (ANSS) http://quake.geo.berkeley.edu/cnss | Jones and Helmberger 1998 |
| Big Bear | 33.5÷34.5°N;<br>116.40÷117.25°W | | |
| Landers | 34.75°N; 116.80°W<br>34.80°N; 116.50°W<br>33.85°N; 116.10°W<br>33.80°N; 116.40°W | | |
| Andreanof Island 1986 | 50 ÷ 52 °N;<br>172÷177°W | Alaska Earthquake Center (AEC) http://giseis.alaska.edu/Seis/ | Engdahl *et al*. 1989 |
| Andreanof Island 1996 | 50.50÷51.75°N;<br>175.80÷179.0°W | ANSS http://quake.geo.berkeley.edu/cnss | Kisslinger and Kikuchi 1997 |
| Hector Mine | 35.0°N; –116.0°W<br>35.0°N; –116.5°W<br>34.5°N; –116.5°W<br>34.2°N; –116.0°W | Southern California Earthquake Data Center (SCEDC) http://www.scecdc.scec.org (or http://www.ncedc.org/anss/) | Wiemer *et al*. 2002, Felzer *et al*. 2002 |
| Northridge | 34.1÷34.5°N;<br>118.3÷ 119.9°W | | Wiemer and Katsumata 1999 |
| British Columbia | 49.7 ÷ 50.9°N;<br>129.5÷130.9°W | Natural Resources Canada (now http://www.earthquakescanada.nrcan.gc.ca/index-eng.php) | Cassidy and Rogers 1995 |

The sequence of Joshua Tree earthquake is regarded as a foreshock sequence of the later Landers quake. It partially overlaps with the region of the quakes of the later Landers earthquake and therefore the end of this sequence coincides with the beginning of the Landers (Jones and Helmberger 1998).

The catalog published in an article by Stephens *et al*. (1980) is used as a data source about St. Elias sequence. One of the most striking features in the distribution of epicenters is that a relatively small number of aftershocks are localized near the epicenter of the main quake and the highest level of activity is observed about 50 km southeast from the epicenter of the main quake (Horner 1983).

It is characteristic of the Nahanni sequence that two earthquakes occurred in the region Mackenzie from the northwest territories of Canada – on 5 October 1985 ($M_S$6.6) and on 23 December 1985 ($M_S$6.9). The hypocenters

of both quakes are localized close to each other – near to the center of the aftershock region and at almost the same focal depth (Horner *et al.* 1990). The catalog is from a CD from WDC-A, Boulder, Colorado and it contains earthquakes with a magnitude $M \geq 3.0$. Only data from the first sequence to the beginning of the second sequence have been analyzed.

Part of the catalog data has been provided by colleagues or published and no further selection has been made in relation to them:

- the data on the earthquake in Strazhitza, Bulgaria, has been taken from the catalog prepared by the Geophysical Institute (now NIGGG), Bulgarian Academy of Science (Solakov and Simeonova 1993); data on the earthquake in Kresna, Bulgaria are from Ranguelov *et al*. (2001);
- short description of the sequences in Greece and Aegean has been found in Papazachos and Papazachou (1997); data about Fruili – in Zollo *et al*. (1997).

In seismology, the well-known Gutenberg–Richter (GR) law dominates the statistics of the occurrence of earthquakes. This law describes the rela-

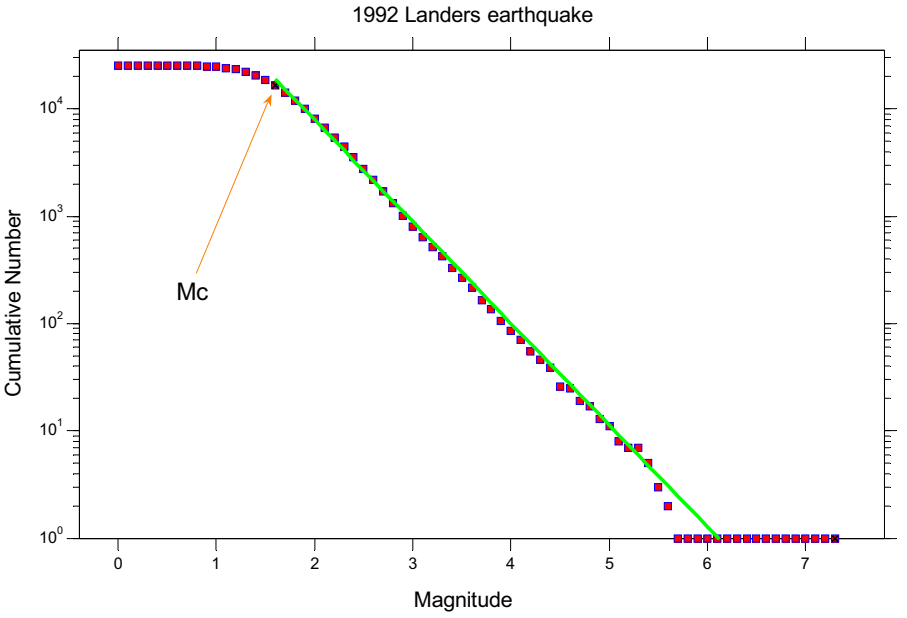


Fig. 1. Frequency-magnitude distribution of events from 1992 Landers aftershock sequence (red squares). The green line represents the best fit to the observations in the area of complete recording (indicated by $M_C$). The slope of the green line is the $b$ value of the Gutenberg and Richter relationship $\log N = a - bM$; the $a$ parameter is determined by the intercept of the green line with the Y axis in the point where the magnitude equals zero.

Table 2

Description of the studied aftershock sequences

| Earthquake | Date | Period | $M_{ms}$ | $M_{th}$ | Number of events | $H$ [km] |
|---|---|---|---|---|---|---|
| St. Elias, Canada | 28 Feb 1979 | 28 Feb 1979 – 30 Mar 1979 | 7.1 | 3.0 | 174 | 0-19 |
| Joshua Tree, California | 23 Apr 1992 | 23 Apr 1992 – 28 Jun 1992 | 6.1 | 3.0 | 234 | 0-18 |
| Landers, California | 28 Jun 1992 | 28 Jun 1992 – 28 Jul 1993 | 7.3 | 3.0 | 783 | 0-20 |
| Big Bear, California | 28 Jun 1992 | 28 Jun 1992 – 8 Jun 1993 | 6.4 | 3.0 | 404 | 0-20 |
| Nahanni, Canada | 5 Oct 1985 | 5 Oct 1985 – 20 Dec 1985 | 6.6 | 3.1 | 167 | 6-10 |
| Andreanof Island ‘86, Alaska | 7 May 1986 | 7 May 1986 – 6 Apr 1987 | 8.0 | 4.8 | 206 | 18-67 |
| Andreanof Island ‘96, Alaska | 10 Jun 1996 | 10 Jun 1996 – 23 May 1997 | 7.7 | 4.5 | 137 | 10-60 |
| Aegean ‘81 | 19 Dec 1981 | 19 Dec 1981 – 14 Dec 1982 | 7.2 | 3.2 | 244 | 0-35 |
| Aegean ‘82 | 18 Jan 1982 | 18 Jan 1982 – 30 Sep 1982 | 6.9 | 3.5 | 75 | 0-72 |
| Aegean ‘83 | 6 Aug 1983 | 6 Aug 1983 – 12 Jun 1984 | 6.9 | 3.6 | 100 | 1-47 |
| Albania | 15 Apr 1979 | 15 Apr 1979 – 10 Oct 1979 | 7.2 | 3.0 | 461 | 0-22 |
| Strazhitza, Bulgaria | 7 Dec 1986 | 7 Dec 1986 – 11 May 1987 | 5.7 | 2.0 | 123 | 0-25 |
| Kresna, Bulgaria | 4 Apr 1904 | 6 Apr 2004 – 29 Mar 2005 | 7.8 | 2.7 | 1224 | 0-50 |
| British Columbia, Canada | 6 Apr 1992 | 6 Apr 1992 – 24 Mar 1993 | 6.8 | 2.7 | 59 | 0-10 |
| Hector Mine, California | 16 Oct 1999 | 16 Oct 1999 – 1 Nov 2000 | 7.1 | 3.0 | 529 | 0-18 |
| Northridge, California | 17 Jan 1994 | 17 Jan 1994 – 16 Jan 1995 | 6.7 | 3.0 | 439 | 0-23 |
| Greece ‘81 | 24 Feb 1981 | 24 Dec 1981 – 25 Feb 1982 | 6.6 | 3.2 | 547 | 0-47 |
| Greece ‘83 | 17 Jan 1983 | 17 Jan 1983 – 13 Jan 1984 | 7.0 | 3.6 | 324 | 0-58 |
| Friuli, Italy | 6 May 1976 | 6 May 1976 – 3 Apr 1977 | 6.5 | 3.0 | 276 | 0-58 |

**Note:** $M_{ms}$ is the main earthquake magnitude, $M_{th}$ is the chosen threshold magnitude, and $H$ is the depth interval for the earthquakes in the sequences.

tionship between the frequency of occurrence and the magnitude of the earthquakes (Gutenberg and Richter 1944):

$$\log_{10} N = a - bM \ , \tag{7}$$

where $N$ is the number of the earthquakes having magnitudes higher than $M$, and $a$ and $b$ are constants.

$M_C$ is the magnitude at which the data departs from the linear trend (Fig. 1) and denoted the magnitude of completeness – a threshold above which all the events in the time-space window can be assumed as having been recorded.

A common practice when studying earthquake sequences is analyzing the GR law. For this purpose, in the present article, the Zmap software (Wiemer 2001) has been used. Zmap calculates the $b$ value and the standard deviation using the maximum-likelihood method. The estimate of the $b$ value based on the mean magnitude (Aki 1965) is as follows:

$$b = \frac{0.4343}{\bar{M} - M_{\min}} \ , \tag{8}$$

where $\bar{M}$ is the mean value of all magnitudes within the selected ranges ($M \geq M_{\min}$). The program Zmap also uses the maximum of the derivative of the frequency magnitude distribution to estimate $M_C$ (Wiemer 2001).

Figure 1 illustrates the frequency-magnitude distribution for Landers aftershocks sequence. The magnitudes of completeness $M_C$ for all studied aftershock sequences vary from 1.5 to 4.8. The chosen threshold magnitudes $M_{th}$, at which the aftershock sequences are studied are given in Table 2. It must be noted that in most cases the chosen thresholds $M_{th}$ equal the magnitudes of completeness $M_C$. The values of $M_C$ are lower only for the California earthquakes – Joshua Tree, Landers, Big Bear, Northridge, as well as British Columbia and Kresna earthquakes.

## 3. METHODOLOGY

The main objective of this work is the study and analysis of the distribution of time intervals between earthquakes from different aftershock sequences.

The pairs of earthquakes are formed by taking only the intervals of time $\Delta t$ between the successive earthquakes. Thus, if the number of events is $N$, then $(N-1)$ time differences are formed. Inter-event times are most often presented using histogram plots of the inter-event times probability distribution. In the present analysis, a histogram of the count using successive bins that are increasing in length is made. One could work with the logarithm of $\Delta t$ but a more direct possibility is to define the bins over which the count is calculated as $A*c^{n-1}$, with $c > 1$ and $n$ labeling consecutive bins. This en-

sures an appropriate bin size for each time scale ($c = 2$ and constant A = 0.001 days were assumed).

The relative frequencies $p_i^*$ for each subinterval are calculated from $p_i^* = n_i / (N-1)$, where $n_i$ is the number of values in the $i$-th subinterval, and $(N-1)$ is the total number of the time intervals used.

Such count histograms are equivalent to the statistical probability distributions (p.d.). In this work, normalized versions of the count histograms are presented, where they are divided by the length of the inter-event time intervals (bin size), as it was done by Jonsdottir *et al.* (2006). The author of this article will further use the term "Rescaled P.D." for these curves.

The function approximating the Rescaled P.D. of the inter-event times $\Delta t$ between the pairs of earthquakes has the form:

$$f(\Delta t) = a_t \, \Delta t^{-b_t} \ , \tag{9}$$

where $a_t$ and $b_t$ are parameters.

Another goal of the present work is to check whether the universal scaling law of the inter-event times distributions (Corral 2004a, 2005) is also applicable to aftershock sequences. The study of the inter-event time probability density $D(\Delta t; M_{th})$ from Eq. 1 is similar to the one described in Corral (2004b) and Marekova (2012). After a strong quake, sequences of weaker earthquakes follow, gradually decreasing with time. Thus, the analysis of the non-stationary seismicity can be generalized by replacing the average intensity $R(M_{th})$ by an instantaneous intensity $R(t; M_{th})$ as a scaling parameter in Eq. 1. The decrease in activity after the main shock can be described by an equation of the type:

$$R\left(t; M_{th}\right) = \frac{K}{\left(c+t\right)^p} \ . \tag{10}$$

The rescaled dimensionless time $\theta_i$ is obtained in the following way:

$$\theta_i = R\left(\Delta t_i; M_{th}\right) \Delta t_i \ . \tag{11}$$

As it was done by Corral (2006b), the results from fitting the real data with Eq. 10 for each sequence were also used here.

## 4. RESULTS AND DISCUSSION

The probability distributions of the time intervals (Fig. 2a) and the Rescaled probability distributions (Fig. 2b) for the studied aftershock sequences are obtained. The Rescaled P.D. are similar, as can be seen from Fig. 2b.

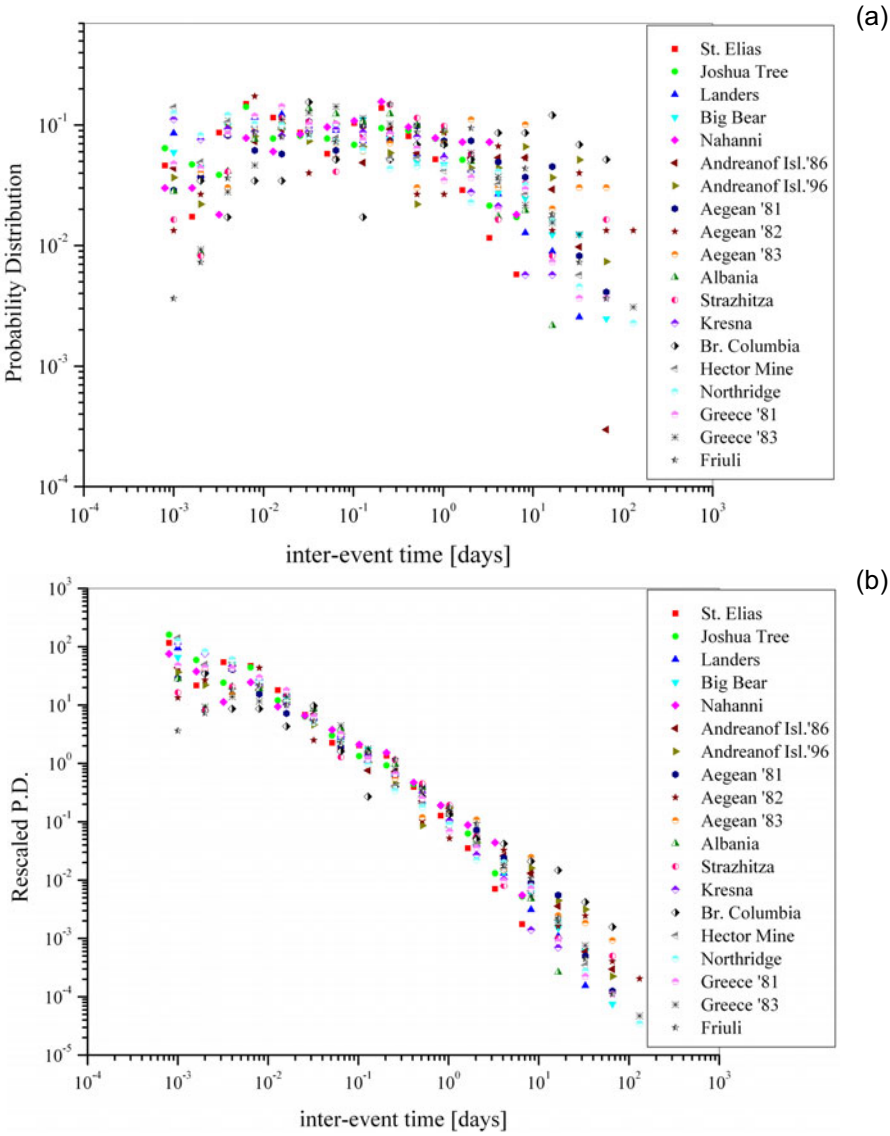


Fig. 2: (a) Probability distribution of the time intervals between successive events for the aftershock sequences, (b) Rescaled probability distributions (P.D.) for the same sequences.

Besides, for all sequences the following parameters are calculated: $p$, $c$, $K$ from MOF Eq. 3, and $a_t$, $b_t$ from the function 9, approximating the Rescaled P.D. They are presented in Table 3. The estimates for the model parameters of MOF are obtained by using the program Zmap.

Table 3

Parameters $a_t$ and $b_t$ of the approximating function 9 for the distributions of the inter-event times between the pairs of earthquakes for the studied aftershock sequences and parameters $p$, $c$, $K$ of the Modified Omori's Formula (Eq. 3)

| Earthquake | $a_t$ | $b_t$ | $p$ | $c$ | $K$ |
|---|---|---|---|---|---|
| St. Elias, Canada | 0.060 (±0.104) | 1.322 (±0.078) | 0.91 (±0.06) | 0.018 (±0.013) | 23.86 (±2.43) |
| Joshua Tree, California | 0.096 (±0.087) | 1.084 (±0.052) | 0.94 (±0.05) | 0.047 (±0.026) | 31.07 (±3.58) |
| Landers, California | 0.061 (±0.071) | 1.343 (±0.055) | 1.22 (±0.03) | 0.787 (±0.147) | 220.72 (±29.01) |
| Big Bear, California | 0.067 (±0.062) | 1.312 (±0.046) | 1.05 (±0.03) | 0.165 (±0.054) | 56.42 (±6.57) |
| Nahanni, Canada | 0.129 (±0.083) | 1.110 (±0.071) | 0.92 (±0.06) | 0.114 (±0.075) | 34.60 (±5.43) |
| Andreanof Island '86, Alaska | 0.089 (±0.056) | 1.183 (±0.042) | 0.90 (±0.03) | 0.005 (±0.006) | 18.53 (±1.85) |
| Andreanof Island '96, Alaska | 0.097 (±0.061) | 1.115 (±0.046) | 0.90 (±0.03) | 0.005 (±0.010) | 13.40 (±1.65) |
| Aegean '81 | 0.085 (±0.060) | 1.205 (±0.060) | 0.91 (±0.03) | 0.020 (±0.015) | 22.65 (±2.45) |
| Aegean '82 | 0.086 (±0.056) | 1.188 (±0.040) | 1.12 (±0.07) | 0.032 (±0.022) | 9.09 (±1.60) |
| Aegean '83 | 0.110 (±0.055) | 1.133 (±0.045) | 0.98 (±0.05) | 0.008 (±0.016) | 10.15 (±1.56) |
| Albania | 0.070 (±0.125) | 1.282 (±0.099) | 1.05 (±0.07) | 1.822 (±0.654) | 114.96 (±32.90) |
| Strazica, Bulgaria | 0.090 (±0.101) | 1.180 (±0.079) | 1.19 (±0.10) | 0.399 (±0.212) | 28.74 (±8.57) |
| Kresna, Bulgaria | 0.585 (±0.085) | 1.278 (±0.060) | 0.93 (±0.01) | 0.070 (±0.016) | 124.70 (±7.04) |
| British Columbia, Canada | 0.117 (±0.061) | 0.901 (±0.042) | 0.63 (±0.05) | 0.000 (±0.009) | 2.67 (±0.63) |
| Hector Mine, California | 0.071 (±0.042) | 1.256 (±0.033) | 1.20 (±0.04) | 0.249 (±0.057) | 104.02 (±11.68) |
| Northridge, California | 0.066 (±0.050) | 1.269 (±0.039) | 1.20 (±0.03) | 0.137 (±0.031) | 80.28 (±7.74) |
| Greece '81 | 0.059 (±0.061) | 1.360 (±0.046) | 1.30 (±0.05) | 1.314 (±0.275) | 222.61 (±41.49) |
| Greece '83 | 0.105 (±0.042) | 1.322 (±0.040) | 1.14 (±0.07) | 3.008 (±1.066) | 106.70 (±35.95) |
| Friuli, Italy | 0.088 (±0.084) | 1.289 (±0.069) | 0.67 (±0.03) | 0.000 (±0.022) | 13.91 (±1.77) |

**Note:** The time taken into account in calculating the seismic activity is measured in days.

It should be noted that when rescaling P.D., deviation from the model line Eq. 9 is observed for almost all sequences at the short time intervals. Therefore, in the present work inter-event times of less than 0.002 days are discarded from the analysis. When calculating the parameters of Eq. 9 the distributions have been used without these values. Talbi and Yamazaki (2009) suggested a formula for inter-event time cutoff, but the values the formula determines exceed the chosen value leading to poor statistics significantly.

Examining whether there existed a relation of the type Eq. 6 between parameters $p$ (from the Omori law) and $b_t$ (from Eq. 9) it was proved that such a relation was not present. The results show that the obtained values for the parameter $b_t$ are a little bit higher than the ones defined by relation 6 (Fig. 3).

The differences between the calculated $q$ values and the values obtained from Eq. 6, were also discussed by Utsu (1971) and Utsu *et al*. (1995). The reasons for the difference between the theoretic relation 6 and the observed values of the $b_t$ parameters can be various. When describing intensity decrease of the aftershocks, the Modified Omori's Formula (MOF) is not observed in all sequences. The decrease of the aftershock activity is better described for some sequences by the models ETAS (Ogata 1988) or RETAS

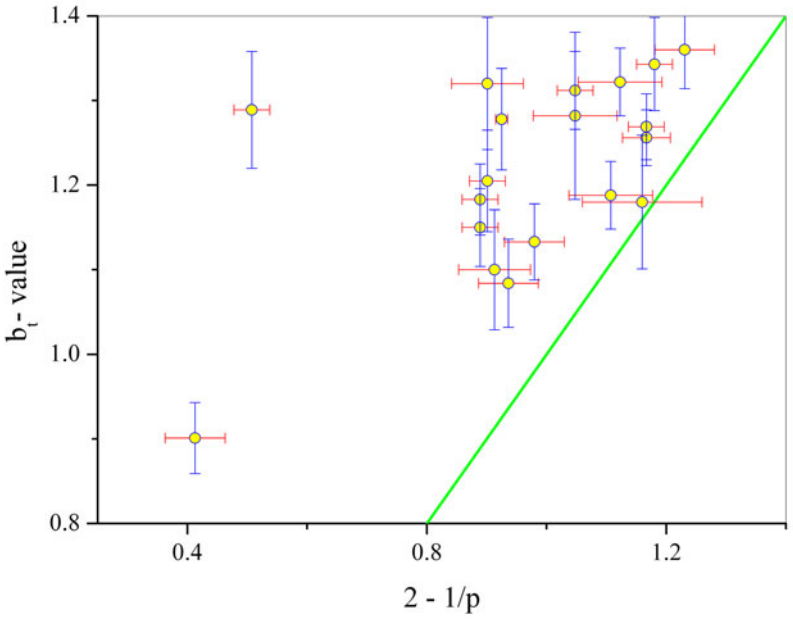


Fig. 3. Comparison between the values of $b_t$ defined based on the real data, and the calculated values $(2 - 1/p)$ from Eq. 6. The green line corresponds to the case when the two parameters are equal.

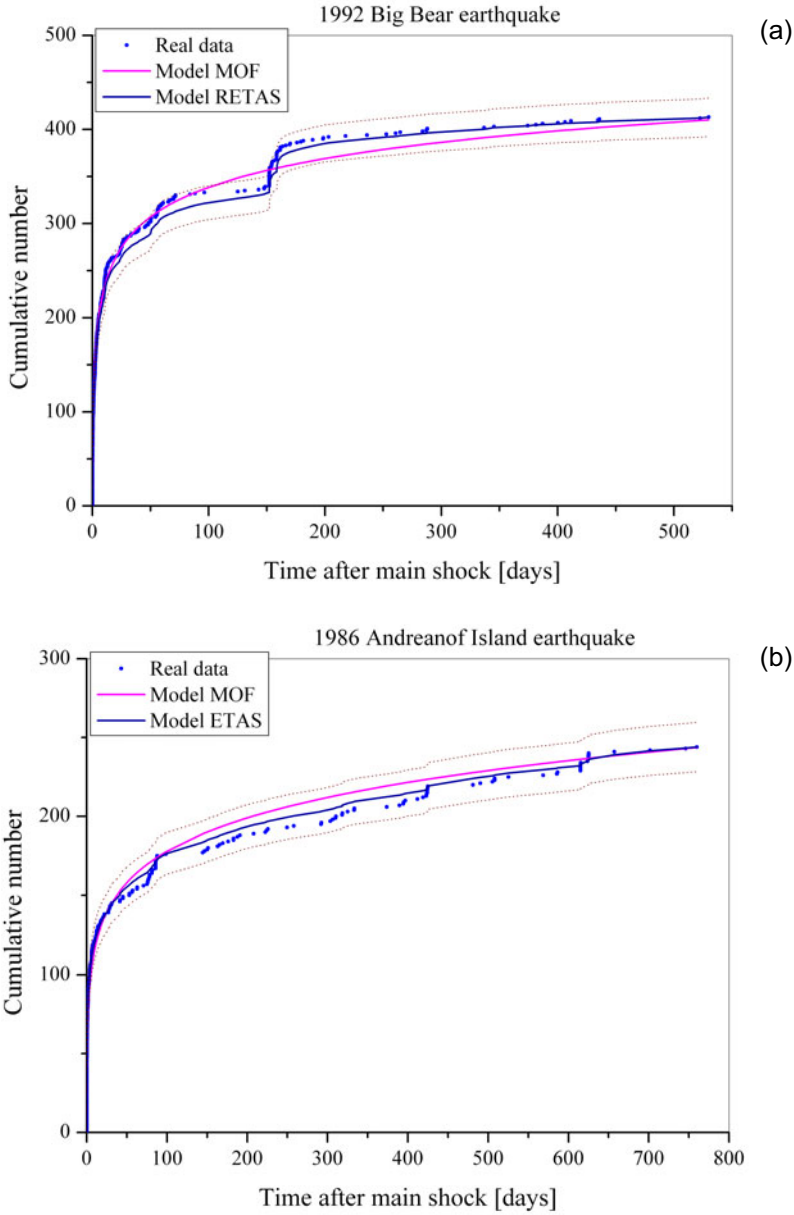


Fig. 4. Real cumulative number of events in time (blue points), calculated expected cumulative number (thick red line) according to the model from the Modified Omori's Formula (MOF) and calculated standard deviation from the model used to present the error in defining the model number (dotted line). The lines of the model RETAS or ETAS are also shown for the sequences (thick blue line).

(Gospodinov and Rotondi 2001), as it is shown in Fig. 4. However, even if we take into account only those sequences for which the intensity decrease follows MOF, such a relation between parameters $p$ and $q$ cannot be obtained.

As it was described by Utsu (1971), the choice of duration of the aftershock sequence influences the parameter $b_t$ – it presents the slope of the straight line, which depicts Eq. 9 in a double-logarithmic scale. When considering longer duration, the slope grows. To reduce this influence, the present study uses a maximum duration of the sequences of 1 year (except for some sequences, as it was discussed above).

When defining the parameters $p$ and $b_t$, also standard errors are estimated. The errors calculated for these parameters are shown by error bars in Fig. 3.

Nowadays, the existence of the scaling behavior in Eq. 1 in models for seismic occurrence has been addressed by means of analytical and numerical investigations. A number of aftershock sequences are studied in the present work in order to show how the universal law is applied in these cases.

The probability densities of the rescaled times $\theta_i$ from Eq. 11, obtained for all sequences, are shown in Fig. 5. Although there is a certain scatter, a characteristic collapse of data in a curve is observed, similar to the cases of stationary seismicity. The obtained curve is approximated by a gamma distribution (Corral 2004a) in the form:

$$f(\theta) = a(b\theta)^{\gamma-1} \exp(-b\theta) \ , \tag{12}$$

where $a$, $b$, and $\gamma$ are the parameters whose values are:

$$a = 0.023 \pm 0.014 \ ; \quad b = 0.042 \pm 0.024 \ ; \quad \gamma = 0.449 \pm 0.086 \ .$$

The analysis used in this paper differs from those made by Corral (2005), Bottiglieri *et al*. (2009b), and Shcherbakov *et al*. (2005).

The specific thing about the present study is the mixing of the data from aftershock sequences realized in different regions. Nevertheless, the distribution curves of the rescaled inter-event times collapse in a master curve and the curve is approximated by a gamma distribution, as described by Corral (2004a, 2005, 2006b).

It should be noted that in the distributions of the rescaled inter-event time intervals a deviation in the ends of the curves is observed. The explanation can be related to the way of identification of the aftershock sequences. Due to decrease in activity, the number of long time intervals between the earthquakes goes down. Besides, the duration of the aftershock sequences depends on the magnitude of the main shock. In such an analysis the time for realization of the sequence can be chosen depending on the magnitude of the

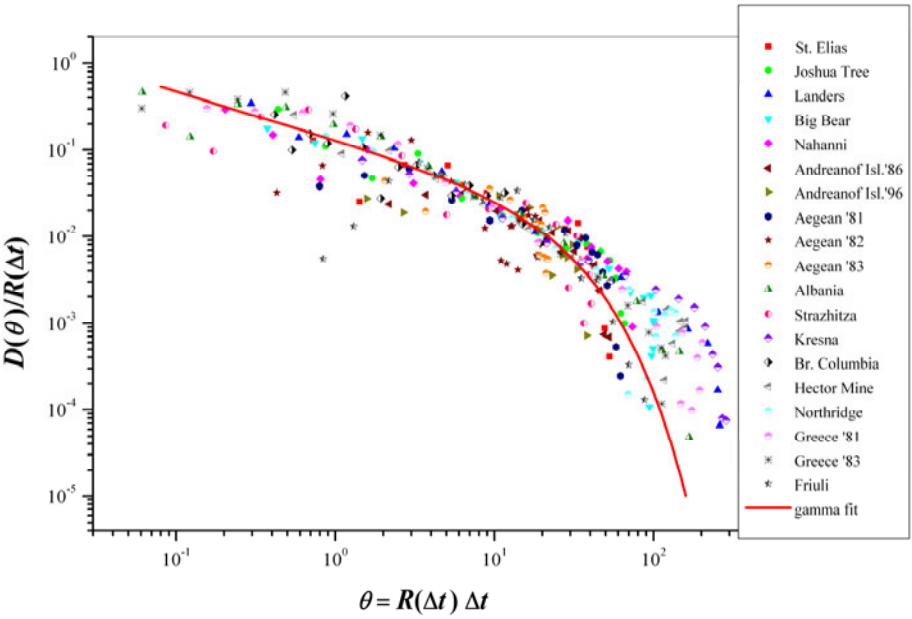


Fig. 5. Probability densities of recurrence times for the aftershock sequences listed in Table 2. The continuous red line is a gamma fit.

main event. The algorithm for defining the duration of the aftershock sequences in California was described in Bottiglieri *et al*. (2009b). According to it, for the Landers and Northridge sequences it was found that they lasted 140 and 110 days, respectively, which is much shorter than the maximum time of 1 year used in the present study.

It is a common practice to study individually main quakes and foreshocks or aftershocks. A reliable algorithm for separating the aftershocks is needed but not available yet (Talbi *et al*. 2013). Multiple seismic surveys use a number of declustering procedures based on subjective criteria to separate the observed clustering (van Stiphout *et al*. 2012).

The algorithms used for separation of the studied aftershock sequences are different and perhaps this leads to the stronger scattering of data around the model curve in Fig. 5.

## 5. CONCLUSION

The paper analyzes the scaling properties of aftershock sequences with different main shock magnitudes, realized in various regions. The study of the temporal properties of aftershocks shows that the aftershock sequences can be modeled as a point process, governed by non-homogeneous Poisson sta-

tistics. Seismic activity in this case decreases as a power dependence, what introduces a self-similar mode of occurrence.

For aftershock sequences following the Omori's law the inter-event times distribution is a power law. The results show that the power law exponents computed from the data are higher than the ones calculated theoretically from Modified Omori's Formula.

The distributions of the inter-event time intervals collapse in a master curve after rescaling by the so-called "instantaneous" intensity. This curve is approximated by a gamma distribution with exponent approximately equal to 0.45.

The probability densities of the rescaled inter-event times appear in good agreement with the results for stationary seismicity. This result suggests once again the existence of a universal mechanism for aftershock generation.

Acknowledgments. The author thanks the two anonymous reviewers whose comments helped improve the earlier version of the manuscript.

## References

Aki, K. (1965), Maximum likelihood estimate of b in the formula log n = a – bM and its confidence limits, *Bull. Earthq. Res. Inst. Tokyo* **43**, 2, 237-239.

Bak, P., K. Christensen, L. Danon, and T. Scanlon (2002), Unified scaling law for earthquakes, *Phys. Rev. Lett*. **88**, 17, 178501, DOI: 10.1103/PhysRevLett. 88.178501.

Bottiglieri, M., C. Godano, and L. D'Auria (2009a), Distribution of volcanic earthquake recurrence intervals, *J. Geophys. Res*. **114**, B10, B10309, DOI: 10.1029/2008JB005942.

Bottiglieri, M., E. Lippiello, C. Godano, and L. de Arcangelis (2009b), Identification and spatiotemporal organization of aftershocks, *J. Geophys. Res*. **114**, B3, 15-16, B03303, DOI: 10.1029/2008JB005941.

Bottiglieri, M., L. de Arcangelis, C. Godano, and E. Lippiello (2010), Multiple-time scaling and universal behavior of the earthquake interevent time distribution, *Phys. Rev. Lett.* **104**, 15, 158501, DOI: 10.1103/PhysRevLett. 104.158501.

Cassidy, J.F., and G.C. Rogers (1995), The rupture process and aftershock distribution of the 6 April 1992 $M_S$ 6.8 earthquake, Offshore British Columbia, *Bull. Seismol. Soc. Am.* **85**, 3, 716-735.

Corral, A. (2004a), Universal local versus unified global scaling laws in the statistics of seismicity, *Physica A* **340**, 4, 590-597, DOI: 10.1016/j.physa.2004.05.010.

Corral, A. (2004b), Long-term clustering, scaling, and universality in the temporal occurrence of earthquakes, *Phys. Rev. Lett.* **92**, 10, 108501, DOI: 10.1103/ PhysRevLett.92.108501.

Corral, A. (2005), Mixing of rescaled data and Bayesian inference for earthquake recurrence times, *Nonlinear Process. Geophys.* **12**, 1, 89-100.

Corral, A. (2006a), Dependence of earthquake recurrence times and independence of magnitudes on seismicity history, *Tectonophysics* **424**, 3-4, 177-193, DOI: 10.1016/j.tecto.2006.03.035.

Corral, A. (2006b), Statistical features of earthquake temporal occurrence. **In:** P. Bhattacharyya and B.K. Chakrabarti (eds.), *Modelling Critical and Catastrophic Phenomena in Geoscience: A Statistical Physics Approach*, Lecture Notes in Physics, Vol. 705, Springer, Berlin, 191-221, DOI: 10.1007/3-540-35375-5_8.

Davidsen, J., and G. Kwiatek (2013), Earthquake interevent time distribution for induced micro-, nano-, and picoseismicity, *Phys. Rev. Lett*. **110**, 6, 068501, DOI: 10.1103/PhysRevLett.110.068501.

Engdahl, E.R., S. Billington, and C. Kisslinger (1989), Teleseismically recorded seismicity before and after the May 7, 1986, Andreanof Islands, Alaska, earthquake, *J. Geophys. Res*. **94**, B11, 15481-15498, DOI: 10.1029/JB094iB11p15481.

Felzer, K.R., T.W. Becker, R.E. Abercrombie, G. Ekström, and J.R. Rice (2002), Triggering of the 1999 $M_W$ 7.1 Hector Mine earthquake by aftershocks of the 1992 $M_W$ 7.3 Landers earthquake, *J. Geophys. Res.* **107**, B9, ESE 6-1–ESE 6-13, DOI: 10.1029/2001JB000911.

Gospodinov, D., and R. Rotondi (2001), Exploratory analysis of marked Poisson processes applied to Balkan earthquake sequences, *J. Balkan Geophys. Soc.* **4**, 3, 61-68.

Gutenberg, B., and C.F. Richter (1944), Frequency of earthquakes in California, *Bull. Seismol. Soc. Am*. **34**, 4, 185-188.

Horner, R.B. (1983), Seismicity in the St. Elias region of northwestern Canada and southeastern Alaska, *Bull. Seismol. Soc. Am.* **73**, 4, 1117-1137.

Horner, R.B., R.J. Wetmiller, M. Lamontagne, and M. Plouffe (1990), A fault model for the Nahanni earthquakes from aftershock studies, *Bull. Seismol. Soc. Am.* **80**, 6A, 1553-1570.

Jones, L.E., and D. Helmberger (1998), Earthquake sourse parameters and fault kinematics in the eastern California shear zone, *Bull. Seismol. Soc. Am.* **88**, 6, 1337-1352.

Jonsdottir, K., M. Lindman, R. Roberts, B. Lund, and R. Bödvarsson (2006), Modelling fundamental waiting time distributions for earthquake se-quences, *Tectonophysics* **424**, 3-4, 195-208, DOI: 10.1016/j.tecto.2006.03. 036.

Kisslinger, C., and M. Kikuchi (1997), Aftershocks of the Andreanof Islands earthquake of June 10, 1996, and local seismotectonics, *Geophys. Res. Lett.* **24**, 15, 1883-1886, DOI: 10.1029/97GL01848.

Lindman, M. (2009), Physics of Aftershocks in the South Iceland Seismic Zone: Insights into the earthquake process from statistics and numerical modelling

of aftershock sequences, Ph.D. Thesis, Digital Comprehensive Summaries of Uppsala Dissertations from the Faculty of Science and Technology 592, Uppsala University, Uppsala, Sweden.

Lippiello, E., A. Corral, M. Bottiglieri, C. Godano, and L. de Arcangelis (2012), Scaling behavior of the earthquake intertime distribution: Influence of large shocks and time scales in the Omori law, *Phys. Rev. E* **86**, 6, 066119, DOI: 10.1103/PhysRevE.86.066119.

Marekova, E. (2012), Testing a scaling law for the earthquake recurrence time distributions, *Acta Geophys*. **60**, 3, 858-873, DOI: 10.2478/s11600-012-0007-y.

Ogata, Y. (1988), Statistical models for earthquake occurrences and residual analysis for point processes, *J. Am. Stat. Assoc*. **83**, 401, 9-27, DOI: 10.1080/01621459.1988.10478560.

Papazachos, B., and C. Papazachou (1997), *The Earthquakes of Greece*, ZITI, Thessloniki.

Ranguelov, B., S. Rizhikova, and T. Toteva (2001), *The Earthquake (M7.8) Source Zone (South-West Bulgaria)*, Acad. Publ. House "M. Drinov", 279 pp.

Senshu, T. (1959), On the time interval distribution of aftershocks, *J. Seism. Soc. Japan, Zisin Ser*. **2**, 12, 149-161 (in Japanese with English abstract).

Shcherbakov, R., G. Yakovlev, D.L. Turcotte, and J.B. Rundle (2005), Model for the distribution of aftershock interoccurrence times, *Phys. Rev. Lett.* **95**, 21, 218501, DOI: 10.1103/PhysRevLett.95.218501.

Shcherbakov, R., D.L. Turcotte, and J.B. Rundle (2006), Scaling properties of the Parkfield aftershock sequence, *Bull. Seismol. Soc. Am.* **96**, 4B, S376-384, DOI: 10.1785/0120050815.

Solakov, D., and S. Simeonova (eds.) (1993), Bulgaria, catalogue of earthquakes 1981-1990, Geophys. Inst. Bulg. Acad. Sci., Sofia, 39 pp.

Stephens, C.D., J.C. Lahr, K.A. Fogleman, and R.B. Horner (1980), The St. Elias, Alaska, earthquake of February 28, 1979: Regional recording of aftershocks and short-term, pre-earthquake seismicity, *Bull. Seismol. Soc. Am.* **70**, 5, 1607-1633.

Talbi, A., and F. Yamazaki (2009), Sensitivity analysis of the parameters of earthquake recurrence time power law scaling, *J. Seismol.* **13**, 1, 53-72, DOI: 10.1007/s10950-008-9115-1.

Talbi, A., K. Nanjo, K. Satake, J. Zhuang, and M. Hamdache (2013), Comparison of seismicity declustering methods using a probabilistic measure of clustering, *J. Seismol.* **17**, 3, 1041-1061, DOI: 10.1007/s10950-013-9371-6.

Tomoda, Y. (1954), Statistical description of the time interval distribution of earthquakes and on its relations to the distribution of maximum amplitude, *Zisin Ser*. **2**, 7, 155-169 (in Japanese).

Utsu, T. (1971), Aftershocks and earthquake statistics (2): Further investigation of aftershocks and other earthquake sequences based on a new classification of earthquake sequences, *J. Fac. Sci. Hokkaido Univ*. *Ser.VII* **3**, 4, 197-266.

Utsu, T. (2002), Statistical features of seismicity. **In:** W.H.K. Lee, H. Kanamori, P.C. Jennings, and C. Kisslinger (eds.), *International Handbook of Earthquake and Engineering Seismology*. *Part A*, IASPEI, 719-732, DOI: 10.1016/S0074-6142(02)80246-7.

Utsu, T., Y. Ogata, and R.S. Matsu'ura (1995), The centenary of the Omori formula for a decay law of aftershock activity, *J. Phys. Earth* **43**, 1, 1-33, DOI: 10.4294/jpe1952.43.1.

van Stiphout, T., J. Zhuang, and D. Marsan (2012), Seismicity declustering, Community Online Resource for Statistical Seismicity Analysis (CORSSA), DOI: 10.5078/corssa-52382934, available from: http://www.corssa.org (accessed: 2 February 2012).

Wiemer, S. (2001), A software package to analyze seismicity: ZMAP, *Seismol. Res. Lett*. **72**, 3, 373-382, DOI: 10.1785/gssrl.72.3.373.

Wiemer, S., and K. Katsumata (1999), Spatial variability of seismicity parameters in aftershock zones, *J. Geophys. Res.* **104**, B6, 13135-13151, DOI: 10.1029/1999JB900032.

Wiemer, S., M. Gerstenberger, and E. Hauksson (2002), Properties of the aftershock sequence of the 1999, $M_W$ 7.1, Hector Mine earthquake: Implications for aftershock hazard, *Bull. Seismol. Soc. Am.* **92**, 4, 1227-1240, DOI: 10.1785/0120000914.

Zollo, A., A. Bobbio, A. Emolo, A. Herrero, and G. De Natale (1997), Modelling of ground acceleration in the near source range: the case of 1976, Friuli earthquake (M = 6.5), northern Italy, *J. Seismol.* **1**, 4, 305-319, DOI: 10.1023/A:1009766214032.

Received 11 December 2014
Received in revised form 24 July 2015
Accepted 28 July 2015

DE GRUYTER OPEN

Acta Geophysica
vol. 64, no. 4, Aug. 2016, pp. 904-929
DOI: 10.1515/acgeo-2016-0044

# Local Recovery of Sub-Crustal Stress Due to Mantle Convection from Satellite-to-Satellite Tracking Data

Michal ŠPRLÁK[1] and Mehdi ESHAGH[2]

[1]NTIS – New Technologies for the Information Society,
Faculty of Applied Sciences, University of West Bohemia, Plzeň, Czech Republic
e-mail: sprlak@ntis.zcu.cz (corresponding author)

[2]Department of Engineering Science, University West, Trollhättan, Sweden
e-mail: mehdi.eshagh@hv.se

A b s t r a c t

Two integral transformations between the stress function, differentiation of which gives the meridian and prime vertical components of the sub-crustal stress due to mantle convection, and the satellite-to-satellite tracking (SST) data are presented in this article. In the first one, the SST data are the disturbing potential differences between twin-satellites and in the second one the line-of-sight (LOS) gravity disturbances. It is shown that the corresponding integral kernels are well-behaving and therefore suitable for inversion and recovery of the stress function from the SST data. Recovery of the stress function and the stress components is also tested in numerical experiments using simulated SST data. Numerical studies over the Himalayas show that inverting the disturbing potential differences leads to a smoother stress function than from inverting LOS gravity disturbances. Application of the presented integral formulae allows for recovery of the stress from the satellite mission GRACE and its planned successor.

**Key words:** integral equation, upward/downward continuation, integral kernel, truncation error, GRACE satellite mission, stress function.

Ownership: Institute of Geophysics, Polish Academy of Sciences;
© 2016 Šprlak and Eshagh. This is an open access article distributed under the Creative Commons Attribution-NonCommercial-NoDerivs license,
http://creativecommons.org/licenses/by-nc-nd/3.0/.

## 1. INTRODUCTION

The sub-crustal stress due to mantle convection is one of the important geophysical phenomenae. It allows for interpretation of seismicity, volcanicity, kimberlite magmatism, ore formation, tectonic and magnetic features (Liu 1977). Runcorn (1964, 1967) was one of the pioneers who proposed modelling the sub-crustal shear stress components in terms of spherical harmonic coefficients of gravity field. His formula was successfully applied, *e.g.*, by Liu *et al*. (1976), Liu (1977, 1978, 1980a, b), and Huang and Fu (1982). Others have also worked on the relation between the stress and other types of gravity data. McKenzie (1967) mentioned that the long wavelength harmonics of the external gravity field cannot be supported by the strength of the lithosphere. Review of stress estimates based on gravity observations and isostatic compensation based on surface deformation was provided by McNutt (1980). Souriau and Souriau (1983) studied correlations between surface tectonics and geoid undulations in terms of harmonic expansion. In a similar way, Ricard *et al*. (1984) investigated the connection between the lithospheric stress and geoidal undulation in terms of spherical harmonics. Mathematical model in terms of a harmonic expansion for convection field of the mantle was provided by Fu (1986, 1990).

Pick and Charvátová-Jakubcová (1988) and Pick (1994) provided integral transformations between geoid or gravity anomaly and the stress components to reduce the contribution of the far-zone gravitational effects. Eshagh (2014) related gradiometric data, such as those provided by the Gravity field and steady-state Ocean Circulation Explorer (GOCE; ESA 1999) satellite mission, and the stress components by integral transformations. In fact, he proposed a scalar function, called stress function (SF), differentiating of which stress components may be obtained. Eshagh (2015) developed this theory further to use the existing model of Moho discontinuity for sub-crustal stress determination. Eshagh and Tenzer (2015) used this method for determination of the sub-crustal stress in different regions with proper geological interpretations. Tenzer and Eshagh (2015) investigated the subduction generated by sub-crustal stress under Taiwan. Eshagh (2016) presented some integral formulae for recovering the sub-crustal stress using terrestrial gravimetric data and applied them for stress modelling under Iran. Tenzer *et al*. (2015) applied this method for evaluation of stress fields on Mars. Eshagh and Romeshkani (2015) used the real GOCE data for recovering the sub-lithospheric stress field in Iran.

In this article, we discuss a model for recovery of the sub-crustal stress from satellite-to-satellite tracking (SST) data, *e.g.*, such as those available from the GRAvity field and Climate Experiment (GRACE; Tapley *et al*. 2004). From the mathematical point of view, we provide two integral trans-

formations of the SF onto the SST data, which are in the form of gravitational potential differences and the line-of-sight (LOS) gravitational accelerations. Local recovery of the sub-crustal stress and/or any other type of gravity data is beneficial as: (a) global coverage of the data is not required; (b) the data with good coverage, uniform distribution and accuracies is used; and (c) local features are more visible. The third reason is highly dependent on the satellite altitude and type of the satellite data. The satellite data may represent the deep interior structure of the Earth much better than the local terrestrial data and especially the GRACE data are more sensitive to the long wavelength structure of the stress field occurring beneath the crust.

We extend the geophysical applications of the GRACE mission, such as those improving models of crustal thickness (Shin *et al*. 2007, Block *et al*. 2009, Tedla *et al*. 2011, Arabelos and Tsoulis 2013, Zhao 2013), lithospheric structures (Ricard *et al*. 2006, Kiamehr *et al*. 2008, Braitenberg and Ebbing 2009a, b; von Frese 2009, Kaban *et al*. 2010, Kaban and Trubitsyn 2012, Köther *et al*. 2012, Tondi *et al*. 2012), and our understanding of tectonic (Mikhailov *et al*. 2004, Kiamehr and Sjöberg 2006, Choi *et al*. 2006, McAdoo *et al.* 2008) and seismic processes (see, *e.g.*, Sun and Okubo 2004, Chen *et al*. 2007, Han *et al*. 2008, Panet *et al*. 2010, Matsuo and Heki 2011, Wang *et al*. 2012, Mikhailov *et al*. 2013, Dai *et al*. 2014, Li *et al*. 2014, Sun 2014).

In Section 2, we describe the SST data and present its relations to the disturbing gravitational field quantities such as disturbing potential differences (DPD) and LOS gravity disturbances. The new integral formulae are developed in Section 3 relating these quantities to the SF (Eshagh and Tenzer 2015). Here, we also study the behaviour of the corresponding sub-integral kernels in the spatial domain. The derived integral formulae are numerically tested in closed-loop simulations in Section 4. We investigate the accuracy of our algorithms by calculating the SST data assuming the SF is known, *i.e.*, the direct problem. We also consider the estimation of the SF and the stress components from known SST data, *i.e.*, the inverse problem. Contributions of this article are summarised in Section 5. Application of the mathematical apparatus to real SST data and geophysical interpretation of the recovered stress function is out of the scope of this paper.

## 2. SATELLITE-TO-SATELLITE TRACKING

SST is an inter-satellite measurement technique for precise determination of the satellite coordinates. It can be performed in two modes: (i) the high-low mode, when position of a low orbiting satellite is determined by satellites at higher altitudes; and (ii) the low-low mode, when two low-orbiting satellites follow each other in approximately the same orbit (see Reigber 1989, Seeber 2003). SST in high-low mode has been successfully realised by the satellite

mission CHAMP (Challenging Minisatellite Payload; Reigber *et al*. 2002). SST in low-low and high-low modes have been exploited on-board of GRACE mission mapping the Earth's gravitational field and GRAIL (Gravity Recovery and Interior Laboratory; Zuber *et al*. 2013) mission, which focused on the Moon's gravitational field.

The high-low SST provides position, velocity and acceleration vectors in the geocentric Earth-fixed frame, namely:

$$\mathbf{x} = [x, y, z]^T , \quad \dot{\mathbf{x}} = [\dot{x}, \dot{y}, \dot{z}]^T , \quad \ddot{\mathbf{x}} = [\ddot{x}, \ddot{y}, \ddot{z}]^T . \tag{1}$$

These are derived from Global Navigation Satellite Systems (GNSS) carrier phase observations. The inter-satellite ranging system between a pair of low-orbiting satellites provides the time series of the following quantities, *i.e.*, the low-low SST data:

$$\rho = |\delta \mathbf{x}| , \quad \dot{\rho} = \delta \dot{\mathbf{x}} \cdot \mathbf{e} , \quad \ddot{\rho} = \delta \ddot{\mathbf{x}} \cdot \mathbf{e} + \frac{|\delta \dot{\mathbf{x}}|^2 - \dot{\rho}^2}{\rho} . \tag{2}$$

Here, $\rho$ is the inter-satellite range, $\dot{\rho}$ and $\ddot{\rho}$ represent its first and second time derivatives, *i.e.*, the inter-satellite velocity difference and inter-satellite acceleration difference (being derived from the inter-satellite range), **e** stands for the LOS inter-satellite unit vector and

$$\delta \mathbf{x} = \mathbf{x}_2 - \mathbf{x}_1 , \quad \delta \dot{\mathbf{x}} = \dot{\mathbf{x}}_2 - \dot{\mathbf{x}}_1 , \quad \delta \ddot{\mathbf{x}} = \ddot{\mathbf{x}}_2 - \ddot{\mathbf{x}}_1 , \tag{3}$$

where the subscript 1 designates the leading satellite and the subscript 2 is assigned to the trailing satellite.

For gravity field modelling, the SST data should be mathematically related to some quantities of the field. The range-rates and velocity measurements have the simplest mathematical relations to the differences of the gravitational potential $V$ between the pair of satellites (see, *e.g.*, Wolff 1969, Fischell and Pisacane 1978, Rummel 1980):

$$\delta V(\mathbf{x}) = |\dot{\mathbf{x}}_1| \dot{\rho} . \tag{4}$$

Note that Eq. 4 holds only approximately. A rigorous model for $\delta V$ was provided and extensively analysed by Jekeli (1999). This model should be preferred for gravity field modelling purposes. Alternatively, the low-low and high-low SST data may rigorously be combined to provide differences of gravitational gradients projected onto the LOS inter-satellite unit vector (see, *e.g.*, Hajela 1974, Rummel 1980, Keller and Sharifi 2005):

$$\frac{|\delta \dot{\mathbf{x}}| - \dot{\rho}^2 - \rho \ddot{\rho}}{\rho} = \frac{\delta \mathbf{x} \cdot \delta \nabla V(\mathbf{x})}{\rho} = \mathbf{e} \cdot \delta \nabla V(\mathbf{x}) . \tag{5}$$

The right hand-side of Eq. 5 is also referred to as LOS gravitational acceleration.

In the following, we will derive the integral formulae between the SF, whose derivatives correspond to the components of the stress due to mantle convection, and the SST data in the form of Eqs. 4 and 5. We introduce the DPD by $\delta T$ and LOS gravity disturbances by $\mathbf{e}\cdot\delta\nabla T$, where $T$ stands for the disturbing gravitational potential. Both, the DPD and LOS gravity disturbances, can be obtained by subtracting the normal gravitational potential, *e.g.*, generated by the GRS80 reference ellipsoid (Moritz 2000), from both sides of Eqs. 4 and 5.

## 3. MATHEMATICAL DEVELOPMENTS

Here, we develop the mathematical relations between each one of $\delta T$ and $\mathbf{e}\cdot\delta\nabla T$ and the SF, which are in fact of integral types. Also, we present the behaviour of the integral kernels to have an idea about the far-zone contribution of the integral formulae.

### 3.1 Integral transformation of the stress function onto disturbing gravitational potential

In this section, we focus on deriving the mathematical link between the SF and the disturbing gravitational potential. The spherical harmonic expansion of the disturbing gravitational potential is:

$$T(\mathbf{x}) = \sum_{n=2}^{\infty} \sum_{m=-n}^{n} \left( \frac{R}{r} \right)^{n+1} \overline{T}_{nm}\, \overline{Y}_{nm}(\Omega) \ , \tag{6}$$

where $R$ is the radius of the reference sphere, the triplet $r$, $\Omega = (\varphi, \lambda)$ represents the spherical coordinates, *i.e.*, the geocentric radius, spherical latitude $\varphi$ and longitude $\lambda$, and they are presented by the vector $\mathbf{x} = \mathbf{x}(r, \Omega)$ on the left-hand side of Eq. 6. $\overline{T}_{nm}$ stand for the fully-normalised spherical harmonic coefficients of the disturbing gravitational potential of degree $n$ and order $m$. These are related to the conventional dimensionless fully-normalised spherical harmonic coefficients $\overline{C}_{nm}$ by the following transformation: $\overline{T}_{nm} = \frac{GM}{R} \overline{C}_{nm}$ , where $G$ stands for the Newtonian gravitational constant and $M$ is the mass of the Earth including oceans and atmosphere. The symbol $\overline{Y}_{nm}$ stands for the fully-normalised surface spherical harmonics. The summation in Eq. 6 starts from degree 2, meaning that the mass of the Earth equals to the mass of the reference ellipsoid and the frame in which the coordinates are defined is geocentric.

Similarly, the SF may be expanded into the following spherical harmonic series (Eshagh 2014):

$$S(\mathbf{x},D)=\frac{R\kappa}{GM}\sum_{n=2}^{\infty}\sum_{m=-n}^{n}\nu_n\,\overline{T}_{nm}\,\overline{Y}_{nm}(\Omega)=\sum_{n=2}^{\infty}\sum_{m=-n}^{n}\overline{S}_{nm}\,\overline{Y}_{nm}(\Omega)\ , \tag{7}$$

where

$$\kappa=\frac{Mg}{4\pi\left[R-D\right]^2},\quad \nu_n=\frac{2n+1}{n+1}\left[\frac{R}{R-D}\right]^{n+1}\ , \tag{8}$$

with $g$ being the mean value of gravity, $D$ is the normal or mean Moho depth and $\overline{S}_{nm}$ are the fully-normalised harmonic coefficients of the SF. By comparing Eqs. 6 and 7 it will not be difficult to find that:

$$\overline{T}_{nm}=\frac{GM}{R\kappa\nu_n}\overline{S}_{nm}\ . \tag{9}$$

Equation 9 shows the direct relation between the spherical harmonic coefficients of the SF and those of the disturbing gravitational potential. However, we can find an integral formula by transforming the SF onto the disturbing gravitational potential in the spatial domain. First, Eq. 9 is inserted back into Eq. 6, and by considering that:

$$\overline{S}_{nm}=\frac{1}{4\pi}\int_{\Omega'}S(\mathbf{x}',D)\,\overline{Y}_{nm}(\Omega')\,\mathrm{d}\Omega(\mathbf{x}')\ , \tag{10}$$

where $\mathbf{x}'=\mathbf{x}(R,\Omega')$ assigns the position of an integration element on the surface of the reference sphere $\Omega'$, we have:

$$T(\mathbf{x})=\frac{GM}{4\pi R\kappa}\sum_{n=2}^{\infty}\frac{1}{\nu_n}\left(\frac{R}{r}\right)^{n+1}\int_{\Omega'}S(\mathbf{x}',D)\sum_{m=-n}^{n}\overline{Y}_{nm}(\Omega')\,\overline{Y}_{nm}(\Omega)\,\mathrm{d}\Omega(\mathbf{x}')\ . \tag{11}$$

Now, according to the addition theorem of the surface spherical harmonics (Hofmann-Wellenhof and Moritz 2005, p. 26):

$$P_{n,0}(\cos\psi)=\frac{1}{2n+1}\sum_{m=-n}^{n}\overline{Y}_{nm}(\Omega)\,\overline{Y}_{nm}(\Omega')\ , \tag{12}$$

where $P_{n,0}$ are the associated Legendre functions of the first kind of degree $n$ and order 0 (also known as Legendre polynomials) and $\psi$ is the spherical distance between the geocentric directions $\Omega$ and $\Omega'$, we get:

$$T(\mathbf{x})=\frac{GM}{4\pi R\kappa}\int_{\Omega'}S(\mathbf{x}',D)\,K(t,u)\,\mathrm{d}\Omega(\mathbf{x}')\ . \tag{13}$$

The series representation of the integral kernel $K(t, u)$ is of the form:

$$K(t,u) = \sum_{n=2}^{\infty} t^{n+1} (n+1) P_{n,0}(u) \quad , \tag{14}$$

with variables $t$ and $u$ defined as follows:

$$t = t(\mathbf{x}, \mathbf{x}') = \frac{|\mathbf{x}'|}{|\mathbf{x}|} = \frac{R}{r}, \quad u = u(\mathbf{x}, \mathbf{x}') = \frac{\mathbf{x} \cdot \mathbf{x}'}{|\mathbf{x}||\mathbf{x}'|} = \cos\psi \quad . \tag{15}$$

We can also find a closed-form formula for the kernel of Eq. 14. To do so, we use the following identities, see, *e.g.*, (Pick *et al*. 1973):

$$\sum_{n=2}^{\infty} t^{n+1} P_{n,0}(u) = t\left(\frac{1}{g} - 1 - tu\right) \quad , \tag{16}$$

$$\sum_{n=2}^{\infty} n\, t^{n+1} P_{n,0}(u) = t^2\left(\frac{u-t}{g^3} - u\right) \quad , \tag{17}$$

where

$$g = g(t,u) = \sqrt{1 - 2tu + t^2} \quad . \tag{18}$$

Exploiting Eqs. 16 and 17, the infinite series of Eq. 14 may be written in the closed form:

$$K(t,u) = -t\left(1 + 2tu - \frac{1-tu}{g^3}\right) \quad . \tag{19}$$

### 3.2 Integral transformation of the stress function onto SST data

By using the integral formula of Eq. 13 we can find corresponding integral transformations between the SF and the SST data in the form of either the DPD ($\delta T$) or LOS gravity disturbance ($\mathbf{e}\cdot\delta\nabla T$). In the following we will develop these transformations.

#### *3.2.1 Integral transformation of the stress function onto disturbing potential differences*

Considering two low-orbiting satellites, $\delta T$ will be nothing else than a difference between disturbing gravitational potentials at the satellites' locations based on Eq. 13. In such a situation $\delta T$ is:

$$\delta T(\mathbf{x}) = \frac{GM}{4\pi R \kappa} \int_{\Omega'} S(\mathbf{x}', D)\, \delta K(t,u)\, \mathrm{d}\Omega(\mathbf{x}') \quad . \tag{20}$$

It is seen that $\delta T$ leads to an integral kernel difference $\delta K(t, u)$, which is a function of three points, *i.e.*, the integration element $\mathbf{x}'$ and the position vectors $\mathbf{x}_1$ and $\mathbf{x}_2$ of both satellites; see also Eq. 15 for the definition of variables $t$ and $u$.

To better understand the properties of the integral formula of Eq. 20 we have investigated the behaviour of the integral kernel $\delta K(t, u)$. For this purpose, we have selected one particular formation of GRACE twin satellites from the product GNV1B (GPS Navigation Data Format Record; Case *et al.* 2010) at GPS time $t_{GPS} = 316363415$ s. The spherical coordinates of the leading satellite are $r_1 = 6854183.3$ m, $\varphi_1 \approx 0.30°$, $\lambda_1 \approx 5.05°$, while the spherical coordinates of the trailing satellite are $r_2 = 6855126.8$ m, $\varphi_2 \approx -1.79°$, $\lambda_2 \approx 5.10°$. It follows that the barycentre of the satellite pair, *i.e.*, the arithme-

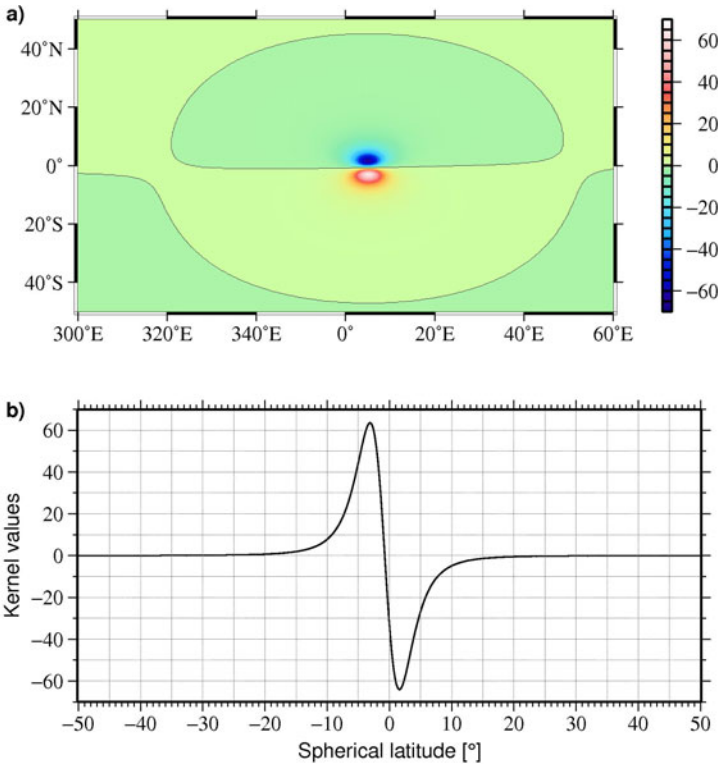


Fig. 1. Graphical illustration of the integral kernel $\delta K$ based on Eq. 20: (a) the total value of the kernel, (b) profile along the meridian with constant longitude $\lambda = 5.125°$. The spherical coordinates of the leading satellite are $r_1 = 6\,854\,183.3$ m, $\varphi_1 \approx 0.30°$, $\lambda_1 \approx 5.05°$. The spherical coordinates of the trailing satellite are $r_2 = 6\,855\,126.8$ m, $\varphi_2 \approx -1.79°$, $\lambda_2 \approx 5.10°$. Value of the mean Moho depth is $D = 30\,000$ m and the radius of the reference sphere is $R = 6\,378\,136.3$ m. The black solid line in Fig. 1a indicates the zero crossings of the integral kernel.

tic average of angular spherical coordinates of both satellites, is defined by the position $\varphi_B \approx -0.75°$, $\lambda_B \approx 5.08°$. Next, we have assumed that the value of the mean Moho depth is $D = 30\,000$ m and the radius of the reference sphere is $R = 6\,378\,136.3$ m. Integral kernel $\delta K(t, u)$ in the closed-form based on Eq. 19 has been computed globally with step 0.25° in both angular directions and depicted in the area bounded by spherical coordinates $\varphi \in [-50.125°, 50.125°]$, $\lambda \in [-60.125°, 60.125°]$; see Fig. 1. Despite of the fact that the kernel $K(t, u)$ is isotropic, the difference $\delta K(t, u)$ is not isotropic anymore and leads to the azimuthal dependence illustrated in Fig. 1a. The extreme behaviour of the integral kernel is seen in the along-track direction that almost coincides with latitude direction. Obviously, value of the integral kernel is zero at the barycentre of the two satellites' positions. Moving from the barycentre along-track by approximately 2.5°, the total integral kernel reaches its extreme values. With increasing distance from the barycentre, one may observe the decay to zero. These facts are clearly demonstrated in Fig. 1b, which represents the behaviour of the integral kernel along the meridian with constant longitude $\lambda = 5.125°$. The integral kernel is much smoother with significantly reduced magnitudes and values close to zero in the cross-track (longitude) direction. Implications of the integral kernel behaviour for the recovery of the SF are further discussed in Section 4.2.

### *3.2.2 Integral transformation of the stress function onto LOS gravity disturbances*

To obtain the integral formula connecting the SF to the LOS gravity disturbance we use the following operator (Šprlák and Novák 2014a, b):

$$\mathbf{e}\cdot\delta\nabla = \frac{1}{R}\delta\left(e_x\, t\sqrt{1-u^2}\cos\alpha\frac{\partial}{\partial u} + e_y\, t\sqrt{1-u^2}\sin\alpha\frac{\partial}{\partial u} - e_z\, t^2\frac{\partial}{\partial t}\right). \qquad (21)$$

In the last equation, $e_x$, $e_y$, and $e_z$ are the components of the LOS inter-satellite unit vector in the spherical local north-oriented reference frame, *i.e.*, the frame with origin at satellite's center of mass, with $x$ axis directed north, $y$ axis pointing west, and $z$ axis pointing in the radial direction, $\alpha = \alpha(\Omega, \Omega')$ is the direct azimuth, and $t$, $u$ are the substitutions defined by Eq. 15. Applying the differential operator of Eq. 21 onto Eq. 13 we get:

$$\mathbf{e}.\delta\nabla T(\mathbf{x}) = \frac{GM}{4\pi R^2\kappa}\int_{\Omega'} S(\mathbf{x}', D)\,\delta\left\{K^u(t,u)\left[e_x\cos\alpha + e_y\sin\alpha\right] - e_z\,K^t(t,u)\right\}\mathrm{d}\Omega(\mathbf{x}'). \qquad (22)$$

The last equation relates the SF to the LOS gravity disturbance. Obviously, the integral kernel is azimuth-dependent due to the presence of the trigonometric functions of the direct azimuth $\alpha$. Similar to Eq. 20, the integral

kernel is a function of three points, *i.e.*, the integration element $\mathbf{x}'$ and the position vectors $\mathbf{x}_1$ and $\mathbf{x}_2$ of both satellites. In addition, the integral kernel is composed of two isotropic kernels, which are defined as follows:

$$K^u(t,u) = t\sqrt{1-u^2}\,\frac{\partial K(t,u)}{\partial u} = \sum_{n=2}^{\infty} t^{n+2}(n+1)P_{n,1}(u) = -t^3\sqrt{1-u^2}\left(2 - \frac{2-tu-t^2}{g^5}\right), \quad (23)$$

$$K^t(t,u) = t^2\frac{\partial K(t,u)}{\partial t} = \sum_{n=2}^{\infty} t^{n+2}(n+1)^2 P_{n,0}(u) = -t^2\left\{1 + 4tu - \frac{1}{g} - \frac{t}{g^3}\left[3u - 4t + \frac{3t(t-u)^2}{g^2}\right]\right\}. \quad (24)$$

Equations 23 and 24 define the spectral and closed forms of the isotropic kernels $K^u(t, u)$ and $K^t(t, u)$. The spectral forms immediately follow by applying the first equalities in Eqs. 23 and 24 to Eq. 14. On the other hand, the closed expressions may be derived making use of the identities of Eqs. 16 and 17 together with (see, *e.g.*, Pick *et al*. 1973, Šprlák and Novák 2014b):

$$\sum_{n=2}^{\infty} n^2\, t^{n+1}\, P_{n,0}(u) = -t^2\left[u - \frac{u-2t}{g^3} - \frac{3t\left(t-u\right)^2}{g^5}\right], \quad (25)$$

$$\sum_{n=2}^{\infty} t^{n+1}\, P_{n,1}(u) = -t^2\sqrt{1-u^2}\left(1 - \frac{1}{g^3}\right), \quad (26)$$

$$\sum_{n=2}^{\infty} n\, t^{n+1}\, P_{n,1}(u) = -t^2\sqrt{1-u^2}\left(1 - \frac{1}{g^3} - \frac{3t\left(u-t\right)}{g^5}\right). \quad (27)$$

We now demonstrate properties of the integral formula of Eq. 22 by investigating the behaviour of its integral kernel. The integral kernel has been evaluated globally with equiangular step of 0.25° and illustrated in the spatial domain bounded by spherical coordinates $\varphi \in [-30.125°, 30.125°]$, $\lambda \in [-30.125°, -40.125°]$. Note that the other kernel parameters, *i.e.*, positions of the satellite pair, the mean Moho depth $D$ and the radius of the reference sphere $R$, have the same values as those already described for the integral kernel $\delta K(t, u)$; see Section 3.2.1.

The total integral kernel of Eq. 22 is illustrated in Fig. 2a, which shows its azimuth-dependent behaviour. The most significant values are again visible in the along-track direction. This direction is approximated by a meridian of constant longitude $\lambda = 5.125°$ in Fig. 2b. We may observe that the integral kernel of Eq. 22 reaches its negative extreme value at the barycentre and then reaches local positive extremes approximately 4.5° from the barycentre. The kernel then decreases to zero with increasing distance from the barycen-

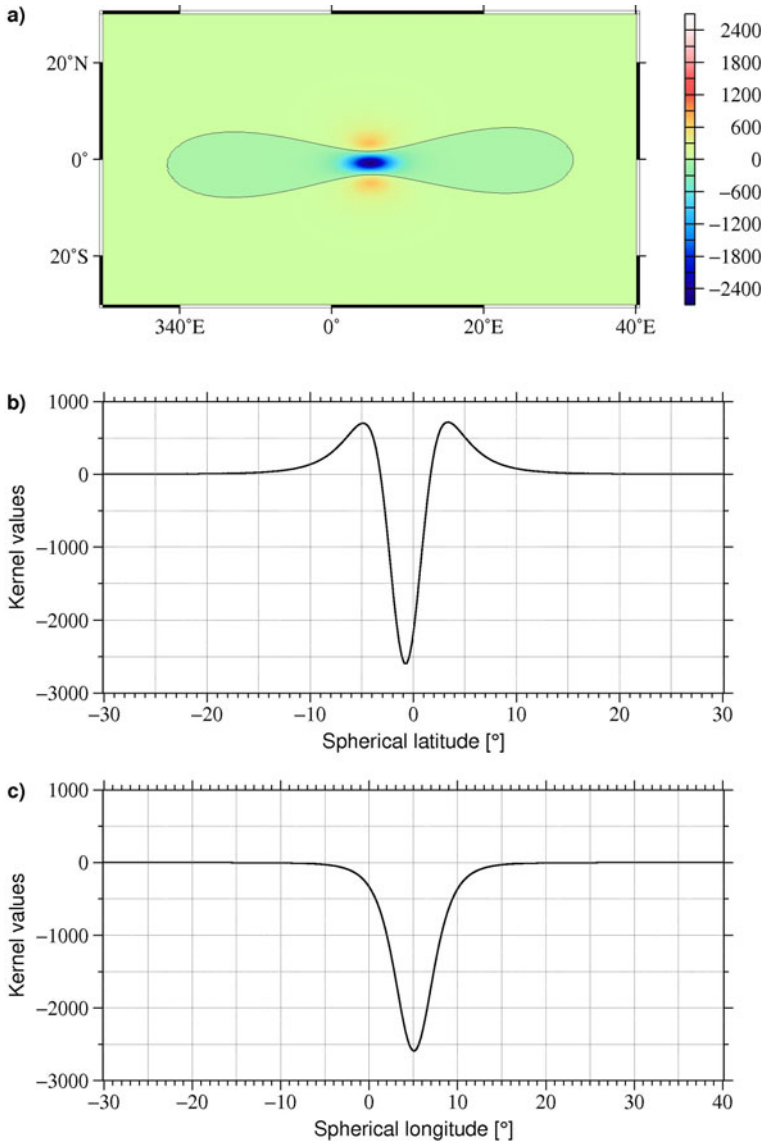


Fig. 2. Graphical illustration of the integral kernel of Eq. 22: (a) the total value of the kernel, (b) profile along the meridian with constant spherical longitude $\lambda = 5.125°$, (c) profile along the parallel with constant spherical latitude $\varphi = -0.625°$. The spherical coordinates of the leading satellite are $r_1 = 6\,854\,183.3$ m, $\varphi_1 \approx 0.30°$, $\lambda_1 \approx 5.05°$. The spherical coordinates of the trailing satellite are $r_2 = 6\,855\,126.8$ m, $\varphi_2 \approx -1.79°$, $\lambda_2 \approx 5.10°$. Value of the mean Moho depth is $D = 30\,000$ m and the radius of the reference sphere is $R = 6\,378\,136.3$ m. The black solid line in Fig. 2a indicates the zero crossings of the integral kernel.

tre. Figure 2c demonstrates the behaviour of the integral kernel along the parallel with constant latitude $\varphi = 0.625°$. This direction represents approximately the cross-track direction and at the same time it is very close to the barycentre. It is seen that in this direction the integral kernel decays to zero faster since the local positive extremes are completely reduced. Behaviour of the integral kernel and its effect on the recovery of the SF are discussed in Section 4.2.

## 4. NUMERICAL EXPERIMENTS

Here, we divide our numerical studies into two parts. First, we will test the direct problem in which the generated SF by EGM2008 (Pavlis *et al*. 2012) is used to reproduce the SST data. In the second numerical experiment, we try to recover the SF by inverting $\delta T$ and $\mathbf{e}\cdot\delta\nabla T$ based on the mathematical apparatus presented in the previous section.

### 4.1 Testing the direct problem

The presented theories have been practically tested in a numerical experiment. First, the correctness of our mathematical derivations has been checked as the direct problem, *i.e.*, direct integration of the SF for calculation of the SST data based on Eqs. 20 and 22. The SF has been generated from EGM2008 global gravity field model (GGFM) up to degree and order (d/o) 180 in a global equiangular grid with spacing of 1°. For evaluation of the SF, we assumed that the value of the mean Moho depth is $D = 30\,000$ m and the radius of the reference sphere is $R = 6\,378\,136.3$ m. Next, the true $\delta T$ and the true $\mathbf{e}\cdot\delta\nabla T$ have been computed from EGM2008 up to d/o 180 at the locations given by real GRACE orbit available from the product GNV1B. Every fifth data record in the period from 1 January 2010 until 30 June 2010 have been considered and restricted to the area bounded by spherical coordinates $\varphi \in [5°, 57°]$ and $\lambda \in [55°, 115°]$. The restricted domain covers the area of India, Himalayas and Southeast Asia and contains 30 036 points in total. The statistics of the SST data is presented in Table 1 and their spatial behaviour is depicted in Fig. 3. We note that the values of the SST data were interpolated from the original locations along the orbit into an equiangular grid with sampling of 0.25° for better visualisation purposes. We also note that values of $\delta T$ have opposite sign for descending and ascending tracks. In Fig. 3a we have opted for ascending tracks when interpolating $\delta T$ and Fig. 3b is a similar map but for $\mathbf{e}\cdot\delta\nabla T$. We observe that the map of $\delta T$, presented in Fig. 3a is smoother than that of $\mathbf{e}\cdot\delta\nabla T$ in Fig. 3b as expected.

In a further step, we have performed the global integration of the SF based on integral formulae of Eqs. 20 and 22. For this purpose, numerical integration method has been implemented in a computer program. Subsequent-

Table 1

Statistics of the differences between the SST data obtained by numerical integration and their true values

| SST data | Equation | Units | Minimum | Maximum | Mean | Std. dev. |
|---|---|---|---|---|---|---|
| $\delta T$ | Signal | $m^2 s^{-2}$ | –44.938 | 46.892 | 0.602 | 18.123 |
| | 20 | | –0.005 | 0.005 | 0.000 | 0.001 |
| $\mathbf{e}\cdot\delta\nabla T$ | Signal | mGal | –10.196 | 8.135 | 0.894 | 2.449 |
| | 22 | | –0.096 | 0.102 | 0.004 | 0.012 |

**Notes:** Closed isotropic kernels were exploited in the numerical integration. The true values were synthesised from EGM2008 up to d/o 180. Statistics of the true values are given in the rows called "Signal".

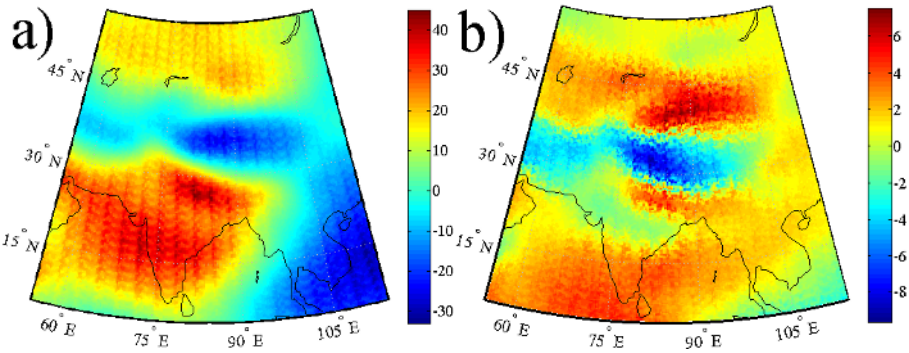


Fig. 3: (a) Disturbing potential differences ($\delta T$) [$m^2 s^{-2}$]; and (b) LOS gravity disturbance ($\mathbf{e}\cdot\delta\nabla T$) [mGal].

ly, $\delta T$ and $\mathbf{e}\cdot\delta\nabla T$ from the global integration have been compared with the true values. Statistics of the differences is presented in Table 1. The standard deviation of differences reaches 0.001 $m^2 s^{-2}$ for $\delta T$ and 0.012 mGal for $\mathbf{e}\cdot\delta\nabla T$. The relative accuracy, defined as the ratio of the standard deviation of differences to the standard deviation of the signal, is two orders higher for $\mathbf{e}\cdot\delta\nabla T$. This indicates that the performance of the numerical integration for $\delta T$ is better. We suppose that the different performance is due to different spectral sensitivity of the quantities in Eqs. 20 and 22. Evaluation of $\delta T$ is more precise as the SF is of similar spectral content. On the other hand, $\mathbf{e}\cdot\delta\nabla T$ is more sensitive to higher frequencies of the gravity field as compared to the SF. Evaluation of $\mathbf{e}\cdot\delta\nabla T$ may therefore be less accurate from a numerical point of view.

### 4.2 Solution of the inverse problem

The integrals 20 and 22 should be inverted to recover the SF. To do so, they are discretised with an equiangular resolution of 1° that corresponds to spherical harmonic expansion up to degree 180. Recovering SF with higher resolution is not meaningful as the GRACE satellite data are not sensitive to higher degrees. The synthesised GRACE data on their real orbit in the area $\varphi \in [5°, 57°]$ and $\lambda \in [55°, 115°]$ are considered as the observations. The discretised integrals represent observation equations connecting the observations to the SF in the same area. According to the size of the study area and the resolution of SF, 3120 values should be determined for SF and the number of synthesised data is 30 036, which means that we have 26 916 data more than the unknown values of SF. Therefore, the systems of equations, organised by the discretisation of the integral formulae, should be solved by the least-squares method. The determinant of the coefficients matrix of the system is very small which makes the inversion process numerically unstable with a condition number of $2 \times 10^{14}$. Regularisation is a method for solving such unstable systems. In this study, we use Tikhonov regularisation (Tikhonov 1963) for stabilising the system and L-curve (Hansen 1998) for estimating the regularisation parameter. For inverting our systems of equations we have used Regularisation Tools (Hansen 2007) of MATLAB. For more information about regularisation, see, *e.g.*, Hansen (1998), Bouman (1998) or Eshagh (2011a).

It should be noted that we have simulated $\delta T$ and $\mathbf{e}\cdot\delta\nabla T$ using the EGM2008 model, while real GRACE orbits have been exploited as the purpose of this study is to investigate how successful our methods for recovering SF are for the noise-free scenario. In this way, we can judge better the theoretical apparatus derived in Section 3 rather than working with the real GRACE data which are of different nature and could make our primary investigations complicated. Recovery of SF from noisy SST data and application of the derived theoretical apparatus for real GRACE data is left for our future research.

#### *4.2.1 Spatial truncation error*

The spatial truncation error is a serious problem in inversion of the spherical integrals like those in Eqs. 20 and 22, in addition to the instability of system of equations organised from them. This is due to lacking data in the integration domain of integral formulae and occurs mainly in the marginal parts of the inversion area. The simplest way for reducing this error is to perform the inversion process in whole area and select the results located in the central part as the final result. Eshagh (2011b) showed that the truncation error may be reduced well when data and unknowns are located within the same area.

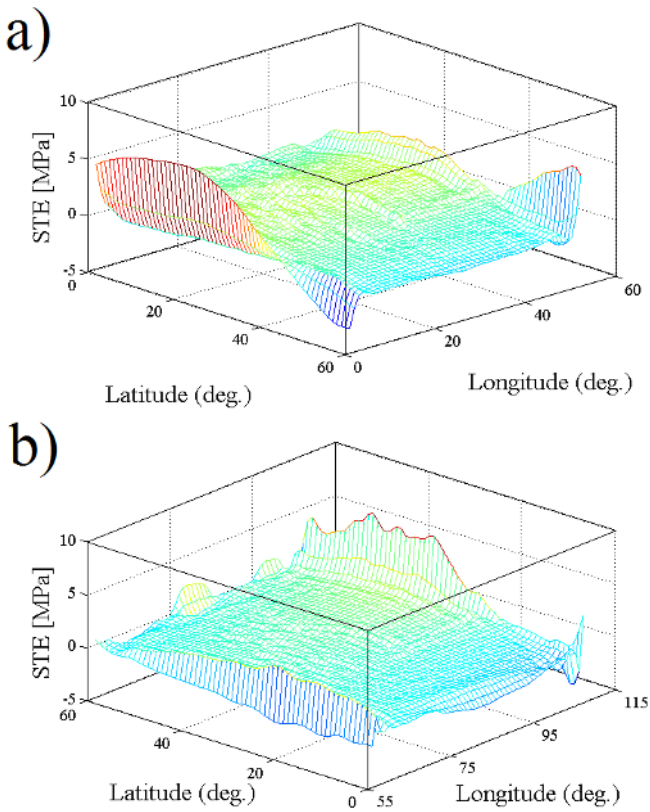


Fig. 4. Spatial truncation error (STE) of recovered SF by inverting integral of: (a) Eq. 20, and (b) Eq. 22.

Also, spatial behaviour of the corresponding integral kernel has a tremendous role to reduce the truncation error. Based on Eshagh (2011b), the truncation error may be considerably reduced for the well-behaving integral kernels, *i.e.*, kernels reaching their extremes at the computational point and decreasing uniformly to zero. Figures 1 and 2 show that the kernels of the integrals 20 and 22 decrease to zero after a geocentric angle of about 15°. Therefore, by considering the inversion area larger by 15° from each side, performing the inversion and selecting the result in the central area (smaller by 15°), the effect of spatial truncation error is reduced. Figures 4a and 4b present the maps of the recovered SF by both integral formulae 20 and 22, respectively, without removing the truncation error. As the figures show, the truncation error is considerably larger than the magnitude of SF in the marginal area. One issue which is visible in these figures is that the SF is

smoother when it is recovered from $\delta T$ via the integral 20 as compared to the recovery by the integral 22.

### *4.2.2 Recovery of the stress function*

Now, the SST data are computed on the real orbit of the twin-satellites. The integrals 20 and 22 are used to invert them to the SF. In order to reduce the effect of the spatial truncation error, we selected the recovered SF in the central part which is smaller by 10°. Figures 5a and 5b show the recovered SF by inverting the integrals 20 and 22. The coastal lines and the tectonic boundaries have been shown in the map by black and green lines. The values of SF are larger when they are recovered from $\delta T$, whilst smaller from $\mathbf{e}\cdot\delta\nabla T$. The maps clearly show that the SF is smoother in the former case than the latter. This could be expected as recovering high frequencies of the Earth gravity field from the potential observables is not possible, while first and second order derivatives of the potential are more capable for high resolution gravity field modelling from space.

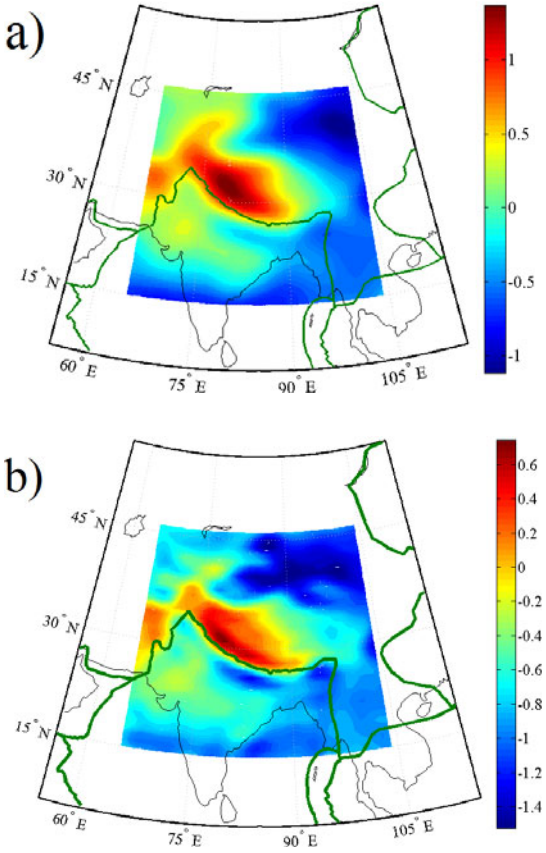


Fig. 5. SF recovered from: (a) disturbing potential differences ($\delta T$), and (b) LOS gravity disturbances ($\mathbf{e}\cdot\delta\nabla T$). Unit: 1 MPa.

### *4.2.3 Determination of sub-crustal stress from the recovered stress function*

Once SF is estimated, computation of its derivatives numerically towards the north and the east is straightforward. One can use the following formulae for generating the meridian and prime vertical sub-crustal stress components:

$$S_x = -\frac{\Delta S}{\Delta \varphi}, \quad S_y = \frac{1}{\cos\varphi}\frac{\Delta S}{\Delta \lambda} \quad , \tag{28}$$

where $S_x$ is the northward and $S_y$ is the eastward component, $\Delta S$ is the difference of the stress function between two adjacent cells towards the north or the east, $\Delta\varphi$ is the resolution in the northward direction and $\Delta\lambda$ in the eastward directions. Note that both of them should be in the radian units.

Here, we compute the magnitudes of the sub-crustal stress by:

$$S_T = \sqrt{S_x^2 + S_y^2} \, , \tag{29}$$

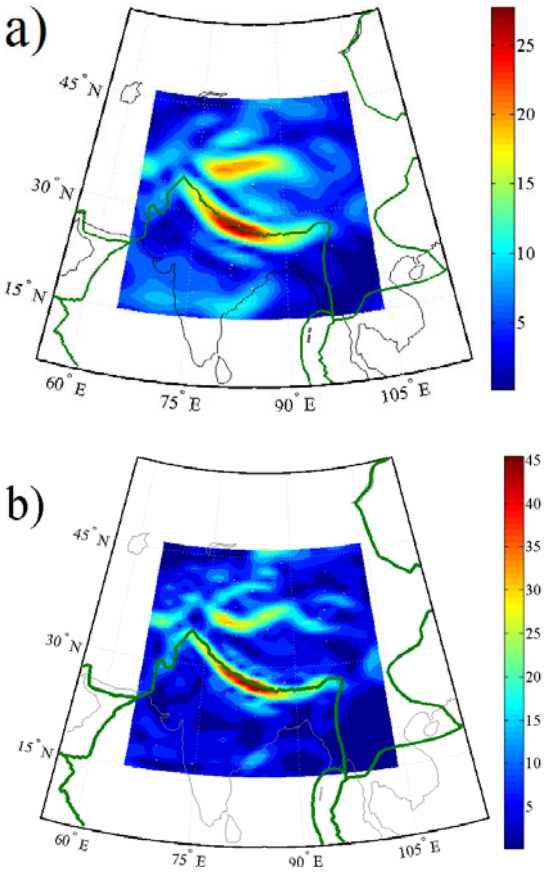


Fig. 6. Magnitudes of sub-crustal stress derived from: (a) $\delta T$, and (b) $\mathbf{e}\cdot\delta\nabla T$. Unit: 1 MPa.

and present them in the maps; see Fig. 6. Figure 6a shows the map of $S_T$ derived from the SF recovered from $\delta T$, and Fig. 6b that from $\mathbf{e}\cdot\delta\nabla T$. In spite of the fact that the values of SF presented in Fig. 5a are larger than those of Fig. 5b, the values of $S_T$ are smaller in Fig. 6a when they are derived numerically from the SF of Fig. 5a. The reason is that when sub-crustal stress components are computed from SF, $\Delta S$ will be smaller in the case of using the SF generated from $\delta T$ than $\mathbf{e}\cdot\delta\nabla T$, which is due to the smooth nature of SF in the first case. Both maps of $S_T$, presented in Figs. 6a and 6b, show large sub-crustal stress under the tectonic boundary in the southern part of Himalayas.

Table 2 presents the statistics of the recovered SF and the sub-crustal stress components recovered numerically from SF. According to the table, $S_x$ ranges from –28.27 to 21.58 MPa when it is derived from $\delta T$, while for $\mathbf{e}\cdot\delta\nabla T$ the range is from –46.42 to 32.02 MPa. The corresponding extreme values for $S_y$ are –9.12 to 14.11 MPa for the former and from –19.28 to 23.75 MPa for the latter functional.

Table 2

Statistics of recovered SF and sub-crustal stress components $S_x$ and $S_y$ derived from $\delta T$ and $\mathbf{e}\cdot\delta\nabla T$

| SST data | Quantity | Minimum | Maximum | Mean | Std. dev. |
|---|---|---|---|---|---|
| $\delta T$ | $S$ | –1.12 | 1.42 | –0.10 | 0.55 |
| | $S_x$ | –28.27 | 21.58 | –1.09 | 6.98 |
| | $S_y$ | –9.12 | 14.11 | –1.18 | 3.55 |
| $\mathbf{e}\cdot\delta\nabla T$ | $S$ | –1.52 | 0.79 | –0.68 | 0.45 |
| | $S_x$ | –46.42 | 32.02 | –0.23 | 9.43 |
| | $S_y$ | –19.28 | 23.75 | –0.98 | 4.93 |

**Note:** Unit: 1 MPa.

## 5. DISCUSSION

In this study, we have used the SST data for recovering the sub-crustal stress components. Generally, a GGFM can be used for modelling these components by the Runcorn's formula. However, Eshagh (2016) showed that Runcorn's formula is not convergent for high degrees. This means that the idea of working with high degree GGFM is not successful.

The mantle convection occurs inside the Earth and only by investigating the long wavelength structure of the Earth gravity field, we can model and investigate it; see, *e.g.*, Eshagh (2015), Eshagh and Tenzer (2015), and Tenzer and Eshagh (2015). The proper selection of the maximum degree of expansion and resolution of recovery play important roles in stress model-

ling. Eshagh (2016) presented a formula for estimating the maximum degree of the expansion and the mean Moho depth. For example, for a mean Moho depth of 35 km, the maximum expansion degree is 372. The larger the Moho depth is the lower the maximum expansion degree will be.

Exploiting terrestrial gravity data means considering all frequencies of the gravity field implicitly. Therefore, the divergence occurs in the computations. In such a case, either kernel functions should be limited to a specific maximum degree or the integral inversion should be performed locally, while the local diverting frequencies of the system of equations are removed, *e.g.*, using the truncated singular value decomposition technique; see Eshagh (2016).

The satellite data are more useful for stress modelling as the satellite altitudes filter out the high frequencies of the gravity field and represent the low frequencies better. For near sub-surface geophysical phenomena the lower altitude satellites are more suitable. On the other hand, for studying deeper structures of the Earth satellites flying at higher altitudes should be preferred. Consequently, SST data provided by GRACE should be more suitable for lithospheric stress modelling. Here, we have investigated two types of the SST data and concluded that $\mathbf{e}\cdot\delta\nabla T$ contains more frequencies of the gravity field and can present the stress better.

Eshagh (2015) reported that the sub-crustal stress reaches up to 100 MPa over Himalayas, when a GGFM is considered to degree 360 with mean Moho depth of 23 km. The magnitude of sub-crustal stress reaches to 5 MPa in Taiwan (Tenzer and Eshagh 2015) using a GGFM and Eshagh and Tenzer (2015) reported a maximum of 70 MPa when a mean Moho depth of 30 km is assumed. Eshagh (2016) reported maximum stress of about 60 MPa over Iran. Eshagh and Romeshkani (2015) used the real GOCE data to recover the stress at the depth of 100 km and found that the stress reaches to about 100 MPa. The values that we have obtained for the stress based on our approaches are about 30 and 45 MPa dependent on the use of $\delta T$ and $\mathbf{e}\cdot\delta\nabla T$ which are consistent with what can be obtained from other data types.

We emphasise that both of our methods have been applied under the same conditions, *e.g.*, the same satellite orbits, spatial resolution, and the mean Moho depth. The difference between these two solutions is dependent on the type of observables and the mathematical models connecting the observables to the unknown SF. It is clear that the second method, which uses the LOS gravity disturbances, is capable of recovering higher frequencies of the sub-crustal stress as compared to disturbing potential differences. Consequently, we can conclude that exploiting the LOS gravity disturbances performs well and may be more suited for real applications. To prove this

finding, recovery of sub-crustal stress from SST data contaminated by noise have to be performed. This task is left for our future research.

## 6. CONCLUSIONS

In this article two integral transformations between the stress function, numerical differentiation of which provides components of the sub-crustal stress, and the SST data have been derived. The first integral transformation assumes that the SST data are in the form of disturbing potential differences. SST data in the form of LOS gravity disturbance are related to the stress function in the second integral transformation.

The corresponding integral kernels have been investigated in the spatial domain showing their azimuthal dependence. The integral kernels are well-behaving, thus suitable for solving the inverse problem, *i.e.*, estimation of the stress function from the SST data. Direct and inverse problems have been tested in the numerical experiments. The results suggest that the stress function (and thus the components of the sub-crustal stress) estimated from the disturbing potential differences is smoother as compared to the estimate from the LOS gravity disturbances. This is due to the type of data being inverted and by using LOS gravity disturbances higher frequencies of the stress field can be recovered. Inversion of such data is better as long as the divergence does not happen in the mathematical model of the stress function. The theoretical apparatus may be applied for the recovery of the sub-crustal stress from satellite mission GRACE and its planned successor.

Acknowledgements. Michal Šprlák was supported by the project No. GA15-08045S of the Czech Science Foundation. Comments of the three anonymous reviewers are gratefully acknowledged.

## References

Arabelos, D.N., and D. Tsoulis (2013), The exploitation of state of the art digital terrain databases and combined or satellite-only Earth gravity models for the estimation of the crust-mantle interface over oceanic regions, *Geophys. J. Int*. **193**, 3, 1343-1352, DOI: 10.1093/gji/ggt081.

Block, A.E., R.E. Bell, and M. Studinger (2009), Antarctic crustal thickness from satellite gravity: Implications for the Transantarctic and Gamburtsev Subglacial Mountains, *Earth Planet. Sci. Lett*. **288**, 1-2, 194-203, DOI: 10.1016/j.epsl.2009.09.022.

Bouman, J. (1998), Quality of regularization methods, DEOS Report no. 98.2, Delft University Press, Delft, The Netherlands.

Braitenberg, C., and J. Ebbing (2009a), New insights into the basement structure of the West Siberian Basin from forward and inverse modeling of GRACE satellite gravity data, *J. Geophys. Res. Solid Earth* **114**, B06402, DOI: 10.1029/2008JB005799.

Braitenberg, C., and J. Ebbing (2009b), The GRACE-satellite gravity and geoid fields in analysing large-scale, cratonic or intracratonic basins, *Geophys. Prospect*. **57**, 4, 559-571, DOI: 10.1111/j.1365-2478.2009.00793.x.

Case, K., G. Kruizinga, and S.-C. Wu (2010), GRACE level 1B data product user handbook, Version 1.3, JPL D22027, Jet Propulsion Laboratory, California Institute of Technology, Pasadena, USA.

Chen, J.L., C.R. Wilson, B.D. Tapley, and S. Grand (2007), GRACE detects coseismic and postseismic deformation from the Sumatra-Andaman earthquake, *Geophys. Res. Lett*. **34**, 13, L13302, DOI: 10.1029/2007GL030356.

Choi, S., C.W. Oh, and H. Luehr (2006), Tectonic relation between northeastern China and the Korean peninsula revealed by interpretation of GRACE satellite gravity data, *Gondwana Res.* **9**, 1-2, 62-67, DOI: 10.1016/j.gr.2005.06.002.

Dai, C., C.K. Shum, R. Wang, L. Wang, J. Guo, K. Shang, and B. Tapley (2014), Improved constraints on seismic source parameters of the 2011 Tohoku earthquake from GRACE gravity and gravity gradient changes, *Geophys. Res. Lett*. **41**, 6, 1929-1936, DOI:10.1002/2013GL059178.

ESA (1999), Gravity field and steady-state ocean circulation mission, Report for mission selection of the four candidate earth explorer missions, ESA SP-1233(1), European Space Agency, ESA Publications Division, Noordwijk, The Netherlands.

Eshagh, M. (2011a), Sequential Tikhonov regularization: an alternative way for inverting satellite gradiometric data, *Z. Vermessungs*. **136**, 2, 113-121.

Eshagh, M. (2011b), The effect of spatial truncation error on integral inversion of satellite gravity gradiometry data, *Adv. Space Res.* **47**, 7, 1238-1247, DOI: 10.1016/j.asr.2010.11.035.

Eshagh, M. (2014), From satellite gradiometry data to sub-crustal stress due to mantle convection, *Pure Appl. Geophys*. **171**, 9, 2391-2406, DOI: 10.1007/s00024-014-0847-2.

Eshagh, M. (2015), On the relation between Moho and sub-crustal stress due to mantle convection, *J. Geophys. Eng.* **12**, 1, 1-11, DOI: 10.1088/1742-2132/12/1/1.

Eshagh, M. (2016), Integral approaches to determine sub-crustal stress from terrestrial gravimetric data, *Pure Appl. Geophys*. **173**, 3, 805-825, DOI: 10.1007/s00024-015-1107-9.

Eshagh, M., and M. Romeshkani (2015), Determination of sub-lithospheric stress due to mantle convection using GOCE gradiometric data over Iran, *J Appl. Geophys*. **122**, 11-17, DOI: 10.1016/j.jappgeo.2015.08.001.

Eshagh, M., and R. Tenzer (2015), Sub-crustal stress determined using gravity and crust structure models, *Computat. Geosci*. **19**, 1, 115-125, DOI: 10.1007/s10596-014-9460-9.

Fischell, R.E., and V.L. Pisacane (1978), A drag-free Lo-Lo satellite system for improved gravity field measurements. **In:** I. Mueller (ed.), *Proc. Ninth Geodesy/Solid Earth and Ocean Physics (GEOP) Int. Symp. "Applications of Geodesy to Geodynamics", 2-5 October 1978, Columbus Ohio State University, USA*, Report No. 280, 213-219.

Fu, R.S. (1986), A numerical study of the effects of boundary conditions on mantle convection models constrained to fit the low degree geoid coefficients, *Phys. Earth Planet. Int*. **44**, 3, 257-263, DOI: 10.1016/0031-9201(86)90074-9.

Fu, R.S. (1990), The Earth's geoid anomalies and the physical mathematical model of the mantle convection, *Chinese J. Geophys*. **33** (Suppl. II), 457-468 (in Chinese).

Hajela, D.P. (1974), Improved procedures for the recovery of 5° mean gravity anomalies from ATS-6/GEOS-3 satellite-to-satellite range-rate observations, Report No. 276, Department of Geodetic Science, Ohio State University, Columbus, USA.

Han, S.-C., J. Sauber, S.B. Luthcke, C. Ji, and F.F. Pollitz (2008), Implications of postseismic gravity change following the great 2004 Sumatra–Andaman earthquake from the regional harmonic analysis of GRACE intersatellite tracking data, *J. Geophys. Res.* **113**, B11, B11413, DOI:10.1029/2008JB005705.

Hansen, P.C. (1998), *Rank-deficient and Discrete Ill-posed Problems: Numerical Aspects of Linear Inversion*, SIAM, Philadelphia, 243 pp.

Hansen, P.C. (2007), Regularization tools, version 4.0 for Matlab 7.3, *Numer. Algorithms* **46**, 2, 189-194, DOI: 10.1007/s11075-007-9136-9.

Hofmann-Wellenhof, B., and H. Moritz (2005), *Physical Geodesy*, 2nd ed., Springer, Wien, 403 pp.

Huang, P.H., and R.S. Fu (1982), The mantle convection pattern and force source mechanism of recent tectonic movement in China, *Phys. Earth Planet. Int*. **28**, 3, 261-268, DOI: 10.1016/0031-9201(82)90007-3.

Jekeli, C. (1999), The determination of gravitational potential differences from satellite-to-satellite tracking, *Celest. Mech. Dyn. Astron*. **75**, 2, 85-101, DOI: 10.1023/A:1008313405488.

Kaban, M.K., and V. Trubitsyn (2012), Density structure of the mantle transition zone and the dynamic geoid, *J. Geodyn*. **59-60**, 183-192, DOI: 10.1016/j.jog.2012.02.007.

Kaban, M.K., M. Tesauro, and S. Cloetingh (2010), An integrated gravity model for Europe's crust and upper mantle, *Earth Planet. Sci. Lett.* **296**, 3-4, 195-209, DOI: 10.1016/j.epsl.2010.04.041.

Keller, W., and M.A. Sharifi (2005), Satellite gradiometry using a satellite pair, *J. Geodesy* **78**, 9, 544-557, DOI: 10.1007/s00190-004-0426-x.

Kiamehr, R., and L.E. Sjöberg (2006), Impact of a precise geoid model in studying tectonic structures – A case study in Iran, *J. Geodyn*. **42**, 1-3, 1-11, DOI: 10.1016/j.jog.2006.04.001.

Kiamehr, R., M. Eshagh, and L.E. Sjöberg (2008), Interpretation of general geophysical patterns in Iran based on GRACE gradient component analysis, *Acta Geophys*. **56**, 2, 440-454, DOI: 10.2478/s11600-007-0050-2.

Köther, N., H.-J. Götze, B.D. Gutknecht, T. Jahr, G. Jentzsch, O.H. Lücke, R. Mahatsente, R. Sharma, and S. Zeumann (2012), The seismically active Andean and Central American margins: Can satellite gravity map lithospheric structures? *J. Geodyn*. **59-60**, 207-218, DOI: 10.1016/j.jog.2011.11.004.

Li, J., J. Chen, and Z. Zhang (2014), Seismologic applications of GRACE time-variable gravity measurements, *Earthq. Sci*. **27**, 2, 229-245, DOI: 10.1007/s11589-014-0072-1.

Liu, H.S. (1977), Convection pattern and stress system under the African plate, *Phys. Earth Planet. Int.* **15**, 1, 60-68, DOI: 10.1016/0031-9201(77)90010-3.

Liu, H.S. (1978), Mantle convection pattern and subcrustal stress under Asia, *Phys. Earth Planet. Int.* **16**, 3, 247-256, DOI: 10.1016/0031-9201(78)90018-3.

Liu, H.S. (1980a), Mantle convection and subcrustal stress under Australia, *Mod. Geol.* **7**, 1, 29-36.

Liu, H.S. (1980b), Mantle convection and subcrustal stress under United States, *Mod. Geol*. **7**, 81-93.

Liu, H.S., E.S. Chang, and G.H. Wyatt (1976), Small-scale mantle convection system and stress field under Pacific plate, *Phys. Earth Planet. Int*. **13**, 3, 212-217, DOI: 10.1016/0031-9201(76)90095-9.

Matsuo, K., and K. Heki (2011), Coseismic gravity changes of the 2011 Tohoku-Oki earthquake from satellite gravimetry, *Geophys. Res. Lett.* **38**, 7, L00G12, DOI:10.1029/2011GL049018.

McAdoo, D.C., S.L. Farrell, S.W. Laxon, H.J. Zwally, D. Yi, and A.L. Ridout (2008), Arctic Ocean gravity field derived from ICESat and ERS-2 altimetry: Tectonic implications, *J. Geophys. Res.* **113**, B5, B05408, DOI:10.1029/2007JB005217.

McKenzie, D.P. (1967), Some remarks on heat flow and gravity anomalies, *J. Geophys. Res.* **72**, 24, 6261-6273, DOI:10.1029/JZ072i024p06261.

McNutt, M. (1980), Implication of regional gravity for state of stress in the Earth's crust and upper mantle, *J Geophys. Res.* **85**, B11, 6377-6396, DOI:10.1029/JB085iB11p06377.

Mikhailov, V., S. Tikhotsky, M. Diament, I. Panet, and V. Ballu (2004), Can tectonic processes be recovered from new gravity satellite data?, *Earth Planet. Sci. Lett.* **228**, 3-4, 281-297, DOI: 10.1016/j.epsl.2004.09.035.

Mikhailov, V., V. Lyakhovsky, I. Panet, Y. van Dinther, M. Diament, T. Gerya, O. deViron, and E. Timoshkina (2013), Numerical modelling of post-seismic rupture propagation after the Sumatra 26.12.2004 earthquake constrained by GRACE gravity data, *Geophys. J. Int.* **194**, 1, 640-650, DOI:10.1093/gji/ggt145.

Moritz, H. (2000), Geodetic reference system 1980, *J. Geodesy* **74**, 1, 128-133, DOI: 10.1007/s001900050278.

Panet, I., F. Pollitz, V. Mikhailov, M. Diament, P. Banerjee, and K. Grijalva (2010), Upper mantle rheology from GRACE and GPS postseismic deformation after the 2004 Sumatra–Andaman earthquake, *Geochem. Geophys. Geosyst.* **11**, 6, Q06008, DOI: 10.1029/2009GC002905.

Pavlis, N.K., S.A. Holmes, S.C. Kenyon, and J.K. Factor (2012), The development and evaluation of the Earth Gravitational Model 2008 (EGM2008), *J. Geophys. Res.* **117**, B4, B04406, DOI: 10.1029/2011JB008916.

Pick, M. (1994), The geoid and tectonic forces. **In:** P. Vaníček and N.T. Christou (eds.), *Geoid and its Geophysical Interpretations*, CRC Press, Boca Raton, 239-253.

Pick, M., and I. Charvátová-Jakubcová (1988), Modification of the Runcorn's equations on the convection flows, *Stud. Geophys. Geod.* **32**, 1, 47-53, DOI: 10.1007/BF01629000.

Pick, M., J. Pícha, and V. Vyskočil (1973), *Theory of the Earth's Gravity Field*, Elsevier, Amsterdam, 538 pp.

Reigber, C. (1989), Gravity field recovery from satellite tracking data. **In:** F. Sansó and R. Rummel (eds.), *Theory of Satellite Geodesy and Gravity Field Determination*, Lecture Notes in Earth Sciences, Vol. 25, Springer, Berlin Heidelberg, 197-234.

Reigber, C., H. Luehr, and P. Schwintzer (2002), CHAMP mission status, *Adv. Space Res*. **30**, 2, 129-134, DOI: 10.1016/S0273-1177(02)00276-4.

Ricard, Y., L. Fleitout, and C. Froidevaux (1984), Geoid heights and lithospheric stresses for a dynamic Earth, *Ann. Geophys*. **2**, 3, 267-286.

Ricard, Y., F. Chambat, and C. Lithgow-Bertelloni (2006), Gravity observations and 3D structure of the Earth, *C. R. Geosci*. **338**, 14-15, 992-1001, DOI: 10.1016/j.crte.2006.05.013.

Rummel, R. (1980), Geoid heights, geoid height differences, and mean gravity anomalies from 'low-low' satellite-to-satellite tracking – an error analysis, Report No. 306, Department of Geodetic Science, Ohio State University, Columbus, USA.

Runcorn, S.K. (1964), Satellite gravity measurements and laminar viscous flow model of the Earth mantle, *J. Geophys. Res*. **69**, 20, 4389-4394, DOI:10.1029/JZ069i020p04389.

Runcorn, S.K. (1967), Flow in the mantle inferred from the low degree harmonics of the geopotential, *Geophys. J. Int.* **14**, 1-4, 375-384, DOI: 10.1111/j.1365-246X.1967.tb06253.x.

Seeber, G. (2003), *Satellite Geodesy*, 2nd ed., Walter de Gruyter, Berlin, 589 pp.

Shin, Y.H., H. Xu, C. Braitenberg, J. Fang, and Y. Wang (2007), Moho undulations beneath Tibet from GRACE-integrated gravity data, *Geophys. J. Int*. **170**, 3, 971-985, DOI: 10.1111/j.1365-246X.2007.03457.x.

Souriau, M., and A. Souriau (1983), Global tectonics and the geoid, *Phys. Earth Planet. Int.* **33**, 2, 126-136, DOI: 10.1016/0031-9201(83)90145-0.

Šprlák, M., and P. Novák (2014a), Integral transformations of deflections of the vertical onto satellite-to-satellite tracking and gradiometric data, *J. Geodesy* **88**, 7, 643-657, DOI: 10.1007/s00190-014-0711-2.

Šprlák, M., and P. Novák (2014b), Integral transformations of gradiometric data onto GRACE type of observable, *J. Geodesy* **88**, 4, 377-390, DOI: 10.1007/s00190-013-0689-1.

Sun, W. (2014), Recent advances of computing coseismic deformations in theory and applications, *Earthq. Sci.* **27**, 2, 217-227, DOI: 10.1007/s11589-014-0077-9.

Sun, W., and S. Okubo (2004), Coseismic deformations detectable by satellite gravity missions: A case study of Alaska (1964, 2002) and Hokkaido (2003) earthquakes in the spectral domain, *J. Geophys. Res.* **109**, B4, B04405, DOI:10.1029/2003JB002554.

Tapley, B.D., S. Bettadpur, M. Watkins, and C. Reigber (2004), The gravity recovery and climate experiment: mission overview and early results, *Geophys. Res. Lett.* **31**, 9, L09607, DOI:10.1029/2004GL019920.

Tedla, G.E., M.V.D. Meijde, A.A. Nyblade, and F.D.V.D. Meer (2011), A crustal thickness map of Africa derived from a global gravity field model using Euler deconvolution, *Geophys. J. Int*. **187**, 1, 1-9, DOI:10.1111/j.1365-246X.2011.05140.x.

Tenzer, R., and M. Eshagh (2015), Subduction generated sub-crustal stress in Taiwan, *Terr. Atm. Oceanic Sci.* **26**, 261-268, DOI: 10.3319/TAO.2014.12.04.01(T).

Tenzer, R., M. Eshagh, and S. Jin (2015), Martian sub-crustal stress from gravity and topographic models, *Earth Planet. Sci. Lett*. **425**, 84-92, DOI: 10.1016/j.epsl.2015.05.049.

Tikhonov, A.N. (1963), Solution of incorrectly formulated problems and regularization method, *Soviet Math. Dokl*. **5**, 1035-1038.

Tondi, R., R. Schivardi, I. Molinari, and A. Morelli (2012), Upper mantle structure below the European continent: Constraints from surface-wave tomography and GRACE satellite gravity data, *J. Geophys. Res.* **117**, B9, B09401, DOI:10.1029/2012JB009149.

von Frese, R.R.B., L.V. Potts, S.B. Wells, T.E. Leftwich, H.R. Kim, J.W. Kim, A.V. Golynsky, O. Hernandez, and L.R. Gaya-Piqué (2009), GRACE gravity evidence for an impact basin in Wilkes Land, Antarctica, *Geochem. Geophys. Geosyst.* **10**, 2, Q02014, DOI:10.1029/2008GC002149.

Wang, L., C.K. Shum, F.J. Simons, B. Tapley, and C. Dai (2012), Coseismic and postseismic deformation of the 2011 Tohoku-Oki earthquake constrained by GRACE gravimetry, *Geophys. Res. Lett*. **39**, 7, L07301, DOI:10.1029/2012GL051104.

Wolff, M. (1969), Direct measurements of the Earth's gravitational potential using a satellite pair, *J. Geophys. Res*. **74**, 22, 5295-5300, DOI:10.1029/JB074i022p05295.

Zhao, S. (2013), Lithosphere thickness and mantle viscosity estimated from joint inversion of GPS and GRACE-derived radial deformation and gravity rates in North America, *Geophys. J. Int.* **194**, 3, 1455-1472, DOI: 10.1093/gji/ggt212.

Zuber, M.T., D.E. Smith, M.M. Watkins, S.W. Asmar, A.S. Konopliv, F.G. Lemoine, H.J. Melosh, G.A. Neumann, R.J. Phillips, S.C. Solomon, M.A. Wieczorek, J.G. Williams, S.J. Goosens, G. Kruizinga, E. Mazarico, R.S. Park, and D.-N. Yuan (2013), Gravity field of the Moon from the gravity recovery and interior laboratory (GRAIL) mission, *Science* **339**, 6120, 668-671, DOI: 10.1126/science.1231507.

Received 21 November 2014
Received in revised form 22 July 2015
Accepted 26 August 2015

DE GRUYTER OPEN

Acta Geophysica
vol. 64, no. 4, Aug. 2016, pp. 930-942
DOI: 10.1515/acgeo-2016-0045

# Spherical Elementary Current Systems Method Applied to Geomagnetic Field Modeling for the Adriatic

Eugen VUJIĆ[1] and Mario BRKIĆ[2]

[1]External Associate of Faculty of Geodesy, University of Zagreb, Croatia
e-mail:eugvujic@gfz.hr (corresponding author)

[2]Faculty of Geodesy, University of Zagreb, Croatia
e-mail: mbrkic@geof.hr

A b s t r a c t

The aim of this work was to derive an accurate regional model of geomagnetic components on the Adriatic. Data of north, east and vertical geomagnetic components at repeat stations and ground survey sites enclosing the Adriatic Sea were used to obtain a geomagnetic model at 2010.5 epoch. The core field was estimated by use of the global Enhanced Magnetic Model, while the crustal field by a mathematical technique for expanding vector systems on a sphere into basis functions, known as spherical elementary current systems method. The results of this method were presented and compared to the crustal field estimations by the Enhanced Magnetic Model. The maps of isolines of the regional model are also presented.

**Key words:** geomagnetic field model, crustal field, spherical elementary current systems method.

## 1. INTRODUCTION

Several methods for modeling of a spatial distribution of geomagnetic field components over a limited region at the Earth's surface have been developed by now (Haines 1985, De Santis *et al.* 1990, Thébault *et al.* 2006). Haines

Ownership: Institute of Geophysics, Polish Academy of Sciences;
© 2016 Vujić-Brkić. This is an open access article distributed under the Creative Commons Attribution-NonCommercial-NoDerivs license,
http://creativecommons.org/licenses/by-nc-nd/3.0/.

(1985) introduced Spherical Cap Harmonic Analysis (SCHA), where the solution of Laplace's equation over the spherical cap includes associated Legendre functions of non-integral degree and integral order. Further modifications of SCHA are given by Adjusted Spherical Cap Harmonic analysis (De Santis 1992) and by Translated Origin of Spherical Cap Harmonic Analysis (De Santis 1991). The Revised Spherical Cap Harmonic Analysis was introduced in order to combine ground, aeromagnetic, and satellite data, and the advantage of this method is improved altitude dependence (Thébault *et al.* 2004, 2006).

The primary objective of this study is testing new method for modelling the crustal field, as well as making a new crustal model over the Adriatic. In this work the regional model is a combination of the Enhanced Magnetic Model (EMM) for the core field, and a model of the crustal field which was derived by the spherical elementary current systems (SECS) method, introduced by Amm (1997). EMM is the high-degree global model up to degree and order of 720 based on spherical harmonic analysis (Maus 2010), and is derived from CHAMP Satellite Data, ØRSTED Satellite Data, INTERMAGNET Observatory Data and GEODAS magnetic data. The core field is described by degrees of 1-15. On the other hand, the SECS method is not based on spectral decomposition of a scalar magnetic potential (Amm and Viljanen 1999). It is based on two sets of basis functions (curl-free and divergence-free) in spherical coordinates, which can be used, *e.g.*, to expand any continuously differentiable vector field on a sphere (Amm 1997, Amm and Viljanen 1999, Juusola *et al.* 2006). The SECS method can expand the measured ground geomagnetic field into a sum of the magnetic field contributions of spherical elementary current systems, placed above the measurement sites and at some depth inside the Earth in geocentric frame (Pulkkinen *et al.* 2003).

## 2. METHOD AND DATA

### 2.1 The SECS method

Two types of spherical elementary sheet currents have been defined by Amm (1997): curl-free and divergence-free. In a case of the ground disturbances continuation, it is necessary to consider only the latter (Amm and Viljanen 1999). The centers of these elementary current systems (their poles) can be placed in the ionosphere and below the Earth's surface at fixed radii in geocentric reference frame (Pulkkinen *et al.* 2003). Within those two planes the poles can be placed freely, such that their locations are most suitable with respect to the type of magnetic variations to be analysed or to the density of measurement sites (Amm and Viljanen 1999).

Although the ground disturbances caused by ionospheric and/or magnetospheric currents were not analysed in this work, the same technique was applied for modeling of the crustal field at the Earth's surface. In this approach the spatial variations of the crustal field were modeled by using the two effective current layers placed in the Earth's interior and at height above the Earth's surface, respectively. For matching all three components of the measured field, field separation into internal and external parts have to be carried out by placing two equivalent current layers, one inside the ground and second above the ground (Vanhamäki *et al.* 2003). In this work a spatial distribution of the crustal field is modeled, not the real sources inside the Earth or the external contributions (and their induced counterparts). Thus, it does not matter where the sources are placed, only their total magnetic effects are modelled by those two current layers.

The definition of one of such divergence-free elementary sheet currents systems (Amm 1997, Amm and Viljanen 1999), in a spherical coordinate system ($r'$, $\theta'$, $\varphi'$) in which the pole of the elementary system is at $\theta' = 0$, is given by: $\boldsymbol{J}_c(\theta') = (I_c/4\pi R_c)\cdot\cot(\theta'/2)\cdot\hat{\varphi}'$, where $c = e$, $i$ ($e$ stands for the external layer and $i$ for the internal layer), $I_c$ is a scaling factor of the elementary system, radii $R_e$ and $R_i$ are defined in geocentric frame as $R_e = R_E + H_e$ and $R_i = R_E - H_i$, and the mean Earth's radius is $R_E = 6371.2$ km.

Thus, there are two infinitely thin horizontal current layers, the first above at height $H_e$ and the second inside the Earth at depth $H_i$, since any divergence-free current system can be composed by superposition of elementary current systems (Amm 1997, Pulkkinen *et al.* 2003). The magnetic effect of these two layers at some point given by radius vector $\boldsymbol{r}$ in geocentric frame on the Earth's surface is:

$$\boldsymbol{B}(\boldsymbol{r}) = \sum_{k=1}^{K} I_i^k \boldsymbol{G}_i\left(\boldsymbol{r}, R_i, \theta_k, \varphi_k\right) + \sum_{l=1}^{L} I_e^l \boldsymbol{G}_e\left(\boldsymbol{r}, R_e, \theta_l, \varphi_l\right), \tag{1}$$

where $\boldsymbol{G}_{i,e}$ are geometric terms related to the internal and the external part ($R_i < r < R_e$) of magnetic field produced by each elementary current system located at ($R_i$, $\theta_k$, $\varphi_k$) and ($R_e$, $\theta_l$, $\varphi_l$), while $K$ and $L$ are the numbers of poles related to the internal and the external layers, respectively. The expressions for $\boldsymbol{G}_{i,e}$ are given in Amm and Viljanen (1999) in detail. The above linear system of equations can be written in a matrix form as (Amm and Viljanen 1999, McLay and Beggan 2010):

$$\mathbf{B} = \mathbf{G}\,\mathbf{I},$$

where

$$\begin{pmatrix} \vdots \\ B_\theta^s \\ B_\phi^s \\ B_r^s \\ \vdots \end{pmatrix} = \begin{pmatrix} & \vdots & \\ G_{i,\theta}^{s,1} & G_{i,\theta}^{s,K} & G_{e,\theta}^{s,1} & G_{e,\theta}^{s,L} \\ G_{i,\phi}^{s,1} \ldots & G_{i,\phi}^{s,K} & G_{e,\phi}^{s,1} \ldots & G_{e,\phi}^{s,L} \\ G_{i,r}^{s,1} & G_{i,r}^{s,K} & G_{e,r}^{s,1} & G_{e,r}^{s,L} \\ & \vdots & \end{pmatrix} \cdot \begin{pmatrix} I_i^1 \\ \vdots \\ I_i^K \\ I_e^1 \\ \vdots \\ I_e^L \end{pmatrix} \tag{2}$$

with $s$ referring to $s$-th measurement site. The matrix **B** (of the order $3N$ by 1), where $N$ is a number of measurement sites, comprises the crustal field $(B_\theta, B_\varphi, B_r)$ estimated at the sites $(1, ..., N)$ on the Earth's surface (in geocentric frame). The matrix **G** is of the order $3N$ by $(K + L)$, where, for example, the term $G_{i,\theta}^{s,l}$ denotes $\theta$-component (in polar direction of geocentric frame) of the magnetic effect of internal origin, of an elementary current system with a scaling factor of 1A and its pole denoted by 1, at the measurement site denoted by $s$.

Matrix **I** can be calculated after deriving the matrices **B** and **G**. The system of equations is highly underdetermined (Amm and Viljanen 1999, Pulkkinen *et al.* 2003, McLay and Beggan 2010, Weygand *et al.* 2011), since the number of unknowns $(K + L)$ is in general much greater than the number of measurements at the Earth's surface $(3N)$. The inversion of matrix **G** can be performed by its singular value decomposition (Press *et al.* 2001), and after that the matrix **I** can be calculated. The procedure is that the stabilization in inversion of matrix **G** is done by choosing the threshold $\varepsilon$ for singular values related to different basis vectors of the decomposition, and if larger $\varepsilon$ is choosen, the smoother solutions for **I** will be in general (Amm and Viljanen 1999, Pulkkinen *et al.* 2003, Vanhamäki *et al.* 2003).

It is also possible to use only one (internal) layer for modeling the spatial variations of the crustal field, which is placed inside the Earth at depth $H = H_i$. In this case, the matrix **G** is of the order $3N$ by $K$, and the matrix **I** is of the order $K$ by 1. The internal SECS produces a different set of scaling factors compared to a case of using the two current layers (McLay and Beggan 2010).

## 2.2 Data

For obtaining the geomagnetic field over the Adriatic Sea region, the values of north ($X$), east ($Y$), and vertical ($Z$) geomagnetic components from 6 Croatian repeat stations, 54 Croatian ground survey stations, 32 Italian repeat stations, and 10 Albanian repeat stations were used (Fig. 1). The distances between the first neighbours are in the range of 5-67 km, with the average of 31 km. The data from Italian and Albanian repeat stations were attained from

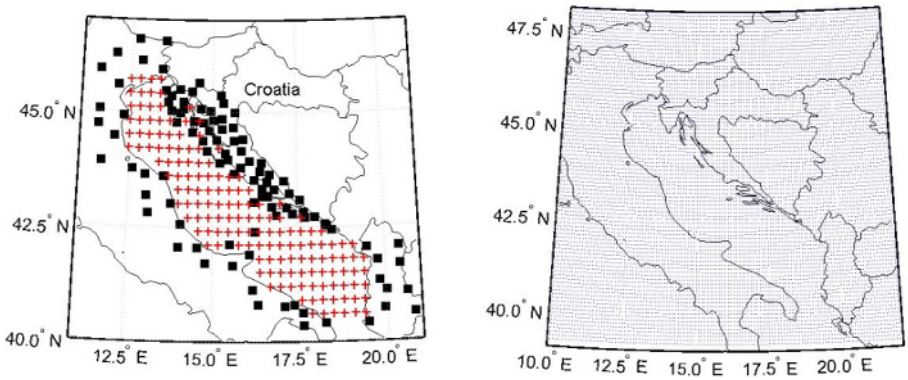


Fig. 1: Left: the positions of measurement sites (squares) used in deriving the regional geomagnetic model. The sites used for finding the optimal values of parameters of the SECS method are denoted with crosses (see Section 3); Right: the SECS poles grid (spacing 0.1°) over the Adriatic Sea region used in this work.

Dominici *et al.* (2012), and these data were reduced to 2010.0 epoch. The measurements of the Basic Geomagnetic Network of Republic of Croatia were performed in 2008 and 2009 (Brkić *et al.* 2013), and the data were reduced to 2008.5 and 2009.5 epochs, respectively, by the method described in Brkić *et al.* (2012).

## 3. RESULTS AND DISCUSSION

To find the optimal values of parameters of the SECS method, implemented for the crustal field modelling, the method was tested by using a known model of crustal magnetic field (degrees higher than 15 of the EMM model), as follows. The crustal field model values of $X$, $Y$, and $Z$ components were calculated at the 102 survey sites (Fig. 1), on which a random noise up to 5.5 nT (the estimated uncertainties due to instrumental and external variations elimination errors) was added (now representing virtual measurements). These values were used as the input into the SECS method.

The SECS method spacing and threshold parameters were tested in the ranges $\delta = 0.05\text{-}0.3°$ (due to the distances between survey sites) and $\varepsilon = 0.01\text{-}0.2$. In this work, due to simplicity, the radii of current layers in geocentric frame were taken as $R_i = R_E - H$ and $R_e = R_E + H$, with heights in the range $H = 5\text{-}30$ km (due to positions of survey sites in geocentric frame). The parameter of the SECS method misfit was the root-mean-square (rms) of residuals (rsd), where rsd = "real values" – "estimations". The residuals of the SECS method were calculated at 151 sites at the sea level over the Adriatic (marked as crosses in Fig. 1, not overlapped with the survey sites). The "real values" at those 151 sites were the EMM crustal field values, while

"estimations" were the crustal field values obtained by the SECS method. It was found that the smallest root-mean-square of residuals were obtained with choice $\delta = 0.1°$, $\varepsilon = 0.036$, and $H = 5$ km, and their values were 15.5 nT in *X*, 15.0 nT in *Y*, and 3.9 nT in *Z*. The regular SECS pole grid with spacing $\delta = 0.1°$ is shown in Fig. 1.

After the process of finding the optimal values of parameters of the SECS method, the aim was to produce the regional crustal field model over the Adriatic. The input values into the SECS method were the annual mean values of *X*, *Y*, and *Z* components at 102 survey sites, subtracted by EMM up to degree of 15, for 2008.5, 2009.5, and 2010.0 epochs, respectively, depending on reduction epoch. Those values were finally corrected for the long-term external variations. This means that the crustal field estimations at survey sites were the input data into the SECS method.

The long-term external variations and their induced effects do not average out completely in observatory annual mean values, and the same is reasonable for the repeat station and ground survey annual mean values (Korte and Thébault 2007). An empirical method for estimation of the long-term external variations can be used, as suggested in detail by (Korte and Thébault 2007). If one can assume that the external influence is homogeneous over some region, it can be estimated by using the data of observatories inside or close to that region. In this study the data from observatories Grocka (20.8 °E, 44.6 °N) and Tihany (17.9 °E, 46.9 °N) were used. The same procedure was used for both observatories, by using observatory data and the corresponding EMM (up to degree 720) estimations. The averaged values of external influences for *X*, *Y*, and *Z* were taken as corrections for all the sites in this study. Their absolute values are smaller than 4 nT in *X*, 1.5 nT in *Y*, and 3.5 nT in *Z*.

The results for rms(rsd) of the SECS method calculated at survey sites are presented in Fig. 2, for all three geomagnetic components. The errors of model increase with the height *H* above (below) the mean Earth's radius, and they are smallest for *Z* component up to 14 km, and for *X* component from 14 km up to 30 km. The corresponding values obtained by EMM crustal field estimations (degrees 16-720) at survey sites were 68.7, 57.4, and 87.2 nT in *X*, *Y*, and *Z* components, respectively. For *H* up to 10 km, rms(rsd) are smaller than 23 nT in *X*, 29 nT in *Y*, and 17 nT in *Z*. The rms values of residuals at survey sites in the case when just one (internal) layer was used in the SECS method, with $\delta = 0.1°$ and $\varepsilon = 0.036$, are also shown in Fig. 2. For the values of $H \leq 10$ km the results are better for *X* component in a case of internal layer, for *Z* in a case of two layers, while for *Y* the results are about the same for both cases.

Figures 3a-c display the isolines of *X*, *Y*, and *Z* components of the crustal field at the sea level over the Adriatic Sea, obtained with the SECS method

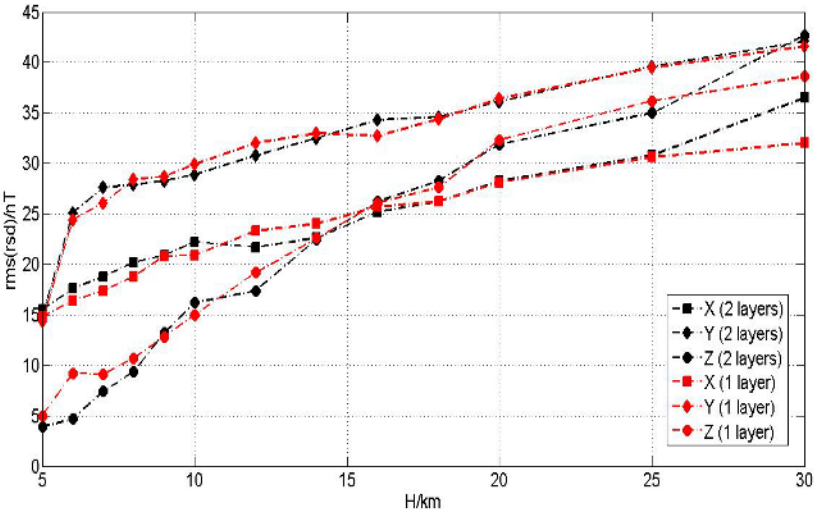


Fig. 2. The root-mean-square values of residuals of $X$, $Y$, and $Z$ components of the crustal field, respectively, derived at survey sites with the SECS method ($\varepsilon = 0.036$, $\delta = 0.1°$), as a function of the current layers height ($H$) above and below the sea level in geocentric frame. The rms values of residuals in the case of just one (internal) layer are also shown, when that layer was placed at depth $H$.

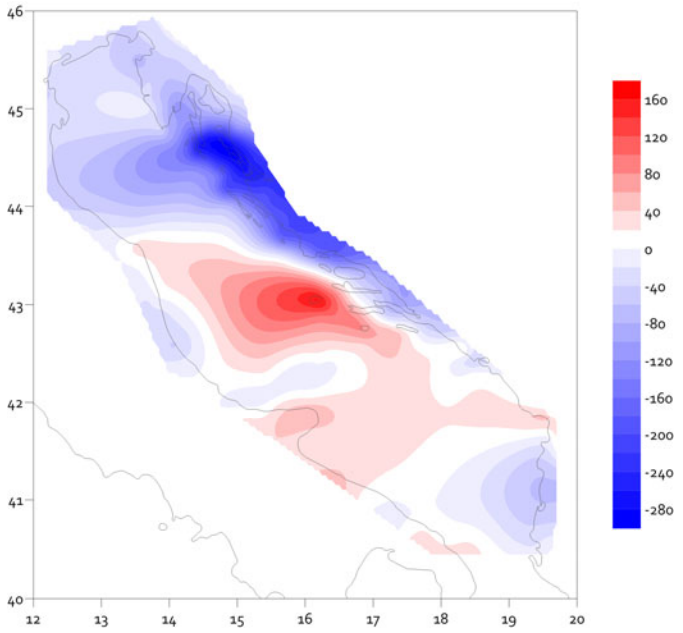

Fig. 3a. The regional model of the crustal field at the sea level of $X$ component over the Adriatic Sea. The scale bar is in nT. It was obtained by the SECS method by using the two current layers (with $H = 5$ km, $\varepsilon = 0.036$, $\delta = 0.1°$).

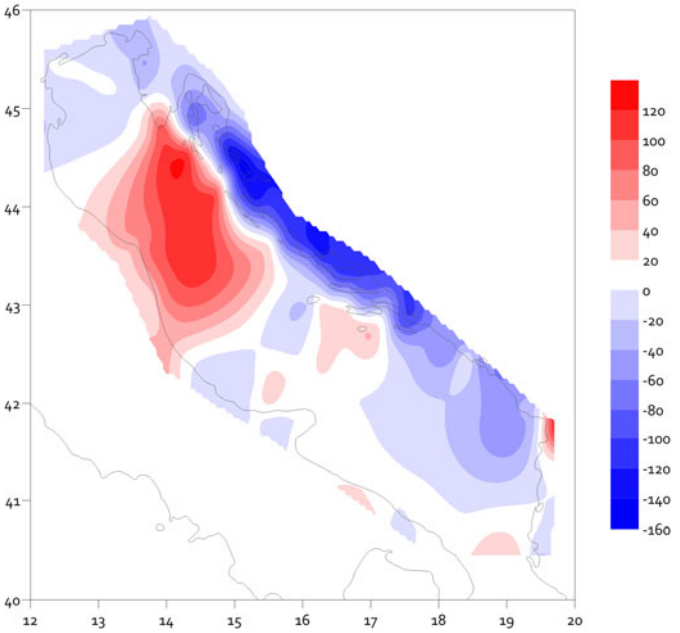


Fig. 3b. The same as Fig. 3a, but for *Y* component.

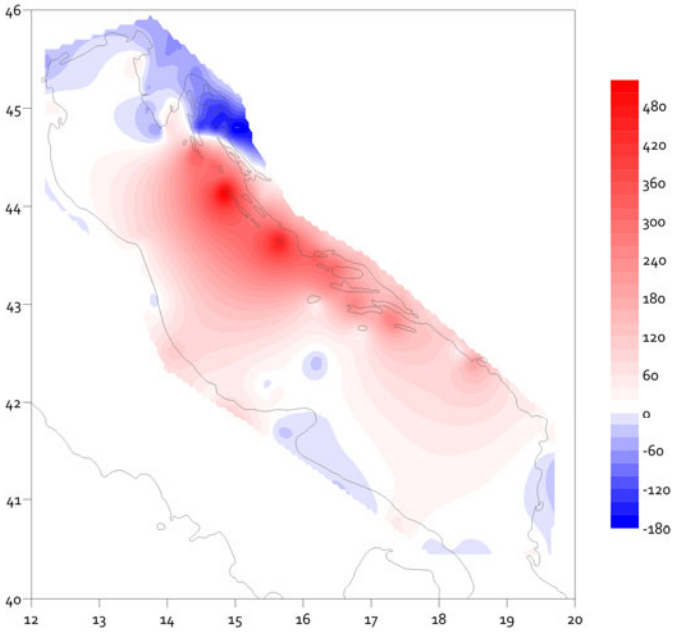


Fig. 3c. The same as Fig. 3a, but for *Z* component.

($H = 5$ km, $\varepsilon = 0.036$, $\delta = 0.1°$). The maximal calculated values of $X$, $Y$, and $Z$ are 158, 124, and 502 nT, respectively, while the minimal values are –300, –146, and –180 nT, respectively. Finally, the regional geomagnetic field model for 2010.5 epoch was equal to a sum of the core field for 2010.5 (obtained with EMM) and of the crustal field derived by the SECS method.

The regional geomagnetic model of $X$, $Y$, and $Z$ components for 2010.5 epoch is presented in Figs. 4a-c, respectively.

Both the crustal and geomagnetic field model maps present an unprecedented view of the crustal and the geomagnetic field features on the Adriatic. However the densification of the data is needed to depict more reliable Adriatic crustal and geomagnetic field.

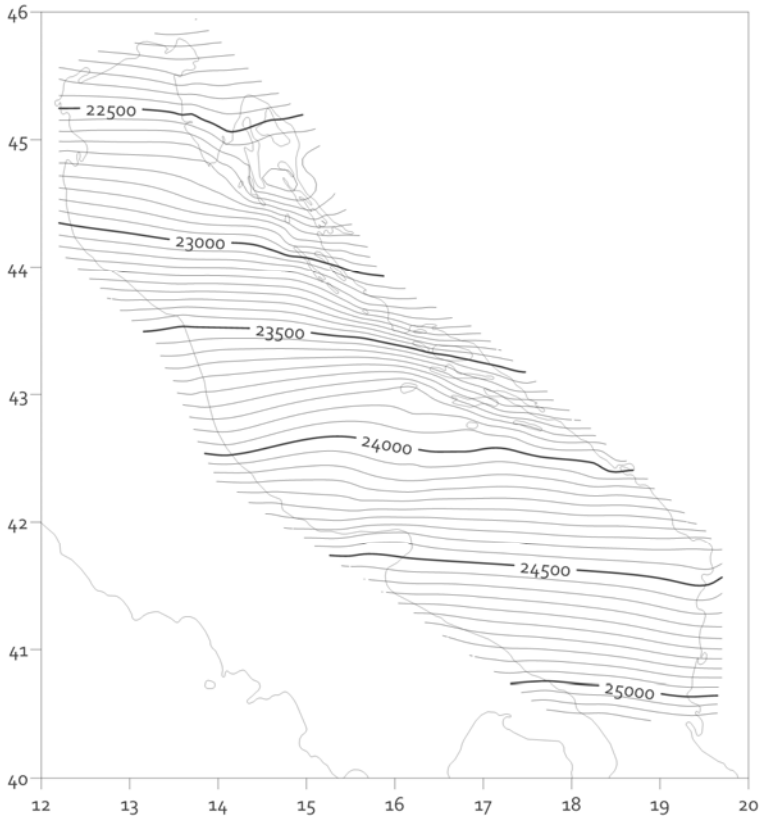


Fig. 4a. The regional model at the sea level of $X$ component over the Adriatic Sea for 2010.5 epoch. The isolines are in nT. The main field was obtained from the EMM, and the crustal field with the SECS method by using the two current layers (with $H = 5$ km, $\varepsilon = 0.036$, $\delta = 0.1°$).

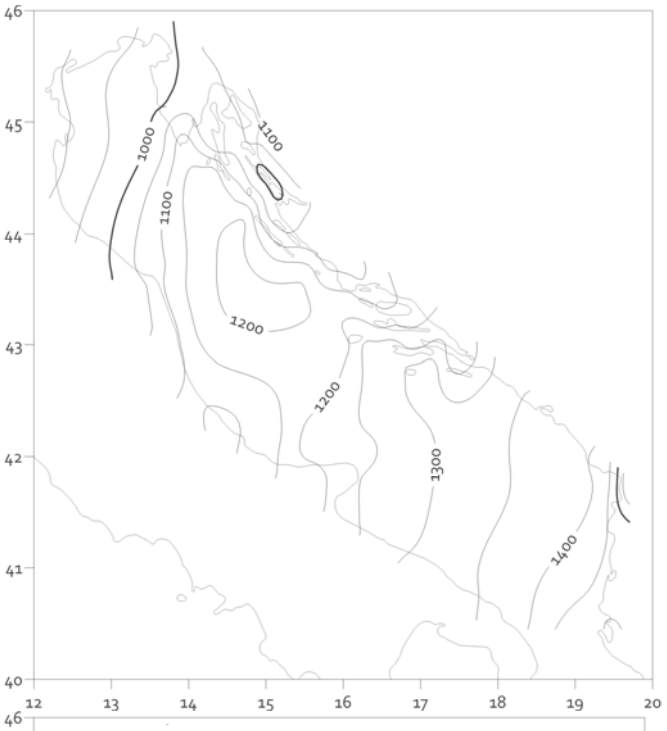


Fig. 4b. The same as Fig. 4a, but for *Y* component.

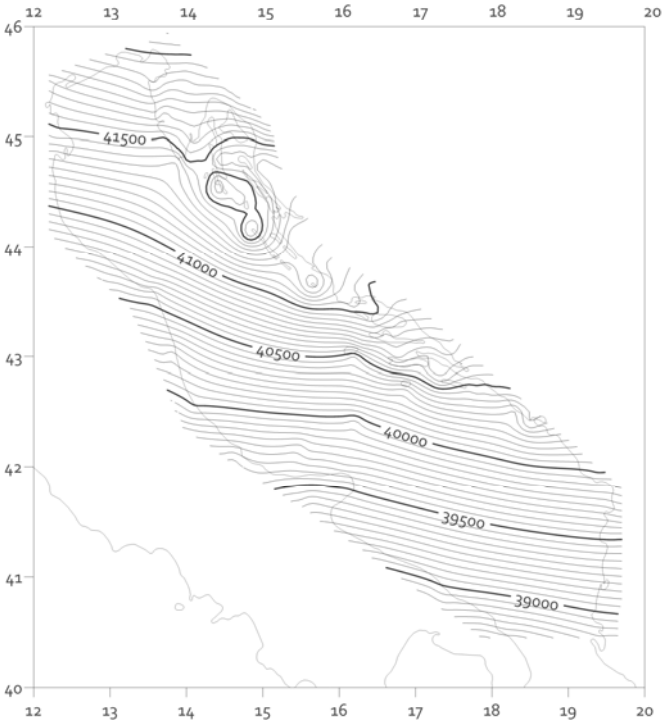


Fig. 4c. The same as Fig. 4a, but for *Z* component.

## 4. CONCLUSION

An alternative approach of modeling the geomagnetic field was envisaged by use of spherical elementary current systems method and investigated on the Adriatic. The presented procedure, in which the main field is removed from the measurements, allows modelling of residuals, or in other words, the crustal field. For a favorable set of parameters (spacing, threshold, and the current layers height), the SECS method gives relatively small modelling errors. The root-mean-square of residuals of the crustal field components were found to be 4-22 times smaller (with $H = 5$ km, $\varepsilon = 0.036$, $\delta = 0.1°$) in respect to the Enhanced Magnetic Model crustal field estimations. Finally, the geomagnetic field was restored by adding back the main field to obtained residuals. The presented crustal and geomagnetic field maps depict features with unprecedented informativeness, but limited by availability and distribution of the input data; thus the maps are expected to be more reliable in the measured areas, close to the Adriatic Sea coast. A new and more accurate crustal and geomagnetic field maps are generally needed for scientific research, *e.g.*, to build tectonic models of oceanic and continental crust, to estimate the crustal thermal states, to contribute to geodynamic models, *etc.* (Thébault *et al.* 2010), while in practical purposes for the natural resources assessment and the navigation, and for some of these reasons could also be used in our future work.

The input data came from the Adriatic coast and islands, while the open sea was without measurements (for both simulated and real cases), and this is a clear drawback of the final model. It would be contrasted by using data in the sea. In a case of "perfect data" there would not be any problem because of the validity of Laplace equation, but here we are quite far from having "perfect data". Furthermore, the satellite data from recent missions should also be used in the future work, in order to fill the gap across the sea, and to understand the real potentiality of the SECS method in case of data at different altitudes as well.

Acknowledgments. The authors acknowledge the Ministry of Defence, the State Geodetic Administration, and the Ministry of Science, Education and Sports of the Republic of Croatia. They are also very thankful to Prof. A. De Santis and an anonymous reviewer for constructive suggestions that significantly improved the manuscript.

## References

Amm, O. (1997), Ionospheric elementary current systems in spherical coordinates and their application, *J. Geomag. Geoelectr.* **49**, 7, 947-955, DOI: 10.5636/jgg.49.947.

Amm, O., and A. Viljanen (1999), Ionospheric disturbance magnetic field continuation from the ground to the ionosphere using spherical elementary current systems, *Earth Planets Space* **51**, 6, 431-440, DOI: 10.1186/BF03352247.

Brkić, M., D. Šugar, M. Pavasović, E. Vujić, and E. Jungwirth (2012), Croatian geomagnetic field maps for 2008.5 epoch, *Ann. Geophys.* **55**, 6, 1061-1069, DOI: 10.4401/ag-5395.

Brkić, M., E. Vujić, D. Šugar, E. Jungwirth, D. Markovinović, M. Rezo, M. Pavasović, O. Bjelotomić, M. Šljivarić, M. Varga, and V. Poslončec-Petrić (2013), Basic geomagnetic network of the Republic of Croatia 2004-2012, with geomagnetic field maps at 2009.5 epoch, Croatian State Geodetic Administration (in Croatian).

De Santis, A. (1991), Translated origin spherical cap harmonic analysis, *Geophys. J. Int.* **106**, 1, 253-263, DOI: 10.1111/j.1365-246X.1991.tb04615.x.

De Santis, A. (1992), Conventional spherical harmonic analysis for regional modelling of the geomagnetic field, *Geophys. Res. Lett.* **19**, 10, 1065-1067, DOI: 10.1029/92GL01068.

De Santis, A., O. Battelli, and D.J. Kerridge (1990), Spherical cap harmonic analysis applied to regional field modelling for Italy, *J. Geomag. Geoelectr.* **42**, 9, 1019-1036, DOI: 10.5636/jgg.42.1019.

Dominici, G., A. Meloni, M. Sperti, G. Manzo, and R. Maseroli (2012), Italian Magnetic Network and Geomagnetic Field Maps of Italy at year 2010.0, Istituto Geografico Militare, Italy.

Haines, G.V. (1985), Spherical cap harmonic analysis, *J. Geophys. Res.* **90**, B3, 2583-2591, DOI: 10.1029/JB090iB03p02583.

Juusola, L., O. Amm, and A. Viljanen (2006), One-dimensional spherical elementary current systems and their use for determining ionospheric currents from satellite measurements, *Earth Planets Space* **58**, 5, 667-678, DOI: 10.1186/BF03351964.

Korte, M., and E. Thébault (2007), Geomagnetic repeat station crustal biases and vectorial anomaly maps for Germany, *Geophys. J. Int.* **170**, 1, 81-92, DOI: 10.1111/j.1365-246X.2007.03387.x.

Maus, S. (2010), An ellipsoidal harmonic representation of Earth's lithospheric magnetic field to degree and order 720, *Geochem. Geophys. Geosyst.* **11**, 6, Q06015, DOI: 10.1029/2010GC003026.

McLay, S.A., and C.D. Beggan (2010), Interpolation of externally-caused magnetic fields over large sparse arrays using Spherical Elementary Current Systems, *Ann. Geophys.* **28**, 9, 1795-1805, DOI: 10.5194/angeo-28-1795-2010.

Press, W.H., S.A. Teukolsky, W.T. Vetterling, and B.P. Flannery (2001), *Numerical Recipes in Fortran 77: The Art of Scientific Computing*, Cambridge University Press, Cambridge.

Pulkkinen, A., O. Amm, A. Viljanen, and BEAR Working Group (2003), Separation of the geomagnetic variation field on the ground into external and internal parts using the spherical elementary current system method, *Earth Planets Space* **55**, 3, 117-129, DOI: 10.1186/ BF03351739.

Thébault, E., J.J. Schott, M. Mandea, and J.P. Hoffbeck (2004), A new proposal for spherical cap harmonic modelling, *Geophys. J. Int.* **159**, 1, 83-103, DOI: 10.1111/j.1365-246X.2004.02361.x.

Thébault, E., M. Mandea, and J.J. Schott (2006), Modeling the lithospheric magnetic field over France by means of revised spherical cap harmonic analysis (R SCHA), *J. Geophys. Res.* **111**, B5, 949-967, DOI: 10.1029/ 2005JB004110.

Thébault, E., M. Purucker, K.A. Whale, B. Langlais, and T.J. Sabaka (2010), The magnetic field of the Earth's lithosphere, *Space Sci. Rev.* **155**, 1, 95-127, DOI: 10.1007/s11214-010-9667-6.

Vanhamäki, H., O. Amm, and A. Viljanen (2003), One-dimensional upward continuation of the ground magnetic field disturbance using spherical elementary current systems, *Earth Planets Space* **55**, 10, 613-625, DOI: 10.1186/ BF03352468.

Weygand, J.M., O. Amm, A. Viljanen, V. Angelopoulos, D. Murr, M.J. Engebretson, H. Gleisner, and I. Mann (2011), Application and validation of the spherical elementary currents systems technique for deriving ionospheric equivalent currents with the North American and Greenland ground magnetometer arrays, *J. Geophys. Res.* **116**, A03305, DOI: 10.1029/ 2010JA016177.

Received 27 March 2015
Received in revised form 25 September 2015
Accepted 22 October 2015

DE GRUYTER OPEN

Acta Geophysica
vol. 64, no. 4, Aug. 2016, pp. 943-962
DOI: 10.1515/acgeo-2016-0001

# Magnetic and Electromagnetic Signatures around Polile Tshisa Hot Spring in the Northern Neotectonic Belt in the Eastern Cape Province, South Africa

Kakaba MADI[1], Peter K. NYABEZE[2], Oswald GWAVAVA[1], Matome SEKIBA[2], and Baojin ZHAO[3]

[1]Department of Geology, University of Fort Hare, Alice, South Africa
e-mail: kmadi@ufh.ac.za

[2]Geophysics Unit, Council for Geoscience, Pretoria, South Africa

[3]Worley Parsons TWP, Johannesburg, South Africa

A b s t r a c t

Finding productive boreholes in the Karoo fractured aquifers has never been an easy task. Fractured Karoo aquifers in the neotectonic zones in the Eastern Cape Province can be targeted for groundwater exploration. The Polile Tshisa hot spring is located in a seismo-tectonic region beset by neotectonics. Hot springs are indicative of circulation of groundwater at great depths along fault zones, and accordingly of neotectonics. The characterisation of hot springs by means of magnetic and electromagnetic methods can help infer the occurrence of structures which are favourable for groundwater potential. The Polile Tshisa hot spring is characterised by faults, fractures, and dolerite dykes. All these structures make the hot spring a good case study for groundwater exploration.

**Key words:** neotectonics, electromagnetic, groundwater, hot springs, Karoo.

Ownership: Institute of Geophysics, Polish Academy of Sciences;
© 2016 Madi *et al*. This is an open access article distributed under the Creative Commons Attribution-NonCommercial-NoDerivs license,
http://creativecommons.org/licenses/by-nc-nd/3.0/.

## 1. INTRODUCTION

The Eastern Cape northern neotectonic belt is mainly characterized by the Kokstad–Koffiefontein seismic belt (formerly known as the Senqu seismotectonic belt) and seven hot springs (Fig. 1). Meissner and Wever (1986) have shown that epicentres of intracontinental earthquakes (*e.g.*, South Africa) are concentrated on lineaments. Recent seismic activity in the South Africa–Lesotho border region is related either to the southwards propagation of the East Africa Rift System at the boundary between the Nubian and Somalian lithospheric plates, or to epirogenic causes involving a lithospheric Quathlamba hot spot (in the Drakensberg volcanic region), which is a seismicity axis (Hartnady 1985).

Olivier (1972) found that during the construction of the Orange–Fish tunnel, flooding occurred after an abnormally well-developed fissure-zone was intersected approximately 550 m south of the shaft 2. The inrush of water was associated with the collapse of the tunnel roof, as part of the roof's major fissure was exposed by the fateful blast. He noted, however, that an influence of earthquakes and accordingly of neotectonics on the pattern of

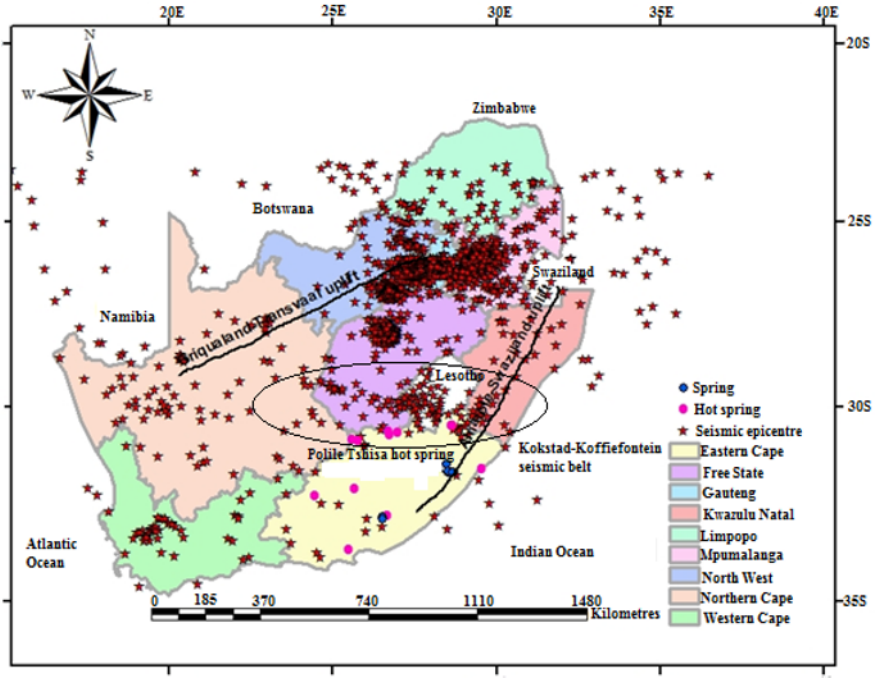


Fig. 1. Seismic epicentres in southern Africa. Note the encircled Kokstad–Koffiefontein seismic belt with its seven hot springs in the Eastern Cape northern neotectonic belt near the country of Lesotho (source of epicentres for new seismic events: IRIS website browser 2012).

semi-diurnal tidal fluctuations is of special interest as regards the flooding problem. Hot springs are indicative of possible neotectonics. It can be suggested that the basaltic eruption of 1983 in Lesotho (Maud *et al.* 1983) might have heated the water from beneath. Moreover, Kent (1969) has shown that the origin of thermal springs is attributed to the presence of deep structures, principally fault-zones, which provide continuously circulating convection or artesian systems. On the other hand, Olivier *et al.* (2011) highlighted that South African thermal springs are some of the most under-researched and under-utilised of all natural resources. Delvaux and Mahon (1993), for instance, compiled a neotectonic map of the Mbeya area in Tanzania from the Quaternary structural elements and volcanic centres, active hot springs, and earthquake epicentres. On the other hand, they highlighted from the works of Spurr (1953) that the hydrothermal activity is rather frequent in the Mbeya area, and is clearly controlled by an active fault. The seven hot springs in the northern neotectonic belt in the Eastern Cape Province are clearly controlled by a neotectonic fault because of the following reasons: the Polile Tshisa hot spring, for instance, is located near the country of Lesotho; the basaltic event of 1983, as reported by Maud *et al.* (1983), is accordingly a neovolcanic event, which has disturbed the crust inducing neotectonics. The Polile Tshisa hot spring is aligned with six other hot springs (on its left) along a neotectonic fault in the Kokstad–Koffiefontein seismic belt (Fig. 1); neotectonics is strongly related to seismic activity.

In a reference guide on geophysical techniques (1993), documented by the Eastern Research Group from Lexington in the United States of America, it was reported that geophysical techniques are used to assess the physical and chemical properties of soils, rocks and groundwater based on response to either (i) various parts of the electromagnetic (EM) spectrum, including gamma rays, visible light, radar, microwave, and radiowaves; (ii) acoustic and/or seismic energy; or (iii) other potential fields such as gravity and the earth's magnetic field. On the other hand, it was shown that the greatest benefits of geophysical methods come from using them early in the site characterization, since they are typically non-destructive, less risky, and require less time and cost than using monitoring wells. Magnetic and electromagnetic surveys can help to characterise potential aquifers as far as the structures are concerned.

## 2. METHODOLOGY

The northern neotectonic belt of the Eastern Cape Province, due to the remarkable seismic belt that runs from the east coast to Koffienfontein and the presence of many hot springs, is considered as an area of remarkable neotectonics. On the basis of this fact it was suggested that this neotectonic belt could be characterized using geophysics (electromagnetic, magnetic, and

radiometric measurements). Magnetic field data were acquired in the walking mode using a Geometrics Proton Processor Magnetometer (G-859) set to operate in the Julian calendar at a cycle time of 1.5 s, with a resolution of 0.1 nT, and an accuracy of 0.5 nT, at temperatures between –20 and 50°C, and a gradient tolerance of 1000 nT/m. The magnetic maps around the Polile Tshisa hot spring were produced using the Geosoft 7.3 first at a grid cell size of 1 m in order to see all the high frequency signals, then the grid cell size was changed to 14 m so that a generalized complete image can be visualized making it easier to depict a preliminary interpretation.

Electromagnetic measurements are mainly used to depict fissured zones, and were conducted using the Geonics EM ground conductivity meter. The data acquisition was not easy due to accessibility problems. In the area of the hot spring of Polile Tshisa, for instance, houses have been built and big gullies, difficult to cross, were great obstacles. For electromagnetic measurements, a 10-, 20-, and 40-m coil separation cable was used .The conductivity was measured both in horizontal and vertical dipole modes. These measurements were then plotted against the station intervals for each coil separation cable on a binary diagram in order to obtain a profile. At Polile Tshisa the electromagnetic survey was done in the southeast-northeast and southwest-northeast directions (*e.g.*, Fig. 8). These survey lines were set in order to possibly cross cut the fault that host the hot springs. The hydrogeological conceptual model was done using the acquired magnetic data.

## 3. RESULTS

### 3.1 Field observations

The Polile hot spring located south of Matatiele near the border of Lesotho is possibly hosted within a major regional fault that connects the hot spring of

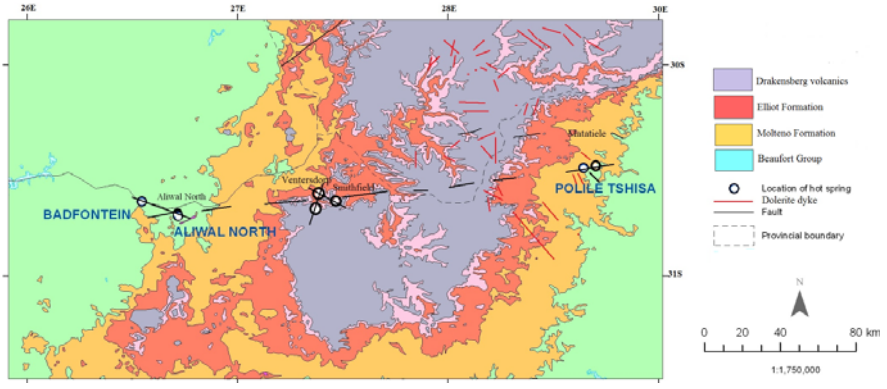


Fig. 2. Geological map showing some structures and the hot springs in the Eastern Cape Province northern neotectonic belt.

Aliwal North and Badfontein (Fig. 2). The water of this hot spring wells up at three different places (Fig. 3a) separated by a distance of almost thirty centimetres aligned in a direction of 75°N. A quartz vein indicating hydrothermal activity occurs near the hot spring. The water of the Polile Tshisa is alkaline (pH of 9.2), and is mainly used by villagers for their domestic

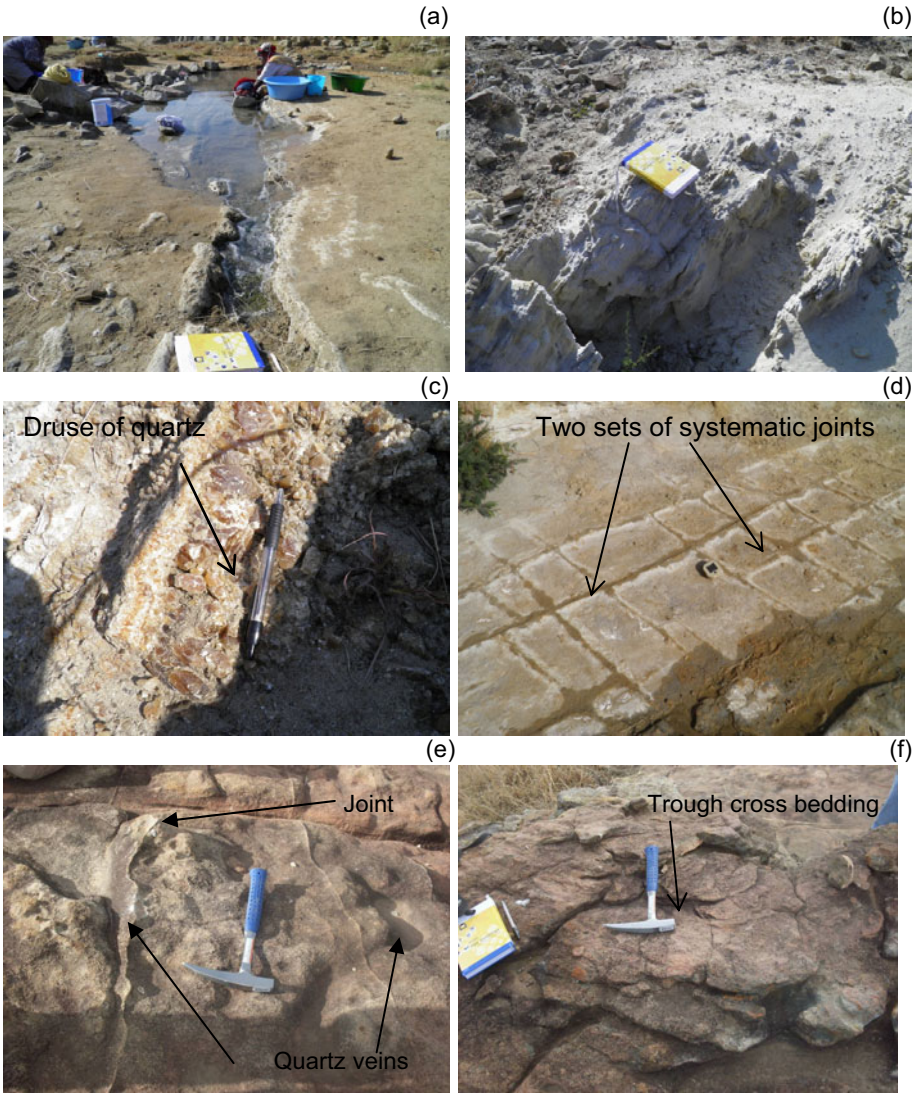


Fig. 3. Caption on next page.

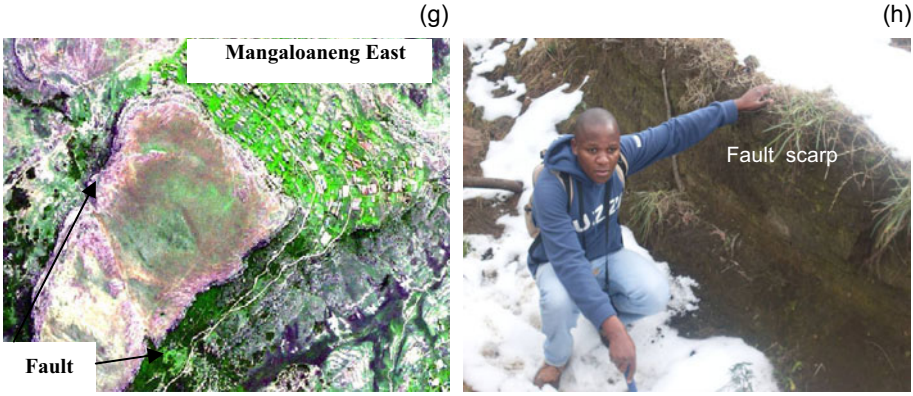


Fig. 3: (a) Polile Tshisa hot spring, (b) intense weathering marked by a kaolinisation, (c) druse of quartz, (d) and (e) centimetric quartz veins, (f) trough-cross bedding, (g) neotectonic fault seen from SPOT data near Mangaloaneng-East village, and (h) fault scarp of the neotectonic fault seen in panel (g).

needs. The temperature of this hot spring water can reach 32°C. The flow rate is of a tiny seep, the water from this hot springs flows along a stream connected to a river nearby. The area itself has outcrops of coarse grains sandstones of the Molteno Formation in the Karoo Supergroup. It is characterized by intense weathering marked by a kaolinisation (Fig. 3b). This weathering indicates an intensive surface water circulation, which is a major source of recharge. The water possibly goes deep down below, and is discharged through the springs. The high degree of weathering has made some of the original rock to completely alter. The sandstone layers have a thickness that varies from 2 to 5 cm. A druse of quartz full of impurities colouring them in brown was seen near the spring (Fig. 3c) and because of weathering, crystals of quartz are easily being loosed up. Two sets of centimetric quartz veins cross cutting each *e* (Fig. 3d) were found on the bed of a non-perennial river near the hot spring; the first set, which is the old one, if the cross cutting relation is applied, has a strike of 320°N; and the second set which is the later one, has a strike of 245°N. The two sets are almost perpendicular, they occur in weathered sandstones with few intercalations of weathered shales. At this place, the beds strike is 250°N, the dip is 15° and the dip direction is 340°N. Similar quartz veins have been found within some coarse-grained sandstones (with a diameter varying between 2 and 5 mm) 10 km north of the Polile Tshisa hot spring near the town of Matatiele around the South Africa–Lesotho border (Fig. 3e). Trough-cross beddings were the only predominant sedimentary structures seen within these sandstones (Fig. 3f). In this area a fault oriented 120°N was depicted from SPOT data around the Mangaloaneng–East village near Matatiele (Fig. 2g); its scarp is visible in

Fig. 3h. This fault indicates neotectonic movement in the area because it has also affected the soil, as can be seen in Fig. 3g.

### 3.2 Magneitc survey at Polile Tshisa hot spring

The magnetic survey (see sample in Table 1) was conducted around the Polile Tshisa hot spring. This survey was complicated by uneasy accessibility marked by the presence of gullies and some few constructions in the vicinity. Data acquisition was carried out using a Cesium vapour high precision magnetometer (Geometrics 859) along four lines (NW-SE, N-S, NE-SW); these lines can be seen in Fig. 4. Figure 5 shows the grid size expanded to 14 m for a better visualisation. The N-S magnetic line at the right hand side has magnetic high values in the southern area. This might be related to the occurrence of a dolerite dyke, which is a good indicator for drilling in order to generate a potential high yield well.

Three magnetic profiles were extracted from the map in Fig. 5. The first line, SE-NW, has a profile that is almost flat at the right side (Fig. 6). It shows an increase from 10 m reaching more than 27634.4 nT at approxi-

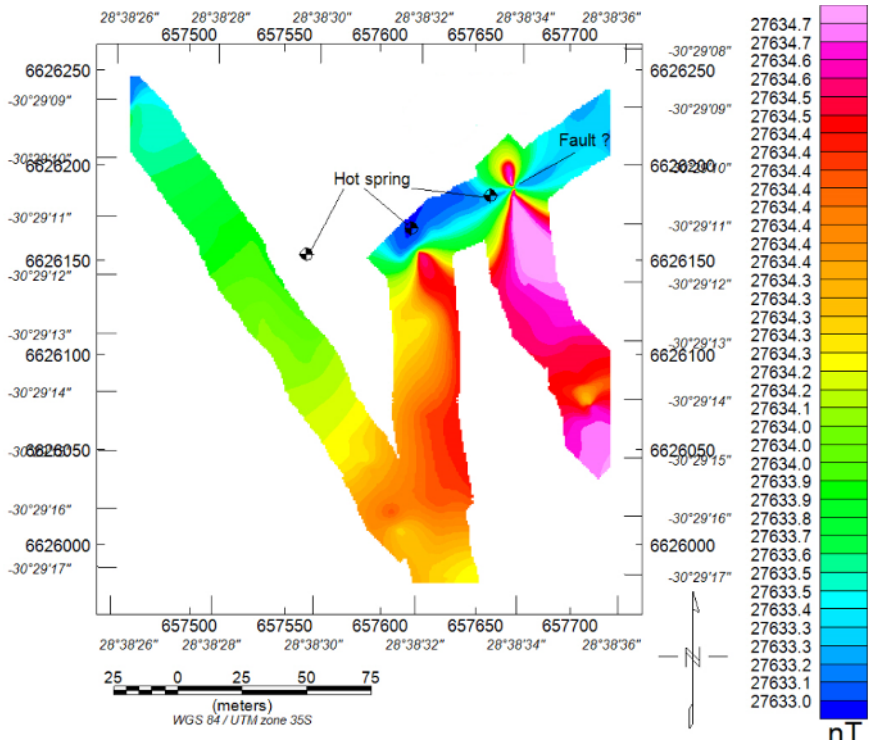


Fig. 4. Magnetic map produced at a grid cell size of 1 m.

Table 1

Sample of magnetic readings at Polile Tshisa

| *X* [°] | *Y* [°] | GPS_height [m] | Reading_1 [nT] | Diurnal_1 [nT] | Corrected [nT] | Time | Date |
|---|---|---|---|---|---|---|---|
| 28.64212 | –30.4866 | 1360.789 | 27616.876 | –16.424 | 27633.3 | 13:49:59.80 | 05/29/12 |
| 28.64212 | –30.4866 | 1360.735 | 27623.534 | –9.766 | 27633.3 | 13:49:59.60 | 05/29/12 |
| 28.64212 | –30.4866 | 1360.681 | 27623.96 | –9.340 | 27633.3 | 13:49:59.40 | 05/29/12 |
| 28.64212 | –30.4866 | 1360.628 | 27621.513 | –11.787 | 27633.3 | 13:49:59.20 | 05/29/12 |
| 28.64212 | –30.4866 | 1360.574 | 27618.573 | –14.727 | 27633.3 | 13:49:59.00 | 05/29/12 |
| 28.64212 | –30.4866 | 1360.54 | 27621.324 | –11.976 | 27633.3 | 13:49:58.80 | 05/29/12 |
| 28.64212 | –30.4866 | 1360.527 | 27624.978 | –8.322 | 27633.3 | 13:49:58.60 | 05/29/12 |
| 28.64213 | –30.4866 | 1360.514 | 27632.037 | –1.263 | 27633.3 | 13:49:58.40 | 05/29/12 |
| 28.64213 | –30.4866 | 1360.501 | 27635.632 | 2.332 | 27633.3 | 13:49:58.20 | 05/29/12 |
| 28.64213 | –30.4866 | 1360.488 | 27633.31 | 0.010 | 27633.3 | 13:49:58.00 | 05/29/12 |
| 28.64213 | –30.4866 | 1360.470 | 27630.625 | –2.675 | 27633.3 | 13:49:57.80 | 05/29/12 |
| 28.64214 | –30.4866 | 1360.449 | 27632.072 | –1.228 | 27633.3 | 13:49:57.60 | 05/29/12 |
| 28.64214 | –30.4865 | 1360.428 | 27634.68 | 1.380 | 27633.3 | 13:49:57.40 | 05/29/12 |
| 28.64214 | –30.4865 | 1360.406 | 27638.985 | 5.685 | 27633.3 | 13:49:57.20 | 05/29/12 |
| 28.64214 | –30.4865 | 1360.385 | 27640.587 | 7.287 | 27633.3 | 13:49:57.00 | 05/29/12 |
| 28.64214 | –30.4865 | 1360.354 | 27637.336 | 4.036 | 27633.3 | 13:49:56.80 | 05/29/12 |
| 28.64215 | –30.4865 | 1360.315 | 27634.981 | 1.681 | 27633.3 | 13:49:56.60 | 05/29/12 |
| 28.64215 | –30.4865 | 1360.276 | 27634.591 | 1.291 | 27633.3 | 13:49:56.40 | 05/29/12 |
| 28.64215 | –30.4865 | 1360.238 | 27635.551 | 2.251 | 27633.3 | 13:49:56.20 | 05/29/12 |
| 28.64215 | –30.4865 | 1360.199 | 27638.56 | 5.260 | 27633.3 | 13:49:56.00 | 05/29/12 |
| 28.64215 | –30.4865 | 1360.166 | 27640.662 | 7.362 | 27633.3 | 13:49:55.80 | 05/29/12 |
| 28.64216 | –30.4865 | 1360.141 | 27636.606 | 3.306 | 27633.3 | 13:49:55.60 | 05/29/12 |
| 28.64216 | –30.4865 | 1360.115 | 27633.287 | –0.013 | 27633.3 | 13:49:55.40 | 05/29/12 |
| 28.64216 | –30.4865 | 1360.089 | 27632.014 | –1.286 | 27633.3 | 13:49:55.20 | 05/29/12 |
| 28.64216 | –30.4865 | 1360.064 | 27634.284 | 0.984 | 27633.3 | 13:49:55.00 | 05/29/12 |
| 28.64216 | –30.4865 | 1360.036 | 27637.53 | 4.230 | 27633.3 | 13:49:54.80 | 05/29/12 |
| 28.64217 | –30.4865 | 1360.007 | 27642.044 | 8.744 | 27633.3 | 13:49:54.60 | 05/29/12 |
| 28.64217 | –30.4865 | 1359.978 | 27639.692 | 6.392 | 27633.3 | 13:49:54.40 | 05/29/12 |
| 28.64217 | –30.4865 | 1359.949 | 27636.889 | 3.589 | 27633.3 | 13:49:54.20 | 05/29/12 |
| 28.64217 | –30.4865 | 1359.920 | 27636.167 | 2.867 | 27633.3 | 13:49:54.00 | 05/29/12 |
| 28.64217 | –30.4865 | 1359.892 | 27639.147 | 5.847 | 27633.3 | 13:49:53.80 | 05/29/12 |
| 28.64218 | –30.4865 | 1359.867 | 27643.981 | 10.681 | 27633.3 | 13:49:53.60 | 05/29/12 |
| 28.64218 | –30.4865 | 1359.842 | 27649.235 | 15.935 | 27633.3 | 13:49:53.40 | 05/29/12 |
| 28.64218 | –30.4865 | 1359.816 | 27648.192 | 14.892 | 27633.3 | 13:49:53.20 | 05/29/12 |
| 28.64218 | –30.4865 | 1359.791 | 27647.845 | 14.545 | 27633.3 | 13:49:53.00 | 05/29/12 |
| 28.64218 | –30.4865 | 1359.774 | 27651.505 | 18.205 | 27633.3 | 13:49:52.80 | 05/29/12 |

to be continued

Table 1 (continuation)

| $X$ [°] | $Y$ [°] | GPS_height [m] | Reading_1 [nT] | Diurnal 1 [nT] | Corrected [nT] | Time | Date |
|---|---|---|---|---|---|---|---|
| 28.64219 | –30.4865 | 1359.767 | 27656.119 | 22.819 | 27633.3 | 13:49:52.60 | 05/29/12 |
| 28.64219 | –30.4865 | 1359.760 | 27662.603 | 29.303 | 27633.3 | 13:49:52.40 | 05/29/12 |
| 28.64219 | –30.4865 | 1359.752 | 27668.121 | 34.821 | 27633.3 | 13:49:52.20 | 05/29/12 |
| 28.64219 | –30.4865 | 1359.745 | 27667.763 | 34.463 | 27633.3 | 13:49:52.00 | 05/29/12 |
| 28.6422 | –30.4865 | 1359.739 | 27668.977 | 35.677 | 27633.3 | 13:49:51.80 | 05/29/12 |
| 28.6422 | –30.4865 | 1359.734 | 27676.68 | 43.380 | 27633.3 | 13:49:51.60 | 05/29/12 |
| 28.6422 | –30.4865 | 1359.729 | 27680.699 | 47.399 | 27633.3 | 13:49:51.40 | 05/29/12 |
| 28.6422 | –30.4865 | 1359.724 | 27688.957 | 55.657 | 27633.3 | 13:49:51.20 | 05/29/12 |
| 28.6422 | –30.4865 | 1359.719 | 27691.569 | 58.269 | 27633.3 | 13:49:51.00 | 05/29/12 |
| 28.64221 | –30.4865 | 1359.717 | 27690.99 | 57.690 | 27633.3 | 13:49:50.80 | 05/29/12 |
| 28.64221 | –30.4865 | 1359.716 | 27694.13 | 60.830 | 27633.3 | 13:49:50.60 | 05/29/12 |
| 28.64221 | –30.4865 | 1359.716 | 27698.642 | 65.342 | 27633.3 | 13:49:50.40 | 05/29/12 |
| 28.64221 | –30.4865 | 1359.716 | 27703.999 | 70.699 | 27633.3 | 13:49:50.20 | 05/29/12 |
| 28.64222 | –30.4865 | 1359.715 | 27709.518 | 76.218 | 27633.3 | 13:49:50.00 | 05/29/12 |
| 28.64222 | –30.4865 | 1359.727 | 27709.386 | 76.086 | 27633.3 | 13:49:49.80 | 05/29/12 |
| 28.64222 | –30.4865 | 1359.751 | 27713.465 | 80.165 | 27633.3 | 13:49:49.60 | 05/29/12 |
| 28.64222 | –30.4865 | 1359.775 | 27722.623 | 89.323 | 27633.3 | 13:49:49.40 | 05/29/12 |
| 28.64223 | –30.4865 | 1359.799 | 27727.628 | 94.328 | 27633.3 | 13:49:49.20 | 05/29/12 |
| 28.64223 | –30.4865 | 1359.823 | 27737.051 | 103.751 | 27633.3 | 13:49:49.00 | 05/29/12 |
| 28.64223 | –30.4865 | 1359.837 | 27740.421 | 107.121 | 27633.3 | 13:49:48.80 | 05/29/12 |
| 28.64223 | –30.4865 | 1359.842 | 27741.883 | 108.583 | 27633.3 | 13:49:48.60 | 05/29/12 |
| 28.64223 | –30.4865 | 1359.847 | 27746.097 | 112.797 | 27633.3 | 13:49:48.40 | 05/29/12 |
| 28.64223 | –30.4865 | 1359.851 | 27749.984 | 116.684 | 27633.3 | 13:49:48.20 | 05/29/12 |
| 28.64224 | –30.4865 | 1359.856 | 27751.505 | 118.205 | 27633.3 | 13:49:48.00 | 05/29/12 |
| 28.64224 | –30.4865 | 1359.855 | 27760.037 | 126.737 | 27633.3 | 13:49:47.80 | 05/29/12 |
| 28.64224 | –30.4865 | 1359.850 | 27765.333 | 132.033 | 27633.3 | 13:49:47.60 | 05/29/12 |
| 28.64224 | –30.4865 | 1359.844 | 27767.607 | 134.307 | 27633.3 | 13:49:47.40 | 05/29/12 |
| 28.64224 | –30.4865 | 1359.838 | 27771.036 | 137.736 | 27633.3 | 13:49:47.20 | 05/29/12 |
| 28.64224 | –30.4865 | 1359.833 | 27778.494 | 145.194 | 27633.3 | 13:49:47.00 | 05/29/12 |
| 28.64225 | –30.4865 | 1359.830 | 27785.487 | 152.187 | 27633.3 | 13:49:46.80 | 05/29/12 |
| 28.64225 | –30.4865 | 1359.830 | 27792.654 | 159.354 | 27633.3 | 13:49:46.60 | 05/29/12 |
| 28.64225 | –30.4865 | 1359.830 | 27804.345 | 171.045 | 27633.3 | 13:49:46.40 | 05/29/12 |
| 28.64225 | –30.4865 | 1359.831 | 27808.339 | 175.039 | 27633.3 | 13:49:46.20 | 05/29/12 |
| 28.64225 | –30.4865 | 1359.831 | 27811.176 | 177.876 | 27633.3 | 13:49:46.00 | 05/29/12 |
| 28.64225 | –30.4865 | 1359.831 | 27817.256 | 183.956 | 27633.3 | 13:49:45.80 | 05/29/12 |
| 28.64225 | –30.4865 | 1359.831 | 27826.289 | 192.989 | 27633.3 | 13:49:45.60 | 05/29/12 |

to be continued

Table 1 (continuation)

| *X* [°] | *Y* [°] | GPS_height [m] | Reading_1 [nT] | Diurnal 1 [nT] | Corrected [nT] | Time | Date |
|---|---|---|---|---|---|---|---|
| 28.64226 | –30.4865 | 1359.831 | 27831.112 | 197.812 | 27633.3 | 13:49:45.40 | 05/29/12 |
| 28.64226 | –30.4865 | 1359.830 | 27837.302 | 204.002 | 27633.3 | 13:49:45.20 | 05/29/12 |
| 28.64226 | –30.4865 | 1359.830 | 27837.878 | 204.578 | 27633.3 | 13:49:45.00 | 05/29/12 |
| 28.64226 | –30.4865 | 1359.825 | 27834.249 | 200.949 | 27633.3 | 13:49:44.80 | 05/29/12 |
| 28.64226 | –30.4865 | 1359.816 | 27836.724 | 203.424 | 27633.3 | 13:49:44.60 | 05/29/12 |
| 28.64226 | –30.4864 | 1359.807 | 27840.916 | 207.616 | 27633.3 | 13:49:44.40 | 05/29/12 |
| 28.64226 | –30.4864 | 1359.798 | 27838.404 | 205.104 | 27633.3 | 13:49:44.20 | 05/29/12 |
| 28.64226 | –30.4864 | 1359.789 | 27842.434 | 209.134 | 27633.3 | 13:49:44.00 | 05/29/12 |
| 28.64227 | –30.4864 | 1359.790 | 27845.238 | 211.938 | 27633.3 | 13:49:43.80 | 05/29/12 |
| 28.64227 | –30.4864 | 1359.802 | 27840.98 | 207.680 | 27633.3 | 13:49:43.60 | 05/29/12 |
| 28.64227 | –30.4864 | 1359.815 | 27846.563 | 213.263 | 27633.3 | 13:49:43.40 | 05/29/12 |
| 28.64227 | –30.4864 | 1359.827 | 27858.536 | 225.236 | 27633.3 | 13:49:43.20 | 05/29/12 |
| 28.64227 | –30.4864 | 1359.839 | 27868.502 | 235.202 | 27633.3 | 13:49:43.00 | 05/29/12 |
| 28.64227 | –30.4864 | 1359.834 | 27877.287 | 243.987 | 27633.3 | 13:49:42.80 | 05/29/12 |
| 28.64228 | –30.4864 | 1359.813 | 27891.319 | 258.019 | 27633.3 | 13:49:42.60 | 05/29/12 |
| 28.64228 | –30.4864 | 1359.792 | 27898.842 | 265.542 | 27633.3 | 13:49:42.40 | 05/29/12 |
| 28.64228 | –30.4864 | 1359.770 | 27905.877 | 272.577 | 27633.3 | 13:49:42.20 | 05/29/12 |
| 28.64228 | –30.4864 | 1359.749 | 27922.575 | 289.275 | 27633.3 | 13:49:42.00 | 05/29/12 |
| 28.64228 | –30.4864 | 1359.727 | 27945.254 | 311.954 | 27633.3 | 13:49:41.80 | 05/29/12 |
| 28.64228 | –30.4864 | 1359.706 | 27962.899 | 329.599 | 27633.3 | 13:49:41.60 | 05/29/12 |
| 28.64229 | –30.4864 | 1359.685 | 27991.921 | 358.621 | 27633.3 | 13:49:41.40 | 05/29/12 |
| 28.64229 | –30.4864 | 1359.664 | 28014.035 | 380.735 | 27633.3 | 13:49:41.20 | 05/29/12 |
| 28.64229 | –30.4864 | 1359.643 | 28013.811 | 380.511 | 27633.3 | 13:49:41.00 | 05/29/12 |
| 28.64229 | –30.4864 | 1359.611 | 28024.038 | 390.738 | 27633.3 | 13:49:40.80 | 05/29/12 |
| 28.6423 | –30.4864 | 1359.569 | 28042.894 | 409.594 | 27633.3 | 13:49:40.60 | 05/29/12 |
| 28.6423 | –30.4864 | 1359.527 | 28035.862 | 402.562 | 27633.3 | 13:49:40.40 | 05/29/12 |
| 28.6423 | –30.4864 | 1359.485 | 28014.74 | 381.440 | 27633.3 | 13:49:40.20 | 05/29/12 |

mately 28 m. At this point it shows a slight decrease, but in general the profile remains constant up to 200 m. The increase in signal at the left side at approximately 28 m is possibly related to a fault resulting in the block to the right having moved up relative to the other block.

The second profile (Fig. 7) displays two peaks, one at 20 m, and the other 80.5 m. These peaks are possibly due to the presence of a wide dolerite dyke or two narrow dykes located directly beneath the peaks. A similar situation can be observed in Fig. 8; groundwater can be targeted besides these peaks related to the occurrence of dolerite dykes. Dolerites always cause a

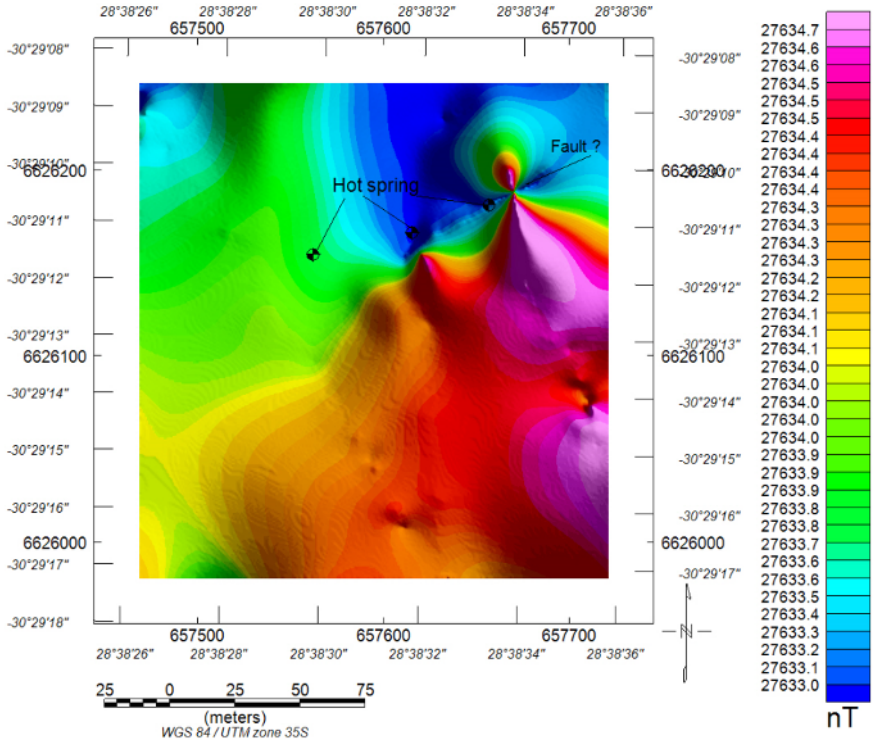


Fig. 5. Magnetic map derived from Fig. 3 but at a grid cell size of 14 m.

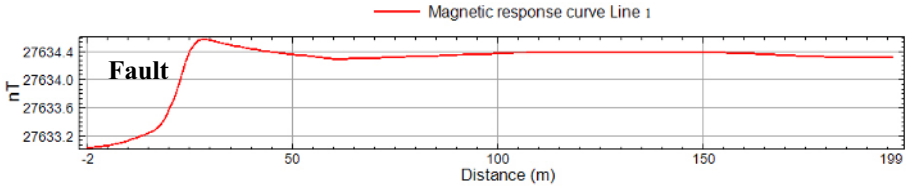


Fig. 6. Polile Tshisa magnetic profile in a SE-NW direction.

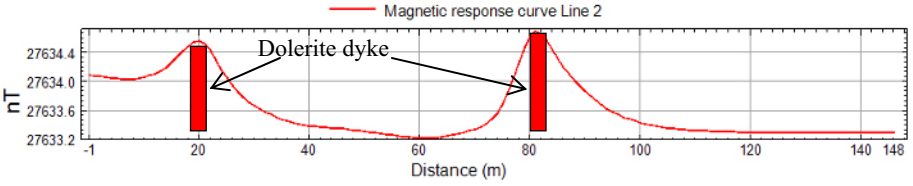


Fig. 7. Polile Tshisa magnetic profile in a SW-NE direction.

chilly margin to occur at the contact with the country rock. All the collected magnetic data can be seen in Table 1.

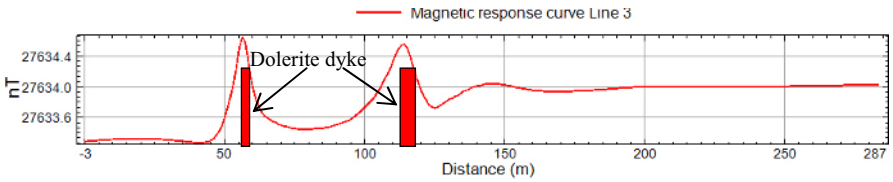


Fig. 8. Polile Tshisa second magnetic profile in a SW-NE direction.

### 3.3 Electromagnetic survey

The acquisition of data was organized for the survey along profiles oriented SE-NW (Lines 1 and 2, see Fig. 9). Profiles were set so in a quasi-perpendicular direction to the one of the structure that hosts the hot springs that wells up at three different places. Another profile, NE-SW (Line 3, see Fig. 9) was also set for a generalized coverage of the area, a better visualization and interpretation.

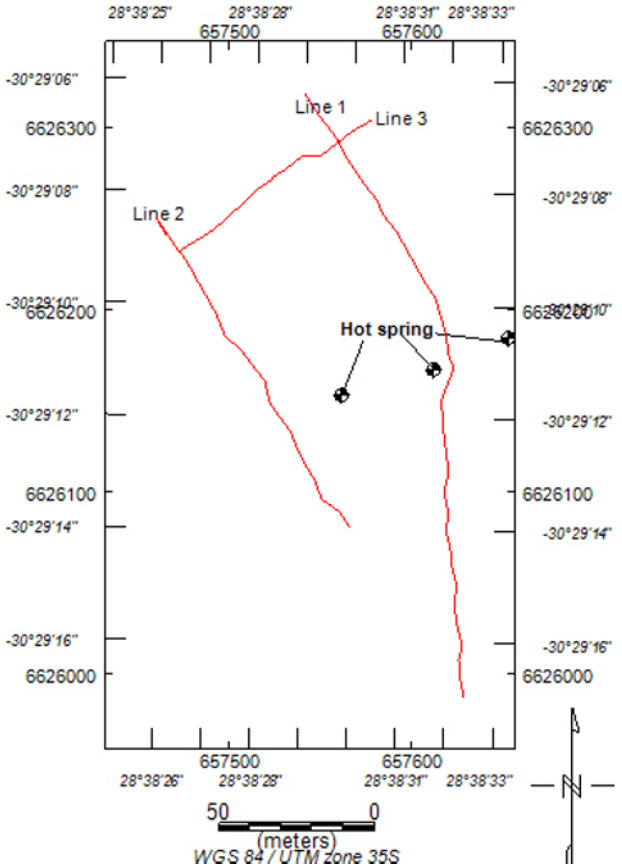


Fig. 9. Lines in red were set for data acquisition using the vertical and horizontal dipoles at intercoil spacing of 20 m at the Polile Tshisa hot spring.

Three lines (Lines 1, 2, and 3, Fig. 9) of combined vertical and horizontal dipole mode were set and data were acquired using an intercoil spacing of 20 m (SE-NW) profiles for Lines 1 and 2, and a third line (Line 3) in an NE-SW profile was set with an intercoil spacing of 20 m. The station spacing was 10 m. For the first line, with 20 m as intercoil spacing (Fig. 10), it was observed that between 0 and 50 m, 70 and 130 m, and from 220 to almost 270 m, the horizontal dipole is higher than the vertical dipole, which is indicative of a conductance that decreases with depth. It is also indicative of a shallow regolith.

Two contrasting anomalies can be seen around 170 m; the vertical dipole showing a positive peak might be indicative of a weathered and fractured zone, and the horizontal dipole showing a low peak at the same place can be

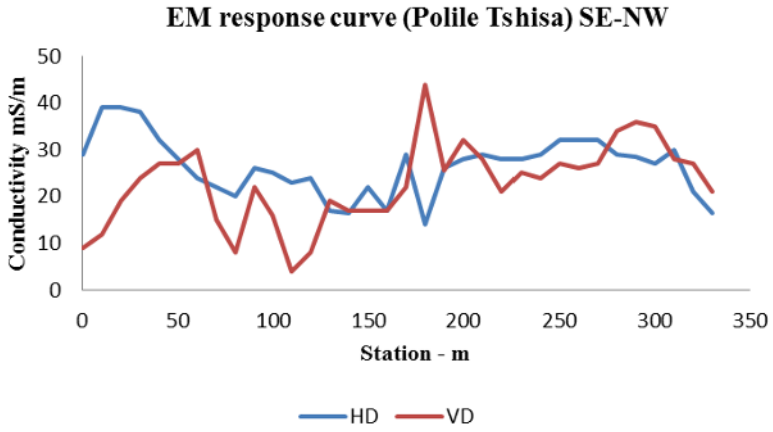


Fig. 10. Line 1 oriented SE-NW (intercoil spacing: 20 m).

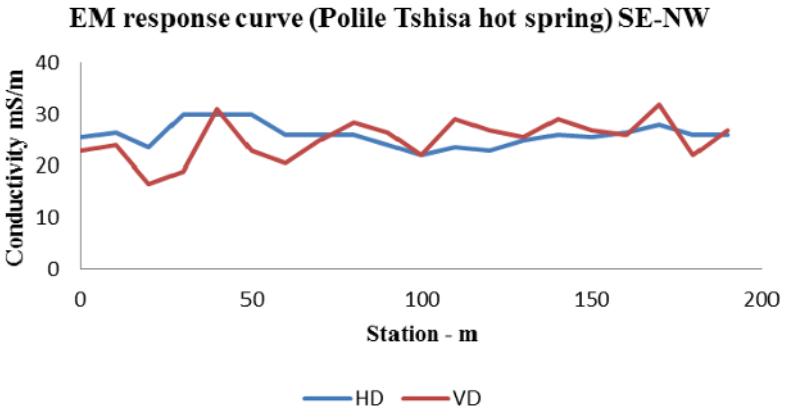


Fig. 11. Line 2 (intercoil spacing: 20 m).

Table 2

Polile Tshisa hot spring L1_20, horizontal and vertical dipole

| Sta [m] | *HD* [mS/m] | *VD* [mS/m] | *X* [m] | *Y* [m] | *Z* [m] | Direction SE-NW |
|---|---|---|---|---|---|---|
| 0 | 29 | 9 | 657629 | 6625987 | 1355 | SE |
| 10 | 39 | 12 | 657627 | 6625996 | 1355 | |
| 20 | 39 | 19 | 657626 | 6626008 | 1356 | |
| 30 | 38 | 24 | 657628 | 6626016 | 1357 | |
| 40 | 32 | 27 | 657625 | 6626027 | 1349 | |
| 50 | 28 | 27 | 657623 | 6626039 | 1350 | |
| 60 | 24 | 30 | 657625 | 6626048 | 1350 | |
| 70 | 22 | 15 | 657622 | 6626059 | 1349 | |
| 80 | 20 | 8 | 657621 | 6626069 | 1349 | |
| 90 | 26 | 22 | 657619 | 6626080 | 1351 | |
| 100 | 25 | 16 | 657620 | 6626087 | 1352 | |
| 110 | 23 | 4 | 657618 | 6626101 | 1354 | |
| 120 | 24 | 8 | 657620 | 6626110 | 1355 | |
| 130 | 17 | 19 | 657619 | 6626121 | 1357 | |
| 140 | 16.5 | 17 | 657618 | 6626132 | 1358 | |
| 150 | 22 | 17 | 657618 | 6626141 | 1359 | |
| 160 | 17 | 17 | 657616 | 6626148 | 1360 | |
| 170 | 29 | 22 | 657619 | 6626157 | 1360 | |
| 180 | 14 | 44 | 657623 | 6626168 | 1361 | |
| 190 | 26 | 25.5 | 657620 | 6626175 | 1361 | |
| 200 | 28 | 32 | 657619 | 6626188 | 1363 | |
| 210 | 29 | 28 | 657613 | 6626206 | 1365 | |
| 220 | 28 | 21 | 657607 | 6626216 | 1366 | |
| 230 | 28 | 25 | 657602 | 6626224 | 1367 | |
| 240 | 29 | 24 | 657598 | 6626233 | 1368 | |
| 250 | 32 | 27 | 657592 | 6626243 | 1369 | |
| 260 | 32 | 26 | 657585 | 6626252 | 1370 | |
| 270 | 32 | 27 | 657581 | 6626260 | 1370 | |
| 280 | 29 | 34 | 657575 | 6626268 | 1371 | |
| 290 | 28.5 | 36 | 657569 | 6626277 | 1372 | |
| 300 | 27 | 35 | 657564 | 6626285 | 1372 | |
| 310 | 30 | 28 | 657559 | 6626294 | 1373 | |
| 320 | 21 | 27 | 657547 | 6626310 | 1374 | |
| 330 | 16.5 | 21 | 657542 | 6626319 | 1376 | NW |

interpreted as a vertical dyke. Dykes in the Karoo aquifers are good indicators for groundwater exploration. This area may have two structures favourable for groundwater. Between 60 and 130 m, the vertical dipole displays two remarkable lows separated by a high. The two peaks can be related to dolerite dykes with a fracture in between them. Thus the potential of finding a productive well is high in this area. There is a quite good variation in conductivity for the horizontal dipole (~40 to 13 mS/m), whilst for the vertical dipole the variation is a bit high (9 to 44 mS/m). The complete set of data is presented in Table 2.

For Line 2, with 20 m as intercoil spacing (Fig. 11), there is no remarkable variation in the conductivity for the horizontal dipole (26-30 mS/m). This may signify that there is no much variation either in mineralogy or porosity. The vertical dipole has higher variation (16.5-32 mS/m) than the horizontal dipole. It is quite clear that between 0 and 40 m and between 42 and 70 m the response of the horizontal dipole is higher than that of the vertical one. This is indicative of a shallow regolith, as observed for the previous profiles. Between 0 and 30 m, both the horizontal and vertical dipole signatures almost dovetail. The set of data is reprised in Table 3.

For Line 3 (Table 4), with intercoil spacing of 20 m (Fig. 12), the vertical dipole response seems higher than that of the horizontal dipole from 0 to 70 m. The signatures of the dipoles (horizontal HD and vertical VD) almost dovetail between 15 and 36 m. On this profile the survey may have intersected a dyke. It may imply that there is a change in the physical properties of the rocks because of the similar responses for the vertical and the horizontal dipoles.

As for Line 2 in Fig. 10 (20 m intercoil spacing), there is similarity in horizontal dipole patterns. It can be seen that from 50 to 110 m, the profile is almost flat like in Fig. 10, and not showing considerable variations.

The vertical dipole shows high conductivities at two points, at 40 and 60 m (> 40 mS/m), with lower conductivities of 18.5 and 24.5 mS/m at 30 and 80 m. These high conductivities from the vertical dipole indicate a possible fault or fracture below the surface. The complete set of data can be seen in Table 4.

The depth-conductivity model (Fig. 13) from Line 1 data at the Polile Tshisa hot spring shows two high conductivity zones (*e.g.*, ≥ 30 mS/m) at the southeastern end of the profile and from about 175 m to the northern end of the profile. Both zones of high conductivity extend from surface to about 8 m depth.

The high conductivity zones can be interpreted as highly weathered sandstones. The area of the Polile Tshisa hot spring was observed to have sandstones that are weathered, leaving loosed particles of sand and whitish kaolinised material. The dashed lines marked in Fig. 12 are inferred to be

Table 3

Polile Tshisa hot spring line 2: L2-20, horizontal and vertical dipole

| Sta [m] | X_Dist | *HD* [mS/m] | *VD* [mS/m] | *X* [m] | *Y* [m] | *Z* [m] | Direction N-S |
|---|---|---|---|---|---|---|---|
| 190 | 0 | 26 | 27 | 657566 | 6626081 | 1359 | SE |
| 180 | 10 | 26 | 22 | 657561 | 6626089 | 1360 | |
| 170 | 20 | 28 | 32 | 657551 | 6626096 | 1361 | |
| 160 | 30 | 26.5 | 26 | 657547 | 6626106 | 1362 | |
| 150 | 40 | 25.5 | 27 | 657542 | 6626115 | 1364 | |
| 140 | 50 | 26 | 29 | 657538 | 6626123 | 1366 | |
| 130 | 60 | 25 | 25.5 | 657533 | 6626134 | 1367 | |
| 120 | 70 | 23 | 27 | 657533 | 6626134 | 1367 | |
| 110 | 80 | 23.5 | 29 | 657528 | 6626141 | 1367 | |
| 100 | 90 | 22 | 22 | 657522 | 6626149 | 1370 | |
| 90 | 100 | 24 | 26.5 | 657520 | 6626161 | 1371 | |
| 80 | 110 | 26 | 28.5 | 657520 | 6626161 | 1370 | |
| 70 | 120 | 26 | 25 | 657512 | 6626170 | 1371 | |
| 60 | 130 | 26 | 20.5 | 657507 | 6626178 | 1371 | |
| 50 | 140 | 30 | 23 | 657498 | 6626186 | 1372 | |
| 40 | 150 | 30 | 31 | 657493 | 6626198 | 1373 | |
| 30 | 160 | 30 | 19 | 657477 | 6626227 | 1375 | |
| 20 | 170 | 23.5 | 16.5 | 657470 | 6626235 | 1376 | |
| 10 | 180 | 26.5 | 24 | 657460 | 6626251 | 1378 | |
| 0 | 190 | 25.5 | 23 | 657466 | 6626241 | 1377 | NW |

Table 4

Polile Tshisa line 3: L3_20, horizontal and vertical dipole

| Sta [m] | X_Dist | *HD* [mS/m] | *VD* [mS/m] | *X* [m] | *Y* [m] | *Z* [m] | Direction |
|---|---|---|---|---|---|---|---|
| 110 | 0 | 32 | 34 | 657472 | 6626232 | 1377 | NE |
| 100 | 10 | 40 | 36 | 657491 | 6626244 | 1376 | |
| 90 | 20 | 39 | 40 | 657499 | 6626250 | 1376 | |
| 80 | 30 | 38 | 24.5 | 657509 | 6626259 | 1376 | |
| 70 | 40 | 38 | 36 | 657515 | 6626266 | 1377 | |
| 60 | 50 | 36 | 47 | 657524 | 6626272 | 1376 | |
| 50 | 60 | 34 | 34 | 657524 | 6626273 | 1376 | |
| 40 | 70 | 40 | 47 | 657531 | 6626277 | 1374 | |
| 30 | 80 | 25.5 | 18.5 | 657540 | 6626284 | 1374 | |
| 20 | 90 | 15 | 20 | 657551 | 6626285 | 1374 | |
| 10 | 100 | 35 | 42 | 657567 | 6626298 | 1372 | |
| 0 | 110 | 36 | 42 | 657578 | 6626304 | 1373 | NW |

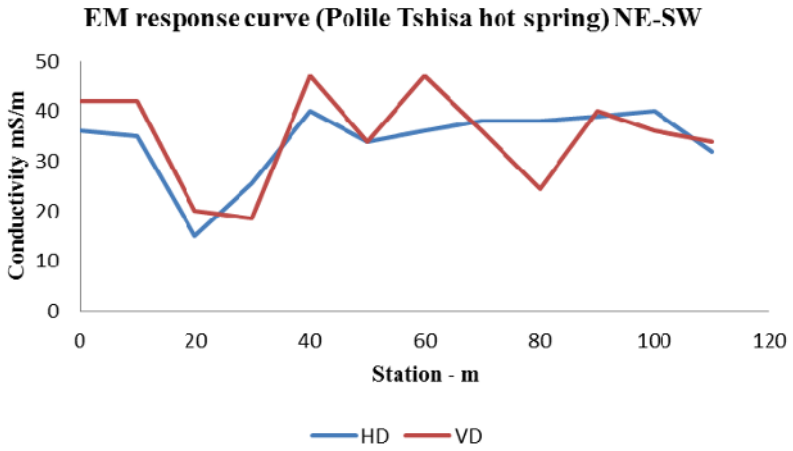


Fig. 12. Line 3 (intercoil spacing: 20).

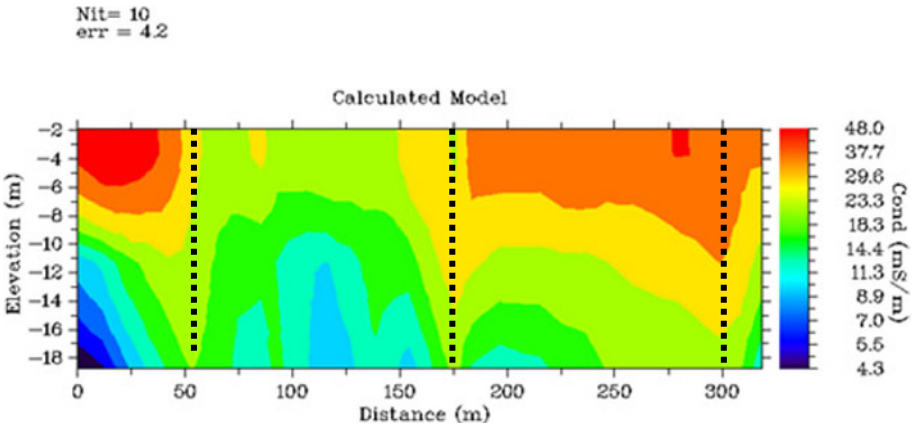


Fig. 13. Polile Tshisa hot spring conductivity-depth model. The dotted lines mark positions of inferred faults. Nit is the number of iterations, and err is the least squares error between calculated and observed conductivities.

either large faults or fractures along which water can migrate upwards easily. Generally, it transpires from the depth modelling that the conductivity is decreasing with depth for the maximum investigated depth (≈ 20 m).

### 3.4 Hydrogeological conceptual model of the Polile Tshisa hot spring area

The hydrogeological conceptual model (Fig. 14) shows that the area of the Polile Tshisa hot spring is structurally controlled by faults and fractures with the intrusion of dolerites. This is indicative of a potential target for high yield aquifers. Fractures and faults are conduits for groundwater flow. The

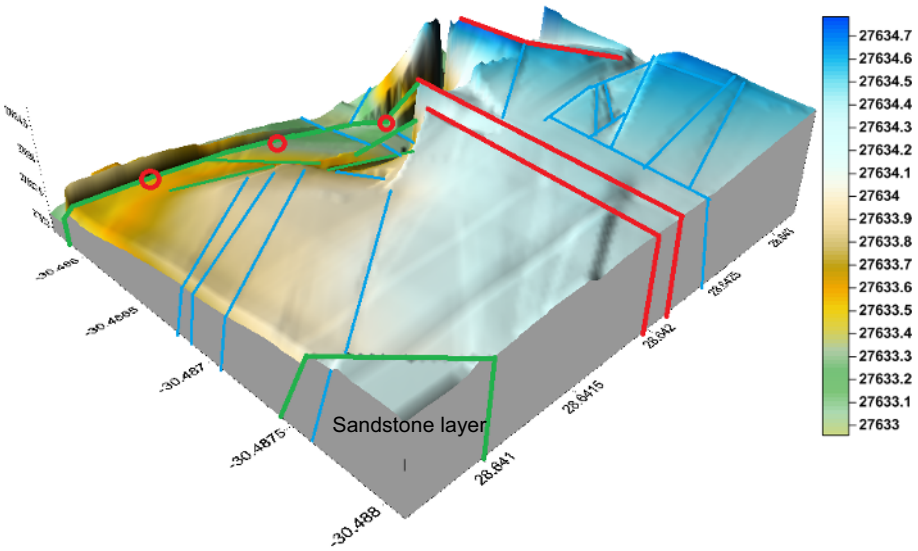


Fig. 14. Hydrogeological conceptual model of the Polile Tshisa hot spring area. Faults are in green, fractures in blue, and dolerites in red. The grey surface represents the sandstone layer.

coarse-grain sandstone of this area is a preferred lithology on the hydrogeological point of view. It is well known that the coarser the grain, the higher the porosity, and the finer the grains, the lower the porosity. The WSW-ENE trending fault, as seen in Fig. 8, along which the water from the three hot springs wells up is very remarkable in this conceptual model. Two dolerite dykes seen in Figs. 6 and 7, oriented N-S, have high magnetic values and are parallel (Fig. 14). It is quite clear that extensional faulting ($\sigma_1$ vertical, $\sigma_2$, and $\sigma_3$ horizontal) prevailed where the magnetic values are low, as can be seen at the north side in Fig. 8.

## 4. DISCUSSION AND CONCLUSIONS

The neotectonics belt near the country of Lesotho is also known for the occurrence of many hot springs, which are indicative of circulation of groundwater at great depths; the occurrence of these springs indicates that they are connected by a major neotectonic fault that stretches from west (Aliwal North) to east (Polile Tshisa). The flooding that occurred in an abnormally well-developed fissure zone, through which a lot of water gushed out during the construction of the Orange–Fish tunnel (Olivier 1972), is a proof that neotectonics is at work in the northern neotectonics belt. Whittingan (1970) noted that the flow of the thermal spring at Badfontein increased markedly

for a period of at least three months after a local earthquake. The Karoo rocks were intruded by dolerite dykes and sills. Strongest magnetic values at the Polile Tshisa hot springs indicate the presence of dolerite dykes or sills, or even unweathered solid geological basement (*e.g.*, Street *et al.* 2002). At Polile Tshisa the magnetic profile in Fig. 6 is typical of a fault that has moved two blocks with a dip-slip component. The water at Polile Tshisa wells up at three different places, which are connected by a fault (Fig. 14) that has possibly cut across the dolerite dykes. Electromagnetic profiles in all the three hot springs are indicative of faults or fractures at some places and dolerite dykes at others. These profiles also show that the weathering process is underway. At Polile Tshisa combined profiles of both horizontal and vertical dipole show that the horizontal dipole is higher than the vertical one at some places; this is always an indication for a shallow regolith (*e.g.*, Barry *et al.* 2010).

The hot springs in the Eastern Cape northern neotectonic belt are connected or occur along an east-west neotectonic fault that is a regional structure. The magnetic and electromagnetic data have helped to identify fractured or faulted zones with different degrees of weathering. At some places one can mention the presence of dolerite dykes, known for their potential to localise groundwater in the Karoo. It is clear that the three places from where the water of the Polile Tshisa hot spring wells up are connected by a WSW-ENE trending fault. The well located near the dolerite dykes, as seen in Fig. 14, is a great target to drill for a productive borehole because dolerite dykes are localisers of groundwater. The combination of seismic activity in the Kokstad–Koffiefontein seismic belt, the occurrence of hot springs in that belt, and the interpreted derived fauts, fractures and dolerite dykes, makes the Polile Tshisa area a potential environment to explore for groundwater.

Acknowledgements. The authors would like to thank the Govan Mbeki development Research Center (GMRDC) at Fort Hare University and the National Research Fund (NRF) of South Africa for financial assistance in this project. The Council of Geoscience of South Africa is greatly acknowledged for the logistical support.

## References

Barry, B., B. Kortatsi, G. Forkuor, M.K. Gumma, R. Namara, L.-M. Rebelo, J. van den Berg, and W. Laube (2010), Shallow groundwater in the Atankwidi Catchment of the White Volta Basin: Current status and future sustainabil-

ity, Res. Rep. 139, International Water Management Institute (IWMI), Colombo, Sri Lanka, 30 pp., DOI: 10.5337/2010.234.

Delvaux, D.F., and M. Hanon (1993), Neotectonics of the Mbeya Area, SW Tanzania, *Mus. Roy. Afr. Centr. Dept. Geol. Min. Rapp. Ann*. **1991-1992**, 87-97.

Hartnady, C.J.H. (1985), Uplift, faulting seismicity, thermal spring and possible incipient volcanic activity in the Lesotho–Natal region, SE Africa: The Quathlamba hotspot hypothesis, *Tectonics* **4**, 4, 371-377, DOI: 10.1029/TC004i004p00371.

Kent, L.E. (1969), The thermal waters in the Republic of South Africa. **In:** *Proc. 23rd Int. Geol. Cong. "Mineral and Thermal Waters of the World", Czechoslovakia 1968*, Vol. 19, 143-164.

Maud, R.R., T.C. Partridge, and J.N. Dunlevey (1998), The Lesotho "volcanic" event of February 1983, *South Afr. J. Geol.* **101**, 4, 313-322.

Meissner, R., and T. Wever (1986), Intracontinental seismicity, strength of crustal units, and the seismic signature of fault zones, *Philos. Trans. Roy. Soc. Lond. A* **317**, 1539, 45-61, DOI: 10.1098/rsta.1986.0024.

Olivier, H.J. (1972), Geohydrological investigation of the flooding at shaft 2, Orange–Fish tunnel, north-eastern Cape Province, *Trans. Geol. Soc. South Afr.* **75**, 197-224.

Olivier, J., J.S. Venter, and C.Z. Jonker (2011), Thermal and chemical characteristics of hot water springs in the northern part of the Limpopo Province, South Africa, *Water SA* **37**, 4, 427-436, DOI: 10.4314/wsa.v37i4.1.

Spurr, A.M.M. (1953), The geology of the Songwe river, Mbeya district, Report AMMS/17, Geological Survey of Tanganyika (unpublished).

Street, G.J., G. Pracilio, and A.M. Anderson-Mayes (2002), Interpretation of geophysical data for salt hazard identification and catchment management in Southwest Western Australia, *Explor. Geophys.* **33**, 2, 65-72, DOI: 10.1071/EG02065.

Wittingham, J.K. (1970), Report of geophysical investigations along the route of the Orange–Fish tunnel, Cape Province, Geol. Surv. South Africa (unpublished).

Received 20 January 2015
Received in revised form 18 April 2015
Accepted 23 June 2015

DE GRUYTER OPEN

**Acta Geophysica**
vol. 64, no. 4, Aug. 2016, pp. 963-977
DOI: 10.1515/acgeo-2016-0039

# Digitized Database of Old Seismograms Recorder in Romania

Daniel PAULESCU[1,2], Maria ROGOZEA[1], Mihaela POPA[1], and Mircea RADULIAN[1,3]

[1]National Institute for Earth Physics, Măgurele, România
e-mails: dpaulescu@infp.ro, mrogozea@infp.ro (corresponding author)

[2]University of Bucharest, Faculty of Physics, Măgurele, România
e-mail: secretariat@fizica.unibuc.ro

[3]Academy of Romanian Scientists, Bucharest, Romania

A b s t r a c t

The aim of this paper is to describe a managing system for a unique Romanian database of historical seismograms and complementary documentation (metadata) and its dissemination and analysis procedure. For this study, 5188 historical seismograms recorded between 1903 and 1957 by the Romanian seismological observatories (Bucharest-Filaret, Focşani, Bacău, Vrincioaia, Câmpulung-Muscel, Iaşi) were used. In order to reconsider the historical instrumental data, the analog seismograms are converted to digital images and digital waveforms (digitization/vectorialisation). First, we applied a careful scanning procedure of the seismograms and related material (seismic bulletins, station books, *etc*.). In a next step, the high resolution scanned seismograms will be processed to obtain the digital/numeric waveforms. We used a Colortrac Smartlf Cx40 scanner which provides images in TIFF or JPG format. For digitization the algorithm Teseo2 developed by the National Institute of Geophysics and Volcanology in Rome (Italy), within the framework of the SISMOS Project, will be used.

**Key words:** historical seismograms, database, digitization, Romania.

Ownership: Institute of Geophysics, Polish Academy of Sciences;
© 2016 Paulescu *et al*. This is an open access article distributed under the Creative Commons Attribution-NonCommercial-NoDerivs license,
http://creativecommons.org/licenses/by-nc-nd/3.0/.

## 1. INTRODUCTION

Consideration of earthquakes from historical perspective is of major interest for seismic hazard and risk assessment, and particularly for strategic buildings and infrastructures, such as nuclear power plants, since in these cases the knowledge about seismicity over long time intervals is required. Instrumental data available for the historical period have, contextually, a crucial scientific significance and allow the earthquake instrumental catalogues to be extended over 100 years period.

Instrumental seismology actually started at the end of the 19th century and the beginning of the 20th century (Dewey and Byerly 1969). Most observatories in the World and in Romania as well, still keep the original recordings (seismograms, bulletins).

The large interest of the international seismological community comes from the 1980s, after IASPEI resolution was set up, followed up by the creation of the World Data Centre A (WDC-A) and the IASPEI/UNESCO Working Group on Historical Seismograms. A systematic activity has started since then to archive seismograms using the microfilming technique (Glover and Meyers 1988).

Digital archiving techniques have been developed recently in order to preserve the unique seismological patrimony consisting in historical seismograms, earthquake bulletins and related documentation (*e.g.*, observatory log books, station books, correspondence, *etc.*). The seismological community has become increasingly aware of the utmost importance to avoid deterioration and loss over time and to save the scientific and informational content of this unique seismological heritage consisting of historical seismograms. At the same time, the digital format allowed the re-analysis of the past earthquakes using modern techniques and re-evaluation of seismic hazard (Kanamori 1988, Michelini *et al.* 2005).

In 2001, Instituto Nazionale di Geofisica e Vulcanologia (INGV) from Italy started an innovative project ("Progetto SISMOS"; *i.e.*, SISMOgrammi Storici) focused on scanning at very high-resolution, and archiving seismological paper records and related material (metadata). In 2002, the SISMOS activity was extended to seismograms and bulletins from 28 countries of the Euro-Mediterranean area, including Romania, through the EuroSeismos Project (Saving and Studying the Seismograms of the Strongest Euro-Mediterranean Earthquakes; http://storing.ingv.it/es_web) conducted by Working Group on the History of Seismometry of European Seismological Commission. In parallel, W.H.K. Lee initiated the project "SeismoArchive" under the auspices of the International Committee for Preservation of WWSSN (World Wide Seismographic Stations Network) and Historical Seismograms (ICPWHS) of the International Association of Seismology and

Physics of the Earth's (IASPEI), in collaboration with Data Management Center (DMC) of the Incorporated Research Institution for Seismology (IRIS) (IRIS 2004).

SISMOS was one of the Transnational Access facilities of the European Commission (EC FP7) NERIES (Network of Research Infrastructures for European Seismology) Project (2006-2010). SISMOS is partner in the GEM Project (2009-2013) for the construction of a Global Instrumental Seismic Catalogue (http://www.globalquakemodel.org/science).

The goal of this paper is to present the database of historical instrumental data (seismograms, seismic bulletins and complementary documentation) developed in digital format for recordings in Romania. Such a database is of highest interest from many points of view: (i) the conservation of the entire information of seismic activity; (ii) the huge volume of data can be used in many scientific fields (seismic risk and hazard, seismic source and seismotectonic studies, *etc*.); (iii) it provides an objective basis for many applications (relocation, retrieval of source parameters, synthetic seismograms); (iv) fast and efficient exchange of data between observatories; (v) structuring and integrating of existing information about historical earthquakes. A brief history of seismology in Romania is presented in Section 2. The methodology to set up the database is described in Section 3.

## 2. BRIEF HISTORY OF SEISMOLOGY IN ROMANIA

The Romanian tradition in geophysical research began with the astronomer and meteorologist Stefan Hepites (1851-1922). Through his contributions to the study and monitoring of earthquakes, he is considered the father of Observational Seismology in Romania. Hepites organized a continuous monitoring of seismic activity in the framework of the National Institute of Meteorology, starting with 400 observation "stations" (locations with volunteer observes).

Specific instructions were set up for the use of volunteers in order to note earthquakes. The first list of old earthquakes recorded in Romania was compiled and was published in the *Register of Earthquakes* in 1893. The *Register* was then published yearly. The model of this seismological survey and collection of information about the earthquakes was adopted for organizing similar networks in other earthquake prone countries, such as Bulgaria and Chile.

Hepites compiled in 1893 the first Romanian catalog of earthquakes, including earthquakes recorded between 1838 and 1892. The catalog was published in Romanian and French in the same year (Hepites 1893).

Hepites founded also, in 1895, the first seismic station in Romania, located in Bucharest, on the Filaret hill. The first instrument for seismic records that worked in Bucharest was a micro-seismoscop Tacchini-Guzzi and a

pendulum. In 1896, he built a new pavilion for terrestrial magnetism measurements and organized an accurate time service.

In 1901 the Romanian Seismological Service was established. Two horizontal Bosch seismographs of 10 kg mass, mechanical amplification of 10 to 15 times and recording on a reel covered with smoked paper (Fig. 1) were installed in 1902. An electric clock marked the minutes on the paper (Radulescu 2009). These pendulums became part of the history of seismology, their records being used by Jeffreys (1935) to demonstrate the existence of deep earthquakes.

In 1935, two pendulums were installed additionally in Bucharest by Demetrescu (1956) from the Astronomical Institute of Bucharest. They had masses of 540 kg and static amplification of 170-180 with air damping. Demetrescu also organized a network of seismic stations to record earthquakes in Romania: two stations at Focsani and Bacau (1942), and three stations at Câmpulung-Muscel (1943), Iaşi (1951), and Vrincioaia (1952).

A seismological observatory was installed at Timisoara (TIM) in 1902 in the western part of Romania (Banat region), under the Austro-Hungarian administration. This seismic station has been working continuously until 1914 (Demetrescu 1956). Ioan Curea, professor at the University of Timisoara, revived the seismic monitoring in Banat by reinstalling at Timisoara in 1943 two horizontal mechanical pendulums of 540 kg. Except of an interrup-

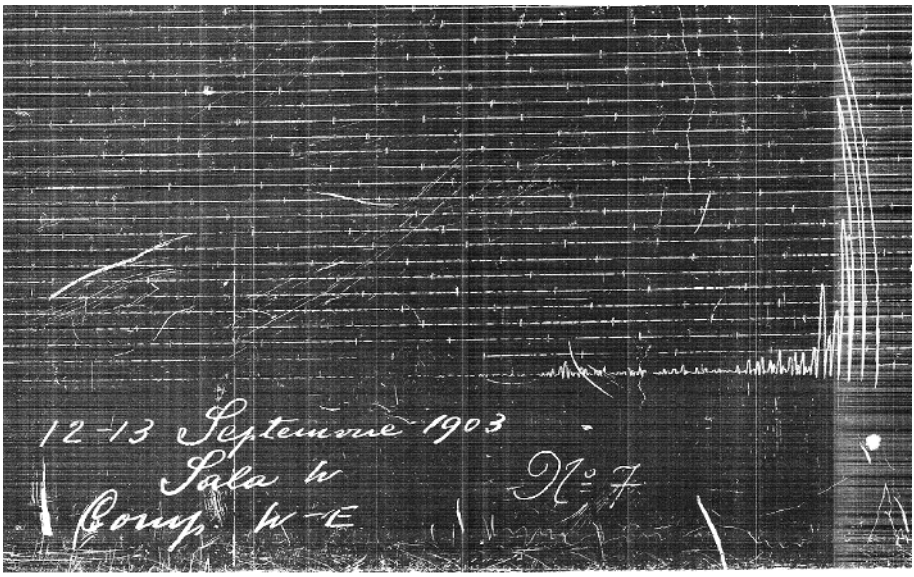


Fig. 1. Bosch mechanical pendulum seismogram recorded by EW component for the Vrancea earthquake of 13 September 1903, at 10:02 GMT ($M$ = 6.3). Half of the motion trace is available.

tion interval from 1944 to 1950, this station has been operating continuously until the present days (Curea 1961). Curea also founded a seismic station at Cluj (1939), belonging to the Astronomical Observatory of the University of Cluj.

## 3. THE DATABASE OF THE STUDIED SEISMOGRAMS

### 3.1 Data

The archive of seismograms of the Bucharest Seismological Observatory was used for this study. We scanned up to now 5188 seismograms recorded at the following seismic stations: Bucharest-BUC (1903), Focşani-FOC (1942), Bacau-BAC (1942), Câmpulung-Muscel-CMP (1943), Iasi-IAS (1951) and Vrincioaia-VRI (1952) – see Fig. 2.

These seismograms were recorded on smoked paper (Mainka-Demetrescu instruments having a speed paper of 30 mm/min) and photo paper (Galitin and Alfany instruments). The characteristics of these seismographs are presented in Table 1. The seismograms contain or not the worldwide earthquakes recorded between 1903 and 1957.

The database of these seismograms includes also information related to seismic bulletins, publications, historical reference to earthquakes and seismic equipment.

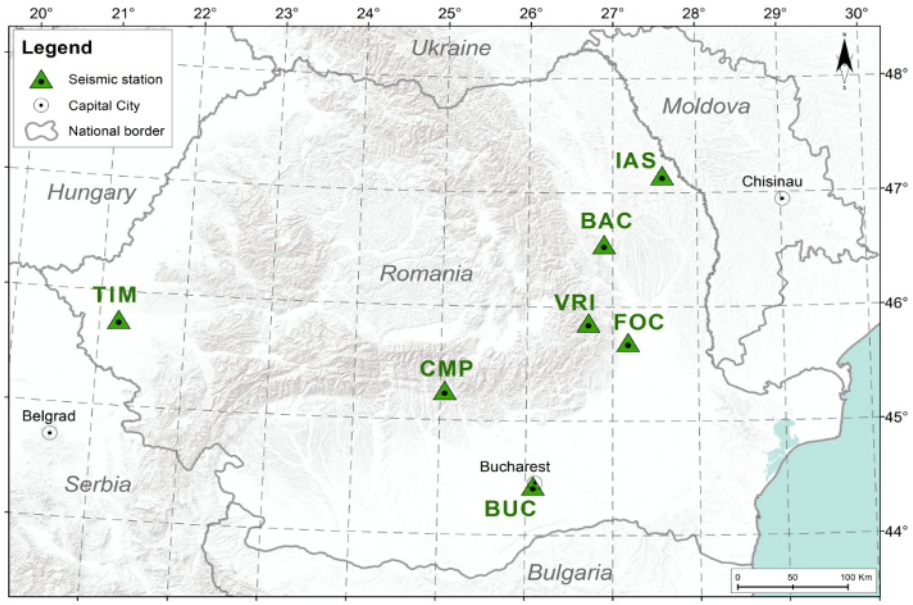


Fig. 2. Seismic stations distribution.

Table 1

List of stations and seismographs
with the associated constants and year of installation

| Station code | Station | Coordinates | | Instruments (seismograph type) | Comp | $M$ [kg] | $T_0$ [s] | $V$ | $\mu^2$ |
|---|---|---|---|---|---|---|---|---|---|
| | | Latitude (°N) | Longitude (°E) | | | | | | |
| BUC | Bucharest Cutitul de Argint | 44.41 | 26.09 | Bosch 1903 | NS<br>EW | 10<br>10 | ?<br>? | 10<br>15 | ?<br>? |
| | | | | Mainka-Demetrescu 1935 | NS<br>EW | 540<br>540 | 12.2<br>12.2 | 165<br>171 | 0.81<br>0.79 |
| | | | | Galitin 1937 | NS<br>EW | 2.7<br>2.7 | 11.5<br>11.5 | 273<br>270 | 0.04<br>0.02 |
| | | | | Alfani 1940 | Z | 7.2 | 4.0 | 400 | ? |
| FOC | Focsani | 45.70 | 27.18 | Mainka-Demetrescu 1942 | NS<br>EW | 105<br>105 | 3.6<br>3.6 | 41<br>37 | 0.84<br>0.77 |
| BAC | Bacau | 46.57 | 26.91 | Mainka-Demetrescu 1942 | NS<br>EW | 105<br>105 | 3.4<br>3.6 | 45<br>42 | 0.82<br>0.82 |
| CMP | Campulung-Muscel | 45.27 | 25.04 | Mainka-Demetrescu 1943 | NS<br>EW | 105<br>105 | 3.5<br>3.5 | 41<br>41 | 0.82<br>0.81 |
| IAS | Iasi | 47.19 | 27.56 | Mainka-Demetrescu 1951 | NS<br>EW | 450<br>450 | 4.8<br>4.8 | 127<br>132 | 0.85<br>0.85 |
| VRI | Vrincioia | 45.87 | 26.73 | Mainka-Demetrescu 1952 | NS<br>EW | 105<br>105 | 3.5<br>3.5 | 41<br>39 | 0.71<br>0.80 |

**Explanations:** Instruments – there are two basic types of seismographs: one type uses a mass suspended by a pendulum; the other is based on a device which responds to strain; Comp – components of a seismograph: Z (vertical), EW (East-West), and NS (North-South). A single seismograph records only one of these three components of motion; $M$ – mass pendulum: mass attached to a fixed base; $T_0$ – natural period of pendulum; $\mu^2$ – damping coefficient; $V$ – magnification.

### 3.2 Methodology

The modern techniques used for imaging and seismic signal processing allows recovering of important information from historical analogue recordings, essential to characterize seismic activity and related seismic hazard

in earthquake prone regions. The major benefit is the possibility of converting analogue to digital data and, thus, analyzing them using modern techniques and methods, specific to the Digital Seismology.

The flow-chart displayed in Fig. 3 explains the procedure followed to set up the database. It is similar with that developed within the framework of the EuroSeismos Project 2002-2007 and has two main stages:

***Stage 1. Scanning and image processing***

The initial scanning is done for all available seismograms at 400 dpi resolution even if they do not contain visible events. They are saved in JPEG format as a useful collection for a preview of the database content. This component is the core of the database.

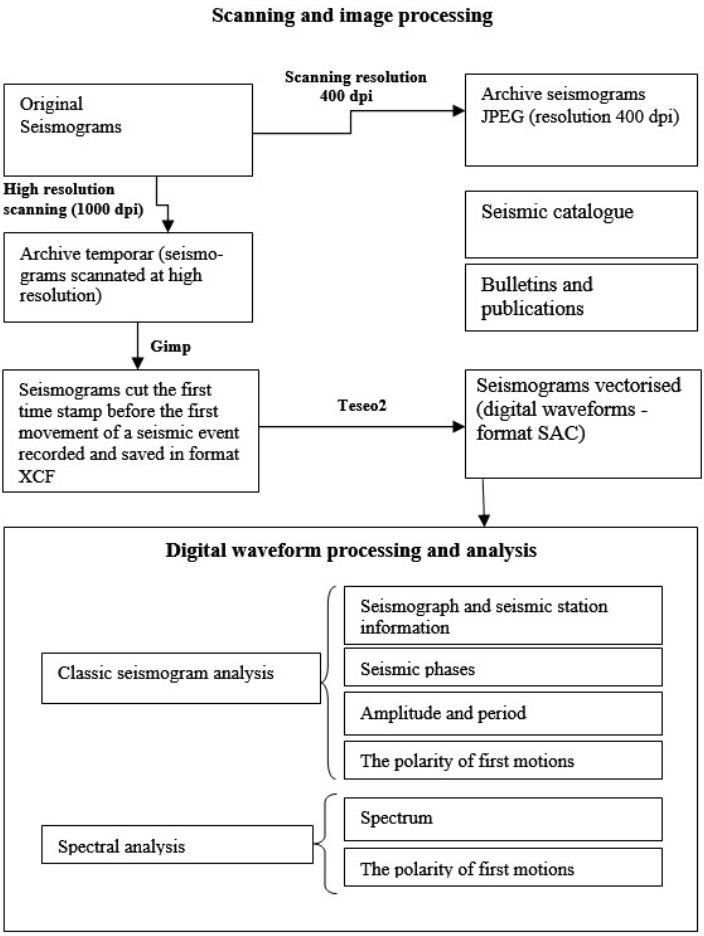


Fig. 3. Flow chart of the procedure proposed in the present work.

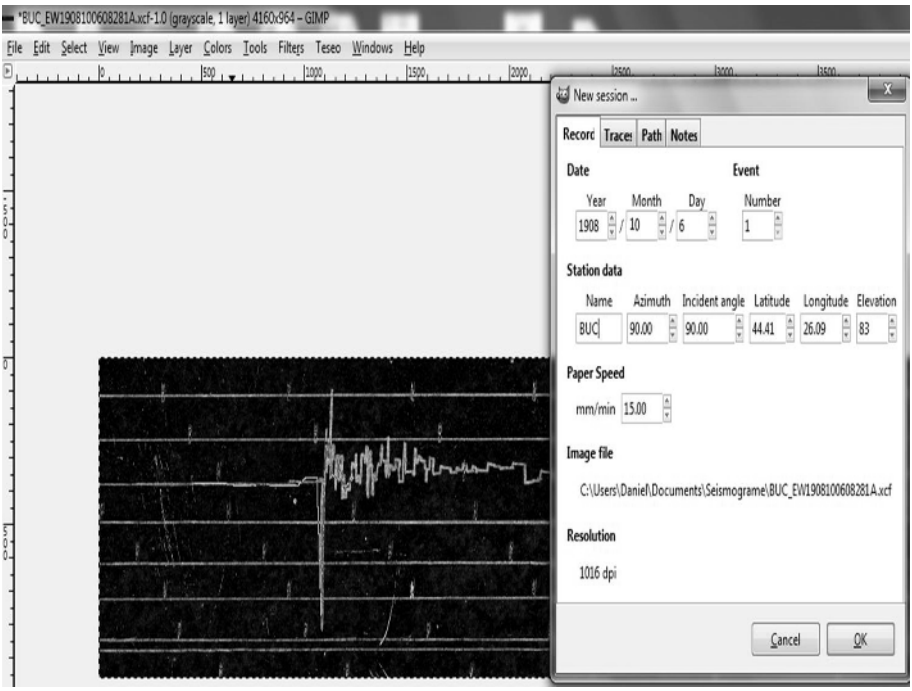


Fig. 4. Example of an extracted seismogram recorded by Bosch seismograph (EW component) for a Vrancea earthquake (6 October 1908, latitude 45.50°N, longitude 26.50°E, $M = 6.8$), prepared to be digitized and vectorized.

The seismograms of an earthquake that show good quality (high contrast) are also scanned at 1000 dpi resolution and saved in a TIFF format. Because the memory required for such a seismogram is very large, only the image that contains the waveform traces of the earthquakes of interest is scanned. Using GIMP software the trace of a given seismic event is (i) processed (*e.g.*, improving the contrast of the seismic traces) and (ii) extracted from the seismogram by marking the window including only the useful recording. The dig out seismogram is saved in XCF format, specific for GIMP (Fig. 4). The outcome files in XCF format can now be digitized and vectorized using Teseo software developed by Pintore *et al.* (2005).

After digitization, the file with the seismogram data points is exported in SAC format in order to be processed (Fig. 5) during the next stage.

### *Stage 2. Digital waveform processing and analysis*

At this stage any standard tool for digital processing of the signals can be applied (Fig. 6). Frequently, good results can be obtained for reassessing the location and magnitude of the earthquakes, estimation the focal mechanism

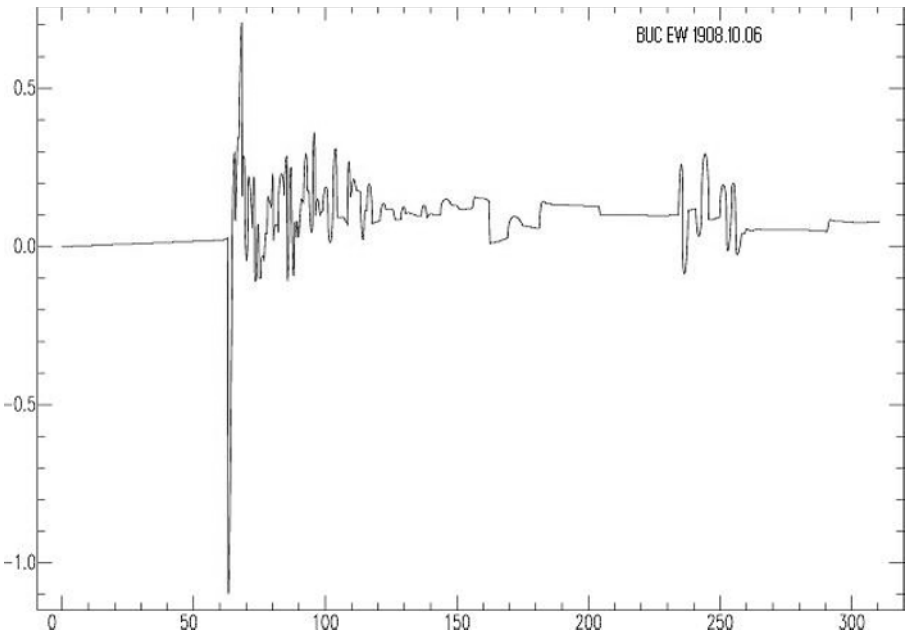


Fig. 5. Example of a seismogram ready to be exported in SAC format (the same event as in Fig. 4).

solutions and their spectral parameters (seismic moment, *Mo*, moment magnitude, *Mw*, corner frequency and seismic fault dimensions). For correcting the seismogram trace curvature, the TESEO2 algorithm is applied (Pinatore *et al*. 2005).

## 4. DATABASE

The new created database has the structure described in Table 2. The number in the second column represents the name designed to the scanned seismogram. The information in Box is a code of the file containing a group of seismograms stored in a separate place. It is useful to search easily the physical seismogram of an event. The other columns refer to the number of seismogram, station which recorded the event, components (EW, NS, Z), date, time of starting and ending of the record, type of instrument and quality factor *Q*, which indicates how well the earthquake was recorded on seismogram (A-very good, B-good, C-low, D-noise). The database includes scanned seismograms even if no earthquake was recorded (empty space in the box of the quality factor means that there is no recorded earthquake on seismogram for that time interval).

The archive of seismograms scanned at 400 dpi resolution is accessible on the website (www.archive.infp.ro). The database contains recordings

Table 2

Database of scanned seismograms

| Box | No. | Station | Component | | | Start date of the record | Start time | End date of the record | End time | Instrument | Q |
|---|---|---|---|---|---|---|---|---|---|---|---|
| A1 | 1 | BUC | NS | | | 25 May 1903 | 10:55 | 26 May 1903 | 10:10 | BS_2 | |
| A1 | 2 | BUC | | EW | | 25 May 1903 | 10:55 | 26 May 1903 | 10:08 | BS_1 | |
| A1 | 3 | BUC | | EW | | 29 May 1903 | 9:46 | 30 May 1903 | 10:52 | BS_1 | |
| A1 | 4 | BUC | NS | | | 29 May 1903 | 9:47 | 30 May 1903 | 10:45 | BS_2 | |
| A1 | 5 | BUC | | EW | | 8 Jun 1903 | 11:08 | 9 Jun 1903 | 8:02 | BS_1 | |
| A1 | 6 | BUC | | EW | | 12 Sep 1903 | 10:19 | 13 Sep 1903 | 10:15 | BS_1 | A |
| A1 | 7 | BUC | NS | | | 12 Sep 1903 | 10:16 | 13 Sep 1903 | 10:20 | BS_2 | B |
| A1 | 8 | BUC | | EW | | 27 Nov 1903 | 10:34 | 28 Nov 1903 | 10:53 | BS_1 | B |
| A1 | 9 | BUC | | EW | | 29 Nov 1903 | 10:18 | 30 Nov 1903 | 10:48 | BS_1 | B |
| A1 | 10 | BUC | | EW | | 5 Dec 1903 | 10:20 | 6 Dec 1903 | 10:35 | BS_1 | B |
| A1 | 11 | BUC | | EW | | 5 Feb 1904 | 10:41 | 6 Feb 1904 | 5:27 | BS_1 | B |
| A1 | 12 | BUC | NS | | | 5 Feb 1904 | 10:40 | 6 Feb 1904 | 5:33 | BS_2 | |
| A1 | 13 | BUC | NS | | | 4 Apr 1904 | 10:32 | 4 Apr 1904 | | BS_2 | B |
| … | … | … | … | … | | … | … | … | … | … | … |
| A4 | 750 | BUC | NS | EW | | 4 Jan 1940 | 17:50 | 5 Jan 1940 | 05:33 | Galitin | A |
| A4 | 832 | BUC | | | Z | 28 Dec 1940 | 17:30 | 29 Dec 1940 | 05:30 | Alfani | |

**Explanations:** Box – code of the file containing a group of seismograms stored in a separate place; No. – number of scanned seismogram; Station – station code; Component – components of the instruments; Start/End of the record – date of beginning of the seismograms; Start/End time – time (hour and minutes) of the beginning/end of the seismogram; Instrument – type of instrument (BS – Bosh), Q – the quality of recorded event (A-very good, B-good, C-low, D-noise).

from local, regional and distant earthquakes occurred since 1903 and will provide information of interest at national, regional/European and global scale. As an example, the seismogram recorded at Bucharest station (Bosch instrument) for an earthquake ($Mw$ = 7.3) occurred in Iran in 1909 is represented in Fig. 6. As a direct consequence, it will contribute to intensification of data exchange with other seismological centers.

The database includes also seismic bulletins, publications, historical references to the earthquakes and the characteristics of the seismic instruments,

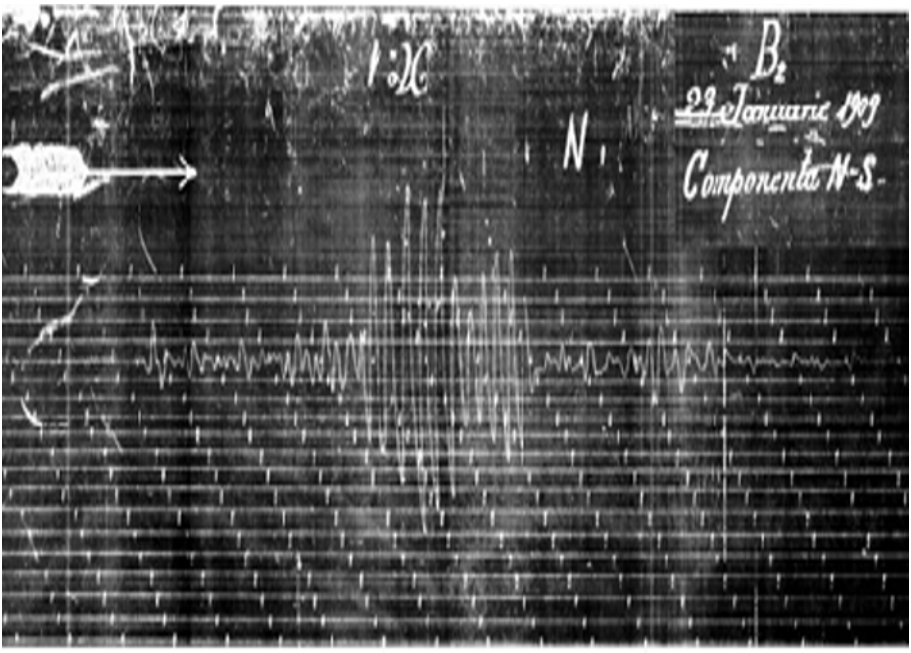


Fig. 6. Event from 23 January1909, Silakhor, Iran (Persia); latitude 33.4°N, longitude 49.1°E, *Mw* = 7.3.

useful for knowing the instrument response function and the time corrections of the seismic phases input (Figs. 7 and 8).

At the same time, all the information provided by other seismological observatories related to strong earthquakes occurred in Romania will be included in the database. The database will be extended with the macroseismic information (notes, reports, documents, papers, maps, photos, *etc.*) whenever they are available.

A lot of such information is now available from the European historical earthquake catalogue (Stucchi *et al*. 2013) and from the integrated macroseismic database for the Vrancea strong events (Kronrod *et al*. 2013).

## 5. CONCLUSIONS

Romania is a country with long history in earthquake activity investigation using instrumental records. Therefore, any tool able to take advantage of the potential information from past recordings is of extreme interest.

We developed a unique instrumental database that archives historical seismograms recorded between 1903 and 1957 by Romanian seismic stations (5188 earthquakes) and as well as all the available complementary documen-

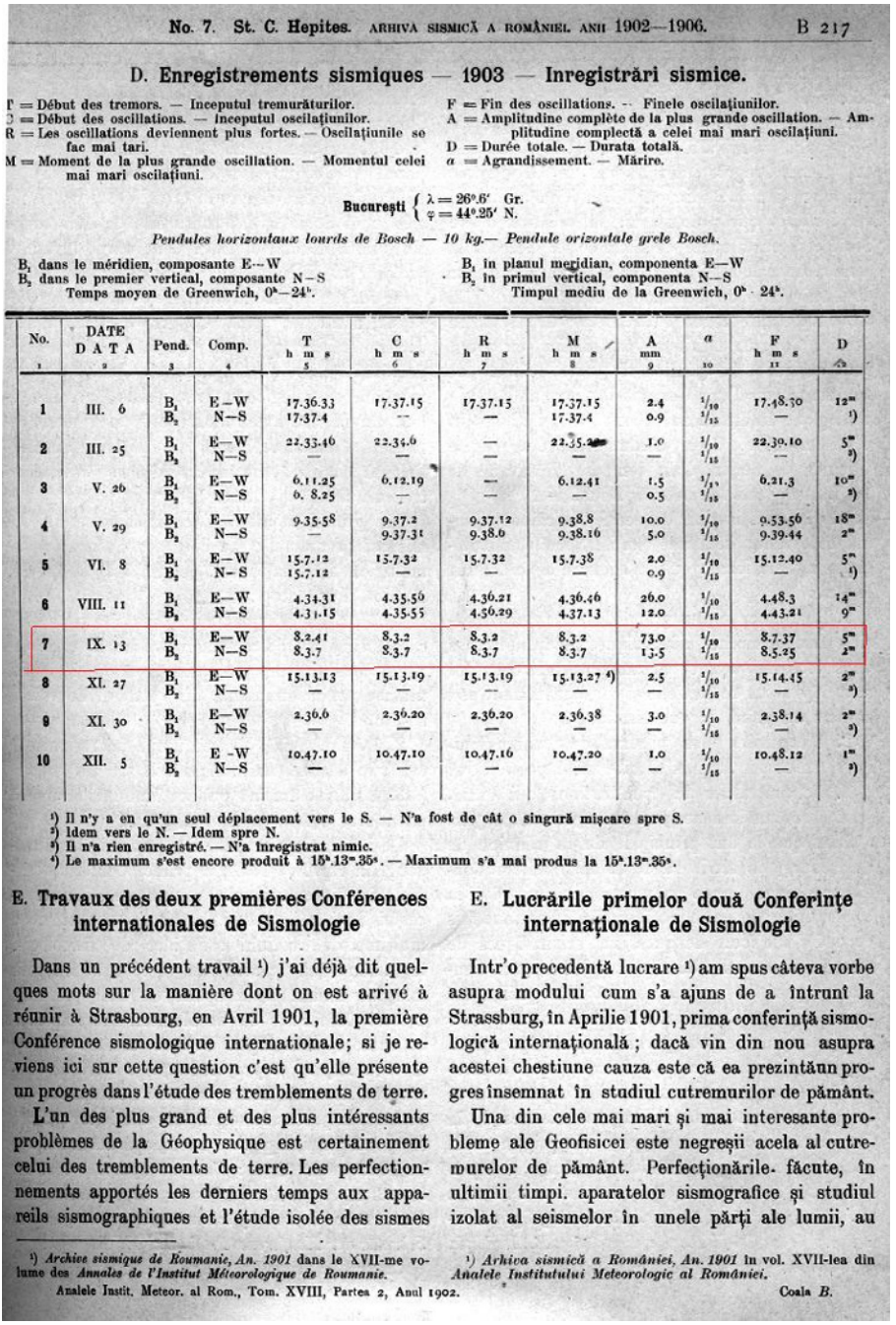

No. 7. St. C. Hepites. ARHIVA SISMICĂ A ROMÂNIEI. ANII 1902—1906. B 217

## D. Enregistrements sismiques — 1903 — Inregistrări sismice.

I = Début des tremors. — Inceputul tremurăturilor.
I = Début des oscillations. — Inceputul oscilaţiunilor.
R = Les oscillations deviennent plus fortes. — Oscilaţiunile se fac mai tari.
M = Moment de la plus grande oscillation. — Momentul celei mai mari oscilaţiuni.
F = Fin des oscillations. — Finele oscilaţiunilor.
A = Amplitudine complète de la plus grande oscillation. — Amplitudine complectă a celei mai mari oscilaţiuni.
D = Durée totale. — Durata totală.
a = Agrandissement. — Mărire.

**Bucureşti** { λ = 26°.6′ Gr. ; φ = 44°.25′ N.

*Pendules horizontaux lourds de Bosch — 10 kg.— Pendule orizontale grele Bosch.*

$B_1$ dans le méridien, composante E—W
$B_2$ dans le premier vertical, composante N—S
Temps moyen de Greenwich, 0h—24h.

$B_1$ în planul meridian, componenta E—W
$B_2$ în primul vertical, componenta N—S
Timpul mediu de la Greenwich, 0h - 24h.

| No. 1 | DATE DATA 2 | Pend. 3 | Comp. 4 | T h m s 5 | C h m s 6 | R h m s 7 | M h m s 8 | A mm 9 | a 10 | F h m s 11 | D 12 |
|---|---|---|---|---|---|---|---|---|---|---|---|
| 1 | III. 6 | $B_1$ | E—W | 17.36.33 | 17.37.15 | 17.37.15 | 17.37.15 | 2.4 | 1/10 | 17.48.30 | 12m |
| | | $B_2$ | N—S | 17.37.4 | — | — | 17.37.4 | 0.9 | 1/15 | — | 1) |
| 2 | III. 25 | $B_1$ | E—W | 22.33.46 | 22.34.6 | — | 22.35.2[illegible] | 1.0 | 1/10 | 22.39.10 | 5m |
| | | $B_2$ | N—S | — | — | — | — | — | 1/15 | — | 2) |
| 3 | V. 26 | $B_1$ | E—W | 6.11.25 | 6.12.19 | — | 6.12.41 | 1.5 | 1/10 | 6.21.3 | 10m |
| | | $B_2$ | N—S | 6. 8.25 | — | — | — | 0.5 | 1/15 | — | 3) |
| 4 | V. 29 | $B_1$ | E—W | 9.35.58 | 9.37.2 | 9.37.12 | 9.38.8 | 10.0 | 1/10 | 9.53.56 | 18m |
| | | $B_2$ | N—S | — | 9.37.31 | 9.38.0 | 9.38.16 | 5.0 | 1/15 | 9.39.44 | 2m |
| 5 | VI. 8 | $B_1$ | E—W | 15.7.12 | 15.7.32 | 15.7.32 | 15.7.38 | 2.0 | 1/10 | 15.12.40 | 5m |
| | | $B_2$ | N—S | 15.7.12 | — | — | — | 0.9 | 1/15 | — | 1) |
| 6 | VIII. 11 | $B_1$ | E—W | 4.34.31 | 4.35.50 | 4.36.21 | 4.36.46 | 26.0 | 1/10 | 4.48.3 | 14m |
| | | $B_2$ | N—S | 4.31.15 | 4.35.55 | 4.36.29 | 4.37.13 | 12.0 | 1/15 | 4.43.21 | 9m |
| 7 | IX. 13 | $B_1$ | E—W | 8.2.41 | 8.3.2 | 8.3.2 | 8.3.2 | 73.0 | 1/10 | 8.7.37 | 5m |
| | | $B_2$ | N—S | 8.3.7 | 8.3.7 | 8.3.7 | 8.3.7 | 13.5 | 1/15 | 8.5.25 | 2m |
| 8 | XI. 27 | $B_1$ | E—W | 15.13.13 | 15.13.19 | 15.13.19 | 15.13.27 4) | 2.5 | 1/10 | 15.14.45 | 2m |
| | | $B_2$ | N—S | — | — | — | — | — | 1/15 | — | 3) |
| 9 | XI. 30 | $B_1$ | E—W | 2.36.6 | 2.36.20 | 2.36.20 | 2.36.38 | 3.0 | 1/10 | 2.38.14 | 2m |
| | | $B_2$ | N—S | — | — | — | — | — | 1/15 | — | 3) |
| 10 | XII. 5 | $B_1$ | E -W | 10.47.10 | 10.47.10 | 10.47.16 | 10.47.20 | 1.0 | 1/10 | 10.48.12 | 1m |
| | | $B_2$ | N—S | — | — | — | — | — | 1/15 | — | 3) |

1) Il n'y a eu qu'un seul déplacement vers le S. — N'a fost de cât o singură mişcare spre S.
2) Idem vers le N. — Idem spre N.
3) Il n'a rien enregistré. — N'a înregistrat nimic.
4) Le maximum s'est encore produit à 15h.13m.35s. — Maximum s'a mai produs la 15h.13m.35s.

## E. Travaux des deux premières Conférences internationales de Sismologie

Dans un précédent travail [1]) j'ai déjà dit quelques mots sur la manière dont on est arrivé à réunir à Strasbourg, en Avril 1901, la première Conférence sismologique internationale; si je reviens ici sur cette question c'est qu'elle présente un progrès dans l'étude des tremblements de terre.

L'un des plus grand et des plus intéressants problèmes de la Géophysique est certainement celui des tremblements de terre. Les perfectionnements apportés les derniers temps aux appareils sismographiques et l'étude isolée des sismes

[1]) *Archive sismique de Roumanie, An. 1901* dans le XVII-me volume des *Annales de l'Institut Météorologique de Roumanie.*

Analele Instit. Meteor. al Rom., Tom. XVIII, Partea 2, Anul 1902.

## E. Lucrările primelor două Conferinţe internaţionale de Sismologie

Intr'o precedentă lucrare [1]) am spus câteva vorbe asupra modului cum s'a ajuns de a întruni la Strassburg, în Aprilie 1901, prima conferinţă sismologică internaţională; dacă vin din nou asupra acestei chestiune cauza este că ea prezintăun progres însemnat în studiul cutremurilor de pământ.

Una din cele mai mari şi mai interesante probleme ale Geofisicei este negreşii acela al cutremurelor de pământ. Perfecţionările făcute, în ultimii timpi, aparatelor sismografice şi studiul izolat al seismelor în unele părţi ale lumii, au

[1]) *Arhiva sismică a României, An. 1901* în vol. XVII-lea din *Analele Institutului Meteorologic al României.*

Coala B.

Fig. 7. Example of historical publication with reference to earthquakes in that period (from Romania Seismic Archive between 1902 and 1906).

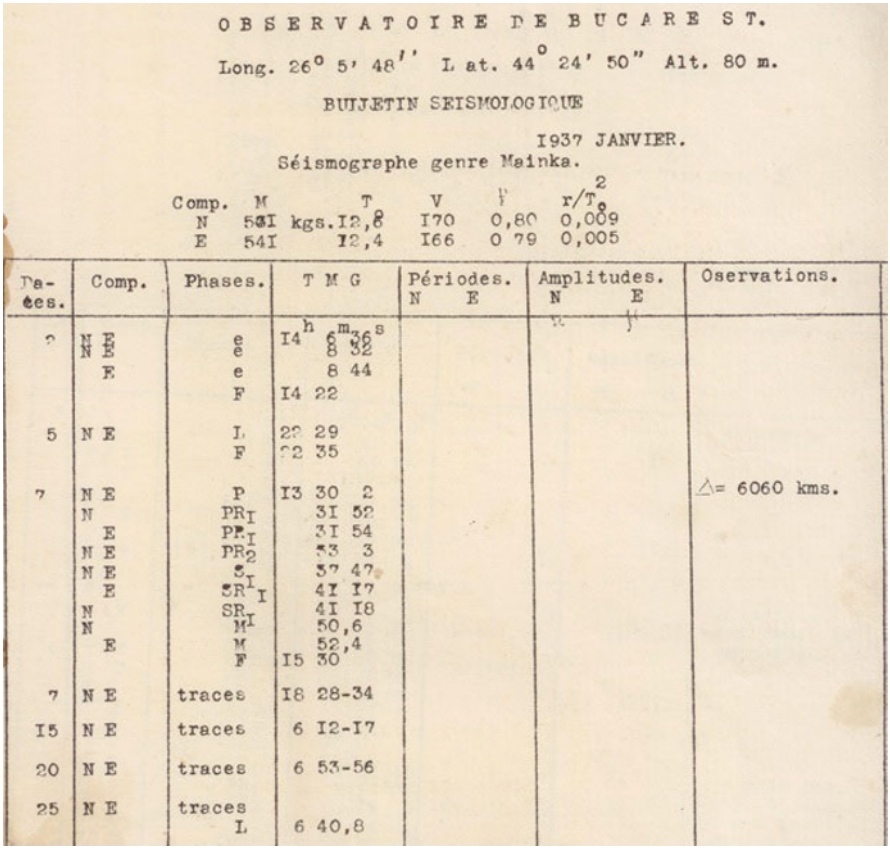

OBSERVATOIRE DE BUCARE ST.

Long. 26° 5' 48'' Lat. 44° 24' 50" Alt. 80 m.

BUJETIN SEISMOLOGIQUE

I937 JANVIER.

Séismographe genre Mainka.

| Comp. | M | T | V | P | r/T$^2$ |
|---|---|---|---|---|---|
| N | 54I kgs. | I2,8 | I70 | 0,80 | 0,009 |
| E | 54I | I2,4 | I66 | 0 79 | 0,005 |

| Dates. | Comp. | Phases. | T M G | Périodes. N E | Amplitudes. N E | Oservations. |
|---|---|---|---|---|---|---|
| 2 | N E | e | I4$^h$ 6$^m$ 36$^s$ | | | |
| | N E | e | 8 32 | | | |
| | E | e | 8 44 | | | |
| | | F | I4 22 | | | |
| 5 | N E | L | 22 29 | | | |
| | | F | 22 35 | | | |
| 7 | N E | P | I3 30 2 | | | △= 6060 kms. |
| | N | $PR_I$ | 3I 52 | | | |
| | E | $PR_I$ | 3I 54 | | | |
| | N E | $PR_2$ | 33 3 | | | |
| | N E | $S_I$ | 37 47 | | | |
| | E | $SR^I_I$ | 4I I7 | | | |
| | N | $SR_I$ | 4I I8 | | | |
| | N | $M^I$ | 50,6 | | | |
| | E | M | 52,4 | | | |
| | | F | I5 30 | | | |
| 7 | N E | traces | I8 28-34 | | | |
| I5 | N E | traces | 6 I2-I7 | | | |
| 20 | N E | traces | 6 53-56 | | | |
| 25 | N E | traces | | | | |
| | | L | 6 40,8 | | | |

Fig. 8. Example of seismic bulletin with information about seismic station equipment and the recording phases of earthquakes.

tation (seismic bulletins, stations books, publications, *etc*.). In a first stage we shall complete the database by scanning all the available old seismograms recorded by the Romanian stations (hundreds of thousands). Then the database will be filled with digitized seismograms associated with identified earthquakes.

A managing system to collect data for historic events, archive (database construction) and analysis procedures was developed. The proposed system follows the same structure as the system developed in the framework of the Euroseismos Project (Saving and Studying the Seismograms of the Strongest Euro-Mediterranean Earthquakes, http://storing.ingv.it/es_web). This project allowed so far the recovery of more than 30000 historical seismograms from 29 countries that joined the project, including Romania. Our database is linked with the EuroSeismos Database.

The organizing of the final database allows an easy access to the main seismic data, like seismograms, bulletins, macroseismic observations, papers, *etc*.

Digital format of the seismograms for significant Romanian earthquakes provides unique data for their advanced study, especially relocation of hypocenters and magnitude determination using more accuracy data, as well as the spectral parameters estimation (seismic moment, moment magnitude, corner frequency, fault dimensions, stress drop, *etc*.), synthetic seismograms and focal mechanism solutions.

On request, seismograms and metadata could be obtained and used for reanalyzing major events recorded at national, regional and global scale.

Acknowledgments. D. Paulescu had benefited of a research NERIES/SISMOS Grant (2008) within the project "Scanning, digitization and vectorization of historical seismograms recorded by Romanian seismic network for some strong Vrancea earthquakes". The first author benefited of a stage of specialization about scanning, digitization and vectorization of historical seismograms at INGV Roma (SISMOS Centre) within the European Commission (EC FP7) NERIES (Network of Research Infrastructures for European Seismology) Project (TA3-006, 12-22/06/2008). The authors are grateful to the editor and the reviewers for their valuable comments and suggestions.

## References

Curea, I. (1961), Recent earthquakes in Banat, *St. Cerc. Astr. Seism.* **6**, 2, 15-35 (in Romanian).

Demetrescu, G. (1956), Seismological office of the Observatory of Bucharest, *St. Cerc. Astr. Seism*. **1**, 85-88 (in Romanian).

Dewey, J., and P. Byerly (1969), The early history of seismometry (to1900), *Bull. Seismol. Soc. Am*. **59**, 1, 183-227.

Glover, D.P., and H. Meyers (1988), Historical seismogram filming project: current status. **In:** W.H.K. Lee, H. Meyers, and K. Shimazaki (eds.), *Historical Seismograms and Earthquakes of the World*, Academic Press, San Diego, 373-379.

Hepites, S.C. (1893), Cutremurele de pamant din Romania in anul 1902 st. n. (1) si in deceniul 1893-1902 (nota a opta), *Anal. Acad. Romane* **35**, 544 (in Romanian).

IRIS (2004), Preservation of WWSSN and historical seismograms, IDEAsRev.doc, Incorporated Research Institutions for Seismology, Washington, USA, available from: http://www.iris.edu/seismo/info/icpwhs/ideas.pdf.

Jeffreys, H. (1935), Some deep-focus earthquakes, *Geophys. J.* **3**, 8, 310-343, DOI: 10.1111/j.1365-246X.1935.tb01741.x.

Kanamori, H. (1988), Importance of historical seismograms for geophysical research. **In:** W.H.K. Lee, H. Meyers, and K. Shimazaki (eds.), *Historical Seismograms and Earthquakes of the World*, Academic Press, San Diego, 16-33.

Kronrod, T., M. Radulian, G. Panza, M. Popa, I. Paskaleva, S. Radovanovich, K. Gribovszki, I. Sandu, and L. Pekevski (2013), Integrated transnational macroseismic data set for the strongest earthquakes of Vrancea (Romania), *Tectonophysics* **590**, 1-23, DOI: 10.1016/j.tecto.2013.01.019.

Michelini, A., B. De Simoni, A. Amato, and E. Boschi (2005), Collecting, digitizing, and distributing historical seismological data, *Eos Trans. AGU* **86**, 28, 261-266, DOI: 10.1029/2005EO280002.

Pintore, S., M. Quintiliani, and D. Franceschi (2005), Teseo: A vectoriser of historical seismograms, *Comput. Geosci.* **31**, 10, 1277-1285, DOI: 10.1016/j.cageo.2005.04.001.

Radulescu, F. (2009), Romanian seismology – historical, scientific and human landmarks, *Rev. Roum. Geophys.* **52-53**, 101-121.

Stucchi, M., A. Rovida, A.A. Gomez Capera, P. Alexandre, T. Camelbeeck, M.B. Demircioglu, P. Gasperini, V. Kouskouna, R.M.W. Musson, M. Radulian, K. Sesetyan, S. Vilanova, D. Baumont, D. Faeh, W. Lenhardt, K. Makropoulos, J.M. Martinez Solares, O. Scotti, M. Zivcic, P. Albini, J. Batllo, C. Papaioannou, R. Tatevossian, M. Locati, C. Meletti, D. Viganò, and D. Giardini (2013), The SHARE European Earthquake Catalogue (SHEEC) 1000-1899, *J. Seismol.* **17**, 2, 523-544, DOI: 10.1007/s10950-012-9335-2.

Received 23 February 2015
Received in revised form 3 August 2015
Accepted 6 August 2015

DE GRUYTER OPEN

**Acta Geophysica**
vol. 64, no. 4, Aug. 2016, pp. 978-1003
DOI: 10.1515/acgeo-2016-0046

# Structural Investigations of Afghanistan Deduced from Remote Sensing and Potential Field Data

Hakim SAIBI[1,2], Masood AZIZI[1], and Saad MOGREN[3]

[1]Kyushu University, Faculty of Engineering,
Department of Earth Resources Engineering, Fukuoka, Japan;
e-mail: saibi-hakim@mine.kyushu-u.ac.jp (corresponding author)

[2]Dept. of Geology, United Arab Emirates University, Al-Ain, United Arab Emirates

[3]King Saud University, Department of Geology and Geophysics,
Riyadh, Saudi Arabia; e-mail: smogren@ksu.edu.sa

A b s t r a c t

This study integrates potential gravity and magnetic field data with remotely sensed images and geological data in an effort to understand the subsurface major geological structures in Afghanistan. Integrated analysis of Landsat SRTM data was applied for extraction of geological lineaments. The potential field data were analyzed using gradient interpretation techniques, such as analytic signal (AS), tilt derivative (TDR), horizontal gradient of the tilt derivative (HG-TDR), Euler Deconvolution (ED) and power spectrum methods, and results were correlated with known geological structures.

The analysis of remote sensing data and potential field data reveals the regional geological structural characteristics of Afghanistan. The power spectrum analysis of magnetic and gravity data suggests shallow basement rocks at around 1 to 1.5 km depth. The results of TDR of potential field data are in agreement with the location of the major regional fault structures and also the location of the basins and swells, except in the Helmand region (SW Afghanistan) where many high potential field anomalies are observed and attributed to batholiths and near-surface volcanic rocks intrusions.

Ownership: Institute of Geophysics, Polish Academy of Sciences;
© 2016 Saibi *et al*. This is an open access article distributed under the Creative Commons Attribution-NonCommercial-NoDerivs license,
http://creativecommons.org/licenses/by-nc-nd/3.0/.

A high-resolution airborne geophysical survey in the data sparse region of eastern Afghanistan is recommended in order to have a complete image of the potential field anomalies.

**Key words:** gravity, magnetic, remote sensing; structure, Afghanistan.

## 1. INTRODUCTION

Regional interpretation and analysis of potential field data (gravity and aeromagnetic data) has been shown to be extremely effective tool to map geology in remote and inaccessible regions and areas buried by shallow cover (Betts *et al.* 2003, McLean *et al.* 2009, Aitken and Betts 2009). The technique is particularly effective for studies of the architecture character of the Earth's crust because the data is effective for interpreting 3D geometry of structure and geological bodies (Aitken and Betts 2009, Blaikie *et al.* 2014, Spampinato *et al.* 2015), overprinting relationships (Betts *et al.* 2003), and fault kinematics (Betts *et al.* 2007). The data is also sensitive to alteration associated with fluid-rock interactions, and igneous intrusions.

Afghanistan preserves some of the most complex and diverse geology in the world associated with the closure of Tethys and the peripherial responses to collision between India and Eurasia. The country is divided into many tectonic blocks bordered by deep-faults that formed or reactivated in response to this collision. These rocks are abundantly rich in natural resources (mineral, petroleum, and natural gas) but much of the Afghanistan's potential remains unknown. The nation is underexplored because it has suffered through decades of war, which affected the education and research progress in the country. Consequently, Afghanistan may represent one of the last bastions of untapped mineral and energy resources on the planet.

In 1966, a German geophysical firm carried out airborne magnetometer measurements in the southern part of Afghanistan in order to explore the depth of the sedimentary basins for oil exploration and possible location of ore bodies for mineral exploration (Bosum *et al.* 1968). The data covered the East Afghan Trough, Helmand, Rosgan, and Ghor basins, and southwestern Afghanistan.

Recently, the USGS started airborne geophysical surveys in cooperation with the Afghanistan Geological Survey (AGS) (USGS 2006, 2008), which covers almost the entire country except of eastern Afghanistan due to security reasons. Here, we present an interpretation of the recent potential field data provided by AGS.

The objective of this study is to delineate the subsurface structure of Afghanistan from the potential field and remote-sensing data. The interpretation techniques applied for the potential field data are tilt derivative (TDR), analytic signal (AS), horizontal derivative of the tilt derivative (HG-TDR),

and Euler Deconvolution (ED). The combination of these methods enhanced the structural definition of Afghanistan. A power spectrum analysis is also performed for gravity and magnetic data in order to detect the depth to the gravity and magnetic sources in Afghanistan. The geophysical data were combined with geological and remote sensing data for better understanding of the subsurface structure to provide context for a wide variety of investigations, such as mineral and energy resources assessments, environmental characterizations, and groundwater studies.

Our approach has been effectively used to constrain the crustal architecture and geology of numerous areas including: Rabie and Ammar (1990), Kamel and Elsirafe (1994) in Egypt, Lunden *et al.* (2001) in Sweden, Lamontagne *et al.* (2003) in Canada, Chen and Zhou (2005) in China, Yassaghi (2006) in Iran, Saadi *et al.* (2008a, b) in Libya, Khamies and El-Tarras (2010) in Egypt, Azizi and Saibi (2015) and Azizi *et al.* (2015) in Aynak-Logar valley, eastern Afghanistan.

The combination of the three types of data (geology, remote sensing, and potential field) is processed in Geographic Information System (GIS) using ArcGIS Ver. 10, ER Mapper Ver. 7.0, and ENVI Ver. 4.7. The geophysical data is processed using Geosoft Ver. 8.

## 2. GEOLOGY, SEISMICITY, AND TECTONIC SETTINGS

The color shaded relief map of Afghanistan and the surrounding area (Fig. 1) shows the large area of mountainous terrain in the country compared with the relative lowlands to the southwest. The relief map emphasizes that the mountain belt is not linear. This tectonic morphology is a direct result of the India–Asia collision to the east of Afghanistan.

The oldest rocks in Afghanistan are of Archean age and succeeded by rocks from the Precambrian up to the Quaternary (Fig. 2). The country has a complicated tectonic history due to its position at the western end of the Himalaya. Information on geology and tectonics of Afghanistan are discussed in detail by Schindler (2002), AGS (2005), and Wheeler *et al.* (2005).

The Arabian plate is moving northward with respect of Eurasian plate at 3.3 cm/year (Wheeler *et al.* 2005) and the Indian plate is subducting beneath the Eurasian plate with a rate of 3.9 cm/year (Jung *et al.* 2013) or faster (Wheeler *et al.* 2005). Consequently, Afghanistan remains extremely seismically active (Fig. 3) with earthquake activity mainly in and around northeastern Afghanistan (Hindu Kush and Pamirs).

Afghanistan can be split into four major tectonic regions: the accreted terranes in the south, the transpressional plate boundary in the east, the north Afghan platform in the north, and the Hindu Kush/Pamirs in the north-east. The high density of faults (Fig. 4) is mainly located along the Hari Rod Fault

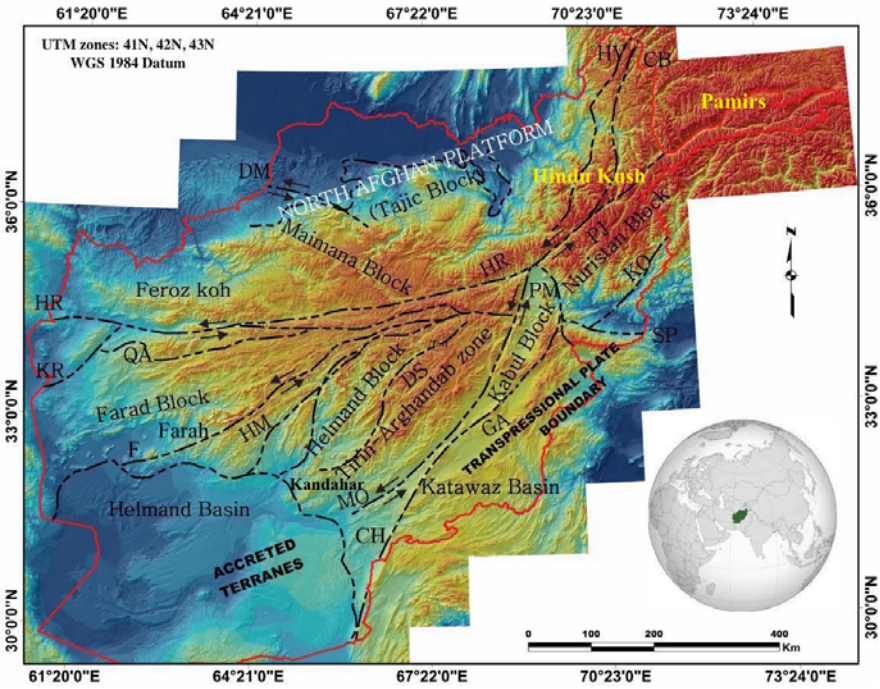


Fig. 1. Color shaded relief map of Afghanistan topography including tectonic block names and abbreviations of major faults: CH – Chaman, CB – Central Badakhsan, DS – Darafshan, DM – Dosi Mirzavalan, GA – Gardez, HR – Hari Rod, HM – Helmand, HV – Henjvan, KR – Kaj Rod, KO – Konar, MO – Mokur, PM – Paghman, PJ – Panjshir, QA – Qarghanaw, SP – Spinghar, F – Farah.

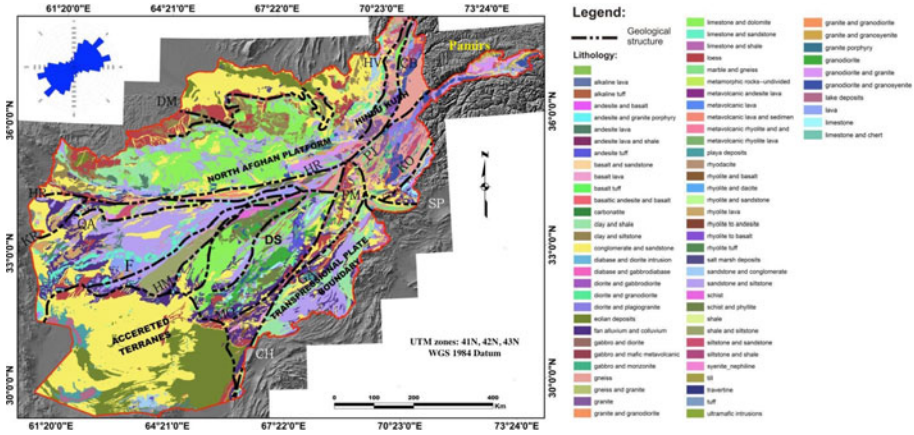


Fig. 2. Geological map showing rock units in Afghanistan and the locations of major faults (modified from Mihalasky *et al*. 2007), overlaid on the shaded relief (SRTM) map.

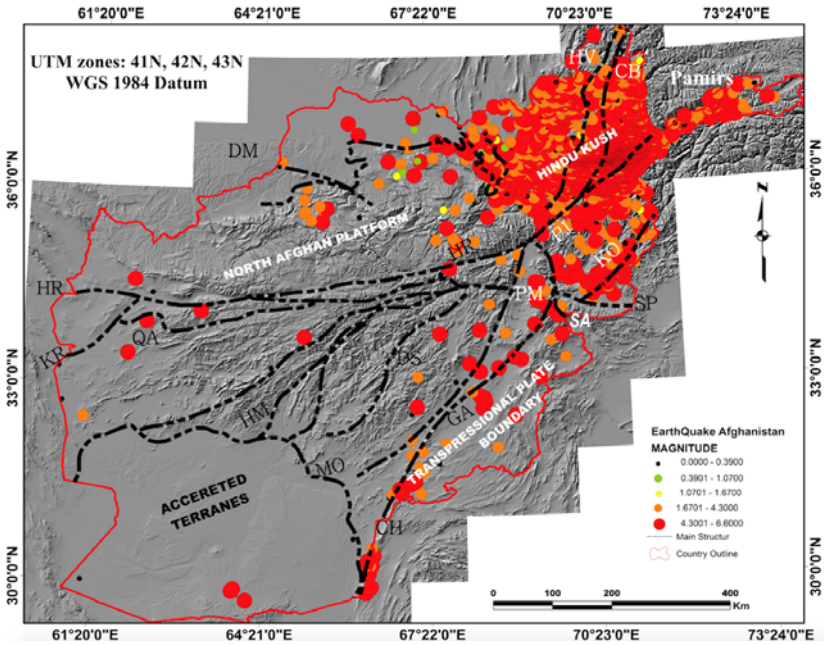


Fig. 3. Seismicity in Afghanistan.

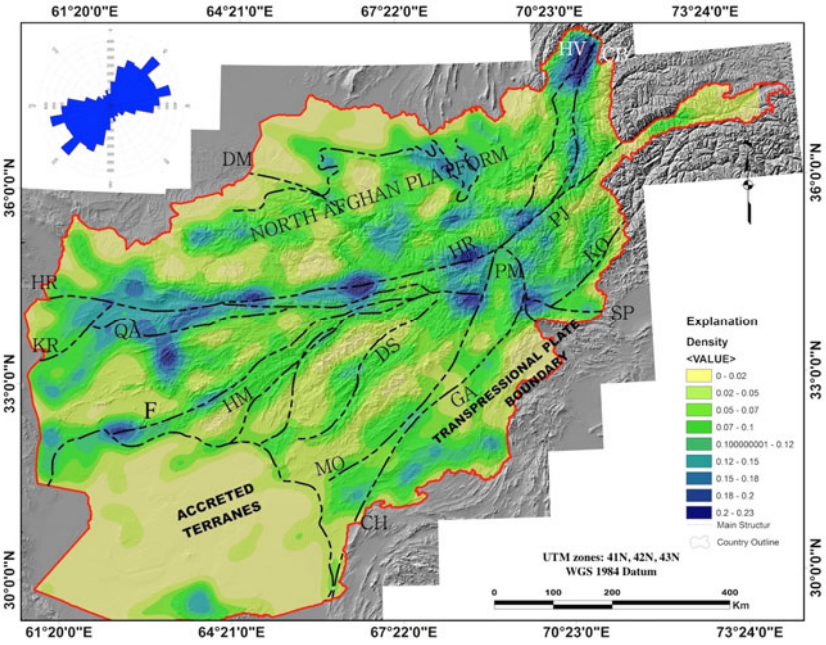


Fig. 4. Density map and rose diagram from known major geological faults in Afghanistan, overlaid on the shaded relief (SRTM) map.

system. These faults are dominated by two orientations, NE-SW and ENE-WSW (Fig. 4).

## 3. REMOTE SENSING DATA

Shuttle Radar Topography Mission (SRTM) images were prepared and interpreted to analyze geological structures in the study area. The SRTM obtained elevation data on a near-global scale to generate the most complete high-resolution digital topographic database of the Earth (Durga Rao *et al.* 2009). In this study, the 90 m resolution SRTM data were used to derive the topographic features of the study area. A series of landform interpretation experiments was conducted on the ETM+ images using contrast stretching methods and Hue-Intensity-Saturation transformation (Mather 2004). The SRTM map was used as the background in all geophysical maps in order to help interpretation.

A kernel density algorithm developed by Silverman (1986) was used in the computation of the lineament density map (Fig. 5). This map shows the number of lineaments per unit area and indicates areas of increased bedrock fracturing. It allows identification of regions with high fault density and areas

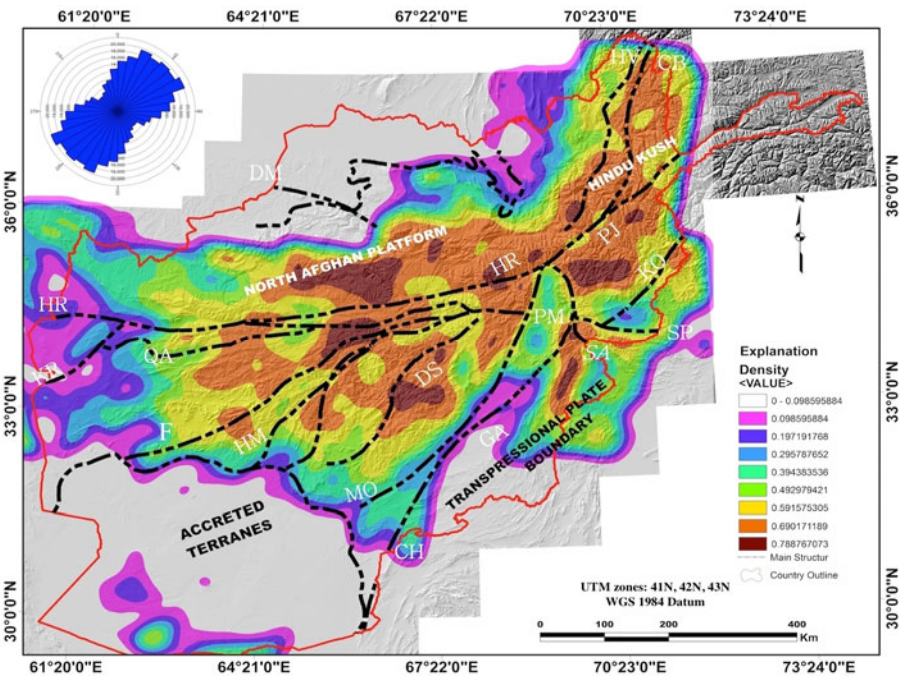


Fig. 5. Automated satellite lineaments density map in Afghanistan, overlaid on the shaded relief (SRTM) map.

lacking faults/joints. To obtain a density map, a grid structure is defined and each linear structure (lineament) that is at least partially within a grid cell is counted toward the total number of lineaments in that grid cell. The density map for Afghanistan was compiled from the digital lineaments extracted from the Landsat imagery and from the shaded relief SRTM. The density map was computed from all lineaments as well as by selecting lineaments within the specific orientation groups determined in each section. Interpreted lineaments occur mainly in the three directions NNE-SSW, NE-SW, and ENE-WSE (Fig. 5), which are the directions of the major faults, CH, HM, and HR, respectively.

## 4. POTENTIAL FIELD DATA

The study of regional gravity and magnetic anomalies has a long and distinguished history of geological and structural investigations of the Earth's lithosphere (Hinze 1985, Aitken and Betts 2009, Jessell *et al.* 2012, Stewart and Betts 2010). The magnetic dataset is derived from 2006 aeromagnetic

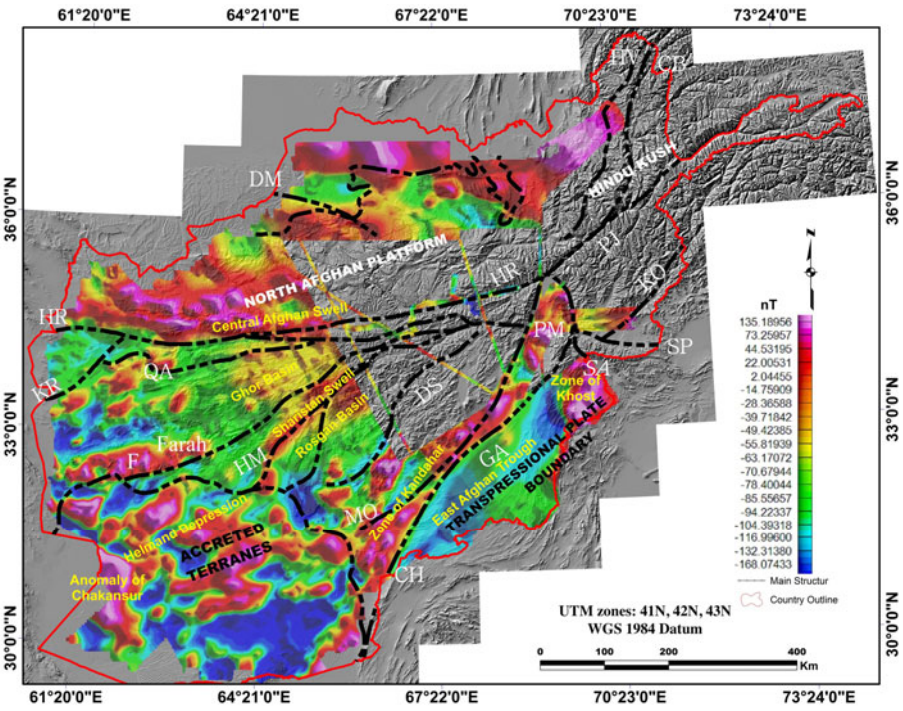


Fig. 6. Reduced-to-pole magnetic map of Afghanistan, overlaid on the shaded relief (SRTM) map. The yellow text shows the major geological and morphological divisions in connection with the magnetic anomalies.

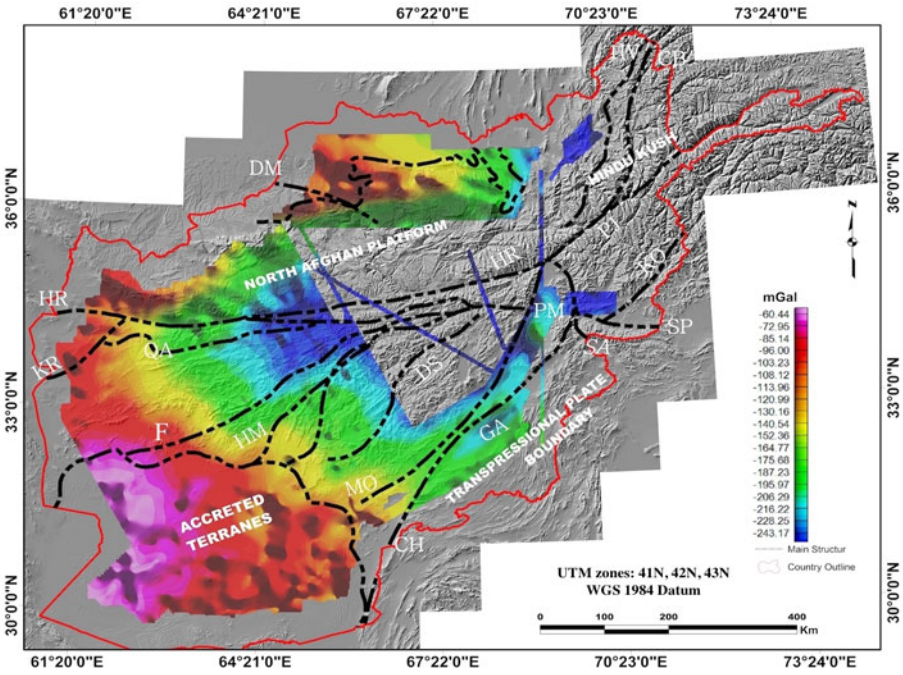


Fig. 7. Complete Bouguer gravity map of Afghanistan, overlaid on the shaded relief (SRTM) map.

surveys provided by U.S. Geological Survey and the grid elevation is 5000 m above terrain (USGS 2006). Five base station magnetometers were used during the survey. In order to correct the airborne magnetic data for time-varying anomalies, a weighted average of data from the five base stations was used to predict the time-varying field at the aircraft (USGS 2011). To overcome bi-polarity related problems, the total magnetic intensity data are gridded by minimum curvature method (with a grid size of 1000 m) and then reduced to the pole (RTP) using a magnetic inclination of 48.74 and a declination of 2.01 degrees. Magnetic data ranges from –168 to 650 nT (Fig. 6).

The gravity dataset comprises ground gravity data collected during 1966 and 1967 by the Afghanistan Water and Soil Survey Authority (McGinnis 1971) and airborne gravity data collected by the USGS in 2006 and 2008 (USGS 2006, 2008). The observed gravity data were corrected by the USGS prior to our utilization. Both data were combined to form the complete Bouguer gravity map of Afghanistan (Fig. 7).

The airborne potential field data do not cover eastern Afghanistan (high topography region).

## 5. POTENTIAL FIELD INTERPRETATION METHODS

### 5.1 Power spectrum analysis

A power spectral analysis yielded information on the depth of a significant density contrast in the crust and on the crustal structure (Gotze and Krause 2002). Saibi *et al.* (2012) applied successfully this method for estimating gravity source depths. Spector and Bhattacharyya (1966) studied the energy spectrum, which was calculated from different 3D model configurations. Spector and Grant (1970) studied the statistical ensemble of 3D maps and concluded a general form of the spectrum

$$E(r,\vartheta) = \langle H(h,r)\rangle\langle S(a,b,r,\vartheta)\rangle\langle C(t,\Phi,r)\rangle \ , \tag{1}$$

where $E$ is the energy spectral density (energy per Hz), $r$ the radial wave number (cycles per distance unit), $\vartheta$ the azimuth of radial wave number (degree), $\langle\rangle$ expresses the ensemble average, $h$ the depth (in meters); $H$ the depth factor, $S$ the horizontal size (width) factor, $C$ the vertical size (thickness or depth extent) factor, $a$ and $b$ the parameters related to the horizontal dimensions of the sources, $t$ and $\Phi$ the parameters related to the vertical depth extent of the source.

Only three factors ($H$, $S$, and $C$) are functions of the radial frequency $r$; thus, in the azimuthally averaged profile form, Eq. 1 can be written as:

$$\ln E(q) = \ln H\left(h^*, q\right) + \ln S\left(a^*, q\right) + \ln C\left(t^*, \Phi, q\right) + \text{constant} \ , \tag{2}$$

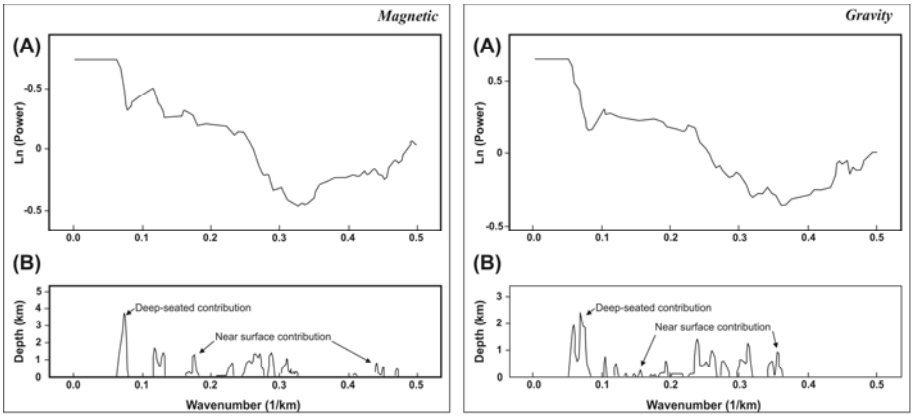


Fig. 8: Left: (A) Azimuthally averaged power spectrum of the RTP magnetic data of Afghanistan, (B) magnetic source depth estimation based on linear segments of the energy decay curve; Right: (A) Azimuthally averaged power spectrum of the complete Bouguer gravity data of Afghanistan, (B) gravity source depth estimation based on linear segments of the energy decay curve.

where $h^*$, $a^*$, $t^*$ are the average depth, half width and thickness of the source ensemble, respectively.

This equation demonstrates that contributions from the depths to the top of layers, widths and thicknesses of the source ensemble can affect the shape of the energy spectral decay curve. Figure 8 (right) shows the averaged power density spectrum of the gravity data of Afghanistan and the instantaneous depths of the gravity sources. Two different gravity contributions can be seen: a deep-seated source at a depth of around 2 to 2.5 km, and a shallow source at a depth of 1 to 1.5 km. Figure 8 (left) shows the averaged power density spectrum of the magnetic data of Afghanistan and the instantaneous depths of the magnetic sources. Two different magnetic contributions can be seen: a deep-seated source at a depth of around 3.8 km, and a shallow source at a depth of 1 to 1.5 km.

### 5.2 Analytic signal method (AS)

The AS method (Nabighian 1972), also called the total gradient method, has been the subject of continuing investigation and improvements since it was first applied (*e.g.*, Nabighian 1974, 1984; Roest *et al.* 1992, MacLeod *et al.* 1993, Hsu *et al.* 1996, 1998; Debeglia and Corpel 1997, Keating and Pilkington 2004). Roest *et al.* (1992) showed that the amplitude (absolute value) of the 3D analytic signal at location $(x, y)$ can be easily derived from the three orthogonal gradients of the total magnetic field. In the analytic signal method, it is assumed that the causative sources are magnetic contacts.

Their counterparts, in the case of gravity data, have been introduced by Klingele *et al.* (1991). The general equation for a 3D source is:

$$\mathrm{AS}(x, y) = \mathrm{SQRT}\left\{\left(\partial F/\partial x\right)^2 + \left(\partial F/\partial y\right)^2 + \left(\partial F/\partial z\right)^2\right\}, \tag{3}$$

where AS $(x, y)$ is the amplitude of the analytic signal at $(x, y)$, $F$ is the potential field observed at $(x, y)$, and $(\partial F/\partial x)$, $(\partial F/\partial y)$, $(\partial F/\partial z)$ are the two horizontal and vertical derivatives of the potential field, respectively.

The maxima of AS is very useful for delineating edges of magnetic sources because of the amplitude of the AS peaks over magnetic sources. The maxima of AS of the magnetic data produce clear resolution of the shallower bodies, but do not delineate the deeper body very well (Arisoy and Dikmen 2013). The analytic signal signature of Afghanistan was calculated (Figs. 9 and 10) in the frequency domain using the fast Fourier transform technique (Blakely 1995). Higher values of the analytic signal of magnetic data are observed mainly in the accreted terranes area and along the HR and CH faults (Fig. 9), indicating that these regions have significant magnetic susceptibility contrasts that produce identifiable signatures on the map.

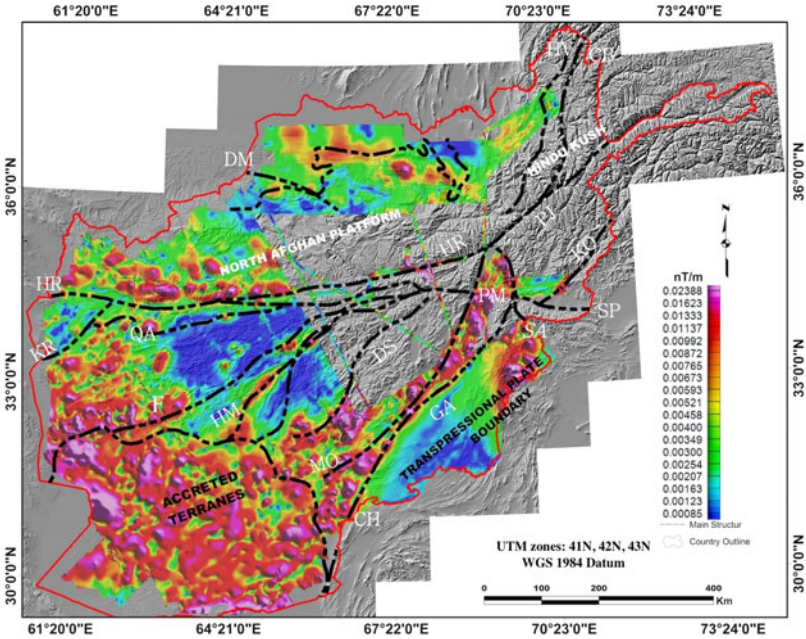


Fig. 9. Analytic signal map of magnetic data of Afghanistan, overlaid on the shaded relief (SRTM) map.

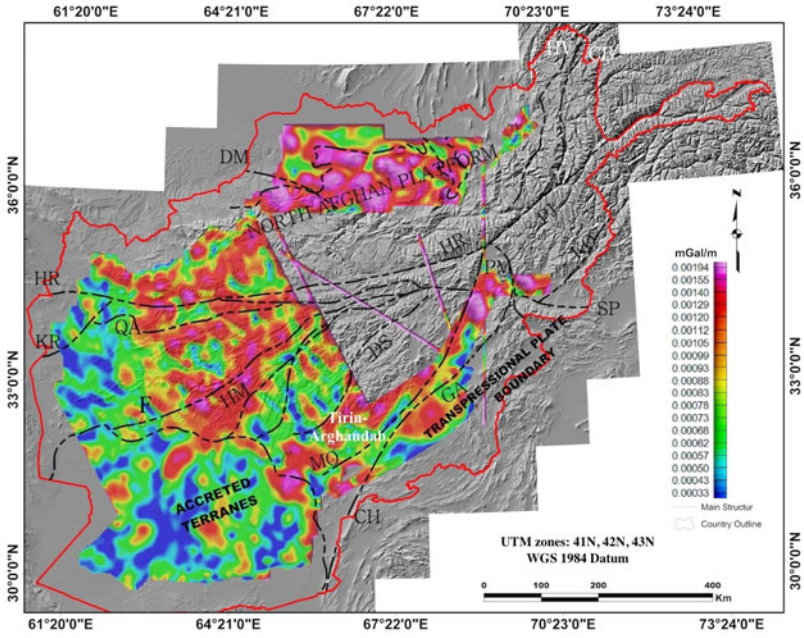


Fig. 10. Analytic signal map of gravity data of Afghanistan, overlaid on the shaded relief (SRTM) map.

High analytic signal of gravity data is observed on the north Afghan platform (Fig. 10) and also along HR and HM fault structures and in the Tirin-Arghandab zone.

### 5.3 Tilt derivative method (TDR)

The tilt derivative method, also called tilt angle method, is a refinement of the analytic signal method suggested by Miller and Singh (1994) and by Verduzco *et al.* (2004). The TDR determines the location and depth of vertical magnetic contacts without prior information on the source configuration by using the horizontal gradient amplitude (first horizontal derivative) of the tilt angle. The method has been further developed by Salem *et al.* (2007, 2008) and Fairhead *et al.* (2008). The TDR method was used to enhance and sharpen the potential field anomalies. The advantage of TDR is that it can show the zero contour line located on or close to a contact. The TDR is defined as:

$$\mathrm{TDR} = \tan^{-1}\left\{\left(\partial F/\partial z\right)\Big/\mathrm{SQRT}\left[\left(\partial F/\partial x\right)^2 + \left(\partial F/\partial y\right)^2\right]\right\}, \qquad (4)$$

where $F$ is the potential field observed at $(x, y)$, and $(\partial F/\partial x)$, $(\partial F/\partial y)$, $(\partial F/\partial z)$ are the two horizontal and vertical derivatives of the potential field, respec-

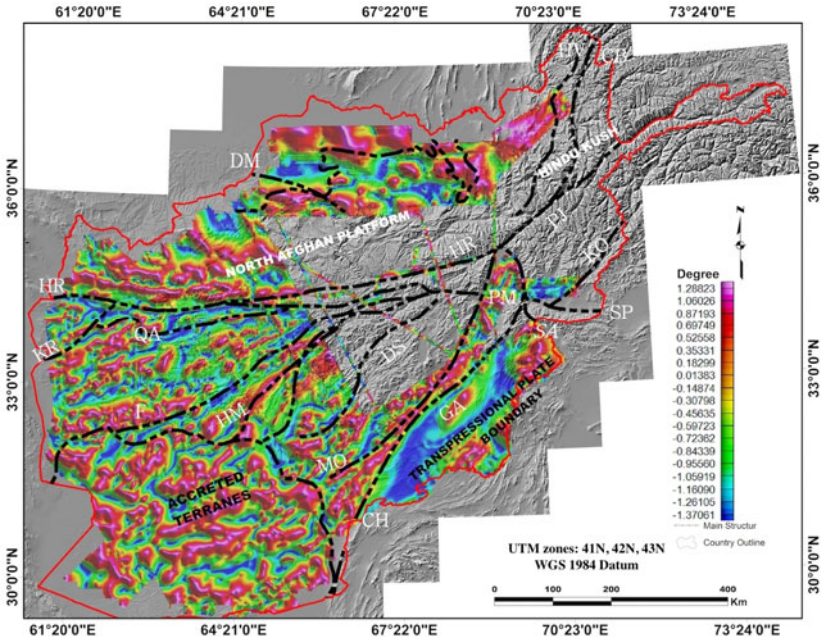


Fig. 11. Tilt derivative map of magnetic data of Afghanistan, overlaid on the shaded relief (SRTM) map.

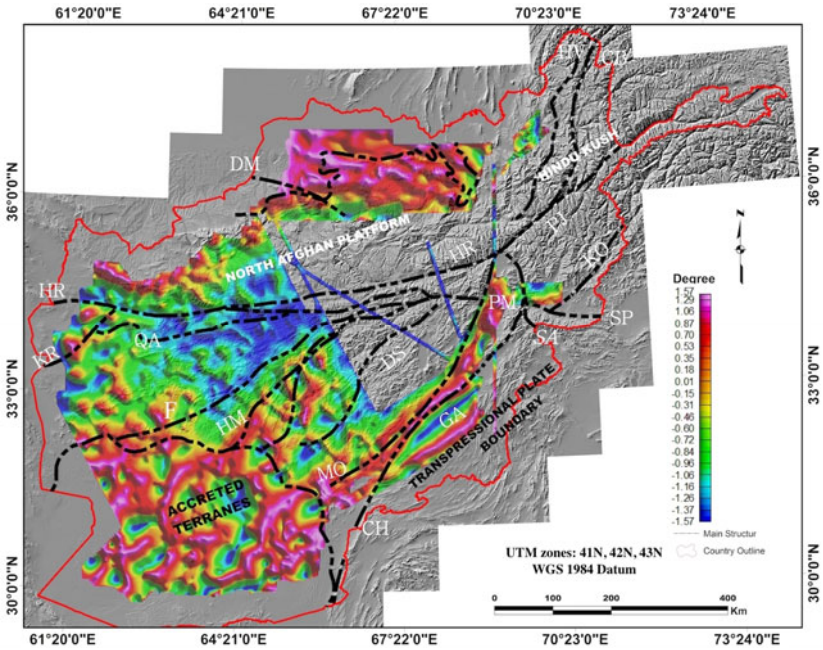


Fig. 12. Tilt derivative map of gravity data of Afghanistan, overlaid on the shaded relief (SRTM) map.

tively. The TDR method has the advantage of responding well to both shallow and deep sources, and the map of TDR recognizes the horizontal location and extent of sources. The TDR of magnetic and gravity data are presented in Figs. 11 and 12, respectively. The TDR has enhanced the potential field anomalies considerably compared to the original maps of magnetic and gravity.

### 5.4 Horizontal gradient of the tilt derivative method (HG-TDR)

Verduzco *et al.* (2004) presented an edge detector, which is the horizontal derivative of the tilt derivative:

$$\text{HG-TDR} = \text{SQRT}\left\{\left(\partial(\text{TDR})/\partial x\right)^2 + \left(\partial(\text{TDR})/\partial y\right)^2\right\} . \quad (5)$$

HG-TDR is independent of the geomagnetic field and generates maximum values over the edges of the magnetized bodies. Figures 13 and 14 show the HG-TDR of the magnetic and gravity data, respectively. The HG-TDR delineates model edges well, as the amplitude of the HG-TDR peaks over magnetic sources, but the results for the deeper bodies are not so effective (Arisoy and Dikmen 2013).

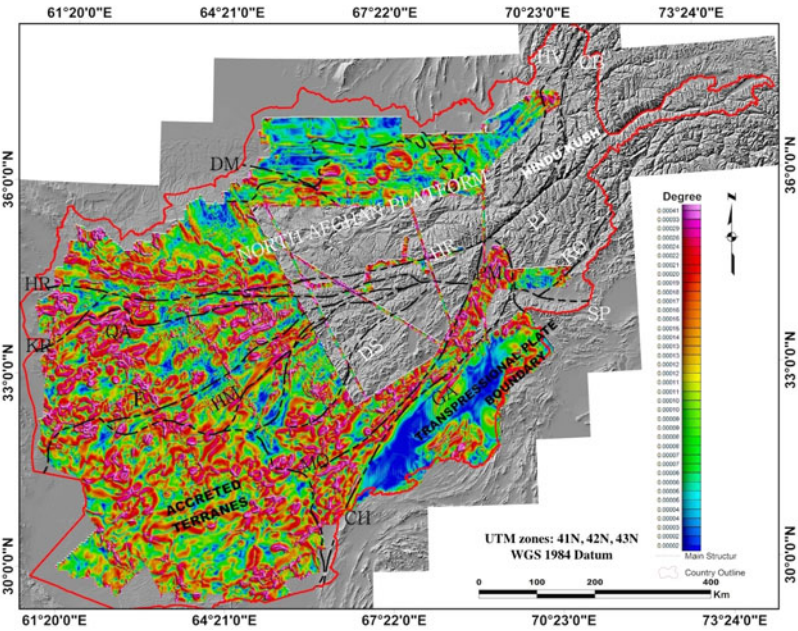


Fig. 13. Horizontal gradient of the tilt derivative map of magnetic data of Afghanistan, overlaid on the shaded relief (SRTM) map.

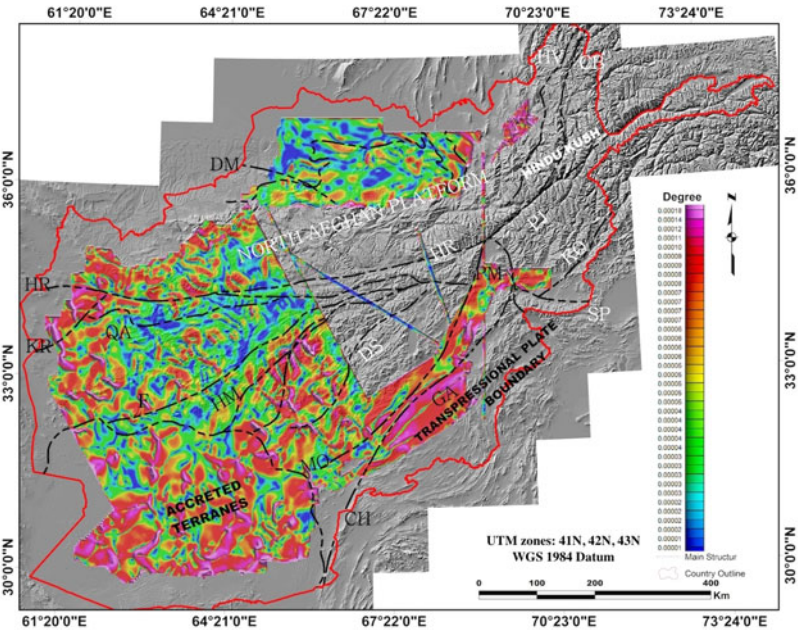


Fig. 14. Horizontal gradient of the tilt derivative map of gravity data of Afghanistan, overlaid on the shaded relief (SRTM) map.

### 5.5 Euler deconvolution method (ED)

The ED is used to estimate the depth and location of magnetic source anomalies. The computerized method was developed by Thompson (1982) and is applied for real magnetic data along profiles. Reid *et al.* (1990) followed up a suggestion in Thompson's paper and further developed the method such that it operates for magnetic grid data. The original technique was referred to as the EULDPH method, but with further development, it has become known as the extended ED technique (Mashayandebvu *et al.* 2001). The significant advantage of this method is that the results are independent of the direction of magnetic polarization and geologic knowledge of the source (Hinze *et al.* 2013).

The ED equation in 3D is given by Reid *et al.* (1990):

$$(x - xo)(\partial M / \partial x) + (y - yo)(\partial M / \partial y) + (z - zo)(\partial M / \partial z) = n(B - M) \ . \qquad (6)$$

Equation 6 can be rewritten as

$$x(\partial M / \partial x) + y(\partial M / \partial y) + z(\partial M / \partial z) + nM = \\ = xo(\partial M / \partial x) + yo(\partial M / \partial y) + zo(\partial M / \partial z) + nB \ . \qquad (7)$$

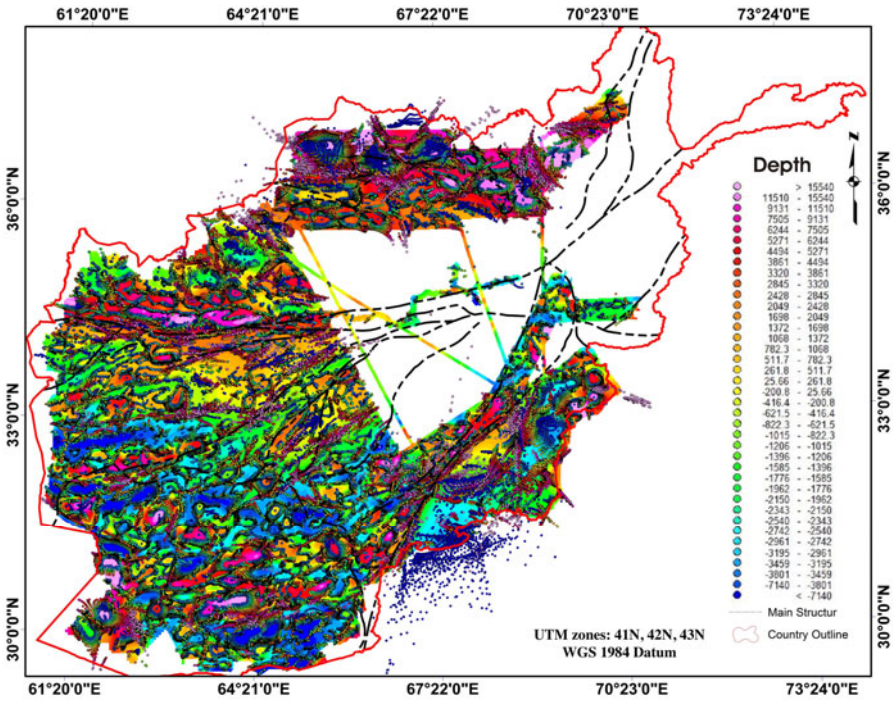


Fig. 15. Euler deconvolution map of the aeromagnetic data of Afghanistan with SI = 0. The background represents the aeromagnetic map.

where ($xo$, $yo$, $zo$) is the position of a source whose magnetic anomaly ($M$) is detected at ($x$, $y$, $z$), $B$ is the regional value of the magnetic, and $n$ is the structural index (SI), which can be defined as the rate of attenuation of the anomaly with distance. The SI must be chosen using prior knowledge of the source geometry. For example, SI = 1 for a dike, SI = 0 for a fault and contact (FitzGerald *et al.* 2004). The horizontal ($\partial M/\partial x$, $\partial M/\partial y$) and vertical ($\partial M/\partial z$) derivatives are used to compute anomalous source locations. By considering four or more neighboring observations concurrently (an operating window), the source location ($xo$, $yo$, $zo$) and $B$ can be computed by solving a linear system of equations generated from Eq. 7. Then, by moving the operating window from one location to another over the anomaly, multiple solutions for the same source are obtained.

The results in Fig. 15 show the Euler solutions by applying Eq. 6 to the aeromagnetic data using a structural index of 0 for faults and contacts. The depth to the magnetic sources ranges from near-surface to 10 km. The Euler solutions are clustered along the major faults and show many circular shapes that may correspond to intrusion bodies underground.

## 6. INTERPRETATION AND DISCUSSIONS

High magnetic anomalies are correlated with major tectonic boundaries of Afghanistan such as along HR, CH, MO, and HM faults. Other high magnetic anomalies are located in the accreted terranes (SW Afghanistan). The qualitative analysis of the RTP magnetic map in connection with the geological and morphological divisions leads to interpretation of the following subdivisions:

### 6.1 The central region

This area starts from Kandahar to the northwest up to central Afghan Swell (see Fig. 6). It includes two sedimentary basins (Ghor Basin and Rosgan Basin) and two swell (horst) regions (Central Afghan Swell and Sharistan Swell).

The RTP magnetic map shows clearly the two basins characterised by regional low magnetic responses. The Sharistan Swell, located between the two basins, is represented by medium amplitude anomalies (around 25 nT), which strike NE-SW similar to that of Kandahar anomalies. This region is intruded by mafic dikes (Fig. 16). High magnetic anomalies along the Helmand Fault (HM) are interpreted to represent magnetized Archean rocks and dikes associated with accretionary terranes in the western part of Afghanistan. The magnetic anomalies in the Sharistan Swell correlates with dikes and Archean rocks (Fig. 16). To the NW, magnetic anomalies decrease in amplitude as magnetic crystalline basement in that area is increasingly cov-

ered by the Ghor Basin. The magnetic anomalies in the Ghor and Rosgan basins differ because of the depths of the depth to the magnetic crystalline rocks. The magnetic response of crystalline basement beneath the Ghor Basin is characterised by longer wavelengths and smaller amplitudes compared with the Rosgan Basin, suggesting that the magnetic basement lies beneath a thicker sedimentary pile of the Ghor Basin. There are high magnetic anomalies in the Central Afghan Swell, reaching 170 nT. The anomalies are parallel to the HR Fault and shifted to the north.

## 6.2 The southeast regions

### *6.2.1 The zone of Kandahar*

This zone is bordered in the east by the Chaman Fault, which forms the border to the southeast Afghan Trough and in the north by two successive faults, the Mokur and Darafshan faults. This subdomain is characterised by the frequent occurrence of magnetic rocks (Fig. 16), which lie beneath relatively thin sedimentary successions. Magnetic anomalies strike NE-SW. The peak amplitude is ~208 nT. These magnetic anomalies are largely caused by the magnetic intrusive volcanic rocks that crop out at the surface or that are

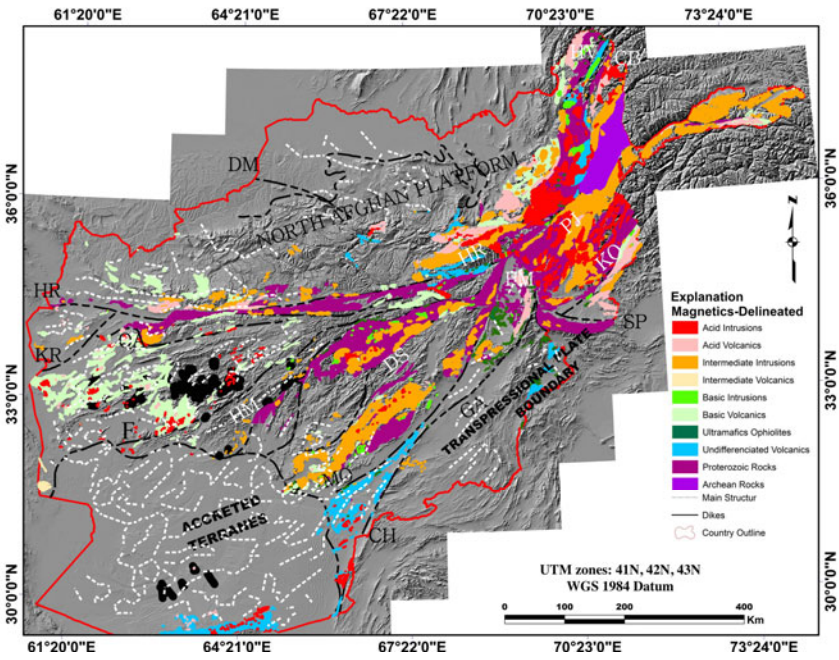


Fig. 16. Magnetic delineated units with dikes in Afghanistan, overlaid on the shaded relief (SRTM) map. White dashed lines show the interpreted fault structure from tilt derivative of aeromagnetic data.

situated underneath a minor cover. The NE-SW magnetic anomaly of this region is parallel to the Chaman Fault.

#### *6.2.2 The East Afghan Trough (EAT)*

Located in the eastern part of the survey area to the east of the Chaman Fault thick Tertiary and possibly Mesozoic sedimentary successions (3 to 6 km) (Bosum *et al.* 1968). This area is characterised by very low negative anomalies (–165 nT in NE and –143 nT in SW of EAT) to moderately low magnetic values (–50 to –80 nT in N and SE of EAT, respectively). These anomalies are interpreted to be related to intermediate depressions and upwarpings.

#### *6.2.3 Zone of Khost*

This zone is located in the eastern boundary of the EAT. It is characterised by high amplitude magnetic anomalies (196 nT in the north to 460 nT in the south), which are interpreted to be sourced from near-surface volcanic rocks (Fig. 16).

### 6.3 The western regions

The magnetic anomalies of the western regions show an entirely different character than those of the eastern regions. This region is characterized by a flat topography and existence of batholiths.

#### *6.3.1 Hilmand depression*

The Hilmand depression is located in the southwestern part of the survey area and consists of large deserts. This area has not been geologically explored compared to other parts of south Afghanistan due to its inaccessibility. The Hilmand depression consists of Neogene and Quaternary sediments with a thickness of around 500 m (Jung *et al.* 2013). This region has magnetic anomalies with amplitudes that range from 145 to 280 nT. These magnetic anomalies are consistent with the presence of an old block of crystalline basement rocks beneath the thin sedimentary layers. Finn and Drenth (2007) interpreted these magnetic anomalies to be related to the arc volcanic rocks within shallow crystalline basement. These volcanic rocks also exist in the northern Pakistan and eastern Iran. The low Bouguer gravity anomaly in a small region inside Helmand Basin is due to the existence of batholiths (Finn and Drenth 2007).

#### *6.3.2 Anomaly of Chakansur*

This region is characterised by high amplitude magnetic anomalies (see Fig. 6) that vary from 190 nT in the south to 650 nT in the north. The source of this high magnetic and gravity anomaly (Fig. 17) is interpreted to be a high magnetic, high density mafic intrusive body.

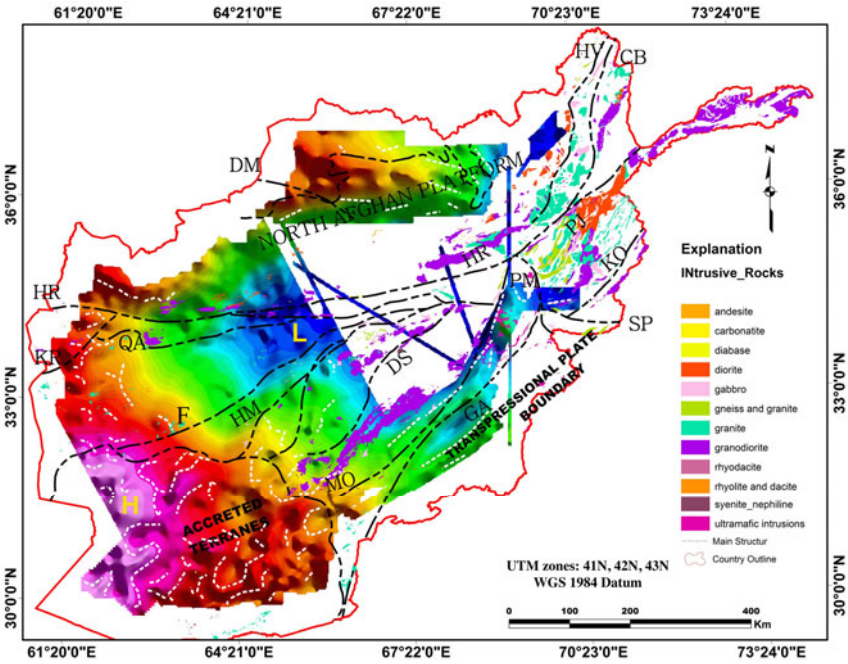


Fig. 17. High density delineated rocks in Afghanistan, overlaid on complete Bouguer gravity map. White dashed lines show the interpreted fault structure from tilt derivative of gravity data. "H" represents high complete Bouguer anomaly while "L" represents low complete Bouguer anomaly.

### *6.3.3 Farah region*

In this region, a predominant magnetic anomaly (around 180 nT) striking mainly E-W extends more than 200 km along the Farah Fault. This region has Tertiary volcanic rocks including granites, which may cause these anomalies and possible upwarping of the magnetic basement is contributing to the magnetic response of the region.

## 7. DISCUSSION

Regional aeromagnetic data and gravity data have been effective tools for mapping inaccessible regions or terranes that are largely buried beneath younger sedimentary cover succession. We have employed analysis and interpretation of these data to characterize first order structural architecture and basement geology of a large part of the poorly understood basement geology of Afghanistan. The data has been effective at imaging major and second order faults and lineaments because they are expressed in the magnetic data as a boundary between high and low magnetic responses. The magnetic data is

also effective at mapping the distribution of volcanic successions and intrusive rocks, which are characterised by high amplitude magnetic responses. The data also shows the extent of basement terranes beneath younger sedimentary basins, although the significance of the magnetic responses are more cryptic because anomalies are characterised by longer wavelengths and lower amplitudes because the distance to the magnetic source is greater.

Interpretation of magnetic and gravity data reveal an excellent correlation with structural architecture that has previously been related to the collision between the Indian and Eurasian plates, and thus provides a tool to assess the extent of deformation associated with this continental collision event.

## 8. CONCLUSIONS

This is the first study presenting potential field and remote sensing data of Afghanistan with the purpose of structural investigation to interpret potential field distributions in Afghanistan and the relationship with subsurface structures and geological data, supported by remote sensing information. These new investigation techniques made it possible to discover structures not yet precisely known.

The rose diagram of geological faults shows two directions: NE-SW and ENE-WSW, while the interpreted faults from remote-sensing maps show three directions: NNE-SSW, NE-SW, and ENE-WSE. The general tectonic direction of NE-SW is related to the collision tectonics of the Indian plate and the Eurasian plate. The NNE-SSW and ENE-WSW fault directions are related to the tectonics of the Arabian plate and the Eurasian plate.

The results of the power spectrum analysis of both gravity and magnetic data in Afghanistan suggest a basement depth in general at 1 to 1.5 km, which is in agreement with the calculated sediment thickness in Afghanistan of the same range (shallow to 1 km) by Jung *et al.* (2013).

The general trend of the Bouguer gravity anomalies is NE-SW along the Indian-Afghan collision zone, which is similar to the trend also found in western Pakistan (Jadoon and Khurshid 1996).

The high Bouguer gravity anomaly in the Helmand Basin suggests a possible existence of an intrusive volcanic body covered by late thin quaternary sediments.

Many magnetic anomalies were observed in the accreted terranes, which could be intrusions of magnetized bodies in the basement rocks. These intrusions are young volcanic rocks, which might be related to the subduction of Arabian oceanic crust beneath Eurasia.

The used data has a low resolution but could provide useful information on the subsurface structures and geological information in Afghanistan and

also the geophysical signatures of volcanic and intrusive rocks in the country. We recommend future high resolutions geophysical surveys in Afghanistan and especially in the no-data regions (eastern parts) in order to enhance the geological, structural, and mineralogical investigations.

Acknowledgments. The authors would like to thank Dr. J.F. Batir (Southern Methodist University, Huffington Department of Earth Sciences, Dallas, USA) for suggesting a number of improvements in this manuscript. We also thank Prof. P.G. Betts (Monash University, School of Earth, Atmosphere and Environment, Australia) for his careful reading of our manuscript and numerous constructive suggestions that helped improve this paper. S. Mogren acknowledges support from the National Plan for Science, Technology and Innovation (MAARIFAH), King Abdulaziz City for Science and Technology, Kingdom of Saudi Arabia, Award Number 09-SPA873-02.

## References

AGS (2005), Geology of Afghanistan, Afghanistan Geological Survey, available from: http://www.bgs.ac.uk/afghanminerals/geology.htm (accessed: 2015).

Aitken, A.R.A., and P.G. Betts (2009), Multi-scale integrated structural and aeromagnetic analysis to guide tectonic models: An example from the eastern Musgrave Province, Central Australia, *Tectonophysics* **476**, 3-4, 418-435, DOI: 10.1016/j.tecto.2009.07.007.

Arisoy, M.O., and U. Dikmen (2013), Edge detection of magnetic sources using enhanced total horizontal derivative of the tilt angle, *Bull. Earth Sci. Appl. Res. Cent. Hacet. Univ.* **34**, 1, 73-82.

Azizi, M., and H. Saibi (2015), Integrating gravity data with remotely sensed data for structural investigation of the Aynak-Logar Valley, eastern Afghanistan, and the surrounding area, *IEEE J. Sel. Top. Appl. Earth Observ. Remote Sens.* **8**, 2, 816-824, DOI: 10.1109/JSTARS.2014.2347375.

Azizi, M., H. Saibi, and G.R.J. Cooper (2015), Mineral and structural mapping of the Aynak-Logar Valley (eastern Afghanistan) from hyperspectral remote sensing data and aeromagnetic data, *Arab. J. Geosci.* **8**, 12, 10911-10918, DOI: 10.1007/s12517-015-1993-2.

Betts, P.G., R.K. Valenta, and J. Finlay (2003), Evolution of the Mount Woods Inlier, northern Gawler Craton, Southern Australia: An integrated structural and aeromagnetic analysis, *Tectonophysics* **366**, 1-2, 83-111, DOI: 10.1016/S0040-1951(03)00062-3.

Betts, P., H. Williams, J. Stewart, and L. Ailleres (2007), Kinematic analysis of aeromagnetic data: Looking at geophysical data in a structural context, *Gondwana Res.* **11**, 4, 582-583.

Blaikie, T.N., L. Ailleres, P.G. Betts, and R.A.F. Cas (2014), Interpreting subsurface volcanic structures using geologically constrained 3-D gravity inversions: Examples of maar-diatremes, Newer Volcanics Province, southeastern Australia, *J. Geophys. Res. Solid Earth* **119**, 4, 3857-3878, DOI: 10.1002/2013JB010751.

Blakely, R.J. (1995), *Potential Theory in Gravity and Magnetic Applications*, Cambridge University Press, Cambridge, 441 pp.

Bosum, W., A. Hahn, E.G. Kind, and D. Weippert (1968), Airborne magnetometer survey in the Kingdom of Afghanistan, Geological Survey of the Federal Republic of Germany, 46 pp.

Chen, S., and Y. Zhou (2005), Classifying depth-layered geological structures on Landsat TM images by gravity data, a case study of the western slope of Songliao Basin, northeast China, *Int. J. Remote Sens.* **26**, 13, 2741-2754, DOI: 10.1080/01431160500104210.

Debeglia, N., and J. Corpel (1997), Automatic 3-D interpretation of potential field data using analytic signal derivatives, *Geophysics* **62**, 1, 87-96, DOI: 10.1190/1.1444149.

Durga Rao, K.H.V., V. Bhanumurthy, and P.S. Roy (2009), Application of satellite-based rainfall products and SRTM DEM in hydrological modelling of Brahmaputra basin, *J. Indian Soc. Remote Sens.* **37**, 4, 587-600, DOI: 10.1007/s12524-009-0051-5.

Fairhead, J.D., A. Salem, S. Williams, and E. Samson (2008), Magnetic interpretation made easy: The tilt-depth-dip-Δ*k* method. **In**: *2008 SEG Ann. Int. Meeting*, Expanded abstracts, Society of Exploration Geophysicists, 779-783.

Finn, C.A., and B. Drenth (2007), Regional gravity and magnetic data help map subsurface geology in Afghanistan. **In:** *GSA Denver Ann. Meeeting*, Abstract # 156-9.

FitzGerald, D., A. Reid, and P. McInerney (2004), New discrimination techniques for Euler deconvolution, *Comput. Geosci.* **30**, 5, 461-469, DOI: 10.1016/j.cageo.2004.03.006.

Gotze, H.J., and S. Krause (2002), The Central Andean gravity high, a relic of an old subduction complex? *J. South Am. Earth Sci.* **14**, 8, 799-811, DOI: 10.1016/S0895-9811(01)00077-3.

Hinze, W.J. (1985), *The Utility of Regional Gravity and Magnetic Anomaly Maps*, Society of Exploration Geophysicists, 469 pp.

Hinze, W.J., R.R.B. von Frese, and A.H. Saad (2013), *Gravity and Magnetic Exploration*, Cambridge University Press, Cambridge, 525 p.

Hsu, S.-K., J.-C. Sibuet, and C.-T. Shyu (1996), High resolution detection of geologic boundaries from potential field anomalies: An enhanced analytic signal technique, *Geophysics* **61**, 2, 373-386, DOI: 10.1190/1.1443966.

Hsu, S.-K., D. Coppens, and C.-T. Shyu (1998), Depth to magnetic source using the generalized analytic signal, *Geophysics* **63**, 6, 1947-1957, DOI: 10.1190/1.1444488.

Jadoon, I.A.K., and A. Khurshid (1996), Gravity and tectonic model across the Sulaiman fold belt and the Chaman Fault zone in western Pakistan and eastern Afghanistan, *Tectonophysics* **254**, 1-2, 89-109, DOI: 10.1016/0040-1951(95)00078-X.

Jessell, M.W., P.O. Amponsah, L. Baratoux, D.K. Asiedu, G.K. Loh, and J. Ganne (2012), Crustal-scale transcurrent shearing in the Paleoproterozoic Sefwi-Sunyani-Comoé region, West Africa, *Precambrian Res.* **212-213**, 155-168, DOI: 10.1016/j.precamres.2012.04.015.

Jung, W., J. Brozena, and M. Peters (2013), Predicting gravity and sediment thickness in Afghanistan, *Geophys. J. Int.* **192**, 2, 586-601, DOI: 10.1093/gji/ggs038.

Kamel, A.F., and A.M. Elsirafe (1994), Delineation and analysis of the surface and subsurface structural lineament patterns in the North Lake Nasser area and its surroundings, Aswan, upper Egypt, *Int. J. Remote Sens.* **15**, 7, 1471-1493, DOI: 10.1080/01431169408954178.

Keating, P., and M. Pilkington (2004), Euler deconvolution of the analytic signal and its application to magnetic interpretation, *Geophys. Prospect*. **52**, 3, 165-182, DOI: 10.1111/j.1365-2478.2004.00408.x.

Khamies, A.A., and M.M. El-Tarras (2010), Surface and subsurface structures of Kalabsha area, southern Egypt, from remote sensing, aeromagnetic and gravity data, *Egypt. J. Remote Sens. Space Sci.* **13**, 1, 43-52, DOI: 10.1016/j.ejrs.2010.07.006.

Klingele, E.E., I. Marson, and H.G. Kahle (1991), Automatic interpretation of gravity gradiometric data in two dimensions: vertical gradient, *Geophys. Prospect.* **39**, 3, 407-434, DOI: 10.1111/j.1365-2478.1991.tb00319.x.

Lamontagne, M., P. Keating, and S. Perreault (2003), Seismotectonic characteristics of the lower St. Lawrence seismic zone, Quebec, insights from geology, magnetics, gravity, and seismic, *Can. J. Earth Sci.* **40**, 2, 317-336, DOI: 10.1139/e02-104.

Lunden, B., G. Wang, and K. Wester (2001), A GIS based analysis of data from Landsat TM, airborne geophysical measurements, and digital maps for geological remote sensing in the Stockholm region, Sweden, *Int. J. Remote Sens.* **22**, 4, 517-532, DOI: 10.1080/01431160050505838.

MacLeod, I.N., K. Jones, and T.F. Dai (1993), 3-D analytic signal in the interpretation of total magnetic field data at low magnetic latitudes, *Explor. Geophys.* **24**, 3-4, 679-688, DOI: 10.1071/EG993679.

Mashayandebvu, M., P. van Driel, A.B. Reid, and J.D. Fairhead (2001), Magnetic source parameters of two-dimensional structures using extended Euler deconvolution, *Geophysics* **66**, 3, 814-823, DOI: 10.1190/1.1444971.

Mather, P.M. (2004), *Computer Processing of Remotely-sensed Images: An Introduction*, 3rd ed., John Wiley & Sons, Chichester, 442 pp.

McGinnis, L.D. (1971), Gravity fields and tectonics in the Hindu Kush, *J. Geophys. Res.* **76**, 8, 1894-1904, DOI: 10.1029/JB076i008p01894.

McLean, M.A., C.J.L. Wilson, S.D. Boger, P.G. Beas, T.J. Rawling, and D. Damaske (2009), Basement interpretations from airborne magnetic and gravity data over the Lambert Rift region of East Antarctica, *J. Geophys. Res.* **114**, B6, B06101, DOI: 10.1029/2008JB005650.

Mihalasky, M.J., J.L. Doebrich, R.W. Wahl, S.D. Ludington, G.J. Orris, J.D. Bliss, D.M. Sutphin, P.G. Schruben, K.S. Bolm, B.E. Hubbard, J.C. Mars, S.G. Peters, C.J. Wandrey, and P. Chirico (2007), Geographic information system (GIS) to accompany the non-fuel mineral resource assessment of Afghanistan. Appendix 1. **In:** S.G. Peters, S.D. Ludington, G.J. Orris, D.M. Sutphin, J.D. Bliss, J.J. Rytuba (eds.), *Preliminary Non-fuel Mineral Resource Assessment of Afghanistan*, U.S. Geological Survey – Afghanistan Ministry of Mines Joint Mineral Resource Assessment Team U.S., Geological Survey Open-File Report, 2007-1214 (Version 1), 2 CD-roms.

Miller, H.G., and V. Singh (1994), Potential field tilt – a new concept for location potential field sources, *Appl. Geophys.* **32**, 2-3, 213-217, DOI: 10.1016/0926-9851(94)90022-1.

Nabighian, M.N. (1972), The analytic signal of two-dimensional magnetic bodies with polygonal cross-section: its properties and use for automated anomaly interpretation, *Geophysics* **37**, 3, 507-517, DOI: 10.1190/1.1440276.

Nabighian, M.N. (1974), Additional comments on the analytic signal of two dimensional magnetic bodies with polygonal cross-section, *Geophysics* **39**, 1, 85-92, DOI: 10.1190/1.1440416.

Nabighian, M.N. (1984), Toward a three-dimensional automatic interpretation of potential field data via generalized Hilbert transforms: Fundamental relations, *Geophysics* **49**, 6, 780-786, DOI: 10.1190/1.1441706.

Rabie, S.I., and A.A. Ammar (1990), Pattern of the main tectonic trends from remote geophysics, geological structures and satellite imagery, Central Eastern Desert, Egypt, *Int. J. Remote Sens.* **11**, 4, 669-683, DOI: 10.1080/01431169008955049.

Reid, A.B., J.M. Allsop, H. Granser, A.J. Millett, and I.W. Somerton (1990), Magnetic interpretation in three dimensions using Euler deconvolution, *Geophysics* **55**, 1, 80-91, DOI: 10.1190/1.1442774.

Roest, W.R., J. Verhoef, and M. Pilkington (1992), Magnetic interpretation using 3-D analytic signal, *Geophysics* **57**, 1, 116-125, DOI: 10.1190/1.1443174.

Saadi, N.M., E. Aboud, H. Saibi, and K. Watanabe (2008a), Integrating data from remote sensing, geology and gravity for geological investigation in the Tarhunah area, Northwest Libya, *Int. J. Digital Earth* **1**, 4, 347-366, DOI: 10.1080/17538940802435844.

Saadi, N.M., K. Watanabe, A. Imai, and H. Saibi (2008b), Integrating potential fields with remote sensing data for geological investigations in the Eljufra area of Libya, *Earth Planets Space* **60**, 6, 539-547, DOI: 10.1186/BF03353116.

Saibi, H., E. Aboud, and S. Ehara (2012), Analysis and interpretation of gravity data from the Aluto-Langano geothermal field of Ethiopia, *Acta Geophys.* **60**, 2, 318-336, DOI: 10.2478/s11600-011-0061-x.

Salem, A., S. Williams, J.D. Fairhead, D. Ravat, and R. Smith (2007), Tilt-depth method: A simple depth estimation method using first-order magnetic derivatives, *The Leading Edge* **26**, 12, 1502-1505, DOI: 10.1190/1.2821934.

Salem, A., S. Williams, J.D. Faihead, R. Smith, and D. Ravat (2008), Interpretation of magnetic data using tilt-angle derivatives, *Geophysics* **73**, 1, L1-L10, DOI: 10.1190/1.2799992.

Schindler, J.S. (2002), Afghanistan: Geology in a troubled land, *Geotimes* **47**, 2, 14-15.

Silverman, B.W. (1986), *Density Estimation for Statistics and Data Analysis*, Monographs on Statistics and Applied Probability, Vol. 26, Chapman & Hall/CRC, New York, 176 pp.

Spampinato, G.P.T., L. Ailleres, P.G. Betts, R.J. Armit (2015), Imaging the basement architecture across the Cork Fault in Queensland using magnetic and gravity data, *Precambrian Res.* **264**, 63-81, DOI: 10.1016/j.precamres.2015.04.002.

Spector, A., and F.E. Grant (1970), Statistical models for interpreting aeromagnetic data, *Geophysics* **35**, 2, 293-302, DOI: 10.1190/1.1440092.

Spector, A., and B.K. Bhattacharyya (1966), Energy density spectrum and autocorrelation function of anomalies due to simple magnetic models, *Geophys. Prospect.* **14**, 3, 242-272, DOI: 10.1111/j.1365-2478.1966.tb01760.x.

Stewart, J.R., and P.G. Betts (2010), Implications for Proterozoic plate margin evolution from geophysical analysis and crustal-scale modeling within the western Gawler Craton, Australia, *Tectonophysics* **483**, 1-2, 151-177, DOI: 10.1016/j.tecto.2009.11.016.

Thompson, D.T. (1982), EULDPH: A new technique for making computer assisted depth estimates from magnetic data, *Geophysics* **47**, 1, 31-37, DOI: 10.1190/1.1441278.

USGS (2006), Aeromagnetic and gravity surveys in Afghanistan: A website for distribution of data, U.S. Geological Survey Open-File Report, 2006-1204.

USGS (2008), Airborne gravity survey and ground gravity in Afghanistan: A website for distribution of data, U.S. Geological Survey Open-File Report, 2008-1089.

USGS (2011), Aeromagnetic surveys in Afghanistan: An updated website for distribution of data, U.S. Geological Survey Open-File Report, 2011-1247.

Verduzco, B., J.D. Fairhead, C.M. Green, and C. MacKenzie (2004), New insights into magnetic derivatives for structural mapping, *The Leading Edge* **23**, 116-119.

Wheeler, R., C.G. Bufe, M.L. Johnson, and R.L. Dart (2005), Seismotectonic map of Afghanistan, with annotated bibliography, U.S.G.S. Open-File Report, 2005-1264.

Yassaghi, A. (2006), Integration of Landsat imagery interpretation and geomagnetic data on verification of deep-seated transverse fault lineaments in SE Zagros, Iran, *Int. J. Remote Sens.* **27**, 20, 4529-4544, DOI: 10.1080/01431160600661283.

Received 24 December 2014
Received in revised form 22 June 2015
Accepted 26 August 2015

DE GRUYTER OPEN

**Acta Geophysica**
vol. 64, no. 4, Aug. 2016, pp. 1004-1033
DOI: 10.1515/acgeo-2016-0038

# Regional Variations of the $\omega$-upper Bound Magnitude of GIII Distribution in the Iranian Plateau

Hiwa MOHAMMADI[1] and Yusuf BAYRAK[2]

[1]Department of Earth Sciences, College of Sciences, Shiraz University, Shiraz, Iran
e-mail: Hiwa.2006.waran@gmail.com (corresponding author)

[2]Agri Ibrahim Çeçen University, Agri, Turkey; e-mail: ybayrak@agri.edu.tr

A b s t r a c t

The Iranian Plateau does not appear to be a single crustal block, but an assemblage of zones comprising the Alborz–Azerbaijan, Zagros, Kopeh–Dagh, Makran, and Central and East Iran. The Gumbel's III asymptotic distribution method (GIII) and maximum magnitude expected by Kijko–Sellevoll method is applied in order to check the potentiality of the each seismogenic zone in the Iranian Plateau for the future occurrence of maximum magnitude ($M_{max}$). For this purpose, a homogeneous and complete seismicity database of the instrumental period during 1900-2012 is used in 29 seismogenic zones of the examined region. The spatial mapping of hazard parameters (upper bound magnitude ($\omega$), most probable earthquake magnitude in next 100 years ($M_{100}$) and maximum magnitude expected by maximum magnitude estimated by Kijko–Sellevoll method ( $M_{max}^{K-S}$ ) reveals that Central and East Iran, Alborz and Azerbaijan, Kopeh–Dagh and SE Zagros are a dangerous place for the next occurrence of a large earthquake.

**Key words:** Iranian Plateau, maximum magnitude, Gumbel's III asymptotic distribution, most probable earthquake magnitude in next 100 years ($M_{100}$), maximum magnitude expected by Kijko–Sellevoll method.

Ownership: Institute of Geophysics, Polish Academy of Sciences;
© 2016 Mohammadi and Bayrak. This is an open access article distributed under the Creative Commons Attribution-NonCommercial-NoDerivs license, http://creativecommons.org/licenses/by-nc-nd/3.0/.

## 1. INTRODUCTION

Tectonically, the Iranian Plateau is located in the main part of the Alpine–Himalayan orogenic belt; therefore, it is one of the most highly seismic regions of the world. Many destructive earthquakes in the last century confirm the high seismicity of Iran. As a result, the need for more accurate seismic hazard studies in the region has become progressively more important for earthquake engineering applications. Statistical methods are useful for characterizing seismic hazard because earthquakes are, for all practical purposes, random phenomena. Statistical analysis complements the deterministic approach to seismic hazard assessment and provides a tool for decision making in matters of resource allocation and public policy (Dargahi-Noubary 2002). Several statistical methodologies and models have been emphasized and being used in different regions of the world to estimate earthquake hazard parameters like expected maximum magnitude, *b*-value of Gutenberg-Richter relationship, activity rate, upper bound magnitude ($\omega$), and modal values among others (Tinti and Mulargia 1985, Kijko and Sellevoll 1989, 1992; Pisarenko *et al*. 1996, Tsapanos *et al*. 2002, Tsapanos 2003, Tsapanos and Christova 2003, Kijko 2004, Wheeler 2009, Mueller 2010, Kijko and Singh 2011, Yadav *et al*. 2010a, b; 2012a, b).

The most common seismic parameter analyzed is the magnitude of the earthquakes. Probabilistic methods are commonly used to compute or forecast the expectation of different magnitudes in an area. In seismic hazard assessment, three types of maximum magnitudes are considered *viz*. maximum historic magnitude, maximum credible magnitude and maximum regional magnitude (Reiter 1990). The maximum historic magnitude is the maximum magnitude which has historical or instrumental confirmation of occurrence in any seismogenic source or fault region and it is lower bound to the maximum size. The maximum credible magnitude is obtained by the reasonable assessment of maximum earthquake potential with respect to the ambient tectonic regime. It does not show actual occurrence and it is less than the maximum regional magnitude but larger or equal to the maximum historic magnitude. The maximum regional magnitude, also called maximum possible magnitude in probabilistic analysis, is the absolute though improbable upper bound magnitude of earthquake size determined by earthquake processes that will occur in a certain time period and a given source region. There is no unique method to estimate maximum magnitude. However, there are two techniques to estimate it, *i.e*., deterministic and probabilistic (Kijko and Sellevoll 1989, 1992; Field *et al*. 1999, Koravos *et al*. 2003, Kijko 2004, Mueller 2010, Kijko and Singh 2011). Kijko and Sellevoll (1989, 1992) and Kijko (2004) introduced a new approach based on maximum likelihood estimation method to estimate maximum magnitude using historical and in-

strumental data. The rank ordering statistic of extreme values is applied by Sornette *et al*. (1996) to the distribution of large earthquakes for extracting the tail of the distribution of sparse data sets. Krinitzsky (2002) proposed the definition of some maximum magnitudes appropriate for use in engineering design. Seismic moment upper bound is considered by Kagan (2002) in order to discuss various theoretical distributions that can be used to approximate the seismic moment data. The Gumbel's third asymptotic distribution of extreme values (GIII) has also proved useful in estimating upper bound magnitude in different regions of the world (Makropoulos 1978, Burton 1979, Makropoulos and Burton 1983, Tsapanos and Burton 1991, Tsapanos 1997, Bayrak *et al*. 2008, Yadav *et al*. 2012b, 2013; Tsapanos *et al*. 2014).

The theory of extreme values described by Gumbel (1958) has the advantage that it does not require analysis of the complete record of earthquake occurrence, but uses the sequence of earthquakes constructed from the largest values of magnitude over a set of predetermined intervals. Both first and third asymptotic distributions of extreme value have been proved useful in mapping seismic hazard (Nordquist 1945, Epstein and Lomnitz 1966, Yegulalp and Kuo 1974, Knopoff and Kagan 1977, Burton 1977, Makropoulos 1978, Makropoulos and Burton 1986, Tsapanos and Burton 1991, Bayrak *et al*. 2008, among others). The advantage of Gumbel's third asymptotic distribution (GIII) over first distribution (GI) is that it includes a parameter known as upper-bound magnitude ($\omega$). The $\omega$ value is directly related with the finite maximum stress which can be stored and released as an earthquake by the rocks of a region (Tsapanos and Burton 1991, Tsapanos 1997). Thus, for calculation of the occurrence or expectation of extreme magnitude earthquakes using probabilistic models, the GIII distribution allows an appropriate and natural physical interpretation. On the other hand, there are different opinions on the use of the GIII distribution for seismicity assessment. Kaila and Narain (1971) suggested that, since GIII mainly involves great earthquakes, it is not an ideal criterion for seismicity parameters assessment. However, Båth (1975, 1983) denoted that the dependency of the method on large events is of important advantage, given that the magnitudes of large earthquakes are more accurately determined than those of small events. Thus for estimation of the occurrence or expectation of extreme magnitude earthquakes using probabilistic models, the GIII allows an appropriate and natural physical interpretation.

Burton (1979) applied this methodology in southern Europe through India to estimate earthquake hazard parameters. Tsapanos and Burton (1991) estimated earthquake hazard parameters using this method for some specific regions of the world and prepared contour maps of most probable maximum magnitudes in next 85 years. Later, Tsapanos (1997) evaluated upper-bound magnitudes in the subduction zones of the Circum–Pacific region. Bayrak *et*

*al*. (2008) used this method for 24 seismogenic regions in Turkey and surroundings to estimate upper-bound magnitude. Yadav *et al*. (2012b) applied this method in 28 seismogenic regions in the Hindukush–Pamir Himalaya to estimate upper-bound magnitude and 100-years magnitude. Yadav *et al*. (2013), by using this method, prepared contour maps of most probable maximum magnitudes in the Hindukush–Pamir Himalaya and adjacent regions in annual and next 100 years. Recently Tsapanos *et al*. (2014) prepared contour maps of most probable maximum magnitudes using this method in the Turkey and its vicinity in annual and next 50 years.

In this study, we have applied GIII distribution in the Iranian Plateau to assess the earthquake hazards in terms of upper bound magnitude ($\omega$) and possible earthquake magnitude that can occur in next 100 years ($M_{100}$). Furthermore, we have computed the maximum earthquake magnitudes ( $M_{\max}^{K-S}$ ) from Kijko–Sellevoll method to correlate and compare $\omega$ values with $M_{\max}^{K-S}$ values for these source zones. The results of this study will be useful to produce a brief atlas to characterize the earthquake hazard.

## 2. TECTONICS

The spatial distribution and magnitude of earthquakes in different regions of the Iranian Plateau are not similar. This is primarily a result of Iran's position in a 1000-km wide zone of compression between the colliding Eurasian and Arabian continents (Engdahl *et al.* 2006) and its location between the Arabian Plate in the south and southwest and the Indian Plate in the east.

Iran does not appear to be a single crustal block, and the distribution of active deformation is not uniform (Fig. 1). The shortening is thought to be concentrated in these main active belts of Zagros, Kopeh–Dagh, Alborz–Azerbaijan, and Central and East Iran (Talebian and Jackson 2004). Based on the global positioning system (GPS), Vernant *et al*. (2004) indicated the rate of deformation of the Iranian Plateau from less than 2 mm/yr in Central and East Iran to 19.5 ± 2 mm/yr in the Makran subduction zone.

Continental-continental collision zone of Zagros in southwest Iran is one the youngest and most active continental collision zone on the earth (Snyder and Barazangi 1986). Seismicity in the Zagros belt is restricted to the region between the main Zagros Thrust and the Persian Gulf. Most of the larger earthquakes occur on high-angle reverse planes that strike parallel to the trend of the fold axes (Jackson and McKenzie 1984). Strong earthquakes are thought to occur on blind active thrust faults that do not reach the surface (Berberian 1995). There is considerable uncertainty about their extent, geometry and the mechanism (Mirzaei *et al*. 1999). Berberian (1983) state that Zagros absorbed a major part of the Arabia–Persia regional shortening by thrust faulting.

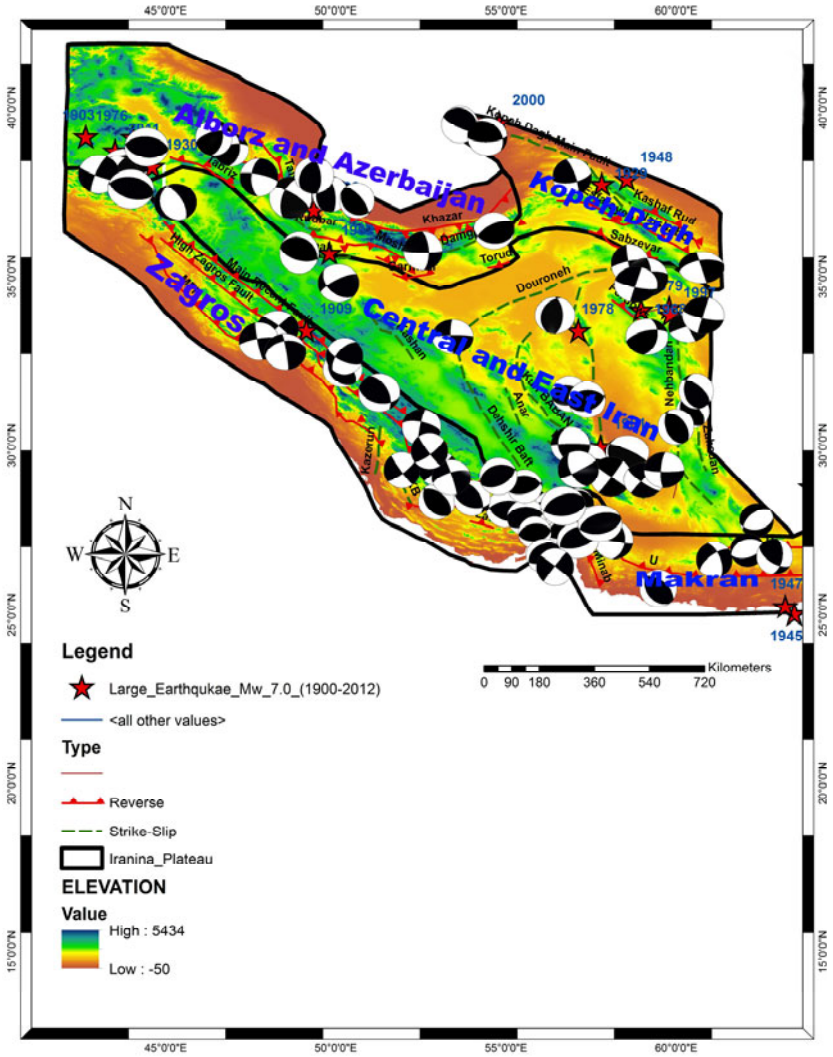


Fig. 1. Tectonic map of the Iranian Plateau showing the major active faults (modified from Berberian (2014)). Focal mechanism solutions of earthquakes with $Mw \geq 5.8$ obtained by Harvard GCMT catalogue during 1976-2012 are also shown. The large and damaging earthquakes with $Mw \geq 7.0$ that occurred during 1900-2012 are shown with stars along with the year of occurrence.

The highly seismic region of Iran is Alborz–Azerbaijan covering north and northwest of Iran. Jackson *et al.* (2002) reported that reliable earthquake depths in the Alborz are above 15 km and that most focal mechanisms present left-lateral strike-slip motions along the faults parallel to the regional

strike of the range and reverse faulting. This seismotectonic province has experienced a severe seismicity during the last century. The Alborz is a stack of thrust sheets, produced by late Cenozoic compressional deformation (Alavi 1996). Exposed thrusts with the greatest throw generally occur in the south of the Alborz. Prominent left-lateral strike-slip faults occur along the length of the Alborz, trending parallel to the thrusts and folds in each region. Structures at both the eastern and western ends of the Alborz change in strike to pass into adjacent fold and thrust belts: the Talesh in the west and the Kopeh–Dagh in the east (Berberian 1997). All faults in the Alborz are parallel to the range and participate in its shortening (Allen *et al*. 2003). Azerbaijan sub-province is a complex tectonic system trapped between Arabia, Anatolia, and Eurasia. One of the most important fault systems in this zone is the North Tabriz Fault system (Berberian and Yeats 2001, Allen *et al*. 2003).

The continental collision zone of Kopeh–Dagh in the northeast shows a northern segment of the Alpine–Himalayan orogenic belt. The characteristic of Kopeh–Dagh seismic activity is the relative frequency of great earthquakes with low depth. In the Kopeh–Dagh, crustal shortening has been taking place in a belt of up to 200-300 km wide as a result of compressional motion of the Central Iran Block against the stable plates of Turkemenistan and Afghanistan. This seismically active area mainly accommodated along a large intra-continental fault system, Ashkabad fault zone (Shabanian *et al*. 2009). Hollingsworth *et al*. (2006, 2007) believe that Kopeh–Dagh central part is an array of active right-lateral strike-slip faults (*e.g*., Quchan fault system), that obliquely affects the mountain range and produce several kilometers offsets in geomorphology. These right-lateral faults are thought to have slipped in major destructive earthquakes during the 19th and 20th centuries.

The Makran Mountains in the southeast are a continuation of the southern arc of the Alpine orogenic system, from the vicinity of Bandar Abbas to West Pakistan. The oceanic-continental subduction zone of Makran, where the consumption of oceanic crust of Arabian plate has occurred continuously since the early Cretaceous along a north dipping subduction zone underneath the Eurasia–Central Iranian microcontinent, covers the southeast of the Iran (Mirzaei *et al*. 1999). The large magnitude events are associated to the down-going plate at the intermediate depths or to the superficial large historical earthquakes in the eastern Makran (Byrne *et al*. 1992).

The Central and East Iranian Block is being compressed between two plates of greater rigidity, Arabia and Eurasia. The Central and East Iranian Block is characterized by discontinuous seismic activity with shallow, large magnitude earthquakes with apparent long recurrence periods (Berberian *et al*. 2000). At the low elevation and apparent lack of seismicity in the Dasht-

e-Lut suggest that the Lut Block is a relatively rigid block within this distributed deforming zone. Some of the roughly N-S right-lateral shear between Central and East Iranian Block and Afghanistan, which is effectively part of stable Eurasia, occurs on the long N-S strike slip faults of Sistan near the Iran–Afghan border (Berberian *et al*. 2000). This block is bordered by the Zagros folded belt in the southwest, the Alborz Mountains in the north, the Kopeh–Dagh Mountains in the northeast, and several strike-slip faults in the east. Several earthquakes are associated with surface faulting in this region. The seismically active area of eastern Iran characterized by long right-lateral strike-slip major faults. Walker *et al*. (2004) and also Walker and Jackson (2004) suggested a total of 100 km right lateral shear between Iran and Afghanistan. The northward motion of central Iran relative to western Afghanistan is accommodated by right-lateral shear across the eastern Iran, on N-S right-lateral strike-slip faults that surround the Dasht-e Lut (*e.g*., Walker and Jackson 2004, Meyer and Le Dortz 2007). The general features of the present-day tectonics in the arid and sparsely populated region of eastern Iran are broadly understood (*e.g*., Berberian 1976, 1977; Jackson and McKenzie 1984, Berberian and Yeats 1999). Also major active strike-slip and thrust faults are observed in several zones (Walker *et al*. 2004)

## 3. DATA USED AND SOURCE ZONATION

We used an earthquake catalogue extending from 1900 to 2012. The Institute of Geophysics, University of Tehran (IGUT) compiled a catalogue including prehistoric, historical and instrumental earthquakes of Iran and adjacent areas until 2000 A.D. It is based on Ambraseys and Melville (1982), Berberian (1994), the International Seismological Centre and the US Geological Survey (USGS). We used the catalogue by IGUT from 1900 to 2000 and extended it to 2012 with the help of data provided by the USGS. The compiled catalogue has been homogenized with respect to the moment magnitude scale (*Mw*) using different empirical regression relationships developed by Karimiparidari *et al*. (2013) between body-wave (*mb*), surface-wave (*Ms*) and local magnitude (*ML*). The homogeneous catalogue contains 5436 earthquakes with magnitude $Mw \geq 4$ between 1900 and 2012. The locations are illustrated in Fig. 2. By using the method of Uhrhammer (1986), dependent events (foreshocks and aftershocks) have been removed. In this method, a scan for the entire catalogue has been performed within a defined spatial and temporal window for each given earthquake. All events (foreshocks and aftershocks) with epicenters falling within the defined two windows are removed. In total, 32.08% of the events in the primary catalogue have been eliminated after filtering out foreshocks and aftershocks and the declustered catalogue contains 3692 independent earthquakes with $Mw \geq 4$. The com-

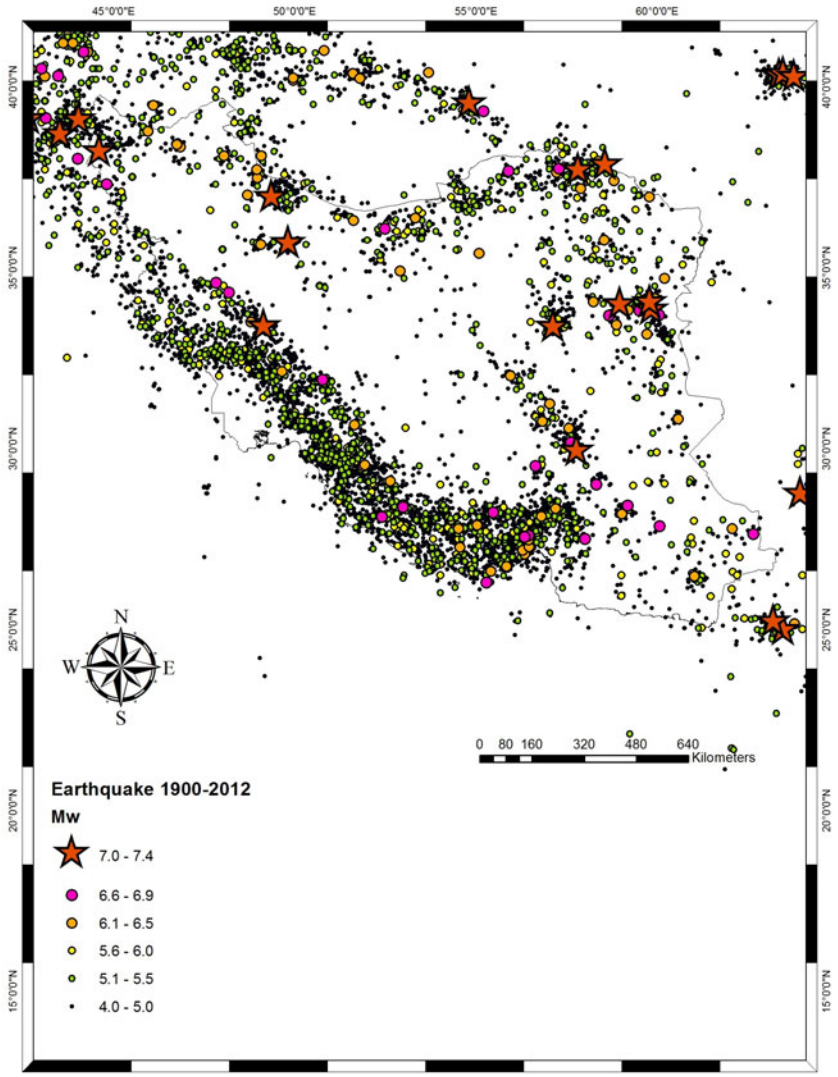


Fig. 2. The epicentral distribution of earthquakes of $Mw \geq 4.0$ occurred during the period 1900-2012.

pleteness of earthquake catalogue has been performed with respect to magnitude and time. The magnitude of completeness (*Mc*), also called threshold or cut-off magnitude is defined as the lowest magnitude at which 100% of events in space-time volume are detected. The methods of Entire Magnitude Range (EMR) and Maximum Curvature (Wiemer and Wyss 2000) have been used to estimate *Mc* that is equal to 4.5. We have also estimated *Mc* for each

and every seismogenic zones in the considered region, keeping in mind that *Mc* varies spatially in a wider region.

The seismotectonic province is considered to be an area that under the present-day geodynamic regimes has a comparable tectonic setting and unified seismicity pattern (Ye *et al*. 1995). Also, it can be defined as a geographic region of some geological, geophysical, and seismological similarity with the assumption of uniform earthquake potential (Tavakoli and Ghafory-Ashtiany 1999). Until now, the several suggestions (*e.g*., Stoklin 1968, Takin 1972, Berberian 1976, Nowroozi 1976, Nogol-Sadat 1994, Tavakoli 1996, Mirzaei *et al.* 1998, Zare 2010) offered for seismotectonic zonation of Iran were partly based on expert opinions, as well as field data. Recently, Karimiparidari *et al.* (2011) proposed 29 seismotectonic provinces with different specification. They used seismicity catalogue, active fault maps, magnetic intensity map, and topography data to determine the borders of each zone.

## 4. THE APPLIED METHODS

In the present study, an assessment of the maximum magnitude or upper bound magnitude is based on the two methods: (a) Gumbel's third asymptotic distribution of extreme values method (GIII), and (b) Kijko–Sellevoll method of maximum likelihood estimate (Kijko and Sellevoll 1989, 1992; Kijko 2004).

### 4.1 Gumbel's third asymptotic distribution (GIII)

In order to analyse earthquake hazard in the Iranian Plateau we shall pursue the method of particular interest for earthquake hazard evaluation, which is the Gumbel's third asymptotic distribution of extremes (GIII). The method needs only the largest earthquake magnitudes occurring in each of a set of predetermined equal time intervals (of 1, 2, 3, *etc.* years) and is satisfied only for the data of the recent catalogues (Yegulalp and Kuo 1974). A most often observation is the absence of data in some of the equal-time selected. These are called "missing years". Burton (1977) suggested that as a rule-of-thumb, if these missing entries are less or equal to 25%, the assessed parameters may be estimated without any noticeable loss of accuracy.

Let *Mi* (with $i = 1, 2, 3, ..., n$) be the largest earthquake magnitudes observed in successive equal-time intervals for a given area. The probability that *M* is an extreme value of the magnitude is given by the cumulative distribution function:

$$P(M) = \exp\left[\left(\frac{\omega - M}{\omega - u}\right)^{k}\right], \tag{1}$$

where $\omega$ is the upper bound to $M$, $k$ is the shape parameter, and $u$ is the characteristic value with $P(u) = 1/e$ and $P(\omega) = 1$. The three parameters allow for curvature through the shape or curvature parameter $k$.

In general, we have extreme intervals of $N$ year duration and the corresponding distribution of $P_N(M)$ is associated to one year extremes of $P_1(M)$ by the relation derived by Burton (1977):

$$\sqrt[N]{P_N(M)} = P_1(M) \ . \tag{2}$$

Equation 3 has been introduced in seismic hazard by Burton (1977). The largest annual earthquake magnitudes ($M_1$, $M_2$, $M_3$, …, $M_N$) are selected from seismic event catalogue of time span of $N$ years and arranged in increasing size. Gringorten (1963) suggested different plotting point values:

$$P(M) = \frac{(i - 0.44)}{N + 0.12} \tag{3}$$

and points out that this equation is more convenient for plotting rule use because it gives a better fit at high magnitudes and long return periods of interest and so is adopted for GIII (Burton 1979). Equation 3 is adopted for the present study.

For curve fitting purposes, Eq. 1 is firstly transposed to

$$M = \omega - (\omega - u)\left[-\ln\left(P(M)\right)\right]^{\lambda} \ , \tag{4}$$

where $\lambda = 1/k$ and plotting $M$ as ordinate and $(-\ln(P(M)))^{\lambda}$ as abscissa draws a straight line with $\omega$ as intercept and $-(\omega - u)$ as slope. Equation 4 is nonlinear and the adopted curve fitting process is described in details by Burton (1979).

Moreover, the most probable magnitude for a time period of $T$ years (Burton 1977) is given by:

$$RM = \omega - (\omega - u)\left[\frac{1-\lambda}{T}\right]^{\lambda} \ . \tag{5}$$

### 4.2 Kijko–Sellevoll method of maximum likelihood estimate

In this study, also we used the approach of Kijko and Sellevoll (1989, 1992) and Kijko (2004) to calculate maximum regional magnitude $M_{\max}$ in 29 seismogenic zones of the Iranian Plateau. Kijko and Sellevoll (1989, 1992) have developed an approach which permits the calculation of maximum likelihood estimates of the parameters related to earthquake hazard. It accommodates the "gaps" in both historical and instrumental parts of the catalogue. It allows the combination between earthquakes of historical epochs and those which are instrumental data of short period.

The probability that $n$ earthquakes will occur in $T$ years can be calculated assuming that the earthquake occurrence is a Poisson process:

$$P(n) = \frac{\exp(\lambda T)(\lambda T)^n}{n!} , \tag{6}$$

where $\lambda$ is the number of occurrences of earthquakes with magnitude greater than or equal to threshold magnitude ($M_{\min}$). Estimation of $M_{\max}$ is based on the equation that compares the largest observed magnitude ( $M_{\max}^{\text{obs}}$ ) and the maximum expected magnitude $E$ ($M_{\max}/T$) during the time span of "T" of catalogue (Kijko 1988, 2004). Following the supposition that earthquake magnitudes are distributed according to the double truncated Gutenberg–Richter relation, the estimator of maximum regional magnitude $M_{\max}$ takes the following form (Kijko 1988):

$$M_{\max} = M_{\max}^{\text{obs}} + \frac{E_1(Tz_2) - E_1(Tz_1)}{\beta \exp(-Tz_2)} + M_{\min} \exp(-\lambda T) . \tag{7}$$

It is not difficult to show that the appropriate variance of the regional maximum magnitude ($M_{\max}$) estimated according to Eq. 6 is equal to that derived by Kijko (2004):

$$Var(M_{\max}) = \sigma_M^2 + \left[ \frac{E_1(Tz_2) - E_1(Tz_1)}{\beta \exp(-Tz_2)} + M_{\min} \exp(-\lambda T) \right]^2 , \tag{8}$$

where it is assumed that the observed magnitude is distorted by an observational error, which is distributed normally with a known standard deviation $\sigma_M^2$ (Kijko and Dessokey 1987).

## 5. RESULTS AND DISCUSSION

The aim of this study is the assessment of earthquake hazard parameters of the Iranian Plateau. For this purpose, we used the computer program HAZAN with many alterations, compiled by Makropoulos and Burton (1986). During a time span of 112 years (1900-2012) a number of successive large earthquakes (with $M \geq 7.0$) occurred in the Iranian Plateau. In GIII distribution method, a sequence of earthquakes with largest magnitude in a set of predetermined equal-time interval was analyzed rather than the whole dataset.

In Table 1 we listed the values of $\omega$, $u$, and $\lambda$, with their uncertainty as they are estimated through Gumbel's III technique. The maximum observed magnitude ( $M_{\max}^{\text{obs}}$ ), recorded during instrumental time, according to the catalogue used, and difference ( $\omega - M_{\max}^{\text{obs}}$ ) are also listed in Table 1. The maxi-

Table 1

The estimated values of $\omega$, $u$, $\lambda$ and their standard deviations, probable earthquake magnitude in the next 100 years ($M_{100}$) and its standard deviation, extreme years ($k$), maximum magnitude estimated by Kijko–Sellevoll method ($M_{\max}^{K-S}$) and its standard deviations, $\omega - M_{\max}^{\text{obs}}$, $\omega - M_{\max}^{K-S}$ and $\omega - M_{100}$, in 29 seismogenic zones of the Iranian Plateau

| Region | $Mc$ | Extreme years $k$ | $M_{\max}^{\text{obs}}$ | $M_{\max}^{K-S}$ | $\sigma M_{\max}^{K-S}$ | $\omega$ | $\sigma\omega$ | $u$ | $\sigma u$ | $\lambda$ | $\sigma\lambda$ | $M_{100}$ | $\sigma M_{100}$ | $\omega - M_{\max}^{\text{obs}}$ | $\omega - M_{100}$ | $\omega - M_{\max}^{K-S}$ |
|---|---|---|---|---|---|---|---|---|---|---|---|---|---|---|---|---|
| 1 | 5 | 2 | 6.5 | 7.09 | 0.12 | 7.14 | 1.31 | 4.38 | 0.18 | 0.34 | 0.28 | 6.64 | 0.29 | 0.64 | 0.5 | 0.05 |
| 2 | 5 | 2 | 6.4 | 6.47 | 0.18 | 6.73 | 0.95 | 3.84 | 0.49 | 0.48 | 0.39 | 6.5 | 0.3 | 0.33 | 0.23 | 0.26 |
| 3 | 4.6 | 1 | 7.3 | 7.43 | 0.15 | 7.64 | 1.42 | 3.37 | 0.59 | 0.27 | 0.21 | 6.51 | 0.3 | 0.34 | 1.13 | 0.21 |
| 4 | 4.4 | 2 | 7.4 | 7.88 | 0.52 | 8.03 | 1.25 | 3.3 | 0.55 | 0.41 | 0.23 | 7.45 | 0.3 | 0.63 | 0.58 | 0.15 |
| 5 | 4.2 | 1 | 7.2 | 7.7 | 0.98 | 7.79 | 1.38 | 3.12 | 0.64 | 0.35 | 0.24 | 6.99 | 0.3 | 0.59 | 0.8 | 0.09 |
| 6 | 4 | 2 | 6.7 | 6.83 | 0.24 | 7.16 | 1.16 | 4.39 | 0.21 | 0.37 | 0.27 | 6.74 | 0.29 | 0.46 | 0.42 | 0.33 |
| 7 | 5 | 2 | 6.1 | 6.28 | 0.27 | 6.45 | 0.44 | 2.99 | 0.92 | 0.57 | 0.54 | 6.3 | 0.3 | 0.35 | 0.15 | 0.17 |
| 8 | 5 | 2 | 6.3 | 6.37 | 0.17 | 6.91 | 1.34 | 3.06 | 0.96 | 0.46 | 0.41 | 6.56 | 0.27 | 0.61 | 0.35 | 0.54 |
| 9 | 4.5 | 1 | 6.9 | 6.98 | 0.22 | 7.31 | 0.84 | 5.02 | 0.1 | 0.33 | 0.19 | 6.87 | 0.21 | 0.41 | 0.44 | 0.33 |
| 10 | 4.7 | 2 | 6.1 | 6.23 | 0.28 | 6.26 | 0.52 | 4.1 | 0.38 | 0.7 | 0.46 | 6.22 | 0.3 | 0.16 | 0.04 | 0.03 |
| 11 | 4.2 | 2 | 6.7 | 6.92 | 0.18 | 7.5 | 1.57 | 3.23 | 0.85 | 0.31 | 0.33 | 6.59 | 0.3 | 0.8 | 0.91 | 0.58 |
| 12 | 4.7 | 4 | 6.6 | 7.05 | 0.49 | 7.32 | 1.9 | 4.53 | 0.15 | 0.21 | 0.19 | 6.31 | 0.3 | 0.72 | 1.01 | 0.27 |
| 13 | 4 | 4 | 6.4 | 6.55 | 0.25 | 6.61 | 0.94 | 4.67 | 0.17 | 0.48 | 0.41 | 6.45 | 0.3 | 0.21 | 0.16 | 0.06 |
| 14 | 4.4 | 1 | 7.2 | 7.54 | 0.57 | 7.73 | 1.46 | 2.93 | 0.74 | 0.36 | 0.26 | 6.95 | 0.28 | 0.53 | 0.78 | 0.19 |
| 15 | 4.7 | 2 | 7.4 | 7.51 | 0.15 | 7.98 | 1.41 | 4.35 | 0.19 | 0.24 | 0.22 | 6.85 | 0.29 | 0.58 | 1.13 | 0.47 |
| 16 | 4.5 | 2 | 6.1 | 6.14 | 0.2 | 6.38 | 0.39 | 5.34 | 0.1 | 0.65 | 0.49 | 6.35 | 0.28 | 0.28 | 0.03 | 0.24 |
| 17 | 5 | 1 | 6.6 | 6.71 | 0.22 | 7.1 | 1.48 | 3.94 | 0.26 | 0.32 | 0.31 | 6.46 | 0.3 | 0.5 | 0.64 | 0.39 |
| 18 | 4.6 | 2 | 7.4 | 7.7 | 0.35 | 7.83 | 1.82 | 2.77 | 0.89 | 0.36 | 0.24 | 7.01 | 0.3 | 0.43 | 0.82 | 0.13 |
| 19 | 4.8 | 1 | 7.2 | 7.32 | 0.24 | 7.66 | 1.81 | 3.59 | 0.45 | 0.22 | 0.21 | 6.26 | 0.29 | 0.46 | 1.4 | 0.34 |
| 20 | 4.5 | 1 | 6.1 | 6.25 | 0.25 | 6.56 | 0.45 | 3.83 | 0.44 | 0.33 | 0.23 | 6.04 | 0.26 | 0.46 | 0.52 | 0.31 |
| 21 | 5 | 2 | 6.8 | 7.3 | 0.24 | 7.76 | 1.05 | 4.62 | 0.15 | 0.21 | 0.14 | 6.62 | 0.29 | 0.96 | 1.14 | 0.46 |
| 22 | 4.2 | 2 | 6.7 | 7.19 | 0.78 | 7.22 | 1.65 | 4.3 | 0.18 | 0.33 | 0.28 | 6.66 | 0.3 | 0.52 | 0.56 | 0.03 |
| 23 | 4.6 | 1 | 5.7 | 5.88 | 0.27 | 6.58 | 1.57 | 3.5 | 0.62 | 0.27 | 0.23 | 5.76 | 0.3 | 0.88 | 0.82 | 0.7 |
| 24 | 4.8 | 2 | 5.6 | 5.85 | 0.32 | 6.28 | 1.71 | 4.19 | 0.31 | 0.33 | 0.3 | 5.88 | 0.31 | 0.68 | 0.4 | 0.43 |
| 25 | 4.4 | 2 | 5.5 | 6 | 0.11 | 6.11 | 1.41 | 3.69 | 0.57 | 0.29 | 0.21 | 5.53 | 0.3 | 0.61 | 0.58 | 0.11 |
| 26 | 5 | 1 | 7.3 | 7.98 | 0.71 | 8.06 | 1.02 | 4.56 | 0.1 | 0.29 | 0.14 | 7.23 | 0.27 | 0.76 | 0.83 | 0.08 |
| 27 | 4.7 | 1 | 5.6 | 5.94 | 0.39 | 6.06 | 1.17 | 3.36 | 0.42 | 0.42 | 0.19 | 5.75 | 0.3 | 0.46 | 0.31 | 0.12 |
| 28 | 4.2 | 3 | 6.4 | 6.94 | 0.28 | 7 | 1.37 | 3.44 | 0.78 | 0.4 | 0.38 | 6.54 | 0.3 | 0.6 | 0.46 | 0.06 |
| 29 | 4.6 | 2 | 6.6 | 7.1 | 0.47 | 7.28 | 1.9 | 4.07 | 0.44 | 0.29 | 0.26 | 6.52 | 0.3 | 0.68 | 0.76 | 0.18 |

mum magnitude estimated by Kijko–Sellevoll method ($M_{\max}^{K-S}$) is also evaluated and its uncertainty is listed in this table along with the values of difference ($\omega - M_{\max}^{K-S}$). The "extreme years", listed in Table 1 have been deduced from the observations since we have rarely full samples of results with extreme years of 1 year. The cumulative probability distribution functions of

GIII have been calculated using annual extreme magnitudes according to Eq. 3; this was followed by the assessment of the GIII estimates by using annual extremes. The Gumbel III graphs including probabilities computed for 29 regions are shown in Fig. 3.

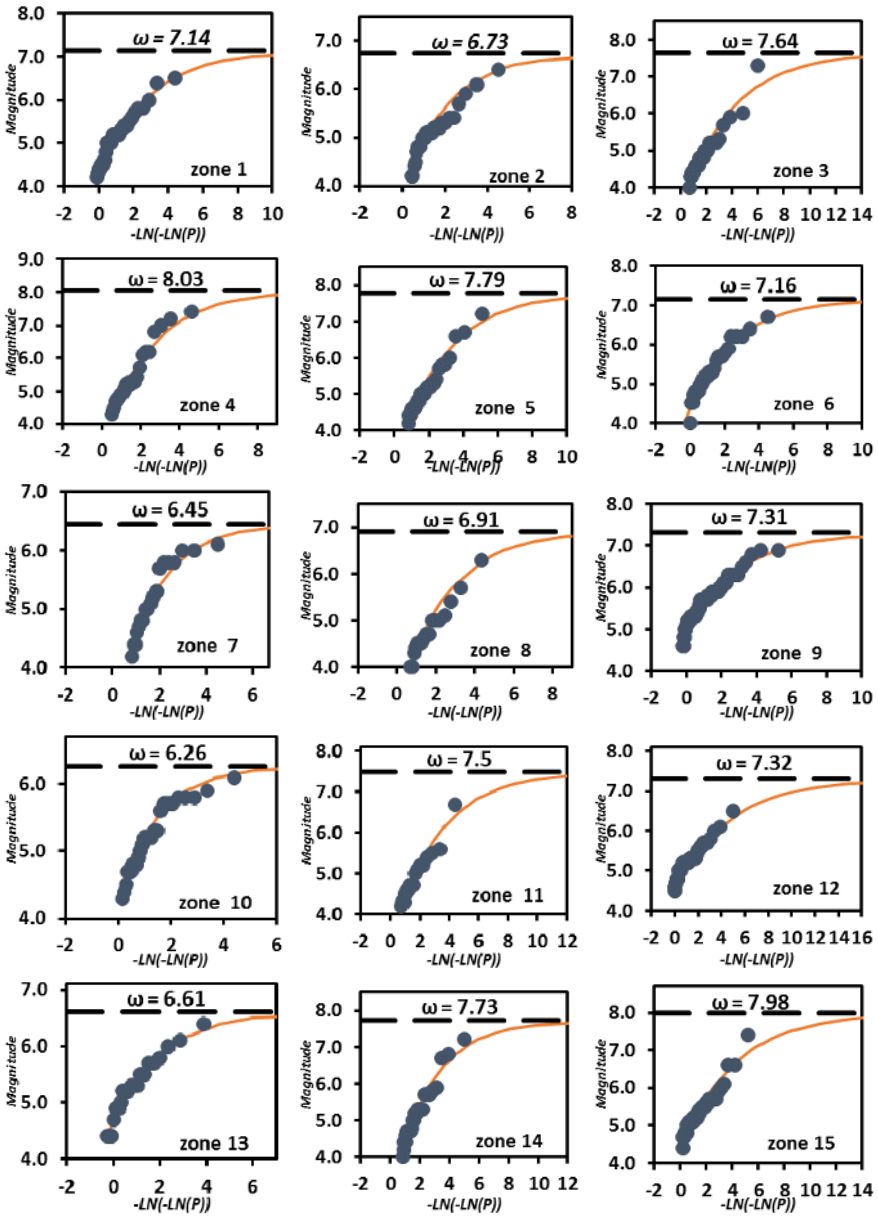


Fig. 3. Caption on next page.

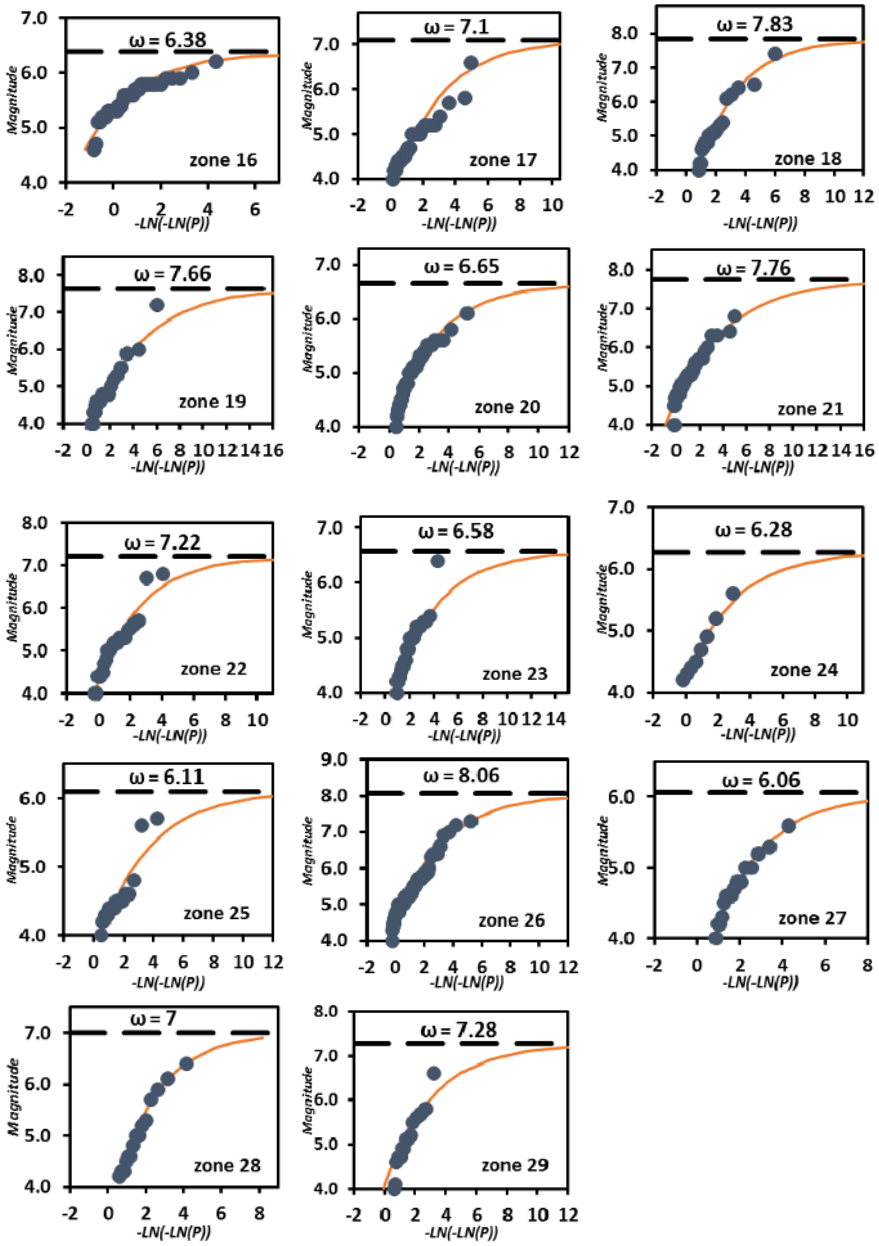


Fig. 3. Gumbel III distribution curves for 29 seismogenic zones of the Iranian Plateau. Solid curve line shows theoretical fitting of observed data (solid circles). Dash line shows the line of maximum magnitude ($\omega$) estimated by GIII distribution.

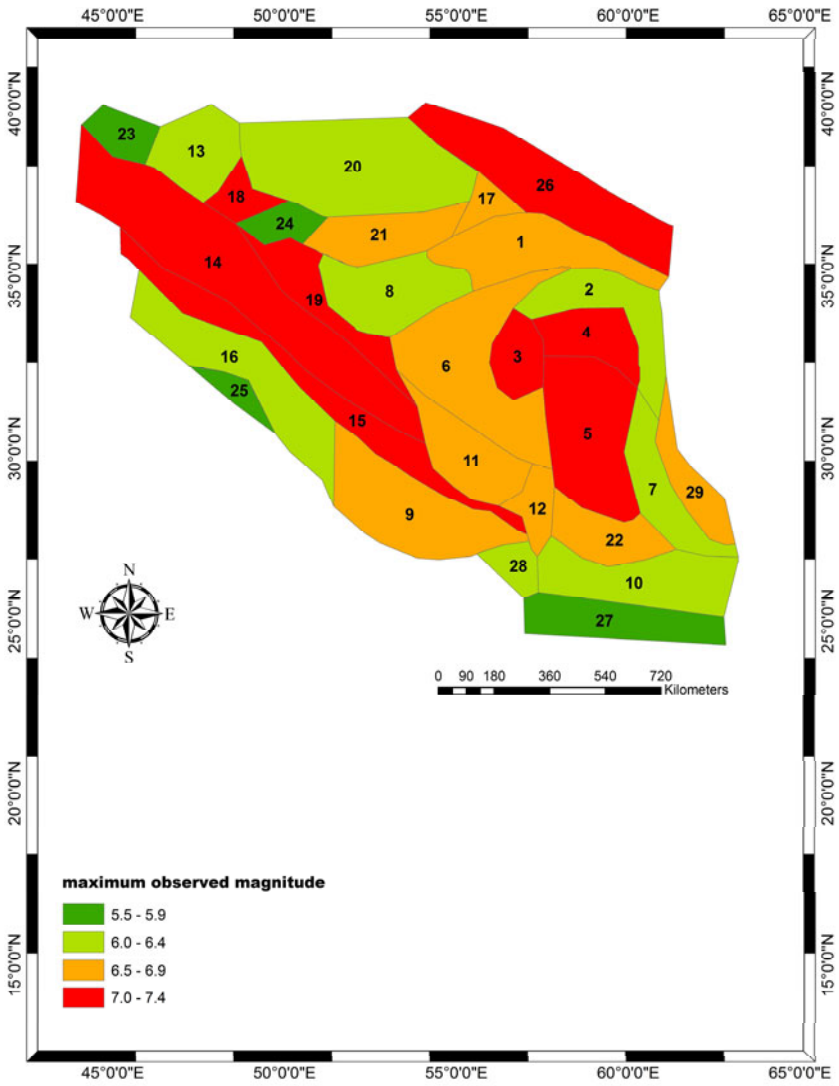


Fig. 4. The $M_{\max}^{\text{obs}}$ value in 29 seismogenic zones in the Iranian Plateau (seismogenic zones defined by Karimiparidari *et al*. (2011)).

Regional variability of $M_{\max}^{\text{obs}}$ and $\omega$ values for each 29 region is shown in Figs. 4 and 5. We divided $M_{\max}^{\text{obs}}$ into four groups as shown by legends with different color scale in Fig. 4, namely: (i) 5.5-5.9, (ii) 6-6.4, (iii) 6.5-6.9, (iv) 7-7.4, and divided $\omega$ into four groups shown by different color scale in Fig. 5, namely: (i) 6.06-6.50, (ii) 6.51-6.99, (iii) 7-7.5, (iv) 7.51-8.06.

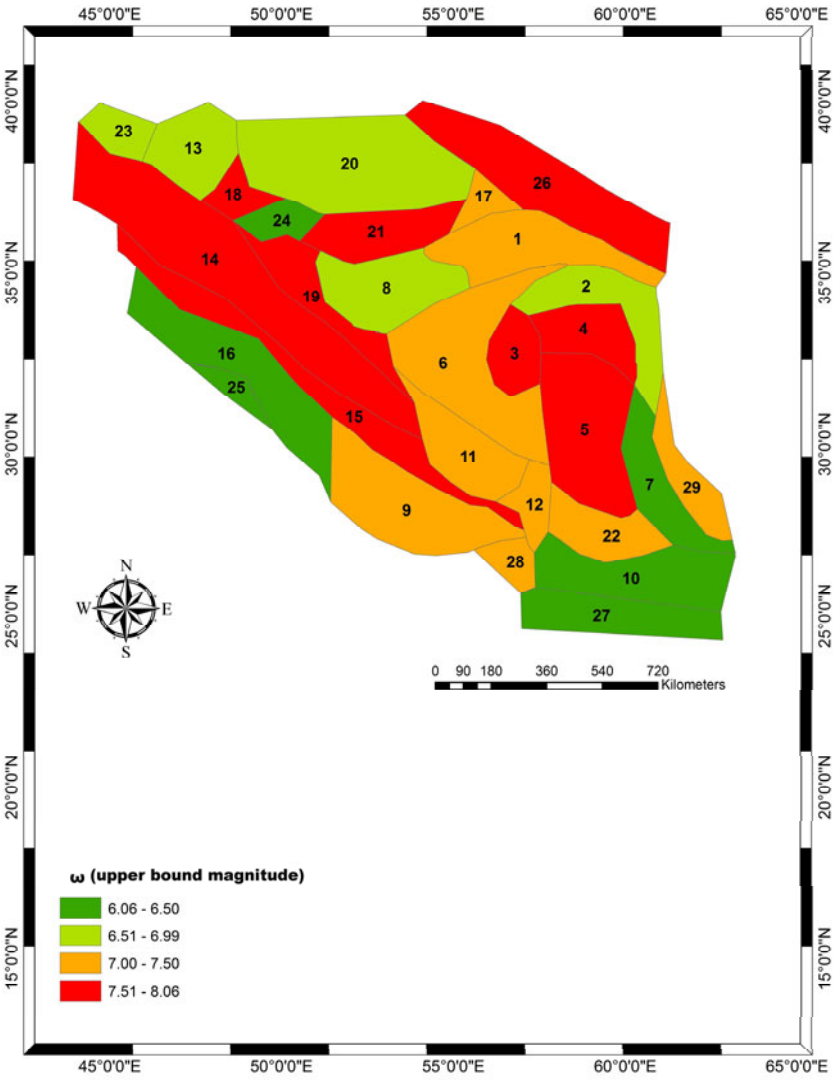


Fig. 5. The $\omega$ value from GUMBEL III in 29 seismogenic zones in the Iranian Plateau (seismogenic zones defined by Karimiparidari *et al*. (2011)).

The regional variation of upper bound magnitude ($\omega$), given in Fig. 5, shows the more hazardous seismogenic zones in the examined region. It may be considered that $\omega$ value associated to a region shows maximum earthquake size which may be occur in the future and we cannot expect a larger earthquake magnitude than the $\omega$ value in this region. In the examined area, the $\omega$ values greater than 8.0 are computed in seismogenic zone 26 related to

the main Kopeh–Dagh fault and seismogenic zone 4 related to Central and East Iran, the $\omega$ values 7.5-8 are computed in regions 15, 18, 5, 21, 14, 19, 3, and 11. These seismogenic zones are related to Central and East Iran, Kopeh–Dagh and Alborz and Azerbaijan. Regions with a high degree of mechanical homogeneity must have high $\omega$ values (Tsapanos 1990, 1997). The rocks in regions of a high degree of mechanical homogeneity can accumulate stress and strain for long time with no energy release through an earthquake. However, the spatial distribution map of $\omega$ values (Fig. 5) shows that Central and East Iran, Alborz and Azerbaijan, SE Zagros and Kopeh–Dagh are highly hazardous seismic regions in the examined area.

Nowroozi and Ahmadi (1986) evaluated that the provinces that are located southwest of the Zagros Thrust and northeast of the Arabian landmass are most likely to produce earthquakes with magnitude of six in less than a decade. However, the northern (Alborz and Azerbaijan) and northeastern (Central and East Iran and Kopeh–Dagh) provinces are each capable of producing an earthquake with a magnitude of 7.5 per century. The highest seismic hazard exists for Alborz, Kopeh–Dagh (KD), Ferdows, and Fars (SE Zagros) provinces. Mirzaei *et al*. (1997, 1999) suggested a maximum possible magnitude of no less than *Ms* = 7.8 in the different regions of Iran. Later Yazdani and Kowsari (2013) (using Bayesian estimation) showed results for the cut-off magnitude of 6.5 which indicate that the highest probability of seismic hazard exists in the Alborz, Kopeh–Dagh, Banndar Abbas (SE Zagros), Kerman (Central Iran), and Zagros regions. The seismic hazard is the lowest for the Esfahan–Sirjan region, the Arabian Platform, the Persian Gulf, and Kavir in Central Iran. Recently Karimiparidari *et al.* (2013) estimated $M_{\max}$ by Kijko and Sellevoll (1989, 1992) method in five major seismogenic zones using the instrumental and historical data. They calculated $M_{\max}$ in Alborz (= 7.8), Azerbaijan (= 7.9), Central and East Iran (= 7.7), Zagros Mountain Range (= 7.5), and Kopeh–Dagh (= 7.7).

For each seismogenic zone, the ($\omega - M_{\max}^{\text{obs}}$) differences, as shown in Fig. 6, are spatially mapped in the 29 seismogenic zones of the examined region for four categories: (i) 0.16-0.35, (ii) 0.36-0.49, (iii) 0.5-0.72, (iv) 0.73-0.96. The difference ($\omega - M_{\max}^{\text{obs}}$) is significantly higher than ($0.5 \leq$) in more seismogenic zones which are related to Central and East Iran, Kopeh–Dagh, and Alborz and Azerbaijan. The observed low (< 0.5) values of the difference ($\omega - M_{\max}^{\text{obs}}$) in the seismogenic zone which are located Zagros and Makran show that these regions have high crustal heterogeneity and the energy is being released in the form of continuous earthquakes.

The maximum expected magnitudes to be observed in the next 100 years ($M_{100}$) are computed in the 29 regions of Iranian Plateau to test whether an earthquake as much as $\omega$ values may occur in each region. The most proba-

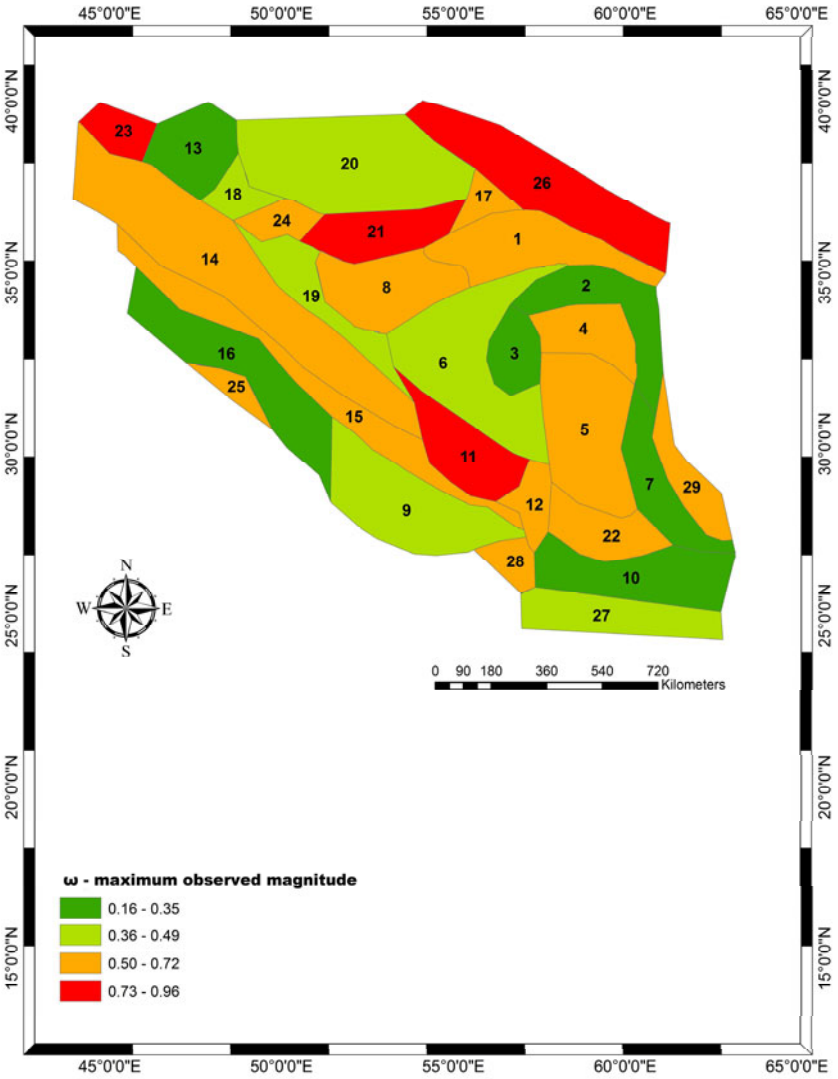


Fig. 6. Spatial distribution of $\omega - M_{\max}^{\text{obs}}$ in 29 seismogenic zones in the Iranian Plateau (seismogenic zones defined by Karimiparidari *et al*. (2011)).

ble magnitudes in next 100 years ($M_{100}$) are listed in Table 1, and its regional variability is shown in Fig. 7. We divided $M_{100}$ in four groups to show its geographical variation in the examined region: (i) 5.53-6, (ii) 6.01-6.50, (iii) 6.51-6.89, (iv) 6.9-7.45. The maximum expected magnitudes to be observed in the next 100 years is higher than 6.5 in the more seismogenic zone which are related Central and East Iran, Kopeh–Dagh, Alborz and Azerbai-

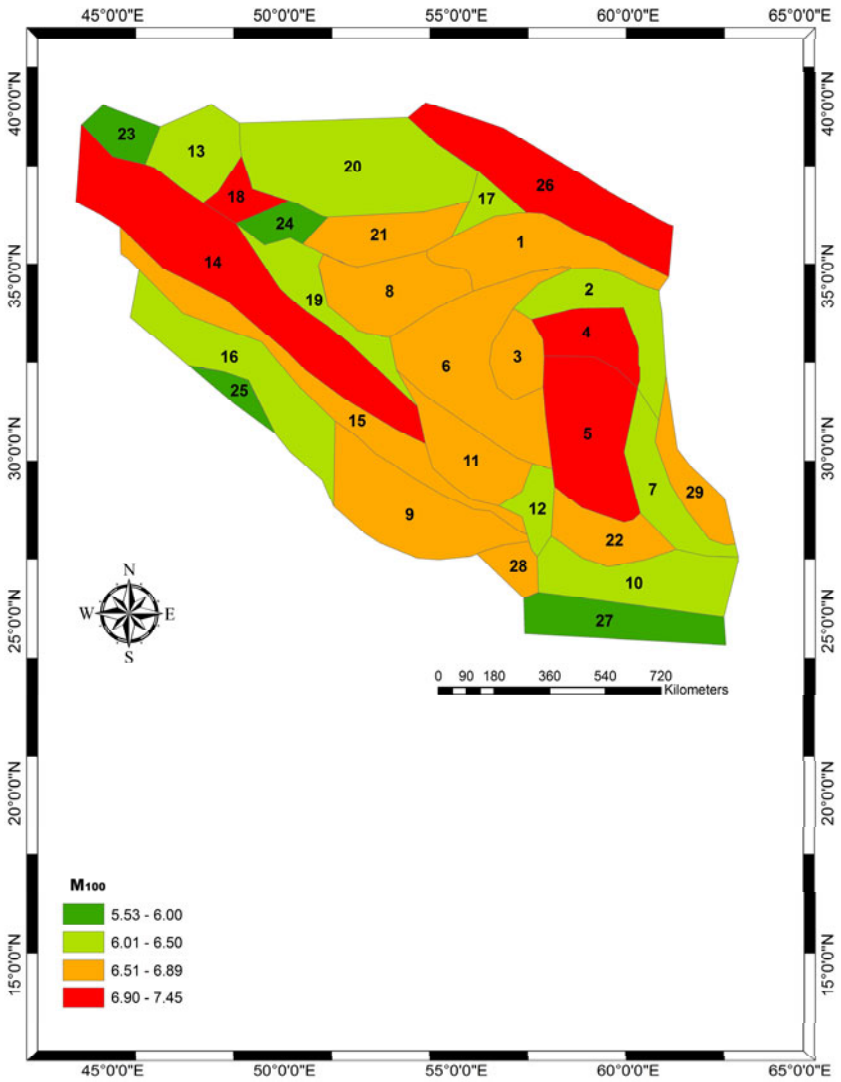


Fig. 7. Spatial distribution of $M_{100}$ in 29 seismogenic zones in the Iranian Plateau (seismogenic zones defined by Karimiparidari *et al*. (2011)).

jan, and SE Zagros. However, for each region the ($\omega - M_{100}$) differences shown in Fig. 8 are spatially mapped in the 29 seismogenic zones of the examined region for four categories. It is observed that all $M_{100}$ values are lower than $\omega$ values in the respective zones. The ($\omega - M_{100}$) differences are observed to be more than 1.0 in seismogenic zones 19, 6, 16, 20, and 22 (Table 1).

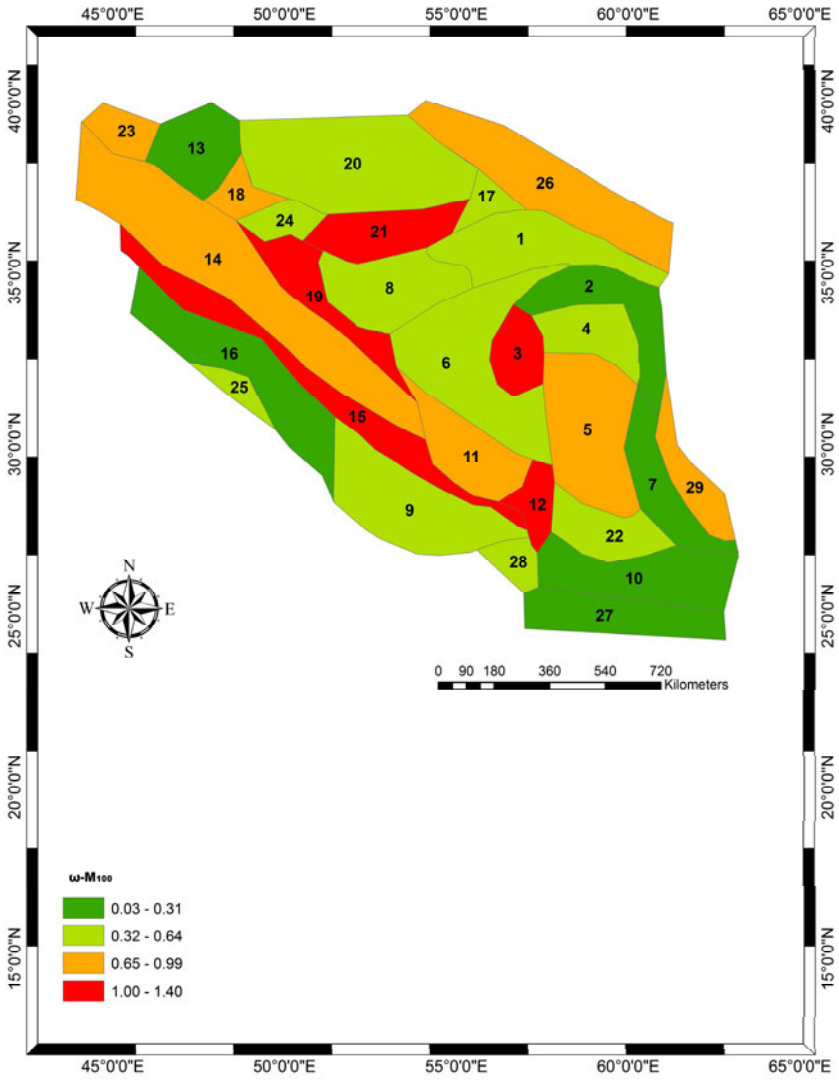


Fig. 8. Spatial distribution of $\omega - M_{100}$ in 29 seismogenic zones in the Iranian Plateau (seismogenic zones defined by Karimiparidari *et al*. (2011)).

We have also calculated the maximum magnitudes in the 29 seismogenic zones using maximum likelihood estimate of Kijko–Sellevoll method ($M_{\max}^{K-S}$) using same earthquake data; the results are listed in Table 1 and shown in Fig. 9. Moreover, the values of difference ($\omega - M_{\max}^{K-S}$) are listed in Table 1.

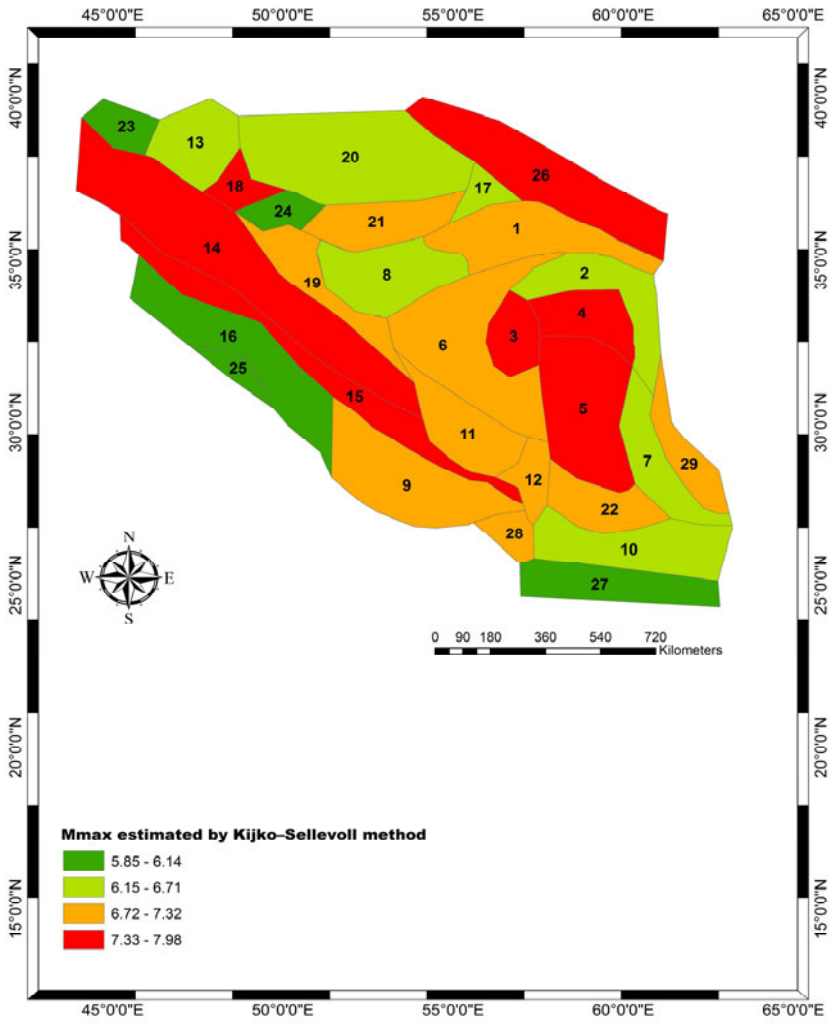


Fig. 9. Spatial distribution of maximum magnitude estimated by Kijko–Sellevoll method ($\omega - M_{\max}^{K-S}$) in 29 seismogenic zones in the Iranian Plateau (seismogenic zones defined by Karimiparidari *et al*. (2011)).

A linear regression relationship has been developed between the two values of $M_{\max}$ estimated by GIII (*i.e.*, $\omega$) and Kijko–Sellevoll method ($M_{\max}^{K-S}$) (Fig. 10). The developed relation takes the form of:

$$\omega = 0.9319\, M_{\max}^{K-S} + 0.7198\ , \qquad R^{20} = 0.92\ .$$

It is observed that the estimated $\omega$ values for the examined area are in good agreement with the $M_{\max}^{K-S}$ for the 29 seismogenic zones. In other

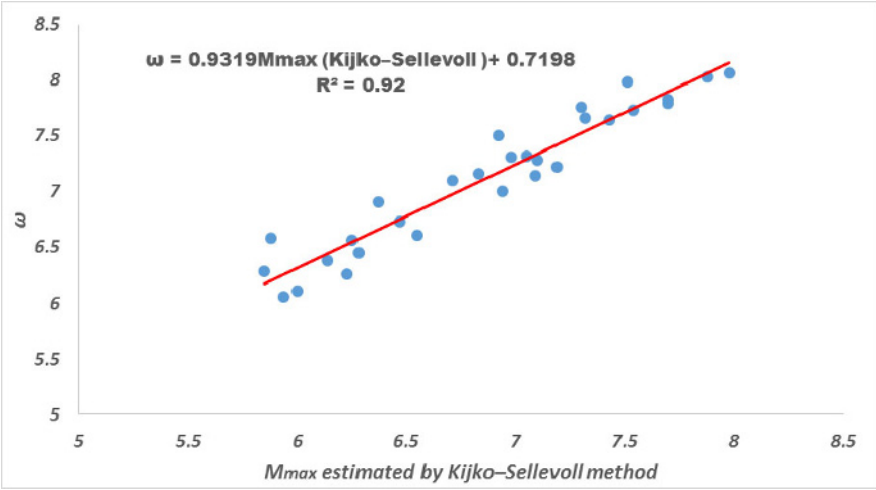


Fig. 10. Linear regression relationship between $\omega$ and $M_{\max}^{K-S}$.

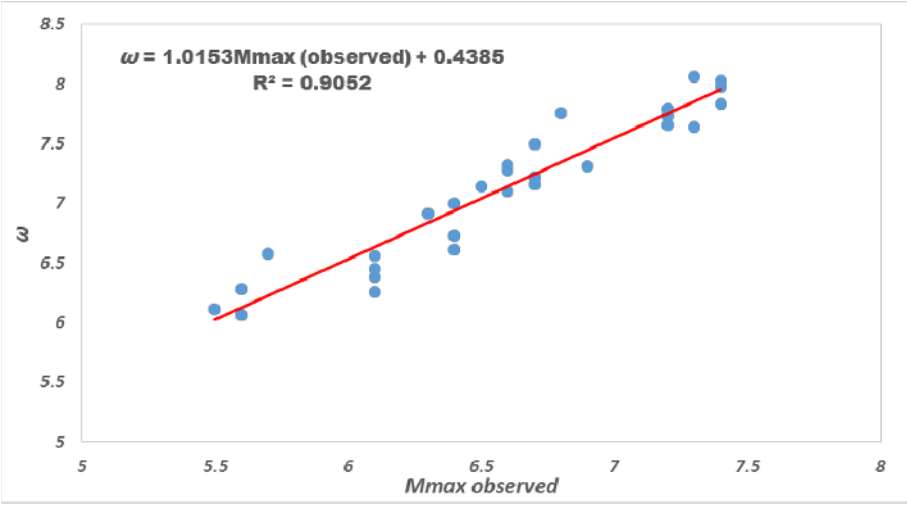


Fig. 11. Linear regression relationship between ω and $M_{\max}^{\text{obs}}$.

words, there is a positive correlation between $M_{\max}$ estimated by GIII ($\omega$) and Kijko–Sellevoll method ($M_{\max}^{K-S}$). Also, the differences between $\omega$ and $M_{\max}^{K-S}$ vary from 0.03 to 0.7 with the average of differences is only 0.25, suggesting both estimates are reliable and significant.

Similarly, we have made correlation between $\omega$ and maximum observed magnitude ($M_{\max}^{\text{obs}}$) (Fig. 11) and the regression relation takes the form:

$$\omega = 1.0153\, M_{\max}^{\text{obs}} - 0.4385 \ , \qquad R^{20} = 0.9052 \ .$$

However, we found out there is a positive correlation between maximum observed magnitude ( $M_{\max}^{\text{obs}}$ ) and that estimated by method of GIII. Also it is observed that their differences vary from 0.16 to 0.96 with a mean of 0.53, suggesting a good linear relation between these two values for the examined region. Thus, if we have the observed magnitude in any zone of the examined region, we can estimate the upper bound magnitude which can be generated by that zone.

## 6. CONCLUSIONS

From the estimated results in this study, it may be concluded that the upper bound magnitude ($\omega$) estimated by method of GIII and maximum magnitude estimated by Kijko–Sellevoll are comparable to each other and a linear relationship exists between them. The calculated lower values of maximum magnitude by Kijko–Sellevoll method than the $\omega$ values suggest that no earthquake with a larger $\omega$ value can occur in any seismogenic zone and it is a characteristic value of any source zone. A linear relationship is also established between the maximum observed magnitude ( $\omega - M_{\max}^{\text{obs}}$ ) and the upper bound magnitude ($\omega$) for the examined region and it will be a benefit relation to get an idea about upper bound magnitude in other regions using the maximum observed magnitude. The difference between these two parameters ( $\omega - M_{\max}^{\text{obs}}$ ) shows the degree of heterogeneity or homogeneity of the rocks. It is observed that more seismogenic zones which are located in Kopeh–Dagh, Central and East Iran, Alborz and Azerbaijan have high value of $\omega - M_{\max}^{\text{obs}}$ . This shows that these seismogenic zones have high degree of homogeneity and the rocks in these seismogenic zones of a high degree of mechanical homogeneity can accumulate stress and strain for a long time with no energy release through an earthquake. Moreover, the value of ( $\omega - M_{\max}^{\text{obs}}$ ) is low in Zagros and Makran. So these regions have high crustal heterogeneity and energy is being released in the form of successive earthquakes.

The two important parameters estimated in this study are the upper bound magnitude ($\omega$) and the most probable earthquake magnitude in the next 100 years ($M_{100}$). It is estimated that the upper bound magnitudes are higher than 8.0 for region 26 related to Kopeh–Dagh and region 4 related to Central Iran. A very interesting result of this study is that the most probable earthquake magnitudes in the next 100 years ($M_{100}$) are higher than the maximum observed magnitude in regions 24, 8, 16, 7, 27, 28, 1, 10, 2, 23, 13, 4, 6, and 25. So this reveals that in the next 100 years, these zones may experi-

ence magnitudes of earthquakes greater than the maximum magnitude that has been observed during past 112 years (1900-2012).

Acknowledgements. We wish to thank the anonymous reviewers for their constructive reviews, which substantially improved the original manuscript. Also the authors would like to express their sincere thanks to Prof. Dr. A. Kijko for providing computer program written in Matlab.

## References

Alavi, M. (1996), Tectonostratigraphic synthesis and structural style of the Alborz mountain system in northern Iran, *J. Geodyn.* **21**, 1, 1-33, DOI: 10.1016/0264-3707(95)00009-7.

Allen, M.B., S.J. Vincent, G.I. Alsop, A. Ismail-Zadeh, and R. Flecker (2003), Late Cenozoic deformation in the South Caspian region: effects of a rigid basement block within a collision zone, *Tectonophysics* **366**, 3-4, 223-239, DOI: 10.1016/S0040-1951(03)00098-2.

Ambraseys, N.N., and C.P. Melville (1982), *A History of Persian Earthquakes*, Cambridge University Press, Cambridge.

Båth, M. (1975), Seismicity of the Tanzania region, *Tectonophysics* **27**, 4, 353-379, DOI: 10.1016/0040-1951(75)90004-9.

Båth, M. (1983), Earthquake frequency and energy in Greece, *Tectonophysics* **95**, 3-4, 233-252, DOI: 10.1016/0040-1951(83)90070-7.

Bayrak, Y., S. Öztürk, H. Çinar, G.Ch. Koravos, and T.M. Tsapanos (2008), Regional variation of the ω-upper bound magnitude of GIII distribution in and around Turkey: tectonic implications for earthquake hazards, *Pure Appl. Geophys.* **165**, 7, 1367-1390, DOI: 10.1007/s00024-008-0359-z.

Berberian, M. (1976), Contribution to the seismotectonics of Iran. Part II, Geological Survey of Iran, Report No. 39.

Berberian, M. (1977), Contribution to the seismotectonics of Iran. Part III, Geological Survey of Iran, Report No. 40.

Berberian, M. (1983), The southern Caspian: A compressional depression floored by a trapped, modified oceanic crust, *Can. J. Earth Sci*. **20**, 2, 163-183, DOI: 10.1139/e83-015.

Berberian, M. (1994), Natural hazards and the first earthquake catalogue of Iran. Vol. 1. Historical hazard in Iran prior to 1900, International Institute of Earthquake Engineering and Seismology (IIEES), Tehran, Iran, 620 pp.

Berberian, M. (1995), Master "blind" thrust faults hidden under the Zagros folds: active basement tectonics and surface morphotectonics, *Tectonophysics* **241**, 3-4, 193-224, DOI: 10.1016/0040-1951(94)00185-C.

Berberian, M. (1997), Seismic sources of the Transcaucasian historical earthquakes. **In:** D. Giardini and S. Balassanian (eds.), *Historical and Prehistorical Earthquakes in the Caucasus*, 233-311, Kluwer Academic Publishers.

Berberian, M. (2014), Earthquakes and Coseismic Surface Faulting on the Iranian Plateau. A Historical, Social and Physical Approach, Elsevier Publishing, Amsterdam, 776 pp.

Berberian, M., and R.S. Yeats (1999), Patterns of historical earthquake rupture in the Iranian Plateau, *Bull. Seismol. Soc. Am.* **89**, 1, 120-139.

Berberian, M., and R.S. Yeats (2001), Contribution of archaeological data to studies of earthquake history in the Iranian Plateau, *J. Struct. Geol.* **23**, 2-3, 563-584, DOI: 10.1016/S0191-8141(00)00115-2.

Berberian, M., J.A. Jackson, M. Qorashi, M. Talebian, M. Khatib, and K. Priestley (2000), The 1994 Sefidabeh earthquakes in eastern Iran: blind thrusting and bedding-plane slip on a growing anticline, and active tectonics of the Sistan suture zone, *Geophys. J. Int.* **142**, 2, 283-299, DOI: 10.1046/j.1365-246x.2000.00158.x.

Burton, P.W. (1977), The application of extreme value statistics to seismic hazard assessments in the European area. **In:** *Proc. Symp. Analysis and on Seismic Risk, 17-22 October 1977, Liblice*.

Burton, P.W. (1979), Seismic risk in southern Europe through to India examined using Gumbel's third distribution of extreme values, *Geophys. J. Int.* **59**, 2, 249-280, DOI: 10.1111/j.1365-246X.1979.tb06766.x.

Byrne, D.E., L.R. Sykes, and D.M. Davis (1992), Great thrust earthquakes and aseismic slip along the plate boundary of the Makran Subduction Zone, *J. Geophys. Res.* **97**, B1, 449-478, DOI: 10.1029/91JB02165.

Dargahi-Noubary, G.R. (2002), The use of modern statistical theories in the assessment of earthquake hazard, with application to quiet regions of eastern North America, *Soil Dyn. Earthq. Eng.* **22**, 5, 361-369, DOI: 10.1016/S0267-7261(02)00027-1.

Engdahl, E.R., J.A. Jackson, S.C. Myers, E.A. Bergman, and K. Priestley (2006), Relocation and assessment of seismicity in the Iran region, *Geophys. J. Int.* **167**, 2, 761-778, DOI: 10.1111/j.1365-246X.2006.03127.x.

Epstein, B., and C. Lomnitz (1966), A model for the occurrence of large earthquakes, *Nature* **211**, 5052, 954-956, DOI: 10.1038/211954b0.

Field, E.H., D.D. Jackson, and J.F. Dolan (1999), A mutually consistent seismic-hazard source model for southern California, *Bull. Seismol. Soc. Am.* **89**, 3, 559-578.

Gringorten, I.I. (1963), A plotting rule for extreme probabilistic paper, *J. Geophys. Res.* **68**, 3, 813-814, DOI: 10.1029/JZ068i003p00813.

Gumbel, E.J. (1958), *Statistics of Extremes*, Columbia University Press, New York, 375 pp.

Hollingsworth, J., J. Jackson, R. Walker, M.R. Gheitanchi, and M.J. Bolourchi (2006), Strike-slip faulting, rotation, and along-strike elongation in the Kopeh Dagh mountains, NE Iran, *Geophys. J. Int.* **166**, 3, 1161-1177, DOI: 10.1111/j.1365-246X.2006.02983.x.

Hollingsworth, J., J. Jackson, J.E. Alarcon, J.J. Boomer, and M.J. Bolourchi (2007), The 4th February 1997 Bojnourd (Garmkhan) earthquake in NE Iran: Field, teleseismic, and strong-motion evidence for rupture directivity effects on a strike-slip fault, *J. Earthq. Eng.* **11**, 2, 193-214, DOI: 10.1080/13632460601031078.

Jackson, J., and D. McKenzie (1984), Active tectonics of the Alpine–Himalayan Belt between western Turkey and Pakistan, *Geophys. J. Int*. **77**, 1, 185-264, DOI: 10.1111/j.1365-246X.1984.tb01931.x.

Jackson, J., K. Priestley, M. Allen, and M. Berberian (2002), Active tectonics of the South Caspian Basin, *Geophys. J. Int.* **148**, 2, 214-245, DOI: 10.1046/j.1365-246X.2002.01588.x.

Kagan, Y.Y. (2002), Seismic moment distribution revisited: I. Statistical results, *Geophys. J. Int.* **148**, 3, 520-541, DOI: 10.1046/j.1365-246x.2002.01594.x.

Kaila, K.L., and H. Narain (1971), A new approach for preparation of quantitative seismicity maps as applied to Alpide Belt–Sunda Arc and adjoining areas, *Bull. Seismol. Soc. Am.* **61**, 5, 1275-1291.

Karimiparidari, S., M. Zaré, and H. Memarian (2011), New seismotectonic zoning map of Iran. **In:** *Proc. 6th Int. Conf. on Seismology and Earthquake Engineering (SEE6)*, CD-ROM, 8 pp.

Karimiparidari, S., M. Zaré, H. Memarian, and A. Kijko (2013), Iranian earthquakes, a uniform catalog with moment magnitudes, *J. Seismol*. **17**, 3, 897-911, DOI: 10.1007/s10950-013-9360-9.

Kijko, A. (1988), Maximum likelihood estimation of Gutenberg–Richter b parameter for uncertain magnitudes values, *Pure Appl. Geophys.* **127**, 4, 573-579, DOI: 10.1007/BF00881745.

Kijko, A. (2004), Estimation of the maximum earthquake magnitude, $m_{max}$, *Pure Appl. Geophys*. **161**, 8, 1655-1681, DOI: 10.1007/s00024-004-2531-4.

Kijko, A., and M.M. Dessokey (1987), Application of extreme magnitude distributions to incomplete earthquake files, *Bull. Seismol. Soc. Am.* **77**, 4, 1429-1436.

Kijko, A., and M.A. Sellevoll (1989), Estimation of earthquake hazard parameters from incomplete data files. Part I: Utilization of extreme and complete catalogs with different threshold magnitudes, *Bull. Seismol. Soc. Am.* **79**, 3, 645-654.

Kijko, A., and M.A. Sellevoll (1992), Estimation of earthquake hazard parameters from incomplete data files. Part II: Incorporation of magnitude heterogeneity, *Bull. Seismol. Soc. Am.* **82**, 1, 120-134.

Kijko, A., and M. Singh (2011), Statistical tools for maximum possible earthquake magnitude estimation, *Acta Geophys.* **59**, 4, 674-700, DOI: 10.2478/s11600-011-0012-6.

Knopoff, L., and Y. Kagan (1977), Analysis of the theory of extremes as applied to earthquake problems, *J. Geophys. Res.* **82**, 36, 5647-5657, DOI: 10.1029/JB082i036p05647.

Koravos, G.Ch., I.G. Main, T.M. Tsapanos, and R.M.W. Musson (2003), Maximum earthquake magnitudes in the Aegean area constrained by tectonic moment release rates, *Geophys. J. Int.* **152**, 1, 94-112, DOI: 10.1046/j.1365-246X.2003.01825.x.

Krinitzsky, E.L. (2002), How to obtain earthquake ground motions for engineering design, *Eng. Geol.* **65**, 1, 1-16, DOI: 10.1016/S0013-7952(01)00098-9.

Makropoulos, K.C. (1978), Statistics of large earthquake magnitude and an evaluation of Greek seismicity, Ph.D. Thesis, University of Edinburgh, Edinburgh, UK, 193 pp.

Makropoulos, K.C., and P.W. Burton (1983), Seismic risk of circum-Pacific earthquakes: I. Strain energy release, *Pure Appl. Geophys*. **121**, 2, 247-267, DOI: 10.1007/BF02590137.

Makropoulos, K.C., and P.W. Burton (1986), Hazan: a FORTRAN program to evaluate seismic-hazard parameters using Gumbel's theory of extreme value statistics, *Comput. Geosci*. **12**, 1, 29-46, DOI: 10.1016/0098-3004(86)90017-8.

Meyer, B., and K. Le Dortz (2007), Strike-slip kinematics in Central and Eastern Iran: Estimating fault slip-rates averaged over the Holocene, *Tectonics* **26**, 5, TC5009, DOI: 10.1029/2006TC002073.

Mirzaei, N., M. Gao, and Y.T. Chen (1997), Seismicity in major seismotectonic provinces of Iran, *Earthq. Res. Chin*a **11**, 4, 351-361.

Mirzaei, N., M. Gao, and Y.T. Chen (1998), Seismic source regionalization for seismic zoning of Iran: major seismotectonic provinces, *J. Earthq. Predic. Res.* **7**, 465-495.

Mirzaei, N., M. Gao, and Y.-T. Chen (1999), Delineation of potential seismic sources for seismic zoning of Iran, *J. Seismol.* **3**, 1, 17-30, DOI: 10.1023/A:1009737719013.

Mueller, C.S. (2010), The influence of maximum magnitude on seismic-hazard estimates in the central and eastern United States, *Bull. Seismol. Soc. Am.* **100**, 2, 699-711, DOI: 10.1785/0120090114.

Nogol-Sadat, M.A.A. (1994), Seismotectonic map of Iran. Teritise on the geology of Iran. 1:1 000 000 scale, Tehran, Iran.

Nordquist, J.M. (1945), Theory of largest values applied to earthquake magnitudes, *Trans. Am. Geophys. Union* **26**, 1, 29-31, DOI: 10.1029/TR026i001p00029.

Nowroozi, A.A. (1976), Seismotectonic provinces of Iran, *Bull. Seismol. Soc. Am.* **66**, 4, 1249-1276.

Nowroozi, A.A., and G. Ahmadi (1986), Analysis of earthquake risk in Iran based on seismotectonic provinces, *Tectonophysics* **122**, 1-2, 89-114, DOI: 10.1016/0040-1951(86)90160-5.

Pisarenko, V.F., A.A. Lyubushin, V.B. Lysenko, and T.V. Golubeva (1996), Statistical estimation of seismic hazard parameters: maximum possible magnitude and related parameters, *Bull. Seismol. Soc. Am.* **86**, 3, 691-700.

Reiter, L. (1990), *Earthquake Hazard Analysis: Issues and Insights*, Columbia University Press, New York, 254 pp.

Shabanian, E., L. Siame, O. Bellier, L. Benedetti, and M.R. Abbassi (2009), Quaternary slip rates along the northeastern boundary of the Arabia-Eurasia collision zone (Kopeh Dagh Mountains, Northeast Iran), *Geophys. J. Int.* **178**, 2, 1055-1077, DOI: 10.1111/j.1365-246X.2009.04183.x.

Snyder, D.B., and M. Barazangi (1986), Deep crustal structure and flexure of the Arabian plate beneath the Zagros collisional mountain belt as inferred from gravity observations, *Tectonics* **5**, 3, 361-373, DOI: 10.1029/TC005i003p00361.

Sornette, D., L. Knopoff, Y.Y. Kagan, and C. Vanneste (1996), Rank-ordering statistics of extreme events: application to the distribution of large earthquakes, *J. Geophys. Res.* **101**, B6, 13883-13893, DOI: 10.1029/96JB00177.

Stocklin, J. (1968), Structural history and tectonics of Iran, *AAPG Bull.* **52**, 7, 1229-1258.

Takin, M. (1972), Iranian geology and continental drift in the Middle East, *Nature* **235**, 5334, 147-150, DOI: 10.1038/235147a0.

Talebian, M., and J. Jackson (2004), A reappraisal of earthquake focal mechanisms and active shortening in the Zagros mountains of Iran, *Geophys. J. Int.* **156**, 3, 506-526, DOI: 10.1111/j.1365-246X.2004.02092.x.

Tavakoli, B. (1996), Major seismotectonic provinces of Iran, Technical Report, International Institute of Earthquake Engineering and Seismology (IIEES), Tehran, Iran (in Persian).

Tavakoli, B., and M. Ghafory-Ashtiany (1999), Seismic hazard assessment of Iran, *Ann. Geophys*. **42**, 6, 1013-1021, DOI: 10.4401/ag-3781.

Tinti, S., and F. Mulargia (1985), Effects of magnitude uncertainties on estimating the parameters in the Gutenberg–Richter frequency-magnitude law, *Bull. Seismol. Soc. Am.* **75**, 6, 1681-1697.

Tsapanos, T.M. (1990), b-values of two tectonic parts in the circum-Pacific belt, *Pure Appl. Geophys.* **134**, 2, 229-242, DOI: 10.1007/BF00876999.

Tsapanos, T.M. (1997), Regional variation of the ω values in the circum-Pacific belt, *Pure Appl. Geophys.* **150**, 1, 113-120, DOI: 10.1007/s000240050066.

Tsapanos, T.M. (2003), Appraisal of seismic hazard parameters for the seismic regions of the east circum-Pacific belt inferred from a Bayesian approach, *Nat. Hazards* **30**, 1, 59-78, DOI: 10.1023/A:1025051712052.

Tsapanos, T.M., and P.W. Burton (1991), Seismic hazard evaluation for specific seismic regions of the world, *Tectonophysics* **194**, 1-2, 153-169, DOI: 10.1016/0040-1951(91)90278-Z.

Tsapanos, T.M., and C.V. Christova (2003), Earthquake hazard parameters in Crete island and its surrounding area inferred from Bayes statistics: an integration of morphology of the seismically active structures and seismological data, *Pure Appl. Geophys*. **160**, 8, 1517-1536, DOI: 10.1007/s00024-003-2358-4.

Tsapanos, T.M., O.Ch. Galanis, G.Ch. Koravos, and R.M.W. Musson (2002), A method for Bayesian estimation of the probability of the local intensity for some cities of Japan, *Ann. Geophys*. **45**, 5, 657-671, DOI: 10.4401/ag-3528.

Tsapanos, T.M., Y. Bayrak, H. Cinar, G.Ch. Koravos, E. Bayrak, E.E. Kalogirou, A.V. Tsapanou, and G.E. Vougiouka (2014), Analysis of largest earthquakes in Turkey and its vicinity by application of the Gumbel III distribution, *Acta Geophys.* **62**, 1, 59-82, DOI: 10.2478/s11600-013-0155-8.

Uhrhammer, R.A. (1986), Characteristics of northern and central California seismicity, *Earthq. Notes* **57**, 1, 21 (abstract).

Vernant, P., F. Nilforoushan, J. Chéry, R. Bayer, Y. Djamour, F. Masson, H. Nankali, J.F. Ritz, M. Sedighi, and F. Tavakoli (2004), Deciphering oblique shortening of central Alborz in Iran using geodetic data, *Earth Planet. Sci. Lett.* **223**, 1-2, 177-185, DOI: 10.1016/j.epsl.2004.04.017.

Walker, R., and J. Jackson (2004), Active tectonics and late Cenozoic strain distribution in central and eastern Iran, *Tectonics* **23**, 5, TC5010, DOI: 10.1029/2003TC001529.

Walker, R., J. Jackson, and C. Baker (2004), Active faulting and seismicity of the Dasht-e-Bayaz region, eastern Iran, *Geophys. J. Int.* **157**, 1, 265-282, DOI: 10.1111/j.1365-2966.2004.02179.x.

Wheeler, R.L. (2009), Methods of $M_{max}$ estimation east of the Rocky Mountains, Open-File Report 2009-1018, U.S. Geological Survey, 44 pp.

Wiemer, S., and M. Wyss (2000), Minimum magnitude of completeness in earthquake catalogs: examples from Alaska, the western United States, and Japan, *Bull. Seismol. Soc. Am*. **90**, 4, 859-869, DOI: 10.1785/0119990114.

Yadav, R.B.S., D. Shanker, S. Chopra, and A.P. Singh (2010a), An application of regional time and magnitude predictable model for long-term earthquake prediction in the vicinity of October 8, 2005 Kashmir Himalaya earthquake, *Nat. Hazards* **54**, 3, 985-1014, DOI: 10.1007/s11069-010-9519-4.

Yadav, R.B.S., J.N. Tripathi, B.K. Rastogi, M.C. Das, and S. Chopra (2010b), Probabilistic assessment of earthquake recurrence in northeast India and adjoining regions, *Pure Appl. Geophys*. **167**, 11, 1331-1342, DOI: 10.1007/s00024-010-0105-1.

Yadav, R.B.S., Y. Bayrak, J.N. Tripathi, S. Chopra, A.P. Singh, and E. Bayrak (2012a), A probabilistic assessment of earthquake hazard parameters in NW Himalaya and the adjoining regions, *Pure Appl. Geophys*. **169**, 9, 1619-1639, DOI: 10.1007/s00024-011-0434-8.

Yadav, R.B.S., Y. Bayrak, J.N. Tripathi, S. Chopra, and E. Bayrak (2012b), Regional variation of the ω-upper bound magnitude of GIII distribution in Hindukush–Pamir Himalaya and the adjacent regions: a perspective on earthquake hazard, *Tectonophysics* **544-545**, 1-12, DOI: 10.1016/j.tecto.2012.03.015.

Yadav, R.B.S., T.M. Tsapanos, G.Ch. Koravos, Y. Bayrak, and K.D. Devlioti (2013), Spatial mapping of earthquake hazard parameters in the Hindukush–Pamir Himalaya and adjacent regions: implication for future seismic hazard, *J. Asian Earth Sci.* **70-71**, 115-124, DOI: 10.1016/j.jseaes.2013.03.007.

Yazdani, A., and M. Kowsari (2013), Bayesian estimation of seismic hazards in Iran, *Sci. Iran*. **20**, 3, 422-430, DOI: 10.1016/j.scient.2012.12.032.

Ye, H., G. Chen, and Q. Zhou (1995), Study on the intraplate potential seismic sources. **In:** *Proc. Fifth Int. Conf. Seismic Zonation, Nice, France*, Vol. 2, 1424-1430.

Yegulalp, T.M., and J.T. Kuo (1974), Statistical prediction of the occurrence of maximum magnitude earthquakes. *Bull. Seismol. Soc. Am*. **64**, 2, 393-414.

Zare, M. (2010), Fundamental of seismic hazard analyses, Technical Report, International Institute of Earthquake Engineering and Seismology (IIEES), Tehran, Iran, 142 pp. (in Persian).

Received 1 October 2014
Received in revised form 9 July 2015
Accepted 28 July 2015

DE GRUYTER OPEN

Acta Geophysica
vol. 64, no. 4, Aug. 2016, pp. 1034-1050
DOI: 10.1515/acgeo-2016-0032

# A New Approach in Coal Mine Exploration Using Cosmic Ray Muons

Reza DARIJANI[1], Ali NEGARESTANI[2], Mohammad Reza REZAIE[2], Syed Jalil FATEMI[3], and Ahmad AKHOND[1]

[1]Department of Physics, Payame Noor University, Tehran, Iran

[2]Department of Physics, Kerman Graduate University of Technology, Kerman, Iran
e-mail: mr.rezaie@kgut.ac.ir (corresponding author)

[3]Department of Physics, Shahid Bahonar University, Kerman, Iran

Abstract

Muon radiography is a technique that uses cosmic ray muons to image the interior of large scale geological structures. The muon absorption in matter is the most important parameter in cosmic ray muon radiography. Cosmic ray muon radiography is similar to X-ray radiography. The main aim in this survey is the simulation of the muon radiography for exploration of mines. So, the production source, tracking, and detection of cosmic ray muons were simulated by MCNPX code. For this purpose, the input data of the source card in MCNPX code were extracted from the muon energy spectrum at sea level. In addition, the other input data such as average density and thickness of layers that were used in this code are the measured data from Pabdana (Kerman, Iran) coal mines. The average thickness and density of these layers in the coal mines are from 2 to 4 m and 1.3 gr/cm$^3$, respectively. To increase the spatial resolution, a detector was placed inside the mountain**.** The results indicated that using this approach, the layers with minimum thickness about 2.5 m can be identified.

**Key words:** muon radiography, coal mines, MCNPX.

Ownership: Institute of Geophysics, Polish Academy of Sciences;
© 2016 Darijani *et al.* This is an open access article distributed under the Creative Commons Attribution-NonCommercial-NoDerivs license,
http://creativecommons.org/licenses/by-nc-nd/3.0/.

## 1. INTRODUCTION

When the primary cosmic ray particles, protons and $\alpha$ particles, penetrate the atmosphere they collide with air nuclei and new particles, mostly pions and kaons are produced. These secondary particles are short lived, and a fraction of them decay into muons instead of interacting with nuclei deeper in the atmosphere. Because these cosmic ray muons weakly interact with air nuclei, and their mean lifespan is long (about $2.2 \times 10^{-6}$ s), they are the dominant charged particles at the Earth's surface. They arrive at angles ranging from vertical to horizontal (Thompson and Whalley 1975), and their energy spectrum has been measured as a function of the zenith angle $\theta$ (Allkofer *et al.* 1981). It is also well known that muons arriving in the horizontal direction have a higher intensity at energies above 100 GeV. Because muons become highly penetrative as their energy becomes higher, these horizontal muons can be used for the purpose of probing the internal structure of gigantic objects. For example, typical horizontally arriving cosmic ray muons with energy of 1 TeV penetrate 2.6 km of water (Tanaka *et al.* 2007). Since muons penetrate through matter their energy decreases. The energy loss depends on the kinetic energy of the muon and, at very high energies, also on the chemical composition of the matter (Malmqvist *et al.* 1979). Some of muons that do not have enough energy to escape from the matter of interest are absorbed in the matter, and as a result the muon flux is reduced. Absorption of muons in matter is independent of geophysical models and directly measures the density length. Geophysical models can be used to predict a host of geophysical measurements and are important ways of calibrating regions in the absence of direct measurements. Meanwhile, geophysical models explain geophysical observations and determine the subsurface Earth properties. By measuring cosmic ray muons intensity in different depths of matter, very useful information regarding the density of matter can be obtained. This information is used for many purposes such as exploration of mines, and prediction of volcanic eruptions and earthquakes. The aim of this research is to obtain a two-dimensional profile of the average density inside a mountain by simulation. To this end, production, tracking, and detection of muons were performed by the MCNPX code. The input data such as the average density and thickness of layers that have been used in MCNPX code are the measured data from Pabdana (Kerman, Iran) coal mines.

## 2. THEORY

The potential use of high-energy near-horizontal cosmic ray muons for exploring the internal structure of large scale objects such as Egyptian pyramids has been recognized (Alvarez *et al.* 1970). The effective use of such near-horizontal cosmic ray muons for muon radiography can be explained through the following steps.

### 2.1 The cosmic-ray muon energy spectrum and its dependence on zenith angle

Pions and kaons are produced through nuclear interactions between primary cosmic ray protons and the atmospheric air, some of which decay and produce cosmic ray muons. The energy spectrum of these cosmic ray muons has been measured at different polar angles (Thompson and Whalley 1975). Furthermore, the flux of incident cosmic muons is of critical importance for geophysical imaging since it is used to determine the attenuation produced by the geological target (Lesparre *et al.* 2010). There are two ways to derive the differential flux of muons. The first approach is the use of a full simulation. These Monte Carlo computations can be accomplished by simulation codes like CORSIKA which allows to take into account the geomagnetic and altitude dependence. The second approach to obtain flux models is the use of fitting. The choice of a particular parameterization of the fitting curves may either be inspired by the physics involved in the production of muons from their parents or be guessed to provide a better fit regardless of the physical meaning of the parameters (Gaisser 1990). Some of fitting models only consider the production of muons from pions and kaons decay and assume a primary proton flux of the form: $P_0 e^{-\gamma}$ with $P_0 = 1.8$ ($\mathrm{cm^{-2}\,sr^{-1}\,GeV^{\gamma-1}}$), and $\gamma = 2.7$. This approach yields the analytical form of the muon spectrum initially proposed by Bugaev *et al.* (1970) and popularized by Gaisser in the form of Eq. 1 (Lesparre *et al.* 2010).

$$\varphi_G\left(\mathrm{E}_0,\theta\right) = A_G E_0^{-\gamma}\left(\frac{1}{1+\dfrac{E_0\cos\theta}{E_{0,\pi}^{\mathrm{cr}}}}+\frac{B_G}{1+\dfrac{E_0\cos\theta}{E_{0,\kappa}^{\mathrm{cr}}}}\right), \tag{1}$$

where $A_G$, $\gamma$, and $B_G$ are the scale factor, the power index, and the balance factor, respectively. The balance factor depends on the ratio of muons produced by the kaons and pions. $E_{0,\pi}^{\mathrm{cr}}$ and $E_{0,\kappa}^{\mathrm{cr}}$ are critical energies of pions and kaons for the vertical incidence ($\theta = 0$).

### 2.2 Range of cosmic ray muons through standard rock

The energy loss of a charged particle with some energy $E$ (TeV) on passage though matter with a density length (density × path length) of $X$ hectogram per $\mathrm{cm^2}$, $X$ ($\mathrm{hg/cm^2} = 100\ \mathrm{gr/cm^2}$), can be written as (Tanaka *et al.* 2007, Nagamine *et al.* 1995).

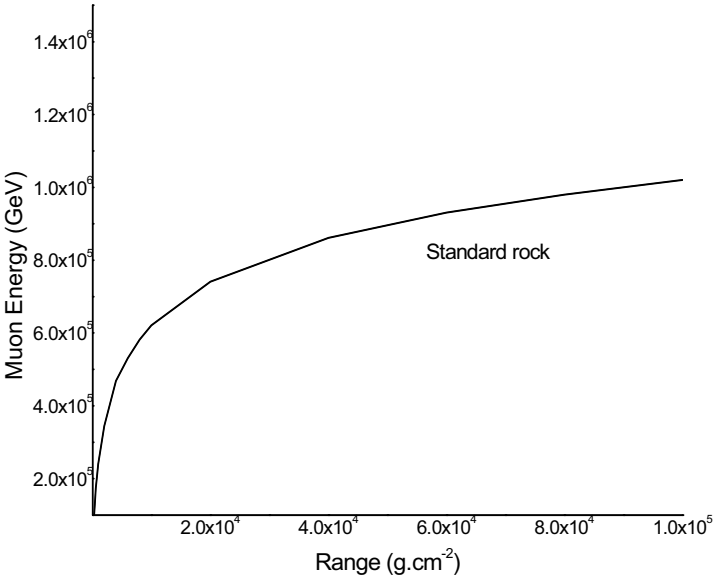


Fig. 1. The muon energy *versus* range in a standard rock.

$$\frac{dE}{dX} = \left[ 1.88 + 0.077\,\mathrm{Ln}\left( \frac{E}{m_\mu} \right) + 3.9E \right] \times 10^{-6} \ \ [\mathrm{TeVcm^2/gr}] \ , \tag{2}$$

where the first two terms represent ionization loss and the third term represents stochastic processes mainly due to bremsstrahlung. Choosing $E = 1$ TeV to yield a relatively small contribution of the logarithmic term, the mean rang (density length) $X$ can be obtained by integrating the energy loss formula as Eq. 3 (Nagamine *et al.* 1995, Nagamine 2003).

$$X = 2.5 \times 10^3 \,\mathrm{Ln}\left(1.56E + 1\right) \ [\mathrm{hg/cm^2}] \ . \tag{3}$$

This equation gives the relationship between range and energy in a standard rock. Standard rock is defined by $z/A = 0.5$, $z^2/A = 5.5$, $Z = 11$, and $\rho = 2.56$ gr/cm$^3$, where $Z$, $A$, and $\rho$ are the mean atomic number, the mean mass number, and density of the rock, respectively. Figure 1 shows the muon energy *versus* range in a standard rock.

### 2.3 Intensity of cosmic ray muons penetrating though rock with density length $X$

Measurement of muons intensity at various depths is important from different aspects. For instance, it provides information on the electromagnetic processes that reduce the flux (Bektasoglu *et al.* 2012). The measured muons

intensity at depth $x$ in the Earth is equal to the intensity of muons at sea level with an energy greater than $E_c(x)$; disregarding the small fraction of muons which decay in the passage from the ground to the depth $x$, $E_c(x)$ is the minimum energy necessary for a muon to penetrate to the depth $x$ (Malmqvist *et al.* 1979). Thus a unique relationship exists between density length $X$ ($X = \rho x$) and the intensity of penetrating cosmic ray muons $N_\mu(E_c(x), \theta_Z)$. Once $X$ is given, the minimum energy $E_c(x)$ is determined through the $X$-$E$ relation (Eq. 3), and the integrated flux $N_\mu(E_c(x), \theta_Z)$ is given as Eq. 4.

$$N_\mu\left(E_c, \theta = 90 - \theta_z\right) = \int_{E_C}^{\infty} \frac{dN}{dE} dE \ . \tag{4}$$

Conversely, for a substance with an unknown density length $X$, the measurement of the muons flux, $N_\mu(\theta_Z)$, penetrating through the substance with a zenith angel, $\theta_Z$, uniquely determines its density length in hg/cm$^2$. Small changes in $X$ due to the existence of a region of lower or higher density inside the broadly uniform object lead to differences in $N_\mu(\theta_Z)$. The change in $N_\mu(\theta_Z)$ informs us of change in $X$ (Nagamine 2003). Figure 2 shows the penetrating muons flux as a function of rock thickness at different zenith angles.

Using Fig. 2, the thickness of rock (in km) is calculated by dividing rock thickness (in km) water equivalent by rock density.

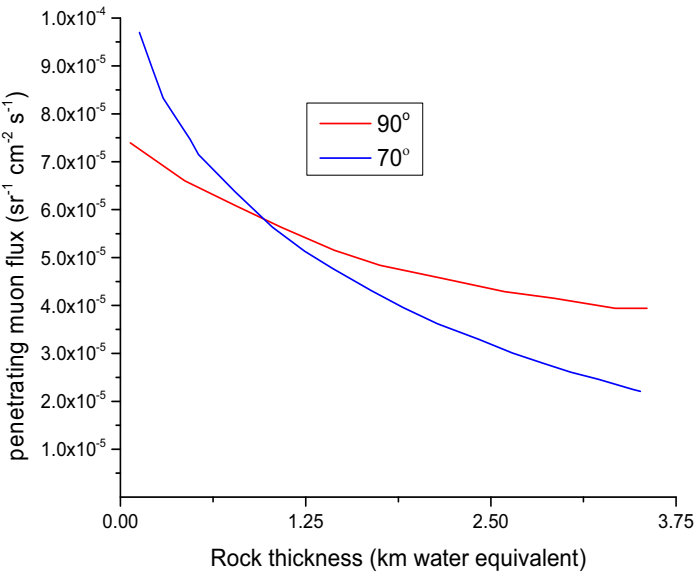


Fig. 2. Penetrating muon flux *versus* rock thickness (Nagamine 2003).

## 3. DETERMINATION COSMIC RAY MUON PATH THROUGH THE MATTER

For determination of the path of the muon penetrating through gigantic objects, there are two types of practical detection systems that are explained in the following.

### 3.1 Telescope of position sensitive detector

In this case, the straight line connecting the points where a cosmic ray muon passes through two (or three) counters determines the particle path (Fig. 3).

There are two representative examples of position determination that are explained in the following:

- The passing points can be determined by the difference in the arrival time of scintillation light from a set of at least three photomultipliers attached to the edges of each scintillator.
- The passing points can be determined more straightly by using segmented counter arrays in both horizontal and vertical directions (Fig. 3b).

In the case of counter telescopes of the position sensitive detectors, the spatial resolution of the detection system at the mountain ($\Delta X, \Delta Y$) can be determined from the resolution of the intersection points with each counter ($\Delta x$, $\Delta y$), the distance between the counters comprising the telescope ($l$), and the distance between the object (mountain) and the detector ($L$). This spatial resolution is calculated by the following Eqs. 5 and 6.

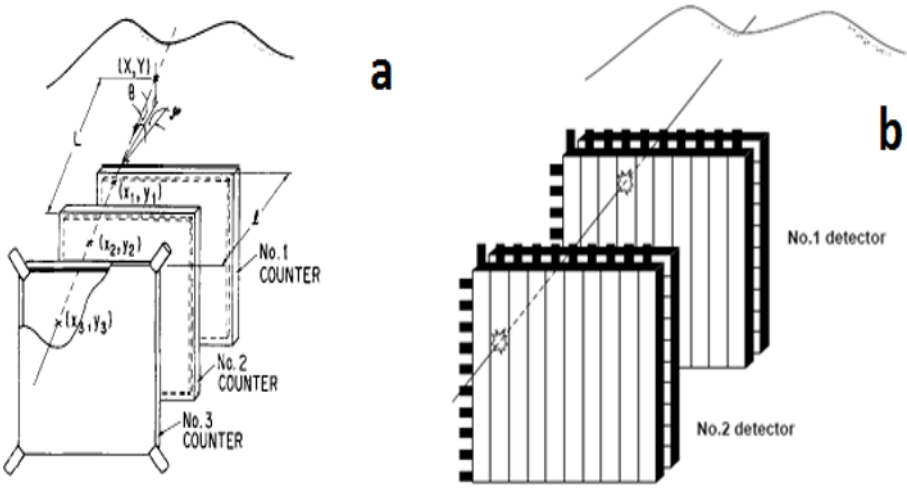


Fig. 3: (a) The counter telescope with three plastic scintillators, and (b) the detection system comprising two segmented plastic counters (Nagamine *et al.* 1995).

$$\Delta X = \frac{L}{l}\Delta x \ , \tag{5}$$

$$\Delta Y = \frac{L}{l}\Delta y \ . \tag{6}$$

### 3.2 Cerenkov light detector

In this case, the passage of the relativistic muon leaves a track of Cerenkov radiation in a selected gas or liquid which can be collected using a concave reflective mirror focused on an array of photomultipliers (Nagamine *et al.* 1995, Tanaka *et al.* 2003).

## 4. KERMAN COAL MINES

Kerman coal mines are situated in the east of central Iran at the distance between 50 and 220 km north west of Kerman. At these areas there are 9 coal ores that the Main Pabdana and the South Pabdana are active and important mines.

### 4.1 Main Pabdana coal mine

This coal mine is around 9 km long and 1.1 km wide, and its area is about 10 $km^2$. It consists of 14 layers of coal which are located at different depths and have different thicknesses. Their maximum thickness is of about 4 m, while for some others the thickness is about 2 m. The average density of coal and that of rock in this mine are about 1.3 and 2.65 $gr/cm^3$, respectively.

### 4.2 The South Pabdana mine

This mine like the Main Pabdana was explored from 1966 to 1977. Its area is about 2 $km^2$. It consists of 13 layers, each one having an average thickness between 1 and 3.15 m and the average density of 1.3 $gr/cm^3$.

## 5. MCNPX CODE

MCNPX is a general-purpose Fortran 90 Monte Carlo radiation transport code that transports more than 34 particle types including neutrons, protons, electrons, muons, *etc*. MCNPX is the product of computer codes that are used for modeling, the interaction of particle with matter, radiography, exploration of mine and oil, medical physics, and shielding. MCNPX has many capabilities that enhance physics, sources, tallies, and graphics (Pelowitz 2008) making the results of simulations more accurate. The simulation performed in the present study has many stages that are explained in the following.

### 5.1 Geometry

In this study geometry is defined as a cone that is 200 m high, parallel to the *z*-axis, and the opening angle of the cone is 45 degrees. This cone is inter-

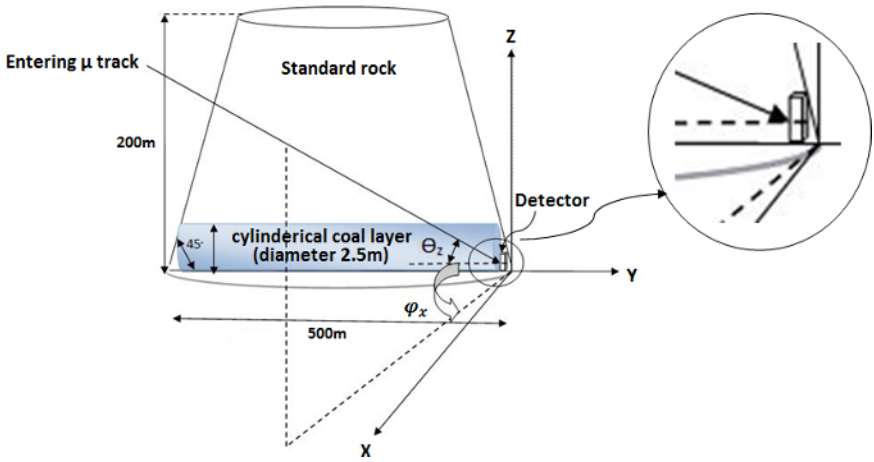


Fig. 4. Simplified model for mountain-detector and polar coordinate system.

sected by two planes parallel to *xy* plane at $z = 0$ and $z = 200$ m, respectively. Inside this cone, there is a cylindrical layer of coal with diameter of 2.5 m which is located at a depth of 200 m from the mountain top (cone) with a width of 500 m; the remaining volume of the cone is standard rock. The coal was replaced by carbon that is defined by $z/A = 0.5$, $z^2/A = 3$, $Z = 6$, and $\rho = 1.3$ gr/cm$^3$, where $Z$, $A$, and $\rho$ are the mean atomic number, the mean mass number, and density of the coal, respectively. A detection system with an area of about 1 m$^2$, perpendicular to the *y* axis, was located at the foot of cone. The geometry and detector that were used in MCNPX code have been shown in Fig. 4.

### 5.2 Source card

The source card of MCNPX code includes all necessary data for generation of particles (positive and negative muons) with energy spectrum at sea level. The energy distribution and life time of positive and negative muons are equal. But due to the fact that the primary cosmic rays, protons (95%) and He (5%), are essentially positively charged, the secondary component in the atmosphere has a positive charge excess (between 20 and 30%), too. These data with energies ranging from 1 to $10^3$ GeV were extracted using Eq. 1. In this equation, values of parameters $A_G$, $\gamma$, and $B_G$ are 0.14 (cm$^{-2}$sr$^{-1}$s$^{-1}$GeV$^{\gamma-1}$), 2.7, and 0.054, respectively. In addition, the values of critical energies of pions and kaons, $E^{cr}_{0,\pi}$ and $E^{cr}_{0,\kappa}$, are 115/1.1 and 850/1.1, respectively. Meanwhile, $E_0$ and $\theta$ are, respectively, the energy and zenith angle of incident cosmic ray muon. In this study, the source has been defined using general source and SDEF card for positive and negative muons separately. The main

control keywords for the SDEF card are position, type, and energy of the particle.

### 5.3 Tally (output)

The appropriate MCNPX tally that is of event-by-event nature and fits the study requirement is the PTRAC card. The main control keywords for the PTRAC card are: (i) output file, (ii) event type filter, and (iii) history filter. The PTRAC card of MCNPX code generates an output file which includes all the information needed for tracking the particle. This information includes: (a) the location ($x$, $y$, $z$) of the particle and its related cell and material number, and (b) the ID number, weight, event time, directional cosine, and energy of the particle. The PTRAC output files by positive and negative muons were equal.

### 5.4 Analysis of the output file (PTRAC)

The simulation of penetrating cosmic ray muons through the mountain by $12 \times 10^9$ muons was performed. The PTRAC output file is simply an ASCII file including the *xyz* (Cartesian coordinates), the *uvw* (directional cosine), the energy, and the event time of the particle (muon) that is being simulated (Zareie 2010 and Tajik *et al.* 2013). Some information that has been extracted from output file (PTRAC) is presented in Table 1. Data in Table 1 have been extracted from Fig. 1A in the Appendix.

Table 1

A portion of typical data which have been extracted from PTRAC output file

| Extracted information from PTRAC output file | | |
|---|---|---|
| Particle number: 374512 | Entrance to geometry | Exit of geometry |
| Location of particle $(x, y, z)$ [cm] | (–7207.9, –19849, 23378) | (45.868, –0.225, –95.656) |
| Directional cosine | (0.22962, 0.62851, –0.74314) | (0.2323, 0.6253, –0.7449) |
| Energy of particle [MeV] | 23000 | 20372 |
| Time of particle [$10^{-8}$ s] | 0.20534 | 105.56 |
| Cell number | 20 | 5 |
| Surface number | 50 | 5 |
| Material number | 1 | 2 |

Using the output file (PTRAC), the distance that muon travels through matter can be calculated. Practically, this distance is calculated by determination of the muon path through matter using the topographic data. Since the PTRAC file gives the directional cosines, the direction of the entrance of muon to detector and the number of muons as a function of $(\theta, \varphi)$, $N_\mu(\theta, \varphi)$,

in every interval of zenith and azimuthal angles with reference to a line perpendicular to the detector plane can be obtained.

## 6. CALCULATION OF THE DENSITY OF MATTER INSIDE THE MOUNTAIN

There are two possibilities to obtain a two dimensional profile of the density of matter inside the mountain that are mentioned as follows.

### 6.1 Using the energy loss of muon inside matter

A unique relationship exists between the range (in gr/cm$^3$) and energy of the penetrating cosmic ray muons (Eq. 3). Thus, for both the input and the output muon energy, the range can be calculated, and from the difference between these calculated ranges, the density length is determined (Darijani *et al.* 2014).

### 6.2 The use of relative flux of muons

The relative intensity of cosmic ray muons transmitted through matter with reference to those directly transmitted through the air is called the relative flux of muons that is introduced as Eq. 7.

$$n(\theta,\varphi)=\frac{N_{\mu}(\theta,\varphi)}{N_{0}(\theta,\varphi)}\ , \tag{7}$$

Equation 7 is a unique relation between density length ($X$) and the intensity of penetrating cosmic ray muons through matter. Figure 5 indicates

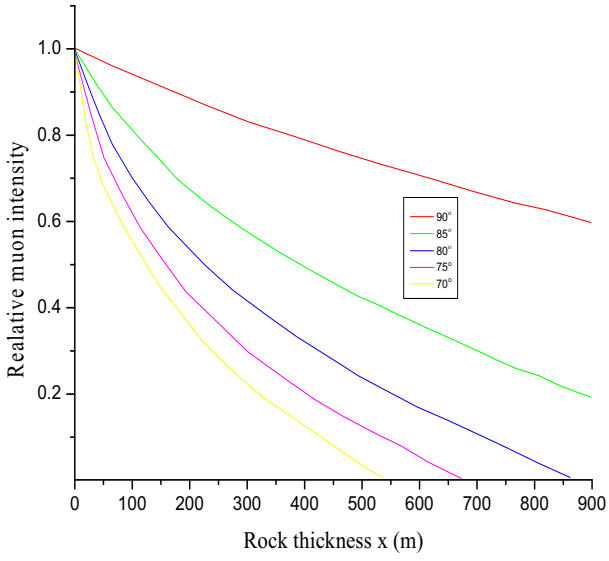


Fig. 5. Relative muon intensity *versus* rock thickness (Nagamine 2003).

relative intensity of muons as a function of standard rock thickness. So, for a substance with an unknown density length, the measurement of the muon flux penetrating through the substance with zenith and azimuthal angels uniquely determines its density length (in gr/cm$^3$) (Nagamine 2003). Using the density length, the substance density is determined.

## 7. RESULTS

The simulation was performed with $12 \times 10^9$ particles. Because of the symmetry, only $6 \times 10^9$ of particles are toward the geometry (Figs. 4 and 6), and the number of muons that were detected after passing through the geometry are about 45720. Figure 6 shows a two-dimensional picture of production and tracking of muons in the simulation code.

Since cosmic ray muons are constantly irradiating every substance on the Earth at rate of about 70 muon per m$^2$ per min, the performed simulation is equal naturally to the detection of muons for about 35 hours. The limitation of time is due to the limitation of the number of input particles ($2 \times 10^9$) in MCNPX code.

Because the size of the detector plane ($100 \times 100$ cm) is much smaller than the object of interest, the path of each muon can be determined in polar system, as shown in Fig. 4. In this figure the detector plane (*xz* plane) is

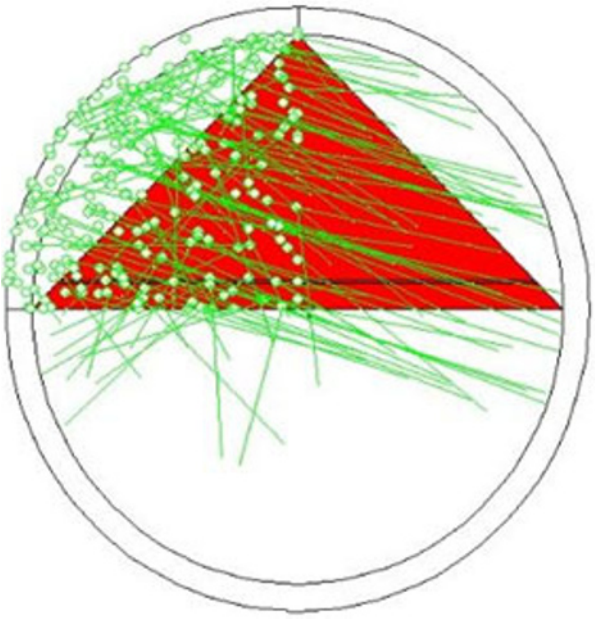

Fig. 6. Two dimensional *yz* profile of production and tracking of muons. The green dots show muon source points and green lines show muon tracks.

perpendicular to the $y$ axes, so the zenith and the azimuthal angles are obtained with reference to the $y$ axes. The angle between muon path and $z$ axis is $\theta$, and $\theta_z$ (zenith angle) is $90 - \theta$ that changes from 0 to 90 degrees (for horizontal and vertical entrance, respectively). The angle between muon path in $xy$ plan and $y$ axis is $\varphi_x$ (azimuthal angle) that changes from –90 to 90 degrees. These angles were divided into steps, $\Delta\theta$ and $\Delta\varphi$, and in every interval the number of muons was recorded. A portion of the typical file in which the number of muons has been recorded in every interval has been shown in Table 2.

Table 2

A portion of the counted muons in angle intervals

| The counted muons in angle intervals $\Delta\theta°$ and $\Delta\Phi°$ | | | | | | | | | | |
|---|---|---|---|---|---|---|---|---|---|---|
| $\Delta\theta°$ / $\Delta\Phi°$ | ··· | [0, 3) | [3, 6) | [6, 9) | [9, 12) | [12, 15) | [15, 18) | [18, 21) | [21, 24) | ··· |
| ··· | ··· | ··· | ··· | ··· | ··· | ··· | ··· | ··· | ··· | ··· |
| [–69, –66) | ··· | 2 | 14 | 7 | 12 | 11 | 7 | 8 | 0 | ··· |
| [–66, –63) | ··· | 0 | 7 | 4 | 7 | 21 | 18 | 5 | 7 | ··· |
| [–63, –60) | ··· | 3 | 12 | 2 | 14 | 16 | 13 | 1 | 9 | ··· |
| [–60, –57) | ··· | 7 | 4 | 13 | 12 | 29 | 19 | 2 | 13 | ··· |
| [–57, –54) | ··· | 9 | 3 | 15 | 13 | 18 | 31 | 0 | 15 | ··· |
| [–54, –51) | ··· | 12 | 1 | 2 | 10 | 15 | 49 | 13 | 2 | ··· |
| [–51, –48) | ··· | 14 | 4 | 9 | 6 | 22 | 18 | 8 | 2 | ··· |
| [–48, –45) | ··· | 6 | 2 | 3 | 10 | 15 | 18 | 16 | 9 | ··· |
| [–45, –42) | ··· | 11 | 6 | 5 | 9 | 6 | 23 | 25 | 8 | ··· |
| ··· | ··· | ··· | ··· | ··· | ··· | ··· | ··· | ··· | ··· | ··· |

Using the output file (PTRAC), two dimensional profiles of the number of muons and density of matter that muons penetrate through it were plotted and have been shown in Figs. 7-10. Figures 7 and 8 indicate the two dimensional profiles of the number of penetrating particles through the mountain without and with a layer of coal, respectively. The two dimensional profiles of the density of the mountain without and with a layer of coal, that muons penetrate through it, have been shown in Figs. 9 and 10. A comparison of Figs. 9, 10a, and 10b shows the existence of the region with lower density (the layer of coal) in the mountain. Figure 10 shows that around $\varphi_x = 0$ (parallel to the $y$ axis) and for $\theta_z$ between 0 and 5 degrees, there is a matter that its density is less than the density of the standard rock. By this approach, the layers with minimum thickness of about 2.5 m are identified.

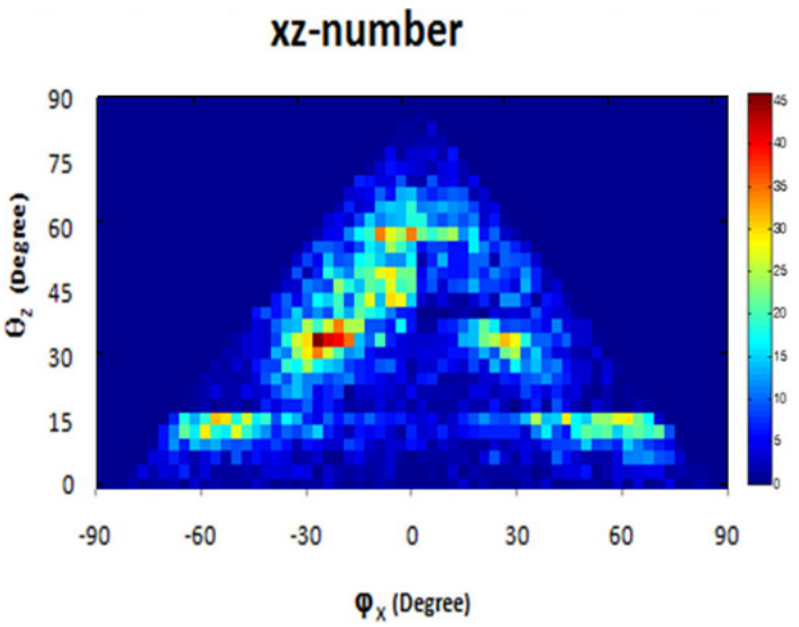


Fig. 7. Two dimensional profile from number of particles in the *xz* plan without any layer of coal.

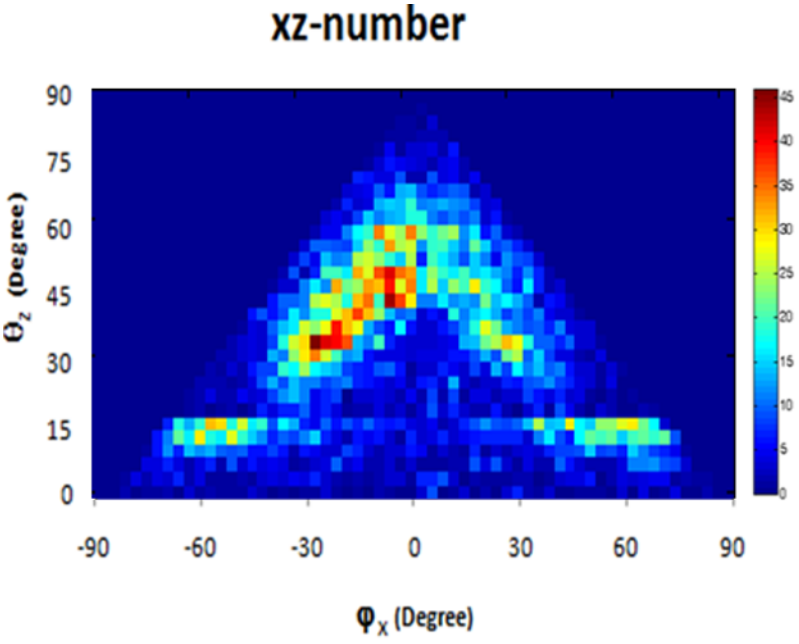


Fig. 8. Two dimensional profile from number of particles in the *xz* plan with a layer of coal.

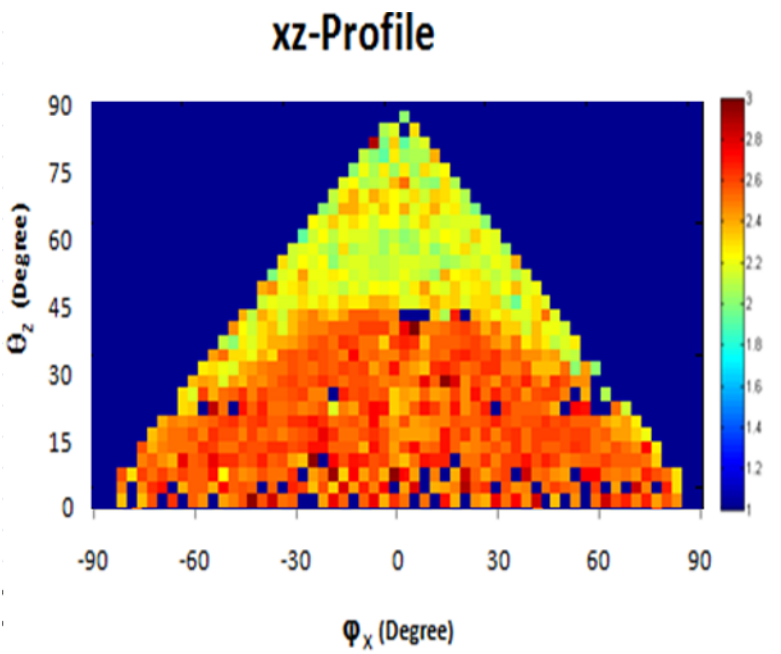


Fig. 9. Two dimensional profile from density of mountain in the *xz* plan without any layer of coal.

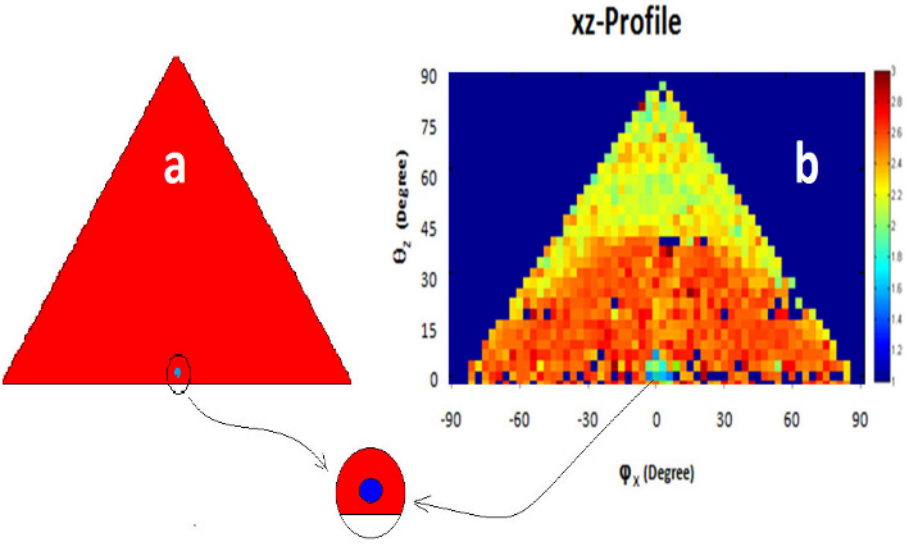


Fig. 10: (a) Two dimensional *xz* profile of geometry that the code provides (the blue circle shows the *xz* profile of cylindrical coal layer), and (b) two dimensional profile from density of mountain in *xz* plan with a layer of coal due to MCNPX simulation results.

## 8. CONCLUSION

Very high energy muons are most suitable for measuring the density profile of a large scale substance like a mountain. These muons also are used for exploration of mines. The spatial resolution to determine the internal intensity of a mountain depends on not only the spatial resolution of detector but also the distance of the detector from the center of mountain. In this study, the detector was placed inside the mountain (Fig. 4) that increased the spatial resolution and decreased the interest area for imaging. Using many detectors at different altitudes of a mountain, radiography can be done from more parts of mountain, the spatial resolution can be increased, and the exact location of coal layers in a mountain can be determined. Figures 7 to 10 are the results of using one detector.

# Appendix

### Interpretation of data in PTRAC output file

PTRAC output file is an ASCII file which includes all information required for tracking a particle. This information includes: (a) the location ($x$, $y$, $z$) of the particle and its related cell, and material number (b) the ID number , weight, event time, directional cosine, and energy of the particle. A portion of typical PTRAC output has been shown in Fig. 1A.

```
                                    374512    3000      30       5
                          3000       2        5       129      20       0       1
-0.72079E+04 -0.19849E+05 0.23378E+05 0.22962E+00 0.62851E+00 -0.74314E+00 0.23000E+05 0.10000E+01
                                                0.20534E+00
                          3000       3        1        94      10       1       2
-0.13960E+03 -0.50173E+03 0.50133E+03 0.22962E+00 0.62851E+00 -0.74314E+00 0.23000E+05 0.10000E+01
                                                0.10289E+03
                          3000       4        7       139     101       2       5
-0.85758E+02 -0.35536E+03 0.32795E+03 0.23029E+00 0.62611E+00 -0.74495E+00 0.21862E+05 0.10000E+01
                                                0.10367E+03
                          3000       5       23        51      10       1       6
-0.83934E+02 -0.35040E+03 0.32205E+03 0.23073E+00 0.62580E+00 -0.74508E+00 0.21836E+05 0.10000E+01
                                                0.10369E+03
                          3000       6       16        20      20       0      10
-0.28438E+02 -0.20017E+03 0.14257E+03 0.23238E+00 0.62530E+00 -0.74499E+00 0.20372E+05 0.10000E+01
                                                0.10450E+03
                          3000       7       12       138      30       0      11
-0.10981E+02 -0.15320E+03 0.86600E+02 0.23238E+00 0.62530E+00 -0.74499E+00 0.20372E+05 0.10000E+01
                                                0.10475E+03
                          3000       8       11        51      20       0      12
0.87891E+01 -0.10000E+03 0.23218E+02 0.23238E+00 0.62530E+00 -0.74499E+00 0.20372E+05 0.10000E+01
                                                0.10503E+03
                          9000       9        5        51      50       0      13
0.45868E+02 -0.22508E+00 -0.95656E+02 0.23238E+00 0.62530E+00 -0.74499E+00 0.20372E+05 0.10000E+01
                                                0.10556E+03
                                    706380    3000      30       5
```

Fig. 1A. A portion of typical PTRAC output.

The first number of the first line (*i.e*., 374512) is an ID number for the particle, number 3000 indicates the entrance of the particle to the geometry, number 30 is the number of the cell that has been filtered, and number 5 determines the entrance surface of the source particles in the geometry. In the second line, numbers 5 and 20 show that the particle has been entered from surface 5 into cell 20, number 0 is the material number, number 2 is the line number, and number 129 is the angle between the particle path and the line perpendicular to the surface 5. In the third line, the first six numbers are Cartesian coordinates ($x$, $y$, $z$) and direction cosines ($u$, $v$, $w$) of the entered particle, respectively. Numbers 0.23000E+05, 0.10000E+01, and 0.20534E+00 in the third line are the energy, weight, and event time of the particle, respectively. In line 16, number 9000 characterizes the exit of the particle from the geometry.

## References

Allkofer, O.C., K. Carstensen, G. Bella, W.D. Dau, H. Jokisch, G. Klemke, Y. Oren, and R.C. Uhr (1981), Muon spectra from DEIS up to 7 TeV. **In:** *Proc. 17th Int. Cosmic Ray Conference, 13-25 July 1981, Paris, France*, Vol. 10, 321-324.

Alvarez, L.W., J.A. Anderson, F. El Bedwei, J. Burkhard, A. Fakhry, A. Girgis, A. Goneid, F. Hassan, D. Iverson, G. Lynch, Z. Miligy, A.H. Moussa, M. Sharkawi, and L. Yazolino (1970), Search for hidden chambers in the pyramids, *Science* **167**, 3919, 832-839, DOI: 10.1126/science.167.3919.832.

Bektasoglu, M., H. Arslan, and D. Stanca (2012), Simulations of muon flux in slanic salt mine, *Adv. High Energy Phys.* **2012**, 751762, DOI: 10.1155/2012/751762.

Bugaev, E.V., Y.D. Kotov, and I.L. Rosental (1970), *Cosmic Muons and Neutrinos,* Atomizdat, Moscow, 320 pp.

Darijani, R., A. Negarestani, M.R. Rezaie, J. Fatami, and A. Akhond (2014), Formulation of muon range 0-100 TeV and transmission through lead, *Indian J. Pure Appl. Phys*. **52**, 1, 7-12.

Gaisser, T.K. (1990), *Cosmic Rays and Particle Physics*, Cambridge University Press, Cambridge.

Lesparre, N., D. Gibert, J. Marteau, Y. Déclais, D. Carbone, and E. Galichet (2010), Geophysical muon imaging: feasibility and limits, *Geophys. J. Int*. **183**, 3, 1348-1361, DOI: 10.1111/j.1365-246X.2010.04790.x.

Malmqvist, L., G. Jönsson, K. Kristiansson, and L. Jacobsson (1979), Theoretical studies of in-situ rock density determinations using underground cosmic-

ray muon intensity measurements with application in mining geophysics, *Geophysics* **44**, 9, 1549-1569, DOI: 10.1190/1.1441026.

Nagamine, K. (2003), *Introductory Muon Science*, Cambridge University Press, Cambridge.

Nagamine, K., M. Iwasaki, K. Shimomura, and K. Ishida (1995), Method of probing inner-structure of geophysical substance with the horizontal cosmic-ray muons and possible application to volcanic eruption prediction, *Nucl. Instrum. Meth. Phys. Res. A* **356**, 2-3, 585-595, DOI: 10.1016/0168-9002(94) 01169-9.

Pelowitz, D.B. (ed.) (2008), MCNPX user's manual, version 2.6.0, LA-CP-07-1743, Los Alamos National Laboratory, Los Alamos, USA.

Tajik, M., N. Ghal-Eh, G.R. Etaati, and H. Afarideh (2013), Modeling NE213 scintillator response to neutrons using an MCNPX-PHOTRACK hybrid code, *Nucl. Instrum. Meth. Phys. Res. A* **704**, 104-110, DOI: 10.1016/j.nima. 2012.12.001.

Tanaka, H., K. Nagamine, N. Kawamura, S.N. Nakamura, K. Ishida, and K. Shimomura (2003), Development of a two-fold segmented detection system for near horizontally cosmic-ray muons to probe the internal structure of a volcano, *Nucl. Instrum. Meth. Phys. Res. A* **507**, 3, 657-669, DOI: 10.1016/ S0168-9002(03)01372-X.

Tanaka, H.K.M., T. Nakano, S. Takahashi, J. Yoshida, and K. Niwa (2007), Development of an emulsion imaging system for cosmic-ray muon radiography to explore the internal structure of volcano, Mt. Asama, *Nucl. Instrum. Meth. Phys. Res. A* **575**, 3, 489-497, DOI: 10.1016/j.nima.2007.02.104.

Thompson, M.G., and M.R. Whalley (1975), The production spectra of the parents of vertical cosmic ray muons, *J. Phys. G* **1**, 48-50, DOI: 10.1088/0305-4616/1/6/004.

Zareie, S.H. (2010), A Monte Carlo simulation of the Compton camera, M.Sc. Thesis, San Diego State University, San Diego, USA.

Received 19 August 2014
Received in revised form 25 April 2015
Accepted 2 June 2015

DE GRUYTER OPEN

**Acta Geophysica**
vol. 64, no. 4, Aug. 2016, pp. 1051-1063
DOI: 10.1515/acgeo-2016-0033

# Practical Implementation of Prestack Kirchhoff Time Migration on a General Purpose Graphics Processing Unit

Guofeng LIU[1,2] and Chun LI[1]

[1]Key Laboratory of Geo-detection, China University of Geosciences, Ministry of Education, Beijing, China; e-mail: liugf@cugb.edu.cn

[2]State Key Laboratory of Continental Tectonics and Dynamics, Institute of Geology, Chinese Academy of Geological Sciences, Beijing, China

A b s t r a c t

In this study, we present a practical implementation of prestack Kirchhoff time migration (PSTM) on a general purpose graphic processing unit. First, we consider the three main optimizations of the PSTM GPU code, *i.e.*, designing a configuration based on a reasonable execution, using the texture memory for velocity interpolation, and the application of an intrinsic function in device code. This approach can achieve a speedup of nearly 45 times on a NVIDIA GTX 680 GPU compared with CPU code when a larger imaging space is used, where the PSTM output is a common reflection point that is gathered as $I[nx][ny][nh][nt]$ in matrix format. However, this method requires more memory space so the limited imaging space cannot fully exploit the GPU sources. To overcome this problem, we designed a PSTM scheme with multi-GPUs for imaging different seismic data on different GPUs using an offset value. This process can achieve the peak speedup of GPU PSTM code and it greatly increases the efficiency of the calculations, but without changing the imaging result.

**Key words:** GPGPU, offset splitting, parallelization, PSTM, texture memory.

Ownership: Institute of Geophysics, Polish Academy of Sciences;
© 2016 Liu and Li. This is an open access article distributed under the Creative Commons Attribution-NonCommercial-NoDerivs license, http://creativecommons.org/licenses/by-nc-nd/3.0/.

## 1. INTRODUCTION

Seismic exploration is an important area of geophysical research, which aims at determining subsurface structures to detect where oil and gas can be found and recovered. Prestack Kirchhoff time migration (PSTM) is one of the most popular migration techniques used for seismic data processing because of its simplicity, efficiency, feasibility, and target-orientated properties (Bevc 1997). However, the practical application of PSTM to tasks during large 3D surveys is still computationally intensive. To accelerate the processing of migration, the parallel processing of prestack time migration has been implemented routinely on distributed parallel computers (Schleicher and Copeland 1993, Chen *et al.* 1993), as well as on PC clusters (Morton *et al.* 1999, Hellman 2000, Dai 2005). In recent years, many other devices have also been used to accelerate PSTM such as FPGAs (He *et al.* 2005).

Recently, programmable graphics processor units (GPUs) have evolved into a computing workhorse. GPUs possess multiple cores with a very high memory bandwidth, which makes them useful resources for graphics and non-graphics processing (NVIDIA 2012). Potentially, GPUs can achieve hundreds or even thousands of GFLOPS, whereas general CPUs are only capable of dozens of GFLOPS at present. NVIDIA's computed unified device architecture (CUDA) provides a C-like programming model for exploiting the massively parallel processing power of NVIDIA's GPU (NVIDIA 2013), and it is now employed widely for many parallel computation applications (Lu *et al.* 2013, Capuzzo-Dolcetta and Spera 2013, Westphal *et al.* 2014). Some studies have also used NVIDIA GPUs to accelerate PSTM. In particular, Liu *et al.* (2009) discussed the possibility of parallel computation with NVIDIA GPUs. Shi *et al.* (2011) proposed a method for accelerating PSTM on GPUs by splitting the PSTM procedure into four consequence kernels according to the GPU memory limitations, as well as considering the floating point error problem, which may lead to differences when comparing PSTM with CPU computations.

In this study, we propose the possible application of computing with PSTM on GPUs by combining the characteristics of GPU and PSTM algorithms. First, we consider three key optimization points, *i.e.*, designing a configuration that achieves a reasonable execution, using texture memory for velocity interpolation, and employing faster intrinsic functions. After analyzing the efficiency of this method, we also propose a multi-GPU scheme that employs a splitting offset to keep the GPU busy. Our test results demonstrate that the proposed method achieves a great speedup.

## 2. REVIEW OF PSTM

PSTM (Fig. 1) uses seismic traces that originate from a source $S$, which are received at $R$ as input data. The variable, $h$, is an offset of the distance be-

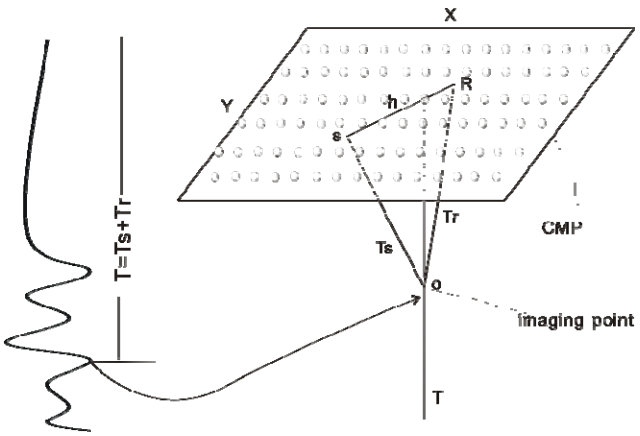


Fig. 1. PSTM scheme.

tween the source and receiver pair, where the 3D imaging space is a uniform common midpoint (CMP) on the ground surface and an imaging point in the depth direction. However, it expresses the depth using a two-way travel time, *T*. For an imaging point, *O*, in the *T* direction, the imaging value for a certain input trace is the amplitude of the input trace at time *t*, *i.e.*, the seismic wave travel time from *S* to *O* and then back to the surface for *O* to *R*. The travel time can be calculated by the straight ray equation:

$$T^2\left(x,y,t_0\right)=t_0^2(x,y)+\frac{x^2}{v^2\left(x,y,t_0\right)}\ , \tag{1}$$

where *T* is the two-way travel time, $t_0$ is the vertical time from the surface to the imaging point, *x* is the distance from the source or receiver to the imaging CMP, and *v* is the root squared mean velocity of the imaging point, which is obtained by the velocity analysis method in seismic processing and it is interpolated to all of the imaging points.

The output of the PSTM for an imaging CMP is called a common reflection gather (CRP), which is used to update *v* in Eq. 1 until we obtain a better image of the subsurface. In Fig. 2 panel (a) is the CRP of a CMP. Stacking all of the traces in this gather can yield the imaging trace of the CMP, while combining all of the CMPs produces the final imaging profile (Fig. 2c), which is a 2D seismic PSTM imaging profile that depicts the geological structure of the subsurface.

In addition to this PSTM kernel, all input seismic traces require an anti-aliasing process (Lumley *et al.* 1993) and an amplitude-preserving weight (Sun and Martinez 2002). The pseudo-code for Algorithm 1 (Table 1) shows how one seismic trace is processed for PSTM imaging.

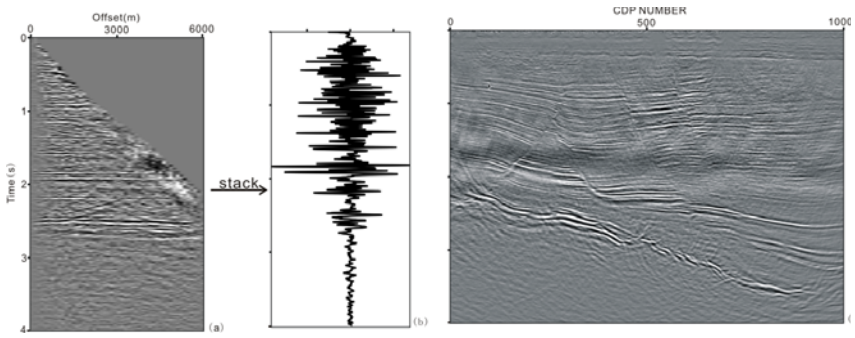


Fig. 2: (a) CRP gather of a midpoint, (b) imaging trace of a midpoint after stacking the CRP gather, and (c) final imaging section obtained by PSTM.

Table 1

Algorithm 1: PKTM kernel

| |
|---|
| Input: velocity model $v[ix][iy][it]$<br>seismic data trace $[ih][it]$ source at $S(x,y)$ and receiver at $R(x,y)$<br>other migration parameters: time interval $dt$, *etc*.<br>Output: common reflection gather $I[ix][iy][ih][it]$ |
| Anti-aliasing processing for input trace;<br>for ($ix = 0$; $ix < nx$; $ix$++) // CMP in $x$ direction<br>for ($iy = 0$; $iy < ny$; $iy$++) // CMP in $y$ direction<br>for ($it = 0$; $it < nt$; $it$++)<br>{ //imaging point in $t$ direction<br>calculate the travel time $t$ with Eq. 1;<br>$I[ix][iy][ih][it]$+ = weight * trace $[t/dt]$; } |

The conventional approach implements parallel processing of Algorithm 1 on a low-cost PC cluster using the message passing interface, where each node calculates all of the imaging points that belong to the same CMPs and they share the same input trace each time. The processing time is longer than the communication time, so the time elapsed is inversely proportional to the number of CPUs, and thus using more CPU nodes can reduce the time elapsed and improve the efficiency (Dai 2005). In this study, we propose a complete GPU solution for PSTM.

## 3. PARALLELIZATION OF PSTM ON GPU

### 3.1 Hardware and real seismic field data

We used a 3.07 MHz Intel (R) core (TM) i7 CPU with 24 GB of DDR3 memory, which was connected to an NVIDIA GTX 680 GPU, where the

main system comprised 2 GB of global memory, eight multiprocessors (MP) and 192 CUDA cores per MP, the total number of registers available per block was 65 536, the maximum number of threads per MP was 1024, and we used CUDA version 5.0. The field seismic data used for testing comprised a 20 GB subse+t of a real 3D dataset with 1 681 920 traces, where each trace had 3000 samples with intervals of 2 ms. The 3D imaging volume had 3000 imaging points with a 2 ms time interval for a CMP. The CMP number in the $X$ direction (the crossline) ranged from 0 to 1000, and the CMP number in the $Y$ direction (the inline) was defined as necessary.

### 3.2 Profiling the PSTM CPU code

Profiling the PSTM CPU code can help to find hotspots and bottlenecks. We used the GUN tool gprof to generate the profile of the seismic field data where the imaging space was equal to 1000 CMPs in the crossline direction, with four inlines. The profiling results (Fig. 3) showed that the PSTM kernel completed nearly 98% of the work with a relatively small amount of code. This value increased when the imaging space was larger. Based on Amdahl's law (Amdahl 1967), the maximum speedup, $S$, of PSTM is:

$$S = \frac{1}{(1-P) + \frac{P}{N}}, \tag{2}$$

where $P$ is the fraction of the total serial execution time required by the portion of code that can be parallelized and $N$ is the number of processors on which the code runs in parallel. When 97% of the running time for PSTM was parallelized, the maximum speedup was > 50, thereby demonstrating that GPU parallelization is a worthwhile procedure.

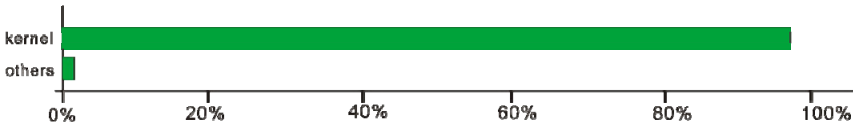


Fig. 3. PSTM kernel runtime percentage for a specific imaging space.

### 3.3 Parallelization strategy for PSTM on a GPU

According to Algorithm 1, the processing of each imaging point is independent. Thus, we can parallelize the three loops, where the CMPs in the $X$ and $Y$ directions can be computed in parallel by blocks in the grid. The CMPs in the $X$ direction are calculated by blockidx.x and the CMPs in the $Y$ direction are calculated by blockidx.y. The imaging point of each CMP is parallelized by threads for each block, where the thread structure of the PSTM is shown in Fig. 4.

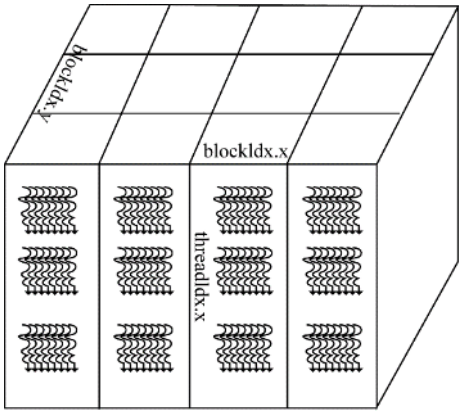


Fig. 4. Thread structure of PSTM.

One approach that improves the GPU performance is keeping the multiprocessors on the device as busy as possible, which has two main features. First, when choosing the number of blocks per grid, the grid size should be larger than the number of multiprocessors so all of the multiprocessors have at least one block to execute. Furthermore, there should be multiple active blocks per multiprocessor so the blocks can keep the hardware busy. This condition can be fulfilled easily, because the number of imaging CMPs in the $X$ and $Y$ directions is much greater than the number of device multiprocessors. Second, when choosing the block size, it is important to remember that multiple concurrent blocks can reside on the multiprocessor, so the occupancy (the ratio of the number of active warps per multiprocessor relative to the maximum number of possible active warps) is not determined by the block size alone. In particular, a large block size does not imply a higher occupancy. For example, it may lead to pressure on a number of registers per multiprocessors and shared memory usage. In the PSTM kernel, the main pressure is the number of registers, which is 31 in the PSTM kernel. If the block size is 128 threads, then based on the GTX 680's maximum register number per multiprocessor, there are 15 active blocks, which is greater than the eight maximum active blocks calculated using the maximum threads per block of 1024; therefore, we can achieve an occupancy of > 99%. According to the NVIDIA programming guide, many factors are involved in selecting the block size and thus some experimentation is required. Therefore, we provide the block size as a program parameter in the PSTM, which is decided by the user. Furthermore, we can apply –maxrregcount at the compilation time to balance the usage of registers and local memory, which is more expensive to access. Figure 5 shows the results of an experiment using GTX

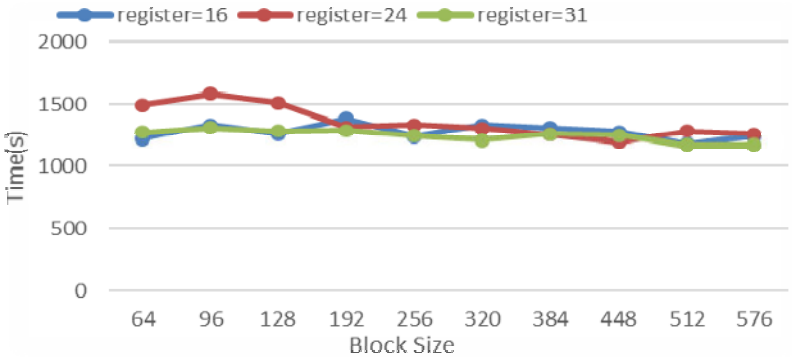


Fig. 5. Comparison of the computing time with different threads and registers.

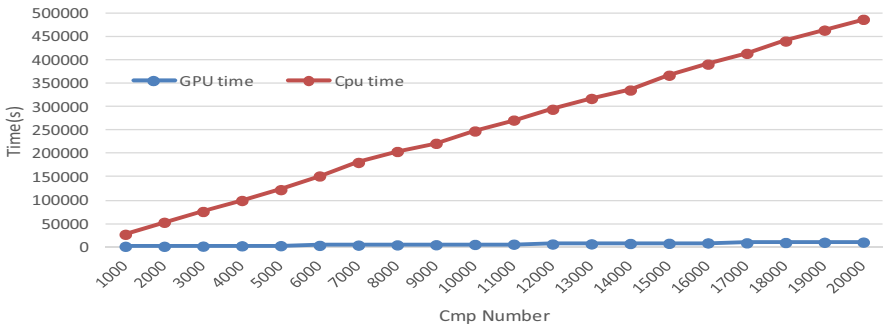


Fig. 6. Comparison of the GPU and CPU computing times with different imaging spaces.

680 with an imaging space of 1000 CMPs for the seismic data mentioned above, where we employed 16, 24, and 31 registers of PSTM elapsed time *versus* different thread numbers per block. This first test was required to obtain the most efficient register and thread pairs.

In PSTM, the root squared mean velocity at the imaging point $t_0$ plays an important role in the imaging accuracy. Thus, a velocity analysis is performed with sparse CMP points and some other points such as the red dots shown in Fig. 6. Traditionally, during the imaging process, the discrete velocity must be interpolated first for all of the imaging points and then passed to the GPU using global memory, which is expensive to access because it needs a relatively large memory space. In our method, we use texture to perform the velocity model transfer and the read-only texture memory space is cached. Therefore, a texture fetch costs only one device memory read for a cache miss; otherwise, it costs one read from the texture cache. Furthermore, threads in the same warp that read texture addresses located close together

will obtain the best performance. Using a function, such as tex3D(), can also provide other capabilities, such as interpolation, and thus based on this characteristic, we can use the texture memory directly for velocity interpolation. This is less expensive to access than global memory and it can save more memory space for the imaging results.

The method used to execute instructions often permits low-level optimizations, which can be useful, especially in code that is run frequently, such as the PSTM kernel. This may involve trading precision for speed when it does not affect the end result, such as using intrinsic instead of regular functions, and including runtime math operations with prepended underscores, *e.g.*, __sinf(),__fmul_rz(). These types of function are mapped directly to the hardware level. They are faster but they have somewhat lower accuracy. When the imaging space of PSTM is 1000, there are 128 threads for a block. We found that if we do not use the intrinsic functions, the number of registers increases to 55 without increasing any variables, which is also a problem that affects the efficiency.

Many possible optimizations can be considered, such as having all read-only input data using the texture memory and employing a constant memory for the transparency function parameters of the device kernel. The final aim is to maximize the use of hardware by maximizing bandwidth and keeping the multiprocessors on the device as busy as possible. Following GPU parallelization, the PSTM kernel can be summarized according to the pseudo-code of Algorithm 2 (Table 2).

Table 2

Algorithm 2: GPU PTKM kernel

| |
|---|
| Input: seismic data trace $[ih][it]$ source at $S(x,y)$ and receiver at $R(x,y)$<br>other migration parameters: time interval $dt$, *etc*.<br>Output: common reflection gather $I[ix][iy][ih][it]$ |
| Anti-aliasing processing for input trace;<br>$ix$ = blockIdx.x // CMP in $x$ direction<br>$iy$ = blockIdx.y // CMP in $y$ direction<br>for ($it$ = threadidx.x; $it < nt$; $it = it$+blockDim.x){ //imaging point in $t$ direction<br>$v$ = tex3D(vel_tex, $it$, blockidx.x, blockidx,y);<br>calculate the travel time $t$ with Eq. 1;<br>$I[ix][iy][ih][it]$+ = weight * trace $[t/dt]$; } |

The final GPU PSTM codes were tested with real seismic field data. The number of CMPs in the crossline direction was 1000 and the CMPs in the inline direction were selected from 1 to 20, where each CMP had 3000 imag-

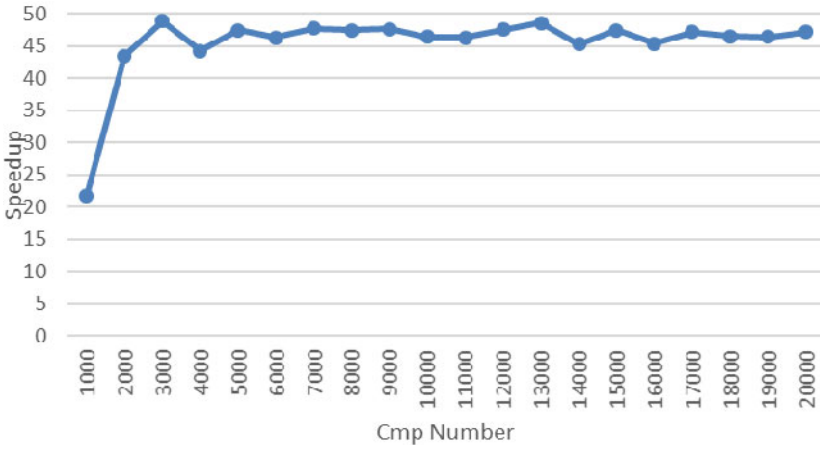


Fig. 7. Speedup in the time elapsed on a GPU compared with one thread on a CPU with different image spaces.

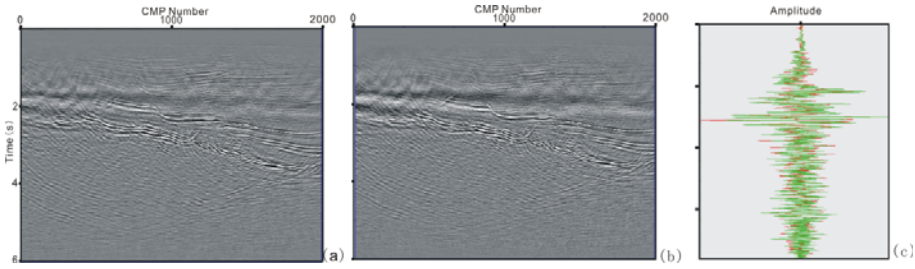


Fig. 8. PSTM section based on real data: (a) migrated section with CPU; (b) migrated section with GPU, and (c) difference in a migrated trace.

ing points. The calculation times obtained with the GPU and CPU are shown in Fig. 6. Figure 7 shows the speedup of the GPU compared with the CPU code where only one thread was used on 3.07 GHz intel i7 processor with different imaging spaces. These two figures demonstrate that the GPU code achieved a speedup of 45 times compared with that of the CPU code, and a larger imaging space reduced the time required significantly.

Figure 8 shows the inline migration results with 1000 CMPs, where panel (a) depicts the CPU migrated result and panel (b) illustrates the GPU migrated result, where it is difficult to see any difference between the two sections. Panel (c) shows the difference in one trace with the same phase and amplitude trend, which may be due to the floating point errors during GPU computation and different velocity interpolation methods, although the results are acceptable in each case.

## 4. MULTI-GPU SCHEME FOR PSTM

The output of the PSTM is a CRP gather in the form of the matrix *I*[*nx*]*ny*][nh][*nt*], where *nx* and *ny* are the surface CMP numbers in the cross-line and sub-line directions, respectively, and *nt* are the imaging points in the depth direction. The final imaging result includes another dimension, *nh*, which is related to the input trace offset. In the imaging parameters, we usually define the offset bin with a minimum and maximum offset, and an offset interval. Therefore, if the input trace is *h*, then *ih* is (*h*-minimum offset)/(offset interval).

The GPU global memory is limited, where the GTX 680 has 2 GB, so it must be split onto multi-GPUs when the imaging space is larger, as shown in Fig. 9.

For the seismic field data tested in this study, if $nx = 1000$, $nt = 3000$, and the offset number = 48, then the GTX 680 can calculate the sub-line number for $ny = 4$ only once with each GPU. As shown in Figs. 7 and 8, it is better to image a larger space to obtain a higher efficiency. Therefore, we propose an alternative method to maximize the GPU efficiency using multi-GPUs. Before image processing, we split the seismic data onto different GPU nodes according to the offset range. When imaging, assuming that *nh* is equal to the GPU node number, the inline *ny* of the imaging space is more than 150 and different GPU nodes are calculated using different offset parts of the same sub-line. After each node finishes imaging, all of the imaging results are collected from the different GPU nodes and the traces are sorted for the CRP gather. Figure 10 shows a flowchart of our proposed method.

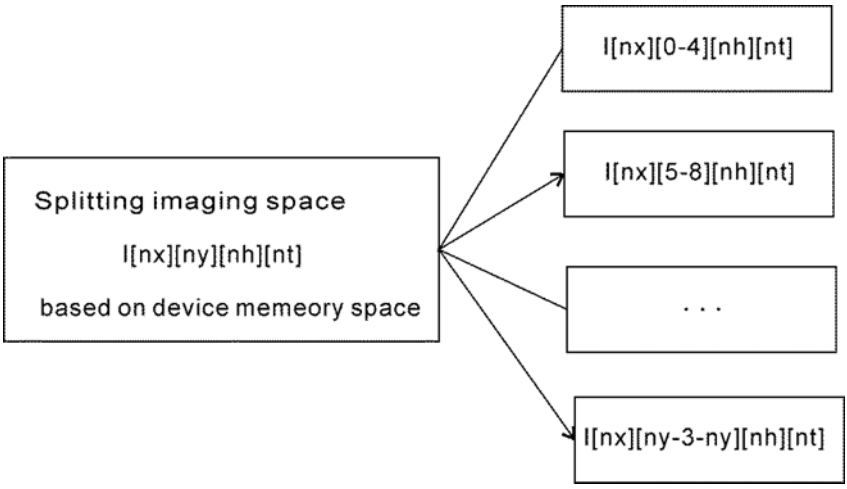


Fig. 9. Splitting the imaging space onto different GPU nodes.

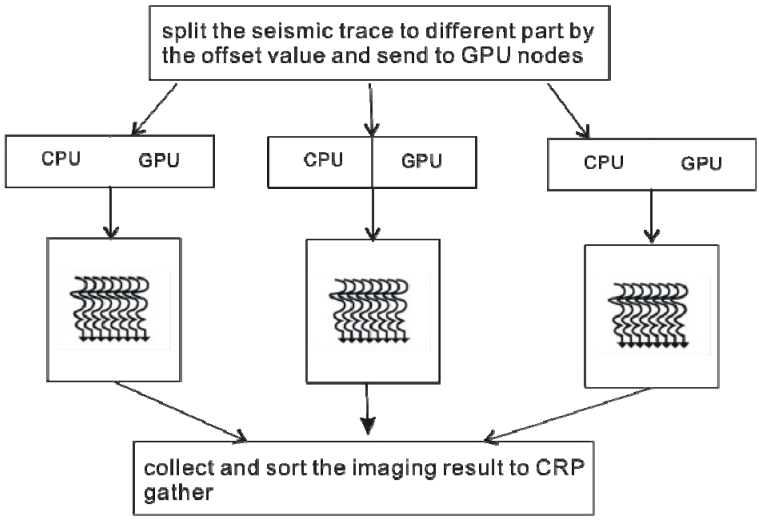


Fig. 10. Flowchart of the proposed multi-GPU scheme.

In large industrial 3D surveys, the offsets of the input data often lack average distributions in a similar manner to joint processing for different surveys, so the following steps are recommend: (i) sort the input trace into the CMP offset order; (ii) split the data into several parts with the same trace numbers according to the number of GPU nodes and send each of them to the GPU nodes; (iii) compute the minimum and maximum offset for the data on each GPU node and set the output offset bins; (iv) migrate all of the imaging space, where several steps may be required depending on the GPU memory and offset number; (v) collect the migrated data from each GPU node and sort them into the CMP offset gather, before stacking the same offset for a CMP gather, thereby completing the migration process and the output is the CRP gather.

## 5. CONCLUSIONS

In this study, we proposed the practical implementation of PSTM on a GPU. We considered three main optimizations, *i.e.*, designing the configuration for execution to maximize the occupancy and make the device as busy as possible, using texture memory for velocity transparency and interpolation to increase the device bandwidth, and employing faster intrinsic functions for the device kernel. We tested the code with 20 GB of real 3D seismic data on an NVIDIA GTX 680 card, which obtained speedups greater than 45 times compared with the CPU. Furthermore, more time was saved when the imaging space was larger. To fully exploit GPUs, we recommend a scheme that

splits the offset onto different GPU nodes, before collecting and sorting to obtain the CRP gather after completing the imaging process. This scheme can be used for data imaging with large volumes. Many possible optimizations can be considered, which requires a large amount of work. However, optimization is easier due to the development of appropriate hardware, and thus the PSTM efficiency can be improved greatly.

Acknowledgments. We would like to thank Dr. Michal Malinowski for his comments and suggestions, which improved this paper significantly, and we also thank the associate editor for his consideration. This study was supported by the NSFC (grant No. 41104083), Beijing Higher Education Young Elite Teacher Project, and Fundamental Research Funds for the Central Universities.

## References

Amdahl, G. (1967), Validity of the single processor approach to achieving large-scale computing capabilities. **In:** *Proc. AFIPS '67 (Spring), 18-20 April 1967*, American Federation Information Processing Society, Vol. 30, 483-485, DOI: 10.1145/1465482.1465560.

Bevc, D. (1997), Imaging complex structures with semirecursive Kirchhoff migration, *Geophysics* **62**, 2, 577-588, DOI: 10.1190/1.1444167.

Capuzzo-Dolcetta, R., and M. Spera (2013), A performance comparison of different graphics processing units running direct N-body simulations, *Comput. Phys. Commun.* **184**, 11, 2528-2539, DOI: 10.1016/j.cpc.2013.07.005.

Chen, T., and D. Hale (1993), Network parallel 3-D phase-shift migration. **In:** *Expanded Abstracts of the 63rd SEG Annual Meeting*, Society of Exploration Geophysicists, Tulsa, USA, 177-180, DOI: 10.1190/1.1822430.

Dai, H. (2005), Parallel processing of prestack Kirchhoff time migration on a PC cluster, *Comput. Geosci*. **31**, 7, 891-899, DOI: 10.1016/j.cageo.2005.02.002.

He, C., C. Sun, M. Lu, and W. Zhao (2005), Prestack Kirchhoff time migration on high performance reconfigurable computing platform. **In:** *Expanded Abstracts of the 75th Annual Meeting of the Society of Exploration Geophysicists, 6-11 November, Houston, USA*, 1902-1905, DOI: 10.1190/1.2148076.

Hellman, K.J. (2000), Distributed memory prestack Kirchhoff time migration: Parallelization and scalability. **In:** *Expanded Abstracts of the 70th Annual Meeting of the Society of Exploration Geophysicists, 6-11 August 2000, Calgary, Canada*, 981-983, DOI: 10.1190/1.1816242.

Liu, G.F., H. Liu, B. Li, Q. Liu, and X.L. Tong (2009), Method of prestack time migration of seismic data of mountainous regions and its GPU implementation, *Chin. J. Geophys.* **52**, 6, 1381-1388, DOI: 10.1002/cjg2.1463.

Lu, F., J. Song, W. Lin, Y. Pang, K. Ren, and P. Shi (2013), Efficient utilization of launched threads on GPUs: The spherical harmonic transform as a case study, *Comput. Phys. Commun.* **184**, 11, 2494-2502, DOI: 10.1016/j.cpc.2013.06.019.

Lumley, D.E., J.F. Claerbout, and D. Bevc (1993), Anti-aliased Kirchhoff 3-D migration: a salt intrusion example. **In:** *Expanded Abstracts of the Annual SEG Summer Research Workshop on 3-D Seismology*, Society of Exploration Geophysicists, 115-123.

Morton, S.A., J.R. Davis, H.L. Duffey, G.L. Donathan, and S.N. Checkles (1999), Seismic processing on commodity supercomputers. **In:** *Expanded Abstracts of the 69th SEG Annual Meeting, 31 October – 5 November 1999, Houston, USA*, Society of Exploration Geophysicists, Tulsa, USA, 956-958, DOI: 10.1190/1.1821269.

NVIDIA (2012), CUDA compute unified device architecture programming guide (v 5.0), NVIDIA Co., Santa Clara, USA.

NVIDIA (2013), GPU computing developer homepage, NVIDIA Co., Santa Clara, USA, available from: http://developer.nvidia.com/object/gpucomputing.html.

Schleicher, K., and J. Copeland (1993), Parallel one-pass 3-D migration. **In:** *Expanded Abstracts of the 63rd SEG Annual Meeting*, Society of Exploration Geophysicists, Tulsa, USA, 174-176, DOI: 10.1190/1.1822429.

Shi, X., C. Li, S. Wang, and X. Wang (2011), Computing prestack Kirchhoff time migration on general purpose GPU, *Comput. Geosci*. **37**, 10, 1702-1710, DOI: 10.1016/j.cageo.2010.10.014.

Sun, C., and R.D. Martinez (2002), Amplitude preserving 3D prestack time migration for VTI media, *First Break* **19**, 618-624.

Westphal, E., S.P. Singh, C.-C. Huang, G. Gompper, and R.G. Winkler (2014), Multiparticle collision dynamics: GPU accelerated particle-based mesoscale hydrodynamic simulations, *Comput. Phys. Commun*. **185**, 2, 495-503, DOI: 10.1016/j.cpc.2013.10.004.

Received 1 August 2014
Received in revised form 22 April 2015
Accepted 2 June 2015

DE GRUYTER OPEN

Acta Geophysica
vol. 64, no. 4, Aug. 2016, pp. 1064-1092
DOI: 10.1515/acgeo-2016-0043

# Deblending of Simultaneous-source Seismic Data using Fast Iterative Shrinkage-thresholding Algorithm with Firm-thresholding

Shan QU[1], Hui ZHOU[1], Renwu LIU[2], Yangkang CHEN[3], Shaohuan ZU[1], Sa YU[1], Jiang YUAN[1], and Yahui YANG[1]

[1]State Key Laboratory of Petroleum Resources and Prospecting, Key Lab of Geophysical Exploration of CNPC, Dept. of Geophysics, China University of Petroleum, Beijing, China;
e-mail address: huizhou@cup.edu.cn (corresponding author)

[2]Dagang Geophysical Prospecting Branch of BGP, CNPC, Tianjin, China

[3]The University of Texas at Austin, Austin, USA

A b s t r a c t

In this paper, an improved algorithm is proposed to separate blended seismic data. We formulate the deblending problem as a regularization problem in both common receiver domain and frequency domain. It is suitable for different kinds of coding methods such as random time delay discussed in this paper. Two basic approximation frames, which are iterative shrinkage-thresholding algorithm (ISTA) and fast iterative shrinkage-thresholding algorithm (FISTA), are compared. We also derive the Lipschitz constant used in approximation frames. In order to achieve a faster convergence and higher accuracy, we propose to use firm-thresholding function as the thresholding function in ISTA and FISTA. Two synthetic blended examples demonstrate that the performances of four kinds of algorithms (ISTA with soft- and firm-thresholding, FISTA with soft- and firm-thresholding) are all effective, and furthermore FISTA with a firm-thresholding operator exhibits the most robust

Ownership: Institute of Geophysics, Polish Academy of Sciences;
© 2016 Qu *et al.* This is an open access article distributed under the Creative Commons Attribution-NonCommercial-NoDerivs license,
http://creativecommons.org/licenses/by-nc-nd/3.0/.

behavior. Finally, we show one numerically blended field data example processed by FISTA with firm-thresholding function.

**Key words:** deblending, regularization, simultaneous-source, firm-thresholding.

## 1. INTRODUCTION

The simultaneous-source technique is an effcient seismic acquisition technology; however, blended seismic data acquired by this technology should be separated before they are processed using the processing methods developed for conventional unblended data. Because of both its economic benefits and technical challenges, this technique has attracted the attention of researchers in both industry and academia (Mahdad *et al.* 2011, Abma *et al.* 2010, Huo *et al.* 2009, Chen *et al.* 2014a).

Different filtering and inversion methods have been applied previously to deblend seismic data. Deblending processing can be considered as a denoising problem because the blending noise appears as random noise when the blended data are sorted into a different domain, *e.g.*, common receiver, common offset or common midpoint domain. According to this property, Beasley (2008) used a geometry-related filter to separate marine blended data in the common midpoint domain. Huo *et al.* (2009) introduced a multi-directional vector median filter after resorting the data into common midpoint gathers. Chen *et al.* (2014b) proposed a deblending method by using normal moveout and median filtering in common-midpoint gathers. However, the denoising methods do not work well when the blended data are complex. Deblending problem can also be formulated as an inversion problem which aims at estimating the desired unknown unblended data. Because of the ill-posedness of such estimation problems, sophisticated regularization plays an important role in the deblending procedure (Doulgeris *et al.* 2012). Akerberg *et al.* (2008) used a sparse constraint to regularize the ill-posed problem in radon domain. Lin and Herrmann (2009) transformed the data into curvelet domain, where the data also present the sparsity, to regularize the inversion. Mahdad *et al.* (2011, 2012), Doulgeris *et al.* (2012), and Chen and Ma (2014) introduced an iterative f-k filtering method that combines the properties of filtering and inversion methods in different domains, but only when the number of simultaneous-source blended shots is greater than or equal to 3, these methods are effective. Chen *et al.* (2014a) proposed a novel iterative estimation scheme using shaping regularization in the seislet domain, but the blending matrix in this method is only a concept matrix, which limits the application of different iterative estimation schemes. In addition, none of the existing methods is suitable for different coding method, such as phase coding or sweep length.

In this paper, an improved algorithm is introduced to separate the blended seismic data. First of all, we define the deblending problem as a regularization problem in both common receiver domain and frequency domain. Then, we compare two basic approximation frames: ISTA and FISTA, and derive the Lipschitz constant. It has been proved that FISTA has a faster convergence speed than ISTA. After that, we propose to use firm-thresholding function as the thresholding function in ISTA and FISTA in order to achieve a higher accuracy. We apply those algorithms to remove blending noise, and meanwhile to preserve useful components of seismic data.

This paper is organized as follows. In Section 2, we present the definition of the deblending problem. In Section 3, we first introduce two basic approximation frames (ISTA and FISTA) and compare their convergence rate. Then, we discuss the reduction of Lipschitz constant used in the approximation frames. Next, we compare the traditional soft-thresholding function and hard-thresholding function with a better choice firm-thresholding. In Section 4, we test the proposed algorithms on two examples of numerically blended synthetic data and one example of numerically blended field data. The algorithms, which are ISTA with soft-thresholding, ISTA with firm-thresholding, FISTA with soft-thresholding, and FISTA with firm-thresholding, are compared before some conclusions are given.

## 2. THE DEFINITION OF DEBLENDING PROBLEM

This deblending model can be applied to any number of sources, while in this paper we only discuss the case of two independent sources. Supposing there are two independent sources corresponding to two shooting vessels in the Ocean Bottom Cable (OBC) acquisition. Here, one source means a collection of shots from one shooting vessel. The two sources are fired with small random time delay. The acquisition geometry is shown in Fig. 1.

The forward problem can be formulated as

$$\mathbf{d} = \mathbf{d}_1 + \mathbf{T}\mathbf{d}_2 \ , \tag{1}$$

where $\mathbf{d}$ denotes the blended data, $\mathbf{d}_1$ and $\mathbf{d_2}$ are unblended seismic datasets excited, respectively, by the two sources, and $\mathbf{T}$ stands for the blending operator in the time domain.

Chen *et al.* (2014a) proposed to augment Eq. 1 with another equation through the inverse blending operator $\mathbf{T}^{-1}$

$$\mathbf{T}^{-1}\mathbf{d} = \mathbf{T}^{-1}\mathbf{d}_1 + \mathbf{d}_2 \ , \tag{2}$$

then the blending problem can be formulated in the common receiver gather and time domain as

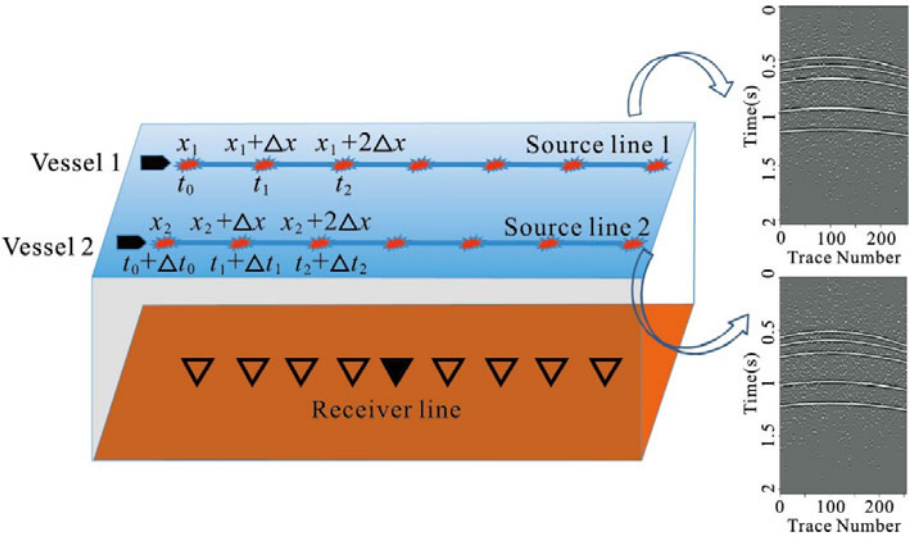


Fig. 1. The illustration of the simultaneous-source technique corresponding to two shooting vessels on the ocean surface in the OBC acquisition. ∇ and ▼ denote, respectively, receivers and a common receiver used to generate the blended data shown on the right side, and ✸ represents shot positions. $x_1$ and $x_2$ stands for the first shot position in source lines 1 and 2, respectively, $\Delta x$ is the shot point interval, $t_k$ denotes the shooting time of the $k$-th shot on source line 1, $\Delta t_k$ represents time delay of the $k$-th shot on source line 2. Two profiles demonstrate the blending seismic datasets in the common receiver domain corresponding to source lines 1 and 2, respectively.

$$\tilde{\mathbf{F}}\tilde{\mathbf{m}} = \tilde{\mathbf{d}} \ , \tag{3}$$

where $\tilde{\mathbf{d}} = \begin{bmatrix} \mathbf{d} \\ \mathbf{T}^{-1}\mathbf{d} \end{bmatrix}$, $\tilde{\mathbf{F}} = \begin{bmatrix} \mathbf{I} & \mathbf{T} \\ \mathbf{T}^{-1} & \mathbf{I} \end{bmatrix}$, $\tilde{\mathbf{m}} = \begin{bmatrix} \mathbf{d}_1 \\ \mathbf{d}_2 \end{bmatrix}$, $\mathbf{I}$ is a unit matrix.

In addition, instead of solving the original forward problem, Chen *et al.* (2014a) turn to solve the augmented Eq. 3, because two datasets can be obtained simultaneously, although this augmented equation is mathematically as ill-posed as the original forward problem. Deblending problem is not like noise attenuation, where the noise part is treated as useless and should be removed. The augmented equation also allows some basic frameworks, which will be discussed in Section 3.1.

Besides, the operator $\mathbf{T}$ in Eq. 3 has the following form

$$\mathbf{T}=\mathcal{F}^{-1}\mathbf{P}\mathcal{F}, \tag{4}$$

where $\mathcal{F}$ and $\mathcal{F}^{-1}$ are forward and inverse Fourier transforms, respectively, and **P** is a block phase-shift operator, which can be expressed as

$$\mathbf{P} = \begin{bmatrix} \mathbf{P}_1 & & & \\ & \mathbf{P}_2 & & \\ & & \ddots & \\ & & & \mathbf{P}_N \end{bmatrix}, \tag{5}$$

where diagonal matrix $\mathbf{P}_n\,(n = 1, 2, \ldots, N)$ denotes the individual phase shift operator for the $n$-th trace having the following form

$$\mathbf{P}_n = \mathrm{diag}\left(e^{-2\pi i f \Delta t_n} \quad e^{-2\pi i f \Delta t_n} \quad \cdots \quad e^{-2\pi i f \Delta t_n}\right)_{M\times M}, \tag{6}$$

where $\Delta t_n$ means the random time delay of the $n$-th trace, and $M$ denotes the number of temporal samples.

According to the representation of **T**, we can see that it is a conceptual blending operator, and it cannot be formulated by a specific matrix. In order to overcome this disadvantage, we transform the forward problem (Eq. 1) into the frequency domain

$$\mathbf{D} = \mathbf{D}_1 + \mathbf{\Gamma}\mathbf{D}_2\,, \tag{7}$$

where **D** denotes the blended data in the frequency domain, $\mathbf{D}_1$ and $\mathbf{D}_2$ represent the frequency domain data of $\mathbf{d}_1$ and $\mathbf{d}_2$, and **Γ** is the blending operator in the frequency domain.

Here, **Γ** is not just a simple Fourier Transform of the blending operator **T** in Eq. 4. For a given frequency, it is a specific matrix. Considering one receiver gather and random time delay coding, **Γ** at frequency $f$ can be formulated by

$$\mathbf{\Gamma} = \mathrm{diag}\left(e^{-2\pi i f \Delta t_1} \quad e^{-2\pi i f \Delta t_2} \quad \cdots \quad e^{-2\pi i f \Delta t_N}\right)_{N\times N}, \tag{8}$$

where $\Delta t_n\,(n = 1, 2, \ldots, N)$ denotes the random time delay of the $n$-th shot, and $N$ stands for the number of shots.

Then, by the same token as Chen *et al.* (2014a), we augment Eq. 7 into the following form

$$\mathbf{F}\mathbf{m} = \tilde{\mathbf{D}}\,, \tag{9}$$

where $\tilde{\mathbf{D}} = \begin{bmatrix} \mathbf{D} \\ \mathbf{\Gamma}^{-1}\mathbf{D} \end{bmatrix}$, $\mathbf{F} = \begin{bmatrix} \mathbf{I} & \mathbf{\Gamma} \\ \mathbf{\Gamma}^{-1} & \mathbf{I} \end{bmatrix}$, $\mathbf{m} = \begin{bmatrix} \mathbf{D}_1 \\ \mathbf{D}_2 \end{bmatrix}$.

There are two main reasons for us to deblend the data in the frequency domain. The first reason is that unlike blending operator described in Eqs. 4-

6, the new blending operator in the frequency domain in Eq. 8 can be formulated by a specific matrix for one frequency. This property turns the deblending problem to a traditional regularization problem for each frequency and allows more approximation frames to be discussed in Section 3. The second reason is that the new blending operator allows more kinds of coding methods, such as phase coding and sweep length coding in the vibroseis acquisition (Qu *et al.* 2014). As a tutorial, $\mathbf{\Gamma}$ is

$$\mathbf{\Gamma} = \mathrm{diag}\left(e^{i\beta_1} \quad e^{i\beta_2} \quad \cdots \quad e^{i\beta_N}\right)_{N\times N}, \tag{10}$$

for phase coding, $\beta_n (n = 1, 2, \ldots, N)$ represents the phase code of the $n$-th shot, and $\mathbf{\Gamma}$ is written as

$$\mathbf{\Gamma} = \mathrm{diag}\left(\frac{1}{\sqrt{q_1}} e^{\left[\frac{q_1-1}{q_1}\pi i\frac{(f-f_0)^2}{2k}\right]} \quad \frac{1}{\sqrt{q_2}} e^{\left[\frac{q_2-1}{q_2}\pi i\frac{(f-f_0)^2}{2k}\right]} \quad \cdots \quad \frac{1}{\sqrt{q_N}} e^{\left[\frac{q_N-1}{q_N}\pi i\frac{(f-f_0)^2}{2k}\right]}\right)_{N\times N}, \tag{11}$$

for sweep length coding, where $k$ represents the sweep rate and $q_n (n = 1, 2, \ldots, N)$ represents that the sweep rate of the encoded signal of the $n$-th shot is $q_n$ times as that of the original signal.

It is known that seismic data often has sparse representation in some transformation domains, *e.g.*, curvelet domain (Candes and Demanet 2005). One way to overcome the ill-posedness of Eq. 9 is to minimize an objective function $J(\mathbf{m})$:

$$\begin{aligned} J(\mathbf{m}) &= f(\mathbf{m}) + g(\mathbf{m}), \\ f(\mathbf{m}) &= \left\|\tilde{\mathbf{D}} - \mathbf{F}\mathbf{m}\right\|_2^2, \\ g(\mathbf{m}) &= \lambda \left\|\mathbf{C}^{-1}\mathbf{m}\right\|_p \quad (0 \le p \le 1), \end{aligned} \tag{12}$$

where $\mathbf{C}^{-1}$ is sparsity-promoting transform that maps the signal to the transformation domain, such as curvelet domain, $f(\mathbf{m})$ is a data-fitting term and $g(\mathbf{m})$ is a regularization term used to penalize the complex model, and $\lambda$ is the penalty term.

## 3. DEBLENDING BY USING IMPROVED ALGORITHM

### 3.1 The basic approximation frames and their convergence rates

Several famous iterative approximation frames for solving regularization problem have been fully developed and applied to image denoising and restoration problems. The optimization problem like Eq. 9 belongs to regularization problem. For the purpose of comparison, we focus on the following two approximation frames.

### *3.1.1 Iterative shrinkage-thresholding algorithm (ISTA)*

The most popular method to solve a regularization problem is ISTA because of its convenient implementation. ISTA was proposed by Daubechies *et al.* (2004), Figueiredo and Nowak (2003), and Chambolle (2004) to solve least-square minimization problem with a constraint to the model. We modify the basic form of ISTA to correspond to the deblending problem as

$$\mathbf{m}_{k+1} = \mathbf{C}T_{\tau,p}\mathbf{C}^{-1}\left[\mathbf{m}_k - \frac{2}{L(\nabla f(\mathbf{m}))}\mathbf{F}^T\left(\mathbf{F}\mathbf{m}_k - \tilde{\mathbf{D}}\right)\right], \tag{13}$$

where $\mathbf{m}_k$ represents the solution at the $k$-th iteration, $L(\nabla f(\mathbf{m}))$ is the Lipschitz constant of $\nabla f(\mathbf{m})$ depending on the maximum eigenvalue of $\mathbf{F}^T\mathbf{F}$. This constant is not as easy to calculate as the traditional inverse problem, because $\mathbf{F}$ depends on the frequency as we discussed in Section 2. We will discuss it in Section 3.2. $T_{\Gamma,p}$ is a thresholding operator corresponding to specific norm regularization to be shown in Section 3.3.

The convergence rate of ISTA has been well investigated for the regularization problem. It is $O(1/k)$, which is also called a "sublinear global rate of convergence". That means each value of the sequence $\{J(\mathbf{m}_k)\}$ converges to the optimal function value $J(\mathbf{m}_*)$, and it is proved to behave like

$$J(\mathbf{m}_k) - J(\mathbf{m}_*) \le \frac{2L(\nabla f(\mathbf{m}))\|\mathbf{m}_0 - \mathbf{m}_*\|^2}{k}, \tag{14}$$

thus

$$J(\mathbf{m}_k) - J(\mathbf{m}_*) \le O(1/k), \tag{15}$$

where $\mathbf{m}_*$ is the optimal solution, and $\mathbf{m}_0$ is an initial model.

### *3.1.2 Fast iterative shrinkage-thresholding algorithm (FISTA)*

FISTA proposed by Beck and Teboulle (2009) is a variation of ISTA. We modify the basic form of FISTA to be suitable for the deblending problem as

$$\mathbf{m}_{k+1} = \mathbf{W}\left(\mathbf{m}_k + \frac{t_k - 1}{t_{k+1}}(\mathbf{m}_k - \mathbf{m}_{k-1})\right), \tag{16}$$

where $t_{k+1} = \left(1+\sqrt{1+4(t_k)^2}\right)\Big/2$, $t_0 = 1$, and the operator $\mathbf{W}$ is given by

$$\mathbf{W}(\mathbf{m}) = \mathbf{C}T_{\tau,p}\mathbf{C}^{-1}\left[\mathbf{m} - \frac{2}{L(\nabla f(\mathbf{m}))}\mathbf{F}^T\left(\mathbf{F}\mathbf{m} - \tilde{\mathbf{D}}\right)\right]. \tag{17}$$

FISTA seems to have the same complexity as the ISTA, but it has been proved to have a faster convergence rate. The sequence $\{\mathbf{m}_k\}$ generated by FISTA achieves

$$J(\mathbf{m}_k) - J(\mathbf{m}_*) \le \frac{2L(\nabla f(\mathbf{m}))\|\mathbf{m}_0 - \mathbf{m}_*\|^2}{(k+1)^2}, \tag{18}$$

and thus

$$J(\mathbf{m}_k) - J(\mathbf{m}_*) \le O(1/k^2). \tag{19}$$

### 3.2 The reduction of Lipschitz constant

It is noted from Eq. 8 that $\mathbf{\Gamma}$ is a function of frequency, and that it is also different from different coding methods as shown in Eqs. 10 and 11. In this part, we prove that $L(\nabla f(\mathbf{x}))$ can be formulated by a constant.

It can be derived from Eq. 8 that $\mathbf{\Gamma}^{-1} = \mathbf{\Gamma}^T$, where $\mathbf{\Gamma}^T$ means the conjugate transpose of $\mathbf{\Gamma}$, then

$$\mathbf{F}^T\mathbf{F} = \begin{bmatrix} \mathbf{I} & \Gamma \\ \Gamma^{-1} & \mathbf{I} \end{bmatrix}\begin{bmatrix} \mathbf{I} & \Gamma \\ \Gamma^{-1} & \mathbf{I} \end{bmatrix} = \begin{bmatrix} 2\mathbf{I} & 2\Gamma \\ 2\Gamma^{-1} & 2\mathbf{I} \end{bmatrix}. \tag{20}$$

According to the linear algebra knowledge, the eigenvalues $\lambda$ of $\mathbf{F}^T\mathbf{F}$ satisfy

$$\left|\mathbf{F}^T\mathbf{F} - \lambda\mathbf{I}\right| = 0, \tag{21}$$

and by using Eq. 20 we have

$$\left|\mathbf{F}^T\mathbf{F} - \lambda\mathbf{I}\right| = \begin{bmatrix} (2-\lambda)\mathbf{I} & 2\mathbf{\Gamma} \\ 2\mathbf{\Gamma}^{-1} & (2-\lambda)\mathbf{I} \end{bmatrix}. \tag{22}$$

According to the block matrix property, Eq. 22 can be modified to

$$\left|\mathbf{F}^T\mathbf{F} - \lambda\mathbf{I}\right| = \left|\lambda(\lambda-4)\right| = 0. \tag{23}$$

Then we obtain that the maximum eigenvalue of $\mathbf{F}^T\mathbf{F}$ is 4, and as a result, $L(\nabla f(\mathbf{m})) = 2\lambda_{\max}(\mathbf{F}^T\mathbf{F}) = 8$ for each frequency.

The whole reduction of Lipschitz constant is also suitable for higher number of blended sources. Now we will try to derive the Lipschitz constant when the number of blended sources is *K*. The blending equation in the frequency domain is as follows

$$\mathbf{F}\mathbf{m} = \tilde{\mathbf{D}}, \tag{24}$$

where $\tilde{\mathbf{D}} = \begin{bmatrix} \mathbf{D} \\ \boldsymbol{\Gamma}_2^{-1}\mathbf{D}_2 \\ \vdots \\ \boldsymbol{\Gamma}_K^{-1}\mathbf{D}_K \end{bmatrix}$, $\mathbf{F} = \begin{bmatrix} \mathbf{I} & \boldsymbol{\Gamma}_2 & \cdots & \boldsymbol{\Gamma}_K \\ \boldsymbol{\Gamma}_2^{-1} & \mathbf{I} & \cdots & \boldsymbol{\Gamma}_2^{-1}\boldsymbol{\Gamma}_K \\ \vdots & \vdots & \ddots & \vdots \\ \boldsymbol{\Gamma}_K^{-1} & \boldsymbol{\Gamma}_K^{-1}\boldsymbol{\Gamma}_2 & \cdots & \mathbf{I} \end{bmatrix}$, $\mathbf{m} = \begin{bmatrix} \mathbf{D}_1 \\ \mathbf{D}_2 \\ \vdots \\ \mathbf{D}_K \end{bmatrix}$,

$\mathbf{D}_k\,(k = 2, \ldots, K)$ is the $k$-th source, $\boldsymbol{\Gamma}_k\,(k = 2, \ldots, K)$ is the frequency blending operator for the $k$-th source.

Then,

$$\mathbf{F}^T\mathbf{F} = \begin{bmatrix} K\mathbf{I} & K\boldsymbol{\Gamma}_2 & \cdots & K\boldsymbol{\Gamma}_K \\ K\boldsymbol{\Gamma}_2^{-1} & K\mathbf{I} & \cdots & K\boldsymbol{\Gamma}_2^{-1}\boldsymbol{\Gamma}_K \\ \vdots & \vdots & \ddots & \vdots \\ K\boldsymbol{\Gamma}_K^{-1} & K\boldsymbol{\Gamma}_K^{-1}\boldsymbol{\Gamma}_2 & \cdots & K\mathbf{I} \end{bmatrix}, \tag{25}$$

$$\left|\mathbf{F}^T\mathbf{F} - \lambda\mathbf{I}\right| = \begin{vmatrix} (K-\lambda)\mathbf{I} & K\boldsymbol{\Gamma}_2 & \cdots & K\boldsymbol{\Gamma}_K \\ K\boldsymbol{\Gamma}_2^{-1} & (K-\lambda)\mathbf{I} & \cdots & K\boldsymbol{\Gamma}_2^{-1}\boldsymbol{\Gamma}_K \\ \vdots & \vdots & \ddots & \vdots \\ K\boldsymbol{\Gamma}_K^{-1} & K\boldsymbol{\Gamma}_K^{-1}\boldsymbol{\Gamma}_2 & \cdots & (K-\lambda)\mathbf{I} \end{vmatrix}. \tag{26}$$

According to the linear algebra knowledge, by using some elementary transformations, Eq. 26 can be simplified as

$$\left|\mathbf{F}^T\mathbf{F} - \lambda\mathbf{I}\right| = \begin{vmatrix} (2K-\lambda)\mathbf{I} & K\boldsymbol{\Gamma}_2 & \cdots & K\boldsymbol{\Gamma}_K \\ 0 & -\lambda\mathbf{I} & \cdots & 0 \\ \vdots & \vdots & \ddots & \vdots \\ 0 & 0 & \cdots & -\lambda\mathbf{I} \end{vmatrix} = \left|(\lambda - 2K)\,\lambda^{K-1}\right|. \tag{27}$$

Now we obtain that the maximum eigenvalue of $\mathbf{F}^T\mathbf{F}$ is $2K$. As a result, $L(\nabla f(\mathbf{m})) = 2\lambda_{\max}(\mathbf{F}^T\mathbf{F}) = 4K$ for each frequency. It can be seen that when $K = 2$, $L(\nabla f(\mathbf{m})) = 8$. This result matches the previous conclusion.

Here is an important part we need to discuss. In terms of complex real simultaneous-source seismic data, $L(\nabla f(\mathbf{m}))$ should be set slightly larger than $4K$, because some parts of the complex blended profiles are actually blended by larger than $4K$ sources.

### 3.3 Thresholding functions

As we discussed in Section 2, in order to overcome the ill-posedness of Eq. 9, we need to recover the single seismic data $\mathbf{m}$ from the blended data $\tilde{\mathbf{D}}$, when $\mathbf{m}$ is of the sparsest structure in a sparse domain; that means, $\mathbf{m}$ has the fewest nonzero components in the sparse domain. Accordingly, the sparsest possible representation of the deblending problem can be modeled as the

minimization of the following objective function $J(\mathbf{m})$ with $L_0$ norm regularization

$$J(\mathbf{m}) = \left\|\tilde{\mathbf{D}} - \mathbf{F}\mathbf{m}\right\|_2^2 + \lambda \left\|\mathbf{C}^{-1}\mathbf{m}\right\|_0 , \tag{28}$$

where $\left\|\mathbf{C}^{-1}\mathbf{m}\right\|_0$ denotes $L_0$ norm regularization.

Thresholding function is related to one specific norm regularization. When we use the objective function with $L_0$ norm regularization as shown in Eq. 28 ($p = 0$), $T_{\Gamma,p}$ in Eqs. 13 and 17 is a hard-thresholding operator with a thresholding value $\tau$ and takes the form of

$$T_{\tau,0} = \begin{cases} v(\mathbf{m}_k), & \text{for} \quad \left|v(\mathbf{m}_k)\right| > \tau , \\ 0, & \text{for} \quad \left|v(\mathbf{m}_k)\right| \le \tau , \end{cases} \tag{29}$$

at the $k$-th iteration, $v(\mathbf{m}_k) = \mathbf{C}^{-1}\left[\mathbf{m}_k - \dfrac{2}{L(\nabla f(\mathbf{m}))}\mathbf{F}^T\left(\mathbf{F}\mathbf{m}_k - \tilde{\mathbf{D}}\right)\right]$.

Unfortunately, Bruce and Gao (1996) have shown that due to the discontinuity, the hard-thresholding ($T_{\tau,0}$) tends to have bigger variance, which would lead to unstable and non-convergent results. Moreover, Candes and Tao (2005) and Donoho (2006) have shown that solving Eq. 28 would appear to require combinatorial optimization, and be utterly intractable to solve. In other words, $L_0$ norm is the most accurate norm, because it conforms to the physical meaning. However, it is sometimes unstable and hard to solve. Therefore, they pointed that $L_1$ norm is in some sense the convex relaxation of the $L_0$ norm and it is more tractable than $L_0$ norm, $L_1$ norm can recover sparse unknown signals in a variety of different situations because of its stability. Equation 28 can be rewritten as

$$J(\mathbf{m}) = \left\|\tilde{\mathbf{D}} - \mathbf{F}\mathbf{m}\right\|_2^2 + \lambda \left\|\mathbf{C}^{-1}\mathbf{m}\right\|_1 . \tag{30}$$

When we use the objective function with $L_1$ norm regularization ($p = 1$), $T_{\Gamma,p}$ is a soft-thresholding operator as the form of

$$T_{\tau,1} = \begin{cases} v(\mathbf{m}_k) - \tau\,\mathrm{sgn}\left(v(\mathbf{m}_k)\right), & \text{for} \quad \left|v(\mathbf{m}_k)\right| > \tau , \\ 0, & \text{for} \quad \left|v(\mathbf{m}_k)\right| \le \tau , \end{cases} \tag{31}$$

where sgn(.) represents sign function.

However, Bruce and Gao (1996) have also shown that because of shrinking all big coefficients towards zero, soft-thresholding ($T_{\tau,1}$) tends to have bigger bias and leads to less accurate results, although it is very stable. To overcome these disadvantages, recent research shows that $L_p$ norm regulari-

zation generates more sparse solutions than $L_1$ norm regularization and more stable than $L_0$ norm regularization. It is possible to use the nonconvex $L_p$ norm in Eq. 12, where $0 < p < 1$ (Chartrand 2007). The objective function $J(\mathbf{m})$ is written as

$$J(\mathbf{m}) = \left\| \tilde{\mathbf{D}} - \mathbf{F}\mathbf{m} \right\|_2^2 + \lambda \left\| \mathbf{C}^{-1}\mathbf{m} \right\|_p . \tag{32}$$

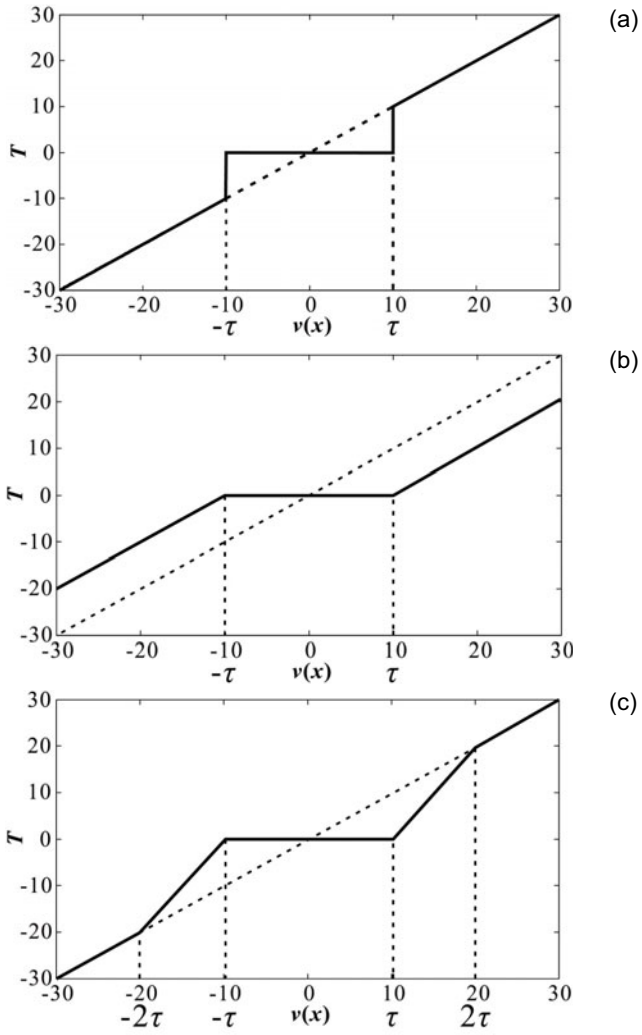


Fig. 2. Comparison of different thresholding functions: (a) hard-thresholding function ($\theta = 1/4$), (b) soft-thresholding function ($\theta \to \infty$), and (c) firm-thresholding function ($\theta = 1/2$).

In this case, we choose firm-thresholding introduced by Gao and Bruce (1997) as thresholding function. It is an intermediate between the soft and hard-thresholding, and can be formulated as

$$T_{\theta,2\tau,p}=\begin{cases} v(\mathbf{m}_k), & \text{for } \left|v(\mathbf{m}_k)\right|>4\theta\tau, \\ \dfrac{4\theta}{4\theta-1}\left[v(\mathbf{m}_k)-\tau\,\mathrm{sgn}\left(v(\mathbf{m}_k)\right)\right], & \text{for } \tau<\left|v(\mathbf{m}_k)\right|\le 4\theta\tau, \\ 0, & \text{for } \left|v(\mathbf{m}_k)\right|\le\tau. \end{cases} \tag{33}$$

To demonstrate that firm-thresholding is an intermediate between soft- and hard-thresholding, we discuss the following cases.

For $\theta = 1/4$, firm-thresholding function becomes hard-thresholding function 29. Furthermore, letting $\theta \to \infty$, firm-thresholding function turns to soft-thresholding function 31. As a result, hard- and soft-thresholding are two extreme cases of firm-thresholding, which can be interpreted as an intermediate between soft and hard-thresholding. Figure 2 displays the shapes of hard-, soft-, and firm-thresholding functions.

## 4. DEBLENDING EXAMPLES

In order to confirm the effectiveness of the proposed method, three deblending examples are demonstrated in this section. We demonstrate two synthetic blended examples and a numerically blended example. Because of the instability of hard-thresholding, only the tests of ISTA and FISTA with soft- and firm-thresholding are shown and compared. All the data are deblended in the common receiver domain, and the curvelet transform is utilized as the sparse transform.

In addition, exponential-decreasing criterion is applied to control the thresholding value $\tau$, which is easy to implement and can somewhat accelerate the convergence rate. And just as a slight clarification, if we use adequate number of iterations, the two approximation frames (ISTA and FISTA) would converge to the same optimal solution at different rates. Obviously, large number of iterations is not practical. With relative small number of iterations, FISTA converges to a better solution than ISTA.

As Chen *et al.* (2014a) did, we also use

$$SNR_{i,n}=10\times\log_{10}\frac{\left\|d_i\right\|_2^2}{\left\|d_i-d_{i,n}\right\|_2^2} \tag{34}$$

to evaluate the convergence performance and accuracy of the methods, where $SNR_{i,n}$ denotes signal-to-noise ratio (SNR) of the $i$-th source at the $n$-th iteration, $d_{i,n}$ represents the estimated model of the $i$-th source at the $n$-th iteration, and $d_i$ stands for the true model for the $i$-th source.

### 4.1 Deblending simple synthetic blended data

This example contains three hyperbolic events without dip conflicts. The unblended and blended data are shown in Fig. 3.

We choose $\tau_{\max} = 0.25 \max\left( \mathbf{C}^{-1} \frac{2}{L\left(\nabla f(\mathbf{m})\right)} \mathbf{F}^T \tilde{\mathbf{D}} \right)$, $\tau_{\min} = 10^{-3}$, $\theta = 1/2$, and the number of iterations is 40. We also add some random noise to the blended sections.

In Figure 4 panels (a) and (b) show the deblended results by using ISTA with soft- and firm-thresholding, and panels (c) and (d) show those by using FISTA with soft- and firm-thresholding. All these deblending results are nearly perfect.

The differences between the deblended and blended data are called blending noise shown in Fig. 5, where the spots are the reflections from other shots. It can be seen that most of the blending noise is removed by all the methods. The differences between the deblended and unblended data denoting the estimation error are illustrated in Fig. 6. It is seen from Fig. 6 that ISTA with soft-thresholding function has some obvious residuals, even though the residuals are very small. However, the estimation error sections of other three algorithms are almost zero.

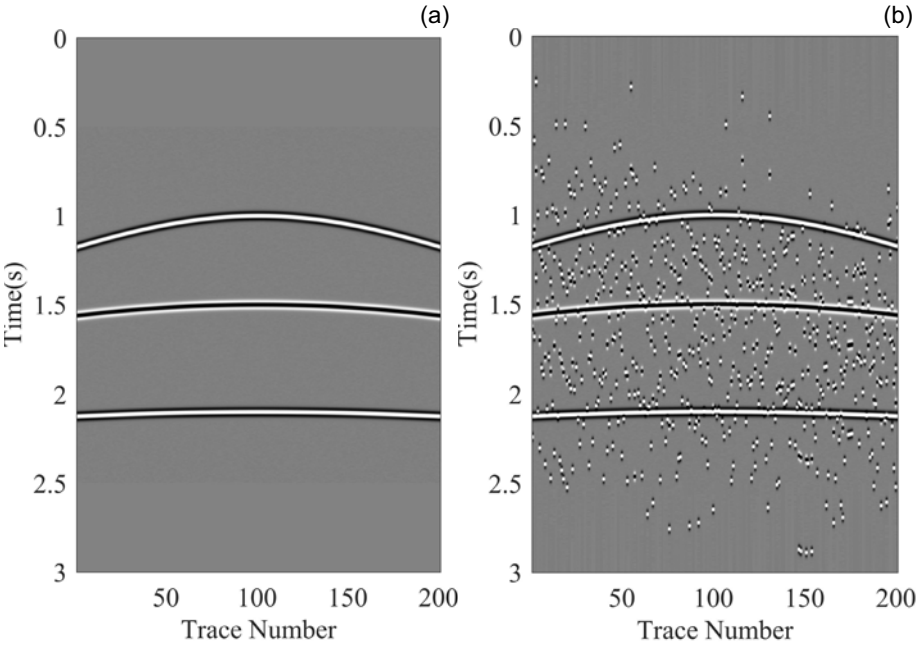


Fig. 3. Two numerical synthetic CRG datasets of the first example, unblended data (a), and blended data (b).

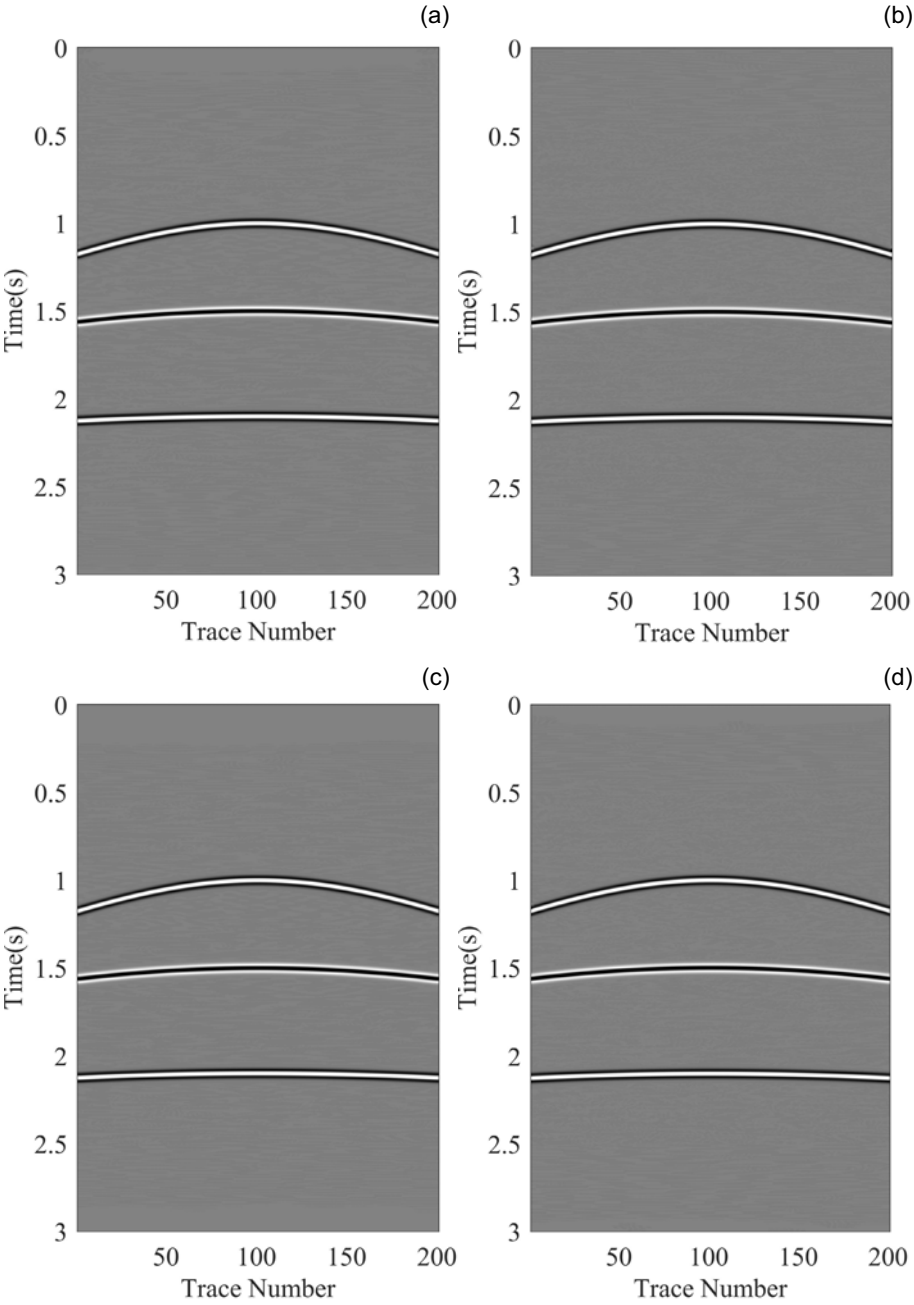


Fig. 4. Deblended result using ISTA with soft-thresholding (a), ISTA with firm-thresholding (b), FISTA with soft-thresholding (c), and FISTA with firm-thresholding (d).

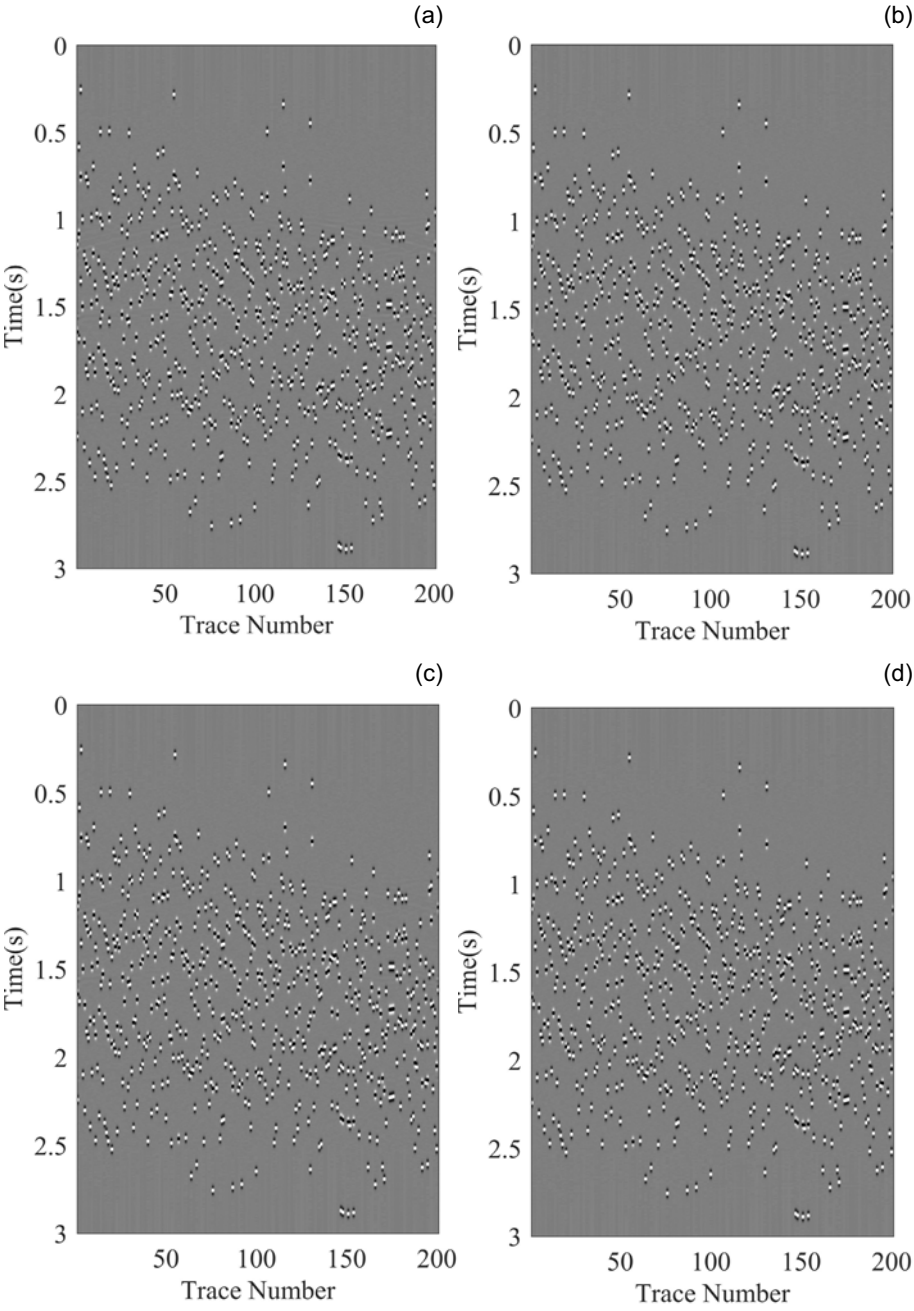


Fig. 5. Blending noise using ISTA with soft-thresholding (a), ISTA with firm-thresholding (b), FISTA with soft-thresholding (c), and FISTA with firm-thresholding (d).

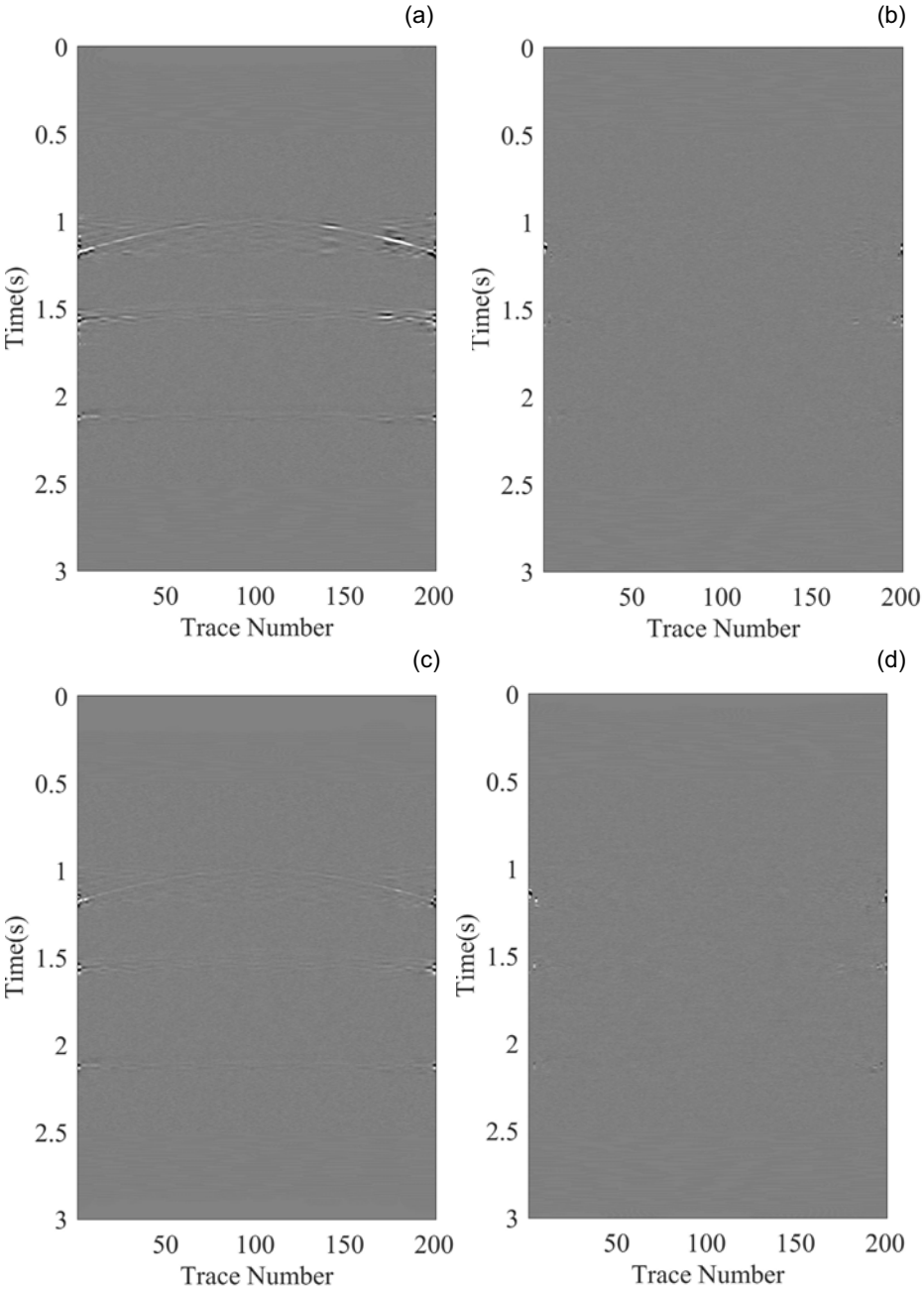


Fig. 6. Deblending estimation error using ISTA with soft-thresholding (a), ISTA with firm-thresholding (b), FISTA with soft-thresholding (c), and FISTA with firm-thresholding (d).

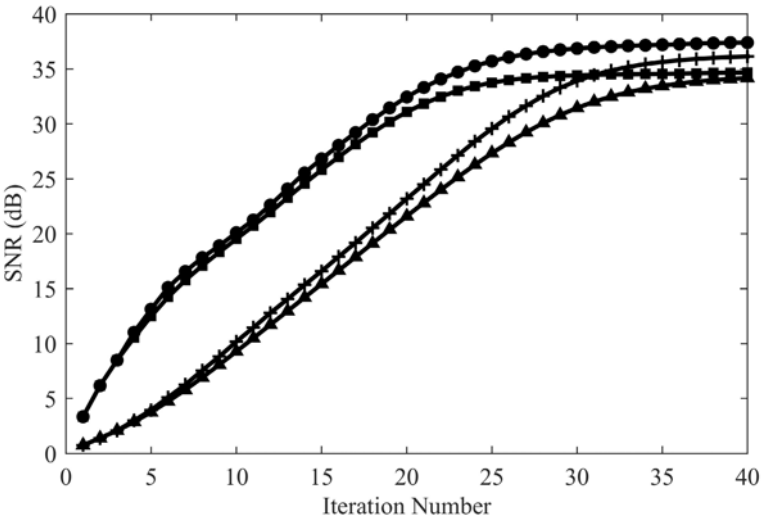


Fig. 7. Curves of SNR with iteration number corresponding to ISTA with soft-thresholding (▲), ISTA with firm-thresholding (■), FISTA with soft-thresholding (+), and FISTA with firm-thresholding (●).

The differences between the deblended and blended data are called blending noise shown in Fig. 5, where the spots are the reflections from other shots. It can be seen that most of the blending noise is removed by all the methods. The differences between the deblended and unblended data denoting the estimation error are illustrated in Fig. 6. It is seen from Fig. 6 that ISTA with soft-thresholding function has some obvious residuals, even though the residuals are very small. However, the estimation error sections of other three algorithms are almost zero.

The curves of convergence rate are shown in Fig. 7, in which FISTA behaves better than ISTA. Figure 7 also depicts that firm-thresholding is a superior choice of thresholding function than soft-thresholding.

### 4.2 Deblending complex synthetic blended data

The synthetic blended data whose geological model is shown in Fig. 8 contain much more events with many dip conflicts. These blended data are numerically calculated by using the staggered-grid finite-difference method. The original unblended and blended sections are shown in Fig. 9.

We choose $\tau_{\max} = 0.5 \max\left( \mathbf{C}^{-1} \frac{2}{L\left(\nabla f(\mathbf{m})\right)} \mathbf{F}^T \tilde{\mathbf{D}} \right)$, $\tau_{\min} = 10^{-1}$, $\theta = 1/2$, and the number of iterations is 40. We add some random noise to the blended sections.

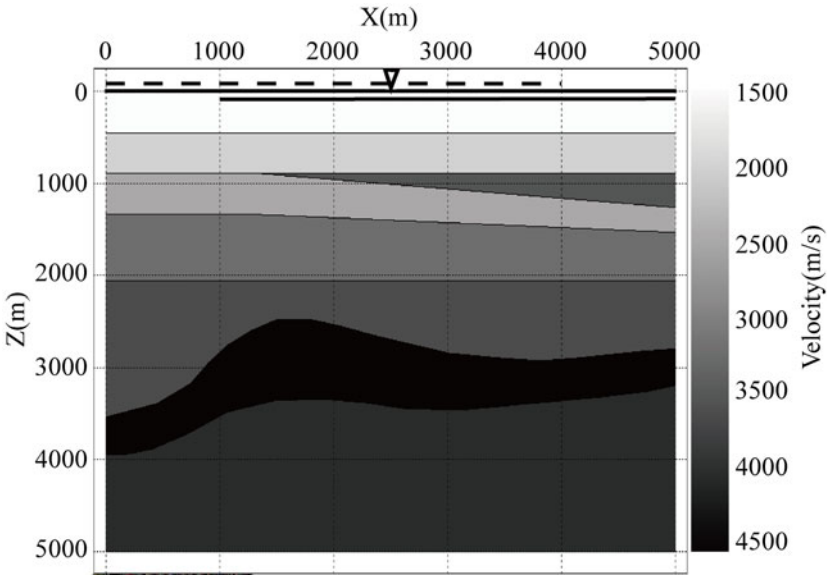


Fig. 8. Geological model used to calculate synthetic CRGs of the second example. ∇ stands for receiver position, the solid and dash line on the surface denote source lines 1 and 2, respectively.

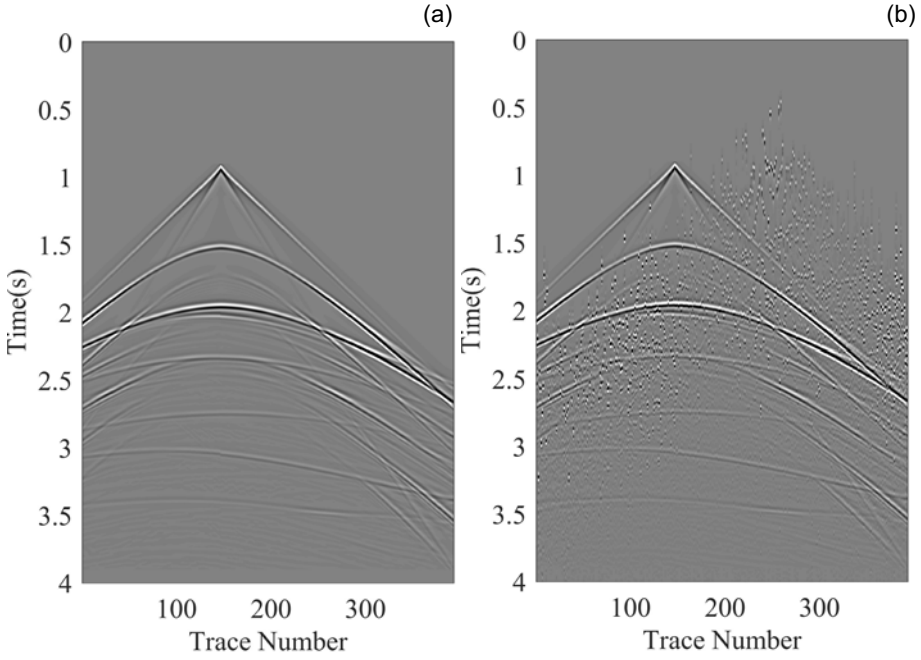


Fig. 9. Two synthetic CRG datasets of the second example: unblended data (a), and blended data (b).

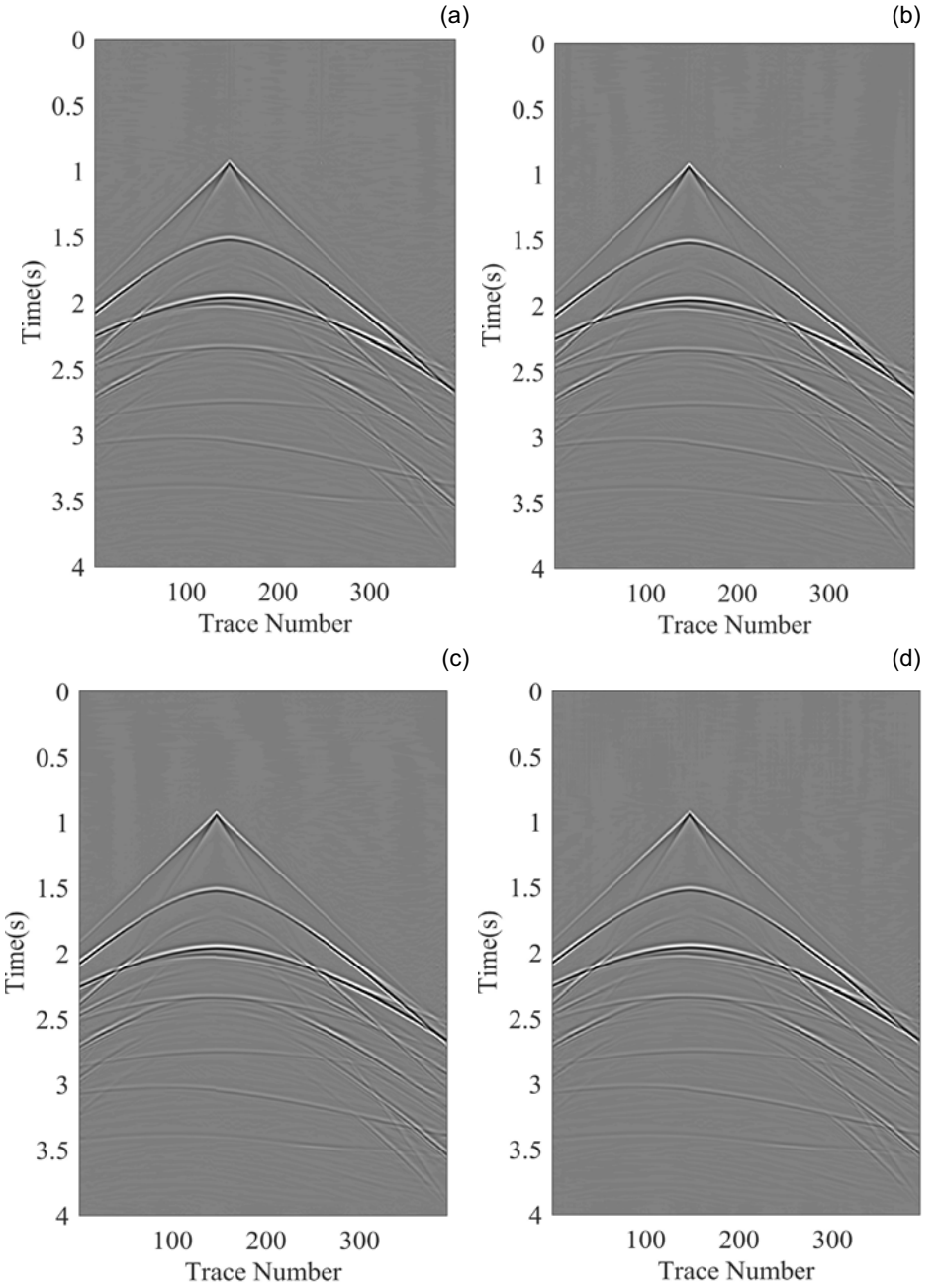


Fig. 10. Deblended result using ISTA with soft-thresholding (a), ISTA with firm-thresholding (b), FISTA with soft-thresholding (c), and FISTA with firm-thresholding (d).

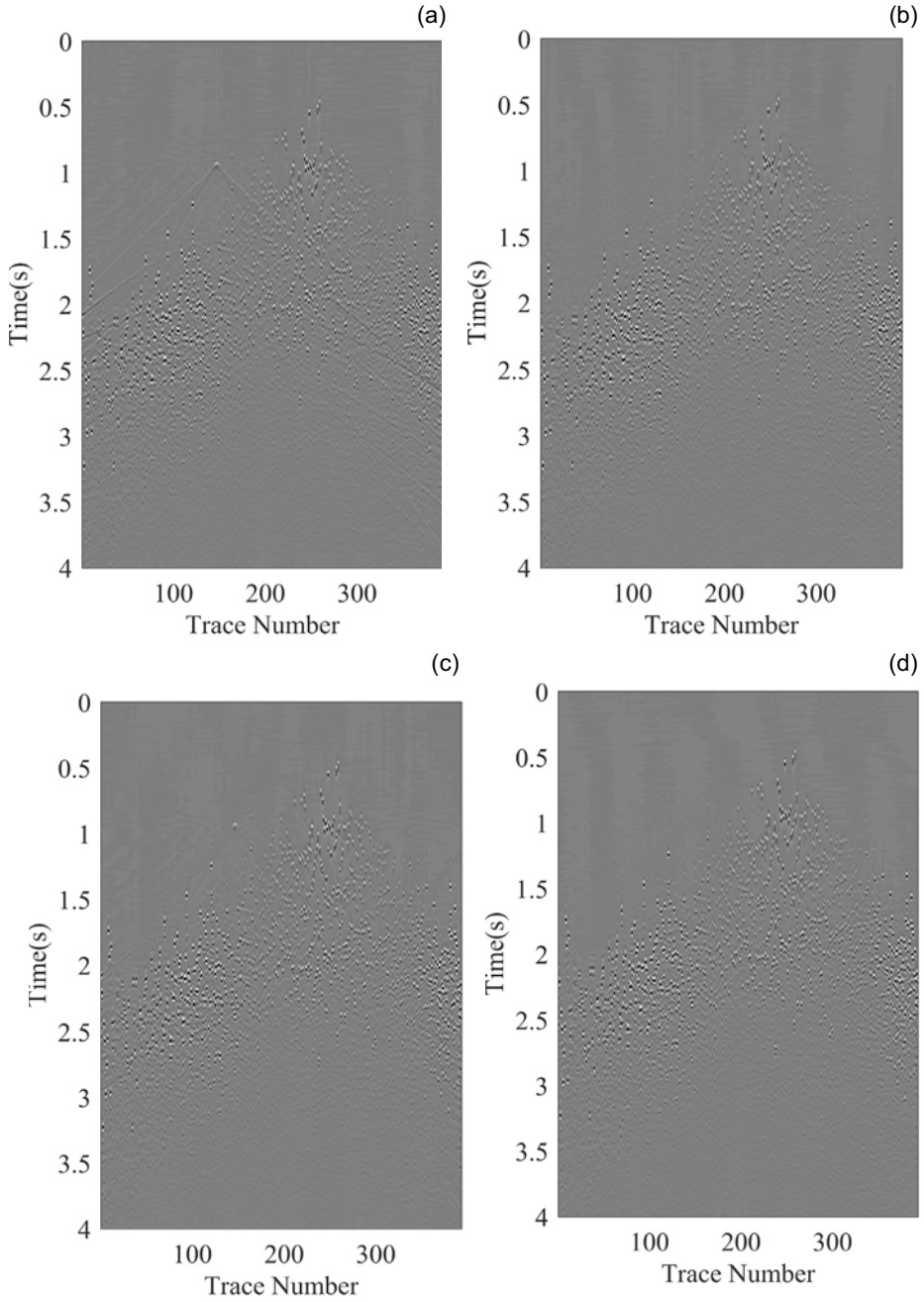


Fig. 11. Blending noise using ISTA with soft-thresholding (a), ISTA with firm-thresholding (b), FISTA with soft-thresholding (c), and FISTA with firm-thresholding (d).

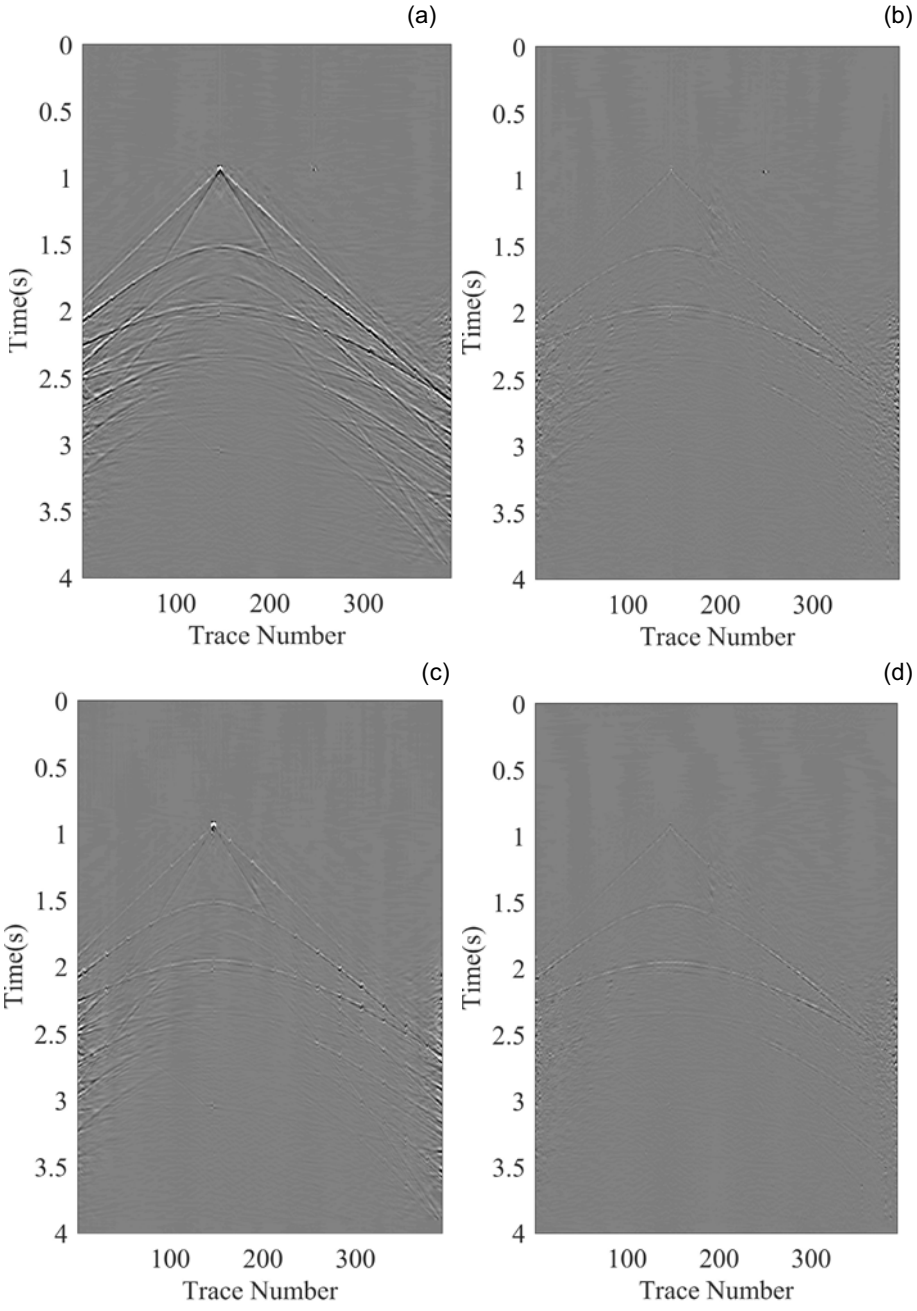


Fig. 12. Deblending estimation error using ISTA with soft-thresholding (a), ISTA with firm-thresholding (b), FISTA with soft-thresholding (c), and FISTA with firm-thresholding (d).

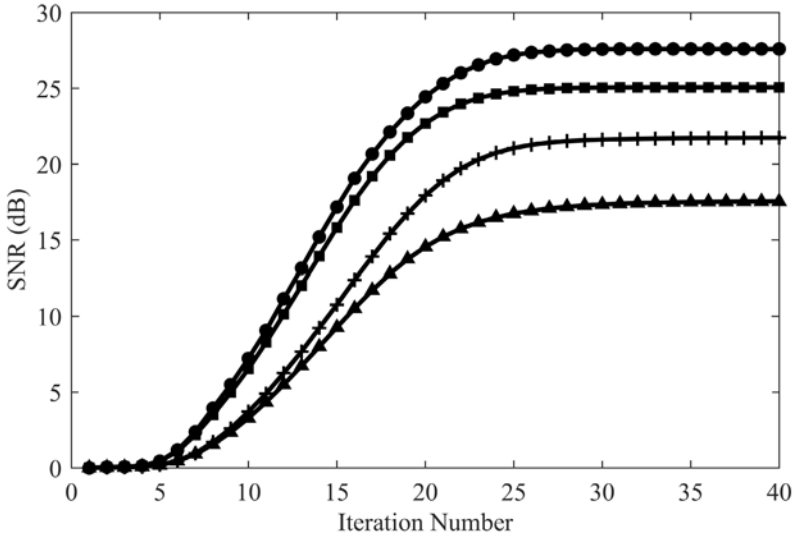


Fig. 13. Curves of SNR with iteration number corresponding to ISTA with soft-thresholding (▲), ISTA with firm-thresholding (■), FISTA with soft-thresholding (+), and FISTA with firm-thresholding (●).

Figure 10 shows the deblending results, in which the useful reflections are very clear and all the results are acceptable. The blending noise sections in Fig. 11 show that most of the blending noise is attenuated by those methods. However, we can obviously find out the different effectiveness among those algorithms from the estimation error sections as shown in Fig. 12. The estimation error sections corresponding to ISTA and FISTA with soft-thresholding function are obviously worse than the sections corresponding to ISTA and FISTA with firm-thresholding. In addition, it can also be seen that when using the same thresholding functions, the results corresponding to ISTA have much more residuals than the results corresponding to FISTA.

Figure 13 shows the curves of SNR. It can be observed that FISTA with firm-thresholding is obviously better than the other methods, and it has the same behavior as the first example.

### 4.3 Deblending numerically blended field data

Common receiver gathers collected by OBC are used to generate two numerically blended field data. These blended data are separated to further test the effectiveness of our proposed method. From the previous tests, it can be seen that the effectiveness of FISTA with firm-thresholding is the best. As a result, we only separate the blended data by using FISTA with firm-thresholding.

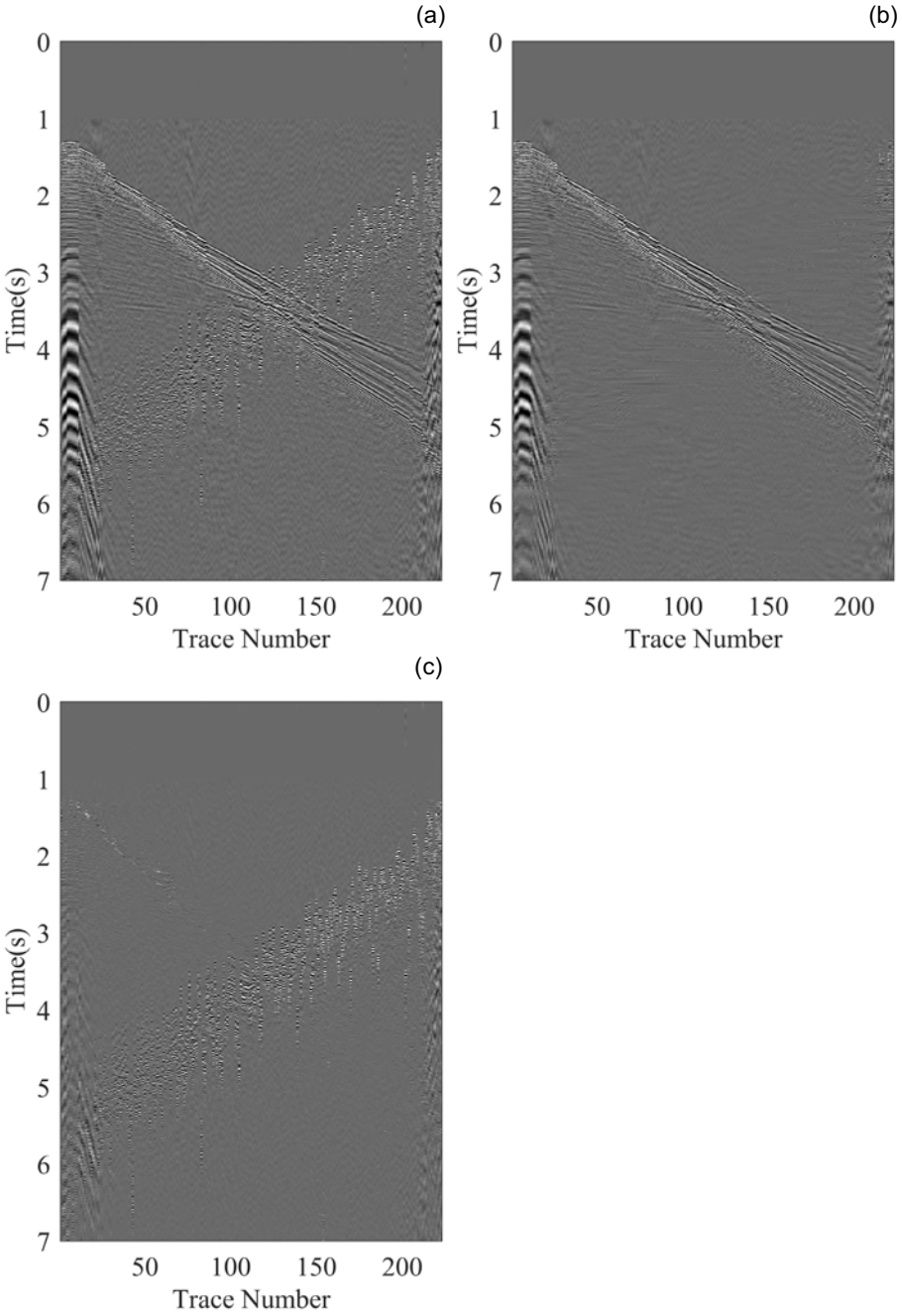


Fig. 14. Deblending example of field data of source line 1: blended gather (a), deblended result (b), and blending noise (c).

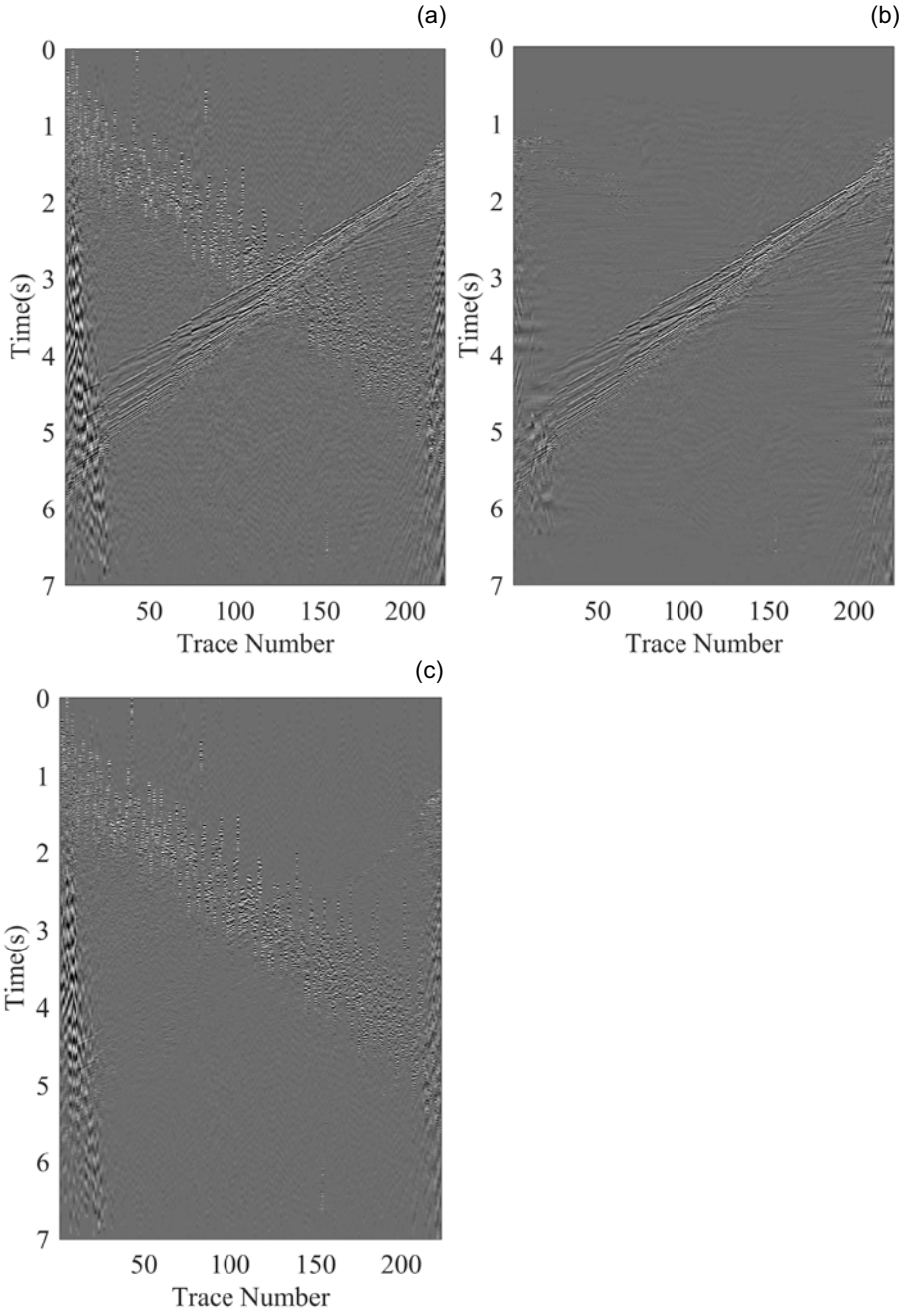


Fig. 15. Deblending example of field data of source line 2: blended gather (a), deblended result (b), and blending noise (c).

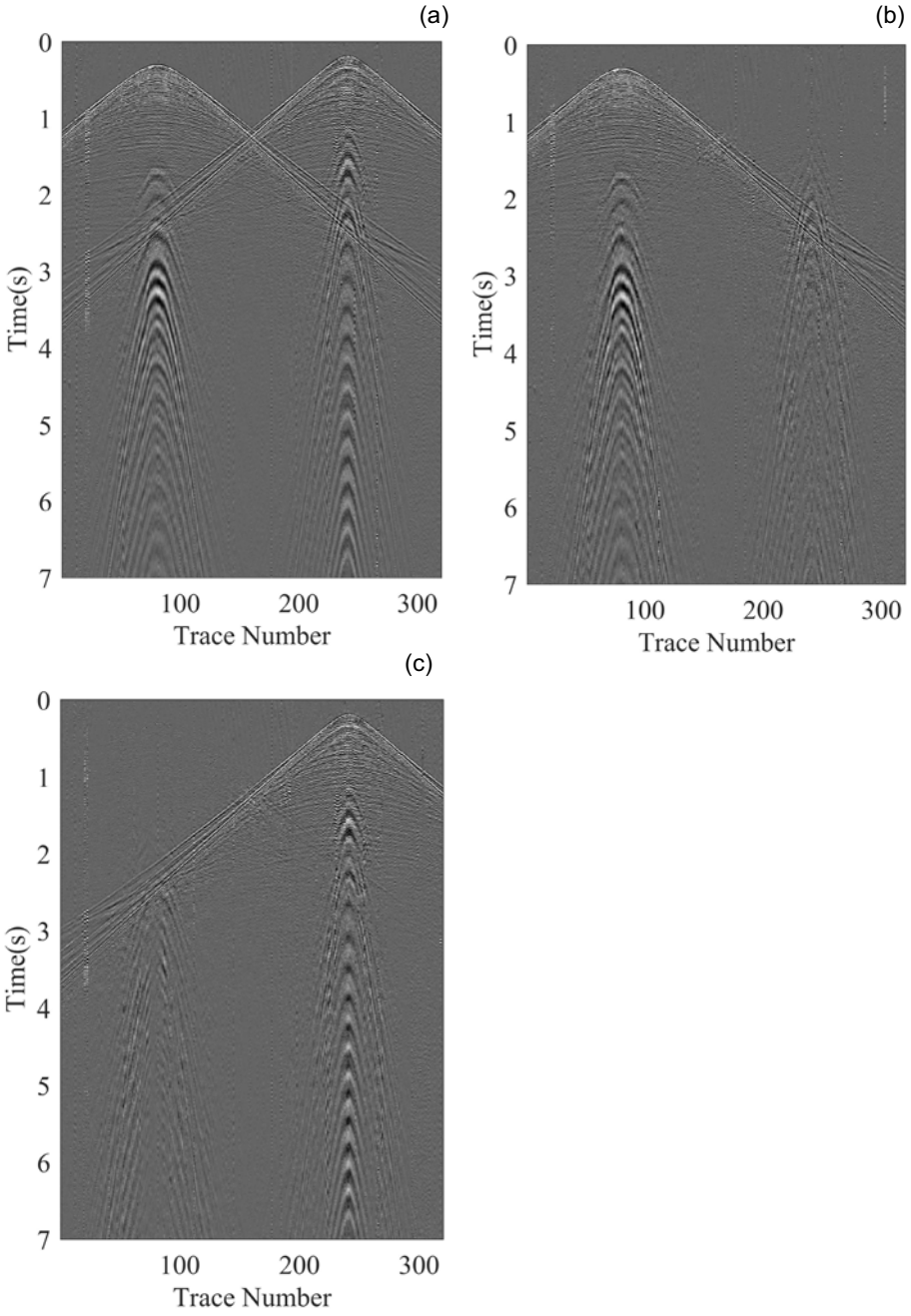


Fig. 16. Deblending example of field data of one common shot gather: blended gather (a), deblended result of shot 1 (b), and deblended result of shot 2 (c).

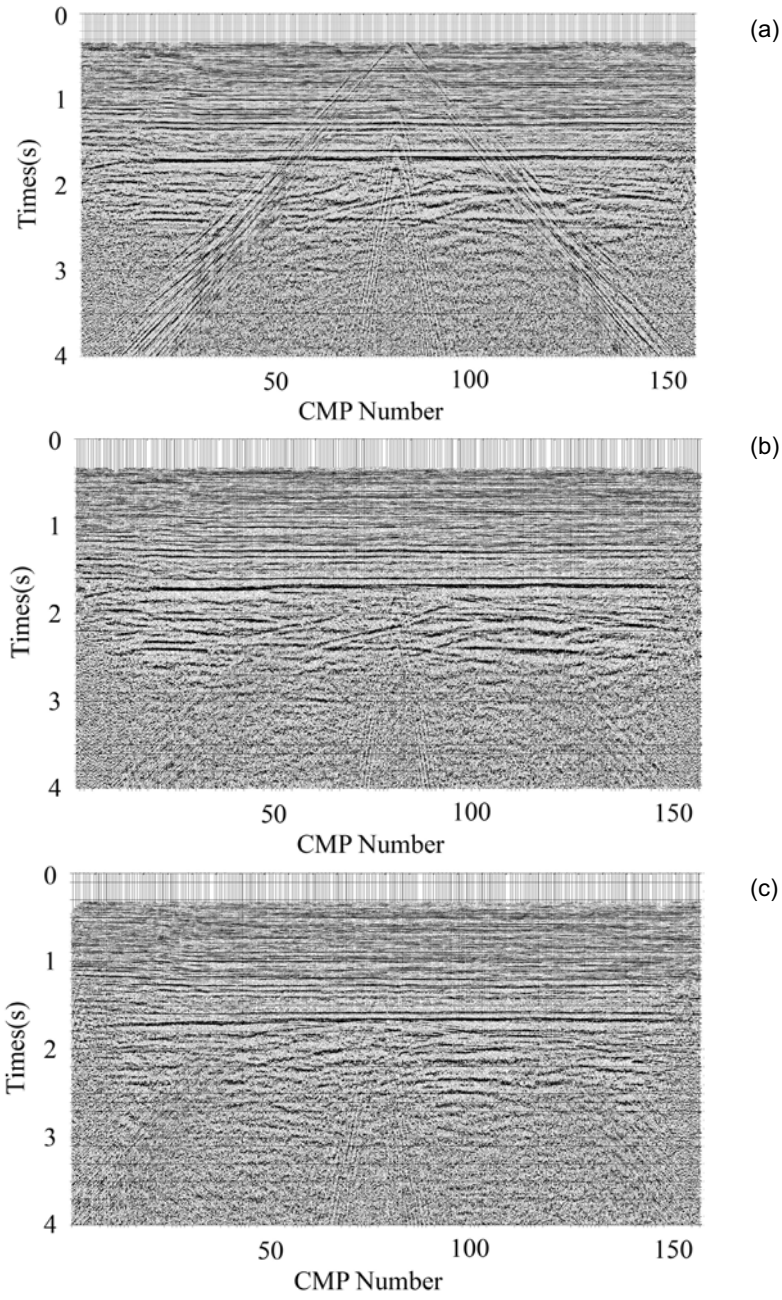


Fig. 17. Deblending example of field data of stack section: blended stack section (a), deblended stack section of source line 1 (b), and deblended stack section of source line 2 (c).

Two typical blended field datasets are shown in Figs. 14a and 15a, which are seriously contaminated by blending noise. After 30 iterations of FISTA with firm-thresholding, deblending results are shown in Figs. 14b and 15b, in which the reflections become much clear. The noise sections are shown in Figs. 14c and 15c, in which most of the blending noise is attenuated, although we can also see that some useful signals near the receiver point are damaged. The SNR increases from 2.2 to 11.6 dB for the first source, and from –2.2 to 9.2 dB for the second source. Although the deblending results are not so perfect, they are acceptable.

After processing all the common receiver gathers, we sort the data into common shot gather. One common shot gather is shown in Fig. 16. Panel (a) illustrates the blended profile, and panels (b) and (c) show deblended common shot gathers of the first and second shot, respectively. The results are likewise acceptable. Figure 17 displays the final stack sections of blended data, and separated data. We can see that the blending noise has been greatly decreased.

## 5. CONCLUSIONS

We have proposed an improved algorithm for deblending simultaneous-source data using FISTA with firm-thresholding. We have compared it with other alternative algorithms. All the algorithms, *i.e.*, ISTA with soft-thresholding, ISTA with firm-thresholding, FISTA with soft-thresholding and FISTA with firm-thresholding, have an acceptable effect to attenuate the blending noise; however, it can be concluded that in terms of approximation frame, FISTA has a faster convergence rate and higher accuracy than ISTA, and in terms of thresholding function, firm-thresholding function has a better convergence behavior and obtains a more accurate result.

When the blended seismic data become more complicated, it is more obvious that FISTA with firm-thresholding is the best choice to deblend the blended data. Moreover, our experiments indicate that it is possible to obtain accurate results within a small number of iterations using the proposed FISTA with firm-thresholding.

Acknowledgment. This work was supported in part by the 973 Program of China (2013CB228603), National Major Science and Technology Program (2011ZX05010-001, 2011ZX05024-001), National Natural Science Foundation of China (40974069, 41174119), and the Research of Novel Method and Technology of Geophysical Prospecting, CNPC (2014A-3609).

## References

Abma, R.L., T. Manning, M. Tanis, J. Yu, and M. Foster (2010), High quality separation of simultaneous sources by sparse inversion. **In:** *Proc. 72nd EAGE Conference and Exhibition incorporating SPE EUROPEC 2010*, DOI: 10.3997/2214-4609.201400611.

Akerberg, P., G. Hampson, J. Rickett, H. Martin, and J. Cole (2008), Simultaneous source separation by sparse radon transform. **In:** *Proc. SEG Annual Meeting, 9-14 November 2008, Las Vegas, USA*, SEG-2008-2801, Society of Exploration Geophysicists.

Beasley, C.J. (2008), A new look at marine simultaneous sources, *The Leading Edge* **27**, 7, 914-917, DOI: 10.1190/1.2954033.

Beck, A., and M. Teboulle (2009), A fast iterative shrinkage-thresholding algorithm for linear inverse problems, *SIAM J. Imaging Sci.* **2**, 1, 183-202, DOI: 10.1137/080716542.

Bruce, A.G., and H.-Y. Gao (1996), Understanding waveshrink: variance and bias estimation, *Biometrika* **83**, 4, 727-745, DOI: 10.1093/biomet/83.4.727.

Candes, E.J., and L. Demanet (2005), The curvelet representation of wave propagators is optimally sparse, *Commun. Pure Appl. Math.* **58**, 11, 1472-1528, DOI: 10.1002/cpa.20078.

Candes, E.J., and T. Tao (2005), Decoding by linear programming, *IEEE Trans. Inf. Theory* **51**, 12, 4203-4215, DOI: 10.1109/TIT.2005.858979.

Chambolle, A. (2004), An algorithm for total variation minimization and applications, *J. Math. Imaging Vis.* **20**, 1-2, 89-97, DOI: 10.1023/B:JMIV.0000011325.36760.1e.

Chartrand, R. (2007), Exact reconstruction of sparse signals via nonconvex minimization, *IEEE Signal Process. Lett.* **14**, 10, 707-710, DOI: 10.1109/LSP.2007.898300.

Chen, Y., and J. Ma (2014), Random noise attenuation by f-x empirical-mode decomposition predictive filtering, *Geophysics* **79**, 3, V81-V91, DOI: 10.1190/geo2013-0080.1.

Chen, Y., S. Fomel, and J. Hu (2014a), Iterative deblending of simultaneous-source seismic data using seislet-domain shaping regularization, *Geophysics* **79**, 5, V179-V189, DOI: 10.1190/geo2013-0449.1.

Chen, Y., J. Yuan, Z. Jin, K. Chen, and L. Zhang (2014b), Deblending using normal moveout and median filtering in common-midpoint gathers, *J. Geophys. Eng.* **11**, 4, 045012, DOI: 10.1088/1742-2132/11/4/045012.

Daubechies, I., M. Defrise, and C. De Mol (2004), An iterative thresholding algorithm for linear inverse problems with a sparsity constraint, *Commun. Pure Appl. Math.* **57**, 11, 1413-1457, DOI: 10.1002/cpa.20042.

Donoho, D.L. (2006), For most large underdetermined systems of linear equations the minimal 1-norm solution is also the sparsest solution, *Commun. Pure Appl. Math.* **59**, 6, 797-829, DOI: 10.1002/cpa.20132.

Doulgeris, P., K. Bube, G. Hampson, and G. Blacquiere (2012), Convergence analysis of a coherency-constrained inversion for the separation of blended data, *Geophys. Prospect.* **60**, 4, 769-781, DOI: 10.1111/j.1365-2478.2012.01088.x.

Figueiredo, M.A., and R.D. Nowak (2003), An EM algorithm for wavelet-based image restoration, *IEEE Trans. Image Process.* **12**, 8, 906-916, DOI: 10.1109/TIP.2003.814255.

Gao, H.-Y., and A.G. Bruce (1997), Waveshrink with firm shrinkage, *Statistica Sinica* **7**, 4, 855-874.

Huo, S., Y. Luo, and P. Kelamis (2009), Simultaneous sources separation via multidirectional vector-median filter. **In:** *Proc. SEG Annual Meeting, 25-30 October 2009, Houston, USA*, SEG-2009-0031, Society of Exploration Geophysicists.

Lin, T.T.Y., and F.J. Herrmann (2009), Designing simultaneous acquisitions with compressive sensing. **In:** *Proc. 71st EAGE Conference and Exhibition incorporating SPE EUROPEC 2009*, DOI: 10.3997/2214-4609.201400276.

Mahdad, A., P. Doulgeris, and G. Blacquiere (2011), Separation of blended data by iterative estimation and subtraction of blending interference noise, *Geophysics* **76**, 3, Q9-Q17, DOI: 10.1190/1.3556597.

Mahdad, A., P. Doulgeris, and G. Blacquiere (2012), Iterative method for the separation of blended seismic data: discussion on the algorithmic aspects, *Geophys. Prospect.* **60**, 4, 782-801, DOI: 10.1111/j.1365-2478.2012.01084.x.

Qu, S., H. Zhou, H. Chen, S. Zu, and L. Zhi (2014), Separation of simultaneous vibroseis data. **In:** *Proc. SEG Annual Meeting, 26-31 October 2014, Denver, USA*, SEG-2014-0182, Society of Exploration Geophysicists.

Received 9 December 2014
Received in revised form 29 May 2015
Accepted 14 July 2015

DE GRUYTER OPEN

**Acta Geophysica**
vol. 64, no. 4, Aug. 2016, pp. 1093-1111
DOI: 10.1515/acgeo-2016-0006

# Application of Ground Penetrating Radar Surveys and GPS Surveys for Monitoring the Condition of Levees and Dykes

Dariusz TANAJEWSKI and Mieczysław BAKUŁA

University of Warmia and Mazury in Olsztyn, Poland
e-mails: d.tanajewski@kgsin.pl (corresponding author); mbakula@uwm.edu.pl

A b s t r a c t

This paper analyses the possibility of using integrated GPS (Global Positioning System) surveys and ground penetrating radar surveys to precisely locate damages to levees, particularly due to the activity of small fossorial mammals. The technology of intercommunication between ground penetrating radar (GPR) and an RTK (Real-Time Kinematic) survey unit, and the method of data combination, are presented. The errors which may appear during the survey work are also characterized. The procedure for processing the data so that the final results have a spatial character and are ready to be implemented in digital maps and geographic information systems (GIS) is also described.

**Key words:** Ground Penetrating Radar surveys, GPS, RTK, levees monitoring, data synchronization.

## 1. INTRODUCTION

### 1.1 Background

Floods are frequent and devastating natural disasters. It is estimated that the effects of floods have affected almost 2.9 billion people in the last 30 years, of whom 550 thousand died, 360 thousand required hospitalization and 4.5 million lost their homes (Doocy *et al.* 2013). The calculation of the total

Ownership: Institute of Geophysics, Polish Academy of Sciences;
© 2016 Tanajewski and Bakuła. This is an open access article distributed under the Creative Commons Attribution-NonCommercial-NoDerivs license, http://creativecommons.org/licenses/by-nc-nd/3.0/.

economic and natural losses is practically impossible. One hundred major floods were recorded in Europe between 1998 and 2002 alone and insured economic losses totaling 25 billion euro (de Vries *et al.* 2003). Although this amount may be shocking, it was only a small fraction of the value of economic assets liable to flooding. The European Commission estimated in the Communication on "Flood risk management; flood prevention, protection and mitigation" (EC 2004) that land worth between 0.5 and 1 billion euro was located within 500 m from the European coastline. In the area liable to extreme flooding along the Rhine river, the potential losses could total another 165 billion euro.

The growing risk of extreme phenomena and potential financial losses forced the European Commission to take action aimed at flood prevention, protection and mitigation. Consultations with governments, non-governmental organizations, scientists and people started to develop an interdisciplinary and comprehensive approach to flood risk management. As a result, "Directive on the assessment and management of flood risks" (EC 2007), which obliged member states to take preventive and protective action, including monitoring and maintenance of a good condition of levees and dykes, was established.

### 1.2 Levee monitoring – technical aspects

The most popular methods of examining the condition of levees are dynamic probing, geotechnical boreholes and laboratory analyses of the collected samples (Bruce 1993, Gołębiowski *et al.* 2012). However, they provide data only for a small ground volume. Borys (2013) and technical guidelines ("Guidelines for evaluations of the condition and safety of levees") recommend that ground samples ought to be collected in places where there is a suspicion of levee construction weakening, but not less frequently than from 3 to 5 samplings per 1 km of the checked structure, depending on the levee class and its subsurface type. This means that a correct levee stability evaluation depends to a large degree on the knowledge, experience and subjective assessment of the person who conducts the field reconnaissance. The human factor can be reduced by increasing the number of probings, but this rises the costs of work and weakens the levee crown.

An alternative to geotechnical levee examination methods is the ground penetrating radar method (commonly called GPR) (Lee *et al.* 2012, Gołębiowski *et al.* 2012, Di Prinzio *et al.* 2010, Song and Guo 2010, Mori 2009, Mydlikowski and Beziuk 2009, Mydlikowski and Szynkiewicz 2009, Szynkiewicz 2000). It allows a near-surface and non-invasive examination of the structure of hydraulic engineering facilities along their entire length and in a relatively short time. In some cases, the survey results are available

in real time and can indicate the areas where the levee structure is weakened at the survey site. Such situations have been examined by the above-mentioned researchers. However, frequently only office survey processing enables the location of dangerous loosenings. A problem with the indication of such places in the field then appears, particularly if several kilometers of a levee were the object of the survey. A comprehensive method for the acquisition of data on the technical condition of hydrotechnical structures, which will determine the location of anomalies in them in geographic space, is therefore needed. This task can be managed by an integrated survey set consisting of a GPS receiver and a ground penetrating radar. Both of these technologies have been designed for completely different purposes. However, in the context of monitoring the condition of levees, only their combination allows for receiving full information on the object of examination (Urbini *et al.* 2001).

The aim of the conducted research was to check the feasibility and evaluate the efficiency of integrated GPR and GPS surveys in detection and spatial location of damage to river embankments. The authors were particularly interested in the tunnels and burrows of small mammals which inhabit the levee crown, because their destructive activity weakens the levee and raises flood risk to the highest degree (Niederleithinger *et al.* 2008). Satellite measurements were also used to determine the levee crown height along the entire examined length. The results have practical application and can be used by public services dealing with water management and flood safety.

## 2. INTEGRATED GPR AND GPS SURVEYS

### 2.1 GPR surveys: theoretical aspects

Detection of objects by the GPR method is based on the principle of electromagnetic wave reflection on boundaries. The transmitting antenna emits single pulses into the examined medium where they reflect and disperse at levels with different lithology, porosity or density. The receiving antenna captures the reflected waves and records them in a digital format (Daniels 2000). The received radargrams reflect the internal composition of the examined structure (Karczewski *et al.* 2011, Jol 2009).

Subsurface components have dielectric properties and can often be described by relative electric permittivity $\varepsilon_r$ and electrical conductivity $\sigma$ (Jol 2009).

The values of these parameters play an important role in ground penetrating radar surveys, because attenuation $\alpha$ and electromagnetic wave velocity $v$ in a given medium are determined on their basis. Attenuation determines the antenna's depth range. The depth reached by the electromagnetic wave is not constant and depends on the degree of wave energy reduction.

The factors attenuating signal energy are: high electrical conductivity of the examined medium, the presence of salts and clayey materials, and ground penetrating radar antenna frequency (Di Prinzio *et al*. 2010, Tillard and Dubois 1995, Smith and Jol 1995). Table 1 shows the values of relative permittivity and electromagnetic wave velocity for different media.

Table 1

Typical electromagnetic properties of the selected materials at 100 MHz (Morey 1998)

| Material | Relative dielectric permittivity $\varepsilon_r$ | Electrical conductivity $\sigma$ [mS/m] | Attenuation $\alpha$ [dB/m] | Velocity $v$ [m/ns] |
|---|---|---|---|---|
| Air | 1 | 0 | 0 | 0.30 |
| Fresh water | 81 | 0.05 | 0.1 | 0.033 |
| Dry sand | 3-5 | 0.01 | 0.01 | 0.15 |
| Saturated sand | 20-30 | 0.1-1.0 | 0.03-0.3 | 0.06 |
| Silts | 5-30 | 1-100 | 1-100 | 0.07 |
| Clays | 5-40 | 2-1000 | 1-300 | 0.06 |

However, the ground medium is usually not homogeneous and consists of several different materials. Relative dielectric permittivity is then not known and wave propagation velocity is measured at the site of the examination. Its value is estimated based on the measurement of an object which is at known depth. Another method is velocity profiling, called a wide angle reflection and refraction (WARR) or a common mid-point (CMP) (Daniels 2004, Fisher *et al.* 1992). It consists in increasing the distance of the receiving antenna from the transmitting antenna with simultaneous recording of the reflected signals. The relationship between the reflected wave transit time and the electromagnetic wave velocity in the medium can then be established (Karczewski *et al.* 2011):

$$t_r = \frac{\sqrt{x^2 + 4 \cdot d}}{v} \quad , \tag{1}$$

where $t_r$ is transit time to and from the target, $x$ distance between GPR antennas, $d$ depth to reflecting interface, and $v$ velocity of propagation.

Another velocity estimation method is fitting the arms of a synthetic hyperbola to the hyperbolas in the radargram. This velocity value is adopted for the one whose theoretical shape best correlates with the shape of the recorded hyperbolas. The correctly determined curve shape is created according to the formula (Sandmeier 2011):

$$t_R = \left[\sqrt{\frac{(x_i - x_d)^2}{v^2} + \left(\frac{t_0}{2} + \frac{r}{v}\right)^2} - \frac{r}{v}\right] + \left[\sqrt{\frac{(x_i + x_d)^2}{v^2} + \left(\frac{t_0}{2} + \frac{r}{v}\right)^2} - \frac{r}{v}\right], \quad (2)$$

where $t_R$ is recording time of the signal reflected from the object in the position $x_i$ , $t_0$ recording time of the signal reflected directly over the object, $x_d$ distance between the transmitting antenna and receiving antenna, $x_i$ antenna position relative to the object, $r$ object (conduit) radius, and $v$ wave velocity in the medium.

The formula shows that the diameter of the examined reference object and the distances between the transmitting and receiving antennas must be known in hyperbola shape determination. The fitting process itself is performed at the data processing stage. The depth determination error for this method is estimated at 10-12% of the real value (Jol 2009, Karczewski *et al.* 2011).

### 2.2 GPS surveys: theoretical aspects

The GPS survey method consists in the determination of the three-dimensional position of the receiver in the global coordinate system, based on the propagation time of radio signals sent by satellites. Coordinate determination accuracy depends on the technical parameters of the receiver and the applied survey technology. Two-frequency receivers, operating in RTK (Real Time Kinematic) survey mode, are commonly used in surveying for precise GPS measurements. From the architectural point of view, this technology consists of: a base receiver set on a point with known coordinates, a rover receiver used to determine the coordinates of successive points, and a communication channel through which the base receiver sends its observations to the rover receiver. The accuracy of position determination by this method is 1-2 cm for the horizontal position and 5 cm for altitude over approximately 10 km of baseline separation (distance between the base station and the rover receiver) (Edwards *et al.* 2010). Rapid and very precise measurement depends on resolving the unknown cycle ambiguities of the double-differenced carrier phase data to integers (ambiguity is the unknown number of whole wavelengths of the carrier signal contained in an unbroken set of measurements from a single satellite at a single receiver). The process is referred to as integer ambiguity resolution and its final solution ("fixed") can be done at the mm-cm level (Henning 2011).

### 2.3 Integrated GPS and GPR surveys: technical aspects

The NMEA 0183 communications protocol is most often used for data exchange between GPS signal receivers and other electronic devices. Data from the receiver are sent to the GPR controller (a laptop or a dedicated

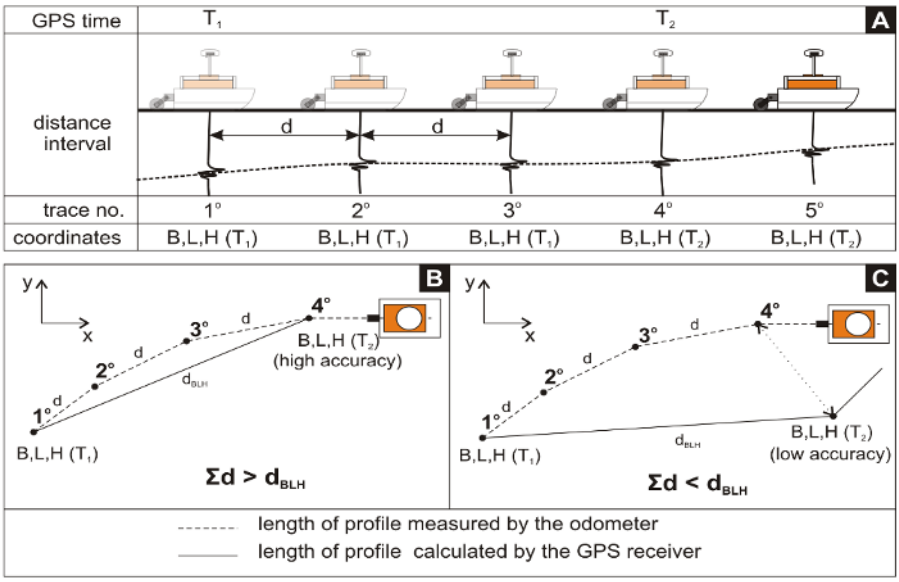


Fig. 1. Schema of the integration of GPS and GPR surveys (A) and errors in determining the length of the profile by a GPS receiver (B) and (C).

monitor) as autonomous sequences of text characters. Each of them contains data on the position (longitude, latitude, and altitude) and time. GPR survey data are also sent to the controller at the same moment. The data acquisition application generates a text file where individual traces, denoted with numbers, are assigned their position and time (Rial *et al.* 2005, Malå GeoScience 2010). However, this solution has some limitations. The signal in a ground penetrating radar is often released with high frequency and the GPS signal receiver cannot update its position equally quickly. This leads to situations where different traces have the same coordinates. The example is presented in Fig. 1A. Then the distance calculated on the basis of the coordinates may be significantly different from the distance measured by the odometer (examples in Fig. 1B). It depends on the speed of GPR movement the interval distance parameter, frequency of satellite measurements and the object that was measured. But, in many cases, low accuracy of GPS coordinates also affects the miscalculation of the length of the profile (Fig. 1C).

In more recent software versions, it is possible to set position interpolation for traces without determined coordinates (Ortyl and Bałut 2006), but it does not eliminate errors in determination of the distance.

Because of the electromagnetic signal nature, Rial *et al.* (2005) suggested in their paper that metal fixings and other elements must be avoided. However, Ortyl (2006) demonstrated in his research that a GPS signal re-

ceiver mounted on a 500 MHz antenna, fixed at around 0.7 m over the GPR antenna, had no significant effect on the results of ground penetrating radar measurements. It has not yet been studied how signals from GLONASS satellites affect the quality of the obtained GPR data, but because both systems use similar frequencies, the authors assumed that their effect would also be low.

## 3. CASE STUDY

The research was carried out along several kilometers of a dyke on the Łyna River in Olsztyn (north-eastern Poland). This structure was selected because in the past heavy rainfall had caused the river to breach the dyke crown, flood the adjacent areas and block an important local road. The conducted terrain inspection showed that the main cause of the ground surface inundation had been burrows of small fossorial mammals which had been weakening the body of the dyke. Fig. 2 shows an example of animal activity harmful to the construction of the structure. The aim of the ground penetrating radar examination was to provide more detailed information on the condition of the structure and the precise location of the damaged places.

The equipment used in the survey was Malå GPR ProEx System, Malå GeoScience, Sweden, fitted with a 500 MHz antenna and a ProEx Control Unit. This is the most universal antenna used for detecting small objects (a minimum of 5 cm in diameter) and, depending on the soil conditions, it provides a depth range from 3 to 5 m (Malå GeoScience 2003). The application Malå GroundVision for ProEx and X3M v. 1.26.1 was used for ground penetrating radar data acquisition. The ground penetrating radar's transmitting antenna released an electromagnetic wave based on the covered distance and measured with an odometer. The distance interval was 0.02 m.

A Trimble R8 SPS882 signal receiver, designed for precise geodetic surveys, was fixed to the ground penetrating radar antenna with a steel bracket

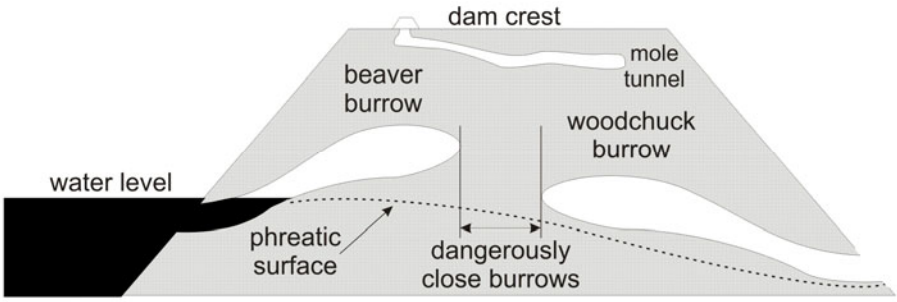


Fig. 2. Impacts of animals on earthen dams (FEMA 2005).



Fig. 3. Integrated survey set (ground penetrating radar antenna and GPS receiver).

and a 50 cm pole. The receiver operated in RTK survey mode and determined the position based on GPS and GLONASS satellites. One of the stations of the national reference station network ASG-EUPOS, located up to 2 km from the survey site, was used as the reference receiver. The receiver position determination frequency was 10 Hz. The survey set is shown in Fig. 3.

Reflex-Win 6.0 software was used for data processing and interpretation (Sandmeier 2011). This is an advanced application for filtering ground penetrating radar survey and seismic survey data. In the study the standard functions of the 2D-data-analysis module described in the REFLEXW 6.0 User Manual (Sandmeier 2011) were used. These included the move start-time, subtract mean (dewow), subtract-DC-shift, background removal, gain function, bandpass Butterworth and correct 3D-topography functions. The move start-time algorithm cuts off several samples from the start of the signal to determine the beginning of the depth scale. The dewow filtering removes subsequent decay of "wow" or low-frequency signal trend present in the data and eliminates a long waved part of the signal caused by the electromagnetic induction (Jol 2009). The DC-shift procedure converts ground penetrating radar signals to a form with the zero mean, subtracting their constant component. This enables subsequent correct survey material processing using other functions, *i.e.*, frequency filtering and gain (Karczewski *et al.* 2011). The "background removal" function removes background noise and reduces

constant horizontal banding across the radargrams (signal ringing effect) (Goodman 2006, Jol 2009). "Bandpass Butterworth" is one of temporal filters and it removes high frequency noise ("speckle"). "Gain function" improves the data display and interpretation (Jol 2009). It enhances a time slice based on manually set two filter parameters: linear gain and exponent (Sandmeier 2011). The "correct 3D-topography" function is a more advanced tool for trace correction in the time axis direction based on topographic data (Sandmeier 2011). The use of other non-standard procedures resulted from the needs which emerged in the interpretation process.

### 3.1 Field experiment description

The survey was conducted in sections of the levees separating the river from the area of a drained lake. The research object was divided into two parts (see Fig. 4). The first fragment (A) was in the immediate vicinity of a housing estate where animal activity seemed low. The second (B) was distant from human agglomerations. A greater damage caused by the action of small

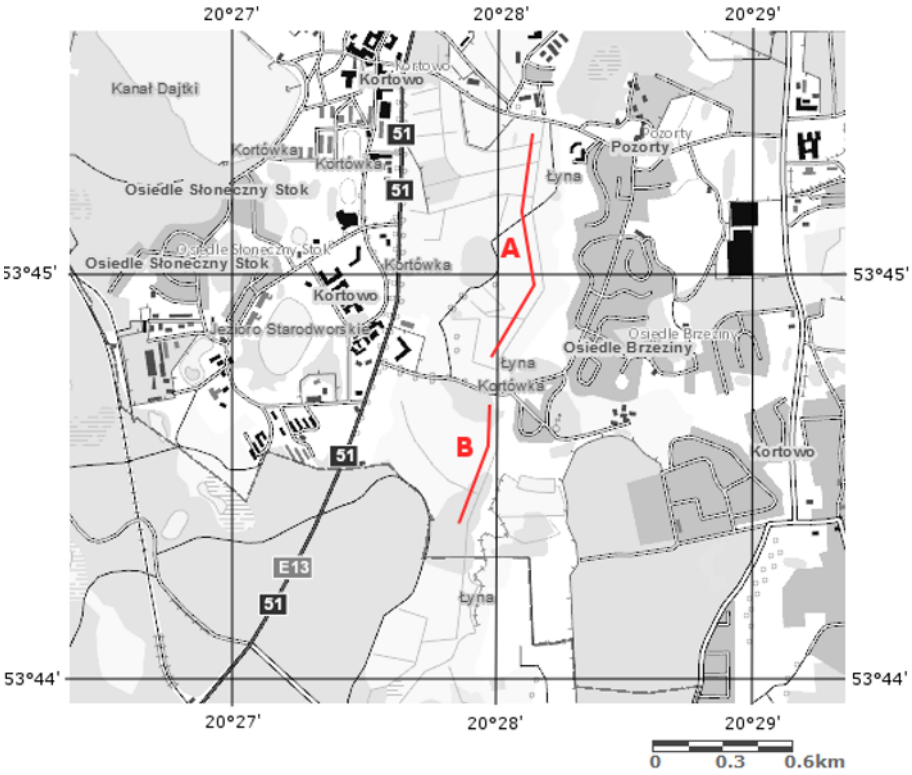


Fig. 4. Distribution map of the measured levee fragments, where (A) means low animals activity expected there, and (B) means high animals activity expected there.

mammals was expected there. Unlike in Di Prinzio *et al.* (2010), the research area was not limited to fragments devoid of factors with a negative effect on survey results, such as arborescent vegetation and shrubs, because, in practice, the occurrence of this type of objects in the immediate vicinity of hydraulic engineering structures cannot be excluded, although this is not desirable.

The embankments were built towards the end of the 1950s in the river dredging process. Soil extracted from its bottom was heaped up on the shores of the former body of water, in places where meadows were to be protected against flooding. The dyke width was designed as 2 m, its height as 1.50 m (altitude 104.21 m), and the slope in a 1:1.5 ratio. The levee consists of peat-mud soils, low moor peats, valley peats, and sandy soils with slightly loamy sand. The levees were modernized in the early 1990s. All of their losses resulting from subsidence and breaching were filled in with material from the river bottom and the dyke was then sown with a grass mixture (ZMiUW 1992).

As it has been mentioned in Section 2, it often happens in practice that the examined ground is composed of several materials. Also the variation of water content in the ground could affect the variations of GPR velocity (Sénéchal and Sénéchal 2010). In this case, the wave velocity determined on the basis of the relative dielectric permittivity parameter may be incorrect. Wave velocity in the medium was evaluated on the basis of a diffraction hyperbola analysis and velocity profile verses two-way travel time from hyperbolic matching data. After applying the "time-depth conversion" filter, the antenna's range was around 1.5 m in depth. The next step was to use "time cut" procedure to clip data after a subjectively identified two-way travel time beyond which noise exceeded the signal.

The terrain conditions in the vicinity of the examined levee were favorable for carrying out a satellite survey. To the west, the horizon was open most of the time and objects which could obstruct satellites (*i.e.*, trees or shrubs) appeared only sporadically. To the east, there were a flowing river, buildings and small clusters of trees and shrubs on a hill which could obscure the satellites at an elevation not higher than 45 degrees. This did not hinder, however, the determination of the receiver's position and the coordinates were determined for all surveyed points. However, a large terrain obstruction in satellite positioning can cause gross errors (Bakuła 2012, 2013).

## 4. DISCUSSION OF THE RESULTS

A set of files containing data on the structure of the levees along 2 km and a set of files with spatial data assigned to the trace numbers were obtained from the field work.

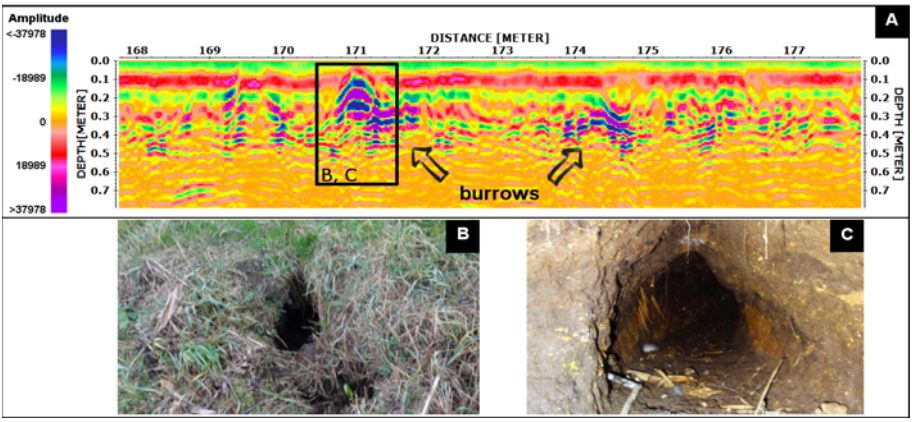


Fig. 5. Tunnel detected during the inspection and its imaging on the radargram (A).

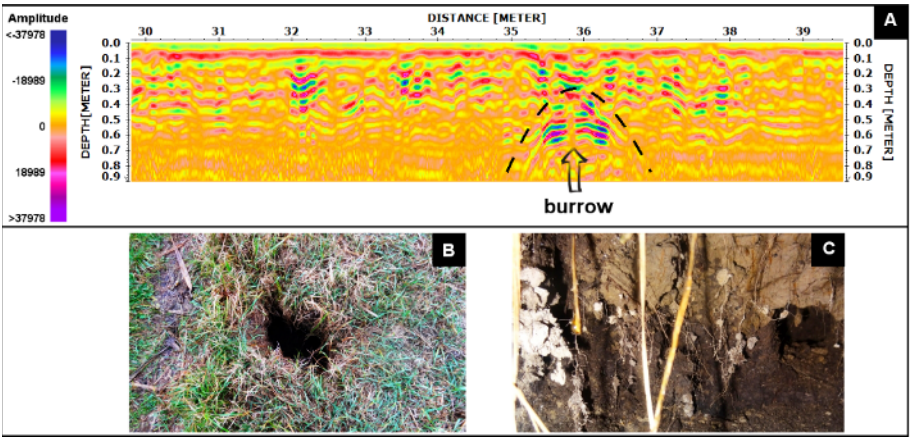


Fig. 6. Tunnel detected after data processing, its imaging on the radargram (A) and photos (B) and (C).

Data processing confirmed the presence of these voids in the levee which had been observed during the inspection of the structure. Figure 5 shows a scan fragment with a visible prelocated burrow at the depth of 10 cm. About 3 m away there was another tunnel, which had not been detected before the measurements. Figure 6 shows the image of the next burrow. It had not been detected during the earlier visual inspection and the survey. These anomalies could be identified only after data processing. These anomalies could be identified only after data processing. Based on their coordinates, places were found in the field and small excavations were made there, which confirmed our suppositions as to the cause of signal interference.

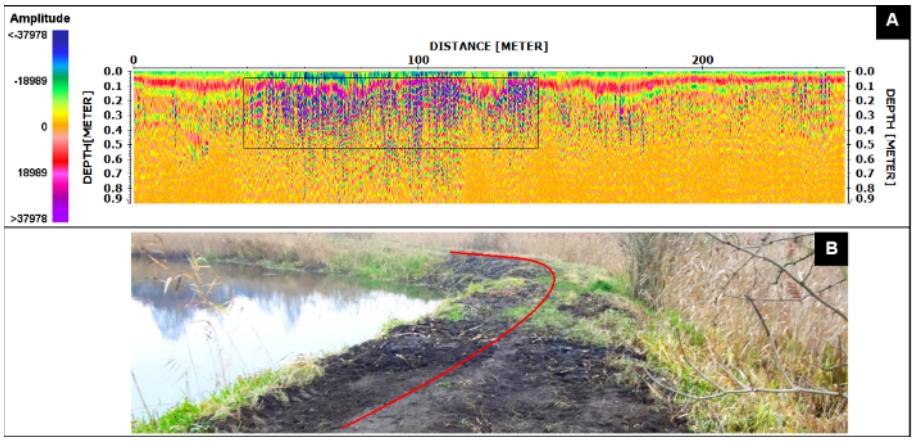


Fig. 7. Repaired levee section, its imaging on the radargram (A) and its photo (B).

Additionally, Fig. 7 presents a radargram fragment with a visible section of distinct signal interference extending from 40 to 140 m. This is the place where the levee had been destroyed by the river. It was repaired using sandbags and material from the river bottom immediately after this event.

The roots of large shrubs growing on the levee banks and collapsed tunnels often disturbed survey data and, in some cases, it was difficult to determine whether they were the cause of the present anomalies or whether it should be sought in other factors. In the places where the levee was flat and free from vegetation, the results were satisfactory.

All anomalies, which were considered as objects with a negative effect on the levee structure, were denoted with markers. A point set was obtained from the accurate GPS survey in the way it can be imported in applications for generating digital maps and Geographic Information Systems. The example was shown in Fig. 8A, where the blue dots are the equivalent of burrows detected during GPR survey. Moreover, the results of the measurement are used as input data in the filter correct 3D-topography.

An accuracy analysis of profiles length determination by the satellite survey was also performed. For this purpose, the distance travelled by the receiver during the survey at individual route sections was computed and compared to the distance recorded by the odometer of the ground penetrating radar equipment. A single profile consisted of around from 1500 to 2000 traces with measured coordinates. The results of these comparisons ($\Delta_1$) are shown in Table 2. The profiles with the numbers 1-5 compose the distance covered in the first direction and numbers 6-10 in the return direction.

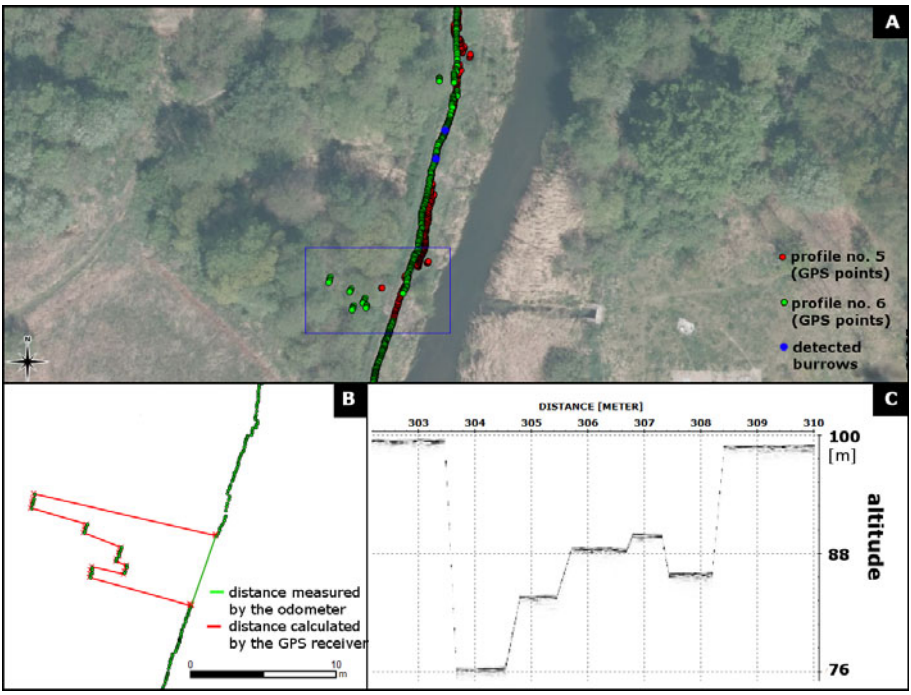


Fig. 8. Gross errors in determined coordinates and altitude (A) and their effect on calculated distance (B) and correct 3D-topography filter (C).

Table 2

Differences between the distance measured with the ground penetrating radar equipment and with the GPS receiver before ($\Delta_1$) and after ($\Delta_2$) coordinates correction

| Profile no. | GPR distance [m] (1) | GPS distance [m] (2) | $\Delta_1$ [m] (2) – (1) | Corrected GPS distance (3) | $\Delta_2$ [m] (3) – (1) |
|---|---|---|---|---|---|
| 1 | 202.25 | 280.73 | 78.48 | 217.48 | 15.23 |
| 2 | 200.25 | 205.87 | 5.62 | 205.62 | 5.37 |
| 3 | 250.08 | 268.48 | 18.40 | 259.43 | 9.35 |
| 4 | 251.16 | 259.59 | 8.43 | 257.81 | 6.65 |
| 5 | 336.77 | 377.02 | 40.25 | 347.22 | 10.45 |
| 6 | 360.34 | 403.30 | 42.96 | 370.04 | 9.70 |
| 7 | 267.85 | 278.50 | 10.65 | 278.31 | 10.46 |
| 8 | 250.09 | 266.30 | 16.21 | 260.05 | 9.96 |
| 9 | 200.45 | 214.70 | 14.25 | 210.00 | 9.55 |
| 10 | 159.51 | 174.50 | 14.99 | 171.00 | 11.49 |

Large values of differences, especially for profiles 1, 5, and 6, indicate gross errors in the determination of distance. This could be caused by failure of the odometer or low accuracy of the designated coordinates. First, odometer has been tested during the measurement profile of a known length. The results of the tests showed no malfunction.

The next step was to control the accuracy of the determination of the coordinate for each of the GPR profiles. The analysis was made on the basis of satellite images and it was set as a background for the determined GPS points. It was noted that the points with low accuracy of the coordinates (standard errors of several meters) were most often near trees and shrubs (Fig. 8A). Trees and other obstacles prevented receiving the signals from satellites and determination high-accuracy three-dimensional coordinates. To obtain the fixed solutions of integer ambiguity during RTK/GPS surveys, at least 5 satellites must be tracked and the quality of signals from satellites also has to be favorable (especially in this method of GPS measurement) (Lee and Ge 2006), so a good condition of measurements is very important.

Sometimes the accuracy of the points was also lower (a dozen or a few tens of centimeters) in places located away from high objects. It could depend on the discontinuities in the time series of carrier-phase measurements due to the receiver temporarily losing lock on the carrier of a GPS signal, known as "cycle slips" (Karaim *et al.* 2013, Kim and Langley 2001, Hofmann-Wellenhof *et al.* 1997). Hofmann-Wellenhof *et al.* (1997) distinguished three causes of cycle slips: obstructions of the satellite signal due to some objects (for example: trees, buildings, mountains); a low signal-to-noise ratio or carrier-to-noise-power-density ratio due to bad ionospheric conditions, signal multipath, high receiver dynamics or low satellite elevation angle and a failure in the receiver software which leads to incorrect signal processing. Then value of a phase ambiguity is determined incorrectly on one or more carrier signals and the coordinates have a lower accuracy.

When the horizontal coordinates have low accuracy, then the attitude is also determined with the gross error (usually much larger than the horizontal coordinates). Thus, the correct 3D-topography filter should not be applied to such satellite surveys as the topography will be inconsistent with the reality, as shown in Fig. 8C.

Based on the analysis of the satellite images and text files with coordinates (*. COR files) points with low accuracy were removed. Then the elimination criteria were used:

- points that are outside the flood embankment and/or are located far away from the other points,
- points with the value of the altitude that is significantly different from the approximate altitude of the flood embankment (more than one meter).

After deleting erroneous data, the distance GPS was recalculated and compared with the results of the odometer. The results ($\Delta_2$) are shown in Table 2. In most cases, the results are better, although they are still not perfect. Besides, the GPR traces for which the coordinates were removed have interpolated BLH values. They also can be calculated with an error (smaller, but difficult to estimate).

So which option ought to be chosen: inaccurate coordinates and the knowledge that they cannot be used to locate anomalies or interpolated values of the coordinates of the unknown accuracy? The authors believe the answer to this question depends on the purpose of surveys. In this case, we recommend using the original coordinates. The authors suggest measuring the profiles twice as one of them is likely to have a better set of BLH values. But in the case of GPR measurements using low-frequency antennas, coordinate interpolation errors will have no meaning.

## 5. CONCLUSION

The results of the survey prove that the GPR method can be used for monitoring the condition of hydraulic engineering structures. Data processing results shown in Figs. 4-6 illustrate examples of interference in the structure of the examined ground. In the first two cases, these are tunnels dug by small mammals. In the third, high disturbance was caused the repair work recently being performed on the levee. That supports Di Prinzio *et al.* (2010) that in places where the levee underwent any changes, the received signals differ from those recorded where the structure was intact.

Since the GPR method is sensitive to interference caused by various geologic and cultural factors (like reflections from nearby vehicles, buildings, fences, power lines, and trees), unprocessed radargrams could provide only approximate shapes and depths. That means some anomalies in the examined structure may be noticed only after data processing. In this situation, GPR data integration with satellite measurements indicates the importance of data processing. Only because accurate geodetic coordinates are assigned to individual traces, they can be located later in the field, plotted on a map and fed into a Geographic Information System.

Nevertheless, the most accurate real-time kinematic surveys, which are commonly used in the geodesy, are not ideal and error-free. Their limitation may be a too small number of observed satellites, a cycle slip and loss of access to the observations sent from the base station. They cause errors in determining the coordinates and height, which do not allow for the correct application of GPS data to locate anomalies and topography modeling during GPR data processing. The solution may be a two-time measurement of one profile or data analysis and removal of inaccurate GPS coordinates. The choice depends on the purpose of measurements. The solution may be a

double measure of the profile or GPS data analysis and removal of inaccurate coordinates. The choice depends on the purpose of GPR surveying.

Precise topographic data are important for levee condition examination. According to the technical documentation, the height of the examined structure was gradually decreasing owing to ground subsidence. In the early 1990s, its height was increased with additional embankments. Having available altitude data at individual points of the levee crown, it can be determined in which place the levee is the lowest and requires repair work. This also allows to predict where the river will overflow the levee and which areas are liable to flooding.

Summing up, the comprehensiveness of integrated GPR and GPS surveys in levee monitoring requires to be stressed. They allow data on levee condition to be acquired quickly and economically without interference to its structure, and all damage is located in a coordinate system. In situations where human life and safety are involved, all information is vital and precise determination of weakened places in the body of the levee is priceless knowledge. Therefore, it is worth employing all technologies which significantly improve the safety. Nevertheless, for public services to be able to use them fully, they must provide optimal conditions for conducting satellite and ground penetrating radar surveys. Trees and shrubs which grow on the levee crown not only prevent correct GPR/GPS measurement, but also weaken the structure.

It must also be remembered that the result of a ground penetrating radar survey is full, however general, information on the condition of the examined structure. According to the "from the whole to the part" principle, boreholes and probings should be made in weakened places to obtain complete and necessary data for correct evaluation of the condition of the levee.

Acknowledgements. The authors are grateful to Mr. Jerzy Dziurdź from the Board of Land Amelioration and Water Facilities (Olsztyn, Poland) for making the technical documentation available. The review comments provided by two anonymous reviewers helped to improve the quality of this paper.

## References

Bakuła, M. (2012), An approach to reliable rapid static GNSS surveying, *Surv. Rev.* **44**, 327, 265-271, DOI: 10.1179/1752270611Y.0000000038.

Bakuła, M. (2013), Study of reliable rapid and ultrarapid static GNSS surveying for determination of the coordinates of control points in obstructed conditions,

*J. Surv. Eng. ASCE* **139**, 4, 188-193, DOI: 10.1061/(ASCE)SU.1943-5428.0000109.

Borys, M. (2013), Principles of the yearly flood embankments technical state controls realisation, *Gospod. Wodna* **2013**, 7, 260-266 (in Polish).

Bruce, D.A. (1993), A review of drilling and grouting methods for existing embankment dams, *Geotech. Spec. Publ*. **35**, 803-819, DOI: 10.1061/9780784412350.0107.

Daniels, D.J. (ed.) (2004), *Ground Penetrating Radar*, IET Radar, Sonar, Navigation and Avionics Series, Vol. 15, The Institution for Electrical Engineers, London.

Daniels, J.J. (2000), Ground penetrating radar fundamentals. Prepared as an appendix to a report to the U.S.EPA, Region V.

de Vries, S., R.A. Verheij, P.P. Groenewegen, and P. Spreeuwenberg (2003), Natural environments – healthy environments? An exploratory analysis of the relationship between greenspace and health, *Environ. Plann*. *A* **35**, 10, 1717-1731, DOI: 10.1068/a35111.

Di Prinzio, M., M. Bittelli, A. Castellarin, and P. Rossi Pisa (2010), Application of GPR to the monitoring of river embankments, *J. Appl. Geophys*. **71**, 2-3, 53-61, DOI: 10.1016/j.jappgeo.2010.04.002.

Doocy, S., A. Daniels, S. Murray, and T.D. Kirsch (2013), The Human impact of floods : a historical review of events 1980-2009 and systematic literature review, *PLoS Curr. Disasters* **5**, PMC3644291, DOI: 10.1371/currents.dis.f4deb457904936b07c09daa98ee8171a.

EC (2004), Flood risk management, flood prevention, protection and mitigation, Communication from the Commission to the Council, the European Parliament, the European Economic and Social Committee and the Committee of the Regions, COM/2004/0472, 11 pp.

EC (2007), Directive 2007/60/EC of the European Parliament and of the Council of 23 October 2007 on the assessment and management of flood risks, Official Journal of European Union on 6 November 2007, L 288/27, 27-24.

Edwards, S.J., P.J. Clarke, N.T. Penna, and S. Goebell (2010), An examination of network RTK GPS services in Great Britain, *Surv. Rev*. **42**, 316, 107-121, DOI: 10.1179/003962610X12572516251529.

FEMA (2005), Technical manual for dam owners. Impacts of Animals on Earthen Dams, FEMA 473, Federal Emergency Management Agency.

Fisher, S.C., R.R. Stewart, and H.M. Jol (1992), Processing ground penetrating radar (GPR) data, *CREWES Res. Rep*. **4**, 1-21.

Gołębiowski, T., S. Tomecka-Suchoń, and J. Farbisz (2012), Use of geophysical methods for non-destructive detection and monitoring of technical level in the river embankments. **In:** *European Symp. "Anti-flood Defences – Today's Problems", 28-30 March 2012, Paris–Orleans, France* (in Polish).

Goodman, D. (2006), GPR Survey at Ft Frederica, Georgia. National Park Service Workshop, May 16-20, 2006, Geophysical Archaeometry Laboratory, Woodland Hills, USA.

Henning, W. (2011), User guidelines for single base real time GNSS positioning, Ver. 2.1, National Oceanic and Atmospheric Administration, National Geodetic Survey, USA.

Hofmann-Wellenhof, B., H. Lichtenegger, and J. Collins (1997), *GPS. Theory and Practice*, 4th ed., Springer, Wien.

Jol, H.M. (2009), *Ground Penetrating Radar: Theory and Applications*, Elsevier Science, Amsterdam.

Karaim, M.O., T.B. Karamat, A. Noureldin, M. Tamazin, and M.M. Atia (2013), Real-time cycle-slip detection and correction for land vehicle navigation using inertial aiding. **In:** *Proc. 26th Int. Technical Meeting of the ION Satellite Division, ION GNSS+ 2013, 16-20 September 2013, Institute of Navigation, Nashville, USA*.

Karczewski, J. Ł. Ortyl, and M. Pasternak (2011), *Zarys Metody Georadarowej*, Wydawnictwa AGH, Kraków (in Polish).

Kim, D., and R.B. Langley (2001), Instantaneous real-time cycle-slip correction of dual-frequency GPS data. **In:** *Proc. Int. Symp. on Kinematic Systems in Geodesy, Geomatics and Navigation KIS 2001, 5-8 June 2001, Banff, Canada*, 255-264.

Lee, D.-H., J.-H. Wu, H.-M. Lin, P.-M. Liao, G.-Z. Zeng, G.-C. Yang, and C.-J. Liao (2012), Classification of the eroded cavities behind concrete-faced embankments by ground penetration radar. **In:** *Proc. 6th Int. Conf. on Scour and Erosion, 27-31 August 2012, Paris, France*, 1393-1399.

Lee, I.-S., and L. Ge (2006), The performance of RTK-GPS surveying under challenging environmental conditions, *Earth Planets Space* **58**, 5, 515-522, DOI: 10.1186/BF03351948.

Malå GeoScience (2003), Antenna 500 MHz for ground penetrating radar investigation. User Manual, Malå GeoScience, Sweden.

Malå GeoScience (2010), Using Malå GPR systems with GPS equipment, Application note, Printed Matter No. 2894, Malå GeoScience, Sweden, 1-5.

Morey, R.M. (1998), *Ground Penetrating Radar for Evaluating Subsurface Conditions for Transportation Facilities*, NCHRP Synthesis 255, Transportation Research Board, National Research Council, National Academy Press, Washington.

Mori, G. (2009), The use of Ground Penetrating Radar and alternative geophysical techniques for assessing embankments and dykes safety, Ph.D. Thesis, Università di Bologna, Bologna, Italy.

Mydlikowski, R., and G. Beziuk (2009), Examination of levee condition by means of GPR, *Studia Geotech. Mech*. **31**, 4, 49-56.

Mydlikowski, R., and A. Szynkiewicz (2009), Non-invasion detection inhomogeneities in structure of levees by radar GPR, *Trans. VSB – Tech. Univ. Ostrava* **9**, 2, 178-192.

Niederleithinger, E., A. Weller, R. Lewis, U. Stötzner, T. Fechner, B. Lorenz, and J. Niessen (2008), Evaluation of geophysical methods for river embankment investigation. **In:** *Proc. 4th Int. Symp. on Flood Defence: Managing Flood Risk, Reliability and Vulnerability, Toronto, Ontario, Canada*.

Ortyl, Ł. (2006), Examination of influence of a GPR-GPS measuring set external elements on results of georadar sensing, *Geodesy* **42**, 45-60.

Ortyl, Ł., and A. Bałut (2006), Application of a RTK-GPS technique in the process of 3-D location of georadar profile traces, *Geodesy* **42**, 27-44.

Rial, F.I., M. Pereira, H. Lorenzo, and P.Arias (2005), Acquisition and synchronism of GPR and GPS data: application on road evaluation, *Image Signal Process. Remote Sens.* **9**, 372-379, DOI: 10.1117/12.627965.

Sandmeier, K.J. (2011), ReflexW version 6.0. User manual, Software Manual, Karlsruhe, Germany, 532 pp.

Sénéchal, P., and G. Sénéchal (2010), Relationships between water flow rate and geophysical measurements in an alluvial aquifer, *Acta Geophys*. **58**, 1, 83-95, DOI: 10.2478/s11600-009-0024-7.

Smith, D.G., and H.M. Jol (1995), Ground penetrating radar: antenna frequencies and maximum probable depths of penetration in Quaternary sediments, *J. Appl. Geophys.* **33**, 1-3, 93-100, DOI: 10.1016/0926-9851(95)90032-2.

Song, H., and Z. Guo (2010), Ground penetrating radar model simulation for detection of coastal embankment, *Electron J. Geotech. Eng.* **15**, 589-600.

Szynkiewicz, A. (2000), GPR monitoring of earthen flood banks/levees. **In:** D.A. Noon, G.F. Stickley, and D. Longstaff (eds.), *Proc. SPIE 4084, Eighth International Conference on Ground Penetrating Radar, 23 May 2000, Gold Coast, Australia*, 85-90, DOI: 10.1117/12.383541.

Tillard, S., and J.C. Dubois (1995), Analysis of GPR data: wave propagation velocity determination, *J. Appl. Geophys*. **33**, 1-3, 77-91, DOI: 10.1016/0926-9851(95)90031-4.

Urbini, S., L. Vittuari, and S. Gandolfi (2001), GPR and GPS data integration: examples of application in Antarctica, *Ann. Geophys*. **44**, 4, 687-702, DOI: 10.4401/ag-3568.

ZMiUW (1992), Construction of levees on the Lyna river, Technical Project, Board of Land Reclamation and Water Facilities (ZMiUW), Warsaw, Poland (unpublished).

Received 20 January 2014
Received in revised form 24 October 2014
Accepted 6 August 2015

DE GRUYTER OPEN

**Acta Geophysica**
vol. 64, no. 4, Aug. 2016, pp. 1112-1138
DOI: 10.1515/acgeo-2016-0042

# Interpretation of Gravity Data using 3D Euler Deconvolution, Tilt Angle, Horizontal Tilt Angle and Source Edge Approximation of the North-West Himalaya

Gopal K. GHOSH

Oil India Limited, Duliajan, Assam, India
e-mail: gk_ghosh@yahoo.com

A b s t r a c t

The collision of the Indian plate and the Eurasian plate created shortening and imbrications with thrusting and faulting which influences northward tectonic movement. This plate movement has divided the Himalaya into four parts, *viz*. Outer Himalaya, Lesser Himalaya, Greater Himalaya, and Tethys Himalaya. The crystalline basement rock plays an imperative role for structural and tectonic association. The study has been carried out near Rishikesh-Badrinath neighborhood in the north-western part of the Himalayan girdle with multifarious tectonic set up with thrusted and faulted geological setting. In this study area, 3D Euler deconvolution, horizontal gradient analysis, tilt angle (TILT) and horizontal tilt angle (TDX) analysis have been carried out using gravity data to delineate the subsurface geology and heterogeneity in the north-western part of Himalaya. The Euler depth solutions suggest the source depth of about 12 km and various derivative analyses suggest the trend of the delineation thrust-fault boundaries along with the dip and strike direction in the study area.

**Key words:** Euler deconvolution, tilt angle (TILT), horizontal tilt angle (TDX), gradient derivative, Indian Plate.

Ownership: Institute of Geophysics, Polish Academy of Sciences;
© 2016 Ghosh. This is an open access article distributed under the Creative Commons Attribution-NonCommercial-NoDerivs license,
http://creativecommons.org/licenses/by-nc-nd/3.0/.

## 1. INTRODUCTION

The area of study, situated in the Rishikesh-Badrinath, extends from 30° N to 31.2° N and 78° E to 80° E (Fig. 1). The tectonic movements of the Indian plate and the Eurasian plate caused overlapping, shortening, stratigraphic changes, and tectonic setting in the north-western part of Himalayan belt (Leech *et al*. 2005). The Himalaya can be divided into four parts: Outer Himalaya, Lesser Himalaya, Greater or Higher Himalaya, and Tethys Himalaya (Gansser 1964). The Main Frontal Thrust (MFT) to the south and the Main Boundary Thrust (MBT) to the north are referred to as Outer Himalaya and have molassic Siwalik super-groups of Miocene and Pliocene ages. The Lesser Himalaya is also subdivided by the MBT to the south and the Main Central Thrust (MCT) to the north and a thick pile of highly folded Proterozoic sedimentary strata with older crystalline rocks (Gansser 1964). The Greater or Higher Himalaya is demarcated by the MCT to its south and the Dar-Martoli Fault or Tethys Fault or the South Tibetan Detachment (STD) to the north. The Tethys Himalaya includes thick pile of sedimentary rocks of Cambrian to lower Eocene ages. The structural and petrological aspects have been studied by Le Fort (1975). Structural and tectonic interpretations of parts of Himalaya have been carried out by Molnar *et al*. (1977) using some geophysical observations. The MCT and its quartz-rich tectonites in Central

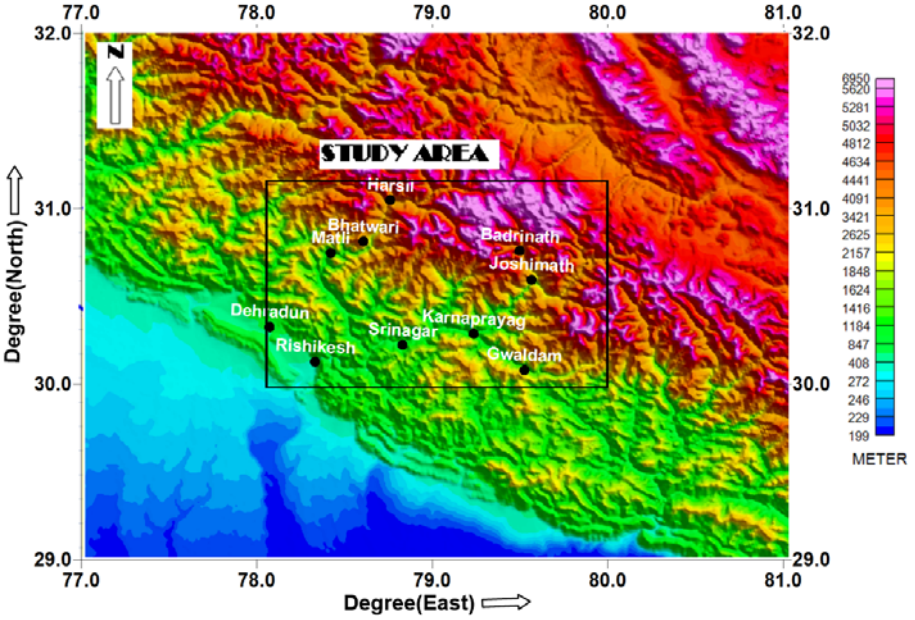


Fig. 1. Computer generated map showing the topography of the study area and its surroundings.

Nepal have been studied by Bouchez and Pecher (1981). The deformation pattern of leucogranites of the Crystalline MCT (CMCT) sheet in southern Tibet was studied by Burg *et al*. (1984). Grasemann *et al*. (1999) represented kinematic flow of decelerating strain path analysis and extrusion of orogenic wedges from the MCT of north-west Himalaya. Beaumont *et al*. (2001) considered the extrusion of low-viscosity crustal channel in the Himalayan tectonics as coupled to focus surface denudation. Vannay and Grasemann (2001) made it clear that the Himalayan inverted metamorphism and syncconvergence extension are a consequence of a general shear extrusion. Bhattacharya and Weber (2004) elucidated the shear deformation in the MCT zone of north-western Himalaya region.

The crystalline basement rock plays a vital role for structural and tectonic involvement which is unperturbed with tectonic movement and deformation. In this text we have dealt with "basement rocks" or "crystalline basement rocks" which are basically of metamorphic or igneous origin and are termed "granitic basement", generally covered by sedimentary rocks or sedimentary basin. Generally, *S*-wave velocity starts around 3500 m/s and *P*-wave velocity starts around 6000 m/s in this layer. This is the high velocity layer. It is generally described as the Indian Shield situated below the sedimentary layers and named the Indian Crystalline Basement.

The study area is located near Rishikesh-Badrinath neighborhood in the north-western part of the Himalayan girdle with multifarious tectonic set up with thrusted and faulted geology. The estimation of crystalline basement depth in folded and thrusted areas of such kind is very difficult. Different authors (Khattri *et al*. 1989, Reddy and Arora 1993, Bhattacharya and Weber 2004, Arora *et al*. 2007) worked for the estimation of basement depth, but the results are not very specific and clear.

Ghosh and Singh (2014) studied the Indian crystalline basement depth in the Dehradun-Badrinath area using spectral analysis and 2D Euler deconvolution technique of gravity data along the few selected profiles. The results are obtained using 2D approach and some geological models have been proposed for shallow crustal configuration based on the gravity data (Ghosh and Singh 2014). The average basement depth estimated was 11.27 km using 2D spectral analysis of gravity data. The 2D Euler de-convolution suggests basement depth varying from 10 to 15 km across the profile from SW to NE in the study area along the three selected profiles. The study suggests that most of the cluster points were located within 10 to 15 km depth range. However, the results provided do not meet in terms of holistic vision to get details in 3D interpretation.

In continuation, to study the area in terms of 3D depth investigation, we have used the published gravity data (Qureshy *et al*. 1974). The old gravity data have been digitized and re-interpreted in terms of geophysical conse-

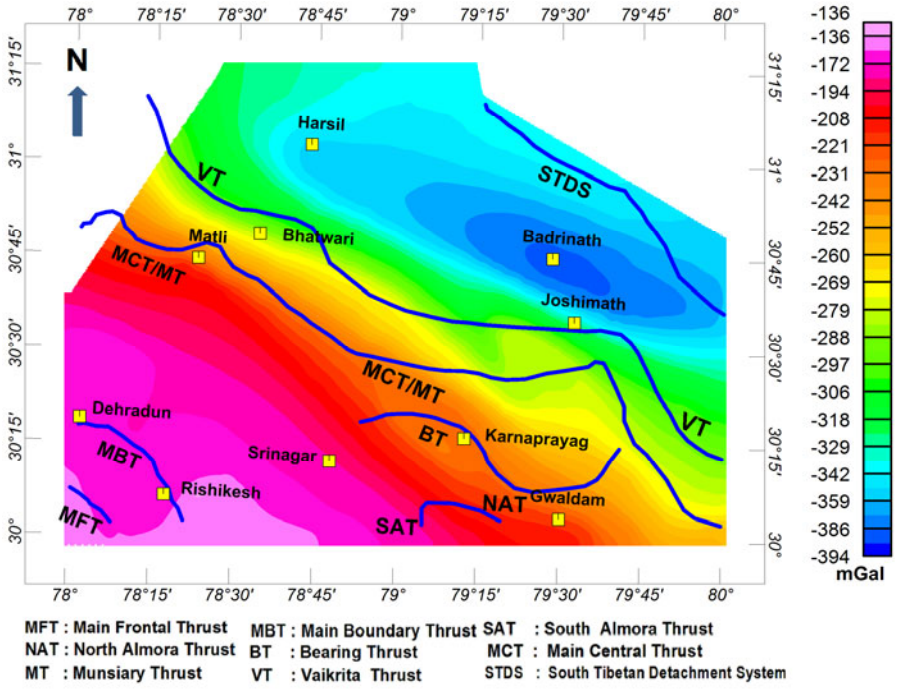


Fig. 2. Bouguer gravity anomaly map (after Qureshy *et al.* 1974) digitized and replotted (Ghosh and Singh 2014). The colour bar denotes the Bouguer gravity anomaly values. Higher gravity value observed at Rishikesh, Srinagar, and Dehradun areas. Lower gravity values are observed at Badrinath, Harsil, and Joshimath areas. Moderate gravity value observed at Gwaldam in the central part orienting NW-SE trends.

quences. The contour maps have been generated using minimum curvature gridding with a grid spacing of 1000 m. The data has been further applied to $3 \times 3$ convolution matrix for better imaging. The different thrust locations (Ghosh and Singh 2014) are superimposed on the digitized gravity anomaly map (Fig. 2).

In the present study, various gravity gradients are interpreted and results are correlated. The horizontal gradient, tilt angle derivative (TILT), horizontal tilt angle derivative (TDX), and Euler deconvolution (ED) of gravity data have been used to delineate the subsurface geology, identifying the subsurface heterogeneity and crystalline basement depth in the study area. Apart from this, to locate the edges (*i.e.*, geological contacts) or peaks, deriving the source edge function have been estimated using gravity data. Source edge detection with dip and strike orientation have been derived from gravity grid data (Cordell and Grauch 1982, Blakely and Simpson 1986, Grauch and Cordell 1987).

## 2. GEOLOGY AND TECTONICS

The study area is enfolded with various kinds of geological formations with thrusting and faulting. It is covered by Ganga Basin, Sub Himalaya, Lesser Himalaya, Vaikrita Group, Higher Himalaya, and Tethys Himalaya. The Main Frontal Thrust (MFT) and Main Boundary Thrust (MBT) are located at the south-western part. South Almora Thrust (SAT) and North Almora Thrust are located in the southern part and mostly outside the study area. Main Central Thrust (MCT) divides into multi-faults/thrusts and prominently into two parts, Munsiyari Thrust (MT) and Vaikrita Thrust (VT), which are located at the central part of the study area oriented NW-SE. The MCT has played a role for the Himalayan mountain development. It connects the Greater Himalayan crystalline series over the Lesser Himalayan series. This MCT itself is a wide fault zone and coincides with several string faults.

The Southern Tibetan Detachment System (STDS) is situated in the north-eastern part of the map. The geologic and the tectonic map of the study area is shown in Fig. 3 (after Ghosh and Singh 2014). Patriat and Achache

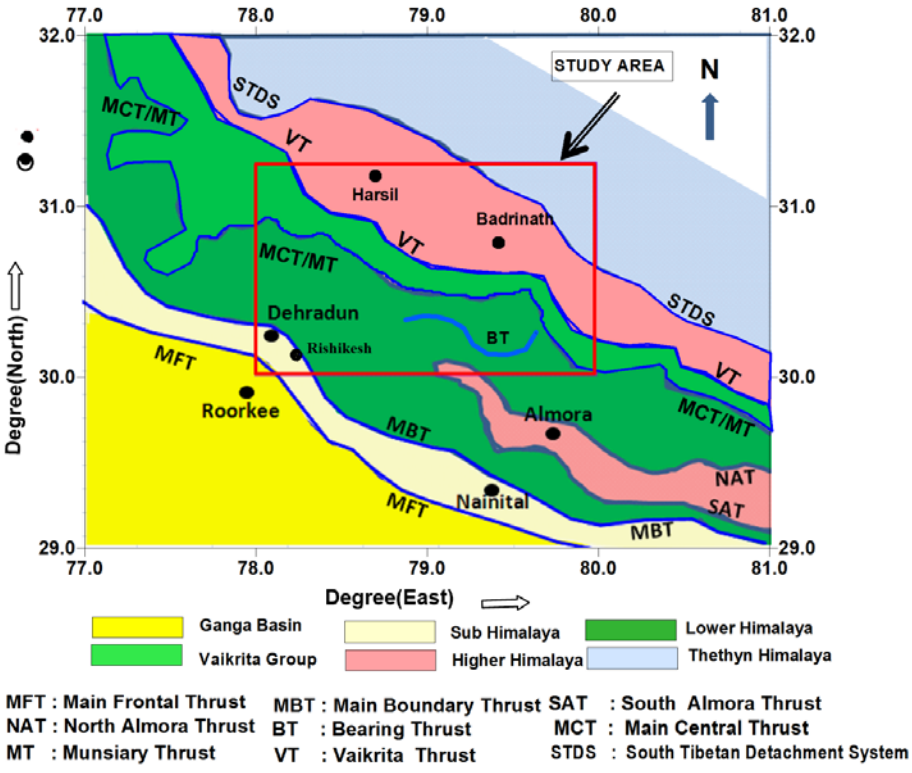


Fig. 3. Geological and tectonic map of the study area (after Ghosh and Singh 2014).

(1984) observed shortening of continental crust in different incidents like subduction of continental crust, intra continental thrusting, internal deformation and lateral extrusion. Sinha (1987) studied the crustal evolution of collision and compressional belts and the tectonic zonation of Himalaya. The crustal movement of the Indian plate and the Eurasian plate causes the overlapping, shortening, and isostatic adjusted with the Tibetan Plateau. The details overall geological framework of the Himalaya have been provided by Heim and Gansser (1939) and Gansser (1964).

## 3. METHODOLOGY: 3D EULER DECONVOLUTION, TILT ANGLE AND TDX ANALYSIS

Euler deconvolution technique was used to estimate the source depth locations of the gravity or magnetic signature in a region; it was applied to profile or gridded data to solve the Euler's homogeneity equation (Thompson 1982) which states that:

$$(x - x_0)\frac{dF}{dx} + (y - y_0)\frac{dF}{dy} + (z - z_0)\frac{dF}{dz} = -N\,F\ , \tag{1}$$

where $x_0$, $y_0$, and $z_0$ are the source depth locations whose gravity field is $F$ measured at $x$, $y$, $z$ and $N$ is the Euler's structural index (SI), which is a function of the source geometry of the causative bodies. Source depth has been estimated based on the Euler deconvolution technique applied to the gridded dataset by solving the Euler's homogeneity equation. Equation 1 in this text clearly explains the details of the theory. This depth estimation depends on the type of structural index (SI) which varies from –1 to 2. In the case of gravity data set, SI = –1 denotes the contact type bodies, SI = 0 for thin sheet edge and thin sill dyke, SI = 1 for cylinder, thin bed and fault, and SI = 2 for point or spherical bodies. In this text, we have used SI = 0, which is theoretically not accurate but provides approximation of contact type bodies for depth calculation using the first vertical derivative of gravity data.

The Bouguer gravity anomaly across the south-western part to north-western part shows large deviation from local isostatic equilibrium. The mass deficiency characterizes the Ganga basin and the excess underlies the Lesser Himalaya. It is understood that the Ganga basin supposed to be over-compensated whereas the Himalayas are undercompensated by as much as 158 mGal (Fig. 2). This combination of mass deficiency over the Ganga basin and the excess mass over the Himalaya Mountains is due to isostatic occurrences within the strong Indian lithosphere being flexed down at the Himalayan front and extended beneath the Himalaya. The isostatic regional correction is applied to Bouguer gravity anomaly using Airy's isostasy model where 38 km crust thickness is considered. However, this 38 km depth

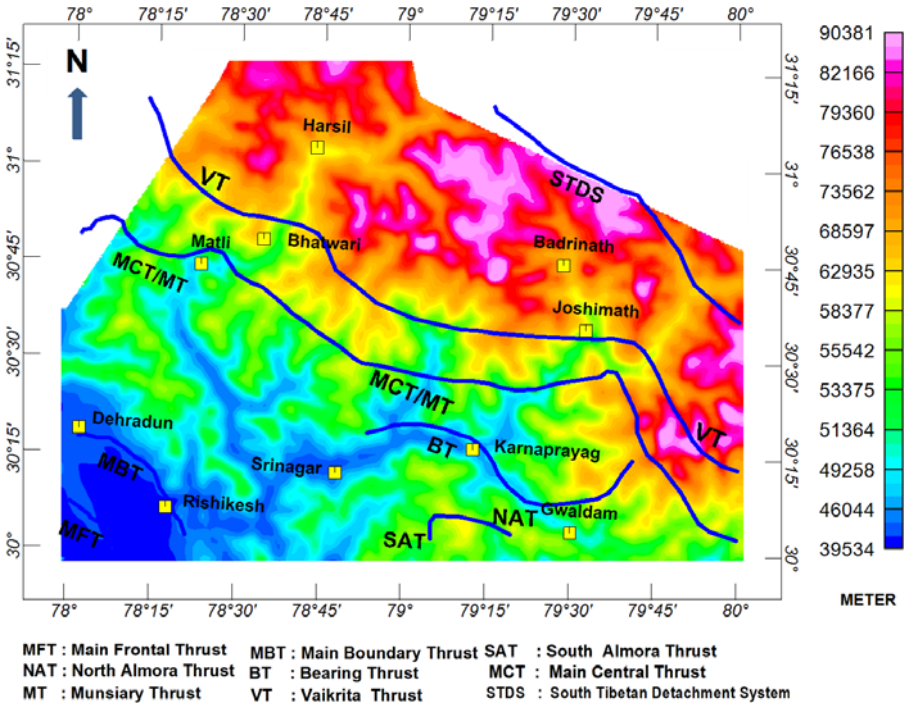


Fig. 4. Isostatic regional depths of the study area (calculated from topo-grid using Airy's isostasy model).

value is not critical and it is varying between 30 and 45 km (Kaila 1982). Bouguer density is considered to be $2.7 \times 10^3$ kg/m$^3$ and Moho density contrast is $0.335 \times 10^3$ kg/m$^3$ (Lyon-Caen and Molnar 1985, Qureshy 2004). Topographic grids are used to calculate the root depth grid below mean sea level by assuming Airy's isostasy for regional anomaly calculation at each grid point (Fig. 4). To calculate the isostatic residual grid, isostatic regional anomaly has been subtracted from the Bouguer gravity anomaly grid after applying upward continuation for 4 km (Fig. 5). The upward continuation has been studied from 1 to 4 km to reduce the short wavelength noise of the data and, finally, the 4 km upward continuation (4 grid cell points) has been applied in this study to smooth the data without changing the physical significance. This corrected isostatic residual anomaly (Fig. 5) is now used to calculate the first vertical gravity gradient (Fig. 6). This first vertical gravity gradient again breaks into three gradients *viz*. one vertical gravity gradient and others two numbers of horizontal gradient components in $x$ and $y$ directions, respectively.

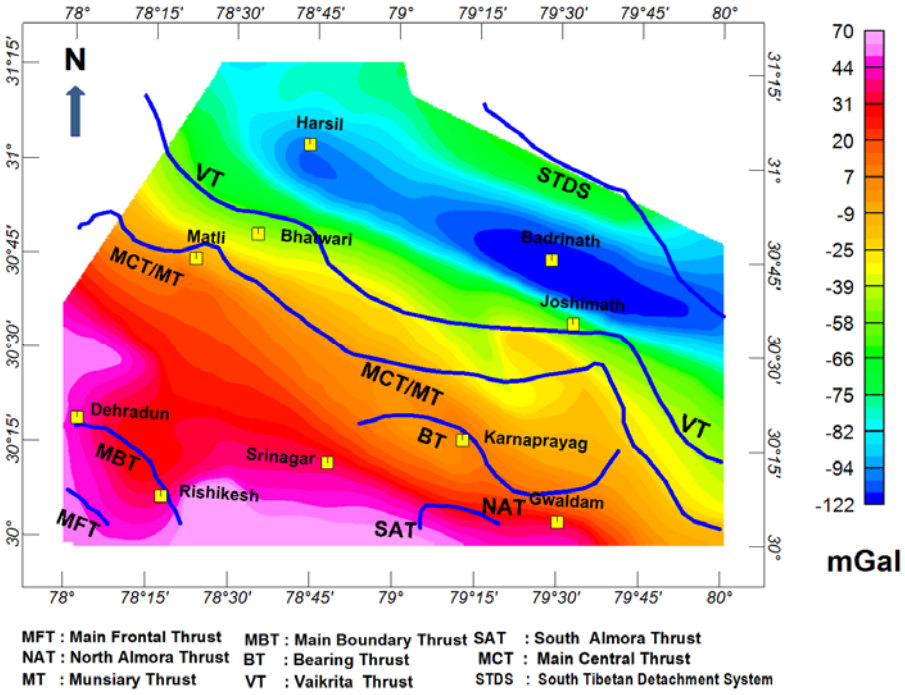


Fig. 5. Isostatic residual map calculated after removing the isostatic regional depth from Bouguer gravity anomaly map and after applying upward continuation of 4000 m. The various thrusts/faults locations are superimposed on the Isostatic residual map.

Structural index (SI) needs to be carefully selected as per the expected geological bodies and structure. Euler depth calculation for fault/contact type bodies used Bouguer gravity anomaly using structural index SI = –1 (Stavrev and Reid 2007, 2010); however, we have used first vertical gravity gradient to calculate Euler depth for fault/contact type bodies using SI = 0, which is theoretically not accurate but provides approximated source depth calculation. As Euler deconvolution generates many solutions, so to accept the best results, the knowledge of the geology is very important. It has been observed that the source depth increases with increasing structural index. The Euler source depth solutions are shown by different symbols with color. In this study, we have used structural index = 0 with a combination of 12 × 12 window size (WS) for correlation purpose.

Reid *et al*. (1990, 2003), and Stavrev (1997) have explained the Euler deconvolution technique, more details in methodology and wider application regarding the Euler's source depth solutions. These Euler depth solutions not

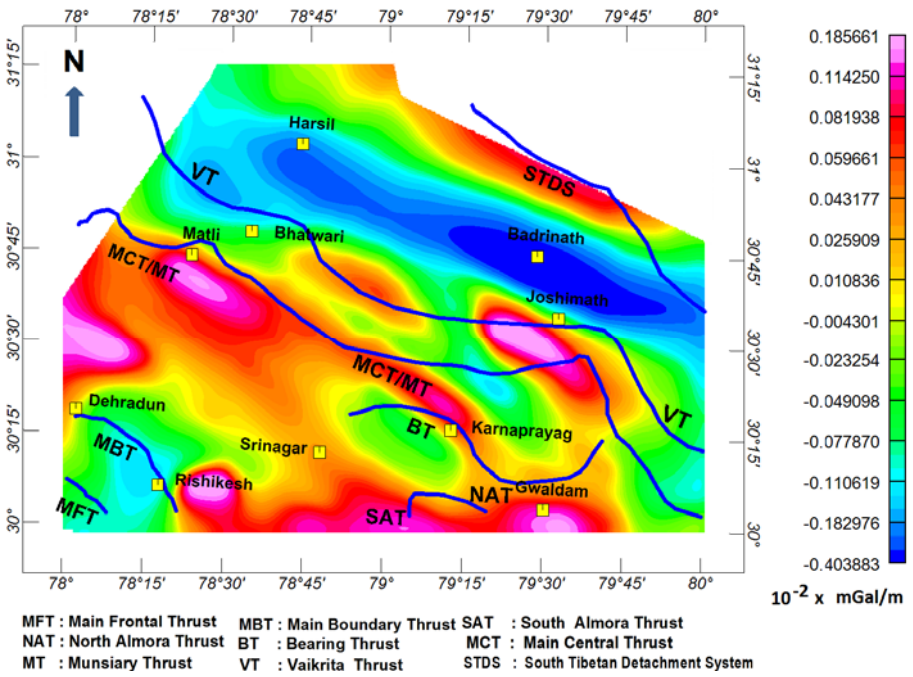


Fig. 6. Map of the first vertical gravity gradient of the study area (vertical gradient calculated from gravity residual isostatic map using Fig. 5).

only estimate the depth ($z_0$), but also delineate the horizontal boundaries (Wilsher 1987, Corner and Wilsher 1989, Klingele *et al*. 1991, Marson and Klingele 1993, Huang *et al*. 1995). In a general case, scattered data points cannot provide superior solutions (Mushayandebvu *et al.* 2004, Yaghoobian *et al*. 1993). Various researchers have used 3D Euler deconvolu-tion technique for source depth estimations (Thompson 1982, Pilkington *et al*. 1995, Smith *et al*. 1998, Nabighian and Hansen 2001, Cooper 2002, Mikhailov *et al*. 2003, Milligan *et al*. 2003, Silva and Barbosa 2003, FitzGerald *et al*. 2004, Mushayandebvu *et al*. 2004, Fedi 2007, Melo *et al*. 2013, Reid and Thurston 2014, Reid *et al.* 2014).

The tilt angle defined by Miller and Singh (1994) and Verduzco *et al*. (2004) is as follows

$$\mathrm{TDR} = \tan^{-1}\left(\frac{\partial g/\partial z}{\sqrt{\left(\partial g/\partial x\right)^2 + \left(\partial g/\partial y\right)^2}}\right), \qquad (2)$$

where $\partial g/\partial z$ is the vertical gradient derivative and $\sqrt{(\partial g/\partial x)^2 + (\partial g/\partial y)^2}$ is the horizontal gradient derivative. Tilt angle (TDR) is varying within the range: $+\pi/2 >$ tilt angle $> -\pi/2$.

The tilt angle is 0 radians at the measuring point ($x = x_0$) above the edges of the contact. It is evident that this property identifies the horizontal location of the source. In addition, one can determine the depth estimation since the tilt angle equals $\pi/4$ when $x - x_0 = z_0$ and $-\pi/4$ when $x - x_0 = -z_0$. Therefore, half the horizontal distance between the $\pm\pi/4$ radians contours of the tilt angle is the depth to source. In addition, the depth to source can be obtained from the distance between zero and $\pm\pi/4$ radians at the point $x = x_0$ over the vertical contact.

Cooper and Cowan (2006) studied the TDX (horizontal tilt angle) as

$$\text{TDX} = \tan^{-1}\left(\frac{\text{THDR}}{\text{VDR}}\right), \tag{3}$$

where VDR is the vertical gradient and THDR is the total horizontal gradient. TDX is varying between the $+\pi/2 > \text{TDX} > -\pi/2$, but has a much sharper gradient over the contrast than tilt angle derivatives.

The tilt angle and TDX analyses for thrust and fault locations have been carried out by many researchers (Blakely and Simpson 1986, Miller and Singh 1994, Hsu *et al*. 1996, Fedi and Florio 2001, Fedi 2002, Williams *et al*. 2005, Wijns *et al*. 2005, Phillips *et al*. 2007, Oruc 2010, Yuanyuan *et al*. 2010, Ansari and Alamdar 2011, Cascone and Campbell 2012, Fedi *et al*. 2012).

## 4. INTERPRETATION OF GRAVITY DATA

The present paper describes the analysis of source depth and thrust/fault locations using the gravity data (Qureshy *et al*. 1974). It has been observed that gradients of Bouguer anomalies increase from Ganga Basin to the Higher Himalaya, varying from 1 to 2 mGal/km. This increases the dipping of Moho rapidly, from 10° to 15° beneath the Higher Himalaya and 1° to 2° below the Lesser Himalaya (Lyon-Caen and Molnar 1985). The published gravity map of Qureshy *et al*. (1974) was further digitized with a grid spacing of 1000 m interval and re-interpreted in terms of geophysical consequences. The isostatic corrected residual anomaly has been calculated after removal of regional and upward continuation of 4 km from the Bouguer gravity data. The first vertical gradient of the isostatic residual anomaly corrected data is used for further 3D Euler deconvolution (ED), tilt angles, and TDX analysis for depths and horizontal boundary of faults or contact-like bodies. The study area comprises a continuous decreasing gravity anomaly

trend from south-west to north-east. The lower gravity anomaly is observed in the north-eastern part at Badrinath (–390 mGal), Harsil (–350 mGal), and Joshimath (–330 mGal) area. However, higher gravity anomaly has been observed at the south-western part near Rishikesh (–160 mGal), Dehradun (–160 mGal), and Srinagar (–185 mGal) area. Moderate gravity anomaly (–260 mGal) was observed at Karnaprayag and Matli areas. The Bouguer gravity anomaly decreases from –134 to –393 mGal while the elevation increases from –199 to 5960 m from south-western to north-eastern direction (Fig. 1). Bouguer gravity anomaly and the topography of the study area follow the opposite pattern due to isostatic adjustment (Qureshy 1981). Based on this observation, the area can be divided into three parts, *viz*. lower gravity anomaly in north-eastern part correlates with higher elevation; the higher gravity anomaly in the south-western part correlates with lower elevation, and the moderate gravity anomaly with moderate elevation is between these higher and lower gravity anomalies.

The gravity observations suggest that Bouguer gravity anomaly decreases rapidly from the Ganga Basin to the Greater Himalaya, causing isostatic adjustment and showing a decrease of crustal density. In various places, like Badrinath and Harsil areas, the crystalline rocks are exposed and might be due to the crustal intrusion, tectonic resettlement or movement process. It was suggested that crystalline rocks are uplifted over the sedimentary surfaces near to the thrusted and faulted area. Hence, it is very difficult to find out the accurate thrust and fault locations through the geological studies accurately. The study suggests that these locations are fragmented in multiple locations.

Various authors (Tripathi *et al*. 2012, Chamoli *et al*. 2011, Arora *et al*. 2007, Gokarn *et al*. 2002) had carried out the depth estimation and provided their views. However, the present study provides better results and detailed information of source depth locations and structural boundaries with dip information. The results carried here are well corroborated with the available thrust fault boundaries, as shown in the tectonic maps of the area (Fig. 10).

Euler solutions are superimposed with the first vertical gradient of the Bouguer gravity map using SI = 0 and window size (WS) = 12 × 12. Different source depth locations are marked with different color circles, which are varying from about 4 to 8 km (Fig. 7). The Euler deconvolution is also used to estimate the delineation of fault or contact at the different depth levels which corresponds to the fractures of basement. It is noted that upward continuation of 4 km has been applied to the gravity data, so the total depth of investigation can vary from approximately 8 km ($\leq 4 + 4$ km) up to 12 km (maximum depth 8 + 4 km), where the isostatic regional root depth calculated from topo grid is more than 90 km.

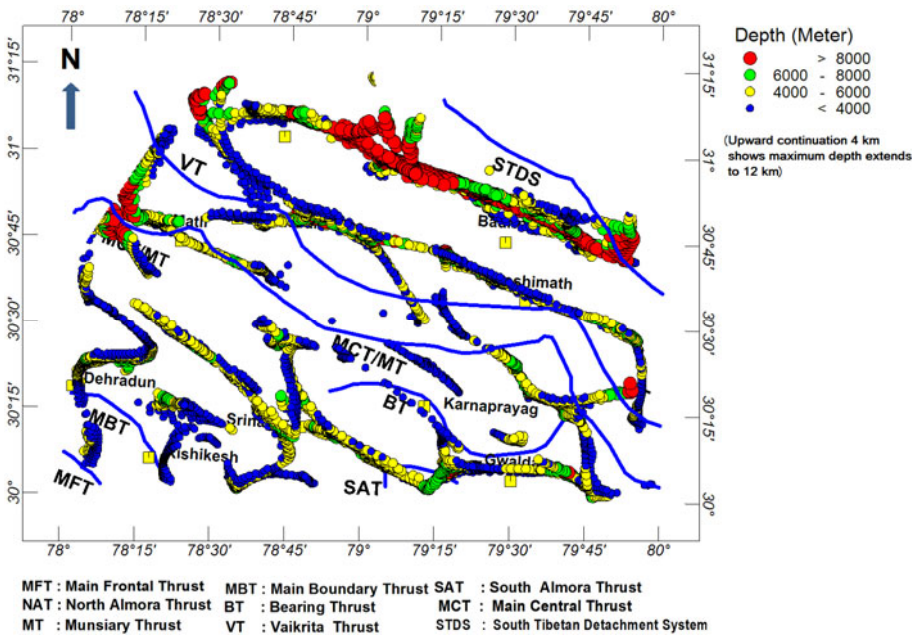


Fig. 7. Map of the Euler source depth solutions superimposed on the geological thrust/fault locations of the Rishikesh-Badrinath area (Euler solutions calculated based on the vertical gravity gradients, SI = 0 (structural index), WS = 12 × 12 (window size).

The various clusters points of the source bodies are evenly connected from shallow to deeper source depth and vary from about 4 to 8 km (alternatively adding 4 km due to upward continuation). It is suggested that the basement depths vary from shallow to the deeper crystalline rocks which are represented in the study. Euler depth solutions are studied from the cluster points located along the thrust boundaries at Main Boundary Thrust (MBT), South Almora Thrust (SAT), North Almora Thrust (NAT), Main Central Thrust (MCT), Munsiary Thrust (MT), Vaikrita Thrust (VT), and South Tibetan Detachment System (STDS). It has been noted that as MCT is a wide fault zone and has divided into several threads faults. However, in broad sense the MCT zone is basically divided into two faults, *i.e.*, upper bounding faults and lower bounding fault. The upper bounding fault is equated with Vaikrita Thrust (VT) and the lower bounding fault is equated as Munsiari Thrust (MT). For this reason, it may be assumed that the 3D Euler deconvolution results in terms of clustering are little scattered. This can also suggests that the thrust/fault boundaries are fragmented in nature, as suggested through Euler deconvolution. Hence, apart from these present thrust

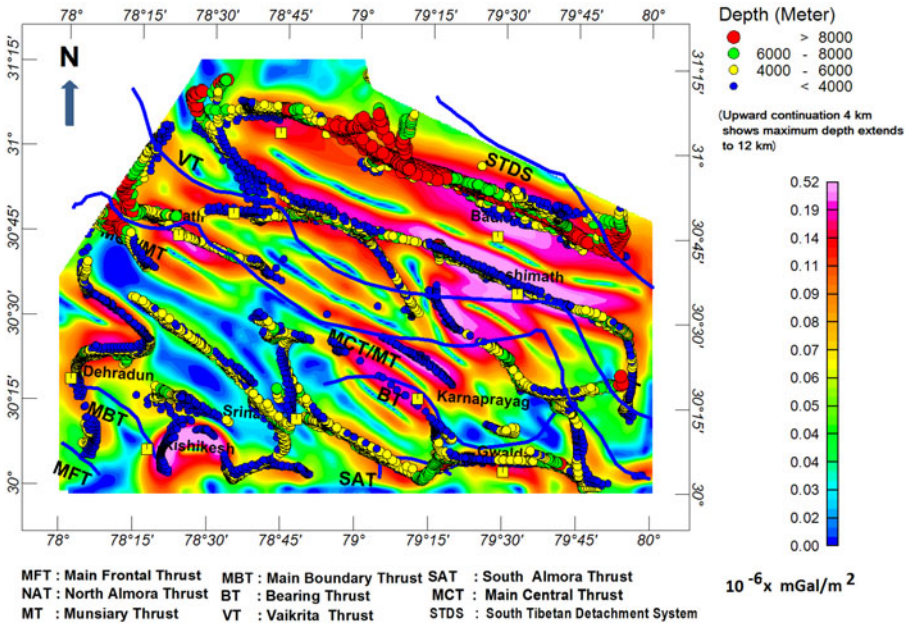


Fig. 8. Map showing the total horizontal component superimposed with the Euler depth solution with SI = 0 and WS = 12 × 12.

locations (Fig. 3), more additional thrust/fault boundaries are acknowledged through cluster solutions (Fig. 7). In Badrinath area, shallow depth < 4000 m suggests the upwarpment of crystalline basement rocks, also observed at the Karnaprayag, Gwaldam, Rishikesh, and Harsil area (Fig. 7).

The horizontal gradient component superimposed with the Euler depth solution SI = 0 and WS = 12 × 12 are shown in Fig. 8. Cluster points are more prominent along the maximum and minimum gradients of gravity field. This horizontal gradient map analysis suggests the trends of major thrust locations and structural boundaries which are poorly exposed. These studies draw attention to weaker structures which can have major tectonic significance in this region. It has been suggested that horizontal gravity gradient analysis with the topography of the area have a strong correlation and need more attention for further study.

Tilt angle and TDX studies suggest the generalized local phase and enhance the weak gravity anomalies. Euler depth solution with structural index 0 and WS = 12 × 12 are superimposed on the tilt angle map (Fig. 9) and TDX map (Fig. 10). The tilt angle map is relatively smoother, with positive values over source and zero over the source edges at which the vertical derivatives is zero. TDX also showed the smoother contour along the peak val-

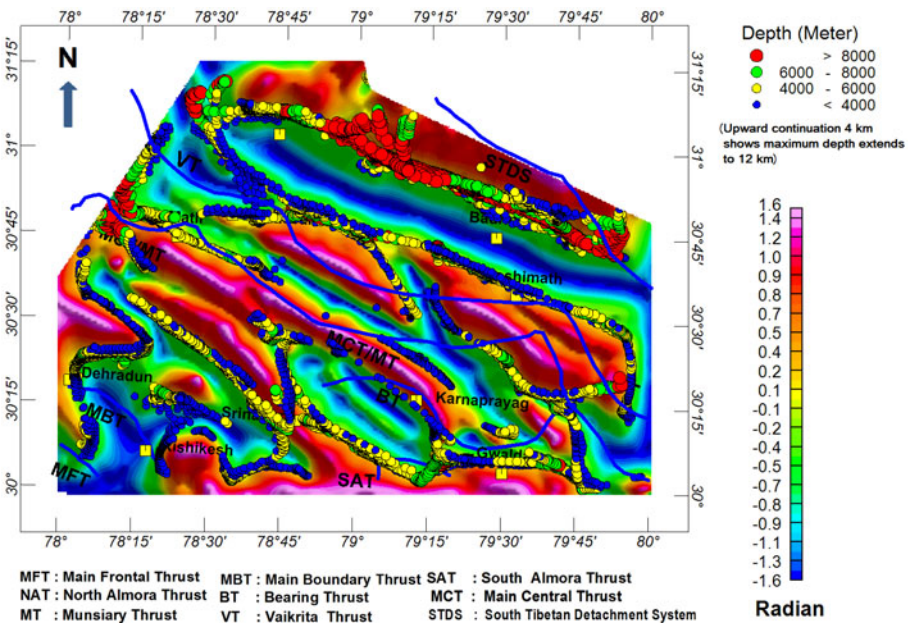


Fig. 9. Map showing the various thrust / fault locations, tilt angle map superimposed with Euler source depth solutions (using SI = 0 and WS = 12 × 12).

ues. However, in both the cases, tilt angle or TDX studies, the vertical contacts are more clearly defined by the zero contour map. The tilt angle map (Fig. 9) provides the source body boundaries elongated in the north-west to south-east direction, which is well correlated along the different known thrust/fault boundaries. The Source Edge Detection (SED) map was superimposed with dip direction and Euler depth solutions using SI = 0 and WS = 12 × 12 (Fig. 11).

The positive and the negative signatures of the gravity anomalies have been considered for processing to estimate in each grid points for calculating dip and strike direction. The map shows the dips of the source bodies with contact representing a symbol "⊥". The right hand is the dip direction standing on the strike direction (Fig. 11). The long axis represented the strike direction of the edge (contact) and the downward gradient directions are the dip directions as shown in Fig. 11. The map shows the four different strike directions varying from $0° \leq \text{strike} \leq 90°$, $90° \leq \text{strike} \leq 180°$, $180° \leq \text{strike} \leq 270°$ to $270° \leq \text{strike} \leq 360°$. This strike is measured in the clockwise direction varying from 0° to 360°, where the Y axis points to north. Dip can also be measured in degrees, varying from 0°-180° relative to the direction perpendicular to the strike (Blakely and Simpson 1986).

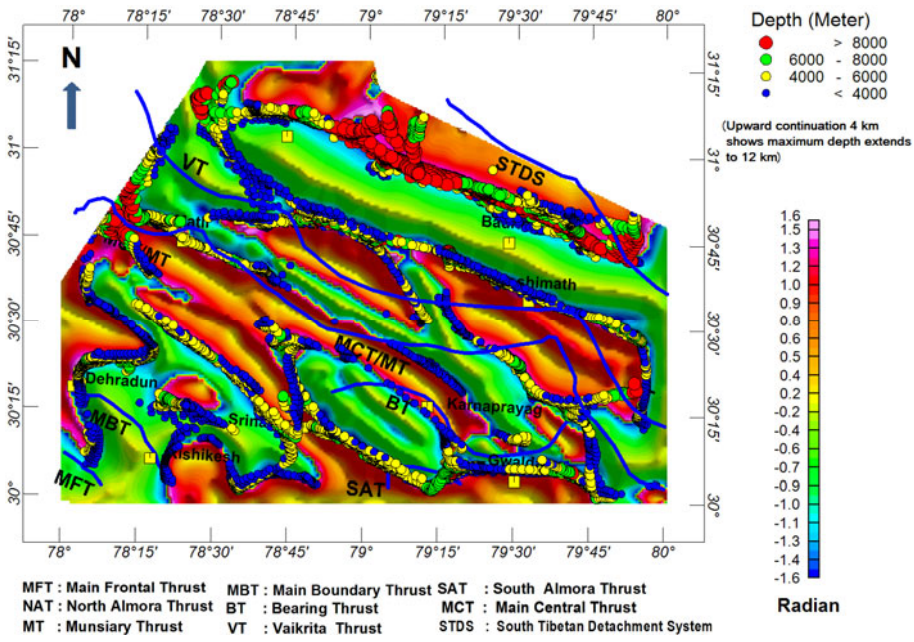


Fig. 10. Map showing the various thrusts/faults locations, TDX (horizontal tilt angle map) superimposed with Euler source depth solutions (using SI = 0 and WS = 12 × 12).

The tilt angle map, SED, Euler depth solution (SI = 0, WS = 12 × 12) and identified thrust/fault boundaries are superimposed, as shown in Fig. 12. Similarly, the TDX analysis, SED, Euler depth solution (SI = 0, WS = 12 × 12) and identified thrust/fault boundaries are superimposed, as shown in Fig. 13. These above studies suggest that the various results derived are well correlated.

Reddy and Arora (1993) reported basement depth from 10.0 to 15.0 km below the Himalayan collision region with a high conductivity layer embedded in the crust at using geomagnetic deep sounding (GDS). Gokarn *et al*. (2002) also observed the basement depth increases upto 15.0 km using magnetotelluric (MT) studies. Khattri *et al*. (1989) also suggested the depth of detachment of 15.0-18.0 km underneath the Lesser Himalaya of Garhwal. Bhattacharya (1999) suggested that during the collision of Indian and Eurasian plate, part of segment of the basement rocks were uplifted from the depth to the surface due to its buoyancy and the rock mass moved along the Main Central Thrust (MCT). It was recommended that most of the collisional stresses were compressive in nature which helped in stirring the mass up and about from the depth. The earthquake's hypocenters are between depths

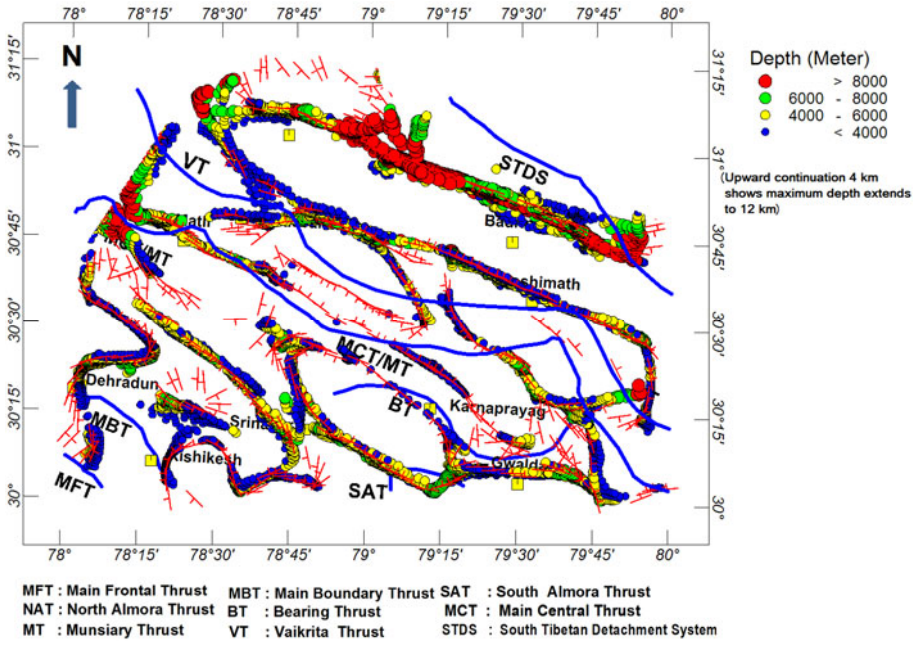


Fig. 11. Map of the Source edge detection (SED) superimposed with dip direction and Euler source depth location (SI = 0 and WS = 12 × 12).

of 10.0 and 20.0 km, due to the under thrusting of Indian Plate and mass upliftment (Molnar and Chen 1982, Ni and Barazangi 1984). Chamoli *et al*. (2011) have studied the Himalayan detachment thrust to be 11.0 km in the north-western part of the present study area. Arora *et al*. (2007) also studied the Deep Resistivity Sounding (DRS) along the western part of the north-western Himalayas and suggest resistivity > 300 Ω·m up to depth of 15 km. Tripathi *et al*. (2012) suggested by coda wave attenuation analysis in the Garhwal region of north-western Himalaya that the earthquakes are mainly concentrated within depths from 10 to 15 km, which suggests that most of the crustal activation takes place within this particular depth. The coeval development of South Tibetan Detachment and the Main Central Thrust studies through simulation analysis and the thrusting dominating nature of Himalaya studies have been done by Shanker *et al*. (2002).

It can be concluded that the results obtained here are well correlated with the results of various scientists in this study area and neighboring areas (Tripathi *et al*. 2012, Chamoli *et al*. 2011, Arora *et al*. 2007, Gokarn *et al*. 2002).

The major thrust locations are identical as per the calculation of Source Edge Detection (SED) technique using the vertical gravity gradient data.

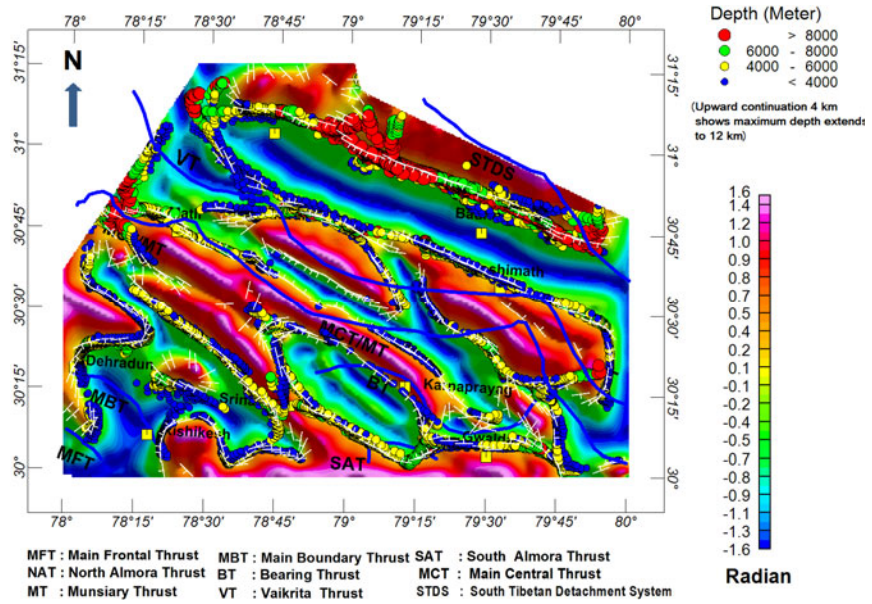


Fig. 12. Tilt angle, SED, Euler depth solution (SI = 0, WS = 12 × 12) and thrust/ fault location map are superimposed which looks a better correlation.

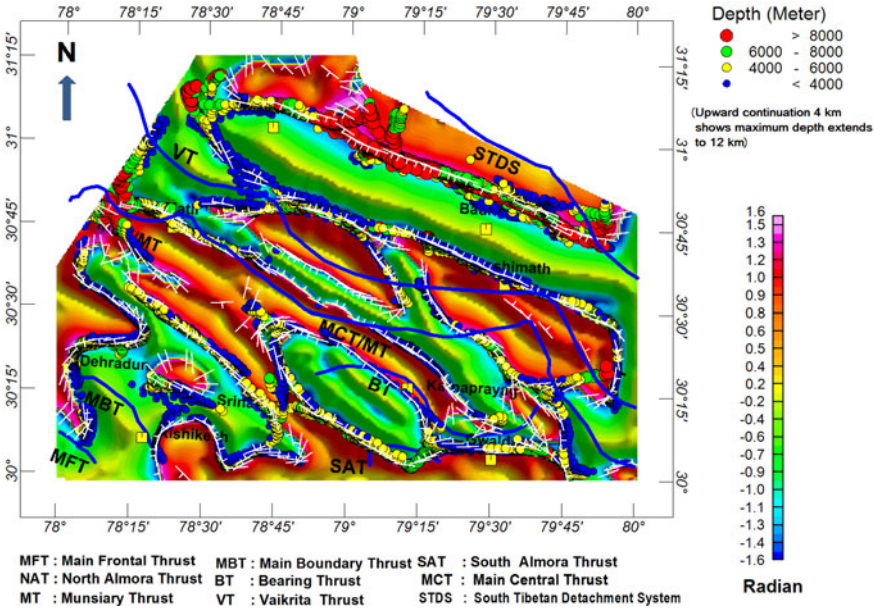


Fig. 13. Map of the Euler source depth solutions (SI = 0, WS = 12 × 12) superimposed on the geological thrust-fault location of the Rishikesh-Badrinath area, horizontal tilt angle (TDX), and source edge detection (SED).

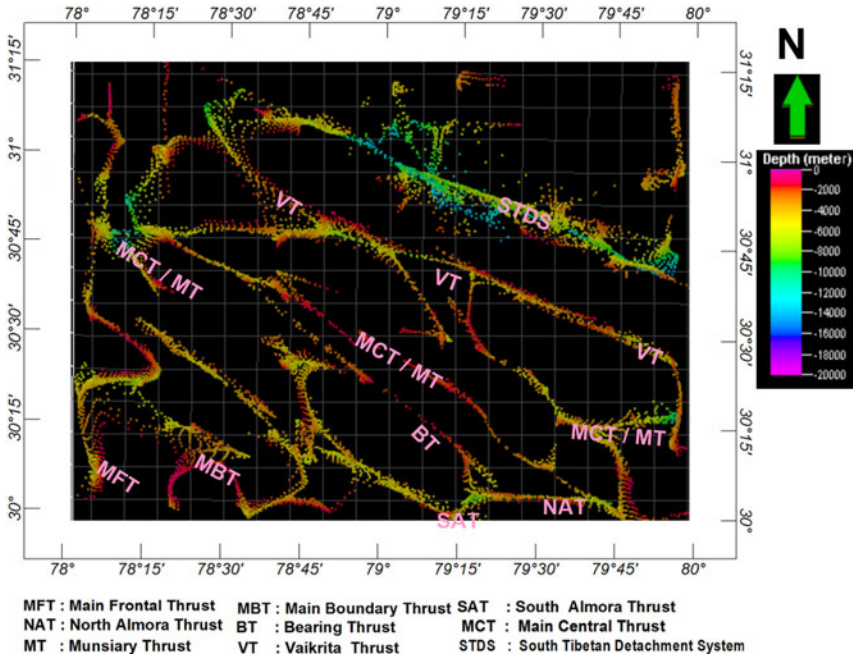


Fig. 14. Map shows the tectonic model (front view) using Euler deconvolution by plotting the cluster points and superimposed with the previously known identified thrust locations.

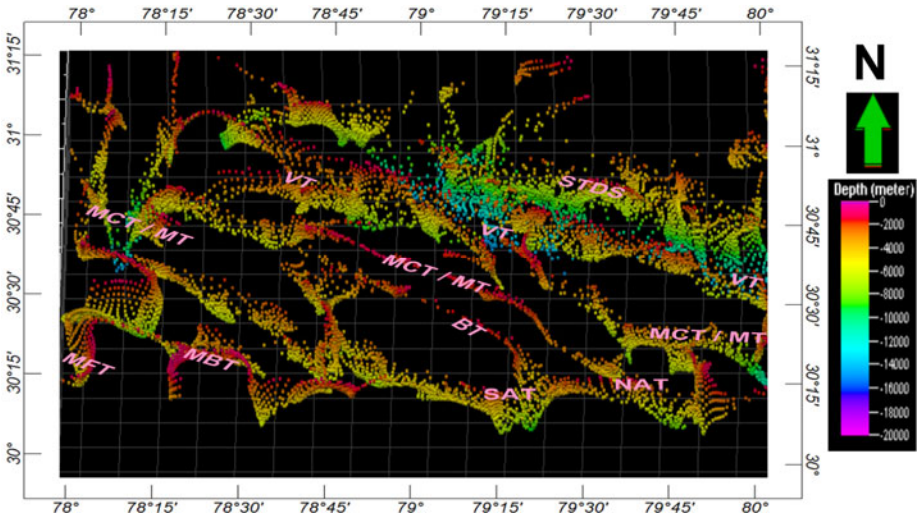


Fig. 15. Map shows the tectonic model (3D view) using Euler deconvolution by plotting the cluster points and superimposed with the previously known identified thrust locations.

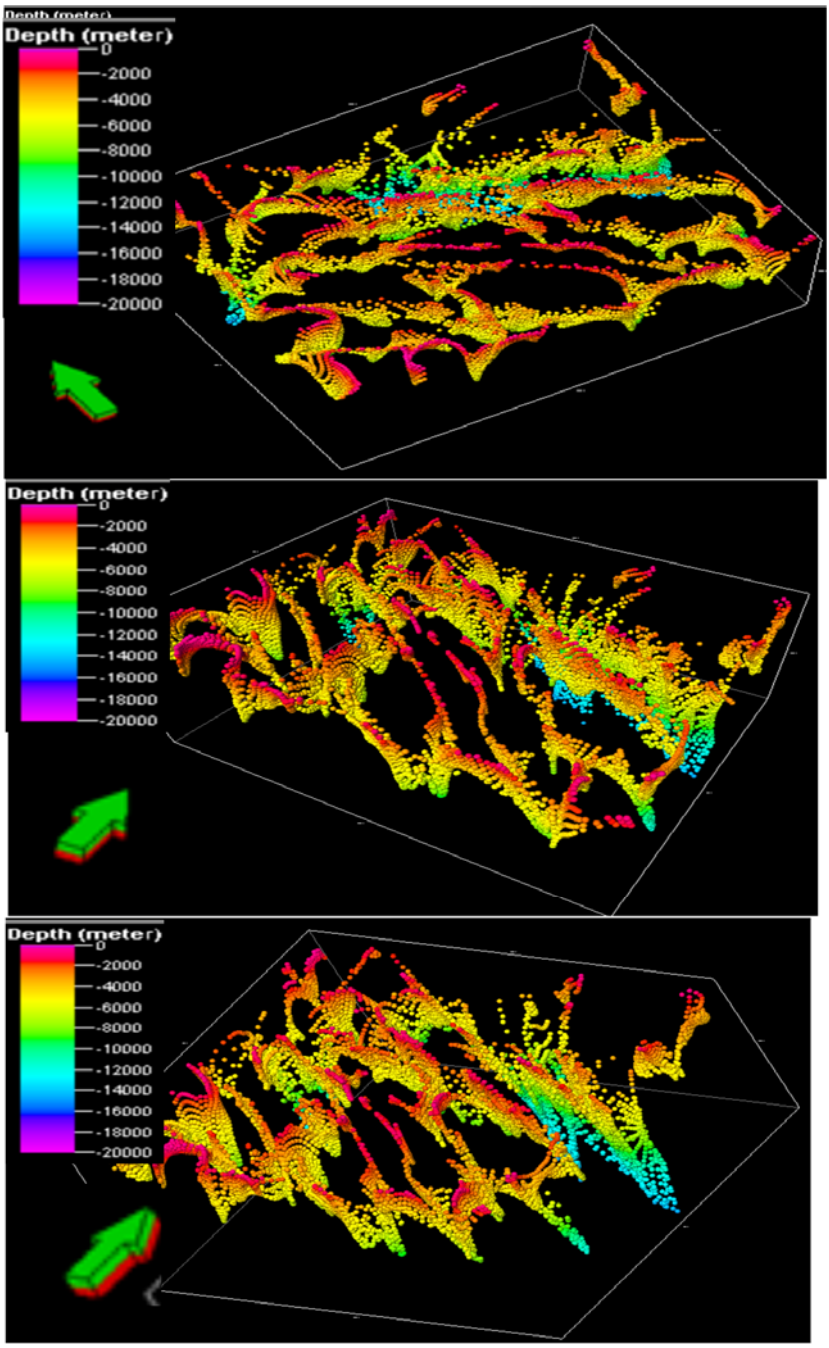


Fig. 16. Map shows the 3D view of the cluster solutions indicating the extension of the cluster points along the thrust locations.

Most of the derived thrust boundaries are well correlated with the various well known thrust boundaries. However, this study provides more additional thrust boundaries, not noticeable earlier. The details identified automatic thrust locations and the dip directions are shown in Fig. 11. Tilt angle, SED and Euler source depth solutions are shown in Fig. 12, and TDX, SED, and Euler source depth solutions are shown in Fig. 13.

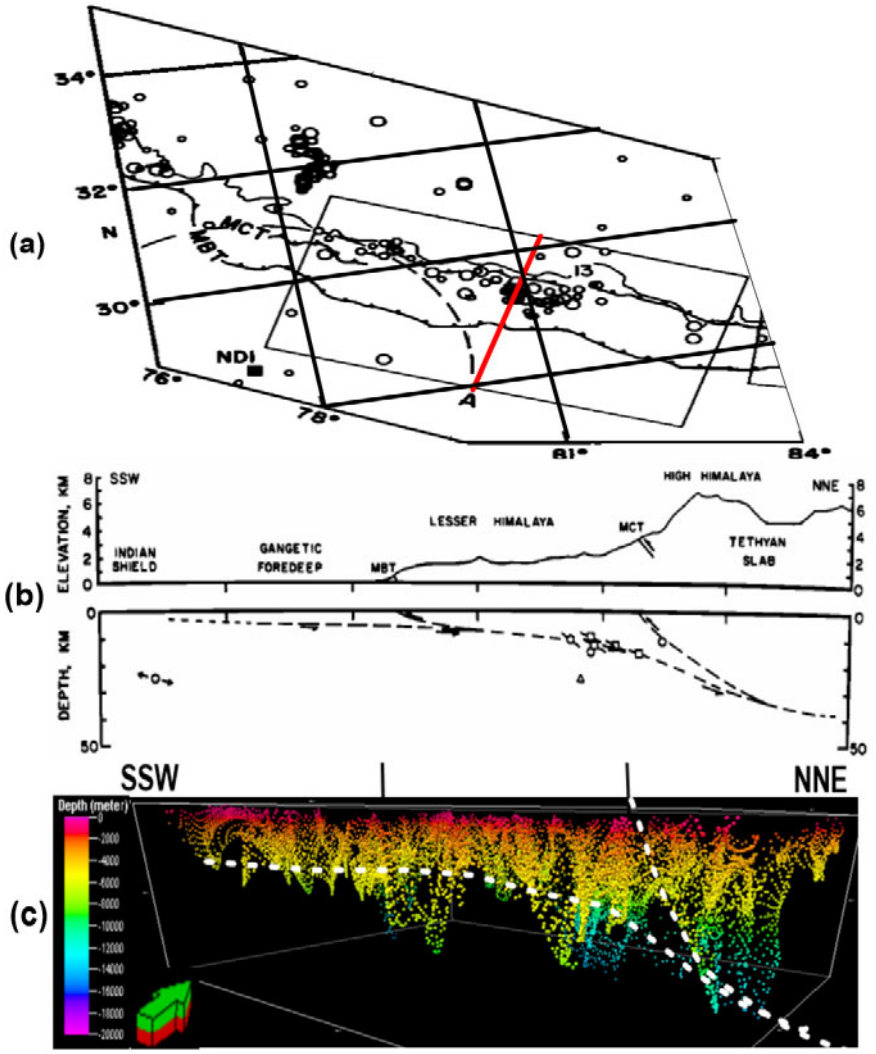


Fig. 17. Map shows the profile location oriented in SSE-NNW direction (profile A) across the area studied by Ni and Barazangi (1984) (a), depth section across the profile A and the relevant thrust locations Ni and Barazangi (1984) (b), and the derived solutions from the 3D Euler deconvolution in the present study(c).

Additionally, a 3D figure (tectonic model) has been developed showing the position of detachment surface with various thrusts like MFT, MBT, SAT, BT, MCT/MT, VT, and STDS. Figures 14 and 15 show the tectonic model using Euler deconvolution by plotting the cluster points and superimposed with the previously known identified thrust locations. Figure 16 shows the 3D view of the cluster solutions indicating the extension of the cluster points along the thrust locations. One of the tectonic profiles (Profile A) oriented SSE-NNW generated by Ni and Barazangi (1984), as shown in Fig. 17a, and the depth solutions model derived by Ni and Barazangi (1984), as shown in Fig. 17b, are correlated with the results derived from the 3D Euler deconvolution (Fig. 17c). The depths estimated along with the thrust locations are well correlated.

It is also to be noted that most of the thrust boundaries in the study area remain unidentified up to now. However, in the present study, additional information of thrust-fault boundaries has been provided. This additional information can be helpful for further detailed geo-scientific research work in the area.

## 5. DISCUSSION AND CONCLUSION

Automatic basement depth study has been carried out using 3D Euler deconvolution of gravity data. These cluster points derived from the Euler's source depth calculation suggest the shallower depth $< 8$ km and deeper depth $> 12$ km (as data is an upward continuation of 4 km). In addition, probable thrust and fault boundaries are identified using tilt angle analysis, TDX angle, and various horizontal gradient analyses of gravity data which have not been marked in the past studies. The Source Edge Detection (SED) technique has been applied and identified the thrust boundaries and dip direction. The various horizontal gradients indicate the structural boundaries in the study area. The information provided in this current study added more supplementary information which was not proposed by earlier study. The results shown here with different aspects are well correlated with the existing available information carried by the various potential workers. However, the present study, providing additional thrust/fault boundary information within Vaikrita Thrust (VT) and Southern Tibetian Detachment System (STDS), with source depth locations and dips directions, provided a need to carry further work with more attention. The gravity data interpretation provides a more reasonable explanation for the depth estimation, structural boundary, and source edge detection. The compilations of details of gravity analysis correlate with the depth and thrust boundaries of buried structures and also clarify the pattern of geological information in the north-western part of India.

Acknowledgement. I thank to the various authors of the journals/text directly or indirectly for their ideas and inspiration during the course of the work. I also thank the anonymous reviewers/editor for their useful comments.

## References

Ansari, A.H., and K. Alamdar (2011), A new edge detection method based on the analytic signal of tilt angle ASTA for magnetic and gravity anomalies, *Iran. J. Sci. Technol.* **35**, A2, 81-88.

Arora, B.R., M.J. Unsworth, and G. Rawat (2007), Deep resistivity structure of the northwest Indian Himalaya and its tectonic implications, *Geophys. Res. Lett.* **34**, 1-4, DOI: 10.1029/2006gl029165.

Beaumont, C., R.A. Jamieson, M.H. Nguyen, and B. Lee (2001), Himalayan tectonics explained by extrusion of low-viscosity crustal channel coupled to focus surface denudation, *Nature* **414**, 6865, 738-742, DOI: 10.1038/414738a.

Bhattacharya, A.R. (1999), Deformational regimes across the Kumaun Himalaya: A study in strain patterns, *Gondwana Res. Mem. (Japan)* **6**, 81-90.

Bhattacharya, A.R., and K. Weber (2004), Fabric development during shear deformation in the Main Central Thrust Zone, NW-Himalaya, India, *Tectonophysics* **387**, 1-4, 23-47, DOI: 10.1016/j.tecto.2004.04.026.

Blakely, R.J., and R.W. Simpson (1986), Approximating edges of source bodies from magnetic or gravity anomalies, *Geophysics* **51**, 7, 1494-1498, DOI: 10.1190/1.1442197.

Bouchez, J.L., and A. Pecher (1981), The Himalayan Main Central Thrust pile and its quartz-rich tectinites in Central Nepal, *Tectonophysics* **78**, 1-4, 23-50, DOI: 10.1016/0040-1951(81)90004-4.

Burg, J.P., M. Brunel, D. Gapais, G.M. Chen, and G.H. Liu (1984), Deformation of leucogranites of the crystalline Main Central Thrust Sheet in southern Tibet China, *J. Struct. Geol*. **6**, 5, 535-542, DOI: 10.1016/0191-8141(84)90063-4.

Cascone, L., and S. Campbell (2012), ACLAS: A new automatic method of defining potential field lineaments using coherency analysis. **In:** *Proc. SEG Annual Meeting, 4-9 November 2012, Las Vegas, USA*, SEG-2012-1254.

Chamoli, A., A.K. Pandey, V.P. Dimri, and P. Banerjee (2011), Crustal configuration of the northwest Himalaya based on modeling of gravity data, *Pure Appl. Geophys.* **168**, 5, 827-844, DOI: 10.1007/s00024-010-0149-2.

Cooper, G.R.J. (2002), An improved algorithm for the Euler deconvolution of potential field data, *The Leading Edge* **21**, 12, 1197-1198, DOI: 10.1190/1.1536132.

Cooper, G.R.J., and D.R. Cowan (2006), Enhancing potential field data using filters based on the local phase, *Comput. Geosci.* **32**, 10, 1585-1591, DOI: 10.1016/j.cageo.2006.02.016.

Cordell, L., and V.J.S. Grauch (1982), Mapping basement magnetization zones from aeromagnetic data in the San Juan Basin, New Mexico. **In:** *Proc. 52nd SEG Annual Meeting, 17-21 October 1982, Dallas, USA*, SEG-1982-0246.

Corner, B., and W.A. Wilsher (1989), Structure of the Witwatersrand basin derived from interpretation of the aeromagnetic and gravity data. **In:** G.D. Garland (ed.), *Proc. Exploration '87: Third Decennial Int. Conf. on Geophysical and Geochemical Exploration for Minerals and Groundwater, Ontario Geol. Survey,* Special Vol. 3, 532-546.

Fedi, M. (2002), Multiscale derivative analysis: A new tool to enhance gravity source boundaries at various scales, *Geophys. Res. Lett.* **29**, 2, 1029-1032, DOI: 10.1029/2001GL013866.

Fedi, M. (2007), DEXP: A fast method to determine the depth and the structural index of potential fields sources, *Geophysics* **72**, 1, l1-l11, DOI: 10.1190/1.2399452.

Fedi, M., and G. Florio (2001), Detection of potential fields source boundaries by enhanced horizontal derivative method, *Geophys. Prospect.* **49**, 1, 40-58, DOI: 10.1046/j.1365-2478.2001.00235.x.

Fedi, M., G. Florio, and L. Cascone (2012), Multiscale analysis of potential fields by a ridge consistency criterion: the reconstruction of the Bishop basement, *Geophys. J. Int.* **188**, 1, 103-114, DOI: 10.1111/j.1365-246X.2011.05259.x.

FitzGerald, D., A.B. Reid, and P. McInerney (2004), New discrimination techniques for Euler deconvolution, *Comput. Geosci.* **30**, 5, 461-469, DOI: 10.1016/j.cageo.2004.03.006.

Gansser, A. (1964), *Geology of the Himalayas*, Interscience Publ., London, 289 pp.

Ghosh, G.K., and C.L. Singh (2014), Spectral analysis and Euler deconvolution technique of gravity data to decipher the basement depth in the Dehradun-Badrinath area, *J. Geol. Soc. India* **83**, 5, 501-512, DOI: 10.1007/s12594-014-0077-3.

Gokarn, S.G., C.K. Rao, and G. Gupta (2002), Crustal structure in the Siwalik Himalayas using magnetotelluric studies, *Earth Planets Space* **54**, 1, 19-30, DOI: 10.1186/BF03352418.

Grasemann, B., H. Fritz, and J.C. Vannay (1999), Quantitative kinematic flow analysis from the Main Central Thrust Zone NW-Himalaya: implications for a decelerating strain path and extrusion of orogenic wedges, *J. Struct. Geol*. **21**, 7, 837-853, DOI: 10.1016/S0191-8141(99)00077-2.

Grauch, V.J.S., and L. Cordell (1987), Limitations on determining density or magnetic boundaries from the horizontal gradient of gravity or pseudogravity data, *Geophysics* **52**, 1, 118-121, DOI: 10.1190/1.1442236.

Heim, A., and A. Gansser (1939), *Central Himalaya: Geological Observations of the Swiss Expedition 1936*, Hindustan Publ., Delhi, 284 pp.

Hsu, S.K., J.C. Sibuet, and C.T. Shyu (1996), High resolution detection of geological boundaries from potential field anomalies. An enhanced analytic signal technique, *Geophysics* **61**, 2, 373-386, DOI: 10.1190/1.1443966.

Huang, D., D. Gubbins, R.A. Clark, and K.A. Whaler (1995), Combined study of Euler's homogeneity equation for gravity and magnetic field. **In:** *57th EAGE Conference and Technical Exhibition; European Association of Exploration Geophysics*, Extended abstr., 144, DOI: 10.3997/2214-4609.201409565.

Kaila, K.L. (1982), Deep seismic sounding studies in India, *Geophys. Res. Bull.* **20**, 3, 309-328.

Khattri, K.N., R. Chander, V.K. Gaur, I. Sarkar, and S. Kumar (1989), New seismological results on the tectonics of the Garhwal Himalaya, *Proc. Indian Acad. Sci. Earth Planet Sci*. **98**, 1, 91-109, DOI: 10.1007/BF02880378.

Klingele, E.E., I. Marson, and H.G. Kahle (1991), Automatic interpretation of gravity gradiometric data in two dimensions: Vertical gradients, *Geophys. Prospect.* **39**, 3, 407-434, DOI: 10.1111/j.1365-2478.1991.tb00319.x.

Le Fort, P. (1975), Himalayas: the collided range. Present knowledge of the continental arc, *Am. J. Sci.* **275A**, 1, 1-44.

Leech, M.L., S. Singh, A.K. Jain, S.L. Klemperer, and R.M. Manickavasagam (2005), The onset of India–Asia continental collision: Early, steep subduction required by the timing of UHP metamorphism in the western Himalaya, *Earth Planet. Sci. Lett.* **234**, 1-2, 83-97, DOI: 10.1016/j.epsl.2005.02.038.

Lyon-Caen, H., and P. Molnar (1985), Gravity anomalies, flexure of the Indian plate, and the structure, support and evolution of the Himalaya and Ganga Basin, *Tectonics* **4**, 6, 513-538, DOI: 10.1029/TC004i006p00513.

Marson, I., and E.E. Klingele (1993), Advantages of using the vertical gradient of gravity for 3-D interpretation, *Geophysics* **58**, 11, 1588-1595, DOI: 10.1190/1.1443374.

Melo, F.F., V.C.F. Barbosa, L. Uieda, V.C. Oliveira Jr., and J.B.C. Silva (2013), Estimating the nature and the horizontal and vertical positions of 3D magnetic sources using Euler deconvolution, *Geophysics* **78**, 6, J87-J98, DOI: 10.1190/geo2012-0515.1.

Mikhailov, V., M. Galdeano, A. Gvishiani, S. Agayan, S. Bogoutdinov, E. Graeva, and P. Sailhac (2003), Application of artificial intelligence for Euler solutions clustering, *Geophysics* **68**, 1, 168-180, DOI: 10.1190/1.1543204.

Miller, H.G., and V. Singh (1994), Potential field tilt – a new concept for location of potential field sources, *J Appl. Geophys*. **32**, 2-3, 213-217, DOI: 10.1016/0926-9851(94)90022-1.

Milligan, P.R., P. Petkovic, and B.J. Drummond (2003), Potential-field datasets for the Australian region: their significance in mapping basement architecture, *GSA Spec. Pap.* **372**, 129-139, DOI: 10.1130/0-8137-2372-8.129.

Molnar, P., and W.P. Chen (1982), Seismicity and mountain building. **In:** K. Hsu (ed.), *Mountain Building Processes*, Academic Press, London, 41-57.

Molnar, P., W.P. Chen, T.J. Fitch, P. Tapponier, W.E.K. Warsi, and F.T. Wu (1977), Structure and tectonics of the Himalaya: a brief summary of relevant geophysical observations, *Colloq. Inter. CNRS* **268**, 269-294.

Mushayandebvu, M.F., V. Lesur, A.B. Reid, and J.D. Fairhead (2004), Grid Euler deconvolution with constraints for 2D structures, *Geophysics* **69**, 2, 489-496, DOI: 10.1190/1.1707069.

Nabighian, M.N., and R.O. Hansen (2001), Unification of Euler and Werner deconvolution in three dimensions via the generalized Hilbert transform, *Geophysics* **66**, 6, 1805-1810, DOI: 10.1190/1.1487122.

Ni, J., and M. Barazangi (1984), Seismotectonics of the Himalaya Collision Zone: Geometry of the underthrusting Indian Plate beneath the Himalaya, *J. Geophys. Res*. **89**, B2, 1147-1164, DOI: 10.1029/JB089iB02p01147.

Oruc, B. (2010), Edge detection and depth estimation using a tilt angle map from gravity gradient data of the Kozaklı-Central Anatolia Region, Turkey, *Pure Appl. Geophys.* **168**, 10, 1769-1780, DOI: 10.1007/s00024-010-0211-0.

Patriat, P., and J. Achache (1984), India-Eurasia collision chronology has implications for crustal shortening and driving mechanism of plates, *Nature* **311**, 5987, 615-621, DOI: 10.1038/311615a0.

Phillips, J.D., R.O. Hansen, and R.J. Blakely (2007), The use of curvature in potential-field interpretation, *Explor. Geophys.* **38**, 2, 111-119, DOI: 10.1071/EG07014.

Pilkington, M., A. Abdoh, and D.R. Cowan (1995), Pre-Mesozoic structure of the Inner Moray Firth Basin: constraints from gravity and magnetic data, *First Break* **13**, 7, 291-300, DOI: 10.3997/1365-2397.1995015.

Qureshy, M.N. (1981), Gravity anomalies, isostasy and crust mantle relations in the Deccan Trap and contiguous regions, India. **In:** K.V. Subha Rao and R.N. Sukheswala (eds.), *Deccan Volcanism and Related Basalt Provinces in Other Parts in the World*, Geological Society of India, Bangalore, 184-197.

Qureshy, M.N. (2004), *Geophysical Framework of India, Bangladesh and Pakistan*, Narosa Publication, 200 pp.

Qureshy, M.N., S.V. Venkatachalam, and C. Subrahmanyam (1974), Vertical tectonics in Middle Himalaya: an appraisal from recent gravity data, *Bull. Geol. Soc. Amer*. **85**, 6, 921-026, DOI: 10.1130/0016-7606(1974)85<921:VTITMH>2.0.CO;2.

Reddy, C.D., and B.R. Arora (1993), Quantitative interpretation of geomagnetic induction response across the thrust zones of Himalaya along the Ganga Yamuna valley, *J. Geomag. Geoelectr*. **45**, 9, 775-785.

Reid, A.B., and J.B. Thurston (2014), The structural index in gravity and magnetic interpretation: Errors, uses, and abuses, *Geophysics* **79**, 4, J61-J66, DOI: 10.1190/GEO2013-0235.1.

Reid, A.B., J.M. Allsop, H. Granser, A.J. Millett, and I.W. Somerton (1990), Magnetic interpretation in three dimensions using Euler deconvolution, *Geophysics* **55**, 1, 80-91, DOI: 10.1190/1.1442774.

Reid, A.B., D. FitzGerald, and P. McInerny (2003), Euler deconvolution of gravity data. **In:** *Proc. 73rd SEG Annual International Meeting, 26-31 October 2003, Dallas, USA*, SEG-2003-0580.

Reid, A.B., J.O. Ebbing, and S.J. Susan (2014), Avoidable Euler errors – the use and abuse of Euler deconvolution applied to potential fields, *Geophys. Prospect.* **62**, 5, 1162-1168, DOI: 10.1111/1365-2478.12119.

Shanker, D., N. Kapur, and B. Singh (2002), Thrust-wedge mechanics and coeval development of normal and reverse faults in the Himalayas, *J. Geol. Soc. London* **159**, 3, 273-280, DOI: 10.1144/0016-764901-059.

Silva, J.B.C., and V.C.F. Barbosa (2003), 3D Euler deconvolution: Theoretical basis for automatically selecting good solutions, *Geophysics* **68**, 6, 1962-1968, DOI: 10.1190/1.1635050.

Sinha, A.K. (1987), Tectonic zonation of the Central Himalayas and the Crustal evolution of collision and compressional belts, *Tectonophysics* **134**, 1-3, 59-74, DOI: 10.1016/0040-1951(87)90249-6.

Smith, R.S., J.B. Thurston, T.F. Dai, and I.N. MacLeod (1998), iSPI$^{TM}$ – The improved source parameter imaging method, *Geophys. Prospect.* **46**, 2, 141-151, DOI: 10.1046/j.1365-2478.1998.00084.x.

Stavrev, P.Y. (1997), Euler deconvolution using differential similarity transformations of gravity and magnetic anomalies, *Geophys. Prospect.* **45**, 2, 207-246, DOI: 10.1046/j.1365-2478.1997.00331.x.

Stavrev, P., and A. Reid (2007), Degrees of homogeneity of potential fields and structural indices of Euler deconvolution, *Geophysics* **72**, 1, L1-L2, DOI: 10.1190/1.2400010.

Stavrev, P., and A. Reid (2010), Euler deconvolution of gravity anomalies from thick contact/fault structures with extended negative structural index, *Geophysics* **75**, 6, 151-158, DOI: 10.1190/1.3506559.

Thompson, D.T. (1982), EULDPH: A new technique for making computer assisted depth estimates from magnetic data, *Geophysics* **47**, 1, 31-37, DOI: 10.1190/1.1441278.

Tripathi, J.N., P. Singh, and M.L. Sharma (2012), Variation of seismic coda wave attenuation in the Garhwal region, northwestern Himalaya, *Pure Appl. Geophys*. **169**, 1, 71-88, DOI: 10.1007/s00024-011-0316-0.

Vannay, J.C., and B. Grasemann (2001), Himalayan inverted metamorphism and syn-convergence extension as a consequence of a general shear extrusion, *Geol. Mag*. **138**, 3, 253-276, DOI: 10.1017/S0016756801005313.

Verduzco, B., J.D. Fairhead, C.M. Green, and C. MacKenzie (2004), New insights into magnetic derivatives for structural mapping, *The Leading Edge* **23**, 2, 116-119, DOI: 10.1190/1.1651454.

Wijns, C., C. Perez, and P. Kowalczyk (2005), Theta Map: Edge detection in magnetic data, *Geophysics* **70**, 4, L39-L43, DOI: 10.1190/1.1988184.

Williams, S.E., J.D. Fairhead, and G. Flanagan (2005), Comparison of grid Euler deconvolution with and without 2D constraints using a realistic 3D magnetic basement model, *Geophysics* **70**, 3, L13-L21, DOI: 10.1190/1.1925745.

Wilsher, W.A. (1987), A structural interpretation of the Witwatersrand basin through the application of automated depth algorithms to both gravity and aeromagnetic data, M.Sc. Thesis, University of Witwatersrand, Johannesburg, South Africa.

Yaghoobian, A., G.A. Boustead, and T.M. Dobush (1993), Object delineation using Euler's momogeneity equation: Location and depth determination of buried ferro-metallic bodies. **In:** *Proc. Symp. on Application of Geophysics to Engineering and Environmental Problems 1993, San Diego, USA*, 613-632, DOI: 10.4133/1.2922042.

Yuanyuan, L., Y. Yushan, and L. Tianyou (2010), Derivative-based techniques for geological contact mapping from gravity data, *J. Earth Sci.* **21**, 3, 358-364, DOI: 10.1007/s12583-010-0099-8.

Received 1 December 2014
Received in revised form 27 September 2015
Accepted 25 November 2015

DE GRUYTER OPEN

**Acta Geophysica**
vol. 64, no. 4, Aug. 2016, pp. 1139-1163
DOI: 10.1515/acgeo-2016-0041

# Effect of Shale Distribution on Hydrocarbon Sands Integrated with Anisotropic Rock Physics for AVA Modelling: A Case Study

Aamir ALI[1], ZUBAIR[1,2], Matloob HUSSAIN[1], Khaista REHMAN[3], and Muhammad TOQEER[1]

[1]Department of Earth Sciences, Quaid-i-Azam University, Islamabad, Pakistan
e-mail: aamirali.geo@gmail.com

[2]Schlumberger Information Solutions, Ocean Tower, Do Talwar, Karachi, Pakistan

[3]National Centre of Excellence in Geology, University of Peshawer, Pakistan

A b s t r a c t

Shales can be distributed in sand through four different ways; laminated, structural, dispersed and any combination of these aforementioned styles. A careful analysis of well log data is required for the determination of shale distribution in sand affecting its reservoir quality. The objective of this study is to characterize the effect of shale distribution on reservoir quality of sands using well log data. The correlation of well data in terms of lithology has revealed four sand and three shale layers in Lower Goru Formation acting as a major reservoir in the study area. Our results indicate that the laminated type of shale distribution prevails at the Basal sand level, which does not affect its reservoir quality greatly. The remaining layers of variable vertical extent show a variety of shale distribution models affecting their reservoir quality adversely. We also present anisotropic rock physics modelling for AVA analysis at Basal sand level.

**Key words:** shaly-sands, reservoir properties, shale distribution, rock physics, anisotropic AVA modelling.

Ownership: Institute of Geophysics, Polish Academy of Sciences;
© 2016 Ali *et al*. This is an open access article distributed under the Creative Commons Attribution-NonCommercial-NoDerivs license,
http://creativecommons.org/licenses/by-nc-nd/3.0/.

## 1. INTRODUCTION

Shales are the most common type of sedimentary rocks present in the Earth's crust. In the context of hydrocarbon exploration, shales are considered as source as well as cap rocks (Sunjay 2011).The presence of shale in porous formations causes problems for interpretation of wireline logs. This is not only due to the gross effect of shale on porosity values, but it can also affect the final calculated original gas in place (OGIP) for a given formation. In most cases, the reservoir sands contain some degree of shaliness which may adversely affect the reservoir quality (Paul 2012). However, physical properties, volume, and distribution of shale are major affecting candidates that may mislead the log reading and consequent interpretation (Clavier *et al*. 1984, Waxman and Smith 1968).

Shales are distributed in sand through four different ways, called laminated, structural, dispersed, and any combination of them (Clavaud *et al*. 2005, Sams and Andrea 2001). The best and common indicator of shale using the well log data is gamma ray (GR) log (Asquith *et al*. 2004, Tiab and Donaldson 2003, Zinszner and Pellerin 2007). This log responds to the changes in natural gamma radiation emitted by the formation. In shaly-sands the level of gamma radiation emitted is generally a function of clay volume only. The gamma ray log does not measure the volume of silts or other inclusions within the shales (Asquith *et al*. 2004, Tiab and Donaldson 2003). Although the gamma ray log is often the best shale indicator available, it is not definitive in identifying the sand-shale boundary by itself. In radioactive sands, gamma ray indicates shale, but responds as sand on neutron and density logs (Minh *et al*. 2008).

The objective of this study is to characterize the effect of shale distribution on reservoir quality of sands encountered in Lower Goru Formation using well log data of Khipro area, Lower Indus Basin, Pakistan. A further aim is to present anisotropic rock physics based amplitude *versus* angle (AVA) model to investigate amplitude variations for reservoir sand in the study area. The data used for this study consists of common suite of wireline logs, recorded in wells of Bilal-01, Inam-Basal-01, Siraj-South-01, and Naimat-Basal-01 with their location and detail given in Fig. 1 and Table 1, respectively. Different logs such as gamma ray, spontaneous potential, resistivity, sonic, porosity, and density were analyzed and interpreted in order to define reservoir geometry and properties. For the accomplishment of the above objectives, the workflow followed in the study for the determination of effect of shale distribution on hydrocarbon sands in Khipro block (study area) is given in Fig. 2. The workflow for the anisotropic rock physics AVA modelling will be presented and discussed in the Section 5.

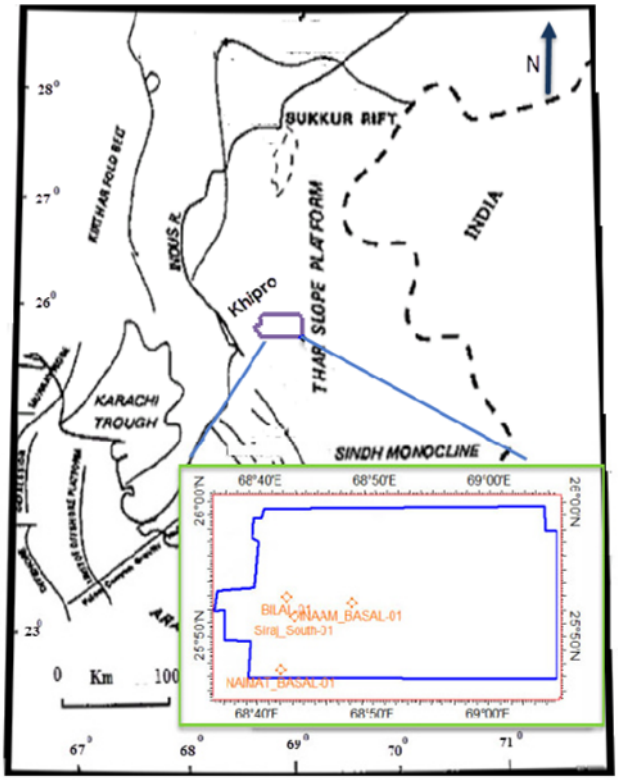


Fig. 1. Map showing the location of Khipro block and wells used in this study (Bender and Raza 1995).

Table 1

Well data used for research work

| Well name | Formation top [m] | | | | Well total depth [m] | Status of well | Discovery |
|---|---|---|---|---|---|---|---|
| | Upper sand | Middle sand | Sand above Talhar Shale | Basal sand | | | |
| Siraj South-01 | 3383 | 2597 | 2905 | 3055 | 3218 | Exploratory | Gas condensate |
| Bilal-01 | 2385 | 2605 | 2929 | 3058 | 3170 | Exploratory | Gas condensate |
| Naimat Basal-01 | 2311 | 3000 | 3389 | 3479 | 3599 | Exploratory | Gas condensate |
| Inam Basal-01 | 2261 | 2445 | 2665 | 2955 | 3153 | Exploratory | Gas condensate |

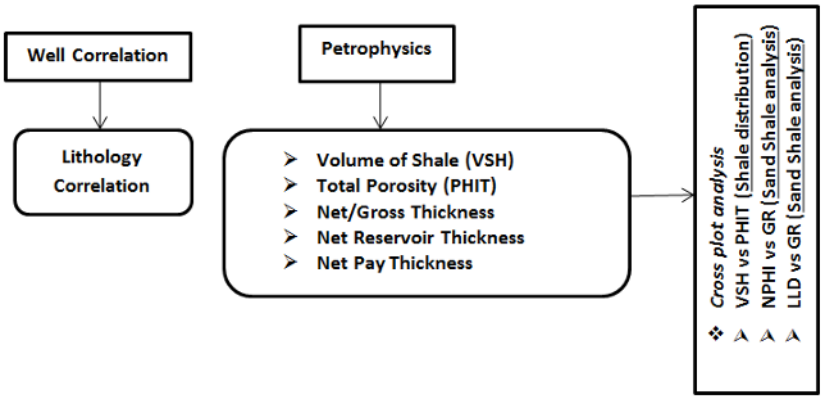


Fig. 2. Workflow followed for the determination of effect of shale distribution on hydrocarbon sands in the study area.

## 2. STUDY AREA

Khipro block is situated between latitude 25°40′N to 26°00′N and longitude 68°20′E to 69°14′E covering an area of 2376 km (Fig. 1). The basinal history of Khipro block is related to rifting and breaks up of Gondwanaland in Jurassic period (Oldham 1982). Khipro lies in Thar platform which is a westward sloping monocline and is controlled by its basement topography (Wandrey *et al*. 2004). After Paleocene there was a continuing oblique convergence of Indian plate and Eurasian plate throughout the Tertiary time and the collision causes tilting of the entire region (Powell 1979).

The presence of Jurassic rocks in area shows deposition during rifting. The rifting has resulted in the formation of normal faulting and horst and grabben structures (Fig. 3). The most important and well developed sedi-

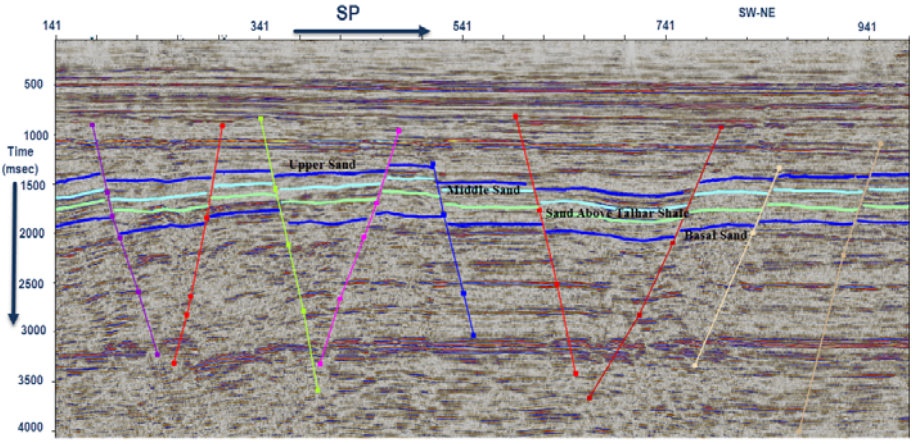


Fig. 3. Existence of normal faults showing start and end of rifting in the study area.

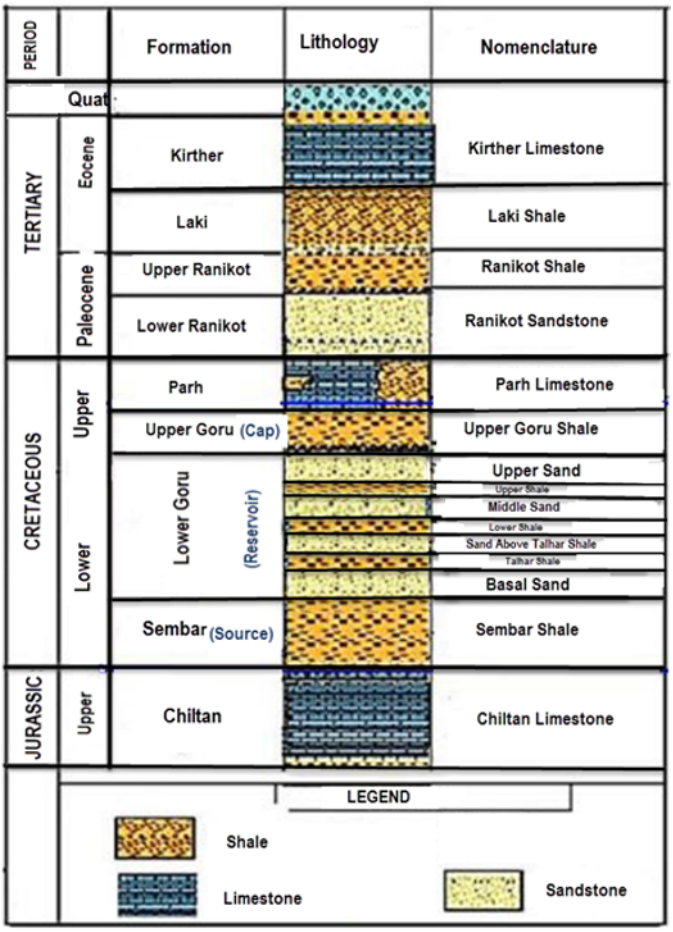


Fig. 4. Stratigraphic chart of the study area showing the petroleum play (Zaigham and Mallick 2000).

mentary rock in this area is Early/Middle Cretaceous sands (Lower Goru Formation) which acts as a good reservoir for oil and gas fields (Ahmad *et al*. 2004). These sands are underlain by shale and marl (Upper Goru) which act as seal for reservoirs (Kazmi and Abbasi 2008). The stratigraphic chart for the study area is given in Fig. 4.

Henceforth we present a brief explanation of workflow followed for characterizing the type of shale distribution in this study.

## 3. METHODOLOGY

For the determination of effect of shale distribution on hydrocarbon sands in the study area we have used the following methodology divided in three parts:

### 3.1 Well correlation

Well correlation entails determination of continuity and equivalence of lithological units, particularly reservoir sands or marker sealing shale across a region of the subsurface (Tearpock and Bischke 1991). It is essential to develop a good understanding of the geometry, continuity, and depositional settings of the sediment packages in order to build predictive geological and basin models, and minimize the risk of well target and performance failure (Li *et al*. 2004). Marker bed correlation is the most widely used and treated as reliable correlation technique even if the lithology or origins of the beds are not known (Li *et al*. 2004).

### 3.2 Petrophysical interpretation for reservoir parameters

Petrophysical interpretation of well logs basically provides us a way to calculate important physical properties like velocity, porosity, volume of shale, water saturation, and hydrocarbon saturation using empirical relations (Akhter *et al*. 2015, Ali *et al*. 2015, Asquith *et al*. 2004, Tiab and Donaldson 2003, Zinszner and Pellerin 2007). In this study, we have followed the workflow presented by Akhter *et al*. (2015) and Ali *et al*. (2015) for the calculation of classical petrophysical properties like velocity, porosity, water saturation, hydrocarbon saturation, and volume of shale.

Furthermore, the analysis of petrophysical logs in this study was also aimed at determining other relevant important reservoir properties (Gross/Net thickness, Net reservoir thickness, Net pay thickness, and Gross porosity) of Lower Goru Sands in Khipro area using cutoff presented in Table 2. Gross/Net thickness is the thickness of a certain facies in that particular zone, net reservoir thickness represents part of net thickness which has a certain amount of porosity, net pay thickness is the thickness contributing to economically viable production, and gross porosity is total porosity.

Table 2

Details of cut-off used for reservoir properties calculation

| Cut-off | GR <= 75 API | 0.1 <= NPHI <= 0.45 | Sw <= 50% |
|---|---|---|---|
| Net thickness [m] | Yes | No | No |
| Net reservoir thickness [m] | Yes | Yes | No |
| Net pay thickness [m] | Yes | Yes | Yes |

### 3.3 Distribution of shale in sand

Shales are distributed in sand through four different ways, called laminated, structural, dispersed, and any combination of the above models (Waxman and Smith 1968). Thomas and Stieber (1975) suggested a shale distribution

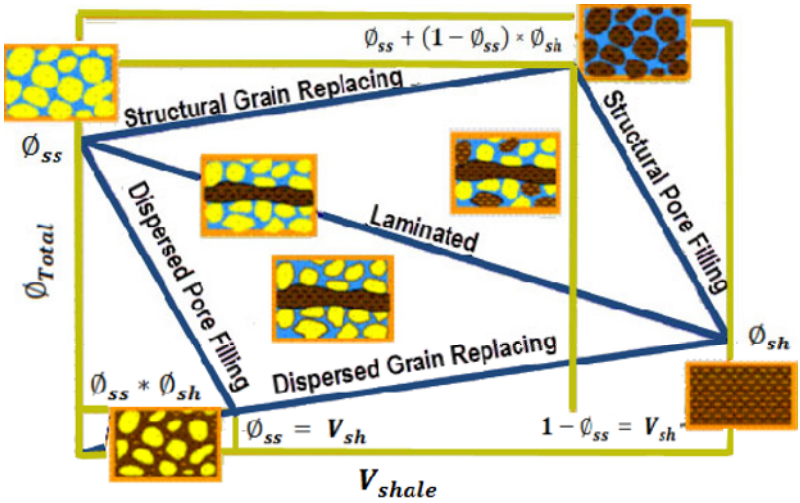


Fig. 5. Shale distribution model proposed by Thomas and Stieber (Tyagi *et al*. 2009). Here $V_{shale}$ is the volume of shale, $\varphi_{total}$ is the total porosity, $\varphi_{max}$ is the maximum porosity, and $\varphi_{sh}$ is the porosity in shale.

model which comprised shale configurations, sand portion, and sand porosity based on volume of shale and porosity (Fig. 5).

Laminar shale is dispersed in reservoir as thin layers of allogeneic clay which does not affect effective porosity, water saturation or horizontal permeability of reservoir rock, but affects the vertical permeability between reservoir rocks (Kurniawan 2005). Laminated shaley-sand repeats sequences of deposition under dual flow regimes considered by dissimilarities in energy levels (Visser 1998).

Dispersed shale is composed of clay minerals that form after deposition because of chemical reactions between minerals and chemicals in formation water due to variety of crystal sizes and shapes (Saxena *et al*. 2006). It significantly decreases the porosity, because shale occupies pore spaces, pore throats, and the water wetness of shale is generally higher than that of sand. Dispersed shale also causes increase in water saturation, reducing resistivity, porosity, and permeability of sands (Kurniawan 2005). The quantity of dispersed shale increasing more than 40% of sand pore space in a reservoir severely affects the pay zones of sands (Visser 1998).

Structural shale is deposited as particles or clasts during early depositional stage (Kurniawan 2005). Although it generally behaves like laminar shale, their permeability, and resistivity properties are similar to the dispersed shale (Kurniawan 2005). It contains shale nodules, which are mixed with sand grains to form part of sandstone having grain size almost same as sand

grains. Structural shales act as framework grains. This may or may not affect reservoir properties by blocking spaces between the grains (Visser 1998).

In most cases, all types of shales are distributed within the sand affecting its reservoir quality in a manner different from each other. Shale distribution can be determined from Thomas–Stieber cross-plot (Fig. 5; Thomas and Stieber 1975, Tyagi *et al*. 2009), where volume of shale (VSH) is plotted on the X-axis and total porosity (PHIT) on the Y-axis. Based on position of data points in the cross plot, laminar, dispersed, structural shale volumes in sand can be recognized and distinguished (Fig. 5).

A common practice is to use the maximum gamma-ray response as the shale point (Heslop 2005). But the mineralogical and compositional heterogeneity of shale may result in a relatively low gamma ray response. For example, sands with kaolinite clays will have a lower gamma ray response as compared to other shaley-sands. It is therefore more accurate to identify the gamma-ray response at the sand-shale boundary (La Vigne *et al*. 1994). Several log combinations may be used to determine the sand-shale boundary, but the most appropriate ones are the laterolog deep resistivity (LLD), neutron porosity (NPHI), and gamma ray (GR) (Heslop 2005). With the help of cross plots between these logs, one can perform detailed sand-shale analysis and also can differentiate between water or gas sand.

## 4. RESULTS AND DISCUSSION FOR SHALE DISTRIBUTION IN SAND

Lithological correlation of Lower Goru Formation has been prepared by matching formation tops from one well to another (Fig. 6). The lithological units are represented in vertical succession by distinct surfaces which represent changes in lithological character. This correlation has revealed sand layers named as: Upper sand, Middle sand, sand above Talhar Shale, and Basal sand of variable thickness from shale layers named as: Upper shale, Lower shale, and Talhar shale of variable thickness (Fig. 6).

After discriminating between sand and shale bodies, the classical reservoir properties (*e.g*., total porosity, volume of shale, and water saturation) are determined by using petrophysical interpretation for wells Naimat Basal-01 (Fig. 7) and Siraj South-01 (Fig. 8). Other relevant important reservoir properties (gross thickness, net thickness, net reservoir thickness, and net pay thickness) are also determined based on the values of cut-offs presented in Table 2. These reservoir properties for both wells are tabulated in Tables 3 and 4. Based on the results of petrophysical analysis, Upper and Basal sand layers show very good quality reservoir rock, while Middle sand and sand above Talhar shale show poor reservoir quality. Overall, the reservoir qualities of Lower Goru Sands vary from very good to poor. Generally the good or bad quality of reservoir depends mainly on its porosity and permeability.

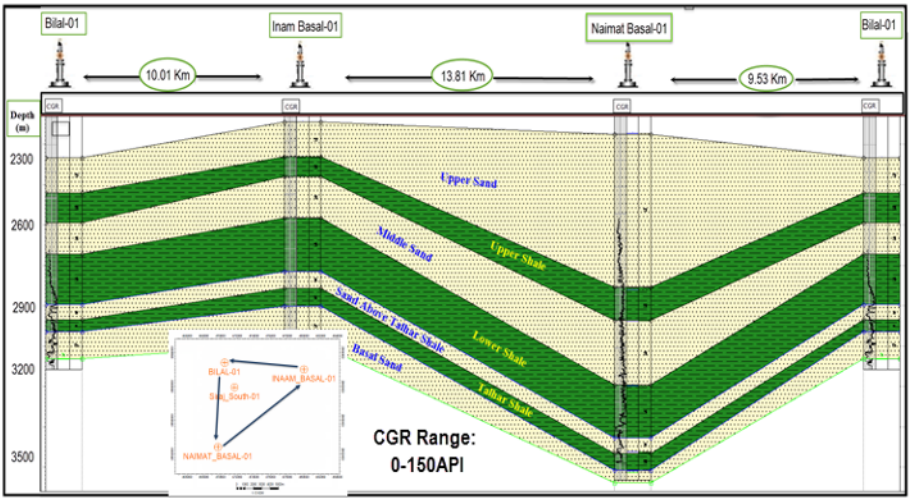


Fig. 6. Well correlation at Lower Goru level.

Here we have tried to describe the reservoir quality in terms of net reservoir thickness and net pay thickness using the cut off values given in Table 2 on classical petrophysical properties. In what follows, the reservoir quality of the sand layers will be related to the type of shale distributed within them.

The type of shale distribution in identified sand packages has been determined from cross-plot of volume of shale (VSH) and total porosity (PHIT) obtained from Siraj South-01 and Naimat Basal-01. Interpretation of this cross-plot on the basis of position of data points indicates that almost all types of shales are distributed within the sand bodies (Figs. 9-12).

Sand above Talhar shale has a small vertical extent (thickness) as compared to all other sand layers with mostly structural along with dispersive shale distribution (Fig. 11). This type of shale distribution in Sand above Talhar shale further affects its reservoir quality along with its small vertical extent. The effect can be in the form of decreased porosity (as dispersive shale occupies pore spaces) and increased water saturation (as water wetness of shale is generally higher than that of sand). The values of porosity and water saturation are used in the cut-off values of net reservoir thickness and net pay thickness.

Middle sand has a large vertical extent as compared to Sand above Talhar shale, but with large distribution of structural and dispersive shales along with some quantity of laminar shale (Fig. 10). Due to the presence of more structural and dispersive shale this sand layer also has a poor reservoir quality as in the case of Sand above Talhar shale.

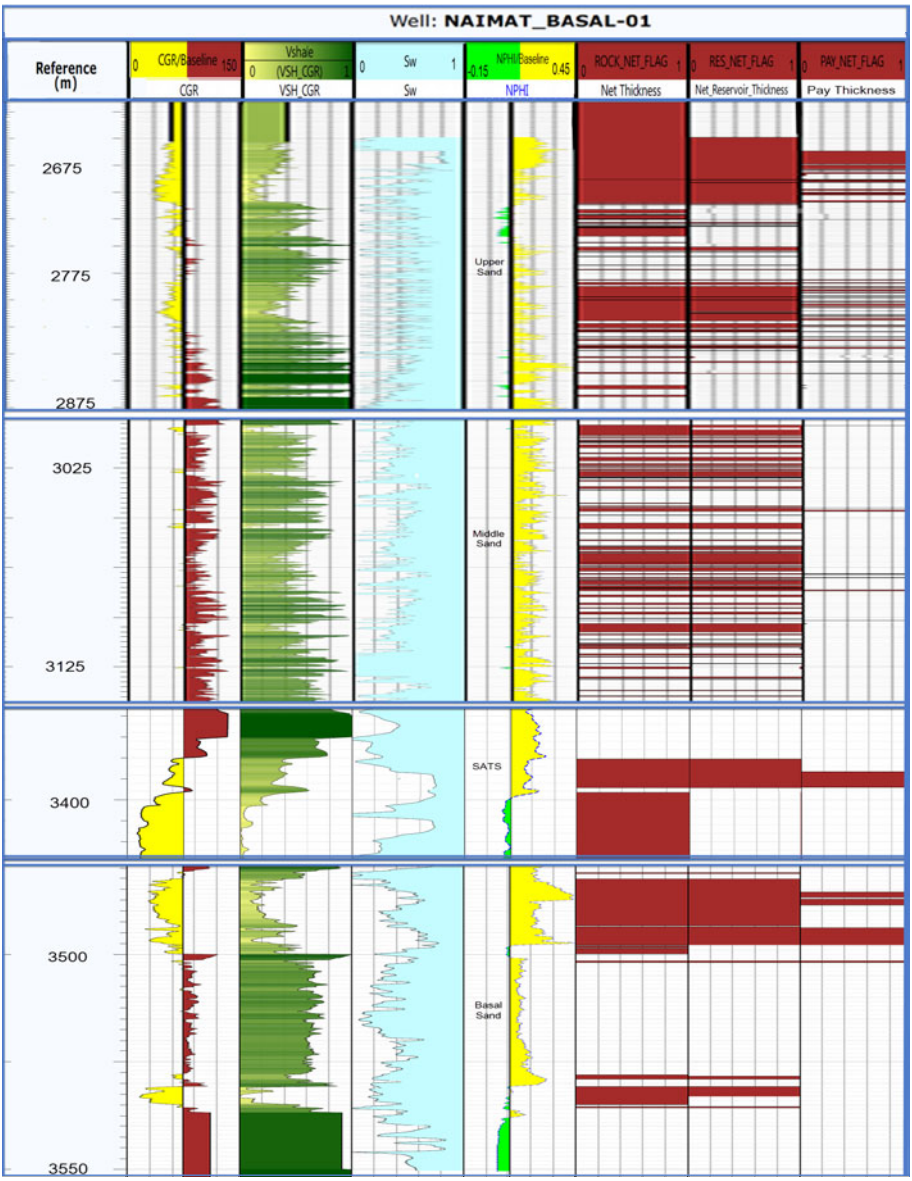


Fig. 7. Petrophysical properties at Lower Goru level for well Naimat Basal-01 with each sand interval shown in different depth scale for better legibility.

Upper and Basal sand layers can be considered as major hydrocarbon bearing sand packages due to their reasonable vertical extent as compared to the other sand layers (Figs. 7-8, Tables 3-4). In geological terms, the sand

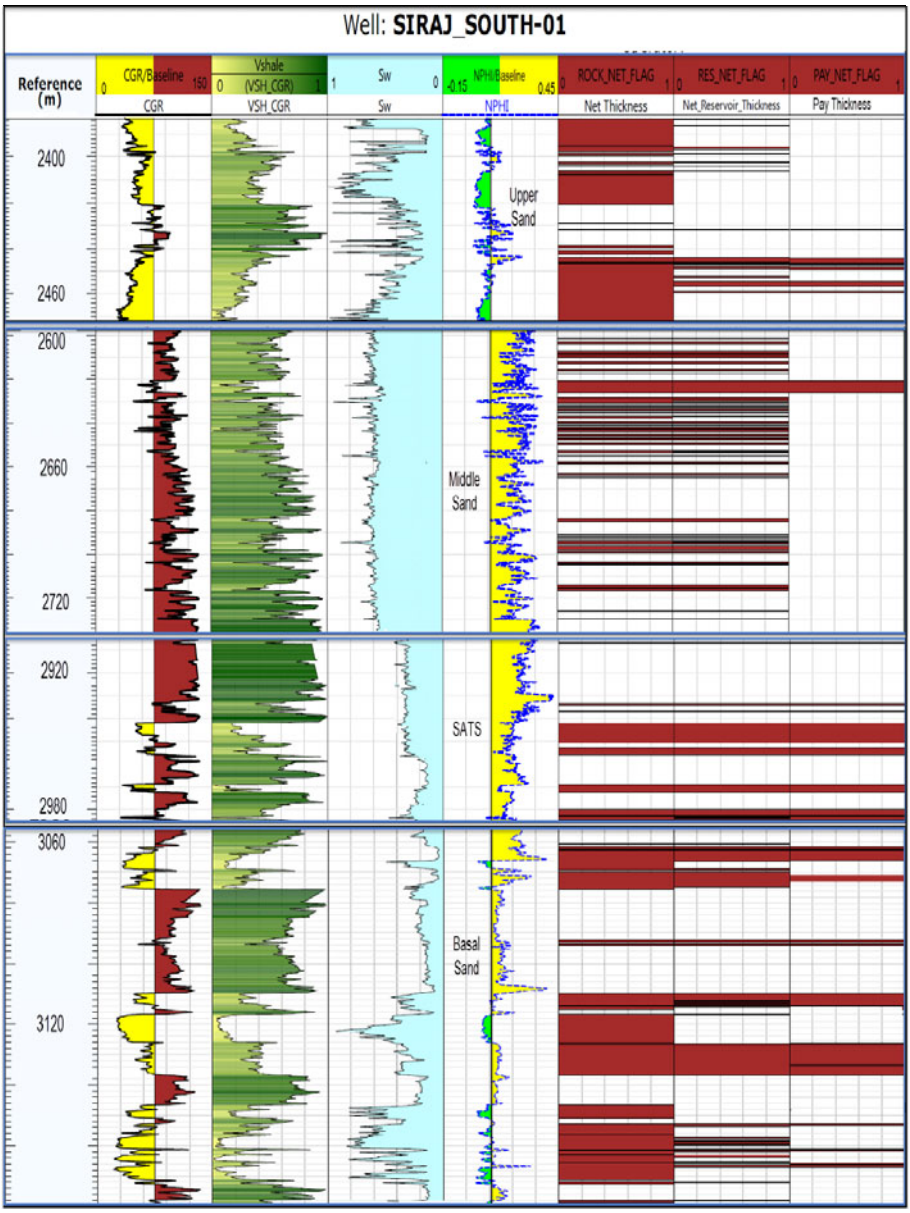


Fig. 8. Petrophysical properties at Lower Goru level for well Siraj South-01.

packages formed in longer deposition time will have a reasonable vertical extent. All types of shales (laminated, structural, and dispersed) are distributed within these layers (Figs. 9 and 12). There is a presence of more dis-

Table 3

Reservoir properties in Lower Goru Sands in Naimat Basal-01 well

| Naimat Basal-01 | Upper sand | Middle sand | Sand above Talhar Shale | Basal sand |
|---|---|---|---|---|
| Depth range [m] | 2311-2878 | 3000-3143 | 3389-3407 | 3479-3570 |
| Gross thickness [m] | 567 | 144 | 18 | 91 |
| Net thickness [m] | 194 | 56 | 12 | 29 |
| Net reservoir thickness [m] | 82 | 47 | 7 | 24 |
| Net pay thickness [m] | 33 | 5 | 4 | 17 |
| Gross porosity [%] | 14 | 21 | 15 | 17 |
| Average volume of shale [%] | 53 | 59 | 40 | 50 |
| Average water saturation [%] | 55 | 62 | 50 | 55 |

Table 4

Reservoir properties in Lower Goru Sands in Siraj South-01 well

| Siraj South-01 | Upper sand | Middle sand | Sand above Talhar Shale | Basal sand |
|---|---|---|---|---|
| Depth range [m] | 2383-2472 | 2597-2736 | 2905-2985 | 3055-3200 |
| Gross thickness [m] | 88 | 139 | 59 | 145 |
| Net thickness [m] | 79 | 35 | 18 | 66 |
| Net reservoir thickness [m] | 20 | 32 | 18 | 43 |
| Net pay thickness [m] | 7 | 5 | 18 | 30 |
| Gross porosity [%] | 8 | 23 | 17 | 13 |
| Average volume of shale [%] | 50 | 60 | 65 | 46 |
| Average water saturation [%] | 56 | 60 | 30 | 35 |

Table 5

Thickness of different shales in Upper and Basal sand level using data from Figs. 9 and 15a in Siraj South-01 well

| Shale type | Upper sand thickness [m] | | Basal sand thickness [m] |
|---|---|---|---|
| Laminated shale | 6 | | 35 |
| Dispersed shale | Pore filling | 28 | 23 |
| | Grain replacing | 19 | 18 |

persed shale at Upper sand level as compared to the structural and laminar shales (Table 5). This reduces porosity and increases water saturation at Upper sand level along with the effects of structural (may or may not affect res-

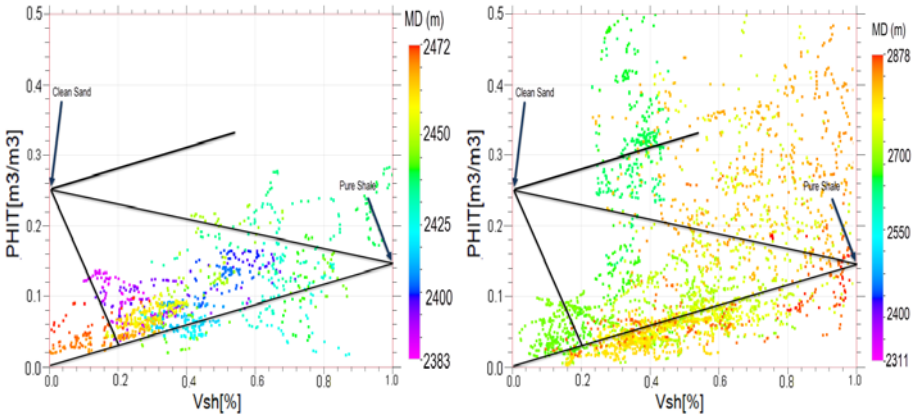


Fig. 9. Shale distribution at Upper sand level in well Siraj South-01 (left) and Naimat Basal-01 (right). Figure 5 is used as a reference for the interpretation of the above cross-plots.

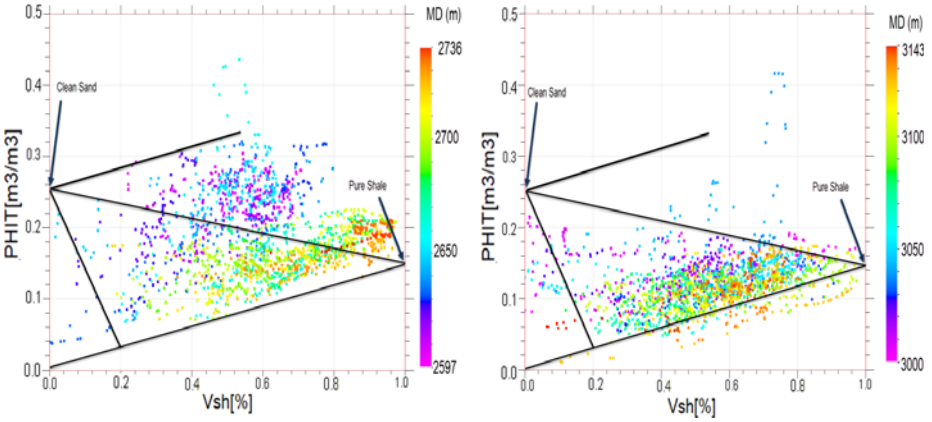


Fig. 10. Shale distribution at Middle sand level in well Siraj South-01 (left) and Naimat Basal-01 (right). Figure 5 is used as a reference for the interpretation of the above cross-plots.

ervoir properties) and laminated shale (only affects the vertical reservoir properties). On the other hand, Basal sand consists mainly of laminar shale along with significant amount of dispersed shale (Table 5). The presence of more laminar shale at Basal sand level as compared to Upper sand level is probably one of the reasons that Basal sand is a major producer in most of the drilled wells in the study area.

A detailed sand-shale analysis was carried out at Basal sand level, which helps in differentiating between hydrocarbon (oil/gas) and non-hydrocarbon

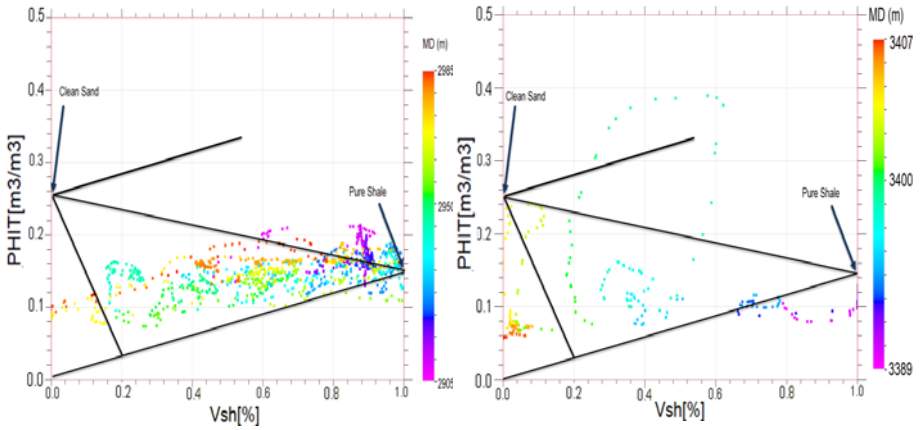


Fig. 11. Shale distribution at Sand above Talhar Shale in well Siraj South-01 (left) and Naimat Basal-01 (right). Figure 5 is used as a reference for the interpretation of the above cross-plots.

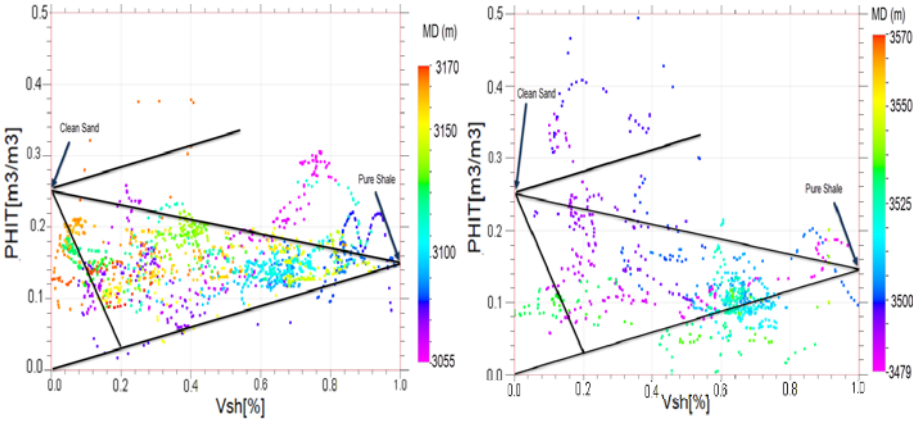


Fig. 12. Shale distribution at Basal sand level in well Siraj South-01 (left) and Naimat Basal-01 (right). Figure 5 is used as a reference for the interpretation of the above cross-plots.

(water) bearing sands using the data of Siraj-South-01 well. The cross-plots of laterolog deep resistivity (LLD), gamma ray (GR) log, and neutron porosity log (NPHI) were used for this purpose. In hydrocarbon bearing formation, the resistivity log signatures show high resistivity values than in water bearing formation (Fig. 13). On the cross-plot of the NPHI *versus* GR using the data of Siraj-South-01 well, we can identify the clean/gas sands at low neutron porosity and low gamma ray value (Fig. 14).

The results obtained from sand-shale analysis (Figs. 13-14) and types of shale distribution at Basal sand level (Fig. 15a) were integrated with the

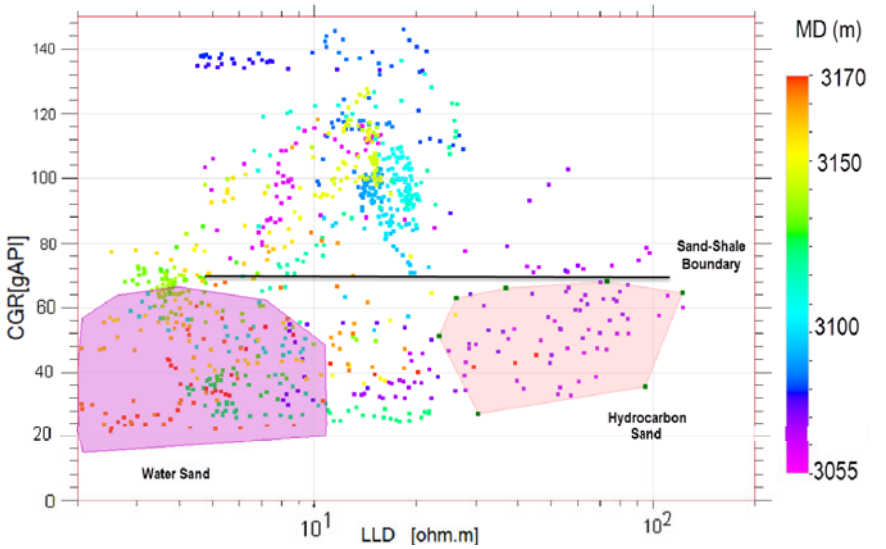


Fig. 13. Detailed sand-shale analysis using the cross-plot of LLD *versus* GR from Siraj South-01 well for the identification of hydrocarbon and water bearing sand at Basal sand level.

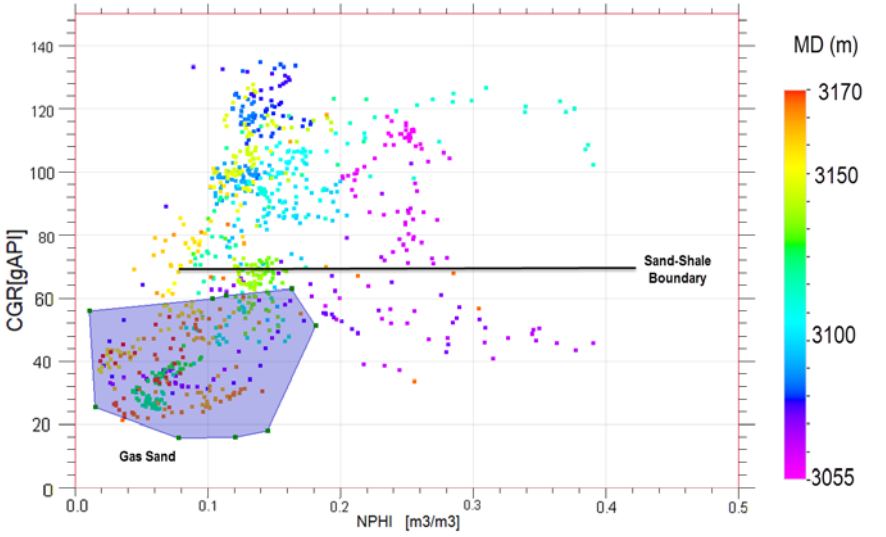


Fig. 14. Detailed sand-shale analysis using the cross-plot of NPHI *versus* GR from Siraj South-01 well for the identification of hydrocarbon and water bearing sand at Basal sand level.

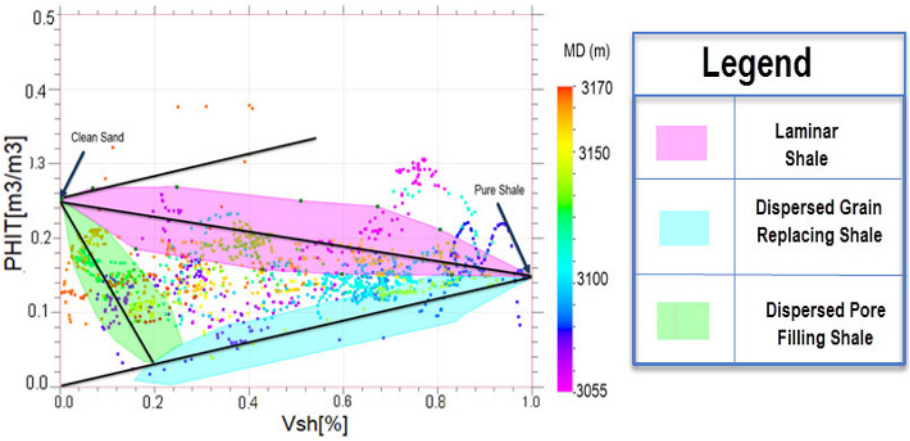


Fig. 15a. Shale distribution at Basal sand level in well Siraj-South-01. Polygons are drawn with reference to Fig. 5 with area between them showing mixture of different shale distributions.

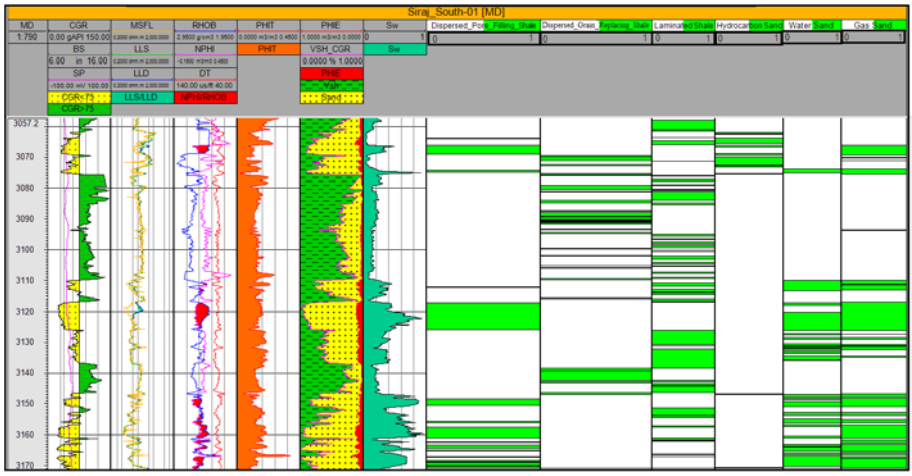


Fig. 15b. Petrophysical interpretation at Basal sand level in Siraj South-01 well showing consistent results (data within polygons of Figs. 13-15a) with Figs. 13-15a.

petrophysical interpretation. Clearly the density-porosity cross-over confirms the presence of hydrocarbons (Fig. 15b). There are different depth ranges that confirm presence of water sand and laminar shale (Fig. 15b) consistent with Figs. 13-15a.

## 5. ANISOTROPIC ROCK PHYSICS BASED AVA MODELLING FOR BASAL SAND

The purpose of this modeling at producing Basal sand level was to identify the class of sand based on AVA response (Rutherford and Williams 1989, Sen 2006). A further aim was to present an application of anisotropic rock physics modeling to generate AVA response based on the type of shale distribution. In reality, shales are often found to behave elastically as transversely isotropic media with a vertical axis of symmetry (Jakobsen and Johansen 1999, 2000). From rock physics modeling point of view, shales can be modeled as layers or in the form of lenses within the host medium (Sayers 1998). For modeling shales as thin layers within the host medium (sand), one can use the Backus averaging typically designed for layered medium modeling (Jakobsen *et al*. 2003, Ali *et al*. 2015, Sayers 1998, Backus 1962). Shales in the form of lenses within the host medium (sand) can be modeled with the help of inclusion based methods (Jakobsen *et al*. 2003, Ali *et al*. 2011). Here in our study area mainly laminar shale along with the dispersed shale are distributed in Basal sand layer. Laminar shale generally fulfills the criteria of being deposited in the form of thin layers. Therefore, the best available choice for rock physics modeling of shales in this study is using a laminar/layered model performed through the Backus averaging.

Shale layers within the sand matrix often show horizontally aligned orientation, thus making a transversely isotropic (TI) medium with a vertical axis of symmetry also known as VTI medium characterized either in terms of five independent elastic/stiffness constants ($C_{11}$, $C_{13}$, $C_{33}$, $C_{55}$, and $C_{66}$) or of two vertical velocities ($V_P$ and $V_S$) and three Thomsen anisotropic parameters ($\gamma$, $\delta$, $\varepsilon$) (Thomsen 1986, Tsvankin 1997a, b; Ali *et al*. 2011).

The effective stiffness of a stratified medium composed of transversely isotropic layers in the limit of long-wavelength is also effectively anisotropic and is given by Backus (1962)

$$\begin{bmatrix} A & B & F & 0 & 0 & 0 \\ B & A & F & 0 & 0 & 0 \\ F & F & C & 0 & 0 & 0 \\ 0 & 0 & 0 & D & 0 & 0 \\ 0 & 0 & 0 & 0 & D & 0 \\ 0 & 0 & 0 & 0 & 0 & M \end{bmatrix}, \qquad M = \frac{1}{2}(A - B), \tag{1}$$

where $A$, $B$, $C$, $D$, and $F$ are the five independent effective elastic constants. In terms of $P$- and $S$-wave velocities ($V_P$ and $V_S$) and densities ($\rho$), the five independent elastic constants can be written as

$$A = \left\langle 4\rho V_S^2 \left[ 1 - \frac{V_S^2}{V_P^2} \right] \right\rangle + \left\langle 1 - 2\frac{V_S^2}{V_P^2} \right\rangle^2 \left\langle \left( \rho V_P^2 \right)^{-1} \right\rangle^{-1}, \tag{2}$$

$$B = \left\langle 2\rho V_S^2 \left[ 1 - \frac{2V_S^2}{V_P^2} \right] \right\rangle + \left\langle 1 - 2\frac{V_S^2}{V_P^2} \right\rangle^2 \left\langle \left( \rho V_P^2 \right)^{-1} \right\rangle^{-1}, \tag{3}$$

$$C = \left\langle \left( \rho V_P^2 \right)^{-1} \right\rangle^{-1}, \tag{4}$$

$$F = \left\langle 1 - 2\frac{V_S^2}{V_P^2} \right\rangle^2 \left\langle \left( \rho V_P^2 \right)^{-1} \right\rangle^{-1}, \tag{5}$$

$$D = \left\langle \left( \rho V_S^2 \right)^{-1} \right\rangle^{-1}, \tag{6}$$

$$M = \left\langle \rho V_S^2 \right\rangle. \tag{7}$$

The brackets $\langle \cdot \rangle$ indicate averages of the enclosed properties weighted by their volumetric proportions. The input parameters $V_P$, $V_S$, and $\rho$ for calculation of constants $A$-$M$ in Eqs. 2-7 for the sand and shale layers at the Basal sand level are obtained from well log data of Siraj South-01 tabulated in Table 6. More specifically, we have used sonic and density log for the estimation of $V_P$ and $\rho$ at Basal sand level. As shear log was not available in any of the wells including Siraj South-01, we have estimated $V_S$ from $V_P$ for both sand and shale using relations given byMavko *et al*. (2009).

Once the five independent constants are obtained using the Eqs. 2-7 in our rock physics model, the Thomsen anisotropy parameters for VTI can be obtained using the relation given by Thomsen (1986, 1995)

Table 6

Mechanical properties used for anisotropic AVA modelling obtained from well Siraj South-01

| Reservoir properties | Sand (matrix) | Shale (layers) | Overburden |
|---|---|---|---|
| *P*-wave velocity, $V_P$ [m/s] | 4355 | 3975 | 3970 |
| *S*-wave velocity, $V_S$ [m/s] | 3403 | 2960 | 2250 |
| Density, $\rho$ [g/cm$^3$] | 2.61 | 2.59 | 2.52 |
| Porosity, $\varphi$ (fraction) | 0.09 | 0.11 | – |
| Volume of shale, $V_{sh}$ (fraction) | 0.46 | – | – |
| Water saturation, $S_w$ (fraction) | 0.18 | – | – |

$$\gamma = \frac{M - D}{2D} , \tag{8}$$

$$\varepsilon = \frac{A - C}{2C} , \tag{9}$$

$$\delta = \frac{(F + D)^2 - (C - D)^2}{2C(C - D)} . \tag{10}$$

In order to calculate the effect of fluid saturation on the effective properties of alternating sand shale layers, one can use the (anisotropic Gassmann) relations of Brown and Korringa (1975) (also see Ali *et al*. 2011, Shahraini *et al*. 2011). The values of porosity, water saturation, and volume of shale have been used in anisotropic Gassmann relation from well data of Siraj South-01 at Basal sand level given in Table 6.

For the purpose of seismic modelling, there exist many approximations, but we have used Rüger's approximation of reflection coefficients for VTI medium, because the influence of anisotropy can be readily analyzed on AVA signatures (Rüger 2002). The Rüger's approximation gives reflection coefficients as a function of polar incidence angle (*i*) written as (Rüger 2002)

$$R_P^{\mathrm{VTI}}(i) = \frac{1}{2}\frac{\Delta Z}{\overline{Z}} + \frac{1}{2}\left\{\frac{\Delta V_{P0}}{\overline{V}_{P0}} - \left(\frac{2\overline{V}_{S0}}{\overline{V}_{P0}}\right)^2 \frac{\Delta G}{\overline{G}} + \Delta\delta\right\}\sin^2 i + \frac{1}{2}\left\{\frac{\Delta V_{P0}}{\overline{V}_{P0}} + \Delta\right\}\sin^2 i \tan^2 i . \tag{11}$$

Here $Z$ is the *P*-wave impedance, $G$ is the shear modulus, $V_{P0}$ is the effective *P*-wave velocity obtained using $V_{P0} = \sqrt{C/\rho}$, and $V_{S0}$ is the effective shear wave velocity obtained using $V_{S0} = \sqrt{D/\rho}$. The constants $C$ and $D$ are obtained using Eqs. 4 and 6. The constants and $\delta$ are the anisotropy parameters for VTI media and obtained using relations in Eqs. 9 and 10. Here symbol $\Delta$ denotes contrast across an interface $(\Delta Z = Z_2 - Z_1)$ and a bar over a symbol denotes the average $\left(\overline{Z} = (Z_1 + Z_2)/2\right)$, where subscript 1 corresponds to the upper-half space (which corresponds to the mechanical properties $V_P$, $V_S$, and $\rho$ of overburden tabulated in Table 6), and subscript 2 corresponds to lower-half space (which corresponds to the effective mechanical properties $V_P$, $V_S$, and $\rho$ at Basal sand level obtained using Backus averaging).

The workflow followed to obtain the AVA response at Basal sand level is given in Fig. 16. The background parameters used in the computation of anisotropic rock physics and seismic modeling are tabulated in Table 6 and obtained from the analysis of data of Siraj South-01 well. It is important to clarify that the mechanical properties of sand and shale given in Table 6 are average values from well log data of Siraj South-01. These values are used

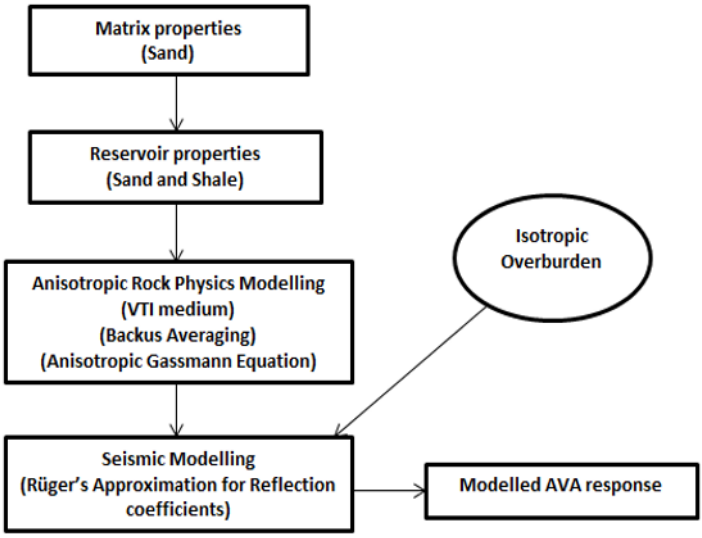


Fig. 16. Workflow followed for anisotropic rock physics based AVA modelling at Basal sand level.

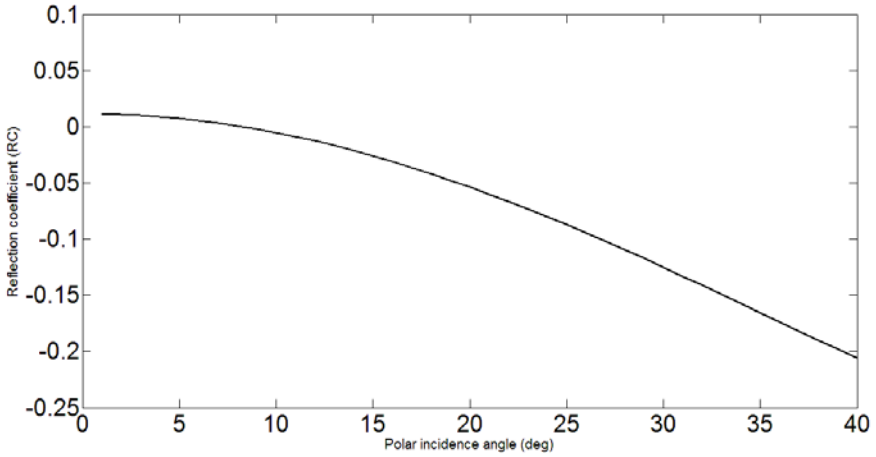


Fig. 17. Plot of reflection coefficient as a function of incidence angle at Basal sand level with $\delta = -0.008$ and $\varepsilon = 0.002$. Isotropic overburden is assumed during the computation with mechanical properties given in Table 6.

as an input by Backus averaging (Eqs. 1-10) to give effective mechanical properties at the Basal sand level. The overburden properties given in Table 6 represent the average mechanical properties obtained in lithologies above the Basal sand level using the well log data of Siraj South-01.

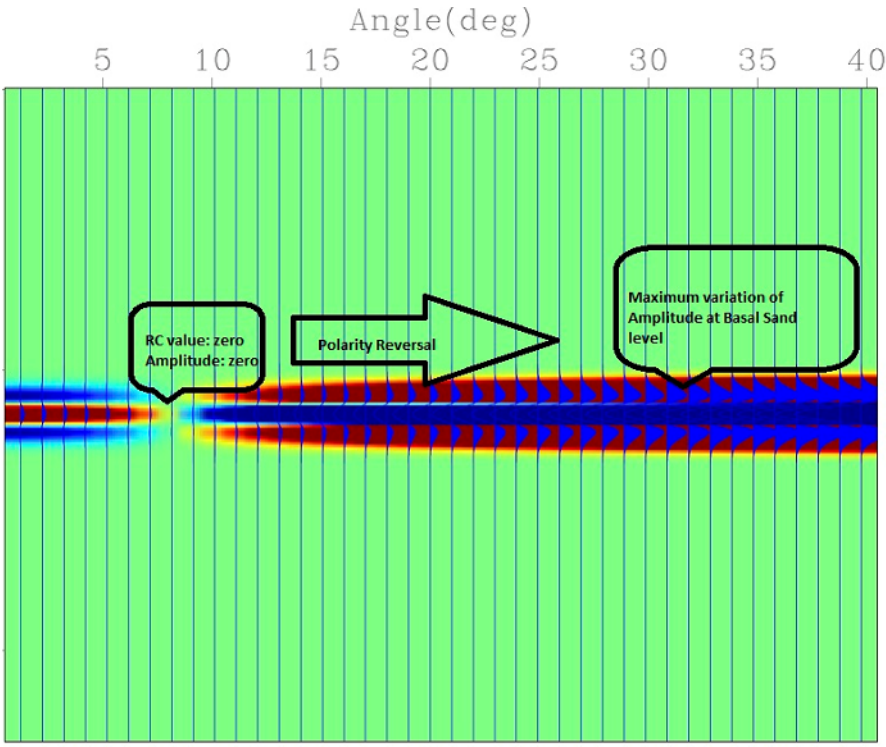


Fig. 18. Anisotropic AVA at Basal sand level. A polarity reversal at near offsets indicates moderately compacted AVO class II sand.

Figure 17 shows the reflection coefficients as a function of polar incidence for Basal sand level. There is a sharp decreasing trend of the reflection coefficients with the increasing angle of incidence (far offsets) at the Basal sand level. Figure 18 shows the AVA response at the top of the Basal sand level clearly indicating the polarity reversal due to negative reflection coefficients and maximum variation of amplitude at increasing polar angle of incidence (far offsets).

## 6. CONCLUSIONS

In this study we have presented a case study to determine the effect of shale distribution on producing sands from Khipro area, Lower Indus basin Pakistan using well log data. The well correlation using well tops at Lower Goru level reveals four sands (Upper sand, Middle sand, sand above Talhar shale, and Basal sand) and three shale (Upper shale, Lower shale, and Talhar shale) layers.

Based on the results of petrophysical analysis, Upper and Basal sand layers show very good reservoir quality in terms of net reservoir thickness and net pay thickness. We have also related the reservoir quality with the type of shale distribution within these two sand layers. Our results further reveal that there is a presence of more dispersed shale at Upper sand level as compared to the structural and laminar shales decreasing the porosity and increasing the water saturation. There is a presence of more laminar shale at Basal sand level as compared to dispersed shale, making this layer viable for hydrocarbon production.

A detailed sand-shale analysis based on LLD, GR, and neutron porosity logs integrated with petrophysical interpretation at the Basal sand level is also presented to discriminate between hydrocarbon and water bearing sands. The detailed sand-shale analysis and petrophysical interpretation results are consistent with each other at the Basal sand level.

We have also presented an anisotropic rock physics based AVA analysis at the Basal sand level using the workflow given in Fig. 16. Our analysis shows that due to negative reflection coefficients a polarity reversal can be observed at near incidence angles (near offsets) which indicate a moderately compacted AVO class II sand. The maximum variation of amplitude can be observed with increasing angle of incidence (far offsets). This way of modelling provides a framework for the calculation of anisotropic parameters ($\gamma$, $\delta$, $\varepsilon$) required for anisotropic AVA. It will also improve the matching of amplitudes with the seismic gather at far offsets as compared to an isotropic AVA model where anisotropy is ignored.

Acknowledgments. Dr. Aamir Ali would like to thank the Directorate General of Petroleum Concessions (DGPC), Pakistan, for allowing the use of seismic and well log data for research and publication purposes and the Department of Earth Sciences, Quaid-i-Azam University, Islamabad, Pakistan for providing the basic requirements to complete this work.

## References

Ahmad, N., P. Fink, S. Strurrock, T. Mahmood, and M. Ibrahim (2004), Sequence stratigraphy as predictive tool in Lower Goru Fairway, Lower and Middle Indus platform, Pakistan". **In:** *Proc. PAPG-SPE Annual Technical Conference, 8-9 October 2004, Islamabad, Pakistan*, 85-104.

Akhter, G., Z. Ahmed, A. Ishaq, and A. Ali (2015), Integrated interpretation with Gassmann fluid substitution for optimum field development of Sanghar area, Pakistan: A case study, *Arab. J. Geosci.* **8**, 9, 7467-7479, DOI: 10.1007/s12517-014-1664-8.

Ali, A., A. Shahraini, and M. Jakobsen (2011), Improved characterization of fault zones by quantitative integration of seismic and production data, *J. Geophys. Eng.* **8**, 2, 259, DOI: 10.1088/1742-2132/8/2/011.

Ali, A., M. Kashif, M. Hussain, J. Siddique, I. Aslam, and Z. Ahmed (2015), An integrated analysis of petrophysics, cross-plots and Gassmann fluid substitution for characterization of Fimkassar area, Pakistan: A case study, *Arab. J. Sci. Eng.* **40**, 1, 181-193, DOI: 10.1007/s13369-014-1500-1.

Asquith, G.B., D.A. Krygowski, S. Henderson, and N. Hurley (2004), *Basic Well Log Analysis*, American Association of Petroleum Geologists, 244 pp.

Backus, G.E. (1962), Long-wave elastic anisotropy produced by horizontal layering, *J. Geophys. Res.* **67**, 11, 4427-4440, DOI: 10.1029/JZ067i011p04427.

Bender, F.K., and H.A. Raza (1995), *Geology of Pakistan*, Borntraeger, Berlin.

Brown, R.J.S., and J. Korringa (1975), On the dependence of the elastic properties of a porous rock on the compressibility of the pore fluid, *Geophysics* **40**, 4, 608-616, DOI: 10.1190/1.1440551.

Clavaud, J.B., R. Nelson, U.K. Guru, and H. Wang (2005), Field example of enhanced hydrocarbon estimation in thinly laminated formation with a triaxial array induction tool: A laminated sand-shale analysis with anisotropic shale. **In:** *SPWLA 46th Annual Logging Symposium, 26-29 June 2005, New Orleans, USA*, SPWLA-2005-WW.

Clavier, C., G. Coates, and J. Dumanoir (1984), Theoretical and experimental bases for the dual-water model for interpretation of shaly sands, *Soc. Petrol. Eng. J.* **24**, 2, 153-168, DOI: 10.2118/6859-PA.

Heslop, K. (2005), *Interpretation of Shaly Sands*, London Petrophysical Society, London.

Jakobsen, M., and T.A. Johansen (1999), A test of ANNIE based on ultrasonic measurements on a shale, *J. Seism. Explor.* **8**, 1, 77-89.

Jakobsen, M., and T.A. Johansen (2000), Anisotropic approximations for mudrocks: A seismic laboratory study, *Geophysics* **65**, 6, 1711-1725, DOI: 10.1190/1.1444856.

Jakobsen, M., J.A. Hudson, and T.A. Johansen (2003), T-matrix approach to shale acoustics, *Geophys. J. Int.* **154**, 2, 533-558, DOI: 10.1046/j.1365-246X.2003.01977.x.

Kazmi, A.H., and I.A. Abbasi (2008), *Stratigraphy and Historical Geology of Pakistan*, Department and National Centre of Excellence in Geology, Peshawar, Pakistan.

Kurniawan, F. (2005), Shaly sand interpretation using CEC-dependent petrophysical parameters, Ph.D. Thesis, Louisiana State University and Agricultural and Mechanical College, Baton Rouge, USA.

La Vigne, J., M. Herron, and R. Hertzog (1994), Density-neutron interpretation in shaly sands. **In:** *Proc. SPWLA 35th Annual Logging Symp., 19-22 June, Tulsa, USA*, 16 pp.

Li, S., C.M. Henderson, and R.R. Stewart (2004), Well log study and stratigraphic correlation of the Cantuar Formation, southwestern Saskatchewan, *CREWES Res. Rep.* **16**, 1-18.

Mavko, G., T. Mukerji, and J. Dvorkin (2009), *The Rock Physics Handbook: Tools for Seismic Analysis of Porous Media*, 2nd ed., Cambridge University Press, Cambridge.

Minh, C.C., J.B. Clavaud, P. Sundararaman, S. Froment, E. Caroli, O. Billon, G. Davis, and R. Fairbairn (2008), Graphical analysis of laminated sand-shale formations in the presence of anisotropic shales, *Petrophysics* **49**, 5, 395-405.

Oldham, R.D. (1982), Report on the geology of Thal Chotiali and part of the Mari Country, *Records Geol. Survey India* **15**, 1, 18-29.

Paul, W.J. (2012), *Petrophysics,* Dept. of Geology and Petroleum Geology, University of Aberdeen.

Powell, C. (1979), A speculative tectonic history of Pakistan and surroundings: some constrains from Indian Ocean. **In:** A. Farah and K.A. De Jong (eds.), *Geodynamics of Pakistan*, Geological Survey of Pakistan, Quetta, 5-24.

Rüger, A. (2002), *Reflection Coefficients and Azimuthal AVO Analysis in Anisotropic Media*, Society of Exploration Geophysicists, Tulsa, 177-182, DOI: 10.1190/1.9781560801764.appd.

Rutherford, S.R., and R.H. Williams (1989), Amplitude-versus-offset variations in gas sands, *Geophysics* **54**, 6, 680-688, DOI: 10.1190/1.1442696.

Sams, M.S., and M. Andrea (2001), The effect of clay distribution on the elastic properties of sandstones, *Geophys. Prospect.* **49**, 1, 128-150, DOI: 10.1046/j.1365-2478.2001.00230.x.

Saxena, K., A. Tyagi, T. Klimentos, C. Morriss, and A. Mathew (2006), *Evaluating Deepwater Thin-Bedded Reservoirs with the RT Scanner*, Petromin, Kuala Lumpur.

Sayers, C.M. (1998), Long-wave seismic anisotropy of heterogeneous reservoirs, *Geophys. J. Int.* **132**, 3, 667-673, DOI: 10.1046/j.1365-246X.1998.00456.x.

Sen, M.K. (2006), *Seismic Inversion*, Society of Petroleum Engineers, Richardson, USA.

Shahraini, A., A. Ali, and M. Jakobsen (2011), Seismic history matching in fractured reservoirs using a consistent stiffness-permeability model: Focus on the effects of fracture aperture, *Geophys. Prospect.* **59**, 3, 492-505, DOI: 10.1111/j.1365-2478.2010.00934.x.

Sunjay, S. (2011), Shale gas: An unconventional reservoir, Department of Geophysics, Banaras Hindu University, Varanasi, India.

Tearpock, D.J., and R.E. Bischke (1991), *Applied Subsurface Geological Mapping,* Prentice-Hall, Inc., Englwood Cliffs.

Thomas, E.C., and S.J. Stieber (1975), The distribution of shale in sandstones and its effect on porosity. **In:** *Trans. SPWLA 16th Annual Logging Symp., 4-7 June 1975*.

Thomsen, L. (1986), Weak elastic anisotropy, *Geophysics* **51**, 10, 1954-1966, DOI: 10.1190/1.1442051.

Thomsen, L. (1995), Elastic anisotropy due to aligned cracks in porous rock, *Geophys. Prospect.* **43**, 6, 805-829, DOI: 10.1111/j.1365-2478.1995.tb00282.x.

Tiab, D., and E.C. Donaldson (2003), *Petrophysics: Theory and Practice of Measuring Reservoir Rock and Fluid Transport Properties*, Gulf Professional Publ., Waltham.

Tsvankin, I. (1997a), Anisotropic parameters and P-wave velocity for orthorhombic media, *Geophysics* **62**, 4, 1292-1309, DOI: 10.1190/1.1444231.

Tsvankin, I. (1997b), Reflection moveout and parameter estimation for horizontal transverse isotropy, *Geophysics* **62**, 2, 614-629, DOI: 10.1190/1.1444170.

Tyagi, A.K., R. Guha, D. Voleti, and K. Saxena (2009), Challenges in the reservoir characterization of a laminated sand shale sequence. **In:** *Proc. 2nd SPWLA-India Regional Symp., 19-20 November 2009, Mumbai, India*.

Visser, J. (1998), Extensile hydraulic fracturing of (saturated) porous materials. Ph.D. Thesis, Department of Civil Engineering and Geosciences, Delft University, Delft, The Netherlands.

Wandrey, C.J., B.E. Law, and H.A. Shah (2004), Sembar Goru/Ghazij composite total petroleum system, Indus and Sulaiman-Kirthar geologic provinces, Pakistan and India, U.S. Geological Survey Bulletin, Report #B 2208-C, 23 pp.

Waxman, M.H., and L.J.M. Smith (1968), Electrical conductivities in oil-bearing shaly sands, *SPE J.* **8**, 2, 107-122.

Zaigham, N.A., and K.A. Mallick (2000), Prospect of hydrocarbon associated with fossil-rift structures of the southern Indus basin, Pakistan, *AAPG Bull*. **84**, 11, 1833-1848.

Zinszner, B., and F.M. Pellerin (2007), *A Geoscientist's Guide to Petrophysics*, Editions Technip, Paris.

Received 31 October 2014
Received in revised form 4 August 2015
Accepted 18 August 2015

DE GRUYTER OPEN

Acta Geophysica
vol. 64, No. 4, Aug. 2016, pp. 1164-1175
DOI: 10.1515/acgeo-2016-0040

# The Influence of a Local Fault Zone on High Energy Tremor Occurrence During Longwall Mining of a Coal Seam

Łukasz WOJTECKI[1], Małgorzata KNOPIK[2], and Wacław Marian ZUBEREK[2]

[1]Kompania Węglowa S.A., Katowice, Poland; e-mail: l.wojtecki@kwsa.pl

[2]University of Silesia in Katowice, Faculty of Earth Sciences, Sosnowiec, Poland; e-mail: gosia_knopik@interia.pl, waclaw.zuberek@us.edu.pl

Abstract

Underground mining of coal seams in the Upper Silesian Coal Basin in Poland is accompanied by seismic activity of varying magnitude. The investigations which have been performed for several years distinguished high energy mine tremors connected directly with mining or coupled with geological structures, such as large faults. In mined seams, local fault zones occur. Faults in these zones are usually small, with throws comparable with coal seams thicknesses. Local fault zone may be responsible for the occurrence of high energy tremors as well as large faults, as presented in this article. An analysis of source mechanism of high energy tremors generated during longwall mining of the coal seam No. 510, with presence of a local fault zone, in one of the Polish hard coal mines in the Upper Silesian Coal Basin was performed. For this purpose, the seismic moment tensor inversion method was used. In most of foci, the process of shear predominated. Determined nodal plane parameters were correlated with parameters of faults forming the local fault zone. High energy tremors were generated mostly by dislocations on faults of the local fault zone. Weakening of roof rocks in the neighborhood of local fault zone takes an important role too, and was responsible for share of implosion in the focal mechanism.

**Key words:** mine tremors, focal mechanism, seismic moment tensor, underground coal mining.

Ownership: Institute of Geophysics, Polish Academy of Sciences;
© 2016 Wojtecki *et al*. This is an open access article distributed under the Creative Commons Attribution-NonCommercial-NoDerivs license, http://creativecommons.org/licenses/by-nc-nd/3.0/.

## 1. INTRODUCTION

Underground mining of coal seams in the Upper Silesian Coal Basin generates mine tremors, including those with high energy. These tremors may be correlated with mining operation and their energy is adequate to specific geological and mining conditions. Some tremors are coupled to geological structures, such as large faults.

An analysis of the tremor source mechanism allows to reconstruct the way of rock mass destruction in the focal zone. The most probable factors affecting the generation of seismic events may be determined. The determination of mechanisms which are responsible for the occurrence of mine tremors is possible with the use of seismic moment tensor inversion method. This method was firstly used in global seismology, and next was adapted to mine tremors analysis (Gibowicz and Kijko 1994, Marcak and Zuberek 1994, Gibowicz 1995, Stec 2009, Kwiatek 2009, Stec and Wojtecki 2011).

The method of seismic moment tensor inversion was applied for determination of source mechanisms of high energy tremors induced during mining of coal seam No. 510 in one of the coal mines in the Upper Silesian Coal Basin, in a certain time interval. The most probable ways of generation of these tremors were defined. The results of the analysis have been compared with local geological and mining conditions.

The presented analyses were performed to determine the factors responsible for the occurrence of high energy tremors during longwall mining under complicated geological and mining conditions. Understanding the processes which take place in the tremors' foci (especially those with high energy) enables a proper assessment of the rockburst hazard in coal mines with the use of seismological method and application of adequate prevention. The local fault zone was the main factor influencing the high energy tremor occurrence. This knowledge was applied for determination of rockburst prevention methods in the longwall and will be also useful for seismicity forecast during planning of further longwall mining.

## 2. GEOLOGICAL AND MINING CONDITIONS

The coal seam No. 510 in the area of the longwall was deposited at a depth of about –835 to –910 m and its thickness varied from 5.3 to 8.1 m. The smallest thickness of the coal seam was correlated with the local fault zone occurrence.

In the floor of the coal seam No. 510, shale, sandy shale, and fine-grained sandstone are deposited. Sandy shale, fine-grained sandstone, another sandy shale, and shale occur in the roof of the coal seam No. 510. The total thickness of these layers is lower than 13 m. The floor of coal seam No. 507 is above. At a distance of more than 70 m above the seam No. 510,

a thick layer of sandstone is deposited. This sandstone has high value of uniaxial compressive strength (up to 80 MPa), and its maximum thickness – with some thin layers of shales and sandy shales – is 60 m.

The longwall with caving was running in the upper layer of coal seam No. 510, from west to east. The longwall advance in the following months (from November 2012 to December 2013) is shown in Fig. 1 (the bold line represents the location of longwall face at the beginning). The longwall started from neighborhood of pillar for flank drifts, in a short distance from large fault, which has strike NW-SE and throw $h = 25$ m (Fig. 1). Mining under the above-mentioned conditions was responsible for the occurrence of high energy tremors (Knopik *et al.* 2015). High energy tremors have seismic energy $E \geq 1 \times 10^5$ J (magnitude $M_L \geq 1.68$). The longwall was running along the gob created in the upper stage (Fig. 1).

In the area of the longwall, the local fault zone occurred. This zone consisted of several faults, with strikes from SW-NE to WNW-ESE, throws from $h = 0.2$ to 5.5 m, and dips from near 20° to near 90° (generally SE, but S and NW as well). The location of local fault zone and values of throws and dips of faults forming this zone are shown in Fig. 1.

In the longwall area, coal seam No. 507 has been mined several years ago. The longwall in the wholeness was running under the gob created in coal seam No. 507. Coal seam No. 502, deposited at a distance of about 126 m above coal seam No. 510, has been mined still earlier. However, the longwall was running under the mining remnant of irregular shape in coal seam No. 501 (Fig. 1), deposited at a distance of about 140 m above coal seam No. 510. This mining remnant was responsible for the observed increase of stress in rock mass, during running of the longwall.

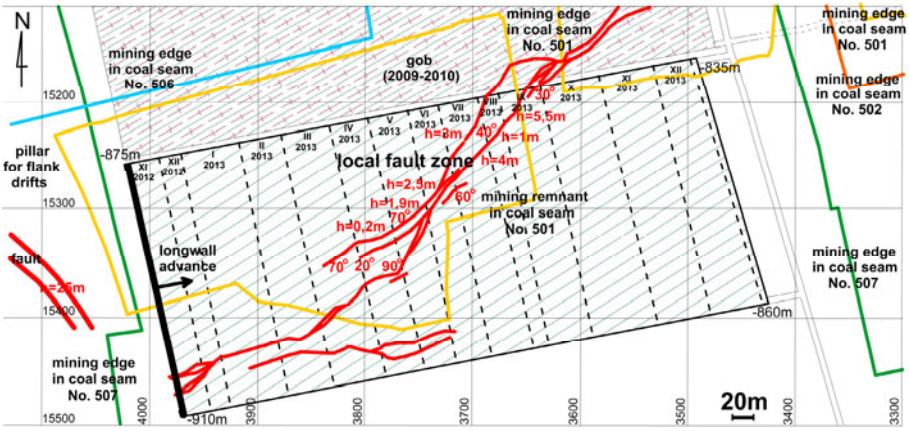


Fig. 1. The longwall area on the coal seam No. 510 map.

## 3. HIGH ENERGY TREMORS IN THE AREA OF LONGWALL

Mining of coal seam No. 510 with the longwall lasted nearly 14 months (from November 2012 to December 2013). High energy tremors accompanied this longwall mining, which indicated a high level of rockburst hazard. Total number of recorded high energy tremors was 61 with magnitude $M_L$ from 1.84 to 2.74. According to seismic activity, correlated to geological and mining conditions, running of the longwall could be divided into two periods.

During the first 6 months, the longwall run away from the neighbourhood of protecting pillar for flank drifts and large fault (throw $h = 25$ m). During this period, 28 high energy tremors occurred with magnitude $M_L$ from 1.84 to 2.74. High energy tremors in this period were caused by a change of stress equilibrium in the pillar for flank drifts and dislocations on large fault (Knopik *et al.* 2015). Some of high energy tremors were caused also by cracking of thick layer of sandstone above mined coal seam and destruction of roof rocks because of gob formation (Knopik *et al.* 2015). In this period, the total longwall advance equalled 225 m.

The second period lasted nearly 8 months. During the first four months of this period the longwall was running through the local fault zone, where the roof was weak. Keeping the stabilization of the roof affected the longwall advance, which equalled only 121 m. During the last four months the roof in the area of the longwall was tougher, which allowed to get longwall advance of 194 m. During the second period, 33 high energy tremors occurred with magnitude $M_L$ from 1.84 to 2.58. Hypocentres of these tremors were localized behind the longwall, mainly in the local fault zone or its direct neighbourhood (with an average error of epicentre location amounting to 20 m). In the area of the longwall, the maximum error of epicentre location achieved about 35 m, and it depended on the seismic stations which had been taken into calculations (Kołodziejczyk 2009). The error of hypocentre location in the area of the longwall was larger and in extreme cases reached over 60 m (Kołodziejczyk 2009). Focal mechanisms of these tremors were determined.

## 4. CALCULATION OF THE FOCAL MECHANISM

Focal mechanism of mine tremors could be calculated with the use of seismic moment tensor inversion method. In this method, the seismic moment tensor components are calculated on the basis of displacement field recorded by seismic network surrounding the source. Displacements at a long distance from the seismic source are a sum of displacements caused by each of force couples (Aki and Richards 1980). The tensor decomposition into the isotropic component (I), the compensated linear vector dipole (CLVD), and a

double couple of forces (DC) is the most often used characterization of the focus of mine tremor (Gibowicz and Kijko 1994, Marcak and Zuberek 1994, Gibowicz 1995, Stec 2009). The isotropic part I describes the volumetric changes in the source ("+" means explosion, "–" means implosion), CLVD describes a mechanism similar to the uniaxial compression ("–") or tension ("+") and DC relates to shear mechanism. The advantage of the isotropic part in full seismic moment tensor concerns tremors generated because of roof weight on coal seam causing the exceedance of its compressive strength (explosive mechanism) or a collapse of roof rocks into cavern caused by mining (implosive mechanism). The compensated linear vector dipole (CLVD) describes cracking of pillars. The advantage of the double couple of forces (DC) indicates sliding of rock masses (Gibowicz and Kijko 1994), for example by activation of faults presented in rock mass.

Focal mechanisms were calculated by the seismic moment tensor inversion based on the analysis of seismic waves generated in the focus and registered by the underground seismic stations surrounding the source. The data set has been obtained from a network of 16 seismic stations, located in underground excavations at depths from 320 to 1000 m below the sea level. The network is composed of vertical SPI-70 seismometers and DLM-2001 geophones installed on bolts and oriented vertically. These sensors measure signals having a frequency from 1 Hz. The upper limit of transmitted frequencies is 50 Hz. Signals are recorded with dynamic range less than 72 dB. Each channel has its own amplitude gain. The sampling rate is 5000 samples per second. The timing of seismological system is synchronized by Global Positioning System.

Seismic moment tensor calculation was performed in the FOCI software (Kwiatek 2009), based on an inversion of *P*-wave amplitude, taking into account the directions of the first deflection in the time domain (Stec and Wojtecki 2011).

Mechanisms of all 33 events that occurred in the second period of mining, mostly in the local fault zone or its neighbourhood, have been estimated. Focal mechanisms were determined on the basis of records registered by seismological network of hard coal mine. For seismic moment tensor determination, 14 or 15 records were used most often (about 64 and 18% of tremors, respectively). The minimal number of records taken into account was 12 (about 6% of tremors). Seismic stations were distributed evenly and optimally around the longwall (Fig. 2). Squares with "S" in Fig. 2 represent seismic stations.

The calculations were made using L1 norm, because of its lower sensitivity to possible large errors, caused, for example, by random noise made by mining machines. Vertical coordinates of focus were improved by the FOCI software (Kwiatek 2009), testing the seismic moment tensor solution and as-

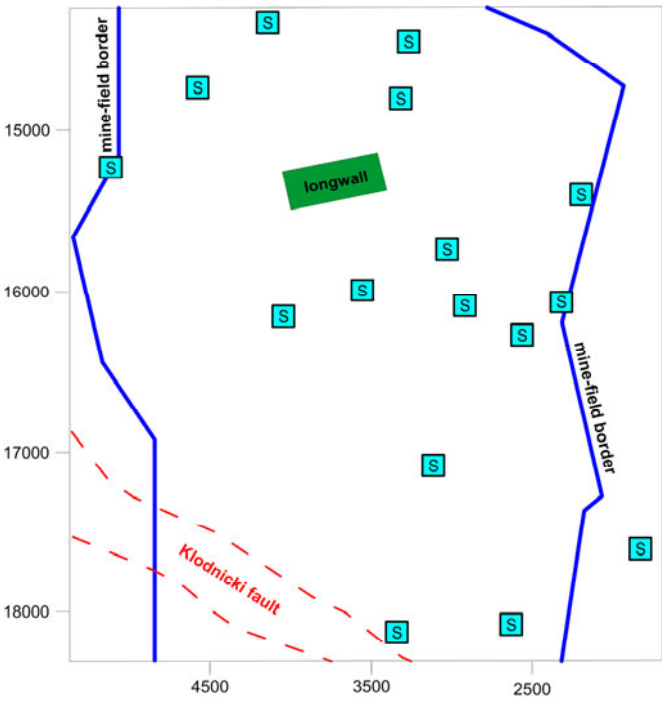


Fig. 2. Configuration of the seismic network around the longwall in coal seam No. 510.

suming the value corresponding to the highest values of quality coefficient (from 29 to 49%, mean 38%) – taking into consideration configuration of seismic stations and error of result – and the smallest error of estimation. Relative error of calculated seismic moments was 3% on average.

## 5. RESULTS

Results of the focal mechanism analysis of tremors recorded during second period of the longwall run are presented in Table 1. The criteria of focal mechanism types were specified by authors. If the share of DC component in full seismic moment tensor solution equals 50% or more, focal mechanism type is classified as normal (NO) or reverse (RE) slip mechanism. The only exception to this criterion is a focal mechanism type (RE) of tremor No. 5 (Table 1), where the share of DC component equals almost 50%, the share of uniaxial compression is higher than 40%, and the implosion practically does not matter (Table 1). For the other tremors, if the share of implosion is higher than 40%, the focal mechanism type is classified as IMPL. Some mixed types of focal mechanism, which do not satisfy the above mentioned

Table 1

Seismological and focal mechanism parameters of high energy tremors occurred during mining of coal seam No. 510 with the longwall

| No. | Date | Time | | $M_L$ | $Z$[1)] [m] | Nodal planes parameters[2)] | | Components of full seismic moment tensor [%] | | | Type mechanism |
|---|---|---|---|---|---|---|---|---|---|---|---|
| | | h | m | | | ΦA/δA λA | ΦB/δB λB | I | CLVD | DC | |
| 1. | 18 Jun 2013 | 3 | 17 | 2.05 | –825 | 19.7°/86.5° 116.2° | 116.8°/26.4° 7.9° | –22.2 | –20.8 | 57 | RE |
| 2. | 28 Jun 2013 | 18 | 11 | 2.00 | –809 | 18°/75.4° 111.6° | 140.4°/25.9° 35.2° | –4.7 | –6.1 | 89.3 | RE |
| 3. | 8 Jul 2013 | 4 | 45 | 2.13 | –829 | 230°/87.6° –115.8° | 135.1°/25.9° –5.5° | –9.4 | –18.4 | 72.2 | NO |
| 4. | 22 Jul 2013 | 22 | 29 | 2.37 | –829 | 219.6°/87.8° –115.3° | 125°/25.4° –5.1° | –23.2 | –24.1 | 52.8 | NO |
| 5. | 27 Jul 2013 | 7 | 9 | 2.00 | –829 | 43.2°/86.5° 107.2° | 144.3°/17.5° 11.7° | –11.8 | –40.7 | 47.4 | RE |
| 6. | 2 Aug 2013 | 17 | 21 | 2.16 | –822 | 217.8°/85.8° –117.2° | 119.7°/27.5° –9.2° | –24.5 | –15.4 | 60.1 | NO |
| 7. | 14 Aug 2013 | 13 | 39 | 2.09 | –801 | 212.4°/81.6° –113.8° | 104°/25.1° –20.2° | –34.4 | –30.8 | 34.8 | NO/IMPL |
| 8. | 18 Aug 2013 | 9 | 28 | 2.19 | –820 | 223.8°/67.3° –114.3° | 93.3°/32.8° –45.4° | –42.3 | –36.5 | 21.2 | IMPL |
| 9. | 20 Aug 2013 | 20 | 9 | 2.19 | –820 | 228.2°/72.9° –113.9° | 104.6°/29° –37.2° | –34.9 | –25.3 | 39.8 | NO/IMPL |
| 10. | 23 Aug 2013 | 4 | 22 | 2.19 | –810 | 254°/76.1° –107.5° | 126.8°/22.2° –39.4° | –15.3 | –1.8 | 82.9 | NO |
| 11. | 26 Aug 2013 | 22 | 1 | 2.46 | –829 | 231.8°/73.3° –113.5° | 108.4°/28.5° –36.9° | –32.1 | –16.3 | 51.6 | NO |
| 12. | 31 Aug 2013 | 8 | 31 | 2.21 | –827 | 230.8°/70.5° –114.1° | 104°/30.7° –41° | –36 | –22.9 | 41.1 | NO/IMPL |
| 13. | 6 Sep 2013 | 8 | 25 | 2.37 | –827 | 224.5°/78.5° –116.1° | 112.4°/28.3° –24.8° | –32.3 | –32.4 | 35.3 | NO/IMPL |
| 14. | 11 Sep 2013 | 11 | 19 | 1.84 | –824 | 225.9°/77.7° –117.4° | 113.6°/29.9° –25.4° | –31 | –13.8 | 55.2 | NO |
| 15. | 20 Sep 2013 | 0 | 38 | 2.16 | –821 | 245.5°/65.3° –110.6° | 104.5°/31.8° –52.6° | –37 | –23.5 | 39.5 | NO/IMPL |
| 16. | 23 Sep 2013 | 17 | 40 | 2.05 | –827 | 48.5°/69.2° 115.1° | 175.5°/32.2° 41.7° | 24.8 | 23.5 | 51.8 | RE |
| 17. | 30 Sep 2013 | 15 | 21 | 2.19 | –823 | 249°/61.4° –106° | 99.9°/32.4° –63.2° | –36.9 | –21.3 | 41.8 | NO/IMPL |

to be continued

Table 1 continuation

| No. | Date | Time | | $M_L$ | $Z^{1)}$ [m] | Nodal planes parameters[2)] | | Components of full seismic moment tensor [%] | | | Type mechanism |
|---|---|---|---|---|---|---|---|---|---|---|---|
| | | h | m | | | ΦA/δA λA | ΦB/δB λB | I | CLVD | DC | |
| 19. | 8 Oct 2013 | 3 | 3 | 1.84 | –828 | 242.3°/60.4° –113.7° | 104°/37.2° –54.7° | –41.9 | –31.2 | 27 | IMPL |
| 20. | 9 Oct 2013 | 21 | 18 | 2.05 | –827 | 237.8°/55.8° –111.4° | 92.8°/39.6° –61.7° | –45.1 | –39.5 | 15.4 | IMPL |
| 21. | 15 Oct 2013 | 7 | 17 | 2.05 | –825 | 245.8°/59.9° –110.2° | 102.1°/35.7° –59.2° | –41.3 | –31.2 | 27.5 | IMPL |
| 22. | 16 Oct 2013 | 16 | 31 | 2.05 | –800 | 235.6°/64.2° –115.9° | 103.7°/35.9° –47.9° | –40.6 | –26.7 | 32.7 | IMPL |
| 23. | 18 Oct 2013 | 17 | 14 | 2.21 | –830 | 235°/74° –114.7° | 114°/29.2° –34.5° | –32.7 | –18.5 | 48.8 | NO/IMPL |
| 24. | 23 Oct 2013 | 20 | 34 | 2.05 | –825 | 256.6°/54.6° –125.5° | 127.5°/48.4° –50.8° | –35 | –39.4 | 25.6 | IMPL/NO |
| 25. | 30 Oct 2013 | 23 | 53 | 2.00 | –818 | 249.6°/61.9° –104.1° | 97.7°/31.2° –65.5° | –37.7 | –21.8 | 40.5 | NO/IMPL |
| 26. | 6 Nov 2013 | 12 | 5 | 2.37 | –808 | 250.6°/67° –108.7° | 111.6°/29.4° –52.9° | –32.1 | –17.1 | 50.7 | NO |
| 27. | 15 Nov 2013 | 4 | 39 | 2.00 | –804 | 254.1°/57.2° –108.9° | 106.5°/37.3° –63.6° | –41 | –19.3 | 39.7 | IMPL |
| 28. | 23 Nov 2013 | 1 | 4 | 2.58 | –720 | 19.2°/65.2° –70.9° | 159.6°/31° –125.3° | –21.3 | –18.6 | 60.1 | NO |
| 29. | 30 Nov 2013 | 12 | 5 | 2.05 | –703 | 23.4°/68.4° –69.8° | 158.5°/29.3° –131° | –25.6 | –24.5 | 50 | NO |
| 30. | 11 Dec 2013 | 9 | 55 | 2.05 | –815 | 274.5°/47.1° –77.3° | 76.2°/44.4° –103.3° | –39.5 | –14.4 | 46.1 | NO/IMPL |
| 31. | 14 Dec 2013 | 2 | 12 | 2.37 | –772 | 148.2°/73.2° 79° | 2.2°/20° 122.4° | 27.6 | 22.1 | 50.2 | RE |
| 32. | 21 Dec 2013 | 23 | 16 | 2.05 | –816 | 156.8°/53.1° 59.2° | 21.6°/46.6° 124.3° | 21 | 18.8 | 60.2 | RE |
| 33. | 4 Jan 2014 | 14 | 20 | 2.00 | –782 | 246.3°/67° –114.2° | 115.2°/32.9° –46° | –34.9 | –15.5 | 49.6 | NO/IMPL |

[1)]focus depth from the best fitting solution by the FOCI software, [2)]nodal plane parameters: ΦA, ΦB – azimuth of nodal planes A, B; $\delta$A, $\delta$B – dip of nodal planes A, B; $\lambda$A, $\lambda$B – rake angle correlated with nodal planes A, B.

criteria, occur too. If the normal slip mechanism dominates the implosion, such a mechanism is classified as NO/IMPL; otherwise, the focal mechanism is classified as IMPL/NO.

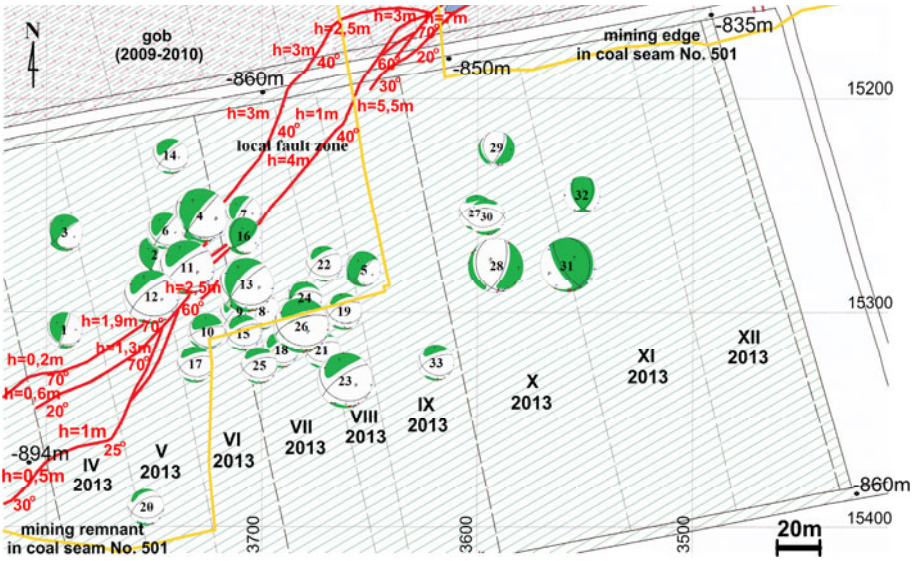


Fig. 3. Location of epicentres and focal mechanisms of analyzed high energy tremors on the coal seam No. 510 map.

Solutions of focal mechanism of all analyzed tremors are graphically presented in Fig. 3 with the use of focal spheres. The equal-area projection (Schmidt's projection) on the lower hemisphere was used. In each sphere the green area represents tension, and the white area – compression. Inside every focal sphere the ordinal number of tremor is included. Small-sized spheres represent tremors with energy of the order of $10^5$ J (magnitude $1.68 \leq M_L < 2.21$). Large-sized spheres represent tremors with energy of the order of $10^6$ J ($2.21 \leq M_L < 2.74$).

In focal mechanisms of near 45.5% of tremors (15 cases) shear mechanism predominated (tremors Nos. 1-6, 10, 11, 14, 16, 26, 28, 29, 31, 32). The DC component achieved maximally 89.3% (mean 59.4%). Participation of other components was lower: the isotropic component varied from 4.7 to 32.1% (mean 21.8%), and the CLVD component ranged from 1.8 to 40.7% (mean 18.8%).

The normal slip mechanism occurred in 60% of tremors' foci with shear component domination (9 cases). An azimuth of one of the nodal planes in 78% of foci with normal slip mechanism ranged from 217.8° to 254° (mean 232.8°), and a dip angle ranged from 67°NW to 87.8°NW (mean 79.3°NW), which is clearly correlated with the local fault zone parameters (Fig. 3). In the foci of tremors Nos. 28 and 29 an azimuth of one of nodal planes equaled 159.6° and 158.5°, which was quasi parallel to the face position of the

longwall. A dip angle of these nodal planes was 31°W and 29.3°W. These tremors occurred after longwall had left the local fault zone (Fig. 3). Displacement of rock mass in these foci was most probably in the direction of gob and local fault zone. The best solutions of seismic moment tensor inversion were achieved for depths of –720 and –703 m, which clearly corresponds to cracking of thick layer of sandstone above the coal seam.

The reverse slip mechanism occurred in 40% of foci with shear component domination (6 cases, including tremor No. 5). An azimuth of one of nodal planes in these foci ranged from 116.8° to 175.5° (mean 147°), which was quasi parallel to the position of longwall face. Dip angles of these nodal planes for the four tremors (Nos. 1, 2, 5, 16) ranged from 17.5°E to 32.2°E (mean 25.5°E), which indicates shallow (near horizontal) reverse thrust faulting in roof-rocks. In foci of tremors Nos. 31 and 32 (Fig. 3), which occurred when the longwall has almost finished, the reverse slip mechanism also occurred, but dip angles of the above-mentioned nodal planes were larger, amounting to 73.2°E and 53.1°E, respectively. The reverse slip mechanism occurs when the horizontal compressive stresses and the vertical tensile stresses dominate together. At a large depth, compressive stresses in rock mass occur naturally. The level of compressive stress is particularly high near the longwall face. Probably rock mass destruction in the area of the local fault zone and large subsidence caused deflection of the layers of tough rocks (sandstones) deposited above, in which the additional vertical tensile stresses appeared. These conditions were responsible for reverse slip mechanism in foci of tremors Nos. 1, 2, 5, 16, 31, and 32.

In foci of nearly 33.3% of tremors – 11 cases (tremors Nos. 7, 9, 12, 13, 15, 17, 18, 23, 25, 30, 33) − the participation of shear component was insignificantly higher than implosion (near 6.2% on average). CLVD component had a lower share (mean 22.6%). Taking into account only the DC component, occurrence of these tremors corresponded with the local fault zone. In these foci the normal slip mechanism occurred (Fig. 3). An azimuth of one of nodal planes ranged from 212.4° to 274.5° (mean 238.7°), and a dip angle ranged from 47.1°NW to 81.6°NW (mean 68.3°NW), which is connected with local fault zone parameters. Participation of implosion was important too. Because of weak roof, the caving process took place largely.

In foci of nearly 21.2% of tremors – 7 cases (tremors Nos. 8, 19-22, 24, 27) − an implosion dominated (Fig. 3). In 6 cases this domination was clear (share of implosion was higher than 40%). In focal mechanism of tremor No. 24 the share of implosion equaled 35%. In full seismic moment tensor solution the I component equaled, on average, 41%, and the CLVD and DC components were 32 and 27% on average, respectively. Taking into account only the DC component, the considered tremors were in some way correlated with local fault zone. An azimuth of one of nodal planes ranged from

223.8° to 256.6° (mean 242.3°), and a dip angle ranged from 54.6°NW to 67.3°NW (mean 59.9°NW), which is well correlated with local fault zone parameters. However, the collapse of weak roof rocks in the area of the local fault zone was the main factor responsible for these tremors occurrence. Stress level coming from mining remnant of coal seam No. 501 was probably also of importance.

## 6. DISCUSSION AND SUMMARY

Focal mechanisms of 33 high energy mine tremors (with magnitudes between 1.84 and 2.58), recorded by mine seismic network during longwall mining of coal seam No. 510 in one of the USCB coal mines, have been determined. Determination of focal mechanism supported the information about factors responsible for the occurrence of analyzed tremors.

Among geological and mining factors, an activation of local fault zone contributed to the highest degree to high energy tremors occurrence. In the source mechanism of analyzed mine tremors, the shear component clearly or insignificantly predominated. The roof rocks' weakening in the neighborhood of local fault zone was significant too. The collapse of roof rocks was reflected in great share of implosion in the full solution of seismic moment tensor. In some foci, an implosion even predominated. Taking into account only the DC part of full solution of seismic moment tensor of the abovementioned tremors, the calculated nodal plane parameters: azimuth (mean 238°) and dip (mean 69°NW) corresponded to the parameters of local fault zone. In the area where foci of analyzed tremors were concentrated, faults forming the local fault zone had strikes from 210° to 240° (calculated in the same way as the nodal plane azimuth) and dips between 60°SE and 70°SE. A difference between the calculated azimuth and dip of nodal planes and average strike and dip of faults forming the local fault zone were 15° and 9° on average, respectively. Some tremors occurred due to cracking of a thick layer of sandstone (normal or reverse slip mechanism).

Occurrence of high-energy tremors was clearly correlated with the local fault zone. This zone was a factor influencing on the level of rockburst hazard during mining of coal seam No. 510 with selected longwall.

Knowing the reason of the occurrence of high energy tremors, appropriate preventive measures were applied for improving the safety of mining. A restriction of crew movement was applied and a lining of galleries was reinforced. Some blastings in coal seam No. 510 were performed to minimize the risk of coal bump, which might be initiated by high energy tremors.

The results obtained will be helpful during planning of further longwall mining in the assigned underground coal mine. On this basis, rockburst prevention methods and parameters of longwall lining will be established.

## References

Aki, K., and P.G. Richards (1980), *Quantitative Seismology – Theory and Methods*, Vols. 1, 2, W.H. Freeman & Co., San Francisco.

Gibowicz, S.J. (1995), Mechanism of tremor foci, mining tremors – mechanism, location and energy. **In:** *Proc. School of Underground Mining, 27 February – 3 March 1995, Szczyrk, Poland*, 5-30 (in Polish).

Gibowicz, S.J., and A. Kijko (1994), *An Introduction to Mining Seismology*, Academic Press, San Diego.

Knopik, M., W.M. Zuberek, and Ł. Wojtecki (2015), Multisources of high-energy mine tremors occuring during longwall mining of coal seam in varied geological and mining conditions, *Prz. Górn*. **12**, 12-19 (in Polish).

Kołodziejczyk, P. (2009), Optimization of the seismic network in Kompania Węglowa S.A., Tech. Report, SITG, Gliwice (in Polish, unpublished).

Kwiatek, G. (2009), Foci-seismic moment tensor – spectral parameters: A description of the program, available from: http://induced.pl/foci.

Marcak, H., and W.M. Zuberek (1994), *Mining Geophysics*, Śląskie Wydawnictwo Techniczne, Katowice (in Polish).

Stec, K. (2009), The focal mechanism and the methods of its calculation. **In:** *Workshop of the "Natural Hazards in the Mining Industry", 17-19 June 2009, Bogatynia-Świeradów Zdrój, Poland*, 287-305 (in Polish).

Stec, K., and Ł. Wojtecki (2011), Characteristics of the mine tremor source mechanism associated with the mining in the seam 510, the longwall 502 in the "Bielszowice" Coal Mine, *Res. Rep. Centr. Min. Inst.: Min. Environ.* **1**, 61-77 (in Polish).

Received 13 November 2014
Received in revised form 6 August 2015
Accepted 18 August 2015

DE GRUYTER OPEN

**Acta Geophysica**
vol. 64, no. 4, Aug. 2016, pp. 1176-1192
DOI: 10.1515/acgeo-2016-0030

# Influence of Elevation Data Source on 2D Hydraulic Modelling

Krzysztof BAKUŁA, Mateusz STĘPNIK, and Zdzisław KURCZYŃSKI

Warsaw University of Technology,
Faculty of Geodesy and Cartography, Warsaw, Poland;
e-mails: k.bakula@gik.pw.edu.pl (corresponding author),
matstepnik@gmail.com, kurczynski@wp.pl

A b s t r a c t

The aim of this paper is to analyse the influence of the source of various elevation data on hydraulic modelling in open channels. In the research, digital terrain models from different datasets were evaluated and used in two-dimensional hydraulic models. The following aerial and satellite elevation data were used to create the representation of terrain – digital terrain model: airborne laser scanning, image matching, elevation data collected in the LPIS, EuroDEM, and ASTER GDEM. From the results of five 2D hydrodynamic models with different input elevation data, the maximum depth and flow velocity of water were derived and compared with the results of the most accurate ALS data. For such an analysis a statistical evaluation and differences between hydraulic modelling results were prepared. The presented research proved the importance of the quality of elevation data in hydraulic modelling and showed that only ALS and photogrammetric data can be the most reliable elevation data source in accurate 2D hydraulic modelling.

**Key words:** digital terrain model (DTM), hydraulic modelling, LIDAR, aerial photogrammetry, satellite imagery.

Ownership: Institute of Geophysics, Polish Academy of Sciences;
© 2016 Bakuła *et al.* This is an open access article distributed under the Creative Commons Attribution-NonCommercial-NoDerivs license,
http://creativecommons.org/licenses/by-nc-nd/3.0/.

## 1. INTRODUCTION

To enable the accurate hydraulic modelling of inundation areas, a detailed and accurate digital terrain model of a watercourse (DTM-W) is required. It is the main input to numerical hydrodynamic modelling (not concerning flow resistance – the impact of the roughness), especially if two-dimensional (2D) modelling is considered. DTM-W is a digital terrain model (DTM) that describes the potential inundation area of a river, including the effects of the river bed and buildings hindering the run-off (Mandlburger and Brockmann 2001). According to a document prepared by a group of experts working in the European Exchange Circle on Flood Mapping (Martini and Loat 2007), the appropriate selection of elevation data source has a significant impact. The vertical accuracy of DTM should be better than 0.5 m (root mean square error – RMSE). Among the possible methods and tools providing DTM for large areas the following may be mentioned: airborne laser scanning, satellite and aerial radar systems, aerial digital images, high-resolution satellite images and DTM obtained from vectorization of contour lines from topographic maps on a scale of 1:10 000 and contour interval of less than 0.5 m for flat areas.

In the literature, some experiments using various elevation sources in hydraulic modelling have been described (Casas *et al.* 2006, Cheveresan 2012). There are studies concerning smaller areas where the most accurate elevation data from airborne laser scanning were utilized in hydraulic modelling (French 2003, Mandlburger *et al*. 2009, Sole *et al.* 2008). This technique replaced photogrammetric methods of 3D data collection, which had been applied before the development of airborne laser scanning in the most accurate hydraulic analyses (Lane *et al.* 2002). For studies concerning large areas or areas sparsely covered with data, the examples of satellite elevation data, *i.e.*, radar interferometry (Farr *et al.* 2007, Yamazaki *et al*. 2012, Wang *et al.* 2012), methods based on satellite stereo pairs providing global DTM (Rauter *et al.* 2009, Wang *et al.* 2012, Gichamo *et al.* 2012) or DTM created from contour lines vectorized from topographic maps at different scales (Casas *et al.* 2006, Cheveresan 2012) can be used. However, there are few studies comparing the available elevation data sources and their impact on the results of hydraulic modelling in the analysis of the same area. This paper presents a variety of height data used in two-dimensional flood wave propagation and assesses such influences.

## 2. REMOTE SENSING ELEVATION DATA FOR HYDRAULIC MODELLING

The digital terrain model is a numerical representation of terrain relief and it is applied as a boundary condition in 2D hydraulic modelling. The term was

first used was by Miller and Laflamme (1958), and since then it was called by different names: digital elevation model (DEM), digital ground model (DGM), digital height model (DHM), and digital terrain elevation model (DTEM), which were associated with the nomenclature of experts from various fields of science and from different countries. In practice, despite their frequent usage as synonyms, their meaning is not the same (Li *et al.* 2005, Höhle and Potuckova 2011). Remote sensing elevation data sources can be divided into two groups: airborne and satellite data. Another classification related to the method of data acquisition distinguishes between active (*i.e.*, laser scanning, radar interferometry) and passive (stereophotogrammetry) techniques.

### 2.1 Airborne data

At present, airborne laser scanning (ALS), also commonly called Light Detection and Ranging (LIDAR), is the most accurate remote sensing method of 3D data acquisition for terrain and its coverage. The principle of this method is a time-of-flight measurement of an outgoing laser pulse interacting with (multiple) targets within the laser beam (Wehr and Lohr 1999), which provide point clouds with specified X, Y, Z coordinates of thousands of points belonging to the surface of a terrain and objects on it (Kurczyński 2006). As a result of laser scanning, quasi-continuous spatial representation of terrain with a height accuracy of a few centimetres is provided. For instance, during the implementation of the EU Flood Directive (Directive 2007) in Poland, DTM based on the ALS technique had a resolution of 1 m and vertical accuracy of at least RMSE = 0.15 m for uncovered, paved surfaces, and at least RMSE = 0.30 m for forested areas (Kurczyński and Bakuła 2013).

The other technology that allows for highly accurate digital elevation model generation is automatic image matching, which also provides point clouds. Photogrammetric technology has a tradition of over 100 years in aerial image application for cartography. Current techniques of image acquisition with large-format digital cameras provide high-resolution data at a pixel resolution lower than 10 cm. These images offer a great opportunity for image matching applications to replace stereo measurements. In recent years, algorithms of this technique have been significantly developed from area-based matching (ABM) and feature-based matching (FBM) methods to specialized algorithms of dense image matching providing point clouds comparable with ALS data (Hirschmüller 2008, Rothermel and Haala 2011). The disadvantage of this technique is the lack of penetration through vegetation, which means that DTM obtained with photogrammetric technology has low-

er accuracy in forested areas and must be integrated with manual stereoscopic measurements or other surveying data.

In Poland, in national or regional repositories, digital terrain models have been prepaired. They were obtained by photogrammetric technology within the Land Parcel Identification System (LPIS). The direct objective of their creation was orthorectification of aerial images needed to produce orthophotomaps for system purposes, as well as to supply a topographic database at a scale of 1:10 000. The basic source of these elevation data was stereoscopic measurements from aerial images (analogue at a scale of 1:13 000 or digital with ground sampling distance GSD = 0.25 m) with interior (parameters of camera) and exterior orientation (location and orientation of each image) defined in a bundle adjustment process. In cases of difficult land cover mostly related to vegetation, both types of measurement were allowed: manual (photogrammetric spatial resection) and automatic (image matching). The vertical accuracy of such a product is much lower due to the objectives of their generation. The approximate error for this DTM was estimated at below 0.6 m for flat and uncovered areas.

In the second half of the twentieth century, aerial photographs and stereoscopic observations in analogue technology became the elevation data source for topographic map generation. Vectorization of contours from these maps allowed for DTM creation, which is sufficient for a regional approximated representation of terrain topography. An example of such a model is EuroDEM – European DTM generated with a large share of contour lines from topographic maps on a scale of 1:100 000. The vertical accuracy of EuroDEM is about 8-10 m (Hovenbitzer 2008); however, in Poland, maps on a scale of 1:50 000 were adopted and so the accuracy of EuroDEM can be estimated at about 3-4 m.

### 2.2 Satellite data

Among the elevation data used to create global satellite elevation models, radar interferometry should be primarily indicated. The example of application of this technique is the space Shuttle Radar Topography Mission (SRTM) (Rabus *et al.* 2003). This global DTM covers 80% of land surface in two standards: SRTM-1 (resolution of 1 arcsec – approx. $30 \times 20$ m) and SRTM-3 (3 arcsec – approx. $90 \times 60$ m). Radar interferometry is still dynamically developed, which can be observed in the German satellite missions of TerraSAR-X and TanDEM-X (Krieger *et al.* 2007).

Another source of DTM is image matching of stereo images. Such high-resolution images are captured by satellite sensors, which are able to change the angle of deflection and consequently register the same area from different locations (oblique imageries) – especially in the case of a single satellite

transition (from one orbit). One of the first proposed DTMs generated with this technology was an ITM-1 (IKONOS Terrain Model-1) derived on request in two standards: ITM-5c w (resolution of 1 arcsec) and ITM-5e (0.2 arcsec). At present, most satellites that register optical imageries are equipped with this measurement solution.

In recent years, another global terrain model has been developed. The ASTER Global Digital Elevation Model (ASTER GDEM) (Jacobsen and Passini 2010) was generated with more than one million stereo-pairs of images collected by the Japanese Advanced Spaceborne Thermal Emission Reflection Radiometer (ASTER). The model covers 99% of the land surface. Its spatial resolution is 1 arcsec and it has a declared vertical accuracy better than 20 m. It is worth mentioning that satellite elevation data are strongly dependent upon the terrain morphology and land coverage, and the fact that they can be affected by systematic and random errors, so homogenous accuracy cannot be expected from this data source (Jacobsen and Passini 2010).

### 2.3 Test area and data used in the experiment

The test area is a part of the Połaniec Basin limited to two sections (M-34-55-A-d-4 and M-34-55-C-b-2) of the topographic map on a scale of 1:10 000 covering about 40 $km^2$ (Fig. 1a). The research area is located in Rytwiany municipality, part of Staszów district in Świętokrzyskie Voivodeship. The river flowing through this area is the Czarna Staszowska. Figure 1 presents all elevation data used in the experiment. As the most accurate elevation data, an airborne laser scanning point cloud from 2012 with an average density of four points per square metre was used to generate the most accurate DTM at a 1 m resolution (Fig. 1b). The second data source was archival analogue aerial images obtained by a photogrammetric large-format camera in 2009 on a scale of 1:13 000 (scanned with the resolution of 14 μm, GSD = 0.19 m). They were used to create DTM at a 3 m resolution (Fig. 1c) using dense image matching techniques supplemented by stereoscopic measurements in forested areas. The third data source was DTM from the LPIS system (Fig. 1d), which has already been prepared and archived in a national repository, with a 10 m spatial resolution. The fourth was a part of EuroDEM (Fig. 1e) in a 2 arcsec (approx. 60 × 40 m) grid created from the vectorization of contours from topographic maps on a scale of 1:50 000. Lastly, the fifth data source was a part of ASTER GDEM (Fig. 1f) at a 30 m resolution whose systematic vertical error was eliminated.

A preliminary analysis of the vertical accuracy of the data was associated with a comparison of heights interpolated from DTMs from different sources with respect to 150 points measured with GNSS observations in an area not covered by high vegetation. The results of this analysis are given in Table 1.

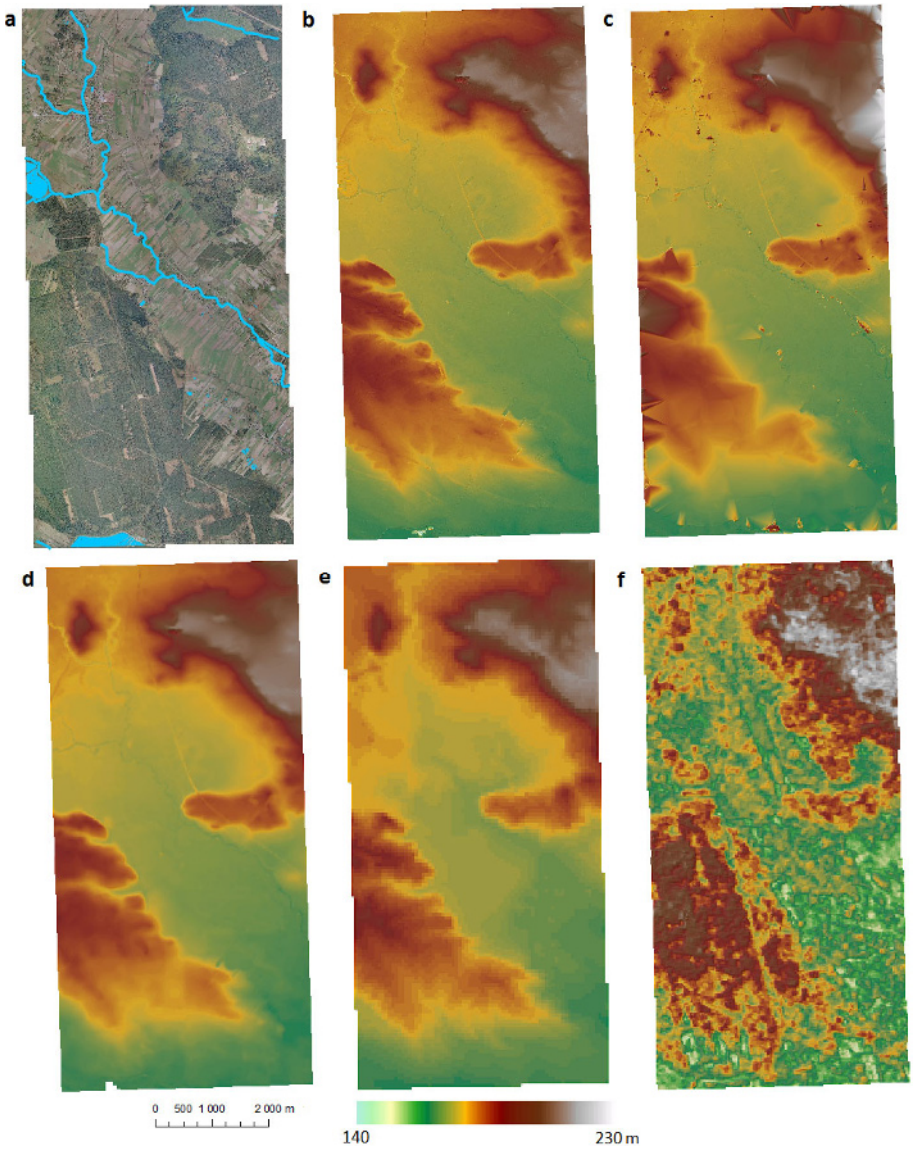


Fig. 1. Test study and data used in research: orthophoto with Czarna Staszowska River highlighted in blue (a); and digital terrain models from various source data: ALS (b), photogrammetry (c), LPIS DTM (d), EuroDEM (e), ASTER GDEM (f).

They confirm the high accuracy of the ALS data related primarily to the robustness to errors associated with low vegetation occurrence, however, a small systematic error (offset) can be noticed, which can be caused by the

Table 1

Analysis of vertical accuracy of different DTM sources on the basis of GNSS measurements

| Parameter | ALS DTM [m] | PHOTO DTM [m] | LPIS DTM [m] | EuroDEM [m] | ASTER GDEM [m] |
|---|---|---|---|---|---|
| Mean | 0.051 | –0.110 | –0.316 | 1.334 | 0.268 |
| Max | 0.546 | 2.307 | 2.510 | 7.077 | 10.976 |
| Min | –0.312 | –2.114 | –2.360 | –1.695 | –10.221 |
| RMSE | 0.171 | 0.624 | 0.950 | 2.686 | 5.081 |
| STD | 0.163 | 0.614 | 0.895 | 2.329 | 5.074 |
| Number of points | 149 | 149 | 161 | 161 | 162 |

accuracy of georeferencing or incomplete penetration of vegetation by the laser beam (RMSE was slightly higher than the tolerance in the Polish program of countrywide laser scanning). The comparative analysis presented in Table 1 shows that the DTM generated from the available aerial images is 2.5-3 times less accurate than the DTM from ALS in uncovered areas in this case. In forested areas a much lower accuracy should be expected. The vertical accuracy of the DTM from LPIS is four times worse than the ALS-based model. The lowest accuracy (few metres) was noticed for EuroDEM and ASTER GDEM. Additionally, the three last models do not reflect characteristic terrain forms (*i.e.*, embankments), which has an important impact on the results of hydraulic modelling.

## 3. METHODOLOGY OF THE RESEARCH

The research methodology consisted of a series of actions related to the preparation and processing of hydraulic modelling using different elevation data and the development of methods for the assessment of the results.

### 3.1 Hydrodynamic model description

The hydrodynamic model of the Czarna Staszowska River was performed using MIKE software by DHI (http://www.mikepoweredbydhi.com/). The module of MIKE FLOOD was used, which allowed for the combination of 1D and 2D hydraulic models with lateral connections. The hydrodynamic model of the watercourse was made in MIKE 11 (module for one-dimensional flow modelling) using hydrological data, cross-sections and observations of engineering structures (bridges, dams). The floodplain models were prepared in MIKE 21 (module for two-dimensional flow modelling) where the digital terrain model (DTM) and digital roughness model (DRM)

were input data. DRM was created on the basis of the Database of Topographic Objects (Baza Danych Obiektów Topograficznych – BDOT) at a scale of 1:10 000 (BDOT is the official topographic database in Poland, stored in the Main Geodetic and Cartographic Documentation Centre). The boundary conditions in the hydraulic model were developed for a water flow of Q1% – 100 years' discharge (discharge with the exceedance probability $p$ = 1%, once per 100 years). The model was calibrated and validated based on the historical observations of water levels and discharges at the Staszów and Połaniec gauging stations located upstream and downstream of the reach where the two-dimensional modelling was implemented. All hydrological data for each variant were identical and spatial resolution of models was resampled to 5 m to unify the results of hydraulic modelling. Resampling of ALS-based DTM decreases its resolution (and consequently accuracy), but significantly accelerates the speed of hydraulic calculations, which was justified by studies on quantitative data reduction conducted by Bakuła (2011). For such lowland areas, DTM downgrading to 5 m is associated with a loss of accuracy of only a few centimetres.

### 3.2 Methods of results evaluation

To analyse the results of hydraulic modelling, a coefficient similar to that used in the assessment of the automatic feature extraction from satellite images (Lee *et al.* 2003) was adopted. The following cases in the evaluation of the results were considered: true positive (Eq. 1), true negative (Eq. 2), false positive (Eq. 3), false negative (Eq. 4), which can be written in algebra as:

$$TP = \left| X \cap R \right| , \tag{1}$$

$$TN = \left| U \setminus (X \cap R) \right| , \tag{2}$$

$$FP = \left| X \setminus R \right| , \tag{3}$$

$$FN = \left| R \setminus X \right| , \tag{4}$$

where $R$ is a reference set, $X$ is a tested set, $U$ is a space.

In this experiment related to hydraulic modelling, the above-mentioned features represent: $TP$ – inundated areas in both sets $R$ and $X$ (pixel-wised), $TN$ – not inundated areas in both sets $R$ and $X$, $FP$ – not inundated areas in $R$ and inundated in $X$, $FN$ – inundated areas in $R$ and not inundated in $X$. In this paper, the results of hydraulic modelling based on DTM from ALS data were used as a reference. Based on these features, correctness – $CR$ (Eq. 5) and completeness – $CP$ (Eq. 6) indexes can be calculated to compare the results:

$$CR = \frac{TP}{TP + FP}\,, \tag{5}$$

$$CP = \frac{TP}{TP + FN}\,. \tag{6}$$

Correctness *CR* indicates how many flooded areas, defined by test data set, would be also flooded in the simulation using the most accurate reference data. Completeness *CP* indicates how many flooded areas defined by the reference data were also identified as flooded by test dataset. For an overall assessment of similarity between two datasets, quality coefficient *Q* can be used (Eq. 7):

$$Q = \frac{TP}{TP + FP + FN}\,. \tag{7}$$

In the literature, such an index is used for the comparison of two inundation areas (Sole *et al.* 2008, Yamazaki *et al.* 2012). It is also known as Jaccard's similarity index. All index values range from 0 to 1, where values closer to 1 are desired. For the *Q* index, a value of 0 represents completely different areas and a value of 1 represents perfect agreement. This factor can also be defined as the ratio of the cardinality of dataset intersection and the cardinality of datasets union as follows:

$$Q = \frac{|X \cap R|}{|X \cup R|}\,, \tag{8}$$

where *R* is a reference set, *X* is a tested set, and $|X|$ is a cardinality of *X* set.

The second method of result evaluation was the calculation of differences in maximum water depth and maximum flow velocity provided by a comparison of rasters from reference and analysed results of hydraulic modelling. For this analysis statistical parameters were also calculated.

## 4. RESULTS

The results of hydraulic modelling, classified by water depth, are shown in Fig. 2. Each inundation class is visualized here with a shaded terrain model in the background corresponding to the relevant data source. In addition, the result of hydraulic modelling with ALS data (reference inundation area) is marked in each case. A visual interpretation of the results shows a similarity of an analysis conducted using airborne data (Fig. 2a-c). In Fig. 2b a TIN (triangular irregular network) structure is clearly visible, which is caused by a low density of points for forested areas where only stereoscopic measurements could be carried out. EuroDEM, which has a lower spatial resolution (Fig. 2d), represents some differences in terms of reference data (ALS). The part of ASTER GDEM (Fig. 2e) exposes the presence of random vertical

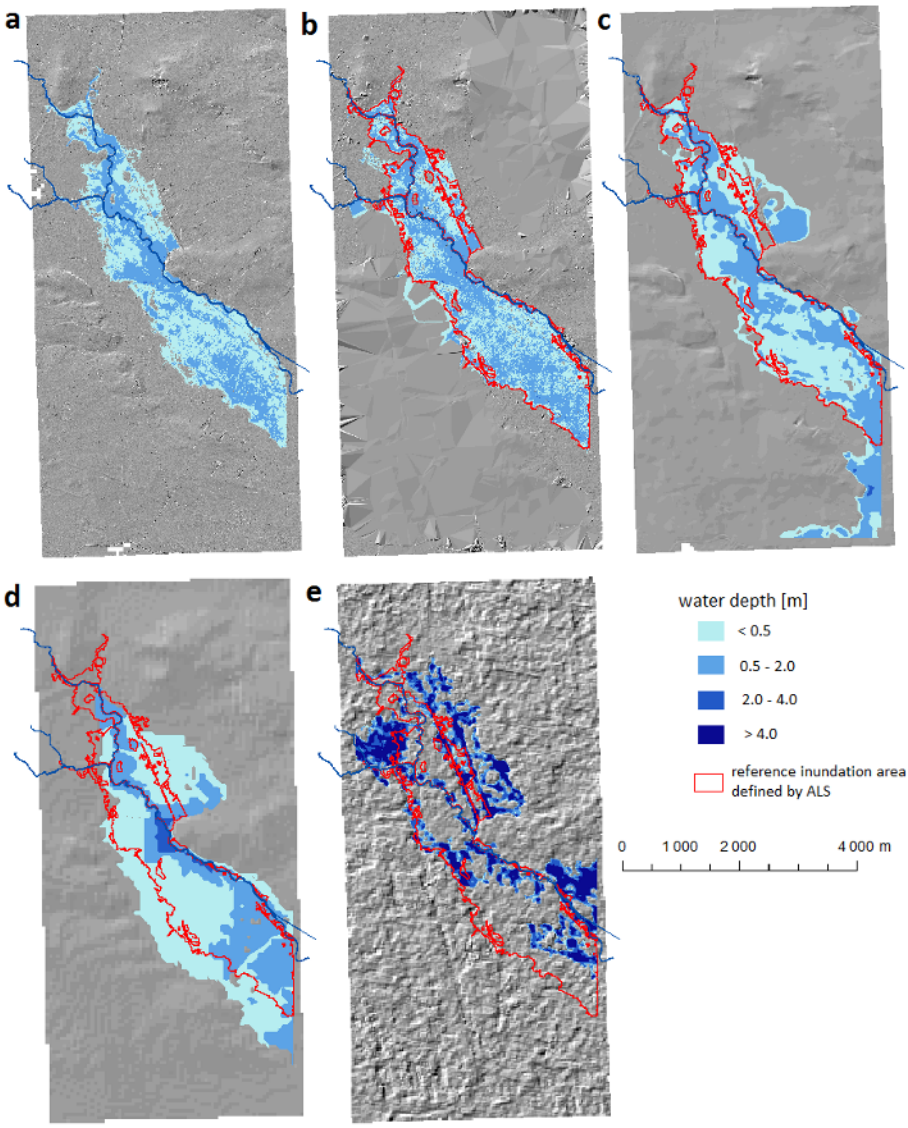


Fig. 2. Results of 2D hydraulic modelling of Czarna Staszowska River using various DTM sources: ALS – reference data (a), matching of aerial images (b), DTM from LPIS (c), EuroDEM (d), and ASTER GDEM (e).

errors in DTM, which significantly influenced the results of hydraulic modelling.

Table 2 shows the values of the following indexes: correctness, completeness, and quality for rasters of inundation zone calculated with different

elevation data in hydraulic modelling. They were calculated on the basis of the shape of flooded areas. Analysis of this table leads to similar conclusions as the visual assessment. All photogrammetric data indicators determine the maximum level of floodwater and flow velocity of the wave in a similar way (quality, completeness, and correctness indexes are above 0.8). It is worth noting that the high rate of *CP* index for EuroDEM and LPIS elevation data can be relevant for the determination of flood hazards. The high rate of the *CP* index provides information that the inundation area, designated by the analysed data source, is also identified by reference data as potentially threatened. The results from Table 2 also prove a significant decrease in similarity in analysis using data at a lower spatial resolution – EuroDEM and ASTER GDEM.

Table 2

Similarity indexes in the analysis of hydraulic modelling using various elevation data sources in comparison to the results of ALS data application

| Raster | DTM PHOTO | | | DTM LPIS | | | EuroDEM | | | ASTER GDEM | | |
|---|---|---|---|---|---|---|---|---|---|---|---|---|
| | *CR* | *CP* | *Q* | *CR* | *CP* | *Q* | *CR* | *CP* | *Q* | *CR* | *CP* | *Q* |
| Indexes value for inundation area quality assessment | 0.88 | 0.95 | 0.84 | 0.72 | 0.94 | 0.69 | 0.59 | 0.89 | 0.55 | 0.43 | 0.32 | 0.23 |

Table 3

Overall comparison of maximum water depth and flow velocity in comparison to the results of ALS data application

| Parameter | Maximum water depth [m] | | | | Maximum flow velocity [m/s] | | | |
|---|---|---|---|---|---|---|---|---|
| | DTM PHOTO | DTM LPIS | Euro DEM | ASTER GDEM | DTM PHOTO | DTM LPIS | Euro DEM | ASTER GDEM |
| Mean | 0.07 | 0.01 | 0.14 | 2.99 | –0.01 | 0.01 | –0.04 | –0.08 |
| Median | 0.03 | –0.01 | 0.03 | 2.44 | –0.01 | 0.00 | –0.06 | –0.12 |
| STD | 0.40 | 0.30 | 0.54 | 2.63 | 0.08 | 0.11 | 0.20 | 0.31 |
| MAD | 0.16 | 0.22 | 0.50 | 2.52 | 0.06 | 0.09 | 0.18 | 0.20 |
| RMSE | 0.40 | 0.30 | 0.55 | 3.98 | 0.08 | 0.11 | 0.20 | 0.32 |

In Table 3, a comparison of the raster presenting maximum water depth and velocity of a flood wave in 2D hydraulic modelling is shown with respect to a model based on ALS data. In this analysis, the mean value, median value, standard deviation (STD), median absolute deviation (MAD), and root mean square error (RMSE) were calculated. Based on these results, it was

noticed that photogrammetric data sources provide the most similar effect to LIDAR data in the inundation area and flow velocity prediction. The RMSE for maximum water depth was 0.4 m in the case of aerial images and 0.3 m for archived DTM at a slightly lower resolution (LPIS). A difference between MAD and STD for maximum water depth of photogrammetric DTM (PHOTO) could be a result of the appearance of inundated areas in forests, where the accuracy of DTM was much lower due to sparse stereo measurements. Differences in flow velocity reached 0.08 and 0.11 m/s, respectively. In the considered analysis, very large differences were noticed for DTM from the ASTER satellite.

## 5. DISCUSSION

European good practice on flood mapping described in the EXCIMAP handbook (Martini and Loat 2007) provides only general guidelines for elevation data sources, whereas our investigation and conclusions from other publications point to the significant impact of elevation data on the results of hydraulic modelling (Casas *et al.* 2006).

The comparative analysis of flood wave propagation proved that the strongest similarity to the inundation area, defined by the most accurate elevation data (ALS), could be reached by using photogrammetric DTMs. This source has huge potential, considering the present images of GSD below 10 cm acquired by large-format, digital and metric cameras. The development of dense image matching algorithms (Rothermel and Haala 2011) also allows for the creation of elevation models that are competitive to LIDAR data. Nevertheless, the limitation of this technique is a lack of reliable representation of terrain shape in areas covered with vegetation.

Considering DTM from LPIS, the results of hydraulic modelling with its usage do not differ significantly from those associated with image matching. It is worth considering whether this data source could be acceptable in precision 2D hydraulic modelling, because it correctly indicated flood inundation areas (very high index of completeness) in the current research.

The results of hydraulic modelling, based on the DTM obtained by digitations of contours from topographic maps on a scale of 1:50 000, did not provide the correct results. This elevation source represents too low a level of accuracy related to a medium scale of map and large contour intervals. On the other hand, the use of larger scale maps, whose contours are defined on the basis of accurate remote sensing or surveying measurements, can lead to achieving better results in hydraulic modelling using this data source, which was also noted by Casas *et al*. (2006).

The possibilities of satellite systems elevation data collection are constantly increasing. However, it is very difficult to avoid systematic and ran-

dom vertical errors, *i.e.*, noise (Jacobsen and Passini 2010), which was particularly visible in our analyses, affecting the accuracy of DTM and preventing raw data usage, and errors related to vegetation and buildings that can impede water flow along river networks (Lehner *et al.* 2008). Data from the satellite systems do not include the terrain height in the riverbed or small structures such as narrow channels connecting the main river and floodplains (Wilson *et al.* 2007). These are reasons why many studies depicting examples of the use of satellite data are more often focused on the elimination of systematic and random errors based on data that represent better accuracy and higher resolution. The results of the present study regarding ASTER data do not recommend this data source in 2D hydraulic modelling, showing larger differences in the prediction of water levels and flooding area than in the research by Wang *et al*. (2012).

## 6. CONCLUSION

This study assessed the influence of an elevation data source of five DTMs (*i.e.*, airborne laser scanning; aerial images on a scale of 13 000; DTM from national repositories dedicated for orthogonalization of images, LPIS; EuroDEM created from topographic maps on a scale of 1:50 000; and ASTER GDEM). Such a validation was carried out using a GNSS evaluation of the vertical accuracy of the datasets and practical research related to hydraulic modelling with the same conditions and parameters for all data series. The following major conclusions can be drawn:

- The geometry of a terrain, described in DTM, is the most influential parameter in hydraulic modelling, and the change of such a data source can affect its results.
- Data from airborne laser scanning have the highest vertical accuracy of the analysed data sources – ALS represents the shape of terrain in the most detailed manner, and its use in 2D hydraulic modelling is nowadays common, but owing to the issue of redundancy and voluminous datasets it should be dedicated to high precision analysis in relatively small areas.
- Photogrammetric data can ensure accuracy quite similar to airborne laser scanning in hydraulic modelling analyses. The only limitation of this technique is in the occurrence of large forested areas where the results of hydraulic modelling may vary due to the problem of the lack of accurate elevation data from this source.
- Data from DTMs archived in national repositories for aerial image orthorectification or included in topographical databases on a scale of 1:10 000, represented by DTM from the LPIS system, do not provide very high accuracy in hydraulic modelling because of their low (10-20 m) spatial

resolution; however, their use can be justified by the absence of more accurate data or integration with a large number of ground-based measurements.

- EuroDEM application in accurate 2D hydraulic modelling led to unsatisfactory results; topographic maps as a source of elevation data should be large-scale, and their contour interval should be small. Nowadays this cartographic elevation data source is seldom used, as highly accurate DTM is archived in national repositories.
- The poorest quality hydraulic modelling results were obtained using elevation data from ASTER GDEM; satellite data have a worse quality than DTMs from airborne sources, and their application in hydraulic modelling should be limited to the use of very large areas without requiring high precision. However, it can be justified in exceptional situations, for example where political affairs cause an inability to comply with airborne missions in border areas.
- The main criterion for assessing the impact of remote sensing elevation data sources on hydraulic modelling can be their spatial resolution, which has a significant influence on the accuracy of the DTM and, consequently, the result of hydraulic modelling.

Future research in elevation data acquisition for 3D modelling will undoubtedly be focused on the further use of LIDAR data in other geographic areas. The capabilities of constantly developing image matching algorithms will increase. There will also be higher quality and better resolution of aerial images in the development of high accuracy DTM, especially for uncovered areas. Airborne data will not be the only data source offering high accuracy and quality in the near future. The development of radar interferometry and image matching of satellite data, as well as the evolution of accuracy enhancement methods, will unquestionably improve the quality of elevation data from satellites, which will find their use in accurate 2D hydraulic modelling.

Acknowledgements. This research was financed by the Foundation for Polish Science – research grant no. VENTURES/2012-9/1 funded by the Innovative Economy program of the European Structural Funds. We would like to thank to Mr. Radosław Radoń from the Regional Water Management Board in Kraków for his indispensable help with hydraulic modelling.

## References

Bakuła, K. (2011), Reduction of DTM obtained from LiDAR data for flood modeling, *Arch. Photogram. Cartogr. Remote Sens*. **22**, 51-61.

Casas, A., G. Benito, V.R. Thorndycraft, and M. Rico (2006), The topographic data source of digital terrain models as a key element in the accuracy of hydraulic flood modelling, *Earth. Surf. Proc. Land*. **31**, 4, 444-456, DOI: 10.1002/esp.1278.

Cheveresan, B. (2012), Digital terrain model accuracy for flooded area delineation. **In:** *Proc. 5th Conf. Water Observation and Information System for Decision Support BALWOIS 2012, 27 May – 2 June 2012, Ohrid, Republic of Macedonia*.

Directive (2007), Directive 2007/60/EC of the European Parliament and of the Council of 23 October 2007 on the assessment and management of flood risks, *Offic. J. Europ. Union* **L288**, 27-34.

Farr, T.G., P.A. Rosen, E. Caro, R. Crippen, R. Duren, S. Hensley, M. Kobrick, M. Paller, E. Rodriguez, L. Roth, D. Seal, S. Shaffer, J. Shimada, J. Umland, M. Werner, M. Oskin, D. Burbank, and D. Alsdorf (2007), The Shuttle Radar Topography Mission, *Rev. Geophys*. **45**, 2, RG2004, DOI: 10.1029/2005RG000183.

French, J.R. (2003), Airborne LiDAR in support of geomorphological and hydraulic modelling, *Earth Surf. Proc. Land.* **28**, 3, 321-335, DOI: 10.1002/esp.484.

Gichamo, T.Z., I. Popescu, A. Jonoski, and D. Solomatine (2012), River cross-section extraction from the ASTER global DEM for flood modeling, *Environ. Modell. Softw*. **31**, 37-46, DOI: 10.1016/j.envsoft.2011.12.003.

Hirschmüller, H. (2008), Stereo processing by semiglobal matching and mutual information, *IEEE Trans. Patt. Anal. Mach. Intell*. **30**, 2, 328-341, DOI: 10.1109/TPAMI.2007.1166.

Höhle, J., and M. Potuckova (eds.) (2011), *Assessment of the Quality of Digital Terrain Models*, European Spatial Data Research, Official Publ. No. 60, EuroSDR.

Hovenbitzer, M. (2008), The European DEM (EuroDEM) – setup and harmonisation. **In:** *The International Archives of the Photogrammetry, Remote Sensing and Spatial Information Sciences, ISPRS Congress, Beijing, China*, Vol. 37, Part B4, 1853-1856.

Jacobsen, K., and R. Passini (2010), Analysis of ASTER GDEM elevation models. **In:** *The International Archives of the Photogrammetry, Remote Sensing and Spatial Information Sciences, ISPRS Congress, Calgary, Canada*, Vol. 38, Part 1.

Krieger, G., A. Moreira, H. Fiedler, I. Hajnsek, M. Werner, M. Younis, and M. Zink (2007), TanDEM-X: a satellite formation for high-resolution SAR interferometry, *IEEE Trans. Geosci. Remote Sens*. **45**, 11, 3317-3341, DOI: 10.1109/TGRS.2007.900693.

Kurczyński, Z. (2006), *Aerial and Satellite Imagery of Earth*, Warsaw University of Technology Publishing House, Warsaw (in Polish).

Kurczyński, Z., and K. Bakuła (2013), The selection of aerial laser scanning parameters for countrywide digital elevation model creation. **In:** *Proc. 13th SGEM GeoConference on Informatics, Geoinformatics and Remote Sensing, 16-22 June 2013*, Vol. 2, 695-702, DOI: 10.5593/SGEM2013/BB2.V2/S10.020.

Lane, S.N., R.J. Hardy, L. Elliott, and D.B. Ingham (2002), High-resolution numerical modelling of three-dimensional flows over complex river bed topography, *Hydrol. Process*. **16**, 11, 2261-2272, DOI: 10.1002/hyp.5034.

Lee, D.S., J. Shan, and J.S. Bethel (2003), Class-guided building extraction from IKONOS imagery, *Photogramm. Eng. Remote Sens*. **69**, 2, 143-150, DOI: 10.14358/PERS.69.2.143.

Lehner, B., K.Verdin, and A. Jarvis (2008), New global hydrography derived from spaceborne elevation data, *Eos Trans. Am. Geophys. Union* **89**, 10, 93-94, DOI: 10.1029/2008EO100001.

Li, Z.L., Q. Zhu, and C. Gold (2005), *Digital Terrain Modelling: Principles and Methodology*, CRC Press, Boca Raton.

Mandlburger, G., and H. Brockmann (2001), Modelling a watercourse DTM based on airborne laser-scanner data using the example of the River Oder along the German/Polish border. **In:** *Proc. OEEPE Workshop "Airborne Laser-scanning and Interferometric SAR for Detailed Digital Elevation Models", 1-3 March 2001, Stockholm, Sweden*, 111-120.

Mandlburger, G., C. Hauer, B. Höfle, H. Habersack, and N. Pfeifer (2009), Optimisation of LiDAR derived terrain models for river flow modelling, *Hydrol. Earth Syst. Sci.* **13**, 8, 1453-1466, DOI: 10.5194/hess-13-1453-2009.

Martini, F., and R. Loat (eds.) (2007), *Handbook on Good Practices for Flood Mapping in Europe*, European Exchange Circle on Flood Mapping (EXCIMAP), 57 pp.

Miller, C.L., and R.A. Laflamme (1958), The digital terrain model – theory and application, *Photogramm. Eng*. **24**, 433-442.

Rabus, B., M. Eineder, A. Roth, and R. Bamler (2003), The shuttle radar topography mission – a new class of digital elevation models acquired by spaceborne radar, *ISPRS J. Photogramm. Remote Sens*. **57**, 4, 241-262, DOI: 10.1016/S0924-2716(02)00124-7.

Rauter, H.I., A. Nelson, P. Strobl, W. Mehl, and A. Jarvis (2009), A first assessment of ASTER GDEM tiles for absolute accuracy, relative accuracy and terrain parameters. **In:** *Proc. IEEE Int. Geoscience and Remote Sensing Symp., 12-17 July 2009, Cape Town, South Africa*, Vol. 5, 240-243, DOI: 10.1109/IGARSS.2009.5417688.

Rothermel, M., and N. Haala (2011), Potential of dense matching for the generation of high quality digital elevation models. **In:** *The International Archives of the Photogrammetry, Remote Sensing and Spatial Information Sciences,*

*ISPRS Workshop, 14-17 June 2011, Hannover, Germany*, Vol. 38-4/W19, 271-276.

Sole, A., L. Giosa, L. Nolè, V. Medina, and A. Bateman (2008), Flood risk modelling with LiDAR technology, *WIT Trans. Ecol. Environ*. **118**, 27-36, DOI: 10.2495/FRIAR080031.

Wang, W., X. Yang, and T. Yao (2012), Evaluation of ASTER GDEM and SRTM and their suitability in hydraulic modelling of a glacial lake outburst flood in southeast Tibet, *Hydrol. Process.* **26**, 2, 213-225, DOI: 10.1002/hyp. 8127.

Wehr, A., and U. Lohr (1999), Airborne laser scanning – an introduction and overview, *ISPRS J. Photogramm. Remote Sens.* **54**, 2-3, 68-82, DOI: 10.1016/ S0924-2716(99)00011-8.

Wilson, M., P. Bates, D. Alsdorf, B. Forsberg, M. Horritt, J. Melack, F. Frappart, and J. Famiglietti (2007), Modeling large-scale inundation of Amazonian seasonally flooded wetlands, *Geophys. Res. Lett*. **34**, 15, L15404, DOI: 10.1029/2007GL030156.

Yamazaki, D., C.A. Baugh, P.D. Bates, S. Kanae, D.E. Alsdorf, and T. Oki (2012), Adjustment of a spaceborne DEM for use in floodplain hydrodynamic modeling, *J. Hydrol*. **436-437**, 81-91, DOI: 10.1016/j.jhydrol.2012.02.045.

Received 11 September 2014
Received in revised form 24 May 2015
Accepted 2 June 2015

DE GRUYTER OPEN

**Acta Geophysica**
vol. 64, no. 4, Aug. 2016, pp. 1193-1210
DOI: 10.1515/acgeo-2016-0034

# Correction of Hydrological and Oceanic Effects from GRACE Data by Combination of the Steric Sea Level, Altimetry Data and GLDAS Model

Farzam FATOLAZADEH, Behzad VOOSOGHI, and Mehdi RAOOFIAN NAEENI

Faculty of Geodesy and Geomatics Engineering,
K.N. Toosi University of Technology, Tehran, Iran;
e-mails: ffatollahzadeh@mail.kntu.ac.ir, vosoghi@kntu.ac.ir,
mraoofian@kntu.ac.ir (corresponding author)

A b s t r a c t

In this study, a scheme to estimate oceanic and hydrological effects in the GRACE (Gravity Recovery and Climate Experiment) data is presented. The aim is to reveal tectonic signals for the case of the Sumatra earthquake on 26 December 2004. The variations of hydrological and oceanic effects are estimated with the aid of data set of GRACE, altimetry, World Ocean Atlas, and the GLDAS model for a period of January 2003 to December 2006. The time series of computed gravity changes over Sumatra region show some correlations to the deformation resulting from the earthquake occurred in December 2004. The maximum and minimum impacts of hydrological and oceanic effects on gravity changes are about 3 μGal in radial direction and –5 μGal in northward direction. The maximum and minimum amounts of gravitational gradient changes after the correction are 0.2 and –0.25 mE, which indicates the significant influences of hydrological and oceanic sources on the desired signal.

**Key words:** hydrological and oceanic effects, GRACE data, World Ocean Atlas, GLDAS model, gravitational gradient changes.

Ownership: Institute of Geophysics, Polish Academy of Sciences;
© 2016 Fatolazadeh *et al.* This is an open access article distributed under the Creative Commons Attribution-NonCommercial-NoDerivs license,
http://creativecommons.org/licenses/by-nc-nd/3.0/.

## 1. INTRODUCTION

Satellite measurements of time-variable gravity field are a new data type, capable of modeling and detecting global mass transfer within the Earth. Such a global mass redistribution may be due to large exchange of water reservoir in the oceans and lands and may lead to significant changes of the Earth's gravity field which can be well detected by gravimetric satellite. The regional mass transfer such as localized tectonic processes due to earthquake, volcano and Tsunami, however, have an indicative influence on gravity fields that may be sensed by space observations (Han *et al*. 2013, Bao *et al.* 2005). This subject, in its present form, began with the launch of GRACE mission (the Gravity Recovery and Climate Experiments) (Tapley *et al.* 2004). The GRACE mission provides a useful apparatus to study the time-variation of the gravity field of the Earth. GRACE is able to monitor changes in a total water supply from the land surface to the base of the deepest aquifer (surface water, soil moisture, groundwater, snow) (Tourian *et al.* 2015, Fatolazadeh *et al*. 2016).

Numerous studies published in the recent years have shown that GRACE can offer useful constraints on ocean mass change (*e.g.*, Lombard *et al.* 2007), mass balance of the ice sheets (*e.g.*, Velicogna and Wahr 2006, Luthcke *et al.* 2006), terrestrial water storage change (*e.g.*, Tapley *et al. 2004*, Wahr *et al.* 2004), polar ice sheet melting (*e.g.*, Velicogna and Wahr 2006), and gravity variations due to localized tectonic processes (*e.g.*, Chen *et al.* 2007).

A large body of researches devoted to evaluations of hydrological effects in the GRACE data which primarily focused on the use of hydrological models. Rajner *et al.* (2012) demonstrated that the hydrological effects would change the gravity field of the Earth up to 6 μGal per year in global scale, whereas its local effects may reach to 10 μGal (see also Creutzfeldt *et al.* 2010). Unfortunately, these models only account the variation of water level in continents and as a result discard the effects due to ocean currents (see, *e.g*., Feng and Jin 2012). In some cases, hydrological effects have been removed without reference to specific hydrological model, by simply using an averaging scheme (see Chen *et al.* 2007, Wang *et al.* 2012).

It should be mentioned that in a similar contributions of this subject (Wang *et al.* 2012), in order to suppress the hydrological effects, the difference between the averaged gravity field of two years before and after the earthquake is considered (as hydrological free signal), which means that the hydrological effects are assumed to have the same influences on the gravity field before and after the earthquake. However, in this study it is shown that in the aforementioned case, some hydrological effects would remain and may contaminate the desired tectonic signal in observations.

In this paper, we present an approach for correction of hydrological and oceanic effects in the GRACE observations of level-2 data from period of January 2003 to December 2006 which considers the variations in the water supply from both the oceans and continents. By this way, we could extract the tectonic signal related to Sumatra earthquake occurred in December 2004. To do so, the outputs of the GLDAS model (Global Land Data Assimilation System model) (see Rodell *et al.* 2004) could be used to account for hydrological effects in lands. For oceanic effects, the difference between altimetry data and World Ocean Atlas (Stephens *et al.* 2002) model is used which may account for the total oceanic mass variations. The last step is to remove the above effects (hydrological effects in land plus oceanic mass transfer) from the GRACE observations. Thus, the remaining signal in the GRACE data would be due to desired tectonic signal. It should be mentioned that since the GRACE observations of level-2 have been corrected for background ocean model (Lyard *et al.* 2006), before subtracting the hydrological and oceanic effects, at first, it is necessary that this model be restored in the GRACE monthly solution via a new Ocean Bottom Pressure product (GAD coefficients) (Flechtner 2007).

## 2. THEORETICAL BACKGROUND

The fundamental result of physical geodesy is that the gravitational potential of the Earth satisfies Laplace equation in its exterior boundary, namely (Heiskanen and Moritz 1967):

$$\nabla^2 V = 0 \qquad \text{out of the Earth} , \tag{1}$$

in which $V$ is the gravitational potential and $\nabla^2$ stands for the Laplace operator. In spherical coordinate system with coordinates $\lambda$, $\varphi$, and $r$, which respectively correspond to longitude, latitude and radial coordinates, and the origin at the center of mass of the Earth (the natural coordinate of the Earth based on its principle moment of inertia), the solution of the above equation can be represented as (Heiskanen and Moritz 1967):

$$V(\lambda,\varphi,r) = \frac{GM}{r}\left\{1+\sum_{n=2}^{\infty}\left(\frac{R}{r}\right)^n \sum_{m=0}^{n}\left[\overline{C}_{mn}\overline{P}_{mn}(\sin\varphi)\cos m\lambda + \overline{S}_{mn}\overline{P}_{mn}(\sin\varphi)\sin m\lambda\right]\right\}. \tag{2}$$

in which $G$ is the universal constant of gravitation, $M$ the total mass of the Earth, $\overline{C}_{nm}$ and $\overline{S}_{nm}$ the non-dimensional Stokes coefficients and $\overline{P}_{nm}(\sin\varphi)$ are associated Legendre polynomial in latitude of degree $n$ and order $m$.

One of the important goals of satellite gravimetry is the determination of the so-called Stokes coefficients up to a maximum degree and orders which mostly depends on the altitude of satellite and its temporal and spatial reso-

lutions. Three space missions have been dedicated to this matter, which are CHAMP, GRACE, and GOCE missions (Tsoulis and Patlakis 2014). GRACE satellite, launched jointly by NASA and the German Aerospace Center (DLR) in March 2002 (Tapley *et al.* 2004), consists of two identical satellites in similar orbits, one following the other by about 220 km and at an altitude of approximately 400 km above the Earth. The satellites use microwave signal to continuously measure their separation distance to an accuracy of better than 1 micrometer. This observation may be converted to information about gravity field of the Earth.

All the data received from the satellite (raw data) are processed at the Raw Data Center (RDC) to level-0 GRACE data type. At this stage, they are transformed into physically meaningful quantities, such as satellite-to-satellite distances, non-gravitational accelerations, spacecraft attitude, *etc*., which are the so-called level-1 data that can be used to construct gravity field solution. Since few users have the capability of working with this type of observation, level-2 products are generated at several project-related processing centers (the Center for Space Research at the University of Texas, Geo Forschungs Zentrump in Potsdam, Germany, and the Jet Propulsion Laboratory), and each of these products is made available to users (Wahr *et al.* 1998). The level-2 gravity products consist of complete sets of spherical harmonic (Stokes) coefficients up to some maximum degree and order (typically 120), averaged over monthly intervals.

Using the GRACE observations of level-1, the gravity field of the Earth could be recovered in terms of aforementioned spherical harmonics which constitute the level-2 data. These coefficients released by temporal resolution of one month. The difference between the monthly index of $\overline{C}_{nm}$ and $\overline{S}_{nm}$ and the average index of $\overline{C}_{nm}$ and $\overline{S}_{nm}$ over definite period of time may be used as an indicator of significant mass change during a specific month.

GRACE can measure the gravity field variations which include any considerable changes occurring in the mass distribution of the Earth, such as changes in the amount of water reservoirs or local mass transfer due to seismic phenomena. Therefore, one may write:

$$\delta M^{\mathrm{GRACE}} = \delta M^{\mathrm{Hydrology}} + \delta M^{\mathrm{Seismic}} + \delta M^{\mathrm{Oceanic}} + \delta M^{\mathrm{Others}} \ , \tag{3}$$

where $\delta M^{\mathrm{GRACE}}$ is a total mass variations observed by GRACE, $\delta M^{\mathrm{Hydrology}}$ is a mass variations due to hydrological effects, $\delta M^{\mathrm{Oceanic}}$ is a mass variations due to oceanic effects, $\delta M^{\mathrm{Seismic}}$ is a mass variations due (for example) to earthquake, and $\delta M^{\mathrm{Others}}$ contains mass changes from Glacial Isostastic Adjustment (GIA), subsurface solid Earth, atmospheric mass changes or other sources of mass transfer which has been corrected in the GRACE observations of level-2.

Since the GRACE satellite can only sense the total mass variation due to all possible sources, the extraction of individual signals from GRACE observations needs the elimination of other impacts such as GIA, subsurface solid Earth, atmospheric mass changes which among them, the hydrological and oceanic signals have prominent contributions and their amplitudes are significant in the GRACE data.

If one considers the monthly level-2 data of the GRACE in terms of Stokes coefficients, by referring to Eq. 2, the potential changes in this period and at the Earth surface ($R \approx r$) (see Wahr *et al.* 1998) can be computed as:

$$\Delta V = \frac{GM}{R}\sum_{n=2}^{\infty}\sum_{m=0}^{n}\left[\Delta\bar{C}_{mn}\bar{P}_{mn}(\sin\varphi)\cos m\lambda + \Delta\bar{S}_{mn}\bar{P}_{mn}(\sin\varphi)\sin m\lambda\right] . \qquad (4)$$

where $\Delta V$ is the potential change which has been represented in terms of variations in Stokes coefficients, namely $\Delta\bar{C}_{mn}$ and $\Delta\bar{S}_{mn}$. This potential change or equivalently its corresponding differential coefficients ($\Delta\bar{C}_{mn}$ and $\Delta\bar{S}_{mn}$) is related to $\delta M^{\mathrm{GRACE}}$ in Eq. 3. Since the gravity acceleration is the gradient of potential, in the spherical coordinate system we have:

$$\mathbf{g} = \frac{1}{r\cos\varphi}\frac{\partial V}{\partial\lambda}\mathbf{e}_{\lambda} + \frac{1}{r}\frac{\partial V}{\partial\varphi}\mathbf{e}_{\varphi} + \frac{\partial V}{\partial r}\mathbf{e}_{r} . \qquad (5)$$

in which $\mathbf{g}$ is the gravity acceleration and $\mathbf{e}_{\lambda}$, $\mathbf{e}_{\varphi}$, and $\mathbf{e}_{r}$ are the unit vectors in the longitude, latitude, and radial directions. Therefore, the computation of gravity changes needs the first derivatives of $\Delta V$ as:

$$\begin{aligned}
\Delta V_r &= \frac{\partial\Delta V}{\partial r}|_{r\approx R} = -\left(\frac{GM}{R^2}\right)\sum_{n=2}^{\infty}\sum_{m=0}^{n}(\mathrm{n}+1)\left[\Delta\bar{C}_{mn}\bar{P}_{mn}(\sin\varphi)\cos m\lambda + \Delta\bar{S}_{mn}\bar{P}_{mn}(\sin\varphi)\sin m\lambda\right] \\
\Delta V_{\varphi} &= \frac{\partial\Delta V}{\partial\varphi}|_{r\approx R} = \left(\frac{GM}{R}\right)\sum_{n=2}^{\infty}\sum_{m=0}^{n}\left[\Delta\bar{C}_{mn}\bar{P}'_{mn}(\sin\varphi)\cos m\lambda + \Delta\bar{S}_{mn}\bar{P}'_{mn}(\sin\varphi)\sin m\lambda\right] \\
\Delta V_{\lambda} &= \frac{\partial\Delta V}{\partial\lambda}|_{r\approx R} = \left(\frac{GM}{R}\right)\sum_{n=2}^{\infty}\sum_{m=0}^{n}m\left[-\Delta\bar{C}_{mn}\bar{P}_{mn}(\sin\varphi)\sin m\lambda + \Delta\bar{S}_{mn}\bar{P}_{mn}(\sin\varphi)\cos m\lambda\right].
\end{aligned} \qquad (6)$$

Since we are interested in the local change, the local Cartesian coordinate with North-East-Down (NED) frame (Eshagh 2010, Eshagh and Abdollahzadeh 2010, 2012; Eshagh *et al.* 2013) at a point in the Earth surface is introduced in such a way that the *x*-axis is directed to the north, the *y*-axis to the east, and the *z*-axis downwards; therefore, in this local coordinates we have:

$$g_x = \Delta V_x = -\frac{1}{r}\Delta V_\varphi, \qquad g_y = \Delta V_y = \frac{1}{r\cos\varphi}\Delta V_\lambda, \qquad g_z = \Delta V_z = \Delta V_r. \tag{7}$$

The components of gravity gradient tensor may be expressed as:

$$\begin{aligned}
\Delta V_{xx} &= \frac{1}{r}\Delta V_r + \frac{1}{r^2}\Delta V_{\varphi\varphi}, & \Delta V_{xy} &= \frac{1}{r^2\cos\varphi}\Delta V_{\varphi\lambda} + \frac{\sin\varphi}{r^2\cos^2\varphi}\Delta V_\lambda \\
\Delta V_{xz} &= \frac{1}{r^2}\Delta V_\varphi - \frac{1}{r}\Delta V_{r\varphi}, & \Delta V_{yy} &= \frac{1}{r}\Delta V_r + \frac{1}{r^2\cot\varphi}\Delta V_\varphi + \frac{1}{r^2\cos^2\varphi}\Delta V_{\lambda\lambda} \\
\Delta V_{yz} &= \frac{1}{r\cos\varphi}\Delta V_{r\lambda} - \frac{1}{r^2\cos\varphi}\Delta V_\lambda, & \Delta V_{zz} &= \Delta V_{rr}.
\end{aligned} \tag{8}$$

in which at the surface of the Earth we have (see also formulas in: Wang *et al.* 2012, Eshagh 2010, Eshagh and Abdollahzadeh 2010, 2012):

$$\begin{aligned}
\Delta V_{rr} &= \frac{GM}{R^3}\sum_{n=2}^{60}(n+1)(n+2)\sum_{m=0}^{n}\left(\Delta\bar{C}_{nm}\cos m\lambda + \Delta\bar{S}_{nm}\sin m\lambda\right)\bar{P}_{nm}(\sin\varphi), \\
\Delta V_{\varphi\varphi} &= \frac{GM}{R}\sum_{n=2}^{60}\sum_{m=0}^{n}\left(\Delta\bar{C}_{nm}\cos m\lambda + \Delta\bar{S}_{nm}\sin m\lambda\right)\bar{P}''_{nm}(\sin\varphi), \\
\Delta V_{\lambda\lambda} &= -\frac{GM}{R}\sum_{n=2}^{60}\sum_{m=0}^{n}m^2\left(\Delta\bar{C}_{nm}\cos m\lambda + \Delta\bar{S}_{nm}\sin m\lambda\right)\bar{P}_{nm}(\sin\varphi), \\
\Delta V_{r\lambda} &= -\frac{GM}{R^2}\sum_{n=2}^{60}\sum_{m=0}^{n}m\left(-\Delta\bar{C}_{nm}\sin m\lambda + \Delta\bar{S}_{nm}\cos m\lambda\right)\bar{P}_{nm}(\sin\varphi), \\
\Delta V_{r\varphi} &= -\frac{GM}{R^2}\sum_{n=2}^{60}(n+1)\sum_{m=0}^{n}\left(\Delta\bar{C}_{nm}\cos m\lambda + \Delta\bar{S}_{nm}\sin m\lambda\right)\bar{P}'_{nm}(\sin\varphi), \\
\Delta V_{\varphi\lambda} &= \frac{GM}{R}\sum_{n=2}^{60}\sum_{m=0}^{n}m\left(-\Delta\bar{C}_{nm}\sin m\lambda + \Delta\bar{S}_{nm}\cos m\lambda\right)\bar{P}'_{nm}(\sin\varphi).
\end{aligned} \tag{9}$$

## 3. COMPUTATIONAL PROCEDURE AND NUMERICAL RESULTS

In this section, the scheme to correct the hydrological and oceanic effects from GRACE data of level-2 is presented. The process could be summarized as a following flowchart in Fig. 1.

### 3.1 GLDAS model and mass transfer in land

With reference to Fig. 1, it is seen that the correction of hydrological effects in lands is done with the help of GLDAS model. It was developed jointly at the National Aeronautics and Space Administration (NASA) Goddard Space Flight Center (GSFC) and the National Oceanic and Atmospheric Administration (NOAA) National Centers for Environmental Prediction (NCEP) (Rodell *et al.* 2004).

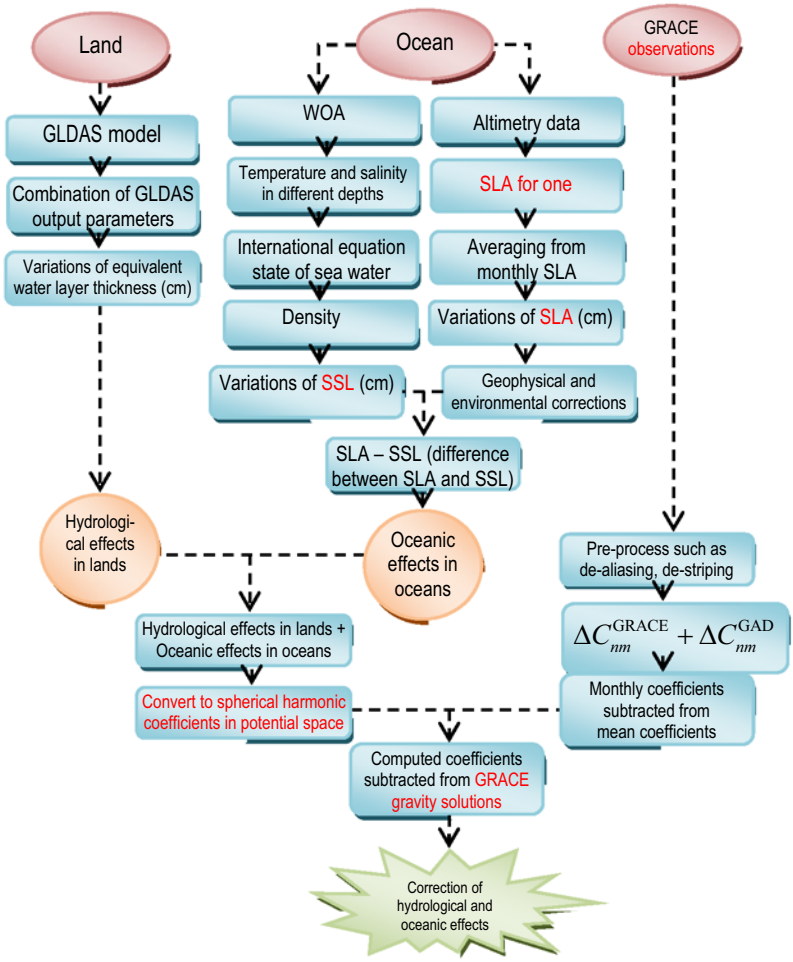


Fig. 1. The technical flowchart of correcting hydrological and oceanic effects from the GRACE data to reveal earthquake signals.

In this study, we use the outputs of the GLDAS model that are combinations of all the affective parameters including average layer soil moisture (0-200 cm), average layer soil temperature (0-200 cm), average surface temperature, ground heat flux, snowfall rate, total canopy water storage, surface runoff, snowmelt and snow water equivalent which are computed in terms of variations in water layer thickness. Since we are interested in the Sumatra earthquake occurred on 26 December 2004, to evaluate the hydrological effects at this epoch, the difference between water layer thickness in January 2005 and its mean value from January 2003 to December 2006 covering 47 months, is computed.

It is worth to mentioned that in spite of a number of analyses and assessment which have shown that the GLDAS could model the complete global hydrological variations in reasonable manner (see, *e.g.*, Jin *et al.* 2012) some other showed how well and often how poorly GLDAS and other models fit to the GRACE data (see Sneeuw *et al.* 2014, Lorenz *et al.* 2014).

### 3.2 Oceanic mass transfer from WOA and satellite altimetry

In the oceans, there are two important factors that cause the variations of water level. One of them is due to raining, evaporation, river discharge and ice sheet melting known as sea level anomaly and the other is due to water becoming warmer or (less) salty. The second effect is referred to as steric component and the first is known as non-steric component.

To correct oceanic effects in oceans, the two sources of variations mentioned above must be collected together as (Chambers 2006a):

$$\Delta\eta_{\text{Ocean}}(\varphi,\lambda,t) = \Delta\eta_{\text{SLA}}(\varphi,\lambda,t) - \Delta\eta_{\text{SSL}}(\varphi,\lambda,t) \tag{10}$$

in which $\Delta\eta_{\text{Ocean}}$ is the total equivalent water thickness variations in oceans, $\Delta\eta_{\text{SLA}}$ is the sea level anomaly, and $\Delta\eta_{\text{SSL}}$ are the steric sea level variations.

To derive $\Delta\eta_{\text{Ocean}}$, we use the WOA model in conjunction with satellite altimetry data. Satellite altimetry could measure the height of the surface of the oceans above the reference ellipsoid (a purely geometric quantity). However, the observed sea surface heights that are measured by satellite altimetry contain both steric and non-steric sea level changes. Steric sea level relates to changes in the structure of atoms in molecule and depends on many factors, the most important being temperature and salinity (Ishii *et al.* 2006), and could be computed with the aid of WOA model (see following sections).

#### *3.2.1 Satellite altimetry data*

In this study we use Jason-1 satellite that is a joint project between the NASA (United States) and CNES (The Centre national d'études spatiales) space agencies. The satellite's cycles used here are 110, 111, 112, and 113 cycles. As the case study in this paper focuses on the Sumatra earthquake occurred in December 2004, the oceanic effects must be computed at this period. To do so, we use global sea level anomaly data of January 2005 derived from Jason-1 altimetry mission which shows the variation in the sea surface height *versus* mean sea height. The Basic Radar Altimetry Toolbox (BRAT) is a software designed to process radar altimetry data. It has the capability to read all altimetry data from official data centers, do some processing strategies and computations and visualize the results. The sea level data have been corrected for some geophysical and environmental effects, such as sea state bias, ionospheric delay, dry and wet tropospheric corrections, tide effects

(ocean tides, pole tide), ocean tide loading, electromagnetic bias and inverse barometer correction (Ducet *et al.* 2000).

### *3.2.2 World Ocean Atlas model*

The World Ocean Atlas (WOA) is a model produced by the Ocean Climate Laboratory of the National Oceanographic Data Center (U.S.). The WOA dataset provides eight oceanographic variables such as: ocean temperature and salinity, dissolved oxygen, apparent oxygen utilization, percent of oxygen saturation, phosphate, silicic acid, and nitrate. The most important data set of the WOA consists of monthly 1° grid points of temperature and salinity down to 1500 m. The temperature and salinity, with the aid of International Equation state of Sea Water (IES) (Jayne *et al*. 2003), are used to compute density distribution of oceans water in different depths. We compute the difference between density in January 2005 consisting of 26 columns (depths from 0 to 1500 m) and the mean density (computed by averaging over one year) consisting of 35 columns (depths from 0 to 3500 m) and divide to standard density of water ($\rho_0 = 1027$ kg/m$^3$). By integrating this density difference over the water column (along the depth) from depth 0 to 1500 m (temperature and salinity variations after this depth are slow and can be neglected for practical purposes) the steric sea level variations for $1° \times 1°$ grid are derived as (Chambers 2006b):

$$\Delta\eta_{\mathrm{SSL}}(\varphi,\lambda,t) = \frac{1}{\rho_0}\int_{-h}^{\mathrm{surface}} \left[\rho(\varphi,\lambda,t,z,T,S) - \bar{\rho}\left(\varphi,\lambda,t,z,\bar{T},\bar{S}\right)\right] dz. \qquad (11)$$

In Eq. 11, $\Delta\eta_{\mathrm{SLL}}$ is the equivalent water thickness changes for steric sea level, $\rho_0$ is the standard density of water, $h$ is 1500 m, $\rho$ is the density and is a function of latitude, longitude, time ($t$), depth ($z$), temperature ($T$) and salinity ($S$), and $\bar{\rho}$ is mean density function.

## 3.3 GRACE data

The geopotential coefficients of monthly gravity data of level-2 computed by Center Space Research (CSR05) have been used in this research. These coefficients have been fully normalized to degree and order 60, corresponding to the spatial resolution of 300 km and above (Tapley *et al.* 2004).

In this study, we use some of the monthly average GRACE gravity solutions between the periods of January 2003 to December 2006 which includes 47 months. We subtract the value of $\bar{C}_{nm}$ and $\bar{S}_{nm}$ in January 2005, from the mean value of these coefficients over time range of January 2003 to December 2006 to evaluate global mass change due to Sumatra earthquake occurred on 26 December 2004 (see Fig. 1).

The impact of atmosphere as well as short-period (periods less than 1 month) ocean and atmospheric signals appearing in the GRACE monthly solutions have been removed from data of level-2 (Tapley *et al.* 2004). Since GRACE samples the Earth with a complicated temporal and spatial pattern during each month, the short-period signals don't get completely averaged out (Elsaka 2014). To minimize these effects, models of the ocean and atmosphere are used to remove their effects from the raw data, before constructing the monthly gravity field solutions. Also, to remove spatial correlation in the GRACE data, we use Gaussian filter with radius of 350 km (Wahr *et al.* 1998) which is necessary to reveal the fine pattern caused by the earthquake. Besides the errors in the orbit determination, measurements from various onboard instruments and the so-called de-aliasing background models, there are geographically correlated high-frequency errors in the GRACE temporal gravity solutions, so the pre-processing in the GRACE data is necessary to reveal the fine pattern caused by the earthquake.

### 3.4 Correction of GRACE data of level-2

Having introduced the required data set and models, in this sub-section we summarize the overall approach for reduction of hydrological and oceanic signals from the GRACE observations of level-2. Consequently, variations of total hydrological and oceanic effects in January 2005 could be computed by combination of hydrological and oceanic effects in lands and oceans as:

$$\Delta^{\text{Oceanic}}_{\text{Hydrological}}(\varphi,\lambda,t) = \Delta\eta_{\text{GLDAS}}(\varphi,\lambda,t) + \Delta\eta_{\text{Ocean}}(\varphi,\lambda,t)\,. \tag{12}$$

According to Eq. 12, the total oceanic and hydrological signals in oceans and lands are computed in terms of equivalent water thickness. To derive the mass variations and gravity changes due to these effects, we must convert the results that are in terms of water layer thickness to gravity space ($\Delta^{\text{Gravity}}(\varphi,\lambda,t)$) using the so-called Love number (Wahr *et al.* 1998, Agnew 2007).

$$\Delta^{\text{Gravity}}(\varphi,\lambda,t) = \left(\frac{1+k_n}{2n+1}\times\frac{3\rho_w}{a\rho_E}\right)\times\Delta^{\text{Oceanic}}_{\text{Hydrology}}(\varphi,\lambda,t)\,. \tag{13}$$

In Eq. 13, $k_n$ is the second Love number defined as the cubical dilation or the ratio of an additional potential (self-reactive force) produced by the deformation of the deforming potential (Agnew 2007). In addition, $\rho_w$ is the average density of water (1027 kg/m$^3$), $\rho_{\text{E}}$ the average density of the Earth (5517 kg/m$^3$), $a$ the mean radius of the Earth and $n$ is the degree in spherical harmonics.

Ultimately to reduce the effects of gravity changes due to hydrological and oceanic impacts from the GRACE measurements of level-2, it is neces-

sary that $\Delta^{\text{Gravity}}(\varphi,\lambda,t)$ is represented by series expansion in terms of orthogonal spherical harmonic as:

$$\Delta^{\text{Gravity}}(\varphi,\lambda,t)=\sum_{n=2}^{\infty}\sum_{m=0}^{n}\left[\Delta\bar{C}_{mn}\bar{Y}_{nm}^{C}(\varphi,\lambda)+\Delta\bar{S}_{mn}\bar{Y}_{nm}^{S}(\varphi,\lambda)\right] \tag{14}$$

in which $\bar{Y}_{nm}^{C}(\varphi,\lambda)$ and $\bar{Y}_{nm}^{S}(\varphi,\lambda)$ are defined as:

$$\begin{cases}\bar{Y}_{nm}^{S}(\varphi,\lambda)\\ \bar{Y}_{nm}^{C}(\varphi,\lambda)\end{cases}=\bar{P}_{mn}(\sin\varphi)\begin{cases}\sin m\lambda\\ \cos m\lambda\end{cases}. \tag{15}$$

In Eq. 14, $\Delta\bar{C}_{mn}$ and $\Delta\bar{S}_{mn}$ are corresponding expansion coefficients and could be determined as:

$$\begin{aligned}\Delta\bar{C}_{mn}&=\frac{1}{H^{*}}\iint_{\sigma}\Delta^{\text{Gravity}}(\phi,\lambda,t)\bar{Y}_{nm}^{C}(\varphi,\lambda)dS\ ,\\ \Delta\bar{S}_{mn}&=\frac{1}{H^{*}}\iint_{\sigma}\Delta^{\text{Gravity}}(\phi,\lambda,t)\bar{Y}_{nm}^{S}(\varphi,\lambda)dS\ ,\end{aligned} \tag{16}$$

where $H^{*}$ is the norm of spherical harmonic defined by:

$$\begin{aligned}H^{*}&=\frac{2\pi}{2n+1}\frac{(n+m)!}{(n-m)!}\ ,\quad m\neq 0\\ H^{*}&=\frac{4\pi}{2n+1},\quad m=0\ .\end{aligned} \tag{17}$$

It is necessary to mention that in the process of recovery of spherical harmonic coefficients of level-2 data, they are corrected for the effects of oceanic signals, known as background ocean model. Thus, to have a correct evaluation of oceanic signal in the GRACE data, we should restore the background ocean model as:

$$\Delta C_{nm}^{T}(t)=\Delta C_{nm}^{\text{GRACE}}(t)+\Delta C_{nm}^{\text{GAD}}(t)\ , \tag{18}$$

where $\Delta C_{nm}^{\text{GAD}}$ are pressure variations based entirely on an ocean model (see Flechtner 2007) and $\Delta C_{nm}^{\text{GRACE}}$ are coefficients of monthly gravity data of level-2.

## 4. CASE STUDY

Having discussed the general procedure for reduction of hydrological and oceanic effects, in this section we illustrate the performance of proposed strategy. For the case study, we choose the active tectonic region of Sumatra to predict the co-seismic gravitational gradient changes which stricken by

9.2 magnitude earthquake at Sunday on 26 December 2004 at 00:58:53 UTC with fault zone that is located at 3.316°N, 95.854°E, with a focal depth of about 30 km. The model consists of 7 sub-fault planes which were determined from seismic records. For convenience, the 7 sub-faults were merged into 3 segments and named Andaman, Nicobar, and Sumatra, respectively. Figure 2 shows the fault planes.

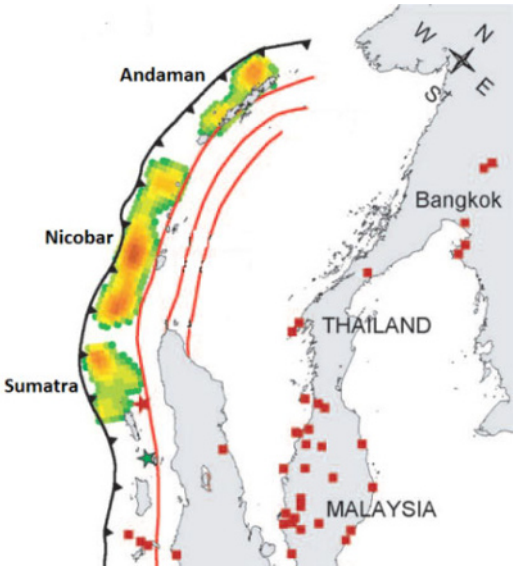


Fig. 2. Finite fault model of segments of Andaman, Nicobar, and Sumatra.

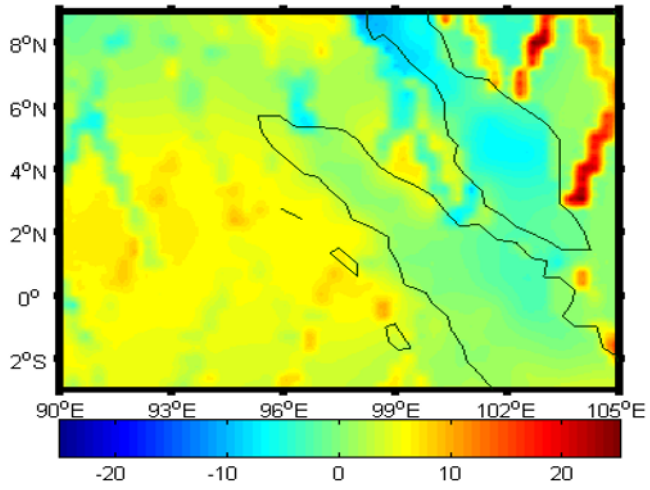


Fig. 3. Variations of hydrological and oceanic effects in January 2005 (in units of cm).

Figure 3 shows the total water layer thickness variations in lands and oceans computed from Eq. 11. All mass changes occurred in a time around December and January but the strongest signals are due to the annual cycle which shows maxima and minima dependent on the seasons and locations which alter from place to place, *e.g.*, between the northern and southern hemisphere. As could be seen in this figure, total water variations in the north of Sumatra and Nicobar segments have negative values which could be a result of sparse vegetation of the region, the larger evaporation and human agricultural irrigation and over-exploitation of groundwater that lead to wastage of groundwater resources.

After combining hydrological and oceanic signals, their effects on gravity variations may be determined. In Fig. 4, hydrological and oceanic effects on gravity field variations have been shown in radial, northwards and eastwards directions in January 2005. These variations could be determined from Eq. 6, considering the $\overline{C}_{nm}$ and $\overline{S}_{nm}$ in Eqs. 14 and 16. As could be seen, the maximum and minimum values of these effects are 3 μGal in radial direction and –5 μGal in northward direction. As a result from all of the observed gravity variations in this region, the maximum and minimum variations of 5 and –5 μGal relate to hydrological and oceanic effects which have been corrected in order to obtained tectonic signal in this region.

Here we compute the gravitational gradient changes (see Eq. 8) and use it to discuss the co-seismic deformation resulting from the Sumatra earthquake. Figure 5 shows the gravitational gradient changes components, such

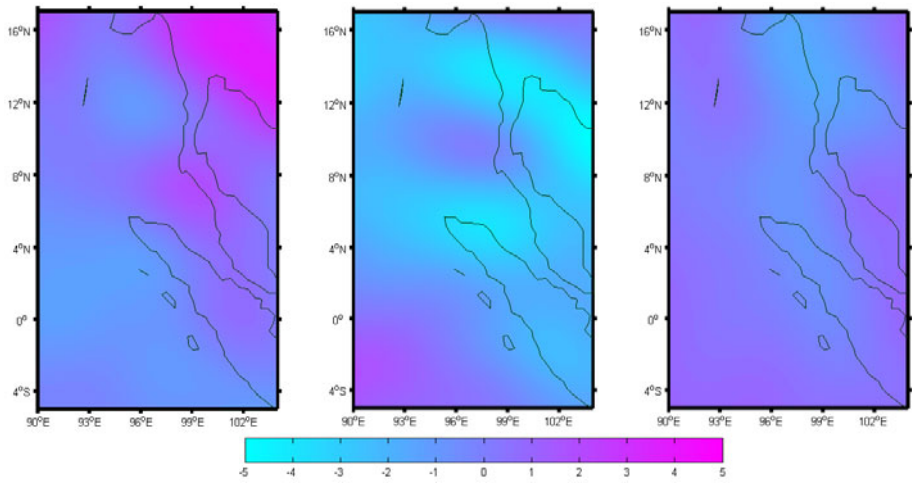


Fig. 4. Variations of hydrological and oceanic signals on gravity changes in January 2005 (in units of μGal) in radial direction (a), northward direction (b), and eastward direction (c).

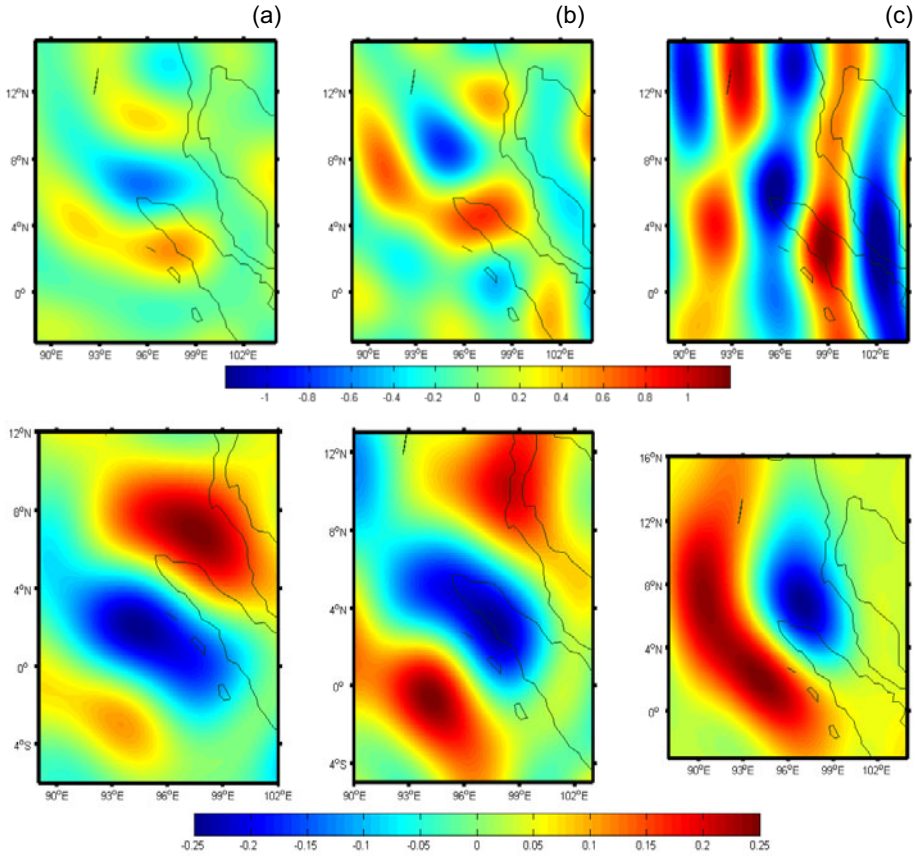


Fig. 5. Gravitational gradient changes components (in units of mE) $\Delta V_{xx}$ (a), $\Delta V_{xz}$ (b), and $\Delta V_{zz}$ (c) before correction of hydrological and oceanic effects (top figures) and after these corrections (down figures).

as $\Delta V_{xx}$, $\Delta V_{xz}$, and $\Delta V_{zz}$, before and after correction of hydrological and oceanic effects. Since the high-frequency contents in gravitational field variation can be amplified by deriving the gravitational gradients, the GRACE-derived co-seismic gravitational gradient changes clearly delineate the fault line, locate significant slips, better define the extent of the co-seismic deformation and reveal refined mass redistribution features caused by the earthquake (see Wang *et al.* 2012).

## 5. CONCLUSIONS

The method for correction of hydrological and oceanic effects from GRACE (the Gravity Recovery and Climate Experiments) data is presented in order to better see the gravity field changes of Sumatra earthquake occurred on 26

December 2004. The hydrological effects in lands are determined by GLDAS (Global Land Data Assimilation System) model which considers the overall influences of soil moisture, precipitation, snow supply, surface temperature, evaporation, and sensible heat flux, on the total water variation in lands. In the oceans, we used the satellite altimetry data in conjunction with WOA (World Ocean Atlas) model. The WOA model produces temperature and salinity with which one could derive the water layer density using international equation state water. This density can be converted to water layer thickness known as steric sea level. By subtracting steric sea level from sea level anomaly obtained from satellite altimetry data, the oceanic effects in oceans are determined. Adding these two sources of variations, the total hydrological and oceanic signals in lands and oceans are determined in terms of equivalent water layer thickness and converted to gravity changes using Love number and represented in terms of spherical harmonic coefficients. The maximum and minimum impacts of hydrological and oceanic effects on gravity changes are obtained to be of about 3 μGal in radial direction and –5 μGal in northwards direction, consistent to other studies. Also the maximum and minimum values of gravitational gradient changes are 0.2 and –.25 mE, as observed in $\Delta V_{zz}$ component.

## References

Agnew, D.C. (2007), Earth tides. **In:** T.A. Herring (ed.), *Treatise on Geophysics: Geodesy*, Elsevier, New York, 163-195.

Bao, L.F., A. Piatanesi, Y. Lu, H.T. Hsu, and X.H. Zhou (2005), Sumatra tsunami affects observations by GRACE satellites, *Eos Trans. AGU* **86**, 39, 353-356, DOI: 10.1029/2005EO390002.

Chambers, D.P. (2006a), Evaluation of new GRACE time-variable gravity data over the ocean, *Geophys. Res. Lett.* **33**, 17, L17603, DOI: 10.1029/2006GL027296.

Chambers, D.P. (2006b), Observing seasonal steric sea level variations with GRACE and satellite altimetry, *J. Geophys. Res.* **111**, C3, C03010, DOI: 10.1029/2005JC002914.

Chen, J.L., C.R. Wilson, B.D. Tapley, and S. Grand (2007), GRACE detects coseismic and postseismic deformation from the Sumatra–Andaman earthquake, *Geophys. Res. Lett.* **34**, 13, L13302, DOI: 10.1029/2007GL030356.

Creutzfeldt, B., A. Güntner, H. Wziontek, and B. Merz (2010), Reducing local hydrology from high-precision gravity measurements: a lysimeter-based approach, *Geophys. J. Int.* **183**, 1, 178-187, DOI: 10.1111/j.1365-246X.2010.04742.x.

Ducet, N., P.Y. Le Traon, and G. Reverdin (2000), Global high-resolution mapping of ocean circulation from TOPEX/Poseidon and ERS-1 and -2, *J. Geophys. Res*. **105**, C8, 19477-19498, DOI: 10.1029/2000JC900063.

Elsaka, B. (2014), Sub-monthly gravity field recovery from simulated multi-GRACE mission type, *Acta Geophys*. **62**, 1, 241-258, DOI: 10.2478/s11600-013-0170-9.

Eshagh, M. (2010), Alternative expressions for gravity gradients in local north-oriented frame and tensor spherical harmonics, *Acta Geophys*. **58**, 2, 215-243, DOI: 10.2478/s11600-009-0048-z.

Eshagh, M., and M. Abdollahzadeh (2010), Semi-vectorization: an efficient technique for synthesis and analysis of gravity gradiometry data, *Earth Sci. Inform.* **3**, 3, 149-158, DOI: 10.1007/s12145-010-0062-3.

Eshagh, M., and M. Abdollahzadeh (2012), Software for generating gravity gradients using a geopotential model based on an irregular semivectorization algorithm, *Comput. Geosci.* **39**, 152-160, DOI: 10.1016/j.cageo.2011.06.003.

Eshagh, M., J.-M. Lemoine, P. Gegout, and R. Biancale (2013), On regularized time varying gravity field models based on GRACE data and their comparison with hydrological models, *Acta Geophys*. **61**, 1, 1-17, DOI: 10.2478/s11600-012-0053-5.

Fatolazadeh, F., B. Voosoghi, and M. Raoofian Naeeni (2016), Wavelet and Gaussian approaches for estimation of groundwater variations using GRACE data, *Ground Water* **54**, 1, 74-81, DOI: 10.1011/gwat.12325.

Feng, G., and S. Jin (2012), Global water cycle and climate change signals observed by satellite gravimetry. **In:** *2012 IEEE Int. Geoscience and Remote Sensing Symposium (IGARSS), 22-27 July 2012, Munich, Germany*, 832-835, DOI: 10.1109/IGARSS.2012.6351432.

Flechtner, F. (2007), GRACE 327-750 (GR-GFZ-AOD-0001). AOD1B product description document for product releases 01 to 04, Rev. 3.1, Gravity Recovery and Climate Experiment, GeoForschungszentrum, Potsdam, Germany.

Han, S.-C., R. Riva, J. Sauber, and E. Okal (2013), Source parameter inversion for recent great earthquakes from a decade-long observation of global gravity fields, *J. Geophys. Res*. **118**, 3, 1240-1267, DOI: 10.1002/jgrb.50116.

Heiskanen, W.A., and H. Moritz (1967), *Physical Geodesy*, W.H. Freeman, San Francisco.

Ishii, M., M. Kimoto, K. Sakamoto, and S.I. Iwasaki (2006), Steric sea level changes estimated from historical ocean subsurface temperature and salinity analyses, *J. Oceanogr.* **62**, 2, 155-170, DOI: 10.1007/s10872-006-0041-y.

Jayne, S.R., J.M. Wahr, and F.O. Bryan (2003), Observing ocean heat content using satellite gravity and altimetry, *J. Geophys. Res.* **108**, C2, 3031, DOI: 10.1029/2002JC001619.

Jin, S.G., AA.. Hassan, and G.P. Feng (2012), Assessment of terrestrial water contributions to polar motion from GRACE and hydrological models, *J. Geodyn.* **62**, 40-48, DOI: 10.1016/j.jog.2012.01.009.

Lombard, A., D. Garcia, G. Ramillien, A. Cazenave, R. Biancale, J.M. Lemoine, F. Flechtner, R. Schmidt, and M. Ishii (2007), Estimation of steric sea level variations from combined GRACE and Jason-1 data, *Earth Planet. Sci. Lett.* **254**, 1-2, 194-202, DOI: 10.1016/j.epsl.2006.11.035.

Lorenz, C., H. Kunstmann, B. Devaraju, M.J. Tourian, N. Sneeuw, and J. Riegger (2014), Large-scale runoff from landmasses: a global assessment of the closure of the hydrological and atmospheric water balances, *J. Hydrometeorol*. **15**, 6, 2111-2139, DOI: 10.1175/JHM-D-13-0157.1.

Luthcke, S.B., H.J. Zwally, W. Abdalati, D.D. Rowlands, R.D. Ray, R.S. Nerem, F.G., Lemoine, J.J. McCarthy, and D.S. Chinn (2006), Recent Greenland ice mass loss by drainage system from satellite gravimetry observations, *Science* **314**, 5803, 1286-1289, DOI: 10.1126/science.1130776.

Lyard, F., F. Lefevre, T. Letellier, and O. Francis (2006), Modelling the global ocean tides: modern insights from FES2004, *Ocean Dynam.* **56**, 5-6, 394-415, DOI: 10.1007/s10236-006-0086-x.

Rajner, M., T. Olszak, J. Rogowski, and J. Walo (2012), The Influence of continental water storage on gravity rates estimates: case study using absolute gravity measurements from area of Lower Silesia, Poland, *Acta Geodyn Geomater*. **9**, 4, 168, 449-455.

Rodell, M., P.R. Houser, U. Jambor, J. Gottschalck, K. Mitchell, C.J. Meng, K. Arsenault, B. Cosgrove, J. Radakovich, M. Bosilovich, J.K. Entin, J.P. Walker, D. Lohmann, and D. Toll (2004), The Global Land Data Assimilation System, *Bull. Am. Meteorol. Soc.* **85**, 3, 381-394, DOI: 10.1175/BAMS-85-3-381.

Sneeuw, N., C. Lorenz, B. Devaraju, M.J. Tourian, J. Riegger, H. Kunstmann, and A. Bárdossy (2014), Estimating runoff using hydro-geodetic approaches, *Surv. Geophys*. **35**, 6, 1333-1359, DOI: 10.1007/s10712-014-9300-4.

Stephens, C., J.I. Antonov, T.P. Boyer, M.E. Conkright, R.A. Locarnini, T.D. O'Brien, and H.E. Garcia (2002), *World Ocean Atlas 2001, Volume 1. Temperature*, NOAA Atlas NESDIS 49, U.S. Gov. Print. Off., Washington, D.C.

Tapley, B.D., S. Bettadpur, M. Watkins, and C. Reigber (2004), The gravity recovery and climate experiment: Mission overview and early results, *Geophys. Res. Lett.* **31**, 9, L09607, DOI: 10.1029/2004GL019920.

Tourian, M.J., O. Elmi, Q. Chen, B. Devaraju, S. Roohi, and N. Sneeuw (2015), A spaceborne multisensor approach to monitor the desiccation of Lake Urmia in Iran, *Remote Sens. Environ*. **156**, 349-360, DOI: 10.1016/j.rse.2014.10.006.

Tsoulis, D., and K. Patlakis (2014), Spectral assessment of isostatic gravity models against CHAMP, GRACE, GOCE satellite-only and combined gravity models, *Acta Geophys*. **62**, 4, 679-698, DOI: 10.2478/s11600-013-0176-3.

Velicogna, I., and J. Wahr (2006), Measurements of time-variable gravity show mass loss in Antarctica, *Science* **311**, 5768, 1754-1756, DOI*:* 10.1126/science.1123785.

Wahr, J., M. Molenaar, and F. Bryan (1998), Time variability of the Earth's gravity field: Hydrological and oceanic effects and their possible detection using GRACE, *J. Geophys. Res.* **103**, B12, 30205-30230, DOI: 10.1029/98JB02844.

Wahr, J., S. Swenson, V. Zlotnicki, and I. Velicogna (2004), Time-variable gravity from GRACE: First results, *Geophys. Res. Lett.* **31**, 11, L11501, DOI: 10.1029/2004GL019779.

Wang, L., C.K. Shum, and C. Jekeli (2012), Gravitational gradient changes following the 2004 December 26 Sumatra–Andaman earthquake inferred from GRACE, *Geophys. J. Int.* **191**, 3, 1109-1118, DOI: 10.1111/j.1365-246X.2012.05674.x.

Received 22 April 2015
Received in revised form 10 July 2015
Accepted 14 July 2015

DE GRUYTER OPEN

**Acta Geophysica**
vol. 64, no. 4, Aug. 2016, pp. 1211-1223
DOI: 10.1515/acgeo-2016-0036

# The 2009-2012 Ionosonde and IRI2012 Variability of *foF*2, *hmF*2, *M*3000*F*2, *B*0, *B*1 Parameters over Warsaw

Michał SZWABOWSKI, Beata DZIAK-JANKOWSKA, Mariusz POŻOGA, and Łukasz TOMASIK

Space Research Centre, Polish Academy of Sciences, Warsaw, Poland
e-mail: mszwabowski@cbk.waw.pl

A b s t r a c t

This paper presents comparisons of variability and accordance of ionospheric parameters *foF*2, *hmF*2, *M*3000*F*2, *B*0, *B*1 over the middle latitude station in Warsaw (52.21°N, 21.06°E). Examination included observational data from Space Research Centre ionosonde in Poland and International Reference Ionosphere (IRI) 2012 model, for the time period of increasing solar activity from 2009 to 2012. The analysis concerned: trend, monthly median differences in twenty-four hours variability, local minima and maxima. Results are presented as tables of semi-annual data, and plots of difference in four-year period. The study indicated good agreement of *foF*2 and *hmF*2 parameters. Underestimations of *B*1 and *M*3000*F*2, variability of *B*0 parameter in Bil-2000, Gul-1987, and ABT-2009 option, were taken into consideration.

**Key words:** ionosonde, IRI, ionospheric sounding.

## 1. INTRODUCTION

Ionospheric soundings in Poland started in Warsaw in the 1960s, and are continued currently by VISRC2 ionosonde of the Plasma Physics Department in the Space Research Centre in Warsaw. Position of the station (geographical coordinates 52.21°N, 21.06°E; geomagnetic coordinates 50.51°N,

Ownership: Institute of Geophysics, Polish Academy of Sciences;
© 2016 Szwabowski *et al.* This is an open access article distributed under the Creative Commons Attribution-NonCommercial-NoDerivs license,
http://creativecommons.org/licenses/by-nc-nd/3.0/.

105.70°E) situates it as a middle latitude one, with solar events characteristic for this region (SRC PAS 2014).

The data obtained from ionosonde was processed by Autoscala software designed for automatic scaling of the main ionospheric characteristics from ionograms, based on an image recognition technique. At the moment of publishing this paper, Autoscala gives an output of the following ionospheric characteristics: *foF*2, *MUF*(3000)*F*2, (3000)*F*2, *foF*1, *h'Es*, *ftEs*, and the estimation of the bottom vertical electron density profile from the base of the ionosphere up to the maximum electron density *NmF*2 (INGV 2014).

In this paper, observational data of the ionosphere were compared to modeled characteristics by URSI IRI model, for days during the period 2009-2012. The international reference ionosphere (IRI) is the international standard for the specification of ionospheric densities and temperatures. It was developed and is being updated by a joint working group of the International Union of Radio Science (URSI) and the Committee on Space Research (COSPAR). As an empirical model, IRI is based on the existing data record, and the IRI working group has been dedicated to deduce the dominant variation patterns of ionospheric parameters from this data record (Bilitza 2001, Bilitza *et al*. 2014).

The study of accordance was made for the main ionospheric parameters:

- the ordinary wave critical frequency in the F region is the most important *F*2 layer characteristic; it corresponds to the maximum radio frequency that can be reflected at vertical incidence,
- the minimum virtual height of the ordinary wave *hmF*2 characterizes the highest stratification in the *F*2 region,
- the *M*(3000)*F*2 is related to Maximum Usable Frequency for 3000 km path length,
- *B*0 describes the thickness of the bottom side profile,
- *B*1 determines the shape of the profile between *hmF*2 and *h*0:24, which is the height where the electron density drops to 0.24*NmF*2.

The description of the *F*2 critical frequency can be done by IRI using two methods: CCIR and URSI. Both are based on the first Fourier analysis with 15 coefficients and seventh order of the monthly median ionosondes diurnal variation and worldwide description in spherical functions. Propagation parameter *M*(3000)*F*2 is obtained from relation *foF*2 and MUF, scaled from ionograms, and CCIR numerical maps. Thus, the obtained *M*(3000)*F*2 factor with created correction factor (dependent on solar activity functions and frequencies of *E* and *F* layers), and solar activity functions, enable calculation of *hmF*2 parameter. URSI prefers the second option, especially at low latitudes. The *B*1 shape bottomside profile function was assumed to take values from in step-like transition 3 to 5 (Bilitza *et al*. 1990, 2014). The IRI

in actual 2012 model offers the three values of *B*0 thickness: Bil-2000, Gul-1987, and ABT-2009.

## 2. DESCRIPTION OF DATA SET AND METHOD OF ANALYSIS

Data used for this study was recorded by VISRC2 ionosonde located at Warsaw position. For the comparisons we used IRI 2012 with STORM correction model (Bilitza *et al*. 2014). IRI is based on ITU-R prediction of monthly median values with decile variability by linear relationship with solar activity (ITU-R 2012). Analysed data set from Warsaw ionosonde contains monthly hour median values of parameters *foF*2, *M*3000*F*2 for URSI, and CCIR, *hmF*2, *B*1, *B*0 option: ABT, BIL, and GUL.

Considered time periods started in January 2009 with a low value of solar radio flux and ended in December 2012 when *R* parameter from January 2011 was rising through increasing sun activity in eleven-year cycle (see Fig. 1, from www.spaceweather.gc.ca database). The plot presents a comparison of daily and median sun solar radio fluxes in specified selected terms.

Results were shown as multiple plots of a 24-hour universal time variability from days in every month for 2009-2012 period of selected parameters. All considered data were presented as a median difference between the IRI values and those observed by Warsaw ionosonde, as in the equation:

$$\text{diff} = \frac{\text{IRI}p - \text{WI}p}{\text{IRI}p + \text{WI}p} \times 100\% \ , \tag{1}$$

where IRI*p* is the selected specific monthly hour median IRI parameter and WI*p* is the selected specific monthly hour median measured Warsaw Ionosonde parameter.

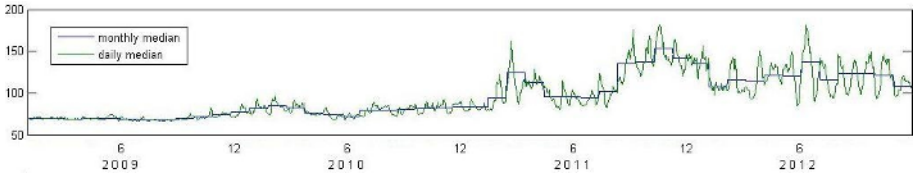


Fig. 1. 2009-2012 comparison of monthly and daily median of solar 10.7 cm flux level.

## 3. ANALYSIS

This paper contains analysed data presented as figures of monthly seasonal variation of parameters *foF*2, *hmF*2, *M*3000*F*2, *B*0, and *B*1 at the Warsaw position. Data is plotted as a difference of IRI and the value measured by the ionosonde, as calculated according to Eq. 1. Colour bars present a difference in percent of the obtained values. The shades of grey under zero value illus-

trate degree of IRI underestimation and above an overestimation. White gaps with "NO DATA" description define the time periods where data was not available for calculations. The terms local minimum and maximum used in the work represent the calculated lowest and highest values of difference between monthly hour medians for years 2009-2012. Trend analysis refers to a comparison of an estimated parameter variability in the annual time period.

Table 1 presents summary of medians differences in 6-month ranges for the considered 2009-2012 period. The results represent $Me_{\text{diff}}$ parameter calculated from Eq. 1. $Me_{\text{IRI}}$ and $Me_{\text{ISD}}$ are, respectively, the median values of the parameter from IRI model and measured by Warsaw ionosonde.

Figures 2 and 3 show monthly variation of maximum frequency of *F*2 layer for URSI and CCIR option. The values predicted by IRI models and those from the Warsaw ionosonde follow the same trend as an annual variable of parameter. Differences occur in the IRI narrower estimation of, extended to the night side part, positive growth of *foF*2 parameter. As a result of an increased solar activity (Fig. 2, years 2011-2012) varying underestimations and overestimations are visible and reduced to night in the time period of low sun activity (years 2009-2010). Generally, the median difference for URSI semi-annual analysed sections reaches values in the range of ± 2.5%, with the lowest at level –6.7%, for the start of analysed time (January-June 2009). CCIR model presents closer value in section January-June 2009 (on –3.1% level) and minimally better from July 2010 to December 2011. The minimum values of the locally observed differences for the models were –24 and –19%, the maximum values being +16 and +19%.

Figures 4 and 5 for URSI and CCIR *hmF*2 parameter present noticeable division into the fields in which low and increased solar radio fluxes are dominant. The level of IRI difference changes from being overestimated for 2009-2010, to underestimation for 2011-2012 periods. Generally, in daytime section in figures, the IRI models in respect to Warsaw ionosonde evaluated a lower value of *hmF*2 and higher value at night from January 2009 to the end of 2010, night overestimate is dominating. The analysis suggests an agreement of trend predicted by IRI and Warsaw ionosonde; both *hmF*2 parameters present higher values at night, and in a second part of the plot (years 2011-2012), where Solar Radio flux level is increased. Noticeable differences are in Warsaw ionosonde data presenting lower value at night and day in the year 2009. Median of the semi-annual difference for all analysed sections reaches low values, from –3 to +1%. The locally observed difference minima reach values from –7% to the maximum level at +13% for both models.

The predicted IRI and Warsaw-ionosonde values for *M*3000*F*2 follow a similar trend. The IRI model presents close results (see Table 1, part 3). In all data, the *M*3000*F*2 parameters are on higher level at daytime, from Au-

Table 1

2009-2012 median difference summary of ionosphere parameters in 6-month ranges

***foF2 URSI***

| | 1-6.2009 | 7-12.2009 | 1-6.2010 | 7-12.2010 | 1-6.2011 | 7-12.2011 | 1-6.2012 | 7-12.2012 |
|---|---|---|---|---|---|---|---|---|
| *Me IRI* | 3,849 | 3,886 | 4,390 | 4,419 | 5,189 | 5,687 | 6,116 | 5,759 |
| *Me WI* | 4,400 | 3,800 | 4,200 | 4,600 | 5,300 | 5,400 | 6,100 | 5,500 |
| *Me diff [%]* | -6,7 | 1,1 | 2,2 | -2,0 | -1,1 | 2,6 | 0,1 | 2,3 |

***foF2 CCIR***

| | 1-6.2009 | 7-12.2009 | 1-6.2010 | 7-12.2010 | 1-6.2011 | 7-12.2011 | 1-6.2012 | 7-12.2012 |
|---|---|---|---|---|---|---|---|---|
| *Me IRI* | 4,135 | 4,034 | 4,616 | 4,541 | 5,320 | 5,678 | 6,003 | 5,772 |
| *Me WI* | 4,400 | 3,800 | 4,200 | 4,600 | 5,300 | 5,400 | 6,100 | 5,500 |
| *Me diff [%]* | -3,1 | 3,0 | 4,7 | -0,6 | 0,2 | 2,5 | -0,8 | 2,4 |

***M3000F2***

| | 1-6.2009 | 7-12.2009 | 1-6.2010 | 7-12.2010 | 1-6.2011 | 7-12.2011 | 1-6.2012 | 7-12.2012 |
|---|---|---|---|---|---|---|---|---|
| *Me IRI* | 3,142 | 3,161 | 3,103 | 3,123 | 3,007 | 3,010 | 2,952 | 3,012 |
| *Me WI* | 3,360 | 3,380 | 3,370 | 3,380 | 3,270 | 3,240 | 3,150 | 3,160 |
| *Me diff [%]* | -3,4 | -3,3 | -4,1 | -4,0 | -4,2 | -3,7 | -3,2 | -2,4 |

***hmF2 CCIR***

| | 1-6.2009 | 7-12.2009 | 1-6.2010 | 7-12.2010 | 1-6.2011 | 7-12.2011 | 1-6.2012 | 7-12.2012 |
|---|---|---|---|---|---|---|---|---|
| *Me IRI* | 261 | 265 | 268 | 270 | 277 | 281 | 286 | 284 |
| *Me WI* | 258 | 260 | 268 | 270 | 288 | 293 | 303 | 300 |
| *Me diff [%]* | 0,5 | 0,9 | 0,0 | 0,0 | -2,0 | -2,1 | -2,9 | -2,7 |

***hmF2 URSI***

| | 1-6.2009 | 7-12.2009 | 1-6.2010 | 7-12.2010 | 1-6.2011 | 7-12.2011 | 1-6.2012 | 7-12.2012 |
|---|---|---|---|---|---|---|---|---|
| *Me IRI* | 259 | 266 | 267 | 270 | 277 | 283 | 286 | 285 |
| *Me WI* | 258 | 260 | 268 | 270 | 288 | 293 | 303 | 300 |
| *Me diff [%]* | 0,3 | 1,0 | -0,2 | 0,1 | -2,0 | -1,8 | -2,8 | -2,5 |

***B0 Gul-1987***

| | 1-6.2009 | 7-12.2009 | 1-6.2010 | 7-12.2010 | 1-6.2011 | 7-12.2011 | 1-6.2012 | 7-12.2012 |
|---|---|---|---|---|---|---|---|---|
| *Me IRI* | 78,5 | 77,8 | 80,6 | 79,7 | 84,1 | 83,7 | 89,2 | 83,6 |
| *Me WI* | 70,0 | 66,0 | 73,0 | 77,0 | 89,0 | 95,0 | 102,0 | 96,0 |
| *Me diff [%]* | 5,7 | 8,2 | 4,9 | 1,7 | -2,8 | -6,3 | -6,7 | -6,9 |

***B0 Bil-2000***

| | 1-6.2009 | 7-12.2009 | 1-6.2010 | 7-12.2010 | 1-6.2011 | 7-12.2011 | 1-6.2012 | 7-12.2012 |
|---|---|---|---|---|---|---|---|---|
| *Me IRI* | 76,2 | 80,3 | 79,4 | 83,8 | 85,1 | 94,5 | 91,8 | 95,9 |
| *Me WI* | 70,0 | 66,0 | 73,0 | 77,0 | 89,0 | 95,0 | 102,0 | 96,0 |
| *Me diff [%]* | 4,2 | 9,8 | 4,2 | 4,2 | -2,2 | -0,3 | -5,3 | -0,1 |

***B0 ABT-2009***

| | 1-6.2009 | 7-12.2009 | 1-6.2010 | 7-12.2010 | 1-6.2011 | 7-12.2011 | 1-6.2012 | 7-12.2012 |
|---|---|---|---|---|---|---|---|---|
| *Me IRI* | 90,9 | 84,2 | 91,6 | 85,3 | 94,1 | 88,5 | 97,4 | 88,3 |
| *Me WI* | 70,0 | 66,0 | 73,0 | 77,0 | 89,0 | 95,0 | 102,0 | 96,0 |
| *Me diff [%]* | 13,0 | 12,1 | 11,3 | 5,1 | 2,8 | -3,5 | -2,3 | -4,2 |

***B1***

| | 1-6.2009 | 7-12.2009 | 1-6.2010 | 7-12.2010 | 1-6.2011 | 7-12.2011 | 1-6.2012 | 7-12.2012 |
|---|---|---|---|---|---|---|---|---|
| *Me IRI* | 1,9 | 2,0 | 1,9 | 2,0 | 1,9 | 2,0 | 1,9 | 2,0 |
| *Me WI* | 3,0 | 3,0 | 3,0 | 3,0 | 3,0 | 3,0 | 3,0 | 3,0 |
| *Me diff [%]* | -22,4 | -20,0 | -22,4 | -20,0 | -22,4 | -20,0 | -22,4 | -20,0 |

***B1 ABT-2009***

| | 1-6.2009 | 7-12.2009 | 1-6.2010 | 7-12.2010 | 1-6.2011 | 7-12.2011 | 1-6.2012 | 7-12.2012 |
|---|---|---|---|---|---|---|---|---|
| *Me IRI* | 2,1 | 2,2 | 2,1 | 2,2 | 2,1 | 2,2 | 2,1 | 2,2 |
| *Me WI* | 3,0 | 3,0 | 3,0 | 3,0 | 3,0 | 3,0 | 3,0 | 3,0 |
| *Me diff [%]* | -17,6 | -15,4 | -17,6 | -15,4 | -17,6 | -15,4 | -17,6 | -15,4 |

gust to April (border value of positive growths), with maximum level in the middle of specified time periods. In Warsaw ionosonde, twenty-four hour distribution presents increased borders, extending to the night-side part. Difference of *M*3000*F*2 parameter shown in Fig. 6 presents dominating under-

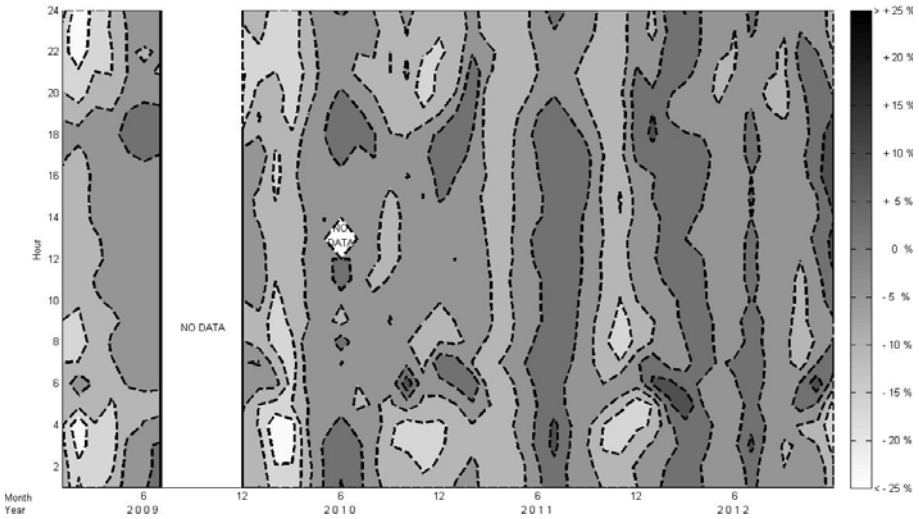


Fig. 2. 2009-2012 comparison of *foF*2 monthly median difference variation for Warsaw ionosonde and IRI 2012 URSI model.

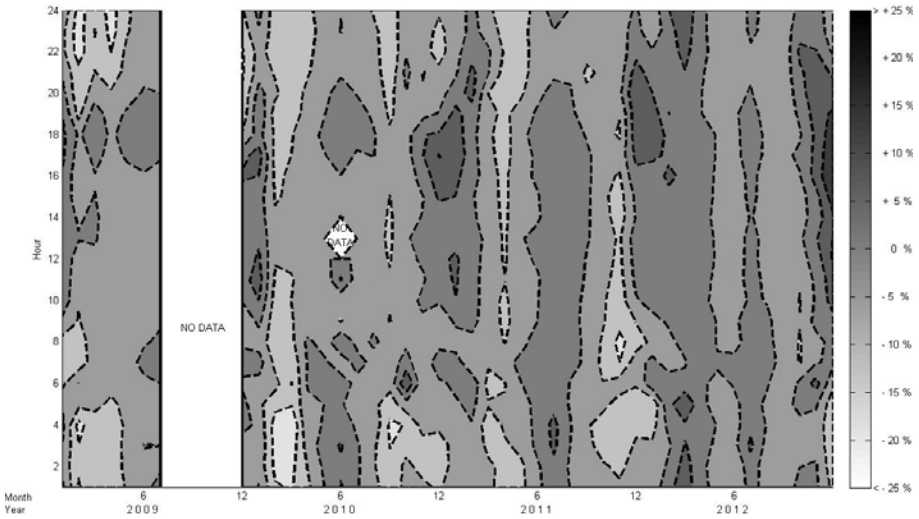


Fig. 3. 2009-2012 comparison of *foF*2 monthly median difference variation for Warsaw ionosonde and IRI 2012 CCIR model.

estimate. The highest local difference can be noticed at night part of the graph, where it reaches a local value to –9%. Positive values appear sporadically in low level, up to +1%. Median difference for semi-annual analysed section reaches low-range negative values approximately at the level of

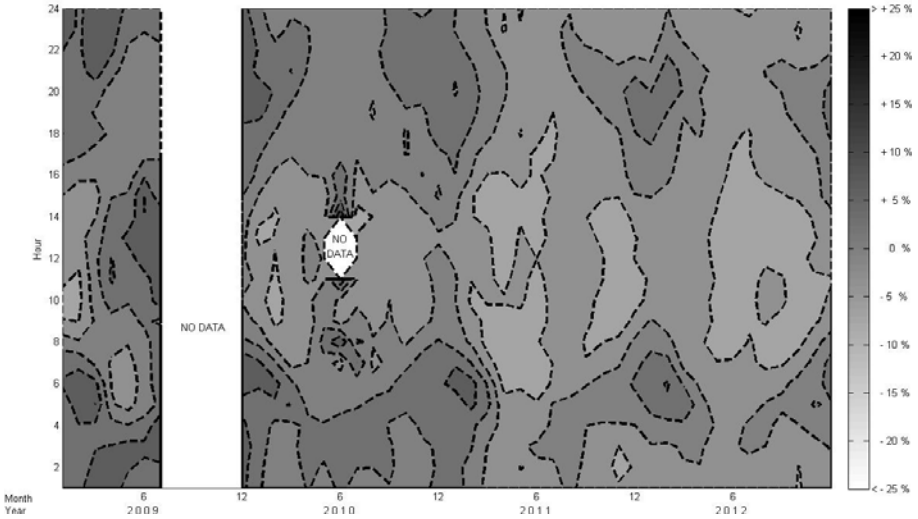


Fig. 4. 2009-2012 comparison of *hmF*2 monthly median difference variation for Warsaw ionosonde and IRI 2012 URSI model.

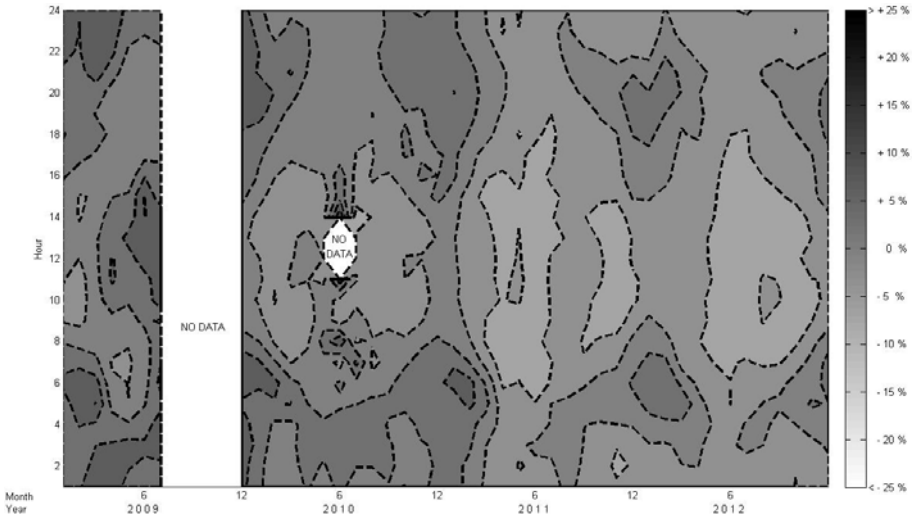


Fig. 5. 2009-2012 comparison of *hmF*2 monthly median difference variation for Warsaw ionosonde and IRI 2012 CCIR model.

–3.5%, from –2.4% for July-December 2012 to –4.2% for January-June 2011.

Difference of *B*0 parameter was presented in Fig. 7 for IRI year Gul-1987, in Fig. 8 for Bil-2000, and in Fig. 9 for a newest IRI 2012 ABT-2009 option.

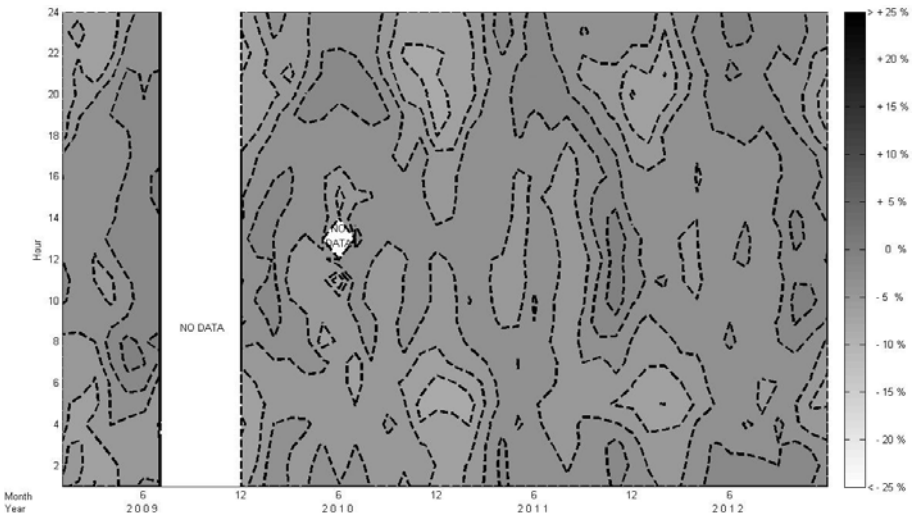


Fig. 6. 2009-2012 comparison of *M*3000*F*2 monthly median difference variation for Warsaw ionosonde and IRI 2012 URSI model.

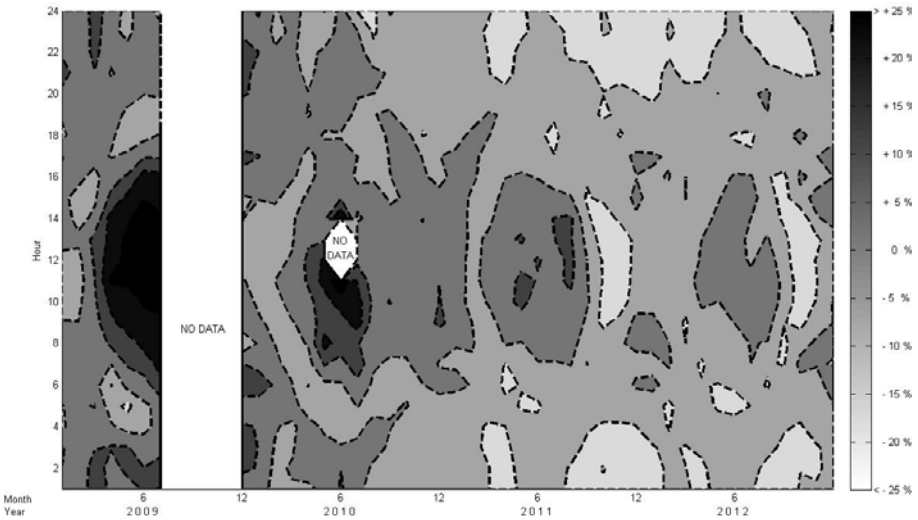


Fig. 7. 2009-2012 comparison of *B*0 monthly median difference variation for Warsaw ionosonde and IRI 2012 Bil-2000 model.

Generally, the IRI models and Warsaw ionosonde follow the same trend. *B*0 modelled parameters present higher values at day from months close to April-August (border value of positive growths), with maximum level close to the middle of specified time periods. Main differences are in the ABT model, evaluating longer borders extending to hours before noon than the

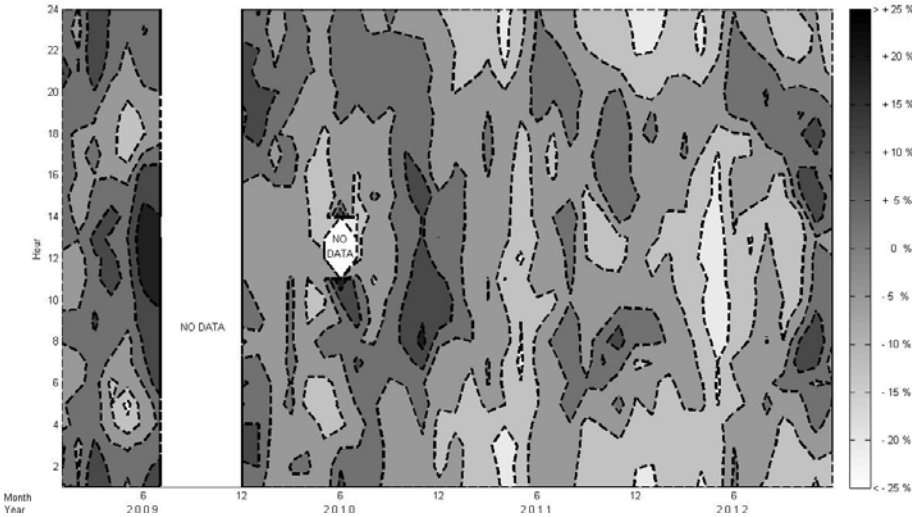


Fig. 8. 2009-2012 comparison of *B*0 monthly median difference variation for Warsaw ionosonde and IRI 2012 Gul-1987 model.

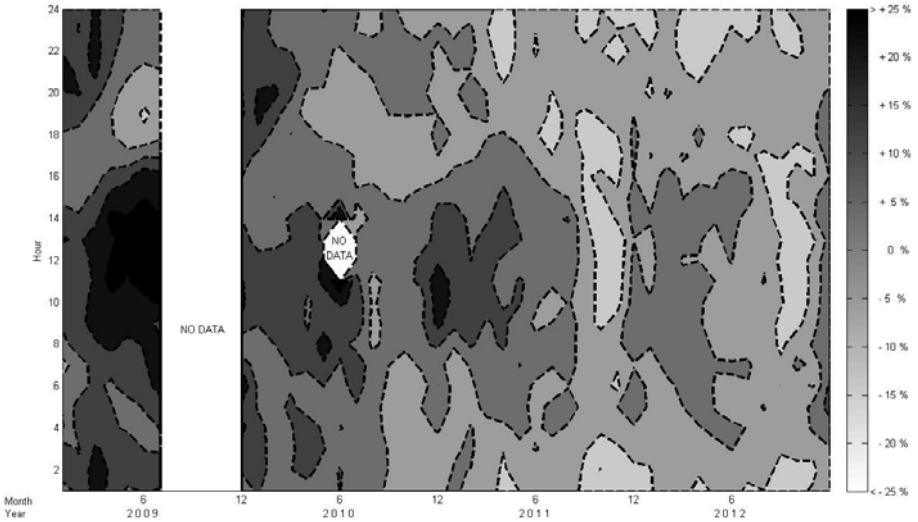


Fig. 9. 2009-2012 comparison of *B*0 monthly median difference variation for Warsaw ionosonde and IRI 2012 ABT-2009 model.

Gul-1987 model, where maximum level range is shorter. Bil-2000 option presents characteristics of lower variable model in twenty-four hour distribution.

In all cases, Figs. 7-9 present noticeable division into two fields where low and increased solar radio fluxes are dominant. All models tend to over-

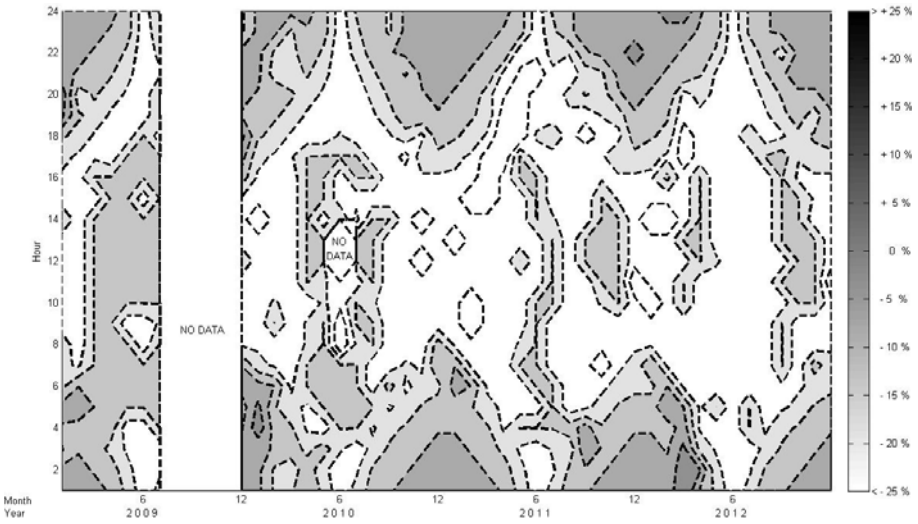


Fig. 10. 2009-2012 comparison of *B*1 monthly median difference variation for Warsaw ionosonde and IRI 2012 model.

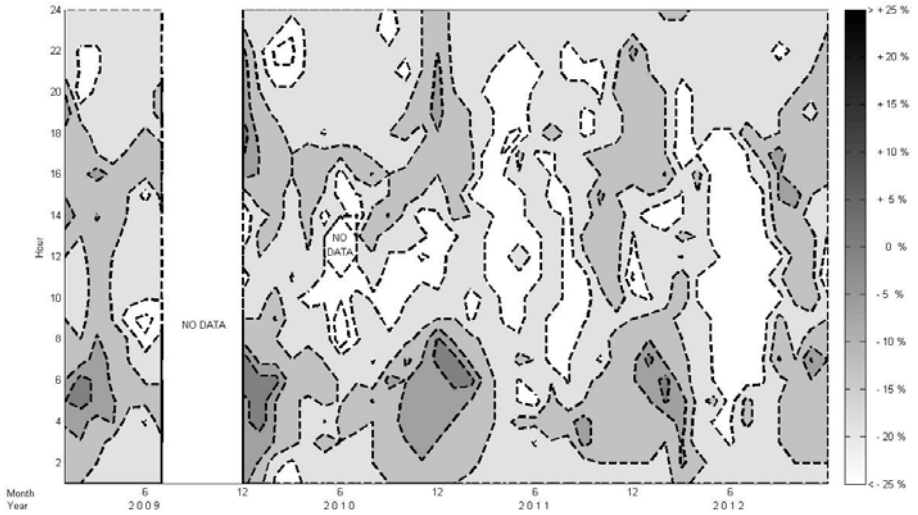


Fig. 11. 2009-2012 comparison of *B*1 monthly median difference variation for Warsaw ionosonde and IRI 2012 ABT-2009 dependent model.

estimate at the first part of graph, presenting data from January 2009 to the end of 2010, when the solar activity level is low. With increasing solar radio flux, from the beginning of 2010 to the end of year 2012, the data present noticeable underestimate.

Level of difference is summarized in Table 1 (parts 6-8). The highest level of difference in the first part of data (January 2009 – December 2010) occurs in ABT-2009 model with positive value from 5.1 to 13.0%. Gul-1987 and Bil-2000 present similar overestimate, respectively, from 1.7 to 8.2% and from 4.2 to 9.8%. In the second part of data with increased solar activity, ABT-2009 model in the first sector for the time period January-June 2011 reaches a positive value of difference, while in other models the underestimation starts to dominate. In the remaining part of graph, from July 2011 to December 2012, the level of difference take values from –2.8 to –4.2% for ABT-2009, –2.8 to –6.9% for Gul-1987, and lastly –0.1 to –5.3% for Bil-2000 option. Observed differences minima and maxima reach respectively values: Gul-1987 from –18 to +42%, Bil-2000 from –20 to +27%, ABT-2009 from –15 to +39%.

Difference of $B1$ parameter was presented in Fig. 10 for the standard model, and Fig. 11 for new $B1$, dependent on a newest IRI 2012 ABT-2009 model. Median difference values for half-year parts of data are presented in Table 1 (parts 9 and 10).

The $B1$ standard model presents trend with the highest values at night with borders of positive growth in June. In Dependent ABT-2009 this variability occurs from August to March, with extension to daytime part. While the standard model calculates one value $B1$ at the level of 1.9, outside the night borders of positive growth, the second model estimates a variable parameter during the days. Analogical variable presents trend from Warsaw ionosonde data with the lowest value at specified parts of the day.

In Figs. 10 and 11 the lowest values occur in the middle part of daytime in months close to half year. From this point, values are increasing in the direction to nighttime and winter season. IRI standard model presented in Fig. 10 reaches continuous underestimate in every part of the graph, from –20.0 to –22.4%, with local difference from –30 to +2%. $B1$ ABT-2009 also underestimates the value but in the level from –15.4 to –17.6%. For this model, the locally observed difference minimum reaches values from –32 to maximum at +6%.

## 4. CONCLUSIONS

Through the usage of IRI model, the monthly median values of $hmF2$, $foF2$ parameters show good agreement with Warsaw ionosonde data. Analysed differences range is on acceptable level. Generally, the variance of difference in $foF2$ parameter is a result of, presented in this paper, IRI model trend estimation at night. Similar results in differences in the CCIR and URSI options leave a choice of model to specified position and time period.

The $HmF2$ parameter presents a very close result to the data obtained from Warsaw ionosonde. Low value of the differences of medians for the

analysed semi-annual sections confirms it. Eventually, the IRI parameters in daytime part underestimations for high solar activity section, and 2009 year overestimations could be taken into consideration.

The IRI evaluated *M*3000*F*2 parameters show constant underestimation for all analysed time. The largest differences occurred in areas where Warsaw ionosonde day trend is extending to night side part. IRI model in twenty-four hour distribution presented a fastest decrease of *M*3000*F*2 parameter in time.

IRI *B*0 factors present noticeable, positive difference in dominating low-level solar radio flux, and negative in time of increasing solar activity. High level of $Me_{\text{diff}}$, local minimum and maximum, should be taken under consideration in examinations of that latitude region. The analysis confirmed that the preferred by CCIR Gul-1987 model is in fact the best long-term fit to parameters measured by the ionosonde. Newest ABT-2009 presents better fitting to ionosonde measured data in twenty-four hour distribution. This model for Warsaw position is a suitable alternative for time periods of increased solar activity. The IRI 2012 Bil-2000 model shows good long-term fit, the lowest value of local difference, and it is sufficient for time periods of low solar activity.

Lastly, the *B*1 parameter, with constant underestimate at the level from –20.0 to –22.4% for a standard model and from –15.4 to –17.6% for *B*1 ABT-2009, needs improvements to reduce a constant difference, which was partially done in 2009. New *B*1 ABT-2009 model noticeably follows a similar trend as the data measured by the Warsaw ionosonde, and the lowest value of median difference indicates that it should be used in the geographical position pertaining to this paper.

Acknowledgment. This study was supported by the National Science Centre (NCN), Poland, grant No. 2011/01/B/ST9/06108.

## References

Bilitza, D. (2001), International Reference Ionosphere 2000, *Radio Sci*. **36**, 2, 261-275, DOI: 10.1029/2000RS002432.

Bilitza, D., K. Rawer, L. Bossy, I. Kutiev, K.-I. Oyama, R. Leitinger, and E. Kazimirovsky (1990), International Reference Ionosphere 1990, Tech. Rep. 19910021307, Science Application Research, Lanham, USA.

Bilitza, D., D. Altadill, Y. Zhang, C. Mertens, V. Truhlik, P. Richards, L.-A. McKinnell, and B. Reinisch (2014), The International Reference

Ionosphere 2012 – a model of international collaboration, *J. Space Weather Space Clim.* **4**, AQ07, DOI: 10.1051/swsc/2014004.

INGV (2014), Autoscala software, Istituto Nazionale di Geofisica e Vulcanologia, Rome, Italy, available from: http://roma2.rm.ingv.it/en/facilities/software/18/autoscala (accessed: 15 April 2014).

ITU-R (2012), ITU-R reference ionospheric characteristics, Recommendation P. 1239-3 (02/2012), P Series Radiowave Propagation, International Telecommunication Union, Geneva, Switzerland.

SRC PAS (2014), Ionospheric sounding in Poland, Space Research Centre, Polish Academy of Sciences, Warsaw, Poland, available from: http://rwc.cbk.waw.pl/RWC2/sisoundpol.html (accessed: 7 April 2014).

Received 29 April 2014
Received in revised form 12 May 2015
Accepted 14 July 2015